POROUS BODY ANALYSIS OF VERTICAL ROD BUNDLES

UNDER MIXED CONVECTION CONDITIONS

by

TAE SUN RO

Vol. I

B.S., Seoul National University

(1974)

M.S., Korea Advanced Institute of Science

(1976)

SUBMITTED TO THE DEPARTMENT OF

NUCLEAR ENGINEERING

IN PARTIAL FULFILLMENT OF THE REQUIREMENTS

FOR THE DEGREE OF

DOCTOR OF PHILOSOPHY

at the

MASSACHUSETTS INSTITUTE OF TECHNOLOGY

Janu.ry 1986

Signature of Author_____

, Department of Nuclear Engineering

January 10, 1986

Certified by _____

Neil E. Todreas

Thesis Supervisor

Accepted by _____

Allan F. Henry

Chairman, Departmental Committee on Graduate Students

POROUS BODY ANALYSIS OF VERTICAL ROD BUNDLES

UNDER MIXED CONVECTION CONDITIONS

by

TAE SUN RO

Submitted to the Department of Nuclear Engineering
on January 10, 1986 in partial fulfillment of the
requirements for the Degree of Doctor of Philosophy in
Nuclear Engineering

ABSTRACT

Approximations and optimum means to apply the porous body approach to rod bundle analysis were investigated. Based on computing time and expected accuracy of the flow and pressure field predictions, the staggered half-pin layout was selected as an optimum control volume geometry. Three-dimensional distributed resistance models were constructed and incorporated into a porous body code, THERMIT, particularly for the selected optimum control volume layout. Satisfactory THERMIT predictions validated these models and verified that the staggered half-pin layout was a successful choice.

Non-radial heat conduction through heater rods fabricated with high thermal conductivity, electrical insulator material (i.e., Boron Nitride) was quantified utilizing a rod conduction model developed using an approximate analytical method. The temperature field predicted by ENERGY-IV code employing the rod conduction model exhibited that the heat conduction through rods reduced the normalized maximum temperature rise by 4% in blanket bundles and by 3% in fuel bundles under mixed convection conditions.

Experiments were performed to investigate an enhanced energy mixing due to turbulent thermal plumes in mixed convection conditions. Turbulent heat flux induced by thermal plumes was measured at various flow and power conditions utilizing a laser Doppler anemometer for velocity fluctuation and a thermocouple for temperature fluctuation measurement. Heat transfer against power skew direction was observed at high Reynolds and Grashof number ranges.

Thesis Supervisor: Dr. Neil E. Todreas

       Title: Professor of Nuclear Engineering

Thesis Reader: Dr. Andrei L. Schor

       Title: Assistant Professor of Nuclear Engineering

ACKNOWLEDGEMENTS

I would like to express my sincere gratitude to Professor Neil E. Todreas, my thesis supervisor, for his guidance and encouragement throughout my research work. I would also like to thank him for the extra time he took to review and correct this manuscript. Professor Andrei L. Schor is gratefully acknowledged for his helpful comments on the THERMIT calculations and for reading this thesis. I am particularly indebted to Professor Tsuyoshi Nakajima (Ken), who was a visiting professor from Japan, who helped me through many valuable discussions and in the experimental work.

Thanks are due to Bob Barra, Tiny Caloggero and Francis Woodworth for their assistance and machining work of the test section. Special thanks are also due to Elenore Kehoe, Lucy Bedirian and Paul Ulbrich for their excellent typing and corrections. I also wish to express appreciation for useful discussions and friendship to all my colleagues and Korean friends.

The financial support of the Korean Government and the Power Reactor and Nuclear Fuel Development Corporation (Japan) is gratefully acknowledged.

Finally, but by no means least, I especially thank my wife, Kyu Bok, and two daughters, Se Jeong and Se Wha, for their constant love, understanding, and patience during my graduate study.

TABLE OF CONTENTS

Table of Contents (Continued)

Table of Contents (Continued)

Table of Contents (Continued)

Table of Contents (Continued)

Table of Contents (Continued)

Table of Contents (Continued)

LIST OF FIGURES

List of Figures (Continued)

List of Figures (Continued)

List of Figures (Continued)

List of Figures (Continued)

Table of Figures (Continued)

LIST OF TABLES

CHAPTER 1

INTRODUCTION

Thermal-hydraulic behavior of rod bundles in mixed convection has received considerable attention in recent years since it is important for a better understanding of fluid flow and heat transfer under off-normal reactor condition. Mixed convection or combined free and forced convection arises when coolant flow rate is low and significant decay heat is generated. In this condition, the buoyancy effect becomes important, and flow and heat transfer characteristics are substantially different from those under forced convection.

In order to predict the flow and temperature fields in rod bundles, the subchannel analysis method is commonly used. It has been proven quite reliable by its application to various rod geometries and operating conditions. However, because of its inherent assumption of existence of a dominantly axial flow, it is doubtful that this method can be applied to the cases of strong transverse flow such as would exist under flow blockage or degraded core geometry which are encountered in LMFBR safety analysis. A new approach, namely, the porous body analysis method, was developed (T-1, S-1) to provide an alternative for rod bundle analysis and for application to general flow cases. The porous body approach is formulated based on porosities of the control volume for which the conservation equations are written. This allows an arbitrary geometric configuration for the control volume since the geometric effect is taken into account

through the surface and volume porosities. In addition, the approach solves the transverse momentum equation as well as the axial momentum equation rigorously.

The approximations involved in applying the porous body analysis method to rod bundles, however, have not been well understood nor have the constitutive correlations required for closure been properly established. Therefore, the objective of this research is to investigate the approximations and optimum means to apply the porous body approach for rod bundle analysis and to provide relevant constitutive correlations under both mixed and forced convection conditions.

To achieve this goal, the following work has been performed and is described in the Chapters indicated.

In Chapter 2 the governing equations for the porous body analysis have been clearly derived. The pressure and the distributed resistance terms in the momentum equation were carefully examined.

In Chapter 3 the practical limitations of the porous body approach and the approximations introduced for numerical implementation were identified and discussed. An optimum control volume for wire-wrapped rod bundle analysis was selected to minimize inaccuracy due to the approximations.

In Chapter 4 the flow resistance was correlated utilizing a distributed resistance model developed for the porous body control volume. The velocity and pressure fields in a wire-wrapped rod bundle predicted using a porous body analysis code, THERMIT(R-1), incorporating the distributed resistance model, were compared against available experimental data to validate the model.

In Chapter 5 a computer code was developed to estimate the non-radial heat conduction through heater rods which is an additional energy transfer in simulated heater rod fabricated with high thermal conductivity, electrical insulator material (i.e., Boron Nitride).

In Chapter 6 a non-radial rod conduction correlation was proposed and calibrated utilizing the code developed.

In Chapter 7 the validation of the correlation was presented and the relative importance maps were described. The temperature field predicted by ENERGY-IV code (C-1) employing the rod conduction model was compared with experimental data. The relative importance of the energy transfer mechanisms, i.e., turbulent mixing including wire sweeping, convective energy transfer by flow redistribution, fluid conduction and rod conduction was investigated and the regions where each parameter was dominant or significant were identified.

In Chapter 8 experimental investigation of the energy mixing due to turbulent thermal plumes has been carried out. The turublent thermal plumes were believed to enhance the energy transfer in low flow, high power condition. Turbulent heat flux induced by thermal plumes was obtained utilizing a laser Doppler anemometer for velocity measurement and a thermocouple for temperature measurement.

Finally, conclusions and recommended future work were presented in Chapter 9.

CHAPTER 2

MATHEMATICAL FORMULATION OF THE POROUS BODY APPROACH

2.1 Introduction

Three methods are widely used for rod bundle thermal-hydraulic
analysis. They are the subchannel, porous body and distributed
parameter methods. The first two methods are categorized as lumped
parameter methods. The lumped parameter method ignores the details
within a control volume chosen by discretizing the whole system volume
into a number of small volumes. It employs a lumped velocity and
temperature to represent average values within a control volume. The
scale of the control volume should be small relative to the size of
the system considered but still large relative to the size of local
phenomena present. The constitutive correlations are modeled
applicable to the geometry of the selected control volume. The
distributed parameter method uses a much smaller mesh size compared to
the typical lumped channel control volume in order to calculate the
detailed velocity and temperature distributions within a rod bundle.
This requires that the constitutive models should be constructed to
describe the local physical phenomena and the rod surface should be
considered as an internal velocity boundary condition in rod bundle
analysis. Thus, the distributed parameter method generally requires
large core memory storage and computing time.

In this chapter, a mathematical formulation of the porous body
approach, also called the porous media approach, is extensively

examined. First, the concept and origin of the porous body approach are described and the terminology used in the formulation of the governing equations is defined. Then, the governing equations and finite difference formulations in the porous body approach are presented. Finally, the pressure term, one of the key parameters in the momentum equations, is thoroughly investigated.

2.2 Porous Media Concept and Definition of Porosity

Flow through porous media has been studied for a century. This topic is encountered in many branches of engineering and science, e.g., ground water hydrology and petroleum production. Recently, the porous media concept has been applied in the field of the rod bundle analysis. While the classical porous media method mainly deals with the diffusive flow through a porous medium dominated by the friction forces, the rod bundle application of this approach is oriented to the convective flow through a rather open medium.

The simple physical description of a porous medium is that of a "solid with holes." According to Bear (B-1), a porous medium is defined as a material which has the following characteristics: (a) a porous medium should be a portion of space occupied by heterogenous or multiphase matter, (b) the solid phase should be distributed throughout the domain of the porous medium, and (c) at least some of the pores comprising the void space should be interconnected. The rod bundle array of most heat exchangers and reactor fuel assemblies has these characteristics and thus, can be treated as a porous medium.

The most important concept of the porous body approach is the

porosity concept. Consider a stationary, nondeformable finite system composed of a fluid and distributed solid. A schematic representation of the system is drawn in Figure 2.1. The total volume is V enclosed by a closed surface A. The fluid portion of the total volume is V_f. A_f is a portion of A through which the fluid may flow, and A_{fs} is the total fluid-solid interface within the volume V.

The volume porosity, γ_V, is defined as the ratio of the fluid volume V_f to the total volume V. Thus,

$$\gamma_V \equiv \frac{V_f}{V} \tag{2.1}$$

γ_V can also be written as,

$$\gamma_V = \frac{1}{V} \int_V I(\vec{r}) dV \tag{2.2}$$

where $\vec{r}$ is the position vector and the indicator function, $I(\vec{r})$, is defined as

$$I(\vec{r}) = \begin{cases} 1, & \text{if the end point of } \vec{r} \text{ is in fluid.} \\ 0, & \text{if the end point of } \vec{r} \text{ is in solid.} \end{cases}$$

The area porosity, γ_A, is defined as the ratio of the free flow area A_f to the surface A (not necessarily closed) of interest.

$$\gamma_A \equiv \frac{A_f}{A} = \frac{1}{A} \int_A I(\vec{r}) dA \tag{2.3}$$

where A_f is the portion of A that is occupied by the fluid. Some authors use the term "surface permeability" instead of "surface porosity." In this work, the term "surface porosity" or "area porosity" is used throughout.

2.3 Governing Equations

The general integral conservation equations have been derived in detail in reference (T-1). The following are the resulting equations for a single phase fluid. The schematic diagram of a general control volume, where the
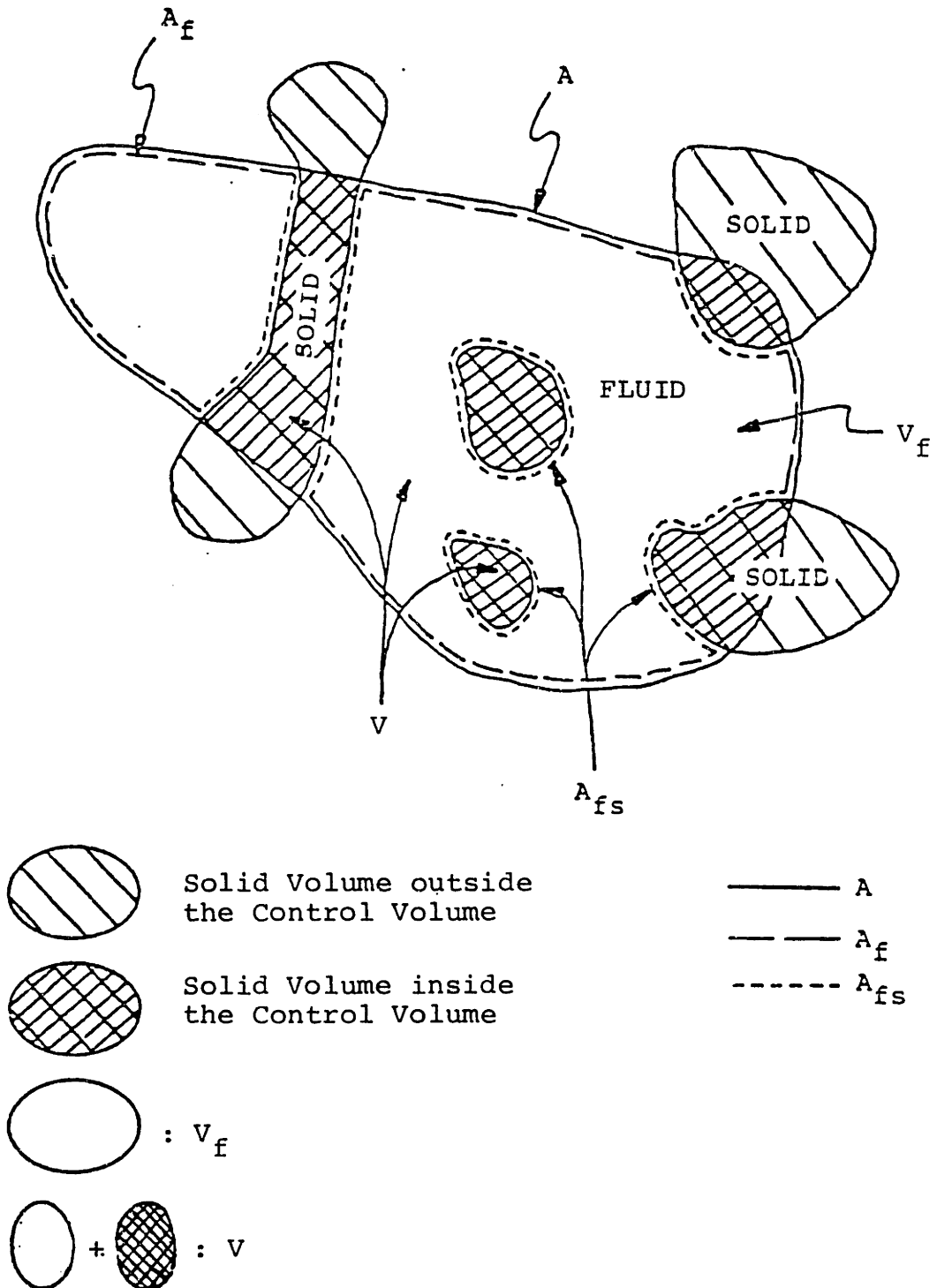
Figure 2.1 Control Volume Containing a Single-Phase Fluid and Solids (Taken from Reference T-1)

conservation equations are written is illustrated in Figure 2.1.

Conservation of Mass:

$$\gamma_V \frac{\partial^i \langle \rho \rangle}{\partial t} + \frac{1}{V} \int_{A_f} \rho \vec{v} \cdot \vec{n} \, dA = 0 \qquad (2.4)$$

$$(1) \qquad\qquad (2)$$

Momentum Equation:

$$\gamma_V \frac{\partial}{\partial t} {}^i \langle \rho \vec{v} \rangle + \frac{1}{V} \int_{A_f} \rho \vec{v} (\vec{v} \cdot \vec{n}) \, dA = \gamma_V {}^i \langle \rho \rangle \vec{g} +$$

$$(3) \qquad\qquad (4) \qquad\qquad (5)$$

$$+ \frac{1}{V} \int_{A_f} (-p\vec{n} + \bar{\bar{\tau}} \cdot \vec{n}) \, dA + \frac{1}{V} \int_{A_{fs}} (-p\vec{n} + \bar{\bar{\tau}} \cdot \vec{n}) \, dA \qquad (2.5)$$

$$(6) \qquad\qquad\qquad (7)$$

Energy Equation in terms of Internal Energy:

$$\gamma_V \frac{\partial}{\partial t} {}^i \langle \rho u \rangle + \frac{1}{V} \int_{A_f} \rho u (\vec{v} \cdot \vec{n}) \, dA = -\gamma_V {}^i \langle p \nabla \cdot \vec{v} \rangle +$$

$$(8) \qquad\qquad (9) \qquad\qquad (10)$$

$$+ \frac{1}{V} \int_{A_f} k_e \vec{n} \cdot \nabla T \, dA - \frac{1}{V} \int_{A_{fs}} \vec{q}'' \cdot \vec{n} \, dA + \gamma_V {}^i \langle q''' \rangle + \gamma_V {}^i \langle \Phi \rangle$$

$$(11) \qquad\qquad (12) \qquad\qquad (13) \qquad (14)$$

$$(2.6)$$

where,

ρ = fluid density

$\vec{v}$ = fluid velocity (u, v, w are the components of velocity in the x, y and z directions respectively)

$\vec{n}$ = outward normal unit vector on the surface

$\vec{g}$ = gravitational acceleration

p = pressure

$\bar{\bar{\tau}}$ = stress tensor

u = internal energy of the fluid (total energy $e \equiv \overset{o}{u}+gz$ where

stagnation internal energy $\overset{o}{u} \equiv u + (1/2)v^2$)

k_e = effective fluid thermal conductivity including both

molecular and turbulent effects

T = fluid temperature

$\vec{q}''$ = heat flux at fluid-solid interface

q''' = heat generation rate

Φ = frictional dissipation energy per unit volume

and the brackets $^i\langle\rangle$ designate the intrinsic local volume average of ψ defined as,

$$^i\langle\psi\rangle \equiv \frac{1}{V_f} \int_{V_f} \psi \, dV \qquad (2.7)$$

The physical meaning of each of the terms composing the conservation equations is explained as the following:

(1) Rate of increase of fluid mass in volume V,

(2) Net mass efflux through the fluid surface A_f,

(3) Rate of increase of linear momentum of the fluid mass in volume V,

(4) Net momentum efflux through the fluid surface A_f,

(5) The body force due to gravity acting on the fluid,

(6) The surface forces due to the fluid normal (pressure) and shear stresses acting on the fluid,

(7) The form and the friction drag forces exerted on the fluid by the dispersed solid within volume V,

(8) Rate of increase of internal energy of the fluid mass in volume V,

(9) Net efflux of internal energy through the fluid surface A_f,

(10) Rate of thermodynamic pressure work,

(11) Conduction heat flow through the fluid surface A_f,

(12) Rate of heat released due to the dispersed solid within volume V,

(13) Heat generation rate within the fluid volume V_f,

(14) Frictional dissipation energy.

2.4 Finite Difference Formulation of the Governing Equations

The previous general integral forms of the conservation equations are discretized to finite difference forms. The finite difference equations are applied to a computational grid which should be determined carefully to yield adequate average quantities. The detailed procedure for determining an optimum computational grid is explained in Chapter 3. The grid provides the control volume unit in which the governing equations are written. In general, lumped density, energy and pressure are determined at the center of a control volume. The velocities including momentum flux and energy flux are usually defined at the control volume boundaries. Accordingly, the axial momentum control volume is staggered in the axial direction with respect to the mass and energy control volume, and the transverse momentum control volumes are staggered in the transverse direction.

A porous body approach can be used in any coordinate system. However, in this paper, the finite difference equations are derived in the Cartesian coordinate system because the derivation in this system is easy to understand and yields less complicated formulations.

2.4.1 Mass Conservation Equation

The orthogonal control volume V ($=\Delta x \Delta y \Delta z$) to which the integral mass conservation equation is applied is drawn in Figure 2.2. The velocity components in the x, y and z directions are u, v and w, respectively. Applying Eq. (2.4) to this control volume yields,

$$\gamma_V \frac{\partial^i \langle \rho \rangle}{\partial t} + \frac{1}{V} \left[\int_{A_f \big|_{x+\frac{\Delta x}{2}}} \rho u dA_x - \int_{A_f \big|_{x-\frac{\Delta x}{2}}} \rho u dA_x + \int_{A_f \big|_{y+\frac{\Delta y}{2}}} \rho v dA_y \right.$$

$$\left. - \int_{A_f \big|_{y-\frac{\Delta y}{2}}} \rho v dA_y + \int_{A_f \big|_{z+\frac{\Delta z}{2}}} \rho w dA_z - \int_{A_f \big|_{z-\frac{\Delta z}{2}}} \rho w dA_z \right] = 0$$

$$(2.8)$$

where $A_f \big|_{x+\frac{\Delta x}{2}}$ denotes the free flow area normal to the x axis at $x+\frac{\Delta x}{2}$

and $A_f \big|_{x-\frac{\Delta x}{2}}$ denotes the analogous area at $x-\frac{\Delta x}{2}$. The corresponding

terms with the y and z subscripts are defined in a similar way.

Now let us define the intrinsic local area average of Ψ as,

$$^{ix}\{\Psi\} \equiv \frac{1}{A_{fx}} \int_{A_{fx}} \Psi \, dA_x \; ; \; \text{etc.} \tag{2.9}$$

and introduce the following notation,

$$\Delta_x (\ ) \equiv (\ )_{x+\frac{\Delta x}{2}} - (\ )_{x-\frac{\Delta x}{2}} \; ; \; \text{etc.} \tag{2.10}$$

Then Eq. (2.8) reduces to,

$$\gamma_V \frac{\partial^i \langle \rho \rangle}{\partial t} + \frac{\Delta_x (\gamma_{Ax} {}^{ix}\{\rho u\})}{\Delta x} + \frac{\Delta_y (\gamma_{Ay} {}^{iy}\{\rho v\})}{\Delta y} + \frac{\Delta_z (\gamma_{Az} {}^{iz}\{\rho w\})}{\Delta z} = 0$$

$$(2.11)$$

This is the general finite difference form of the mass conservation equation.
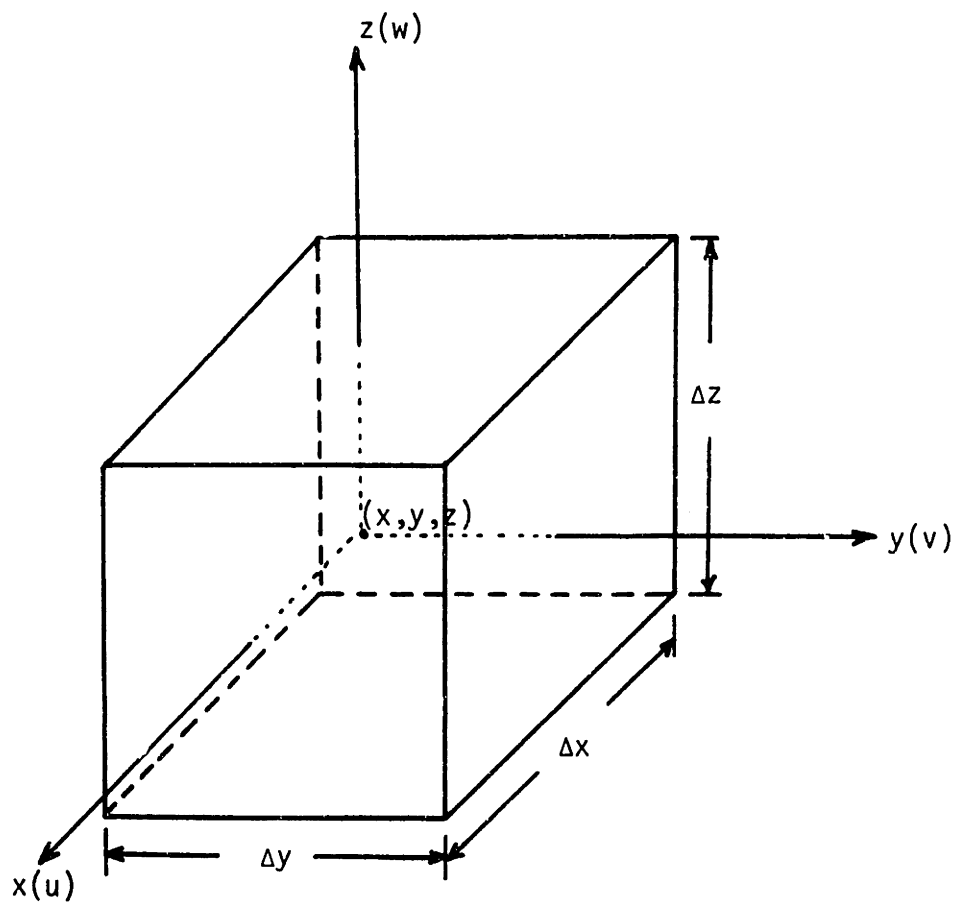
Figure 2.2   Mass and Energy Control Volume in Cartesian
             Coordinate System

2.4.2 Energy Equation

The energy equation is also written for the same control volume shown in Figure 2.2 in terms of the internal energy. By using the definitions of Eqs. (2.9) and (2.10), application of Eq. (2.6) to the control volume gives,

$$
\gamma_V \frac{\partial^i \langle \rho u \rangle}{\partial t} + \frac{\Delta_x (\gamma_{Ax}^{ix} \{\rho u u\})}{\Delta x} + \frac{\Delta_y (\gamma_{Ay}^{iy} \{\rho u v\})}{\Delta y} + \frac{\Delta_z (\gamma_{Az}^{iz} \{\rho u w\})}{\Delta z}
$$

$$
= -\gamma_V^i \langle p \nabla \cdot \vec{v} \rangle + \frac{\Delta_x (\gamma_{Ax}^{ix} \{k_e \frac{\partial T}{\partial x}\})}{\Delta x} + \frac{\Delta_y (\gamma_{Ay}^{iy} \{k_e \frac{\partial T}{\partial y}\})}{\Delta y}
$$

$$
+ \frac{\Delta_z (\gamma_{Az}^{iz} \{k_e \frac{\partial T}{\partial z}\})}{\Delta z} + \gamma_V (^i\langle q_{rb}''' \rangle + {}^i\langle q''' \rangle + {}^i\langle \Phi \rangle) \qquad (2.12)
$$

where the heat release rate per unit volume of the fluid at the fluid-solid interface, sometimes called the distributed heat source (or sink), is defined as,

$$
{}^i\langle q_{rb}''' \rangle \equiv \frac{1}{V_f} \int_{V_f} q_{rb}''' \, dV \equiv -\frac{1}{V_f} \int_{A_{fs}} \vec{q}'' \cdot \vec{n} dA \qquad (2.13)
$$

2.4.3 Momentum Equation

The momentum equation can be also applied to the same control volume in a similar fashion. However, most thermal-hydraulic analysis codes recently developed have employed the staggered mesh (or grid) representation in numerical schemes for the momentum equation. As mentioned earlier, in the staggered grid system, the density, energy (or enthalpy) and pressure are calculated at the center of the mass and energy control volume (M-E control volume) as usual, but the velocity component is defined at the point that lies on the face of this control volume. Thus, to calculate the velocity components, the momentum

control volume is staggered relative to the M-E control volume.

The reasons for introducing the staggered grid for the momentum equation have been well explained by Patankar (P-1). The main reasons are summarized as follows: by defining the velocity components at the faces of the M-E control volume, we can eliminate the possibility that wrong wavy velocity field solutions are obtained from the continuity equation. In addition, the pressure difference between two adjacent grid points (where the pressures are calculated) yields the driving force for the velocity component located between these two grid points. It should also be noted that the staggered mesh system leads to complications in providing geometrical information and formulating practical numerical schemes. However the advantages described above are significant.

The staggered momentum control volume together with the M-E control volume is presented in Figure 2.3. The quantities defined in each control volume are also shown in the figure. The x, y and z momentum control volumes are staggered with respect to the positive x, y and z directions, respectively. Note that the boundary of the staggered momentum control volume passes through the center of the M-E control volume.

Applying the x-component of the integral momentum equation (Eq.(2.5)) to the x momentum control volume (XM control volume) in Figure 2.3 yields,

Y-MOMENTUM
CONTRCL VOLUME

v

(i,j+1/2,k)

y

z ⊙ → x Δy

(i,j,k)

(i+1/2,j,k)

X-MOMENTUM
CONTROL VOLUME

(x,y,z)

u

ρ,𝑢,p

Δx
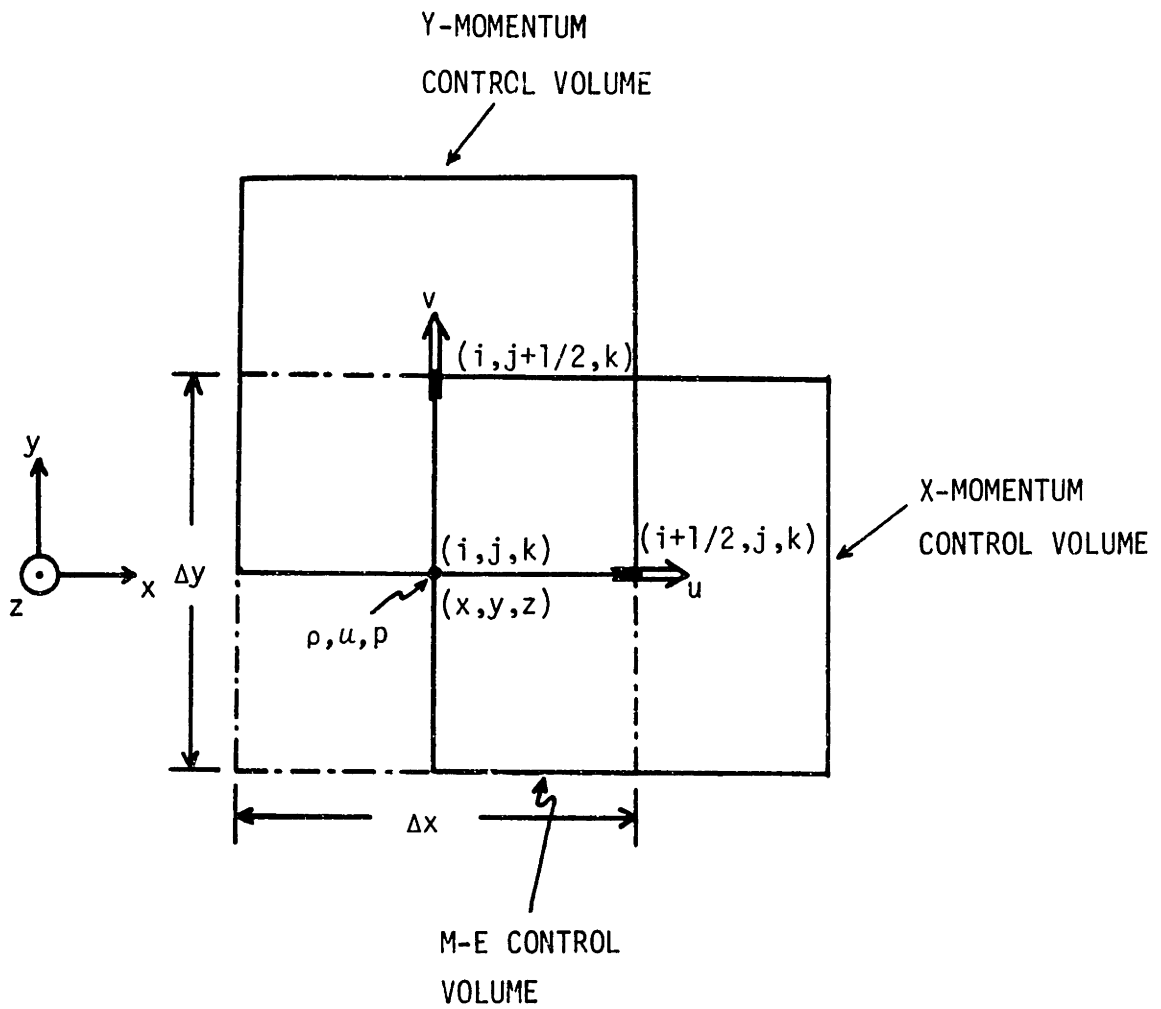
M-E CONTROL
VOLUME

Figure 2.3 Staggered Momentum Control Volume (Plane View)

$$\gamma_V \frac{\partial}{\partial t} {}^i\langle \rho u \rangle + \frac{1}{V} \left[\int_{A_{fx}} \bigg|_{(x+\Delta x, y, z)} \rho u^2 dA_x - \int_{A_{fx}} \bigg|_{(x,y,z)} \rho u^2 dA_x \right.$$

$$+ \int_{A_{fy}} \bigg|_{(x+\frac{\Delta x}{2}, y+\frac{\Delta y}{2}, z)} \rho u v dA_y - \int_{A_{fy}} \bigg|_{(x+\frac{\Delta x}{2}, y-\frac{\Delta y}{2}, z)} \rho u v dA_y$$

$$+ \int_{A_{fz}} \bigg|_{(x+\frac{\Delta x}{2}, y, z+\frac{\Delta z}{2})} \rho u w dA_z - \int_{A_{fz}} \bigg|_{(x+\frac{\Delta x}{2}, y, z-\frac{\Delta z}{2})} \rho u w dA_z$$

$$= \gamma_V {}^i\langle \rho \rangle g_x - \frac{1}{V} \left[\int_{A_{fx}} \bigg|_{(x+\Delta x, y, z)} p dA_x - \int_{A_{fx}} \bigg|_{(x,y,z)} p dA_x \right]$$

$$+ \frac{1}{V} \int_{A_{fx}} \overset{=}{\tau} \cdot \vec{n} \, dA + \gamma_V {}^i\langle R_x \rangle \qquad (2.14)$$

where $A_{fx}\big|_{(x+\Delta x, y, z)}$ denotes the free flow area normal to the x axis and

centered at $(x+\Delta x, y, z)$. Eq. (2.14) is reduced to the following form,

$$\gamma_V \frac{\partial}{\partial t} {}^i\langle \rho u \rangle + \frac{\Delta_{x'}(\gamma_{Ax}{}^{ix}\{\rho u^2\})}{\Delta x} + \frac{\Delta_{y'}(\gamma_{Ay}{}^{iy}\{\rho u v\})}{\Delta y} + \frac{\Delta_{z'}(\gamma_{Az}{}^{iz}\{\rho u w\})}{\Delta z}$$

$$= \gamma_V {}^i\langle \rho \rangle g_x - \frac{\Delta_{x'}(\gamma_{Ax}{}^{ix}\{p\})}{\Delta x} + \frac{\Delta_{x'}(\gamma_{Ax}{}^{ix}\{\tau_{xx}\})}{\Delta x} + \frac{\Delta_{y'}(\gamma_{Ay}{}^{iy}\{\tau_{yx}\})}{\Delta y}$$

$$+ \frac{\Delta_{z'}(\gamma_{Az}{}^{iz}\{\tau_{zx}\})}{\Delta z} + \gamma_V {}^i\langle R_x \rangle \qquad (2.15)$$

utilizing the increment notations defined as,

$$\Delta_{x'} \equiv ( )_{x+\Delta x, y, z} - ( )_{x, y, z} \qquad (2.16)$$

$$\Delta_{y'} \equiv ( )_{x+\Delta x/2, y+\Delta y/2, z} - ( )_{x+\Delta x/2, y-\Delta y/2, z} \qquad (2.17)$$

$$\Delta_{z'} \equiv ( )_{x+\Delta x/2, y, z+\Delta z/2} - ( )_{x+\Delta x/2, y, z-\Delta z/2} \qquad (2.18)$$

The distributed resistance $^i\langle\vec{R}\rangle$, which will be discussed in Section 2.5, is the total force per unit volume of fluid exerted on the fluid by the dispersed solid. It is defined as,

$$^i\langle\vec{R}\rangle \equiv \frac{1}{V_f} \int_{V_f} \vec{R}dV \equiv \frac{1}{V_f} \int_{A_{fs}} (-p\vec{n} + \bar{\bar{\tau}}\cdot\vec{n})dA \qquad (2.19)$$

The y and z components of the momentum equation can be obtained in an analogous fashion as the x component momentum equation.

It should be noted that the volume average quantities of Eq. (2.15) are defined as the values averaged over the XM control volume centered at $(x+\Delta x/2, y, z)$ which is different from the M-E control volume. The area average quantities and the surface porosities are calculated at the six faces surrounding the center, $(x+\Delta x/2, y, z)$. Since volume and surface averaged velocity components are specified in the momentum equation and surface averaged velocities are specified in the energy equation, it is necessary to find either reasonable approximations or a relationship among these velocities defined at different surfaces or volumes of the two control volumes. In the next section, possible approximations or assumptions required to get practically applicable finite difference equations are examined in detail.

2.4.4 Approximations Required for the Numerical Formulation

While the derived conservation equations (Eqs. (2.11), (2.12) and (2.15)) are general forms, they require some approximations for numerical application. First let us examine the volume and area average values of the cross product terms, e.g., $\{uv\}$. The thermal-hydraulic quantities $(\rho, u, \vec{v}, p, \text{etc.})$ have their own spatial distributions within

a control volume or on a suface. Thus, the quantity at a specific location can be expressed as the sum of an average and fluctuating component. The average is a spatial average over a control volume or surface and the fluctuating term is a local variation from the average value. The x and y components of the velocity can be expressed as,

$$u = \{u\} + u'$$ (2.20)

$$v = \{v\} + v'$$ (2.21)

Then,

$$\{uv\} = \{u\}\{v\} + \{u'v'\}$$ (2.22)

The average of the cross product of the fluctuating terms $\{u'v'\}$ is usually neglected compared to other terms in the equation. This assumption is reasonable in most practical situations. However, this assumption should be verified in case of highly non-uniform distributions of the subject quantities. An assessment of this cross product term for the analysis of a wire-wrapped rod bundle is given in Section 3.3.

As mentioned in Section 2.4.3, the typical quantities of interest are expressed as the values averaged over various surfaces and volumes. Table 2.1 summarizes the average representations of the quantities employed in the conservation equations. The expression of the volume or surface in terms of grid notation (I,J,K) represents the position of the center of the volume or surface where the quantity is averaged. In order to estimate each representation exactly, the spatial distribution of each quantity must be known. However, the spatial distribution of a quantity is not given a priori and is different case by case.

Table 2.1 Lists of the Volume and Area Average Quantities Used in the

Conservation Equations*

Quantity	Representation	Location of the Volume or Surface
Energy	$^i\langle u \rangle$	(i,j,k)
	$^{ix}\{u\}$	$(i+\frac{1}{2},j,k)$
	$^{iy}\{u\}$	$(i,j+\frac{1}{2},k)$
	$^{iz}\{u\}$	$(i,j,k+\frac{1}{2})$
Density	$^i\langle \rho \rangle$	$(i,j,k),(i+\frac{1}{2},j,k),(i,j+\frac{1}{2},k),(i,j,k+\frac{1}{2})$
	$^{ix}\{\rho\}$	$(i,j,k),(i+\frac{1}{2},j,k),(i+\frac{1}{2},j,k+\frac{1}{2}),$ $(i+\frac{1}{2},j+\frac{1}{2},k)$
	$^{iy}\{\rho\}$	$(i,j,k),(i,j+\frac{1}{2},k),(i+\frac{1}{2},j+\frac{1}{2},k),$ $(i,j+\frac{1}{2},k+\frac{1}{2})$
	$^{iz}\{\rho\}$	$(i,j,k),(i,j,k+\frac{1}{2}),(i+\frac{1}{2},j,k+\frac{1}{2}),$ $(i,j+\frac{1}{2},k+\frac{1}{2})$
Velocity** (x-component)	$^i\langle u \rangle$	$(i+\frac{1}{2},j,k)$
	$^{ix}\{u\}$	$(i,j,k),(i+\frac{1}{2},j,k),(i+\frac{1}{2},j+\frac{1}{2},k),$ $(i+\frac{1}{2},j,k+\frac{1}{2})$
	$^{iy}\{u\}$	$(i+\frac{1}{2},j+\frac{1}{2},k)$
	$^{iz}\{u\}$	$(i+\frac{1}{2},j,k+\frac{1}{2})$
Pressure	$^{ix}\{p\}$	(i,j,k)
	$^{iy}\{p\}$	(i,j,k)
	$^{iz}\{p\}$	(i,j,k)

*   Only terms which are within one-half a mesh interval in the positive direction (i.e., $+\Delta x/2$, $+\Delta y/2$, $+\Delta z/2$) from the origin are shown.
** The y and z components of the velocity can be obtained in a similar way.

In order to eliminate this difficulty, several approximations can be suggested based on physical grounds. First, since the density and energy are generally the quantities defined for a unit volume or mass, it is reasonable to choose the volume average quantities as their representatives. In addition, since the density does not vary much spatially, if the control volume is taken small, the variation can be neglected. Therefore it is appropriate to set the area average values equal to the volume average value, i.e.,

$$^{ix}\{\rho\}_{i,j,k} = {^{iy}}\{\rho\}_{i,j,k} = {^{iz}}\{\rho\}_{i,j,k} = {^{i}}\langle\rho\rangle_{i,j,k} \qquad (2.23)$$

The area averages defined at the interfaces between the M-E control volumes can be calculated by employing a donor cell concept. Since the density and energy have a convective characteristic, their properties are transported downstream along the direction of fluid flow. Using the donor cell concept, the area average values can be estimated as,

$$^{ix}\{\rho\}_{i+\frac{1}{2},j,k} = {^{i}}\langle\rho\rangle_{i,j,k} \quad \text{if } {^{ix}}\{u\}_{i+\frac{1}{2},j,k} \geq 0 \qquad (2.24)$$

$$^{ix}\{\rho\}_{i+\frac{1}{2},j,k} = {^{i}}\langle\rho\rangle_{i+1,j,k} \quad \text{if } {^{ix}}\{u\}_{i+\frac{1}{2},j,k} < 0 \; ; \text{ etc.} \quad (2.25)$$

Another approximation for the area average quantities is to interpolate neighboring volume average values. This approach is reasonable when the spatial distribution of the quantity is quasi-linear.

For the velocity components, both the area and the volume averages can be used as a representative value. The principal area averages,

i.e., $^{ix}\{u\}_{i+1/2,j,k}$, $^{iy}\{v\}_{i,j+1/2,k}$ and $^{iz}\{w\}_{i,j,k+1/2}$ are

commonly used for the representative values. Then, the other average

quantities are approximately obtained from the interpolation of

neighboring principal velocity components. Further examination of the

velocity components in the application of the wire-wrapped rod bundle

analysis is performed in Section 3.3.

There are three area averages for the pressure term as shown in

Table 2.1. It is difficult to find a plausible relationship among those

quantities. As a rough approximation, one can simply assume that,

$$^{ix}\{p\} - ^{iy}\{p\} = ^{iz}\{p\} \tag{2.26}$$

where $^{iz}\{p\}$ is usually taken as a representative quantity for axial flow

field in a rod bundle.

Although the momentum equation (Eq.(2.15)) is written in terms of

the area averages ($^{ix}\{p\}$, $^{iy}\{p\}$ and $^{iz}\{p\}$ from the y and z

momentum equations), it can be rewritten in terms of the volume average

pressure, i.e., $^{i}\langle p\rangle$ through some mathematical manipulation. In such

a case, only the volume average pressure is employed and, accordingly,

no relationship is required. However, each formulation has its own

advantages and disadvantages. Since the choice between expressing the

momentum equation in terms of area averages or a volume average is quite

important, we will investigate it in more detail within the framework of

one-dimensional problems in the next section.

Further assumptions required for practical numerical applications

are described in Chapter 3. Detailed explanation of the temporal and

spatial discretization schemes of the THERMIT code, which is employed as

our numerical tool in this work, can be found in reference (R-1).

2.5 Pressure Term Analysis in the Momentum Equations

2.5.1 Introduction

There has been much debate regarding the use of the volume porosity, γ_V or the surface porosity (or surface permeability), γ_A in the pressure term of the momentum equation. These porosities result from the average representation of the pressure term. The utilization of the volume porosity means that the volume averaged pressure is employed in the difference formulation, while the utilization of the area porosity means the area averaged pressures are used. From a numerical point of view, the choice of the volume porosity may be best because the pressure is usually defined as a volume-averaged quantity at the center of a main control volume. The pressure also can be defined as an area average quantity, but this requires additional information or some approximations about the relationship between the area average values at different planes as mentioned in Section 2.4.4. However, in a physical sense, the surface porosity seems to be a better choice since the pressure is defined as the force per unit area, and the net force gives rise to the driving force of the flow. Some porous body codes such as the COMMIX code (S-2) employ the volume porosity in the pressure term, while some other opinions suggest that the surface porosity be used.

In order to analyze this problem rigorously, the following tasks have been done sequentially: First, the distributed resistance and the pressure term are examined. Three forms of the pressure term are considered; the COMMIX model, the Area model (the pressure term in Eq.(2.15)) and a model suggested in this work. The assumptions introduced in each model to get a final working form are investigated.

Secondly, to demonstrate its applicability to the flow field analysis, each model is utilized to solve two simple hydraulic problems, i.e. a hydrostatic case and an inviscid flow case with a linearly varying flow area. The error involved in each model is evaluated by comparing the numerical result using each model against an analytical solution. Finally, some concluding remarks are drawn from the error analysis and for numerical implementation.

2.5.2 Distributed Resistance Term

The distributed resistance $^i\langle\vec{R}\rangle$ which is the total force per unit volume of fluid exerted on the fluid by the dispersed solid is defined in Eq. (2.19) as,

$$^i\langle\vec{R}\rangle = \frac{1}{V_f} \int_{V_f} \vec{R}dV = \frac{1}{V_f} \int_{A_{fs}} (-p\vec{n} + \bar{\bar{\tau}}\cdot\vec{n})dA \qquad (2.19)$$

Since the evaluation of $^i\langle\vec{R}\rangle$ is based on friction and drag correlations which represent the force exerted on the solid by the fluid, an alternate notation for the distributed resistance force which has the same magnitude but is oppositely directed to $\int_{V_f} \vec{R}dV$ is introduced and defined as,

$$\vec{F} \equiv - \int_{V_f} \vec{R} \, dV = - \int_{A_{fs}} (- p\vec{n} + \bar{\bar{\tau}}\cdot\vec{n}) \, dA \qquad (2.27)$$

The distributed resistance force $\vec{F}$ is the total force exerted on the solid by the fluid. This force is conventionally correlated (S-3) in terms of a velocity, $\vec{v}$, and a fluid viscosity, μ, as

$$F \approx C \mu v^n \qquad (2.28)$$

where C and n are constants. Some questions concerning the definition of the resistance force arise in limiting cases, i.e., the hydrostatic case with no fluid motion and the case of inviscid fluid flow in a varying flow area. If there is no motion of the fluid or the fluid is assumed to be inviscid, the correlated resistance force (Eq.(2.28))

will be zero. However, the distributed resistance force defined in Eq.(2.27) is not zero although $\vec{v}$ equals zero or μ goes to zero when the flow area changes along the vertical or flow direction. Instead, $\vec{F}$ equals the remaining term, $\int_{A_{fs}} p\vec{n}\ dA$, which represents the pressure distribution on the solid surface. This requires a modification of the resistance term to correct the above discrepancy.

In order to make the resistance force consistent with the correlations used, the pressure at the solid surface is separated into two components as,

$$p \equiv p_{no\ wake} - \Delta p_{wake} \tag{2.29}$$

where $p_{no\ wake}$ is the pressure distribution in case of the ideal flow where no wake is generated downstream the obstacle

and Δp_{wake} is the difference between the actual pressure and the $p_{no\ wake}$.

Then a possible alternative is to define the distributed resistance force, $\vec{F}'$ (or $\vec{R}'$) as,

$$\vec{F}' \equiv - \int_{V_f} \vec{R}'\ dV \equiv - \int_{A_{fs}} (\Delta p_{wake}\ \vec{n} + \overline{\overline{\tau}}\cdot\vec{n})\ dA \tag{2.30}$$

A detailed description of the alternative for the resistance force is given in Appendix A.

Then, the integral momentum equation of Eq.(2.5) becomes,

$$\gamma_V \frac{\partial}{\partial t}\ ^i\langle\rho\vec{v}\rangle + \frac{1}{V}\int_{A_f} \rho\vec{v}(\vec{v}\cdot\vec{n})\ dA = \gamma_V\ ^i\langle\rho\rangle\ \vec{g} - \frac{1}{V}\ (\int_{A_f} p\vec{n}\ dA$$

$$+ \int_{A_{fs}} p_{no\ wake}\ \vec{n}\ dA) + \frac{1}{V}\int_{A_f} \overline{\overline{\tau}}\cdot\vec{n}\ dA + \frac{1}{V}\int_{V_f} \vec{R}'\ dV \tag{2.31}$$

Eq. (2.31) shows that a different definition of the pressure term is required to be consistent with the alternative distributed resistance force $\vec{R}'$.

2.5.3 Models of the Pressure Term

In this section three models for the pressure term are investigated separately. The control volume and the grid index for a one-dimensional analysis are presented in Figure 2.4. The quantities defined at grids are also shown in the figure.

2.5.3.1 COMMIX Model

The pressure term in Eq.(2.31) is numerically modeled in the COMMIX code (S-2) as follows, using the expression for the divergence of an intrinsic local volume average (T-1),

$$\frac{1}{V} \left(\int_{A_f} p\vec{n} \, dA + \int_{A_{fs}} p_{no \ wake} \ \vec{n} \, dA \right) \approx \frac{1}{V} \int_{A_f} p\vec{n} \, dA$$

$$= \nabla(\gamma_V \ ^i\langle p \rangle) \qquad (2.32)$$

and for the x direction,

$$\nabla(\gamma_V \ ^i\langle p \rangle) \approx \gamma_{V_{i+1/2}} \frac{\Delta_x(^i\langle p \rangle)}{\Delta x} \qquad (2.33)$$

Note that an approximation is introduced in the volume porosity manipulation. Additionally, the COMMIX model neglects the term, $\int_{A_{fs}} p_{no \ wake} \vec{n} \, dA$. However, as one can see from the later examples, the combination of the approximation of γ_V and the neglect of the integral term on the surface A_{fs} gives excellent results since these two effects compensate.

2.5.3.2 Area Model (or COBRA-type Model)

The pressure term of the Area model is obtained in the following way. The x component of the pressure term in Eq.(2.31) can be written as,

$$\frac{1}{V} \left(\int_{A_f} p\vec{n} \, dA + \int_{A_{fs}} p_{no \ wake} \ \vec{n} \, dA \right)_x$$

$$= \frac{1}{V} \left(\int_{A_f} p \, dA_{fx} + \int_{A_{fs}} p_{no \ wake} \ (-dA_{fsx}) \right) \qquad (2.34)$$
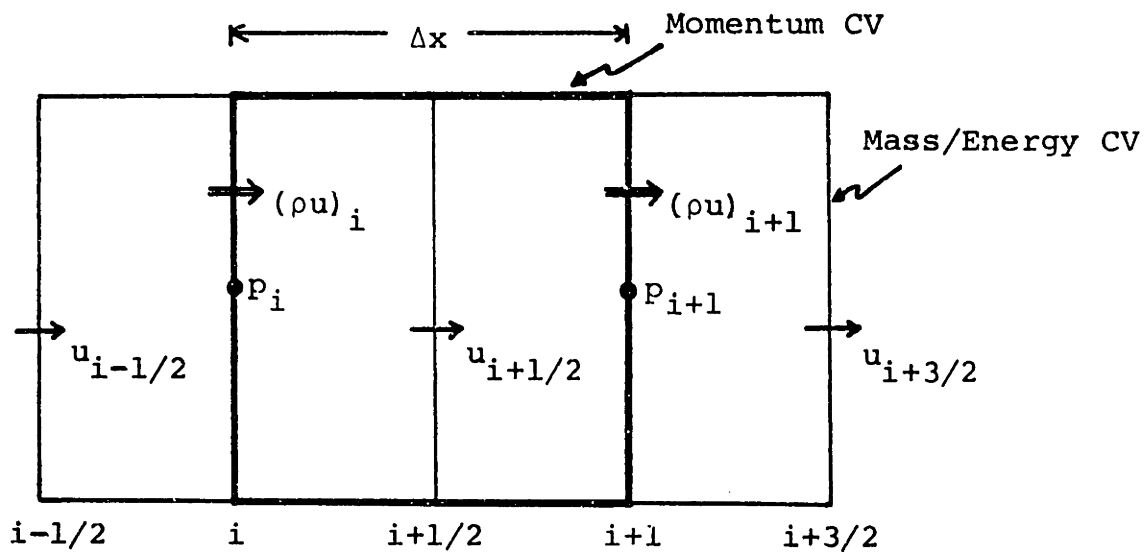
Figure 2.4 Control Volume for a 1-Dimensional Flow

The negative sign in the differential solid area is shown since the direction of the pressure force acting on the solid is always opposite to the normal direction of the solid surface.

The first term of the RHS in Eq.(2.34) is transformed as,

$$\frac{1}{V}\int_{A_f} p \; dA_{fx} = \frac{\Delta_x(\gamma_{Ax}{}^{ix}\{p\})}{\Delta x}$$ (2.35)

To reduce the second term of the RHS in Eq.(2.34) into a numerically tractable form, the following assumptions are introduced:

(1) $p_{no \; wake}$ is linear along the principal direction (here, x direction). This assumption requires that the pressure variation around the obstacle is småll compared to the pressure distribution without the obstacle.

(2) Flow area variation is linear. From these assumptions and by introducing an average pressure as,

$$\bar{p}_{no \; wake} \approx \frac{1}{2}({}^{ix}\{p\}_i + {}^{ix}\{p\}_{i+1})$$ (2.36)

one can derive the following relation,

$$\frac{1}{V}\int_{A_{fs}} p_{no \; wake} \; (-dA_{fsx}) \approx \frac{\bar{p}_{no \; wake}}{V}(A_{fx_i} - A_{fx_{i+1}})$$ (2.37)

By substituting Eq.(2.36) into Eq.(2.37) and adding Eq.(2.35) to Eq.(2.37), one can obtain,

$$\frac{1}{V}\int_{A_f} p \; dA_{fx} + \frac{1}{V}\int_{A_{fs}} p_{no \; wake} \; (-dA_{fsx})$$

$$= \frac{\Delta_x(\gamma_{Ax}{}^{ix}\{p\})}{\Delta x} + \frac{1}{V}\frac{1}{2}({}^{ix}\{p\}_i + {}^{ix}\{p\}_{i+1})(A_{fx_i} - A_{fx_{i+1}})$$

$$= \frac{\gamma_{Ax_{i+1}}{}^{ix}\{p\}_{i+1} - \gamma_{Ax_i}{}^{ix}\{p\}_i}{\Delta x} + (\frac{{}^{ix}\{p\}_i + {}^{ix}\{p\}_{i+1}}{2})(\frac{\gamma_{Ax_i} - \gamma_{Ax_{i+1}}}{\Delta x})$$

$$= \frac{\gamma_{Ax_i} + \gamma_{Ax_{i+1}}}{2} \frac{\Delta_x({}^{ix}\{p\})}{\Delta x}$$ (2.38)

The area porosity in the RHS of Eq.(2.38) can be rewritten as follows if the assumption (2) is valid,

$$\frac{\gamma_{Ax_i} + \gamma_{Ax_{i+1}}}{2} = \frac{\bar{A}_{fx}}{\Delta y \Delta z} \qquad (2.39)$$

where the average flow area, $\bar{A}_{fx} \equiv \frac{1}{2} (A_{fx_i} + A_{fx_{i+1}})$.

Then, Eq.(2.38) yields,

$$\frac{1}{V} \left(\int_{A_f} p\vec{n} \, dA + \int_{A_{fs}} p_{no \ wake} \ \vec{n} \ dA \right)_x = \frac{\bar{A}_{fx}}{V} \Delta_x(^{ix}\{p\}) \qquad (2.40)$$

This result is the same as the pressure term used in the COBRA code (R-2). The y and z components of the pressure term can be obtained in the similar way.

This model works well for one-dimensional analysis as one can see from the later examples. However, it has some difficulties in the numerical implementation. For a general three-dimensional analysis, three kinds of the area-averaged pressure ($^{ix}\{p\}$, $^{iy}\{p\}$ and $^{iz}\{p\}$) are employed in a calculational mesh. This requires that some relationship among the three directional area-averaged pressures should be provided. No relevant correlation has been provided yet, although the correlation may depend on the control volume geometry and the distribution of the pressure field.

As one can see from the later examples, this model does not neglect the pressure force term on the solid surface, $\int_{A_{fs}} p\vec{n} \, dA$, while the COMMIX model does. Thus, this portion of the pressure term is retained in the momentum equation.

2.5.3.3 Suggested Model

We suggest a model for the pressure term by introducing similar assumptions as used in the Area model. However, the suggested model is based on the volume porosity and the volume-averaged pressure, while the

Area model is based on the area porosity and the area-averaged pressure. The same assumptions as in the Area model are used except the average pressure is approximated as,

$$\bar{P}_{no\ wake} = \frac{1}{2} (^{1}\langle p \rangle_{i} + {}^{1}\langle p \rangle_{i+1}) \tag{2.41}$$

The first term of the RHS in Eq.(2.34) is expressed as,

$$\frac{1}{V}\int_{A_f} p\ dA_{fx} = (\nabla \langle p \rangle)_x \approx \frac{\Delta_x (\gamma_V {}^{1}\langle p \rangle)}{\Delta x} \tag{2.42}$$

From assumption (2), i.e., the linear flow area approximation in the x direction, the following relation between the volume and area porosities is obtained,

$$^{\gamma}Ax_i = {}^{\gamma}V_i \quad \text{and} \quad {}^{\gamma}Ax_{i+1} = {}^{\gamma}V_{i+1} \tag{2.43}$$

Then, the second term of the RHS in Eq.(2.34) yields,

$$\frac{1}{V}\int_{A_{fs}} P_{no\ wake} (-dA_{fsx}) \approx \bar{P}_{no\ wake} \frac{(A_{fx_i} - A_{fx_{i+1}})}{V}$$

$$= -\bar{P}_{no\ wake} \frac{\Delta_x(^{\gamma}V)}{\Delta x} \tag{2.44}$$

By adding Eq.(2.42) to Eq.(2.44) with use of Eq.(2.41), using the same procedure as for Eq.(2.38), the RHS of Eq.(2.34) yields,

$$\frac{1}{V}\int_{A_f} p\ dA_{fx} + \frac{1}{V}\int_{A_{fs}} P_{no\ wake} (-dA_{fsx}) = \frac{^{\gamma}V_{i+1} + {}^{\gamma}V_i}{2} \frac{\Delta_x(^{1}\langle p \rangle)}{\Delta x} \tag{2.45}$$

Comparing the suggested model with the COMMIX model, i.e., Eq.(2.45) with Eq.(2.33), shows an identical formulation for the pressure term with the difference existing in the preceding volume porosity term. If the assumption of the linear flow area variation is applied,

$$^{\gamma}V_{i+1/2} = \frac{1}{2} (^{\gamma}V_i + {}^{\gamma}V_{i+1}) \tag{2.46}$$

Therefore, two models for the pressure term are exactly the same for the linearly varying flow area case even though they are based on different assumptions.

2.5.4 Examples and Results

To demonstrate the capability of each model and the error involved in each model, two simple one-dimensional problems are chosen. The first example is a static case, i.e., no fluid motion in a vertical channel with a varying flow area. The second is a steady flow case with an incompressible and inviscid (negligible viscous force) fluid in a horizontal channel with a linearly varying flow area. For these problems, the unsteady term and the viscous term can be neglected.

The convective term in the finite difference form may be transformed as follows, for the x direction,

$$\frac{1}{V}\int_{A_f} \rho uu \; dA = \frac{1}{V}\left[\Delta y \Delta z \gamma_{Ax}\Big|_{x+\Delta x} {}^{1x}\{\rho u^2\}_{x+\Delta x} - \Delta y \Delta z \gamma_{Ax}\Big|_{x} {}^{1x}\{\rho u^2\}_{x}\right]$$

(2.47)

or

$$\frac{1}{V}\int_{A_f} \rho u^2 \; dA = \frac{\Delta_x \left(\gamma_{Ax} {}^{1x}\{\rho u^2\}\right)}{\Delta x}$$

(2.48)

where the increment Δ_x is defined as

$$\Delta_x \equiv (\;)_{x+\Delta x} - (\;)_x$$

(2.49)

This notation for a one-dimensional case is equivalent to the definition of Eq.(2.16) for a three-dimensional case.

Equation (2.31) can now be rewritten for steady state conditions for each model utilizing

    1) Eq.(2.48)

    2) $\gamma_V {}^1\langle\rho\rangle g_x \approx \gamma_{V_{i+1/2}} \rho g$

        where ${}^1\langle\rho\rangle = {}^1\langle\rho\rangle_{i+1/2} = \rho$ since the fluid is assumed incompressible

and 3) Eq.(2.33) (COMMIX Model), Eq.(2.40) (Area Model) and

Eq.(2.45) (Suggested Model)

The resulting working equations for these examples are summarized in Table 2.2.

Table 2.2 Momentum Equation for the Chosen One-Dimensional Examples

COMMIX Model	$\dfrac{\Delta_x(\gamma_{Ax}{}^{1x}\{\rho u^2\})}{\Delta x} = \gamma_{V_{i+1/2}}\rho g - \gamma_{V_{i+1/2}}\dfrac{\Delta_x(^1\langle p\rangle)}{\Delta x}$
Area Model	$\dfrac{\Delta_x(\gamma_{Ax}{}^{1x}\{\rho u^2\})}{\Delta x} = \gamma_{V_{i+1/2}}\rho g - \dfrac{\gamma_{Ax_i} + \gamma_{Ax_{i+1}}}{2}\dfrac{\Delta_x(^{1x}\{p\})}{\Delta x}$
Suggested Model	$\dfrac{\Delta_x(\gamma_{Ax}{}^{1x}\{\rho u^2\})}{\Delta x} = \gamma_{V_{i+1/2}}\rho g - \dfrac{\gamma_{V_i} + \gamma_{V_{i+1}}}{2}\dfrac{\Delta_x(^1\langle p\rangle)}{\Delta x}$

These momentum equations will be evaluated for two cases. The convective term in all the equations will be evaluated using the spatial index system of Figure 2.4, i.e.,

$$\frac{\Delta_x(\gamma_{Ax}{}^{1x}\{\rho u^2\})}{\Delta x} = \frac{1}{\Delta x}\left[(\gamma_{Ax}{}^{1x}\{\rho u^2\})_{i+1} - (\gamma_{Ax}{}^{1x}\{\rho u^2\})_i\right] \qquad (2.50)$$

One assumption to be employed in the calculation is that the flow area is extended linearly beyond the momentum control volume boundary. In other words, the selected momentum control volume is a small portion of the total volume with a linearly varying flow area. By doing this, the volume porosity can be determined without ambiguity.

An analytical solution of each example can be obtained from the Bernoulli equation. The corresponding Bernoulli equation is given as,

$$p + \rho gh + \frac{1}{2}\rho v^2 = \text{constant along streamline} \qquad (2.51)$$

To determine the error involved in each model, the error of the pressure term is defined as,

$$\text{Error } (\Delta p) = \frac{(\Delta p)_{pred} - (\Delta p)_{analy}}{(\Delta p)_{analy}} \qquad (2.52)$$

where, $(\Delta p)_{pred}$ = Model predicted pressure drop

$(\Delta p)_{analy}$ = Analytical solution using the Bernoulli equation.

2.5.4.1 Example 1 - Hydrostatic Case

A schematic geometry for this case is depicted in Figure 2.5. The convective term is zero since there is no fluid flow. Let us evaluate the error for each model separately. Algebraic details for all cases are given in Appendix B.

(a) COMMIX model

The working momentum equation incorporating the COMMIX model can be reduced as,

$$\gamma_{v_{i+1/2}} \, \rho g - \gamma_{v_{i+1/2}} \, \frac{\Delta_x (^1\langle p \rangle)}{\Delta x} = 0 \qquad (2.53)$$

Then, the predicted pressure drop using the COMMIX model is given as,

$$\Delta (^1\langle p \rangle)_{pred} = \rho g h \qquad (2.54)$$

where $h = \Delta x$.

Using the Bernoulli equation, one can calculate the volume-averaged pressure analytically such as,

$$^1\langle p \rangle = \frac{1}{V_f} \int_{V_f} p(x) A_f(x) dx \qquad (2.55)$$

where, $p(x)$ is the local pressure which can be calculated from the Bernoulli equation, and $A_f(x)$ is the free flow area at a position x.
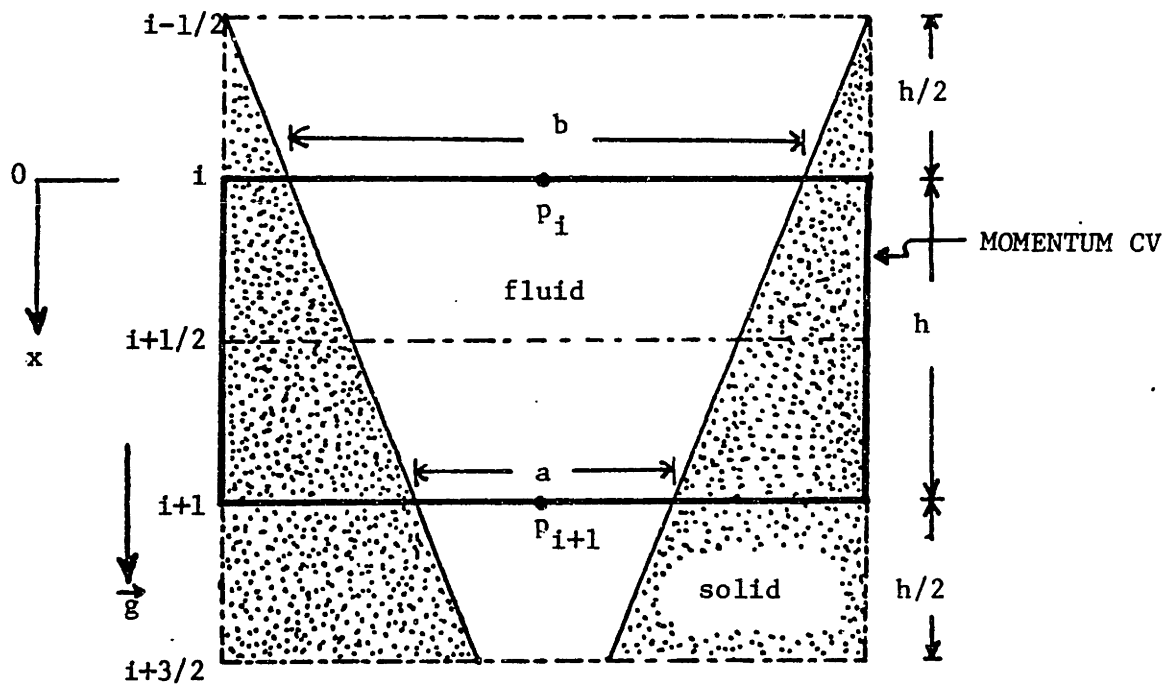
Figure 2.5 Geometry for hydrostatic Case

One can obtain,

$$^i\langle p\rangle_i = P_i - \frac{1}{12}\,\frac{b-a}{b}\,\rho gh$$

$$^i\langle p\rangle_{i+1} = P_i + (\frac{13}{12} - \frac{1}{12}\,\frac{b}{a})\,\rho gh$$

Then the analytical solution of the pressure drop yields,

$$\Delta(^i\langle p\rangle)_{analy} = \rho gh\,(1 - \frac{1}{12}\,\frac{(b-a)^2}{ab}) \qquad (2.56)$$

From Eq.(2.52), the error of the COMMIX model compared to the analytical solution is obtained as,

$$Error\,[\Delta(^i\langle p\rangle)] = \frac{\frac{1}{12}\,\frac{(b-a)^2}{ab}}{1 - \frac{1}{12}\,\frac{(b-a)^2}{ab}} \qquad (2.57)$$

The predicted pressure drop is thus obtained based on the mesh difference, $\Delta x(=h)$ while the analytical solution is obtained using the distance $h(1 - \frac{1}{12}\,\frac{(b-a)^2}{ab})$ which equals the distance between the centers of the pressures weighted by the volume. Therefore, the source of the error in the numerical model comes from the use of an incorrect distance between the centers of the volume-averaged pressures.

(b) Area model

For the hydrostatic case, the working momentum equation with the Area model is written as,

$$^\gamma V_{i+1/2}\,\rho g - \frac{^\gamma Ax_i + {}^\gamma Ax_{i+1}}{2}\,\frac{\Delta_x(^{ix}\{p\})}{\Delta x} = 0 \qquad (2.58)$$

Then, the predicted pressure drop yields,

$$\Delta(^{ix}\{p\})_{pred} = \rho gh \qquad (2.59)$$

The analytical solution using the Bernoulli equation also yields,

$$\Delta(^{ix}\{p\})_{analy} = P_i + \rho gh - P_i = \rho gh \qquad (2.61)$$

Thus, the error of the Area model compared with the analytical solution is given as,

$$\text{Error } \left[\Delta(^{1x}\{p\})\right] = 0$$

There is no error as expected, since the area and the pressure variations are linear which are the assumptions of the Area model.

(c) Suggested model

As described earlier, the pressure drop formulation of the suggested model is identical to that of the COMMIX model for the linearly varying flow area case. Therefore, the result of the error analysis is exactly the same as that of the COMMIX model.

The error of each model is plotted as a function of an area ratio, a/b in Figure 2.6. The error of the COMMIX model or the suggested model increases as the area ratio decreases, while that of the Area model remains zero. If a/b is less than 1/3, the flow area will be negative at plane i+3/2 and our analysis is not applicable to that limiting case.

2.5.4.2 Example 2 - Inviscid flow with a linearly varying flow area

A schematic geometry of this example is drawn in Figure 2.7. Geometrical parameters such as the volume porosity and the area porosity are the same as those of Example 1. For this flow case, it is assumed that the flow field is one-dimensional and the Bernoulli equation is also applicable. Since the flow direction is taken normal to the direction of the gravity force, the gravity term is zero for this problem.

(a) COMMIX model

The working momentum equation is written as,

$$\frac{\Delta_x(\gamma_{Ax}\,^{1x}\{\rho u^2\})}{\Delta x} = -\,\gamma_{V}\Big|_{i+1/2}\;\frac{\Delta_x(^{1}\langle p \rangle)}{\Delta x} \tag{2.62}$$
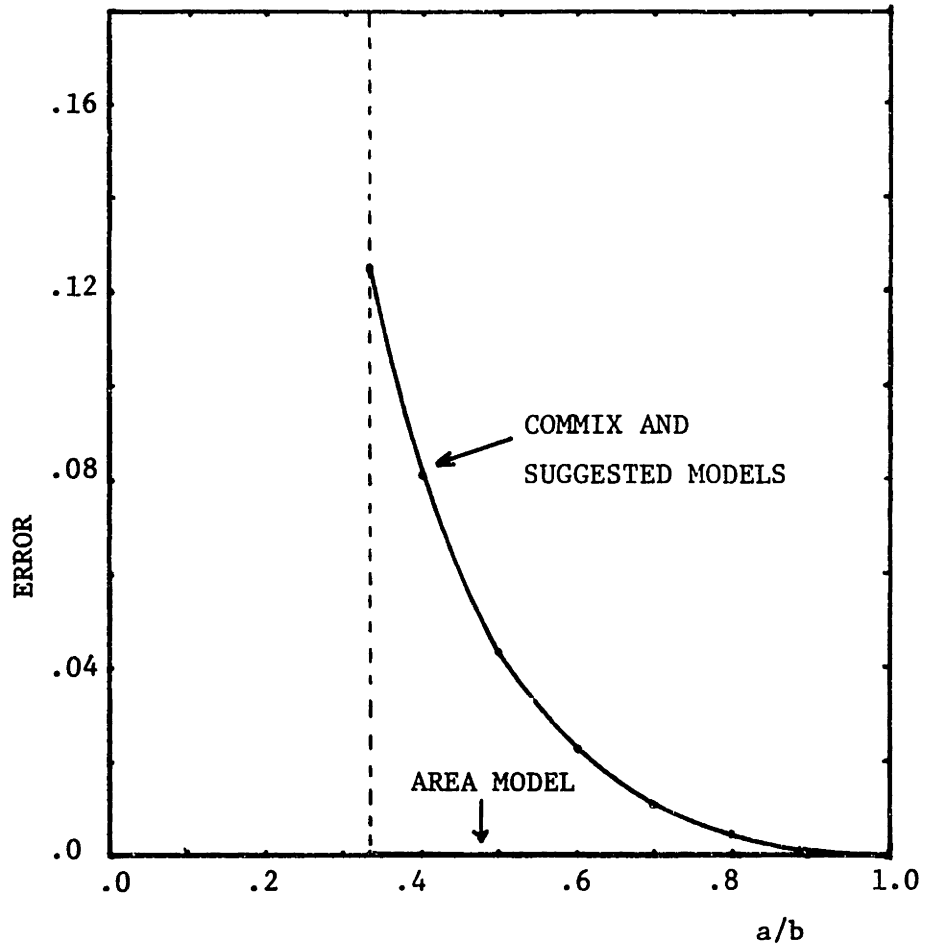
Figure 2.6 Pressure Drop Error of Each Model for the
Hydrostatic Case
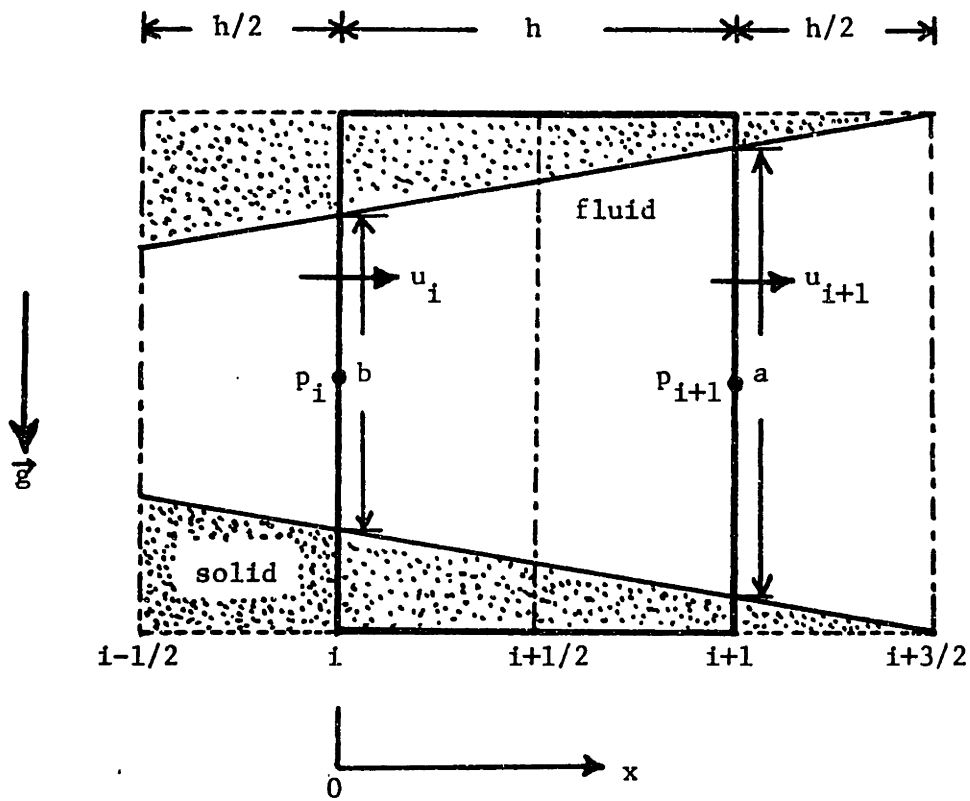
Figure 2.7   Geometry for Inviscid Flow Case in a Linearly Varying
             Flow Area

The convective term can be evaluated using continuity ($u_i b = u_{i+1} a$).

Then, the predicted pressure drop using the COMMIX model yields,

$$\Delta(^i\langle p \rangle)_{pred} = - \frac{2b}{a+b} (\frac{b}{a} - 1) \rho u_i^2 \qquad (2.63)$$

Using Eq.(2.55), the analytical solution of the pressure drop is calculated as,

$$\Delta(^i\langle p \rangle)_{analy} = \frac{1}{2} \rho u_i^2 [\frac{b^2}{a(b-a)} \ln \frac{3a-b}{a+b} - \frac{b}{b-a} \ln \frac{a+b}{3b-a}] \qquad (2.64)$$

By utilizing Eq.(2.63) and Eq.(2.64), the error of the COMMIX model is estimated as,

$$\text{Error } [\Delta(^i\langle p \rangle)] = \frac{- \frac{4(b-a)^2}{a(a+b)} - [\frac{b}{a} \ln \frac{3a-b}{a+b} - \ln \frac{a+b}{3b-a}]}{\frac{b}{a} \ln \frac{3a-b}{a+b} - \ln \frac{a+b}{3b-a}} \qquad (2.65)$$

The sources of the error stem from two reasons: (1) as Example 1, the correct distance between the weighted centers of the volume-averaged pressures is not used, and (2) the assumptions employed in the model derivation contribute to the error.

(b) Area model

The working momentum equation is given as,

$$\frac{\Delta_x(\gamma_{Ax}{}^{ix}\{\rho u^2\})}{\Delta x} = - \frac{\gamma_{Ax_i} + \gamma_{Ax_{i+1}}}{2} \frac{\Delta_x(^{ix}\{p\})}{\Delta x} \qquad (2.66)$$

The predicted pressure drop obtained from Eq.(2.66) is the same as that of the COMMIX model, i.e., Eq.(2.63) since

$$\gamma_{V_{i+1/2}} = \frac{1}{2} (\gamma_{Ax_i} + \gamma_{Ax_{i+1}}) \quad \text{for the linearly varying flow area case.}$$

The analytical solution is calculated from the Bernoulli equation in the same way,

$$\Delta(^{ix}\{p\})_{analy} = \frac{1}{2} \rho u_i^2 [1 - (\frac{b}{a})^2] \qquad (2.67)$$

Therefore, the error of the Area model is

$$\text{Error } \left[\Delta\left(^{1x}\{p\}\right)\right] = -\frac{(a-b)^2}{(a+b)^2} \qquad (2.68)$$

The source of the error comes from the model assumption that the pressure field is linear along the x direction. The pressure field is not actually linear although the flow area and the velocity field are linear.

(c) Suggested model

For this linearly varying flow area case, the suggested model is identical to the COMMIX model. Thus, the result of the error analysis is the same as that of the COMMIX model.

The error of each model for this example is plotted as a function of an area ratio, a/b, in Figure 2.8. The errors of all models increase as the area ratio decreases. Throughout the range of the area ratio, the errors of the COMMIX model or the suggested model are larger than those of the Area model. As explained in Example 1, our analysis fails if a/b is smaller than 1/3.

2.5.5 Summary

The pressure term in the momentum equation has been examined to determine whether the volume porosity with the volume-averaged pressure or the surface porosity with the area-averaged pressure should be used. An alternative distributed resistance force has been defined to satisfy the limiting cases, which accordingly requires a different definition of the pressure term. Three possible formulations of the newly defined pressure term have been derived, which are the COMMIX model, the Area model and the suggested model. The estimation of the error involved in each model has been performed for two one-dimensional problems.
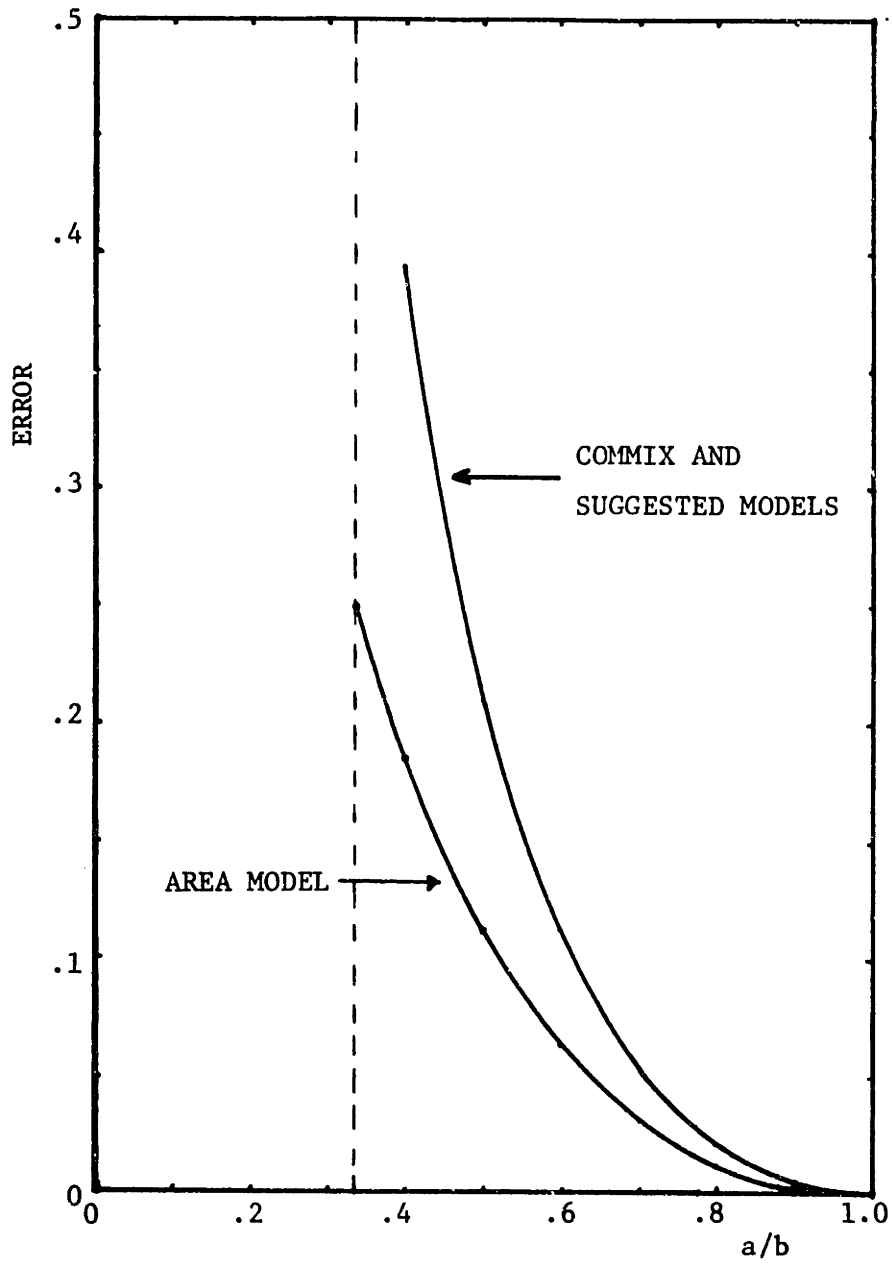
Figure 2.8 Pressure Drop Error of Each Model for the
Inviscid Flow Case

The following concluding remarks are drawn in this work:

(1) An alternative formulation for the pressure term is suggested which does not neglect the pressure distribution on the solid surface. This suggested model is formulated based on reasonable assumptions which are also employed in the derivation of the Area model.

(2) The errors of both the COMMIX and the suggested models increase as the area ratio a/b decreases except that the error of the Area model remains zero for the hydrostatic case. Both models show small error (less than 5%) for the two examples when a/b is greater than 0.7.

(3) The errors of the Area model are always smaller than those of the COMMIX model (or suggested model) throughout the range of the area ratio. However, for general three-dimensional problems, the Area model requires a correlation providing a relationship among the area-averaged pressures of three principal directions. It is difficult to obtain the correlation without information about the detailed pressure distribution which is not known. Therefore, the suggested model is recommended since it does not require any correlation and minimizes the approximations required in the formulation.

CHAPTER 3

POROUS BODY APPROACH FOR THE WIRE-WRAPPED ROD BUNDLE

3.1 Introduction

In this chapter we discuss the application of the porous body approach to the analysis of a wire-wrapped rod bundle. The inherent limitations of the porous body approach deduced from the approximations described in Chapter 2 are clarified. The difficulties in the flow field calculation for the wire-wrapped rod bundle are identified. An optimum control volume layout is selected which may relieve the difficulties and may minimize inaccuracy due to the approximations.

The porous body approach has been successfully used in a rectangular bare rod array analysis. Basically, the porous body approach is almost identical to the subchannel approach in the rectangular geometry since a similar computational mesh configuration is employed for both approaches and the flow direction is predominantly axial in most nuclear applications. However, for triangular wire-wrapped rod bundles, typical of those used in the LMFBR reactor core bundle, the computational mesh cells are no longer identical and strong crossflow is expected by virtue of the wire spacers. Therefore, the assumptions and limitations should be validated for this specific geometry.

First, different characteristics between the porous body and the subchannel approaches are identified. Then, in order to examine the applicability of the porous body approach to the flow field analysis of the triangular wire-wrapped rod bundle, inherent assumptions in the porous body analysis are addressed. Finally, a wide variety of possible control volume layouts for the porous body approach are considered. By examining these layouts with respect to the available experimental data, we suggest an optimum control volume layout.

3.2 Comparisons between the Porous Body and the Subchannel Approaches

Principle differences between the two approaches exist in the formulation of the momentum equations and in the choice of the computational mesh cell. Thus, our discussion is mainly focused on the mathematical formulations and approximations introduced in the derivation of the momentum equations and emphasis is put on the control volume geometry employed by each approach.

3.2.1 Momentum Equation

For the porous body approach, the finite difference form of the linear momentum equation in the x direction is given in Eq.(2.15). The momentum equations in the y and z directions can be obtained in a similar manner.

The axial momentum equation of the subchannel approach can be derived from the general integral momentum equation, i.e., Eq.(2.5). The detailed derivation can be found in reference (T-1). The finite difference form including the turbulent mixing is written as,

$$\frac{\partial \langle \dot{m}_i \rangle}{\partial t} + \frac{\Delta(\dot{m}_i w_i)}{\Delta z} + \sum_j W_{ij}\{w^*\} = -A_{fi}\langle \rho \rangle g_z - A_{fi}\frac{\Delta(^z\{p\})}{\Delta z}$$

$$- \sum_j W_{ij}^{*M}(w_i - w_j) - \{\frac{F_{iz}}{\Delta z}\} \qquad (3.1)$$

The transverse momentum equation can be derived as,

$$\frac{\partial}{\partial t}(W_{ij}) + \frac{\Delta(W_{ij}\{w\})}{\Delta z} + \frac{\Delta(W_{ij}\{u\})}{\Delta x'} = -s_{ij}\frac{\Delta(^t\{p\})}{\Delta x'} - \{\frac{F_{ix}}{\Delta x'\Delta z}\} \qquad (3.2)$$

where,

$\dot{m}_i$ - area averaged mass flow rate for subchannel i $(=\{\rho w\}A_{fi})$

$\langle \dot{m}_i \rangle$ - volume averaged mass flowrate for subchannel i

w_i - area averaged axial velocity $(=\{w\})$

W_{ij} - diversion crossflow rate between subchannels i and j

$\{w_i^*\}$ - effective velocity transported by diversion crossflow rate,

$$(= \frac{\{\rho uw\}}{\{\rho u\}})$$

A_{fi} - axial cross-sectional subchannel flow area

W_{ij}^{*M} - turbulent momentum interchange flow rate

s_{ij} - gap thickness

$\{\frac{F_{iz}}{\Delta z}\}, \{\frac{F_{ix}}{\Delta x \cdot \Delta z}\}$ - total drag force in the z and x directions acting on the solid surface

$^t\{p\}$ - pressure averaged over the control volume surface normal to the transverse direction

The assumptions used in deriving these equations are tabulated and compared with those of the porous body approach in Table 3.1. Most approximations presented for the porous body approach result from the discussion of Section 2.4.4. In addition, the approximations used in computer codes are also addressed.

The fundamental difference between the momentum equations of these two approaches can be described as follows: The porous body approach considers full 3-dimensional flow convection simultaneously, whereas the subchannel approach only considers the momentum interaction between adjacent subchannels. Therefore, the cross product term of the transverse momentum convection in the transverse momentum equation is not usually incorporated in the subchannel approach. Thus, the porous body approach is superior to the subchannel approach in the mathematical sense if the governing equations can be properly formulated in a numerical code.

Table 3.1 Approximations Employed in the Derivation of the Momentum

Equations and Required for Numerical Implementation of the

Porous Body and the Subchannel Approaches

Porous Body Approach	Subchannel Approach
The cross products of the spatial fluctuation terms, $\{u'w'\}$, $\{\rho'u'w'\}$ etc. are neglected. $\{\rho uw\} = \{\rho\}\{u\}\{w\}$	$\{\rho uw\} = \{\rho u\}\{w\}$
The volume average quantities are assumed equal to the surface average or a simple relation based on continuity is used. $\langle \rho u \rangle = \{\rho u\}$ or $\langle \rho u \rangle = \dfrac{\gamma_{Ax}}{\gamma_V}\{\rho u\}$ (COMMIX)	$\langle \rho w \rangle = \{\rho w\}$
	The lateral cross products in the momentum convection and the molecular shear force on the fluid are neglected. $^{it}\{\rho uv\} = 0$, $\{\tau_{xy}\} = 0$

Table 3.1 (continued)

Porous Body Approach	Subchannel Approach
$\nabla\langle p\rangle \approx \gamma_V \nabla^i \langle p\rangle$ (COMMIX) or different surface-averaged pressures are assumed equal to each other, i.e., $^x\{p\} \approx {}^y\{p\} \approx {}^z\{p\}$ (THERMIT)	$^t\{p\} = {}^z\{p\}$ and the pressure varies linearly in each direction (COBRA).
Relationship between $^x\{u\}$, $^y\{u\}$ and $^z\{u\}$ etc. is required, e.g., $^y\{u\} \approx {}^z\{u\} \approx {}^x\{u\}$	$^z\{\rho u\} \approx {}^t\{\rho u\}$
Linear flow area variation is assumed. (THERMIT)	The flow area variation is linear axially. (COBRA)
Calculated velocity should be interpreted as an averaged value over a given control volume. (THERMIT)	

3.2.2 Computational Mesh Cell

Another big difference between the two approaches is the choice
of the computational mesh cell. As mentioned before, the control
volume geometries are different from each other for a triangular
array. In the subchannel approach, the control volume is uniquely
chosen so as to include the fluid portion only. Typical grid layouts
for subchannel analysis are depicted in Figures 3.1(a) and 3.1(b) for
the mass/energy/axial momentum control volume and the transverse
momentum control volume respectively. The axial momentum control
volume should be staggered in the axial direction with respect to the
mass/energy control volume.

In the porous body approach, the grid layout chosen depends on
the coordinate system employed. Although some computer codes use the
cylindrical coordinate system, it leads to a coarse mesh
representation for mesh cells far from the center of a system. Also
the control volume boundaries become too complicated. Since our
primary interest is to obtain the flow field in coolant regions of
subchannel size, meshes that are too coarse should be avoided in our
analysis. Moreover, since the THERMIT code, which is our numerical
tool for the porous body approach, uses the Cartesian coordinate
system, our discussion on the computational mesh cell of the porous
body approach will be concentrated on this system.

In the porous body approach with the Cartesian coordinate system,
the control volume should be chosen as an orthogonal parallelepiped
which includes both fluid and solid. The solid portion is treated as
a distributed resistance for the calculation of the velocity and the
pressure fields, and is treated as a distributed heat source or sink
for the calculation of the temperature field. The grid layout of the
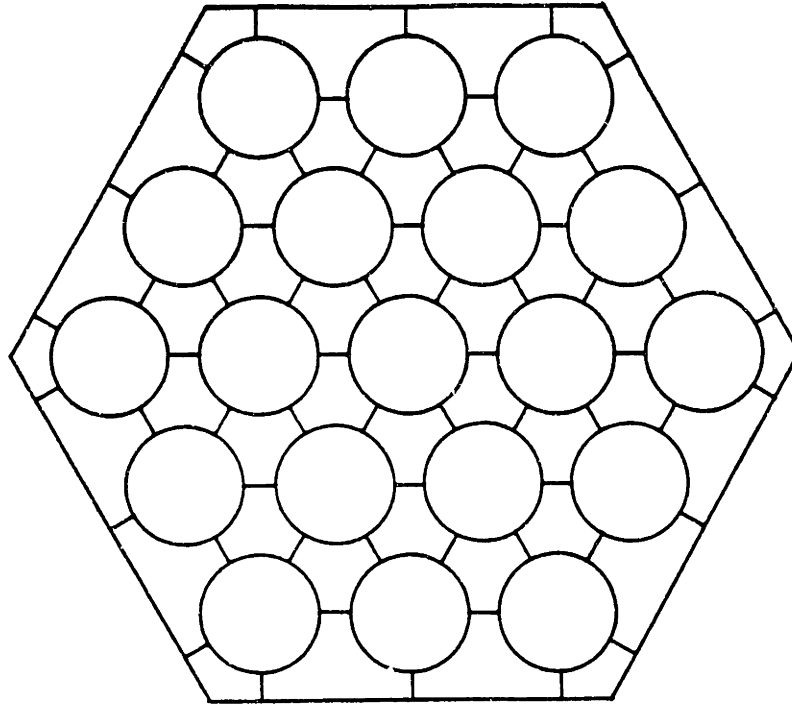
Figure 3.1(a)   Control Volume Geometry of the Subchannel
Analysis - Mass/Energy/Axial Momentum
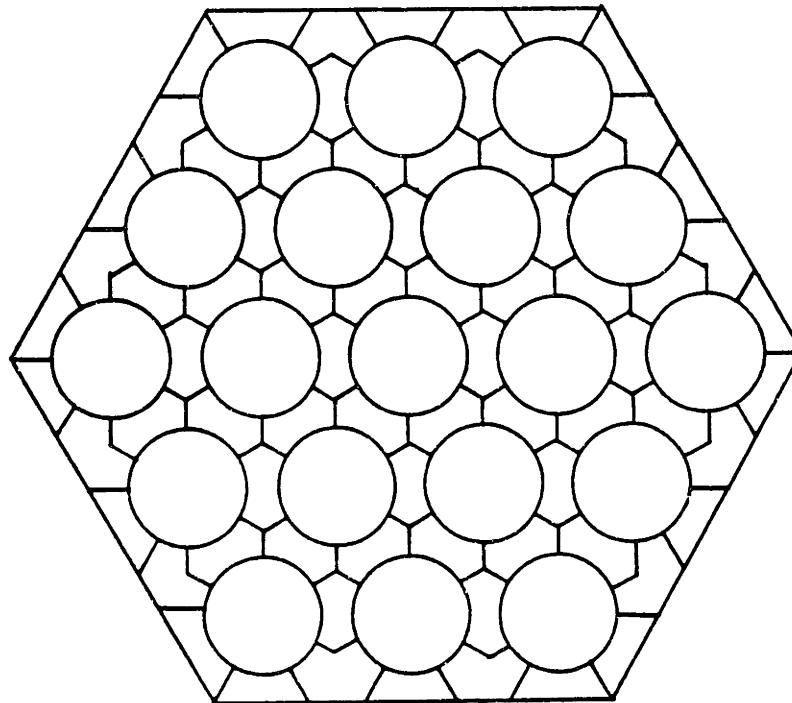
Figure 3.1(b)   Control Volume Geometry of the Subchannel
Analysis - Transverse Momentum

porous body approach can be chosen arbitrarily. However, the choice of a
relevant control volume is a very difficult task. Detailed analyses
supporting the choice of an optimum control volume will be presented in
Section 3.4. For the purpose of comparing with the subchannel analysis, a
typical mesh configuration, i.e., single-pin layout, is shown in Figures
3.2(a), 3.2(b) and 3.2(c) for the mass/energy/z-momentum, the x-momentum
and the y-momentum control volumes, respectively.

3.3 Assumptions of the Porous Body Approach in Wire-Wrapped Bundle Analysis

In this section several fundamental assumptions addressed in Section
3.2.1 are examined and the validity of these assumptions in the wire-
wrapped rod bundle analysis is checked.

3.3.1 Cross Product of the Spatial Fluctuation Terms

The important spatial fluctuation terms in the momentum equations
come from the cross product of the velocity components. Although some
cross product terms of the density with the velocity component appear in
the equations, these terms may be neglible or small compared with the
cross product of the velocity components in a single phase flow. The
spatial velocity fluctuation terms, e.g., $^x\{u'u'\}$, $^y\{u'v'\}$, $^z\{u'w'\}$, etc.
for the wire-wrapped rod bundle geometry may not be negligible as they are
in the bare rod bundle geometry, since the velocity profile is more
nonuniform due to the presence of the wire spacers.

The correct execution of the averaging process to obtain the
fluctuation terms as $^x\{u'u'\}$ is impossible without prior information on
the detailed distribution of the velocity field within a control volume.
The velocity field can be obtained by a fine mesh calculation with a
distributed parameter code, or directly from experimental data.
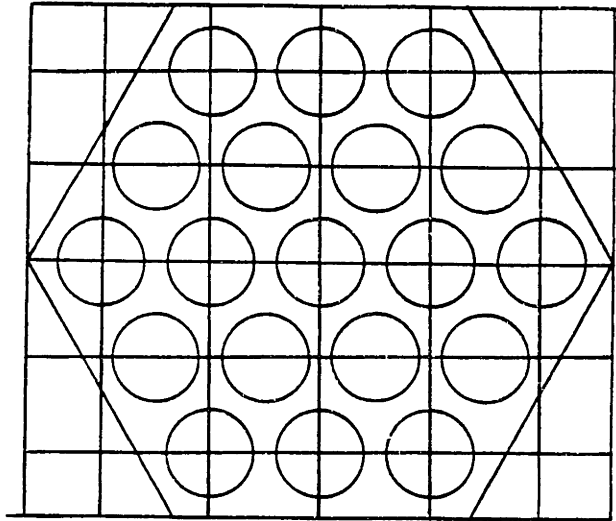
(a) Mass/Energy/Z-Momentum
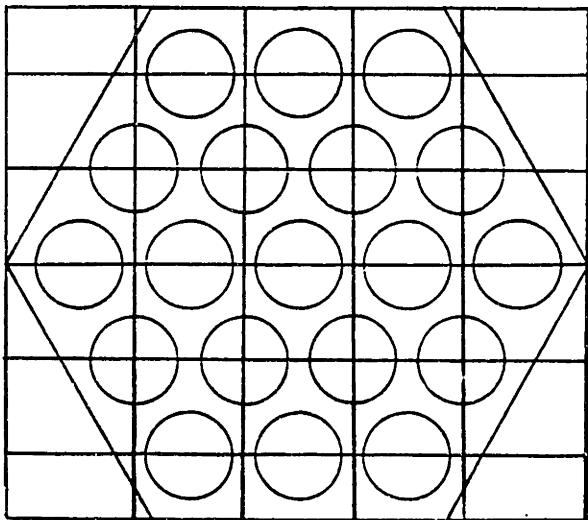
(b) X-Momentum
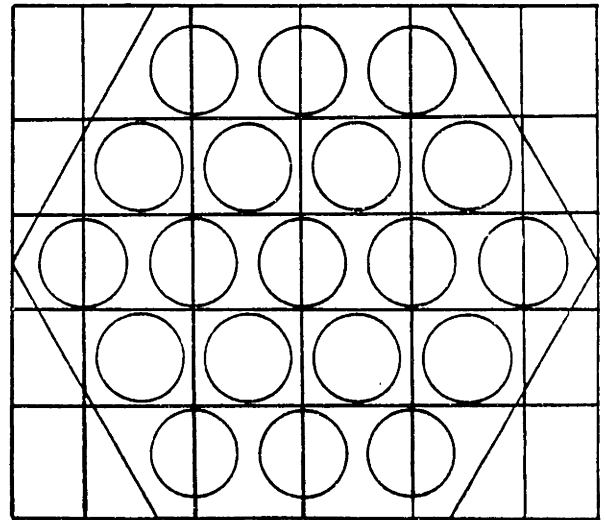
(c) Y-Momentum

Figure 3.2 Control Volume Geometry of the Single-Pin Layout

By decomposing the velocity into three principal directions and finding the average and fluctuating velocity component for each direction the cross products of the fluctuating velocities can be calculated. Another approach is to find the functional dependencies of the fluctuation terms and to make a proper correlation. The undetermined constants in the correlation should be provided by experimental data or a fine mesh calculation. The fluctuation terms may be functionally dependent on position, average velocity, velocity gradient and the parameters appearing in the boundary conditions. An example of this approach is the analysis of the dispersion equation for a single, nonreacting, nonabsorbing species presented in reference (W-1). However, a great deal of effort and time are required to evaluate the cross product fluctuating terms by either method mentioned above. Instead, by choosing an appropriate control volume layout we can make these terms quite negligible.

For example consider the convection terms in Eq.(2.15) in more detail. The x direction convective fluctuation term which is obtained by applying Eq.(2.22) can be approximated as,

$$\frac{\Delta_{x'}{}^{x}\{\rho u'u'\}}{\Delta x} \approx \rho \frac{\Delta_{x'}{}^{x}\{u'u'\}}{\Delta x} \approx \frac{\rho}{\Delta x} \left[{}^{x}\{u'u'\}_{RHS} - {}^{x}\{u'u'\}_{LHS}\right] \quad (3.3)$$

where ${}^{x}\{u'u'\}_{RHS}$ stands for the fluctuation value at the right-hand side of the x-momentum control volume surface, and ${}^{x}\{u'u'\}_{LHS}$ at the left-hand control volume surface. This term can be small if both ${}^{x}\{u'u'\}_{RHS}$ and ${}^{x}\{u'u'\}_{LHS}$ are small or if their difference is small. The difference between these terms can be made negligible if the control volume

boundaries are chosen properly to give the same velocity profile at both boundaries. A good example is the single-pin control volume layout which will be explained later.

3.3.2 Surface and Volume Averaged Quantities

In the governing equations, two kinds of quantities were defined: surface averaged values, $\{\psi\}$, and volume averaged values, $\langle\psi\rangle$. Sha and Chao (S-1) have employed a number of assumptions to develop a relationship between these two quantities. However no general relationship between the two has been presented in the literature. The relationship is a function of geometry and the spatial distribution of the given property. The property, ψ, can be density, velocity and enthalpy. The spatial distribution of these properties cannot be known a priori except for special cases such as an isothermal flow condition. In most porous body and subchannel codes, the volume averaged quantity is assumed to be equal to the surface averaged quantitity. This approximation is not valid if the distribution of the quantity within a control volume is highly nonuniform as in the case of the wire-wrapped rod bundle geometry.

3.3.3 Surface Averaged Properties in the Different Directions

Most of the velocity components in the governing equations are averaged over the surface areas of a control volume. Each velocity component has three kinds of surface averaged velocity, for example, $^x\{u\}$, $^y\{u\}$, $^z\{u\}$ for the x component velocity. Moreover, since the momentum control volume is staggered, the areas where the averaging is

performed will be the surfaces of both momentum and mass/energy control volumes. All the surfaces where the averaging of the velocity is performed are explicitly identified in Table 2.1. This variety of surface areas requires some correlations or approximations which can relate a representative velocity, e.g., $^x\{u\}$ with the others.

For the THERMIT code, no rigorous formulation has been made. Instead, by introducing some assumptions, the code effectively takes all these values as equal. Appendix D of the THERMIT manual (R-1) describes a derivation of the momentum equations of the THERMIT code from the control volume momentum balance equation, and shows which assumptions are necessàry to get the final first-order approximate equation. The main concept of the assumptions is that the solid is uniformly distributed within a control volume, i.e., the free flow area is constant in all directions. For the z direction parallel to the rods in the wire-wrapped rod bundles, this assumption is acceptable. However, for the x and y directions, the flow area changes significantly across the control volume. In the THERMIT code, to overcome this difficulty, a compromise is made such that the surface flow area is obtained by dividing the sum of two adjacent volumes by the total thickness. This leads to some error in the solution of the mass and energy equations since the true area average of the mass/energy control volume is not utilized. Therefore, the calculated transverse velocity should be interpreted as the velocity at the hypothetical surface with such an averaged flow area.

3.4 Determination of the Optimum Control Volume Layout

In the previous section, we mentioned the importance of the control volume choice in the porous body approach. In this section we investigate some representative control volume layouts and show how to determine an optimum control volume. In order to choose the optimum control volume layout among the various layouts, four control volume layouts were selected for examination. These are the single-pin, half-pin, quarter-pin, and staggered half-pin layouts. The first three have been generally used in triangular wire-wrapped rod bundle analysis. The last one was generated during this work and appears to have a favorable geometry. The grid configurations of these four layouts are shown in Figures 3.2(a), 3.3, 3.4 and 3.5. All these layouts represent the mass/energy/z-momentum control volume geometry. For the x- and y-momentum control volume geometries, the grid should be staggered in the positive x and y directions. Figures 3.2(b) and 3.2(c) illustrate the staggered x- and y-momentum control volumes for the single-pin layout.

For the axial direction, an axial mesh size should be selected to account for the variation of the velocity field along the axial direction. Figure 3.6 shows the transverse flow as a function of the wire wrap angle or equivalently the axial location (R-3). From this figure, one can infer that the axial mesh size equal to H/12, i.e., 30°, where H is the wire wrap lead length, is a satisfactory compromise between resolution of the flow field variation and computing time.

The optimum control volume is the volume which balances accuracy and computing time. Computing time is the more easily assessed quantity since it is proportional to the number of mesh points. From this point of view, the single-pin layout shown in Figure 3.2 is the most cost effective
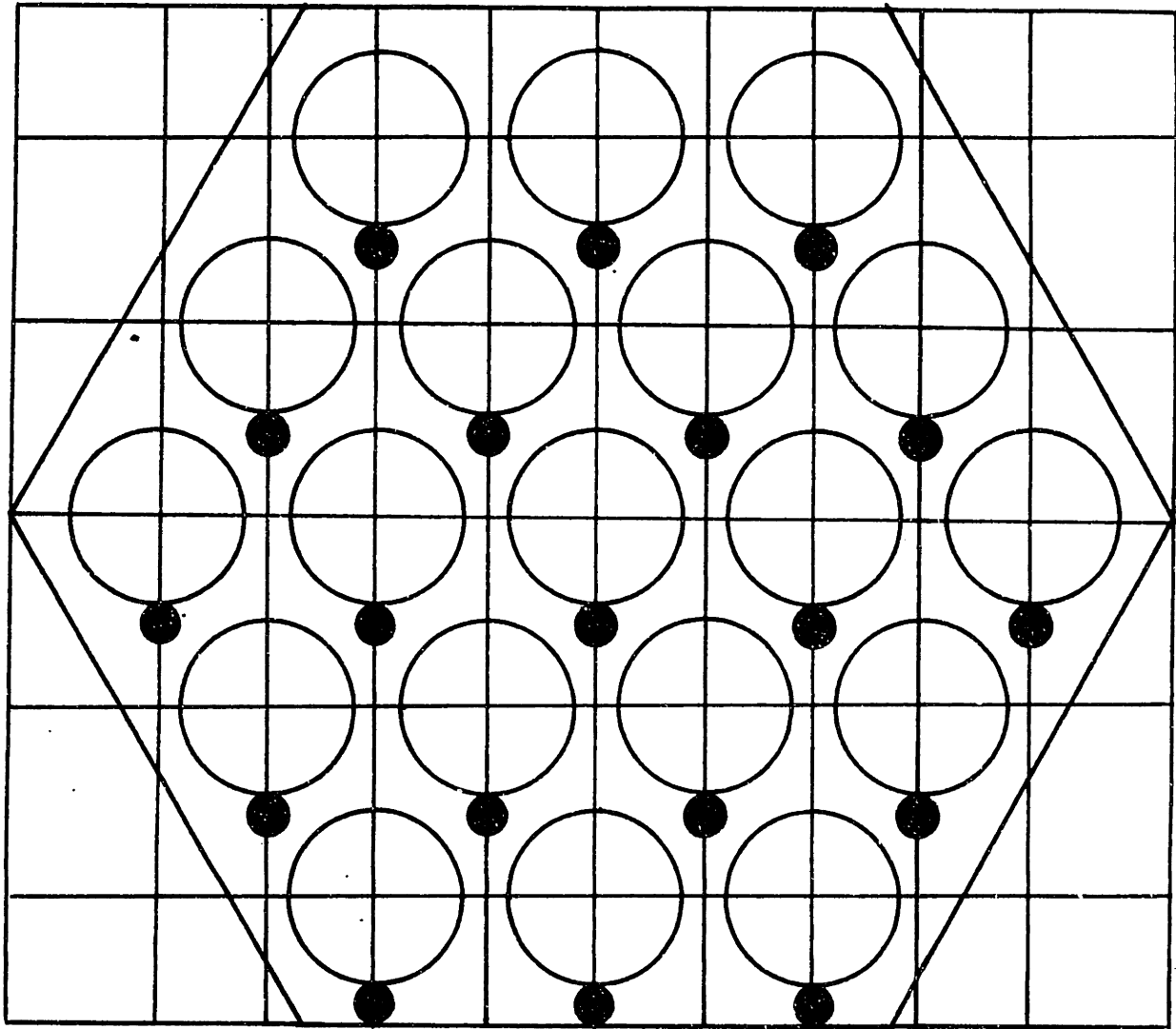
Figure 3.3 Control Volume Geometry of the Half-Pin Layout
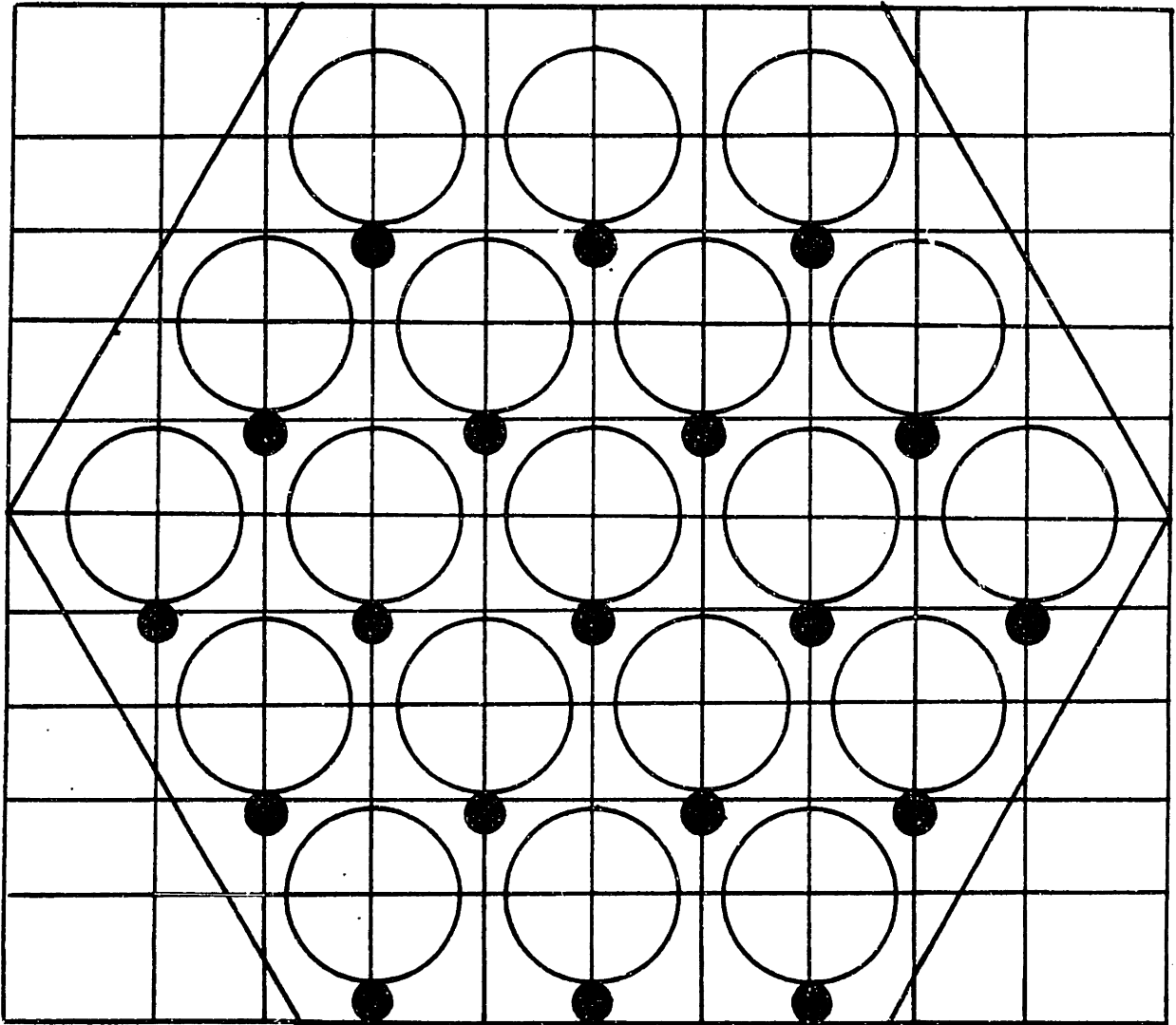
Figure 3.4 Control Volume Geometry of the Quarter-Pin Layout
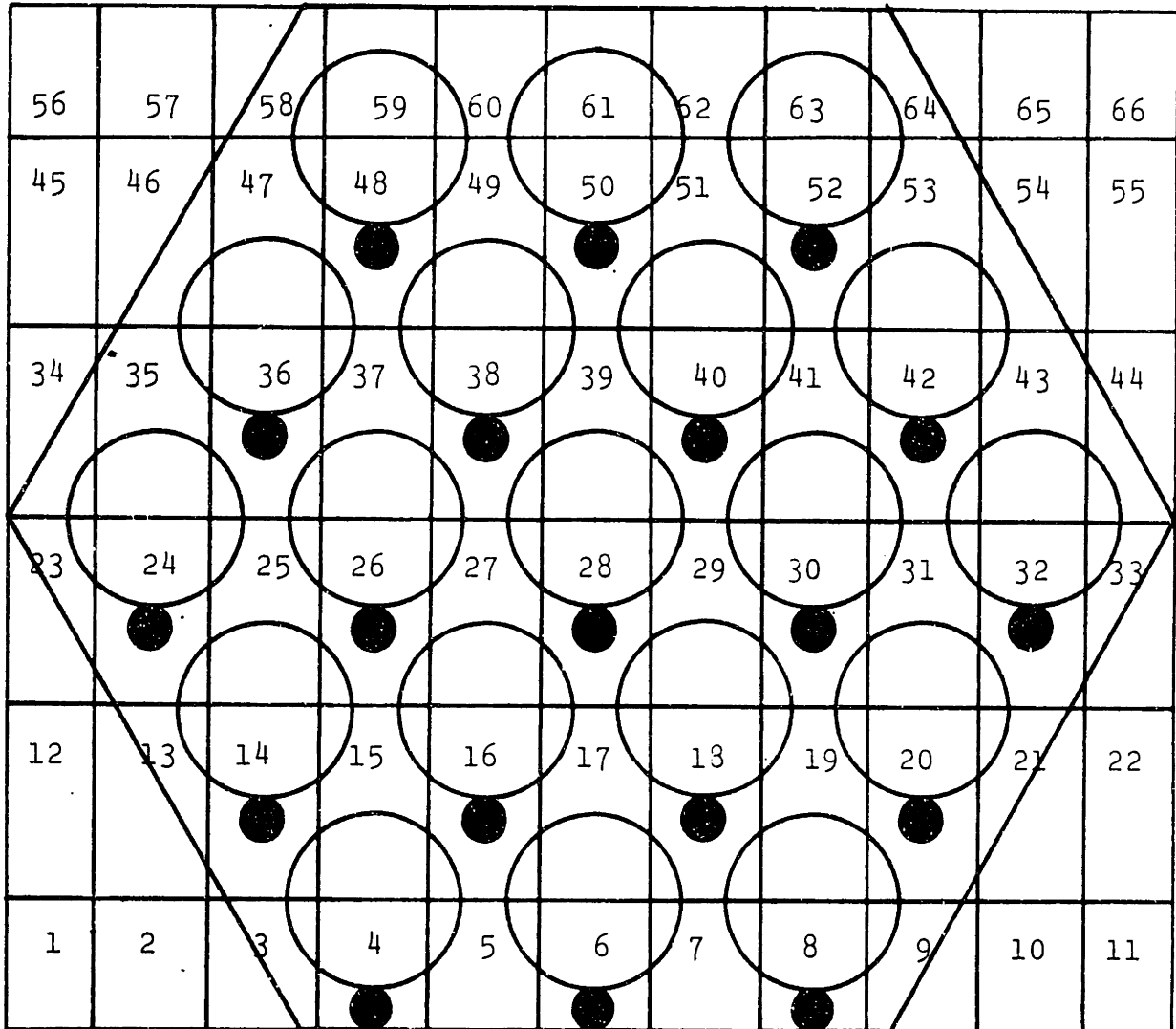
Figure 3.5   Control Volume Geometry of the Staggered Half-Pin
Layout
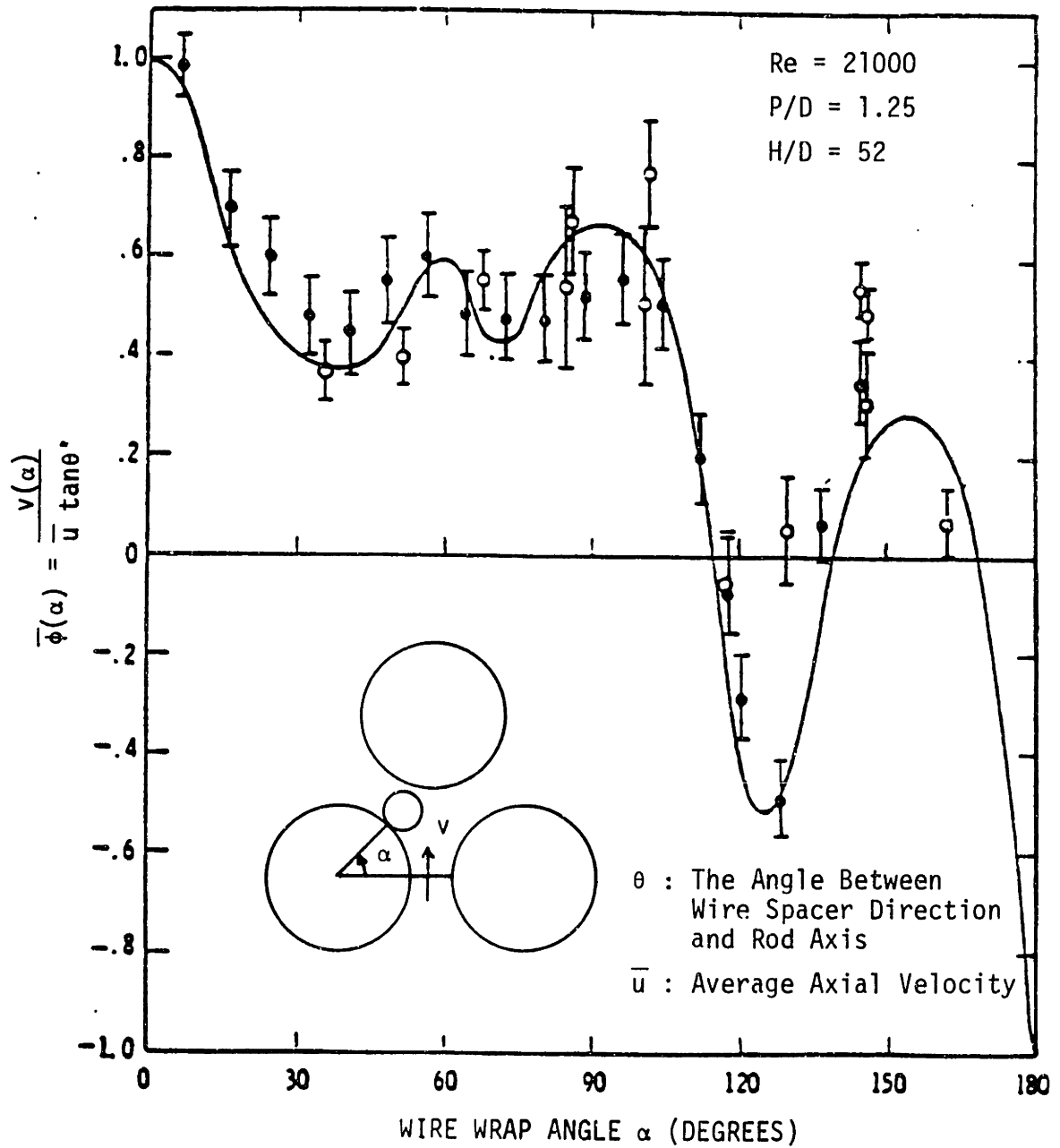
Figure 3.6 Transverse Flow Variation Along the Axial Direction
in Interior Gap (Taken from Reference R-3)

approach among the selected control volume layouts. Total number of radial mesh points for a 19 pin triangular array bundle is 32 for the single-pin layout. The half-pin or the staggered half-pin layout employs around 55 mesh points, which requires more than twice the computing time compared with the single-pin layout. For the quarter-pin layout, the number of mesh points is 92, which requires more than three times the computing time of the single-pin layout. However, use of a more refined mesh layout does not guarantee improvement in accuracy. Therefore, if the accuracy is not substantially improved, one should avoid choosing a smaller mesh size such as the quarter-pin layout.

To assess the accuracy the terms of the axial and transverse momentum equations will be examined. From Eq. (2.31) for steady state, the following terms should be evaluated for both the axial and transverse momentum balances, i.e.,

(1) The spatial velocity fluctuations involved in the momentum convection term:

$$\frac{1}{V} \int_{A_f} \rho \vec{v}(\vec{v} \cdot \vec{n}) dA$$

(2) The pressure term:

$$\frac{1}{V} \int_{A_f} p \vec{n} dA$$

(3) The distributed resistance:

$$\frac{1}{V} \int_{V_f} \vec{R}' dV$$

3.4.1 Spatial Velocity Fluctuations

The spatial velocity fluctuations appear in the momentum equations, e.g., Eq. (2.15) by introducing Eq. (2.22). They are,

$$^x\{u'u'\}, \quad ^y\{u'v'\}, \quad ^z\{u'w'\} \quad \text{for x-momentum,}$$

$$^x\{v'u'\}, \quad ^y\{v'v'\}, \quad ^z\{v'w'\} \quad \text{for y-momentum,}$$

$$^x\{w'u'\}, \quad ^y\{w'v'\}, \quad ^z\{w'w'\} \quad \text{for z-momentum.}$$

The fluctuating cross products with different velocity components (e.g., $^y\{u'v'\}$) are expected to be smaller than their own cross products (e.g., $^x\{u'u'\}$) since the spatial distribution of the velocity component is different from each other. Therefore, only three terms, $^x\{u'u'\}$, $^y\{v'v'\}$ and $^z\{w'w'\}$ will be examined in this section.

A few experimental studies have been performed to measure the local axial and transverse velocity fields within wire-wrapped rod bundles. Japanese experiments (O-1) have produced detailed flow maps within a subchannel, but the experimental data were obtained only at two axial planes. Westinghouse experiments (B-2, B-3) were performed at various axial planes, but since transverse velocities were measured only at the gap, detailed transverse flow maps within a control volume were not obtained. MIT laser Doppler experiments (C-2) measured the velocity field only in the edge subchannels. Complete transverse velocity maps were not obtained because of the interference of the rod geometry with the laser beams near the edge-interior subchannel boundary. Therefore, for interior subchannels, the Japanese experimental data are the most useful for our purpose of investigating the velocity field. For a side subchannel, both the MIT laser Doppler measurements and Japanese experimental data are useful.

The typical axial and transverse velocity fields for the interior subchannels are shown in Figures 3.7 and 3.8. For the side subchannels, the axial and the transverse velocity fields are shown in Figures 3.9 and
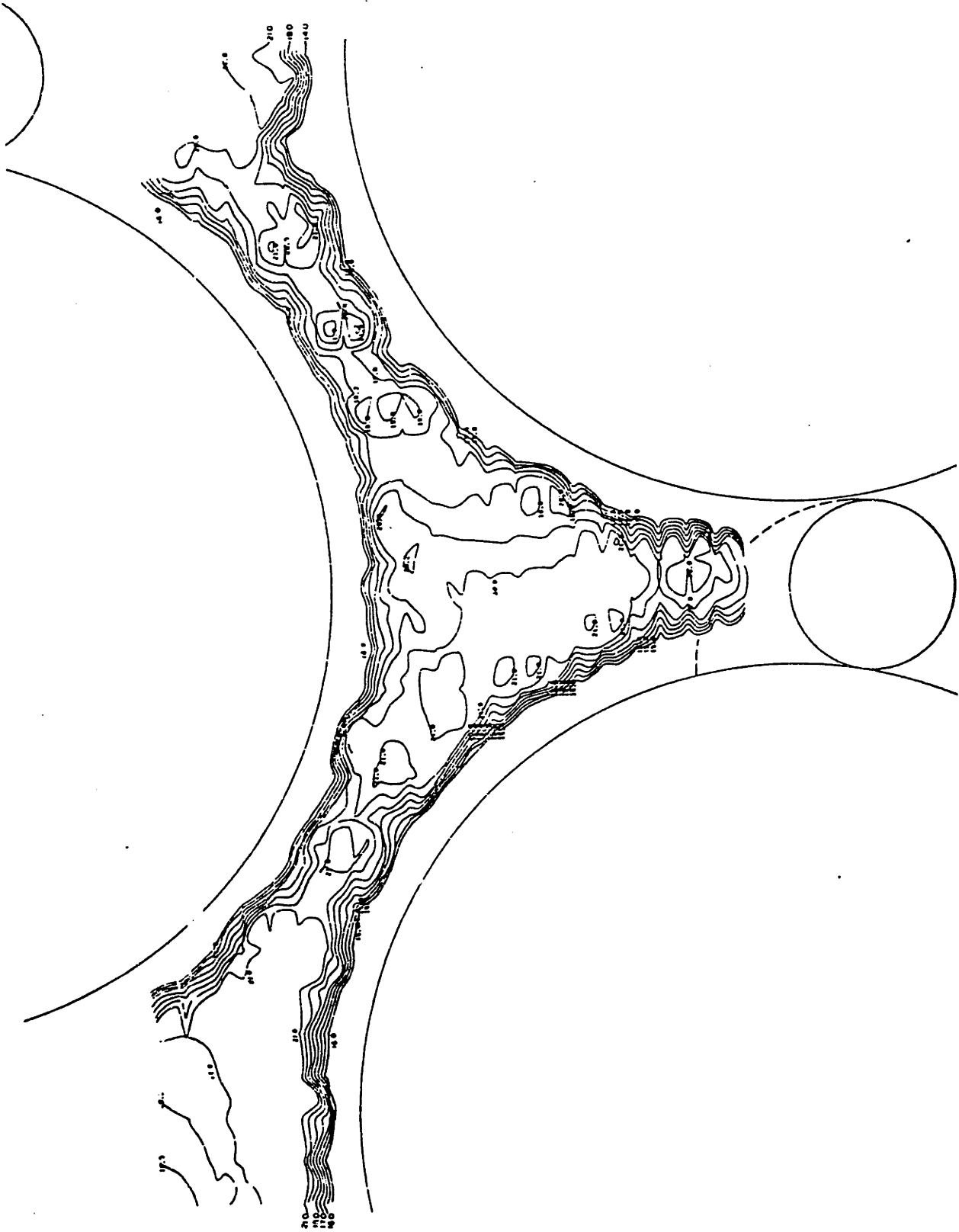
Figure 3.7 Axial Velocity Distribution in Interior Subchannel
(Taken from Reference 0-1)
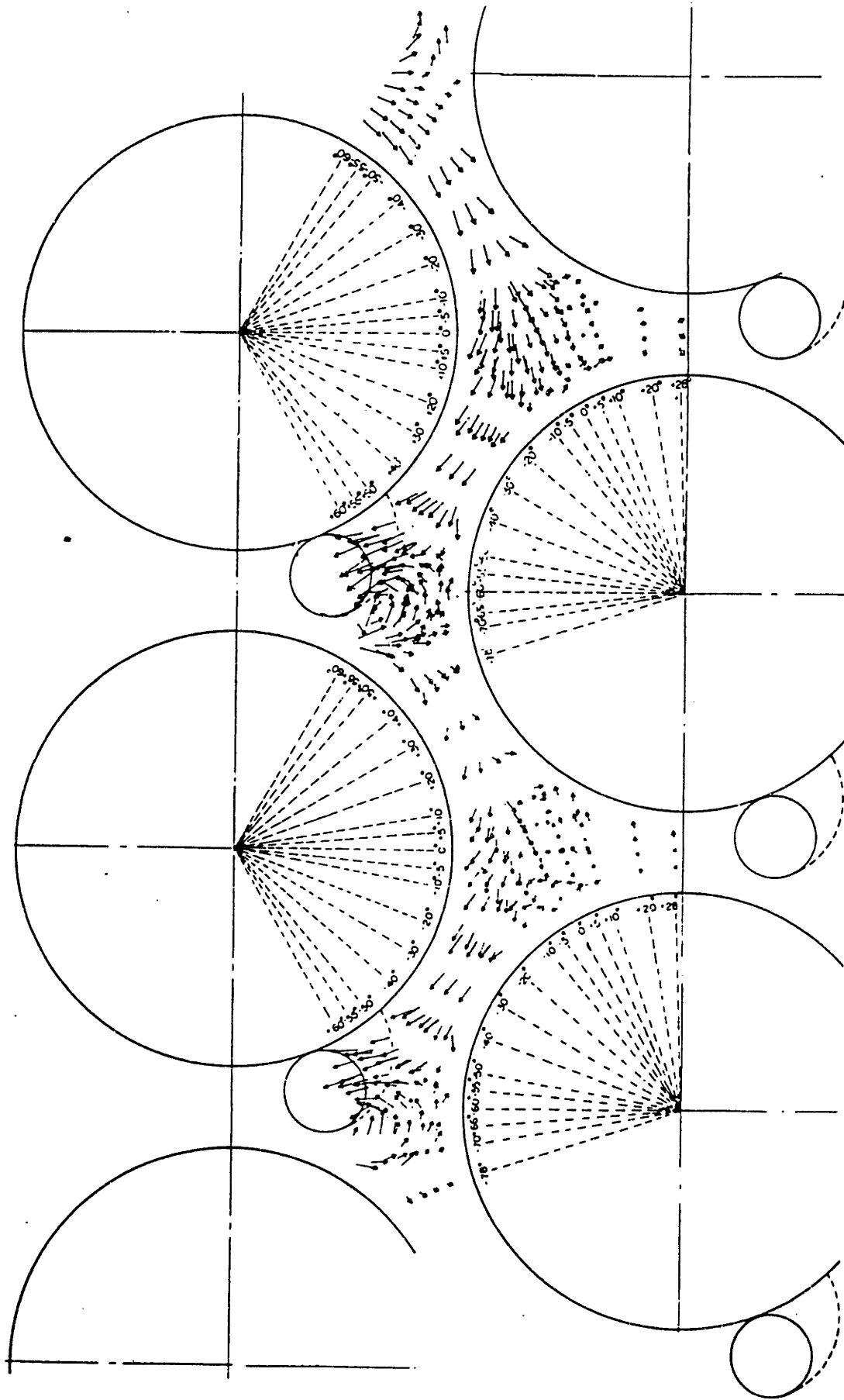
Figure 3.8 Transverse Velocity Distribution in Interior Subchannel
(Taken from Reference 0-1)

Re ≈ 670
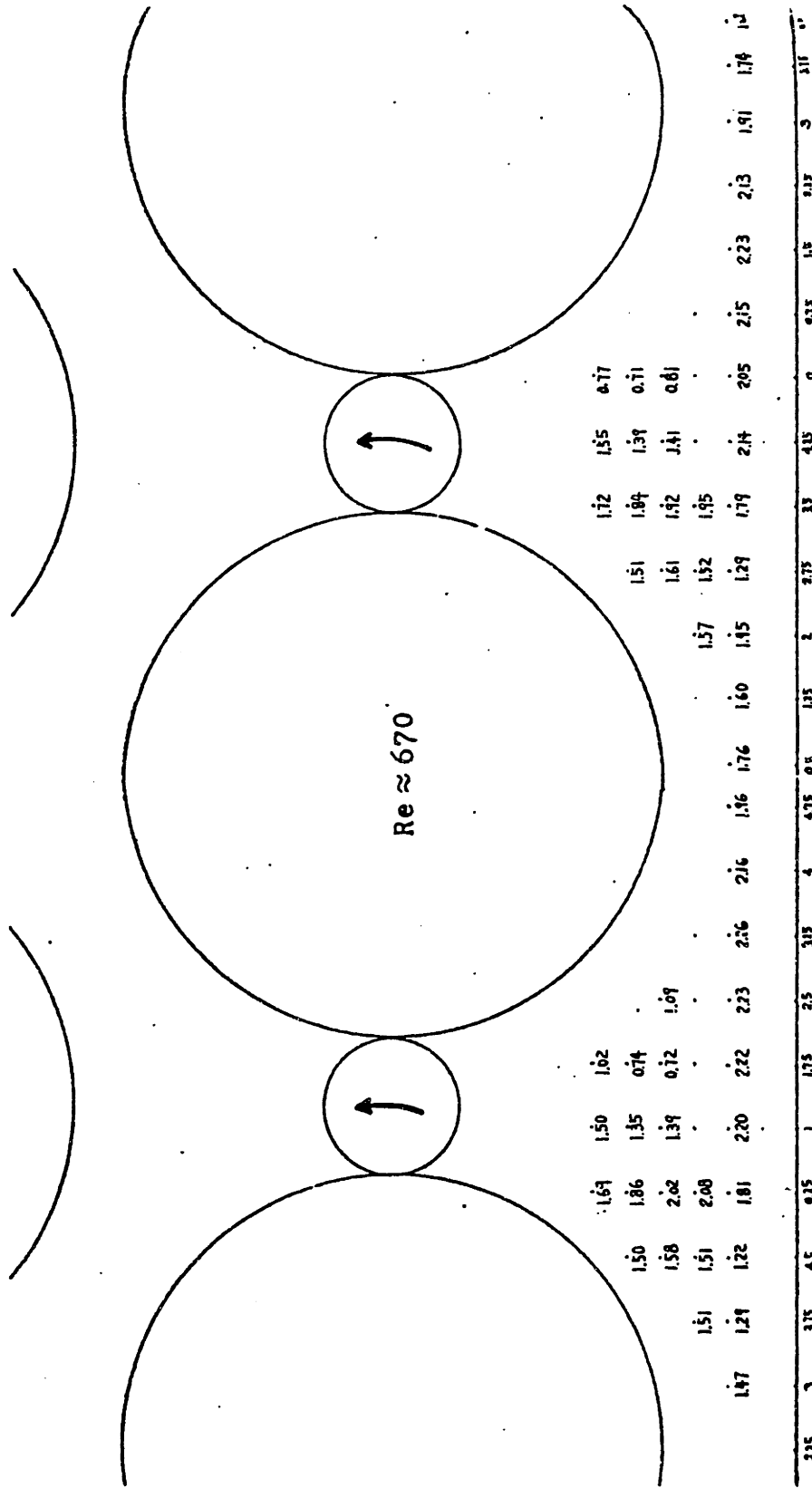
Figure 3.9 Axial Velocity Distribution in Edge Subchannel
(Taken from Reference C-2)
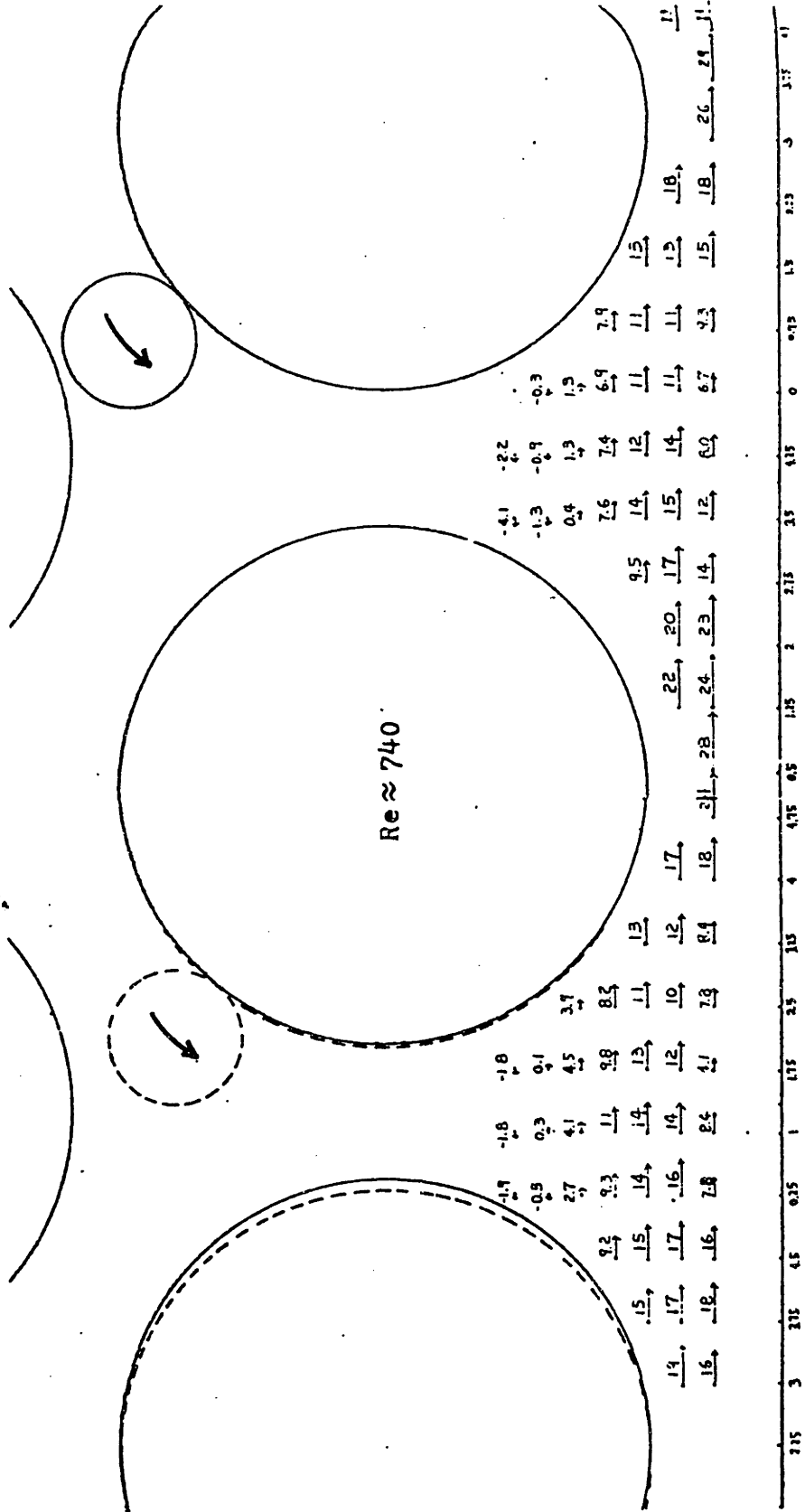
Figure 3.10 Transverse Velocity Distribution in Edge Subchannel
(Taken from Reference C-2)

3.10. As one can observe from these figures, the velocity field within a control volume is neither uniform nor linear. This nonlinearity of the velocity field as well as the complexity of the wire-wrapped rod bundle geometry requires that the approximations made for the momentum equations be checked.

3.4.1.1 Axial Velocity Fluctuation Term, $^z\{w'w'\}$

The axial velocity data (see Figure 3.7) show a large deviation from the average velocity near the solid wall. This observation infers that the magnitude of the spatial velocity fluctuation is proportional to the ratio of the solid surface area to the free flow area within a control volume. Table 3.2 shows the ratio for each control volume layout for the conditions of the wire present and absent from the control volume. The overall evaluation of the fluctuating term for these layouts must consider both these conditions of wire present and absent but it is not obvious how to weight these components, i.e., while S/F is greatest for the quarter-pin layout with the wire present, this condition occurs only over 25% of an axial lead length. Therefore the table includes the ratio S/F averaged over a full wire lead length and this is the condition upon which the layouts are compared. The ratio averaged over one wire lead length shows similar values for all control volume layouts. The single-pin layout yields slightly smaller ratio than other layouts which corresponds to less spatial velocity fluctuations. The quarter-pin layout yields the largest ratio, i.e., largest spatial velocity fluctuations. In all these cases the effect of wake generated by the wire spacer on the axial velocity profile is neglected.

3.4.1.2 Transverse Velocity Fluctuation Terms, $^x\{u'u'\}$ and $^y\{v'v'\}$

The transverse velocity profile has been investigated by

Table 3.2   The Ratio of the Solid Surface Area to the Free Flow Area

for Each Layout

Layout	Fraction of Wire Spacer Present in Each Control Volume Over a Wire Lead Length	Wire Present		No Wire Present		One Wire Lead Length Averaged S/F
		Per-cent	S/F*	Per-cent	S/F	
Single-Pin	12/12	100%	$$\dfrac{\pi D + \pi D_W}{\dfrac{\sqrt{3}}{2}P^2 - \dfrac{\pi}{4}D^2 - \dfrac{\pi}{4}D_W^2}$$ $$\approx 7.57/D$$	0%	$$\dfrac{\pi D}{\dfrac{\sqrt{3}}{2}P^2 - \dfrac{\pi}{4}D^2}$$ $$\approx 5.53/D$$	7.57/D
Half-Pin	6/12	50%	$$\dfrac{\dfrac{1}{2}\pi D + \pi D_W}{\dfrac{1}{2}(\dfrac{\sqrt{3}}{2}P^2 - \dfrac{\pi}{4}D^2) - \dfrac{\pi}{4}D_W^2}$$ $$\approx 10.04/D$$	50%	same	7.79/D
Quarter-Pin	3/12	25%	$$\dfrac{\dfrac{1}{4}\pi D + \pi D_W}{\dfrac{1}{4}(\dfrac{\sqrt{3}}{2}P^2 - \dfrac{\pi}{4}D^2) - \dfrac{\pi}{4}D_W^2}$$ $$\approx 16.92/D$$	75%	same	8.38/D
Staggered Half-Pin	6/12	50%	same as the Half-Pin	50%	same	7.79/D
Sub-channel	6/12	50%	same as the Half-Pin	50%	same	7.79/D

*S/F = the ratio of the solid surface area per unit axial length to the free flow area. Numerical values are obtained based on P/D=1.25 and D_W=P-D :wire spacer diameter.

superimposing the flow maps onto each specific control volume. For the single-pin layout, the velocity distributions at the surfaces perpendicular to the transverse direction in the transverse control volume are not uniform (see Figure 3.8), which yields nonnegligible fluctuation terms. However, although both $^x\{u'u'\}_{RHS}$ and $^x\{u'u'\}_{LHS}$ are neither small nor negligible, the difference between these terms is negligible for the single-pin layout since the velocity field at the boundaries is periodic as shown in Figure 3.8. Consequently, the convective fluctuation terms (refer to Eq.(3.3)) in the transverse directions are negligible. This logic cannot apply to the side subchannels and subchannels near the wall since the periodicity is lost. For the other porous body layouts as well as the subchannel analysis control volume, the velocity distributions at the transverse control volume boundaries are neither uniform nor periodic. Therefore, the spatial fluctuation terms may cause a large error. However, the staggered half-pin layout has an advantage in the calculation of the y-momentum equation. The y-momentum control volume of this layout is staggered to the y direction relative to the mass/energy control volume shown in Figure 3.5. Then, the y component of the velocity is alternatively zero since this velocity component is taken at the center of the control volume which is occupied by the fuel rod. This reduces the error otherwise involved in the convection terms as well as the computing time.

3.4.2 Pressure Term

Few measurements of the pressure field within subchannels are available so far. Experiments performed by Sarno et al. (S-4) have provided a rough idea on the pressure field in the subchannels. This result is presented in Figure 3.11. This figure indicates that the stagnation region upstream of the wire wrap spacer has higher pressure

WIRE SPACER
POSITION AND DIRECTION
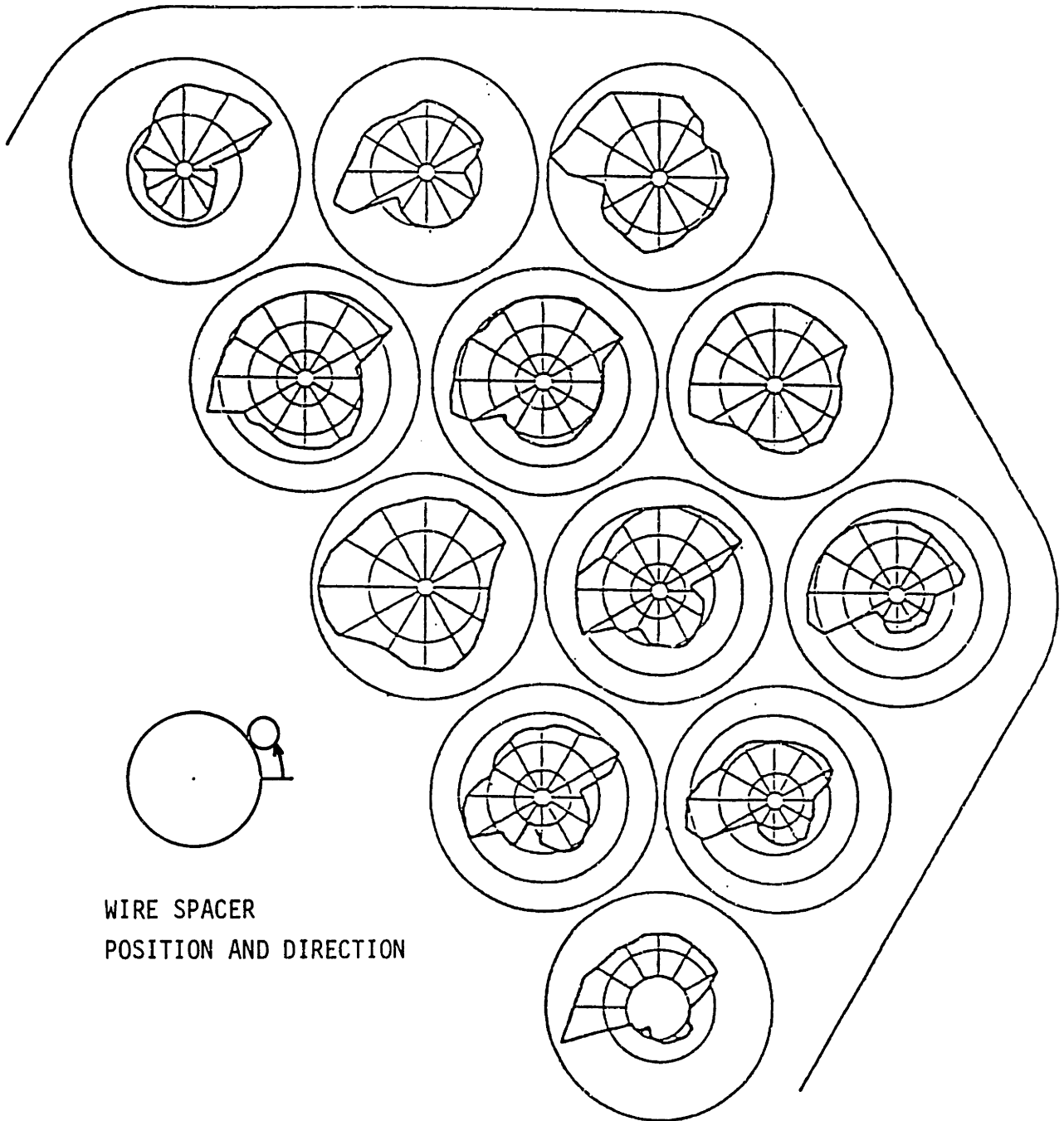
Figure 3.11 Pressure Distribution Around Wire-Wrapped Rods
(Taken from Reference S-4)

than the wake region downstream. This result agrees well with the experimental result obtained by Lafay et al. (L-1).

From Figure 3.11, it is observed that the pressure field is strongly dependent upon the wire spacer location. The wire spacer changes the axial free flow area. The flow area difference between adjacent subchannels leads to an axial pressure drop difference which enhances the crossflow driving force. Therefore, in order to obtain the correct diversion crossflow between the interior subchannels, the control volume layout should be selected so that the adjacent subchannels have different flow areas, e.g., a subchannel includes the wire spacer while the neighboring subchannel does not. For the single-pin layout, the control volume geometries of adjacent interior subchannels are always the same at every axial elevation. Thus, there is no driving force for diversion crossflow induced by the geometrical differences, although a small driving force may be present because of the effect of the flow area differences between peripheral and interior subchannels. On the other hand, the other control volume layouts satisfy this requirement by alternative appearance of the wire spacers in adjacent subchannels.

When the assumption of the equality among the pressures averaged over different surfaces, i.e., $^x\{p\}=^y\{p\}=^z\{p\}$ is used, detailed pressure distributions both in the axial and radial directions should be provided. Since the detailed axial pressure distribution for each control volume surface is not available, relevant examination cannot be performed.

3.4.3 Applicability of the Constitutive Correlations

3.4.3.1 Availability of the Friction Factor Correlations

The distributed resistance model (DRM) developed and explained in Chapter 4 requires friction factors as coefficients of the force

components in the axial and transverse directions. The friction factors are usually obtained from pressure drop experiments. Most of the pressure drop experiments have been performed on a bundle basis with only a few accompanying flow split measurements which are necessary to provide all subchannel friction factors desirable for subchannel analysis. Therefore, the friction factor correlations developed so far in the literature have been constructed on a bundle averaged or subchannel scale.

Relevant friction factor correlations are not available for the porous body control volume. Since considerable effort is required to develop a new friction factor correlation for a specific control volume, we instead choose a control volume properly so as to use available friction factors by allowing a minimal error. From this point of view, the staggered half-pin layout which has a similar geometrical configuration to the subchannel control volume is the best choice among the selected layouts.

3.4.3.2 Geometrical Shape of the Wire Spacer

Another factor to be considered in determining the optimum control volume layout regarding the correlations is the wire spacer shape within a control volume to which the model is applied. Since the friction factor correlations are based on full cylindrical wire cross-section, any wire spacer present within a control volume should be of as cylindrical a shape as possible. This will not be the case if the control volume boundary intersects the wire spacer so that only a small portion of the wire cross-section lies in a given control volume. It is quite difficult to set up a resistance model that can accommodate such a general geometry of the wire spacer. For the quarter-pin layout, a substantial portion of the wire spacer is cut out vertically by the given control volume boundary.

Therefore, only a part of the wire spacer is in the control volume and contacts the fluid. Thus, the quarter-pin layout is not a good choice from this aspect. For other layouts, the control volume geometries are acceptable regarding the wire spacer shape. Especially, for the single-pin layout, a control volume includes a wire spacer with a complete cylindrical shape. Although some portion of the wire spacer is cut out vertically, the wire spacer fraction which appears on the other side of the control volume compensates for this loss.

3.4.4 An Optimum Control Volume Layout

In the previous sections, the single-pin, quarter-pin, half-pin and staggered half-pin layouts are selected as possible candidates of the optimum control volume layout and are examined with regard to the various factors which should be considered to determine the optimum control volume layout. All the important factors are summarized and the merits and demerits for each geometry are indicated in Table 3.3. For comparison purposes, the subchannel control volume case is also included in Table 3.3. From this table, the following conclusion is drawn: The staggered half-pin layout is the best choice among the selected porous body control volumes. This layout is comparable to the subchannel control volume in every aspect of the listed factors. The quarter-pin layout is not expected to result in a correct prediction despite the large number of computational mesh points. Although the optimum control volume layout has been determined here indirectly by examining the flow fields and control volume geometry, etc., it was partially verified through direct numerical calculations as discussed in Chapter 4.

Table 3.3 Important Factors Considered in Determining
the Optimum Control Volume Layout

Factors \ Layouts	Single-Pin	Quarter-Pin	Half-Pin	Staggered Half-Pin	Subchannel Control Volume
Computing Time (Number of Meshes)	O (32)	X (92)	Δ (56)	Δ (54)	O (42)
Spatial Velocity Fluctuations					
(1) Axial	O	Δ	O	O	O
(2) Transverse	O	Δ	Δ	O	O
Pressure Term					
(1) Wire Spacer Effect	X	O	O	O	O
(2) Pressure Distribution	Δ	Δ	Δ	Δ	Δ
DRM					
(1) Available Friction Factors	X	X	X	O	O
(2) Wire Spacer Shape	O	X	O	O	O

Note: O: Good choice
       Δ: Acceptable choice
       X: Poor choice

CHAPTER 4

APPLICATION OF THE THERMIT CODE TO THE WIRE-WRAPPED ROD BUNDLE

4.1 Introduction

In this chapter, we demonstrate the capability of the porous body

code in predicting the hydrodynamic fields in the wire-wrapped rod

bundle. As mentioned ealier, the THERMIT code is used as our numerical

tool for the porous body analysis. To account for the effect of the wire

spacer in the wire-wrapped rod bundle, the flow resistance should be

properly modeled. Calculations were made just using conventional pressure

drop correlation based on the equivalent diameter concept but an

acceptable flow field result could not be obtained. Therefore,

distributed resistance models (DRMs) for the porous body approach have

been developed by generalizing those formulated by Efthimiadis (E-1) for

the subchannel analysis approach. It has been performed by expanding the

2-dimensional models to 3-dimensional models, and by adjusting them to

apply the porous body control volume.

As discussed in Chapter 3, the optimum control volume layout was

chosen as the staggered half-pin layout. Therefore, the distributed

resistance models are especially tailored for this layout. However, one

can easily apply them to other configurations with minor modifications.

4.2 Distributed Resistance Models (DRMs)

The distributed resistance models for the subchannel analysis codes

were presented in reference (E-1) together with the description of the

important physical phenomena affecting the velocity and the pressure

fields due to the wire spacers in the hexagonal rod bundles. Thus our

work mainly concentrated on the extension of the DRMs tailored for the

subchannel analysis codes to the porous body codes. This section explains how to represent the distributed resistance force in an integral form and how to formulate each force component.

4.2.1 Representation of the Distributed Resistance Forces

In Chapter 2, the general integral form of the momentum equation was presented. The distributed resistance force $\vec{F}_{DR}$ was defined as,

$$\vec{F}_{DR} \equiv \int_{V_f} \vec{R} \, dV \equiv -\int_{A_{fs}} (-p\vec{n} + \bar{\bar{\tau}} \cdot \vec{n}) \, dA \qquad (2.27)$$

The physical interpretation of $\vec{F}_{DR}$ is that it represents the form and the friction drag forces exerted on the solid by the surrounding fluid flow. A_{fs} is the area of solid-fluid interface within the control volume. For the rod bundles with the wire wrap spacers, A_{fs} is written as,

$$A_{fs} = A_R + A_W \qquad (4.1)$$

where A_R is the surface area of the rods, and A_W is the surface area of the wire wrap spacers.

As described in Section 2.5.2, we have proposed an alternative definition of the distributed resitance force $\vec{F}'_{DR}$ as Eq.(2.30). Although the mathematical representations of the conventional definition and the proposed one differ, the principles implied in the definitions are identical: The distributed resistance force is the sum of the form drag and the friction drag. Thus, both definitions can be used to construct the distributed resistance model.

If we assume that the interference effect due to coexistence of the rods and the wire spacers is negligible, Eq.(2.27) can be written as,

$$\vec{F}_{DR} = -\int_{A_R} (-p\vec{n} + \bar{\bar{\tau}} \cdot \vec{n}) \, dA - \int_{A_W} (-p\vec{n} + \bar{\bar{\tau}} \cdot \vec{n}) \, dA \qquad (4.2)$$

or

$$\vec{F}_{DR} = \vec{F}_R + \vec{F}_W \tag{4.3}$$

where

$$\vec{F}_R \equiv - \int\limits_{A_R} (-p\vec{n} + \bar{\bar{\tau}}\cdot\vec{n}) \, dA \tag{4.4}$$

$$\vec{F}_W \equiv - \int\limits_{A_W} (-p\vec{n} + \bar{\bar{\tau}}\cdot\vec{n}) \, dA \tag{4.5}$$

These forces should be further decomposed along the principal directions (x, y and z directions) since the x, y and z direction momentum equations of the THERMIT code require x, y, and z components of the distributed resistance force $\vec{F}_{DR}$ respectively. Figure 4.1 illustrates the force components for the rod and the wire wrap spacer. Since the rod axis is along the principal direction z, the force components for the rod are modeled directly in the principal directions. On the other hand the force components for the wire spacer are modeled parallel and perpendicular to the wire spacer whose axis is an angle ϕ to the principal direction z. Thus, each component of the total distributed resistance force along each principal direction can be given as,

$$F_{DR}^Z = F_R^A + F_W^T \cos\phi + F_W^N \sin\phi \tag{4.6}$$

$$F_{DR}^X = F_R^X + (F_W^T \sin\phi - F_W^N \cos\phi) \cos\theta \tag{4.7}$$

$$F_{DR}^Y = F_R^Y + (F_W^T \sin\phi - F_W^N \cos\phi) \sin\theta \tag{4.8}$$

where ϕ is the angle between the wire wrap spacer direction and the rod axis, and θ is the angle between the wire wrap spacer direction
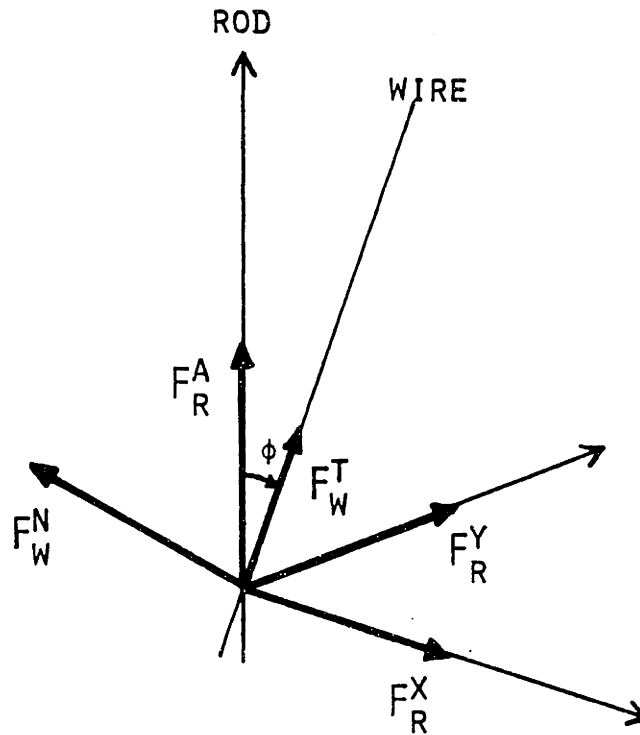
Figure 4.1   Schematic Diagram of Drag Force Components
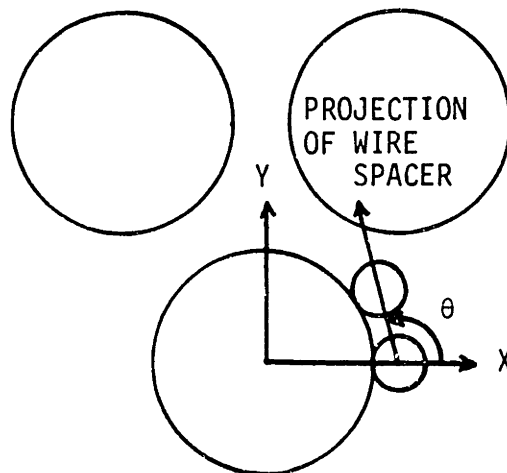
Figure 4.2   Wire Direction in the Control Volume of an
Axial Mesh H/12

projected on the x-y plane and the x axis in a plane perpendicular to the rod axis. The positive directions of these angles are shown in Figure 4.2.

Each component of the total resistance force can be determined if five force components, i.e., F_R^A, F_R^X, F_R^Y, F_W^T and F_W^N are correlated in proper ways. Thus, the distributed resistance models are developed for these five force components separately. The DRMs described in the next section can be applied to both interior and peripheral subchannels.

4.2.2 Modeling of Each Force Component

In contrast to the typical subchannel code, the THERMIT code employs a three-dimensional, Cartesian coordinate system. The velocity $\vec{v}$ of a control volume is composed of three calculated velocity components, u, v, w for the x, y, z directions respectively. In addition, the calculated velocity $\vec{v}$ of the THERMIT should be interpreted as the control volume averaged velocity while the transverse velocity of the subchannel code is defined at the gap. Therefore, careful choice of the velocity components as constituents of the pressure drop correlations is important to get correct results.

4.2.2.1 F_R^A (Axial Force Component of the Rods)

The axial force component of the rods consists of only the friction drag force (no form drag) since the axial direction is taken parallel to the rod direction. The axial friction drag force on the rods and the wire wrap spacers is approximately given as,

$$F_{R+W}^A = \Delta P_A \, A_f \tag{4.9}$$

where ΔP_A is the axial friction pressure drop, and A_f is the cross-sectional flow area averaged over the control volume (However, there are other choices for determining A_f).

If we assume that the total friction drag is uniformly distributed over the rod and the wire wrap spacer surfaces, the axial force component of the rods only yields,

$$F_R^A = \Delta P_A \, A_f \quad \left(\frac{A_R}{A_R + A_W}\right) \tag{4.10}$$

The pressure drop, ΔP_A can be correlated in terms of a friction factor and average velocity. However, the average velocity $\vec{v}$ is generally not parallel to the rod axis but is oriented at some angle α with the rod axis as shown in Figure 4.3. In the case of free stream flow over a yawed cylinder, Ebeling-Koning and Todreas (E-2) suggested that the axial pressure drop be correlated based on the magnitude of the average velocity, $\left|\vec{v}\right|$ instead of the axial velocity component w when a Blasius type pressure drop correlation is employed. Then the frictional pressure drop resulting from the Blasius type correlation should be multiplied by $\cos\alpha$ to yield the axial friction pressure drop, ΔP_A. Thus, the axial pressure drop may be written as,

$$\Delta P_A = f_A \frac{\rho \left|\vec{v}\right| \left|\vec{v}\right|}{2} \frac{\Delta z}{D_e} \cos\alpha \tag{4.11}$$
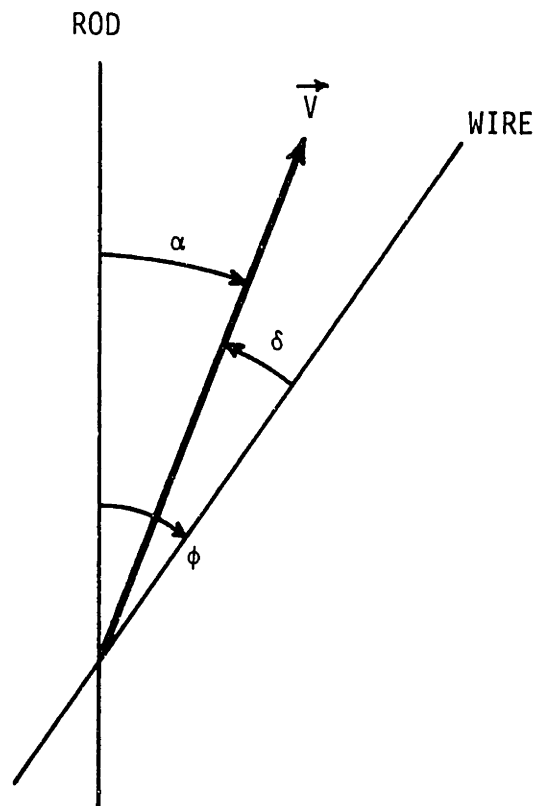
Figure 4.3 Angle Representation in a Wire-Wrapped Rod

where f_A is the friction factor as a function of Reynolds number Re

and geometry. Δz is the length of the axial segment where the ΔP_A

is measured, and D_e is the equivalent hydraulic diameter including

the wire wrap spacers ($D_e = \dfrac{4A_f}{P_w}$, where P_w is the wetted perimeter

$P_w = \dfrac{A_R + A_W}{\Delta z}$).

Substituting Eq.(4.11) into Eq.(4.10) yields,

$$F_R^A = f_A \frac{\rho |\vec{v}| |\vec{v}|}{2} \frac{\Delta z}{D_e} \cos\alpha \, A_f \frac{A_R}{A_R + A_W} \tag{4.12}$$

or

$$F_R^A = f_A \frac{\rho |\vec{v}| |\vec{v}|}{8} \cos\alpha \, A_R \tag{4.13}$$

where $|\vec{v}| = (u^2 + v^2 + w^2)^{1/2}$ (4.14)

and

$$\cos \alpha = \frac{w}{|\vec{v}|} \tag{4.15}$$

In this research, no attempt has been made to obtain a correct

friction factor f_A since the general friction factor correlations

for the subchannel analysis may be used with a minor error for the

optimum control volume layout. Thus, we used the following simple

correlations for f_A,

$$f_A = \begin{cases} \dfrac{64}{Re_v} & , \ Re_v \leq 2000 \ (\text{laminar flow}) \\[3mm] \dfrac{0.3164}{Re_v^{0.25}} & , \ Re_v > 2000 \ (\text{turbulent flow}) \end{cases} \tag{4.16}$$

where Re_v is the Reynolds number based on the average velocity, $\vec{v}$, i.e.,

$$Re_v = \frac{\rho \left| \vec{v} \right| D_e}{\mu} \tag{4.17}$$

4.2.2.2 $\quad F_W^T$ (Tangential Force Component of the Wire Wrap Spacer)

The same methodology used for the correlation of F_R^A can be applied. Although the wire wrap spacers are helically wrapped around the rods with a shape of winding cylinder, they can be assumed straight cylinders within a short axial mesh length. The tangential friction drag of the wire wrap spacers, with the assumption of the uniform distribution of the total friction drag, can be written as,

$$F_W^T = f_A \frac{\rho \left| \vec{v} \right| \left| \vec{v} \right|}{2} \frac{\Delta z}{D_e} \cos\delta \ A_f \frac{A_W}{A_R + A_W} \tag{4.18}$$

or

$$F_W^T = f_A \frac{\rho \left| \vec{v} \right| \left| \vec{v} \right|}{8} \cos\delta \ A_W \tag{4.19}$$

where δ is the angle between the wire wrap spacer direction and the average velocity direction shown as Figure 4.3. In general, since the velocity $\vec{v}$ does not lie on the plane made by the axes of the rod and the wire wrap spacer, the angle ϕ is not equal to the sum of the angles α and δ. Using some vector algebra, the angle δ can be obtained as,

$$\cos\delta = \frac{1}{\left|\vec{v}\right|} \{u \sin\phi \cos\theta + v \sin\phi \sin\theta + w \cos\phi\} \qquad (4.20)$$

where the angle θ is defined in Figure 4.2.

4.2.2.3 F_R^X (X-direction Force Component of the Rods)

The transverse pressure drop cannot be correlated using the Blasius type correlation since F_R^X includes both the form and the friction drag terms. The Gunter-Shaw correlation (G-1) which is simple and generally used in the rod bundle analysis was incorporated. The effect of the wire wrap spacers was simply included in the calculation of the volumetric diameter D_V'' where the double prime superscript indicates that the rods and wire wrap spacers are both included in the volumetric diameter calculation.

The geometrical parameters and the gap velocity for the x-direction momentum calculation are indicated in Figure 4.4. The x-direction resistance force of the rods and the wire wrap spacers in a control volume can be written as,

$$F_{R+W}^X = \Delta P_L \, A_{avg}^X \qquad (4.21)$$

where A_{avg}^X is the x-direction flow area averaged over the control volume, i.e., $A_{avg}^X = \frac{V_f}{\Delta x}$. The Gunter-Shaw correlation for the pressure drop over one stage S_L is,

$$\Delta p_L = f_L \cdot \frac{\rho u_g |u_g|}{2} \, \frac{S_L}{D_V''} \left(\frac{D_V''}{S_T}\right)^{0.4} \left(\frac{S_L}{S_T}\right)^{0.6} \qquad (4.22)$$

where

$$D_V'' = \frac{4V_f}{A_R + A_W} \qquad (4.23)$$
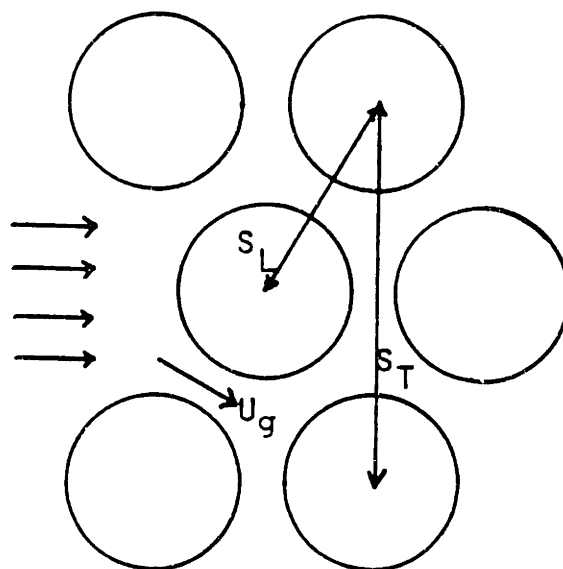
Figure 4.4   Gap Velocity and Geometry Parameters in the
X-Momentum Calculation
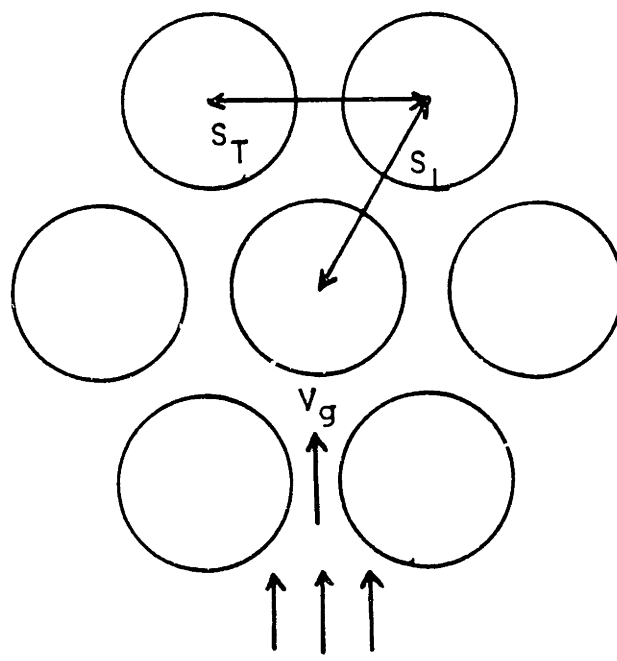
Figure 4.5   Gap Velocity and Geometry Parameters in the
Y-Momentum Calculation

and V_f is the fluid volume in a control volume, f_L is the lateral friction factor, and u_g is the transverse velocity at the gap. For the practical application to the THERMIT code, the transverse gap velocity was assumed to be,

$$u_g = u \frac{A^x_{avg}}{A_g} \qquad (4.24)$$

where A_g is the gap area.

If it is assumed that the total resistance force is uniformly distributed among the rods and the wire wrap spacers, the x-direction force component of the rods only can be obtained as,

$$F^X_R = \Delta p_L \; A^x_{avg} \; \frac{A_R}{A_R + A_W} \qquad (4.25)$$

or

$$F^X_R = f_L \; \frac{\rho u_g |u_g|}{8} \; (\frac{D^{..}_V}{S_T})^{0.4} \; (\frac{S_L}{S_T})^{0.6} \; A_R \qquad (4.26)$$

where f_L is correlated based on the gap velocity u_g.

In our THERMIT calculations, the following correlation for the lateral friction factor was used,

$$f_L = \begin{cases} \dfrac{180}{Re_{u_g}}, & Re_{u_g} \leq 200 \\[2em] \dfrac{1.92}{Re_{u_g}^{0.145}}, & Re_{u_g} > 200 \end{cases} \qquad (4.27)$$

and

$$Re_{u_g} = \frac{\rho |u_g| D^{..}_V}{\mu} \qquad (4.28)$$

4.2.2.4 F^Y_R (Y-direction Force Component of the Rods)

The schematic layout of the y-momentum control volume geometry is depicted in Figure 4.5. In the same way as F^X_R, the y-direction resistance force for the rods can be obtained as,

$$F_R^Y = f_L \frac{\rho v_g |v_g|}{8} \left(\frac{D_V{}''}{S_T} \right)^{0.4} \left(\frac{S_L}{S_T} \right)^{0.6} A_R \qquad (4.29)$$

where v_g is the y-direction velocity at the gap, and is assumed to be,

$$v_g = v \frac{A_{avg}^y}{A_g} \qquad (4.30)$$

where A_{avg}^y is the y-direction flow area averaged over the control volume.

4.2.2.5 F_W^N (Normal Force Component of the Wire Wrap Spacers)

Figure 4.6 presents the characteristics of the flow field over the wire spacer wrapping the rod, and indicates the velocity component normal to the wire wrap spacer. The wake distribution due to the wire wrap spacers is different from that of bare rod bundle geometry. Thus, the drag force concept instead of the Gunter-Shaw correlation was selected for the DRM in the subchannel analysis code (E-1) in order to calculate the normal force component of the wire wrap spacers. The same approach was employed in this work. Using this concept, F_W^N can be written as,

$$F_W^N = C_p \, C_D \, \frac{1}{2} \, \rho \, v_N \, |v_N| \, \frac{D_w \Delta z}{\cos \phi} \qquad (4.31)$$

where D_W is the diameter of the wire wrap spacer, and $D_W \Delta z / \cos \phi$ is the frontal area of the wire wrap spacer. The normal velocity component can be obtained by some vector algebra as the following,

$$v_N = - u \cos \phi \cos \theta - v \cos \phi \sin \theta + w \sin \phi \qquad (4.32)$$

C_D is the drag coefficient which can be expressed as a function of Reynolds number (W-2), i.e.,

$$C_D = 1 + \frac{10}{Re^{2/3}} \qquad (4.33)$$
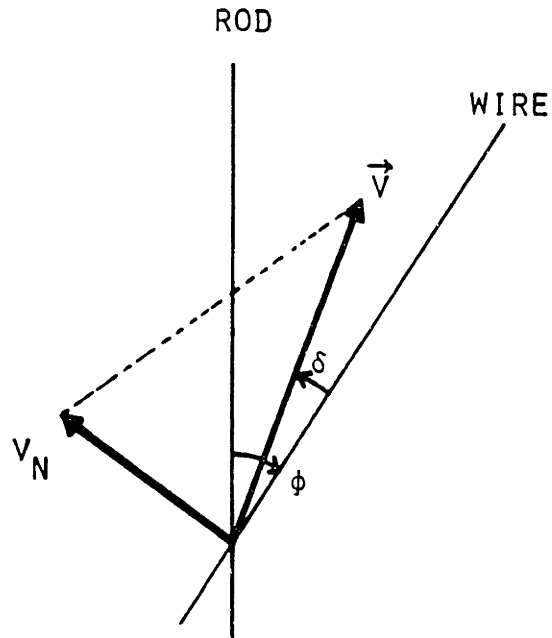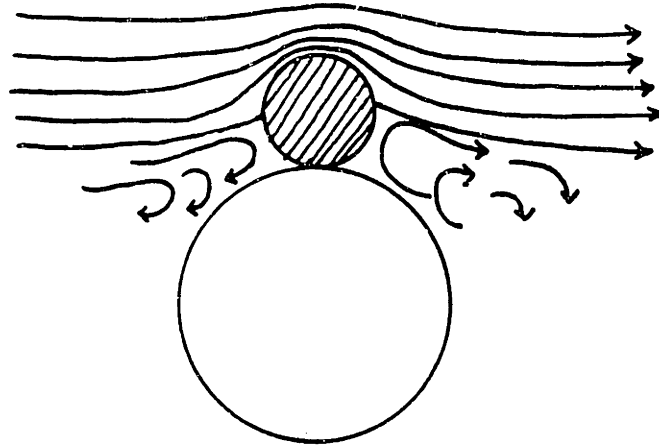
Figure 4.6 Flow Characteristics and Normal Velocity Component
to Wire Wrap Spacer

where

$$Re_{v_N} = \frac{\rho |v_N| D_e}{\mu} \qquad (4.34)$$

and v_N is the normal component of the velocity averaged over a control volume. In Eq.(4.31), C_p is added to account for the difference between the normal component of the average velocity, i.e., v_N and the normal component of the local velocity over the surface of the wire spacer. The difference is expected to be quite large for the following reasons: Flow is accelerated by continuity as it passes through the small free flow area between the wire spacer and the neighbor rod. Thus, the flow velocity in the vicinity of the wire spacer is larger than the control volume average velocity, and by continuity it is proportional to the flow area ratio, i.e., the average flow area to the minimum flow area between the wire spacer and the neighbor rod. In addition, from experiment (L-1), it has been observed that the fluid spilling over the wire spacer tends to follow the direction normal to the axis of the wire spacer. This may have resulted from the pressure difference between the upstream stagnation region and downstream wake region of the wire spacer. Thus, the normal velocity component should be increased to account for this physical observation.

In the THERMIT code, the correction factor C_p is an input parameter which should be determined by comparing the results against experimental data. This factor is very important since the normal drag force to the wire spacer is predominant compared to other force components in the wire-wrapped rod bundle. The calibration of this factor is discussed in the subsequent section.

4.3 Porous Body Code, THERMIT

4.3.1 General Feature of the THERMIT Code

THERMIT is a three-dimensional Cartesian coordinates computer code developed at MIT under EPRI sponsorship for the thermal-hydraulic analysis of reactor cores (R-1). It solves two fluid, six equations for the two-phase flow and heat transfer dynamics. The numerical method employed is a semi-implicit scheme which has a Courant time step stability limit. Several versions of the THERMIT code have been developed for various engineering applications. THERMIT-4E code, a recent version of the THERMIT code incorporating a four-equation model, was used in this study. A detailed description on the THERMIT-4E code can be found in reference (S-5).

The friction model of the original THERMIT-4E code was made based on a simple friction factor correlation for a whole wire-wrapped rod bundle. Therefore, it cannot take account of the wire spacer effect on the local variations of the velocity and pressure fields. The schematic calculational flow diagram of the THERMIT-4E code is drawn in Figure 4.7.

4.3.2 Numerical Implementation of the Distributed Resistance Models

The built-in friction models in the THERMIT-4E code have been eliminated and new resistance models developed in this study have been adapted. The following work has been performed to implement the new distributed resistance models:

(1) Fractions of the fuel rod and the wire spacer for all control volume meshes are identified to calculate the surface areas of the rod and the wire spacer. This should be provided for all the radial and axial nodal meshes for the x, y and z-momentum control volumes. Those are,
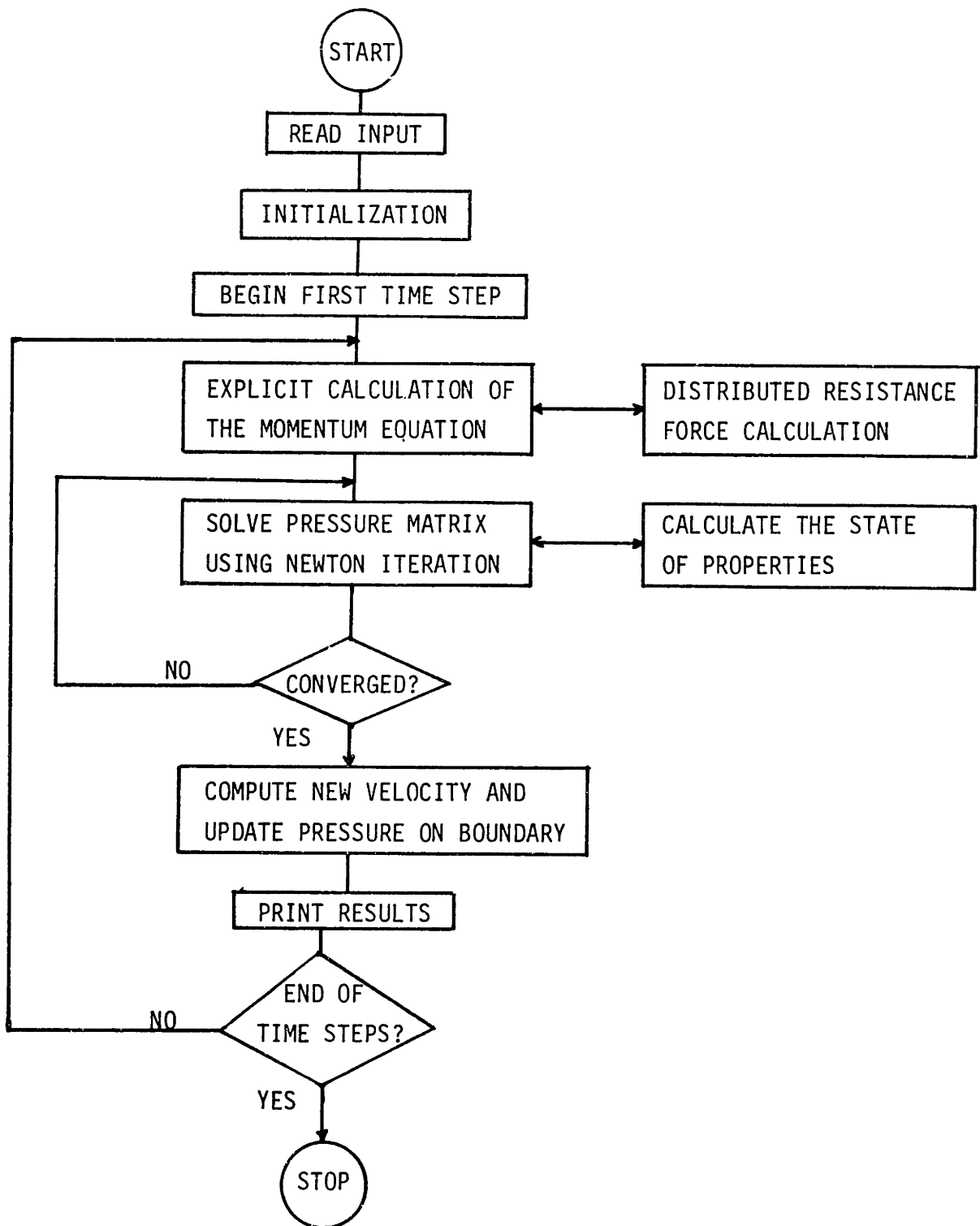
Figure 4.7 Calculational Flow Diagram of the THERMIT Code
(No Heat Transfer Calculation)

XROD(J,I), YROD(J,I), ZROD(J,I) for the rod fractions and,

XLENG(J,I), YLENG(J,I), ZLENG(J,I) for the wire spacer

fractions in terms of the wire length. J denotes the axial mesh

number and I the radial mesh number.

(2) Duct wall areas are also given for the mesh cells which

contact the surrounding duct wall. Those are,

XWALL(J,I), YWALL(J,I), ZWALL(J,I) for the x, y, z-momentum control

volumes, respectively.

(3) The projection angles between the direction of the wire spacer

and the x axis are prepared along the axial position. Those are,

XYANGLE(J), ZANGLE(J) for x and y and z-momentum control volumes,

respectively.

(4) The data sets of the input parameter C_p are tabulated for all

mesh cells. Those are,

CGX(J,I), CGY(J,I), CGZ(J,I) for the x, y and z-momentum control

volumes, respectively.

(5) Since the distributed resistance models require three

principal velocity components for each mesh cell, undetermined

velocity components should be evaluated before the distributed

resistance force calculations are performed. In the main program,

the unknown velocity components are determined by averaging the

velocity components of four neighboring mesh cells.

(6) Subroutine FWALL has been extensively modified to calculate

the distributed resistance forces. All the distributed resistance

models described in Section 4.2 as well as the above geometrical

information were written in the subroutine in numerical form. A

Fortran listing of subroutine FWALL is given in Appendix C.

4.3.3 Volume Porosity Calculation

One of the input variables required by the THERMIT code is the flow volume available to the fluid. The volume porosity can be obtained by dividing this fluid volume by total control volume. The fluid volume cannot be prepared easily since the porous body control volume geometry is complicated due to the presence of a fraction of the wire spacer. In this section, we will briefly explain how to calculate the wire spacer volume as a function of the wire position.

The cross section of the wire spacer is not circular but elliptic. However, to simplify the calculation, it was assumed to be circular. As shown in Figure 4.8, the cross-hatched area of the chopped wire spacer is calculated as,

$$A_W = \frac{\pi}{4} D_W^2 (1 - \frac{\theta}{\pi}) + OP \cdot PM \tag{4.35}$$

where,

$$OP = S - \frac{1}{2} (D_R + D_W) \cos (\frac{\pi}{2} - \phi) \tag{4.36}$$

$$PM = (\frac{1}{4} D_W^2 - OP^2)^{1/2} \tag{4.37}$$

$$\theta = \cos^{-1} \frac{2 \cdot OP}{D_W} \tag{4.38}$$

and, D_R is the rod diameter and D_W the wire spacer diameter. The angles θ and ϕ are indicated in Figure 4.8. If the left-hand side of the boundary is taken as our control volume, the wire spacer volume within the control mesh can be obtained by integrating this wire spacer area with respect to the wire position from the bottom to the top of the control mesh.

$$V_W = \int_{Z_{BOT}}^{Z_{TOP}} A_W \, dz \tag{4.39}$$
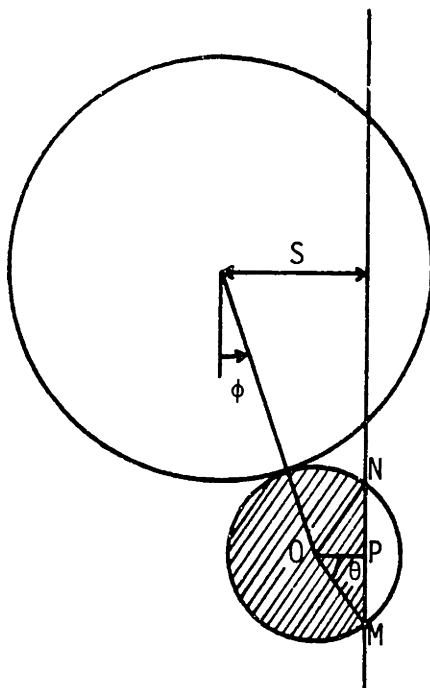
Figure 4.8 Schematic Diagram for Wire Spacer Volume
Calculation

or

$$V_W = \frac{H}{2\pi} \int_{\phi_{BOT}}^{\phi_{TOP}} A_W \, d\phi \qquad (4.40)$$

where,

if $OP > \frac{1}{2} D_W$, then $OP = \frac{1}{2} D_W$ (full wire spacer within the control mesh)

if $OP < -\frac{1}{2} D_W$, then $OP = -\frac{1}{2} D_W$ (no wire spacer within the control mesh)

and,

$$\phi = 2\pi \frac{z}{H} \qquad (4.41)$$

The fluid volume is obtained as,

$$V_f = V_{TOT} - (V_R + V_W) \qquad (4.42)$$

where V_{TOT} is the total volume of the control mesh and V_R is the volume occupied by the rod fraction.

For different control volume geometries and wire spacer locations, the fluid volume can be calculated in a similar manner.

4.4 Calibration and Numerical Results

4.4.1 Calibration of the Parameter C_p

As mentioned earlier, the correction factor C_p is an important parameter to be determined by calibrating against the experimental data. This factor includes two effects on the velocity component normal to the wire spacer: flow acceleration due to the flow area contraction near the wire spacer, and flow orientation in the direction normal to the wire spacer axis which was observed in the experiments. Thus, the

normal component of the local velocity just over the wire spacer is expressed as,

$$v_N^{local} = C_o \left(\frac{A_{avg}}{A_{min}}\right) v_N \tag{4.43}$$

where,

C_o — some constant to account for the flow orientation effect

v_N — control volume average normal velocity in Eq.(4.31)

A_{avg} — free flow area averaged over the specific control volume in the axial direction

A_{min} — free flow area averaged over the gap area between the wire spacer and the neighbor rod as shown in Figure 4.9

The normal force component of the wire wrap spacer can also be written as,

$$F_W^N = C_D \frac{1}{2} \rho v_N^{local} \left|v_N^{local}\right| \frac{D_w \Delta z}{\cos\phi}$$

$$= C_D \frac{1}{2} \rho C_o^2 \left(\frac{A_{avg}}{A_{min}}\right)^2 v_N \left|v_N\right| \frac{D_w \Delta z}{\cos\phi} \tag{4.44}$$

Then, C_p can be correlated from Eqs.(4.31) and (4.44) as,

$$C_p = C \left(\frac{A_{avg}}{A_{min}}\right)^2 \qquad \text{where } C = C_o^2 \tag{4.45}$$

For each control volume geometry, the calibration constant C and the area ratio A_{avg}/A_{min} should be determined as a function of the wire position. Figures 4.9 and 4.10 show the various control volume patterns and selected wire positions for the interior and the side control volumes, respectively. The average versus selected wire positions with respect to each control volume are shown in Table 4.1. A proper choice of the calibration constant requires many iterations and case studies
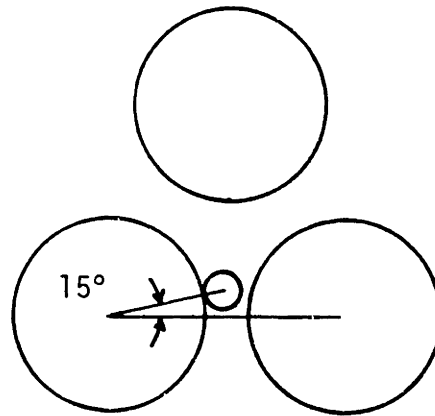
(a) Pattern 1
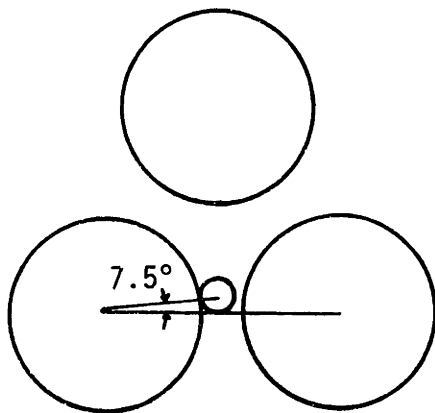
(b) Pattern 2
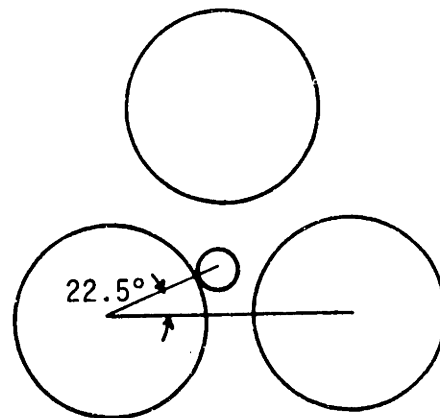
(c) Pattern 3

Figure 4.9 Average Positions of the Wire Wrap Spacers in Various
Interior Subchannels for H/12 Mesh
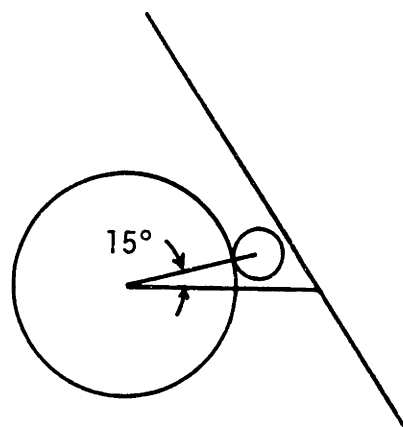
(a) Pattern 4
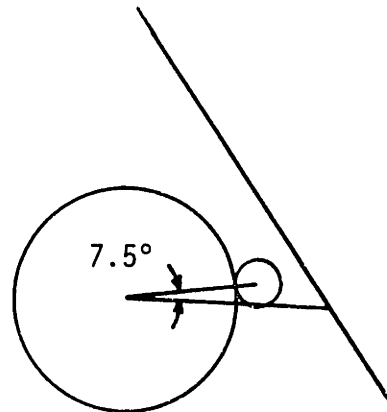
(b) Pattern 5
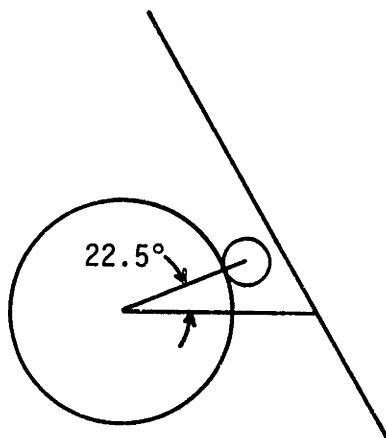
(c) Pattern 6
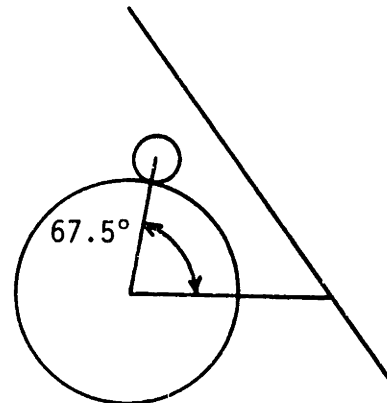
(d) Pattern 7

Figure 4.10   Average Positions of the Wire Wrap Spacers in Various
Side Subchannels for H/12 Mesh

Table 4.1 Selected Wire Positions and Corresponding Patterns

Control Volume (and Location)	Average Wire Positions	Selected Wire Positions	Patterns
X and Y Momentum (Interior)	15°,45°,75°, ..., 345°	same	1
Z Momentum (Interior)	0°,30°,60°, ...,330°	7.5°,22.5°,67.5°, ...,327.5° (See below*)	2,3
X and Y Momentum (Side)	15°,45°,75°, ..., 345°	same	4
Z Momentum (Side)	0°,30°,60°, ...,330°	7.5°,22.5°,67.5°, ...,327.5°	5,6,7

* The selected positions must be different than 0°, 30°, etc., for proper area averaging because the array has 30° symmetry. For example, for wire movement from 345° to 15° about the average position of 0°, the flow area between the rod and wire spacer is not zero because of symmetry from 345° to 0° and 0° to 15°. Therefore, the selected position should be at 7.5° or equivalently at 352.5°.

for different geometries. Further, the correct value of the area ratio
of each control volume is not easily calculated. The calibration work
has been performed based on the experimental conditions of Lafay et al.
(L-1). The calibration constant C and the area ratio as well as the
correction factor C_p for each control volume pattern are tabulated
in Table 4.2. These values provide a data set for each momentum control
volume in subroutine FWALL. The calibration constants were determined
to match the predictions with the experimental results in the following
two respects: The maximum transverse velocity should be reasonably
predicted, and the shape of the velocity and pressure profiles should be
qualitatively similar.

Further, although the calibration study has been carried out for a
single flow rate condition, it is expected that the correction factors
obtained in this work can be also applied to other flow rate conditions
in the experiment. In order to generalize the correction factors, more
calibration work is required to apply to the various bundle geometries,
i.e., different pitch to rod diameter ratio and wire lead length to rod
diameter ratio.

4.4.2 Results and Discussion

The available experimental data with which the numerical results
can be compared are listed in Table 4.3. These parameters include the
transverse velocity, axial velocity and pressure profile for the
interior and the side subchannels. Since our work is aimed at the
assessment of the THERMIT capability in predicting the global flow field
characteristics such as the peripheral swirl flow, the non-uniform
pressure variation and the axial velocity distribution in the

Table 4.2   Correction Factor for Each Control Volume Pattern

Pattern	Calibration Constant, C	Area Ratio, A_{avg}/A_{min}	Correction Factor, C_p
1	5.	$30 \left(1 - \frac{1}{P/D}\right)$	110
2	0.35	$118 \left(1 - \frac{1}{P/D}\right)$	120
3	20.	$14 \left(1 - \frac{1}{P/D}\right)$	100
4	5.	$59 \left(1 - \frac{1}{P/D}\right)$	430
5	20.	$26 \left(1 - \frac{1}{P/D}\right)$	340
6	0.35	$234 \left(1 - \frac{1}{P/D}\right)$	470
7	40.	$10 \left(1 - \frac{1}{P/D}\right)$	100

Table 4.3 Experimental Data for the Wire-Wrapped Rod Bundles Available in the Literature

Investigators	Geometry	Fluid	Pressure field	Axial Velocity	Transverse Velocity
Lafay et al. (L-1)	19 Pins P/D=1.19 H/D=18.75	Water	Side Re=3000 to 28000	N/A	Side Re=23000
Ohtake et al. (O-1)	37 Pins P/D=1.19 H/D=34.8	Air	N/A	Interior (local) Re=15100	Side (local) Interior (local) Re=15100
Roidt et al. (R-3)	Fuel 217 Pins P/D=1.25 H/D=52 Blanket 61 Pins P/D=1.07 H/D=7.9	Air	Side Re=22000	Interior Side Re=4300, 11800, 22000, 73000	Interior Side Re=4300, 11800, 22000, 73000
Chen et al. (C-2)	61 pins P/D=1.25 H/D=48 or 24	Water	N/A	Side Re=640, 4500	Side Re=640, 4500
Sarno et al. (S-4)	19 Pins P/D=1.15 H/D=20.9	Water	Interior Side Re=700 to 2000	Side (local) Re=700 to 2000	N/A
MIT (E-1)	19 Pins P/D=1.248 H/D=35.3	Water	N/A	Side Interior Re=80 to 320	N/A

wire-wrapped rod bundle, the experiments performed on the subchannel
scale are preferred to those on the local scale within a subchannel.
From this point of view, the experimental results of Lafay et al. were
chosen as the benchmark test for comparison with the THERMIT swirl flow
and pressure results. This experiment was done in a 19-pin wire-wrapped
bundle with water as the working fluid. The pitch to diameter ratio of
the bundle is 1.19, and the wire lead length to rod diameter ratio is
18.8. For the axial velocity distribution, the MIT data obtained in
this project was compared with the THERMIT results. The Lafay
transverse velocity and pressure distribution tests and the MIT test
were carried out at bundle Reynolds numbers of 3000 to 28,000 and 320
respectively. Because of prohibitive computer costs only one THERMIT
run was performed which corresponded to the Lafay test geometry and
bundle Reynolds number of 23,000 for the transverse velocity test.
However qualitative comparisons can still be made betweeen THERMIT
predictions and the Lafay pressure tests and the MIT axial velocity
tests.

4.4.2.1   Velocity Field

Before the distributed resistance models (DRMs) were adapted to the
THERMIT-4E code, the velocity and pressure fields were calculated
including only the flow blockage effect of the wire spacers utilizing
the volume porosity. The transverse velocity map is shown in Figure
4.11, when the wire spacers move from 240° to 300°. In this
calculation, the single-pin layout was used, and H/6 was used for the
axial mesh size as a preliminary run. Consistent peripheral swirl flow
characteristics could not be obtained. Moreover, the magnitude of the
transverse velocity was too small compared with the experimental data.
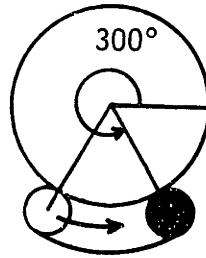
WIRE LOCATION
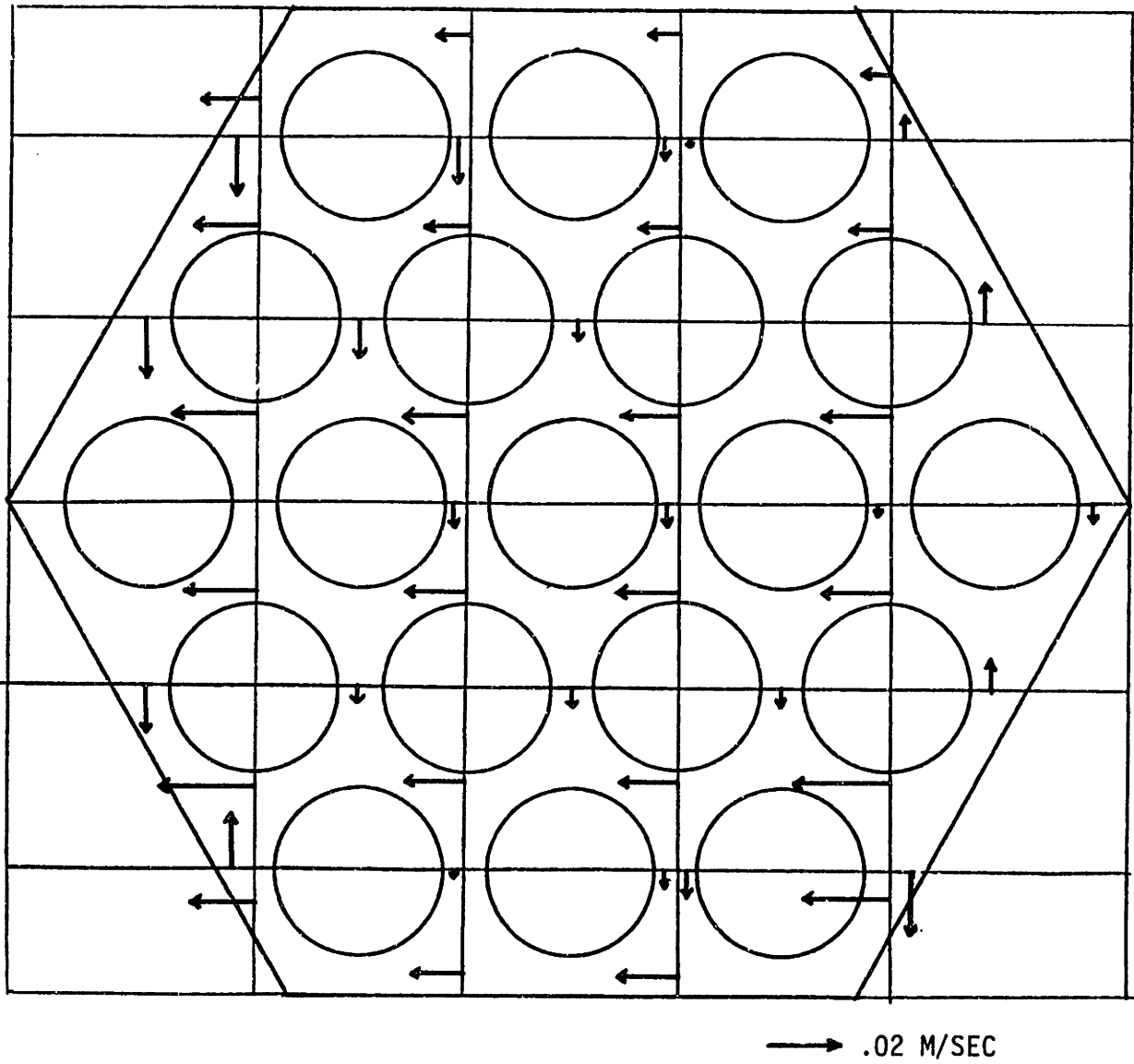
Figure 4.11   Transverse Velocity Distribution Without Distributed
             Resistance Model

After the DRMs were adapted, the flow field calculation was performed with an H/12 axial mesh size and the staggered half-pin layout which had earlier been selected as the optimum control volume geometry as described in Chapter 3. The transverse velocity profile is shown in Figure 4.12, when the wire spacers move from 240° to 270°. Note that the unit length of the arrows of this figure is increased 10 times compared with that of Figure 4.11. The swirl flow around the hexagonal duct is clearly observed. The diversion crossflows in the interior subchannels are also presented. Here note that the velocity drawn in this figure should be interpreted as the mean velocity averaged over the specific control volume.

Predicted ratios of the transverse velocity of the side subchannel at the peripheral gap to the bundle average axial velocity are depicted in Figure 4.13 as well as the experimental results of Lafay et al. The gap velocity was obtained by multiplying the control volume average velocity by the ratio of the experimental gap velocity to the experimental subchannel average velocity. Here, the ratio of the experimental values was calculated by examining the local transverse velocity distribution of the experimental data (C-2). In the averaging process some uncertainties might be included since the experimental data did not provide so much detailed velocity profile and the geometries were different from each other. However, the errors are not expected to be so large, and it is believed that this procedure is the most reasonable way to interpret the porous body results. The transverse velocity prediction of the THERMIT is also compared with the results of

WIRE LOCATION

→ .2 M/SEC
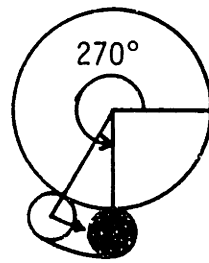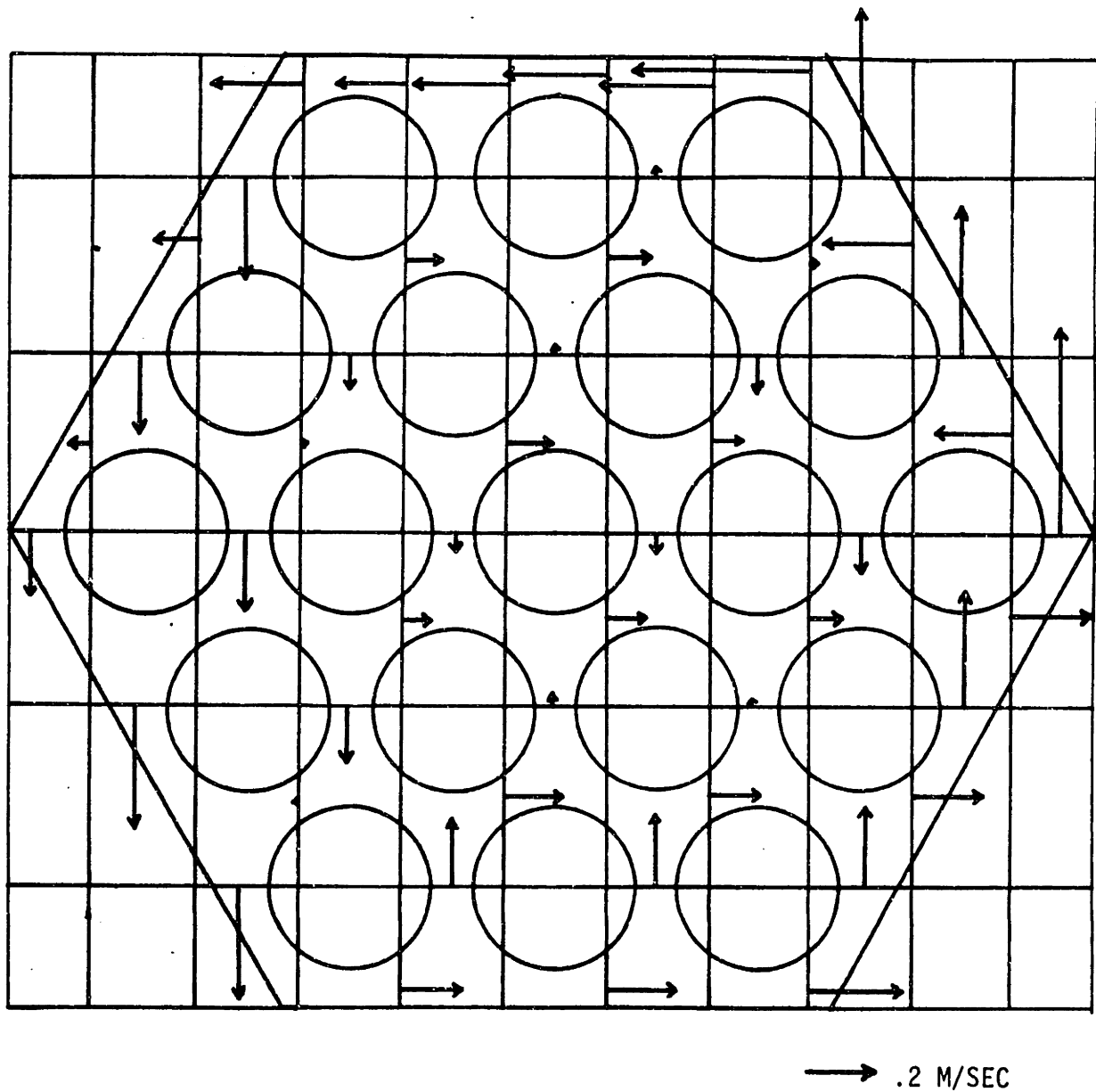
Figure 4.12   Transverse Velocity Distribution in Staggered
Half-Pin Layout with Distributed Resistance Model
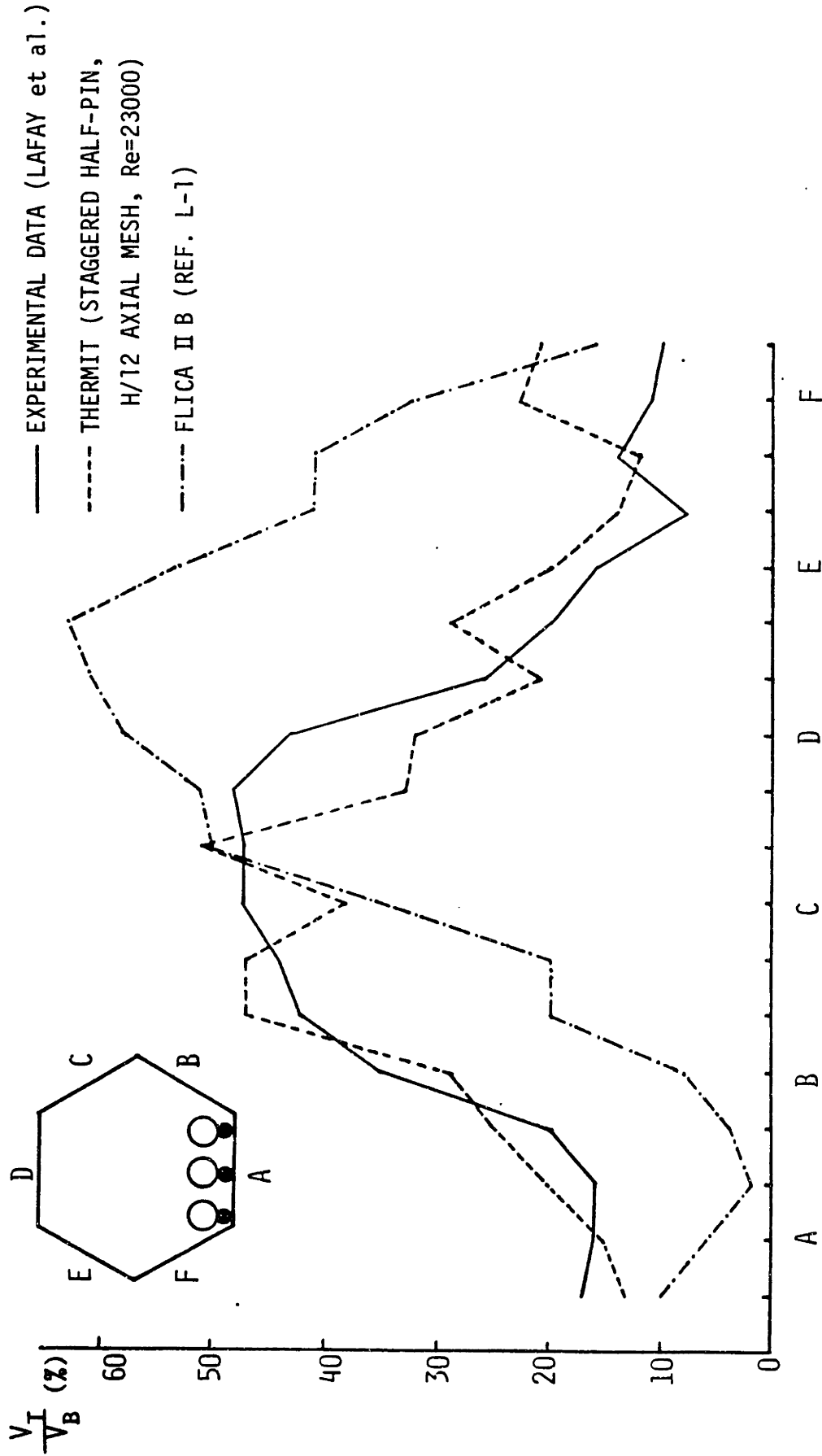
Figure 4.13 Transverse Velocity Profile Along the Hexagonal Duct Wall

the FLICA-IIB code (L-1) in Figure 4.13. Agreement between the THERMIT
prediction and the experimental data is excellent. The maximum
transverse velocity of the THERMIT prediction is 52% of the bundle
average axial velocity while the experimental value of the maximum V_T/V_B
is equal to 48%. The THERMIT prediction shows a dip at the side C. The
reason has not been clearly resolved. The prediction of the FLICA-IIB
code is quite poor. It underpredicts the ratio V_T/V_B by a factor of two
at the sides A, B and C and overpredicts at the sides D,E and F.

Figure 4.14 shows the axial variation of the transverse velocity
profile at the central gap of a peripheral subchannel. The THERMIT
results were compared against the experimental data and the ASFREMIT
subchannel code prediction (E-1). The THERMIT results qualitatively
predict well the trend of the axial variation, but the maximum velocity
ratio of the THERMIT is lower than that of the experimental data as much
as by a factor of two. The ASFREMIT prediction shows a trend and
magnitude similar to the THERMIT prediction over the entire range of the
wire angle.

The axial velocity profile across the 19-pin rod bundle at the exit
plane is plotted in Figure 4.15 and compared against the MIT experi-
mental data. The MIT experiment was done in the laminar flow condition
(Re = 320) and in a different geometry from the Lafay test and the
THERMIT prediction (P/D = 1.25 and H/D = 35). Since the THERMIT run was
performed in the turbulent flow region (Re = 23,000) and the flow split
among the subchannels depends upon the Reynolds number, the two results
cannot be directly comparable. It was shown by Cheng (C-1) that the
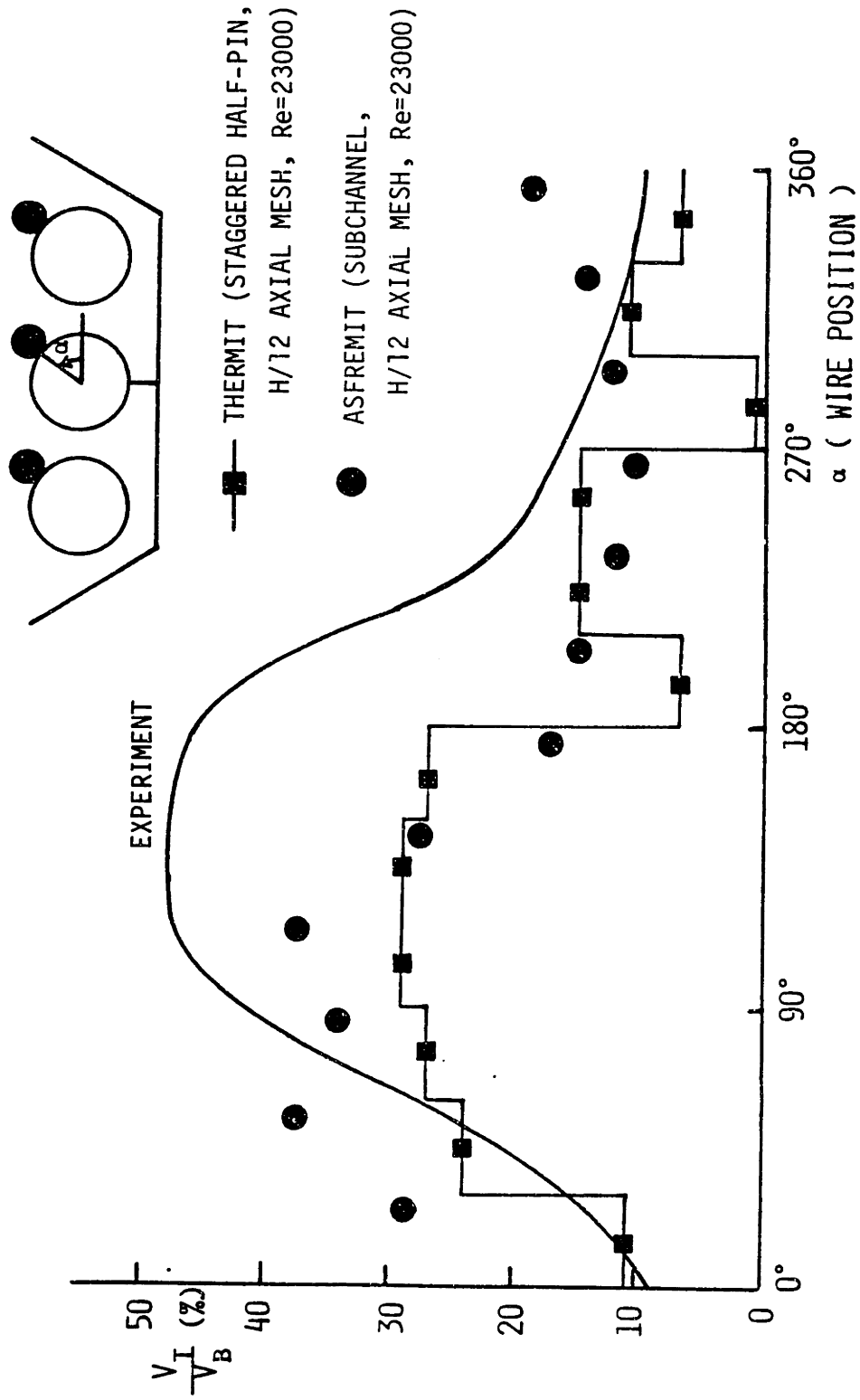
Figure 4.14 Axial Variation of Transverse Velocity at the Central Gap
in Side Subchannel
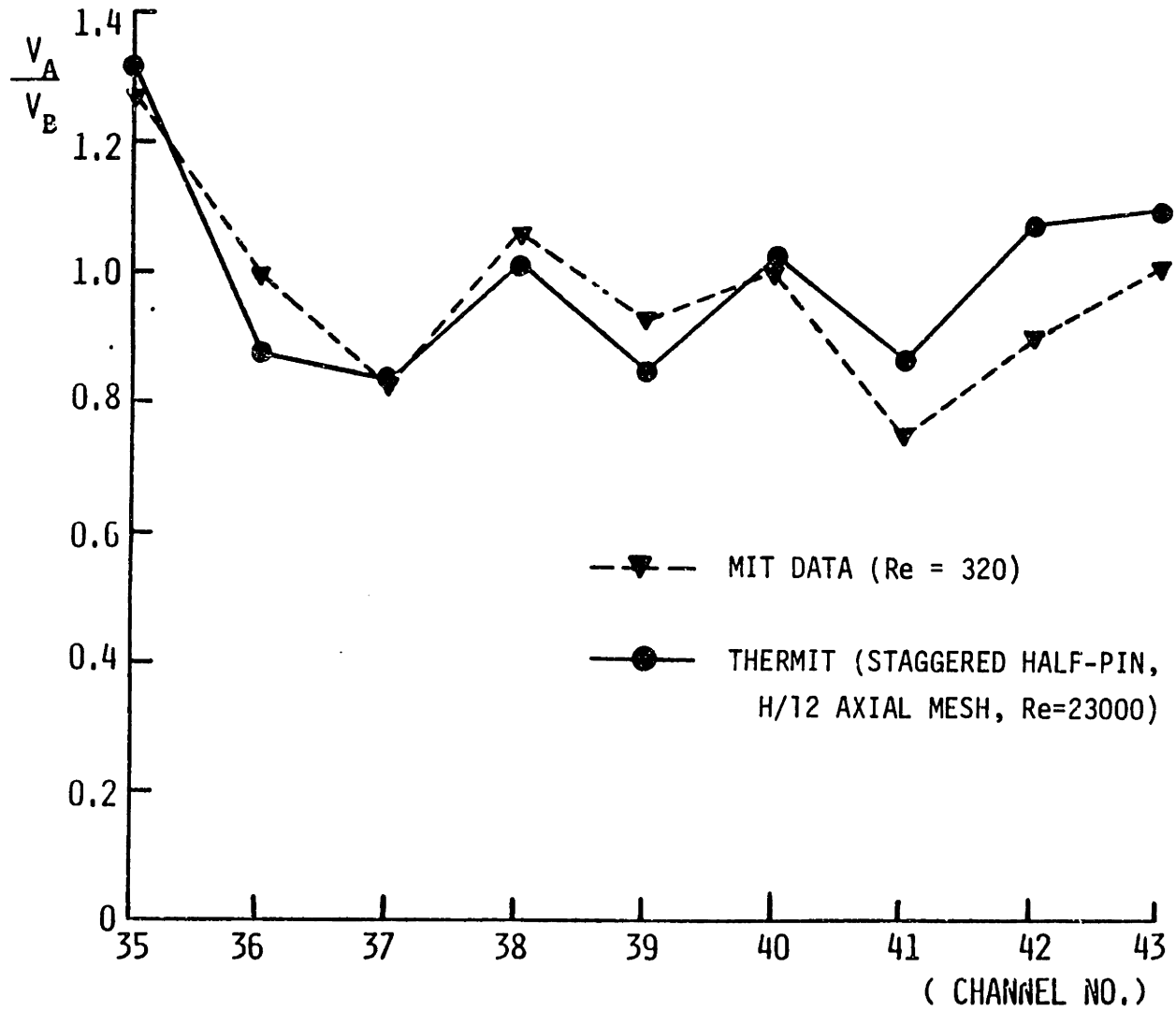
Figure 4.15 Axial Velocity Profile at the Exit Region

flow rate of the side subchannels increased as Re decreased in low flow
condition (Re<10,000). Therefore the THERMIT prediction versus the data
seems inverted by only a small amount for side subchannels 35 and 43.
However, it may be qualitatively verified that the THERMIT can
reasonably predict the axial velocity profile.

4.4.2.2   Pressure Field

The THERMIT prediction of the pressure field was also compared with
the experimental data. Figure 4.16 plots the THERMIT prediction of the
pressure field along the peripheral hexagonal duct for the inlet axial
velocity at 2 m/s (Re = 23000). The experimental data for this pressure
field are shown in Figure 4.17 at a different velocity, 8m/s (Re =
27,000). Direct agreement between the magnitude of the maximum
circumferential pressure differences of the experiment and the THERMIT
simulation are not possible because the axial velocities of these two
cases are different. The axial Reynolds numbers however are about the
same because of different viscosities although the experiment used water
at 65°F with an axial velocity of 8 m/s while the THERMIT-4E simulation
used sodium at 710°F with an axial velocity of 2 m/s. However, the
overall pressure profile of the THERMIT shows a similar shape as that of
the experiment. The maximum pressure is obtained on the side where the
wire spacer is entering to the peripheral subchannel. This corresponds
to the stagnation region upstream of the wire spacer. The minimum
occurs on the side where the wire spacer is leaving the subchannel.
This corresponds to the wake region downstream.

Figure 4.18 shows the axial evolution of the pressure difference,
$P_2 - P_1$ between two side subchannels. The THERMIT prediction was compared
against the experimental data at the same velocity condition. The
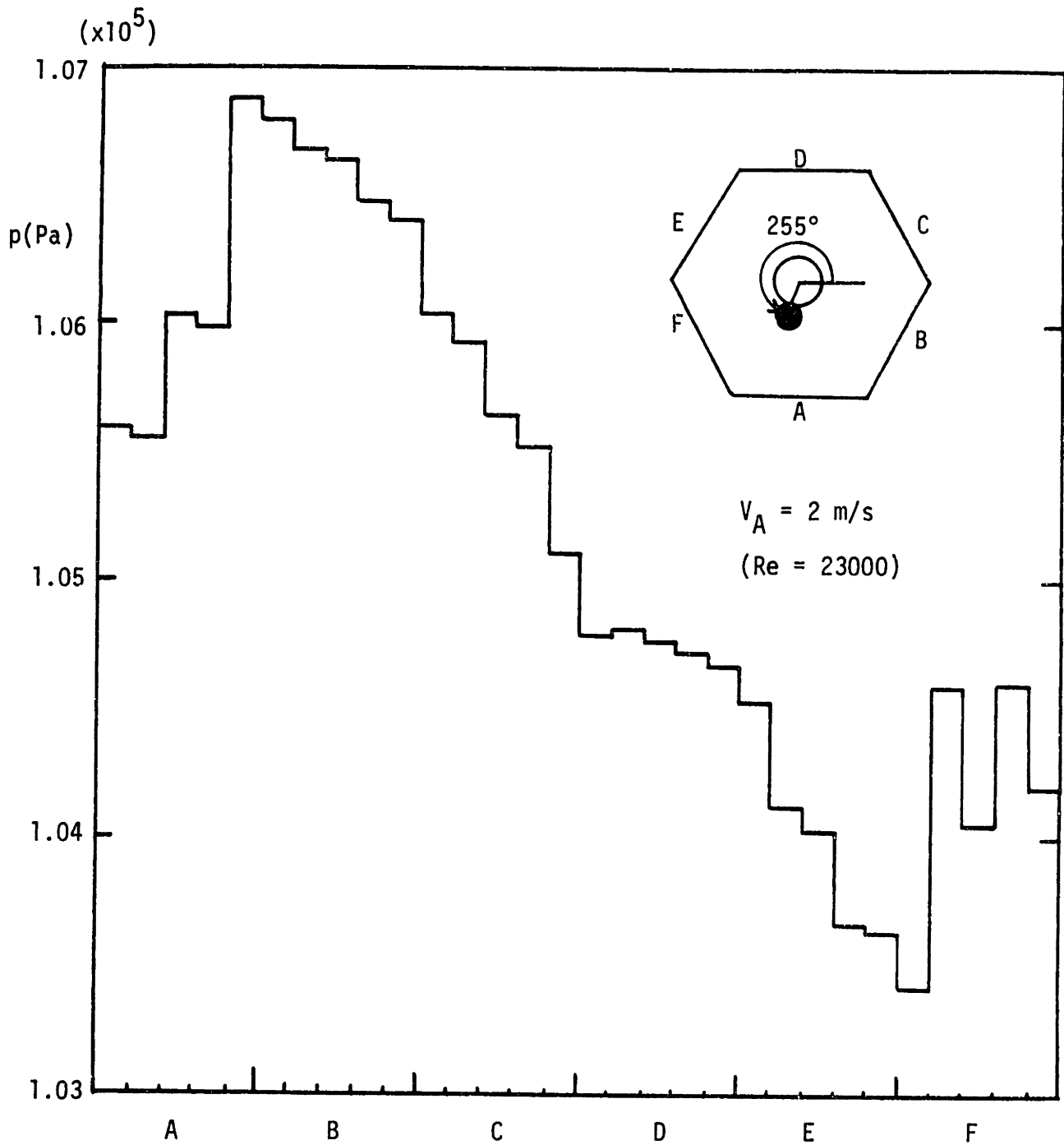
Figure 4.16   THERMIT Predicted Pressure Field Results Along the
Hexagonal Duct Wall
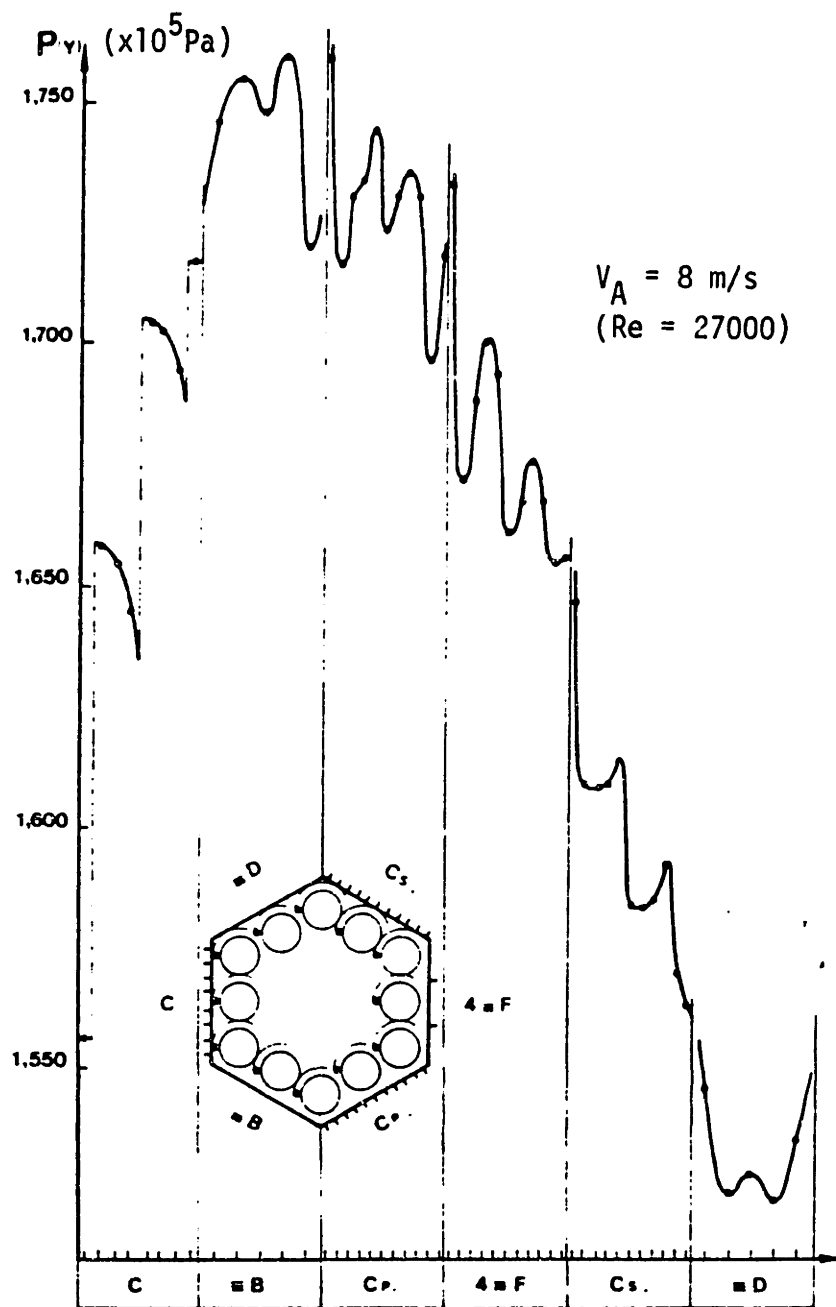
Figure 4.17 Experimental Data of Transverse Pressure Field
(Taken from Reference L-1)
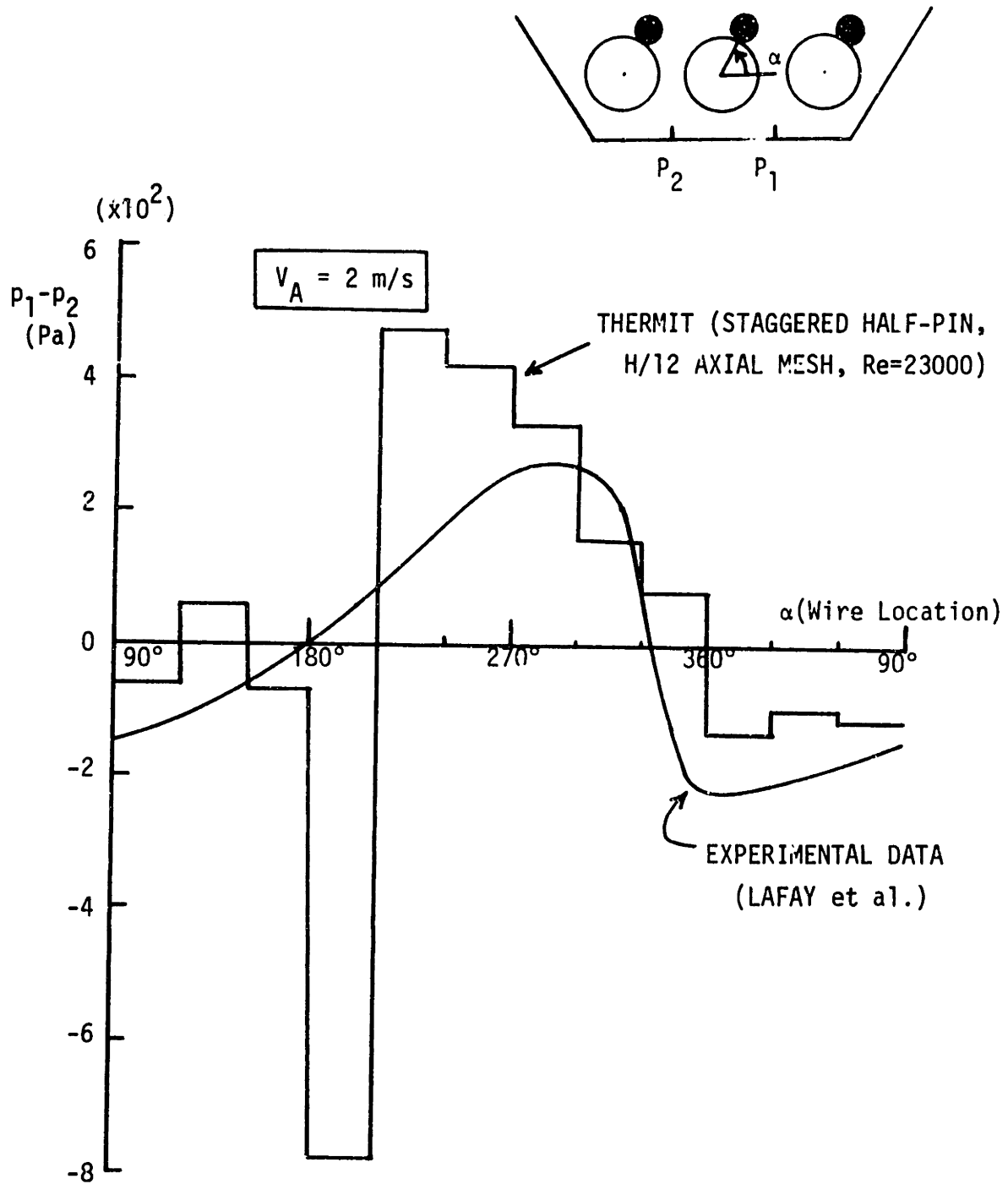
Figure 4.18 Axial Variation of Pressure Difference Between
Two Side Subchannels

agreement was largely satisfactory except an abnormal peak in the prediction at the wire positions of 180° to 210°. Reasons for this abnormality have not been established, but one of the reasons may come from the fact that high pressure in the subchannel 2 is not properly relieved through the gap to an adjacent interior subchannel in the numerical calculation since the wire spacer at 180° to 210° blocks this pathway.

The axial variation of the pressure field at a side subchannel is drawn in Figure 4.19. The difference between the local pressure of the side subchannel and the average pressure at the same plane is plotted as a function of the wire spacer position, i.e., axial elevation. The experimental data corresponding to this figure is presented in Figure 4.20. Since the flow velocity conditions were different between experiment and THERMIT calculation, quantitative comparison could not be made, but the behavior of the local pressure relative to the average planar pressure is quite reasonable. This behavior can best be explained by reference to Figure 4.21 which idealizes the result of Fig. 4.19 and explicitly shows the axial variation of both the local side subchannel pressure, p, and the planar average pressure, $\bar{p}$. Over the axial increment of wire movement from 0° to 180°, no wire exists in the control volume while the converse is true for wire movement from 180° to 360°. With no wire present, the subchannel hydraulic diameter, De, is larger than the case with the wire present. Since pressure drop is inversely proportional to De, the relative axial change in side subchannel pressure is smaller from 0° to 180° than from 180° to 360° as Figure 4.21 shows.
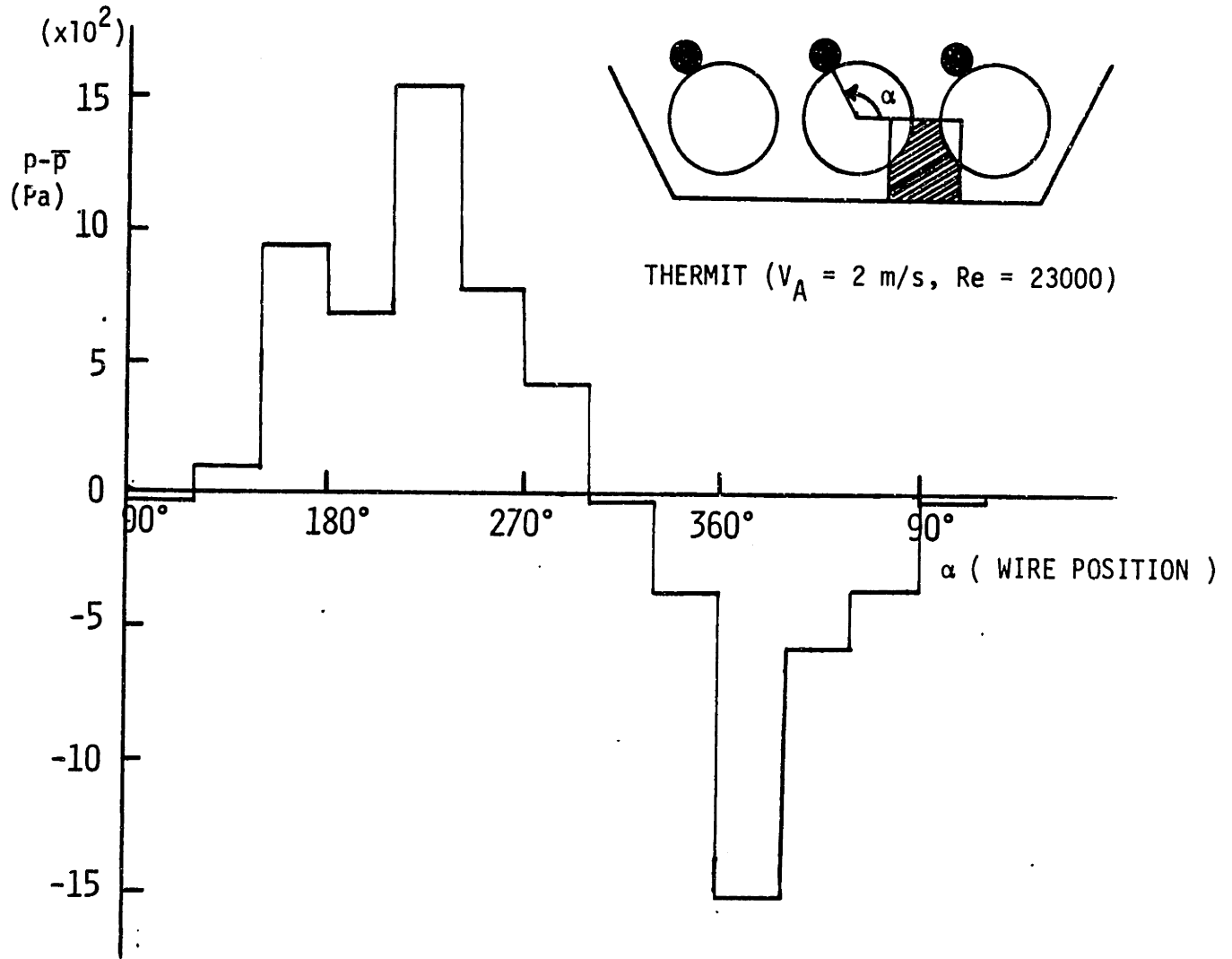
Figure 4.19 Axial Variation of Pressure Field in a Side
                  Subchannel
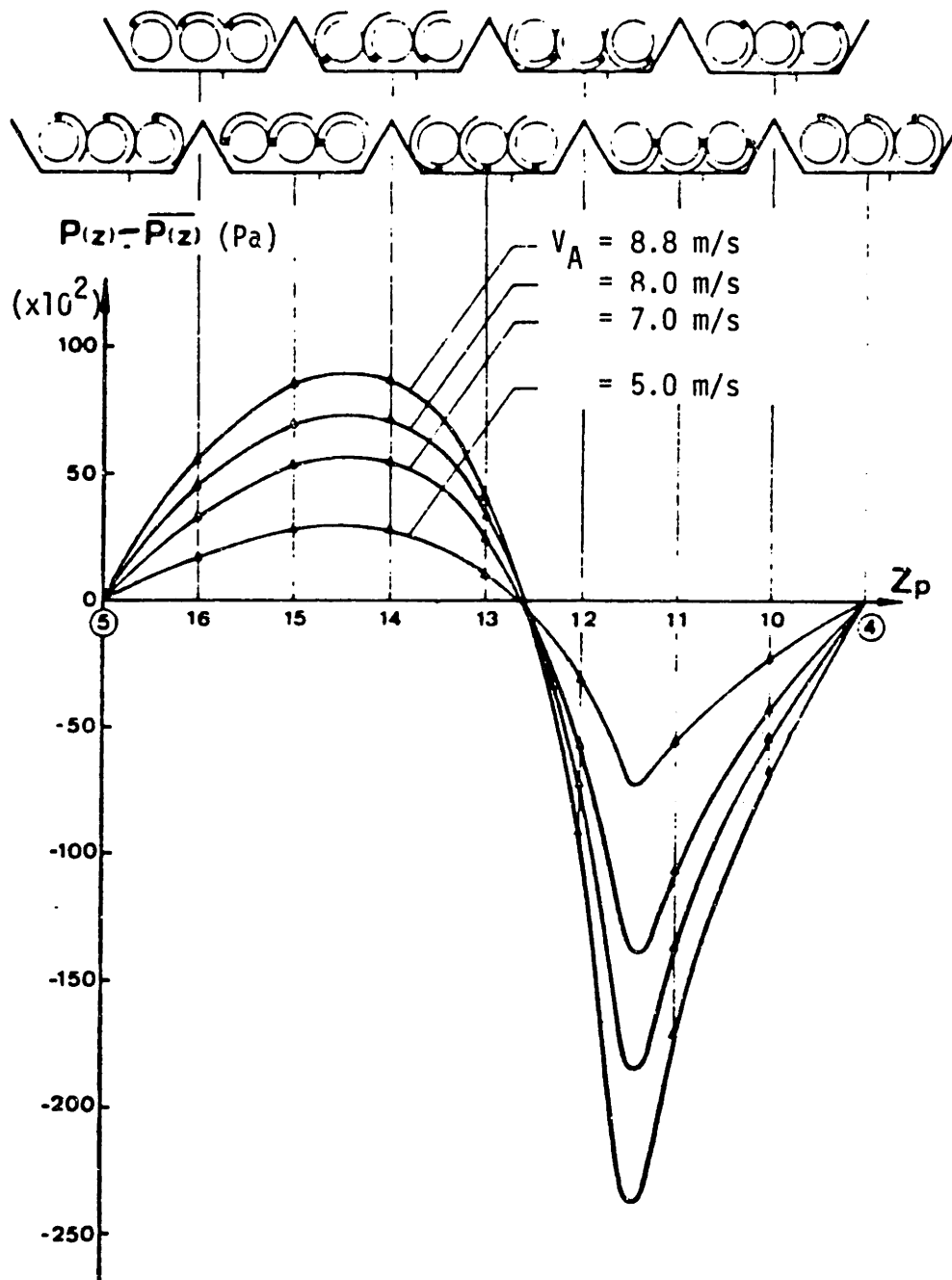
Figure 4.20   Experimental Data of the Axial Pressure Variation
(Taken from Reference L-1)
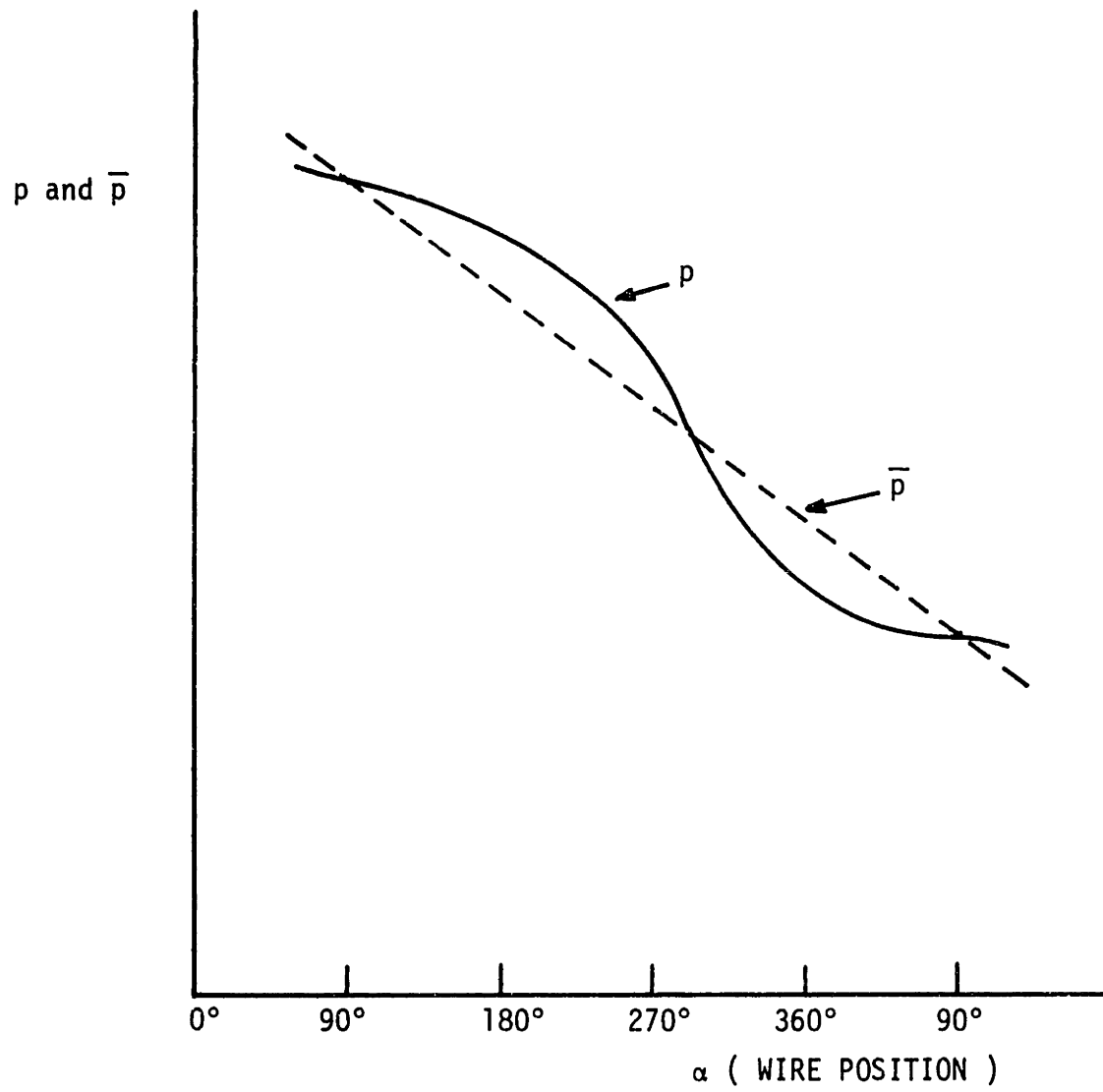
Figure 4.21   Idealized Representation of the Axial Pressure
             Variation

4.4.2.3 Conclusions

To prove the THERMIT capability for predicting the velocity and pressure fields and to generalize the calibration constant to apply to the whole spectrum of bundle geometry, significantly more THERMIT calculations should be performed. However, each run requires substantial computing time for the following reason: When the value of the correction factor C_p is greater than 2, convergence is not achieved in one execution. Thus, to obtain a converged solution, the C_p should be gradually increased after a steady state condition is established. This process requires lots of computing time with our computer facility. A numerical scheme should be developed to accelerate the convergence.

From comparisons between the THERMIT prediction and the experimental data or the ASFREMIT prediction, the following conclusions were drawn:

- The overall THERMIT prediction of the velocity field in a wire-wrapped rod bundle is very satisfactory. The swirl flow behavior is predicted correctly.

- The pressure profile of the THERMIT prediction shows qualitative agreement with the experimental data. Further study is required to validate the pressure field predictions compared with the experimental data by simulating the same velocity condition.

- The choice of the optimum control volume geometry as the staggered half-pin layout appears appropriate and is verified by comparison with experimental data.

- The correction factor C_p should be refined and generalized by calibration for other geometries and flow conditions.

CHAPTER 5

NON-RADIAL ROD CONDUCTION EFFECT IN ROD BUNDLES

5.1 Introduction

5.1.1 Motivation of Work

Correct prediction of the temperature profile within a rod bundle is essential in the thermal-hydraulic design and analysis of LMFBR rod bundle. Fuel and cladding integrity can be maintained by limiting the operating temperature within a maximum allowable temperature. For correct prediction of the temperature field, all energy transfer mechanisms involved in the range of reactor operation should be taken into account. In the forced convection region, turbulent mixing and the energy transfer induced by crossflow due to wire spacers, i.e., the wire sweeping are dominant over other energy transfer mechanisms. In the mixed convection region where the buoyancy effect is important, a significant net crossflow caused by the buoyancy force results in redistribution of the subchannel flow and renders the temperature distribution flatter than in the forced convection region. In addition to this flow redistribution effect, heat conduction through the fluid becomes more important since the turbulent and the wire sweeping effect decreases from the forced to the mixed convection region. At high $Gr_{\Delta T}/Re$ conditions, it is expected that thermal plumes generated from the heated rod surfaces promote the energy mixing between subchannels. Chapter 8 is focused on the experimental exploration of this thermal plume effect.

Besides the above-mentioned effects, in the mixed convection region, non-radial conduction through the rods becomes important. In most subchannel analyses, the heat flux distribution at the cladding surface

is assumed to be uniform. This assumption is no longer valid if a power

skew or a severe temperature gradient exists across the bundle.

Moreover, since most experiments performed in out-of-pile tests use

electrically heated simulation rods instead of actual UO_2-filled fuel

rods, the non-radial conduction through boron nitride (BN) or magnesium

oxide (MgO) insulator is increased due to its high thermal conductivity.

Therefore, the purpose of this work is to investigate and to

quantify the non-radial heat conduction through heater rods and to

construct a rod conduction energy transfer model to be applied to

lumped parameter analysis codes. By doing this, the accuracy of code

prediction of the temperature field in the mixed convection region can be

further increased.

5.1.2 Literature Review

To evaluate the non-radial conduction effect analytically or

numerically, it is essential that the analytical method or the computer

code should have a capability to calculate detailed temperature and heat

flux distributions within a multirod geometry.

An extensive review on the distributed parameter method for a single

cell geometry was presented by Todreas (T-2). Methods to obtain the

detailed velocity field in the coolant region and the heat flux variation

at the cladding surfaces were explained for laminar and turbulent flow

conditions and for various P/D ratios. Nijsing and Eifler (N-1) have

reported a multiregion analysis for a single cell geometry for the

turbulent flow condition taking into account the turbulent eddy

diffusivity and the secondary flow effect. A multirod analysis was

performed by Yeung and Wolf (Y-1) by using the boundary matching

techniques at the cell boundary. They utilized approximate analytical

solutions to determine the temperature distribution within the coolant region and within the fuel rods composed of two regions, i.e., fuel and cladding. Our approach is basically an extension of Yeung and Wolf's work to analyze a multirod and multiregion geometry, the boundary condition of which is uniform heat flux at the heating element.

For numerical applications of the distributed parameter method, finite difference and finite element method are widely used, but the partitioning of the grid is complicated since the boundary conditions at the rod surface cannot be exactly matched. The BODYFIT code (C-3) which was developed based on the technique of boundary-fitted coordinate systems can handle boundary conditions accurately without interpolation. In the BODYFIT code, all the physical boundaries are transformed to be coincident with constant coordinate lines in the transformed space. However, this code has some drawbacks for evaluation of the non-radial rod conduction effect, e.g., the energy equation in the fuel rod region is solved in radial 1-dimensional form. Thus, the current version of BODYFIT code cannot take into account the circumferential heat conduction through rods correctly.

The conduction effect through a boron nitride (BN) simulator rod was first evaluated by Engel and Markley (E-3, E-4, E-5). They calculated the ratio of the peak temperature difference to the average temperature rise $((T_{UO_2}-T_{BN})/\Delta T_{UO_2})$ which took into account the thermal conductivity difference between UO_2 rod in the reactor and BN in their blanket test assembly. The calculated results of the ratio of the peak temperature difference are shown in Figure 5.1 (E-3) as a function of heat input gradient. For the peak subchannel, the ratio was 3-4% and a weak function of the heat input gradient. Engel in an earlier paper
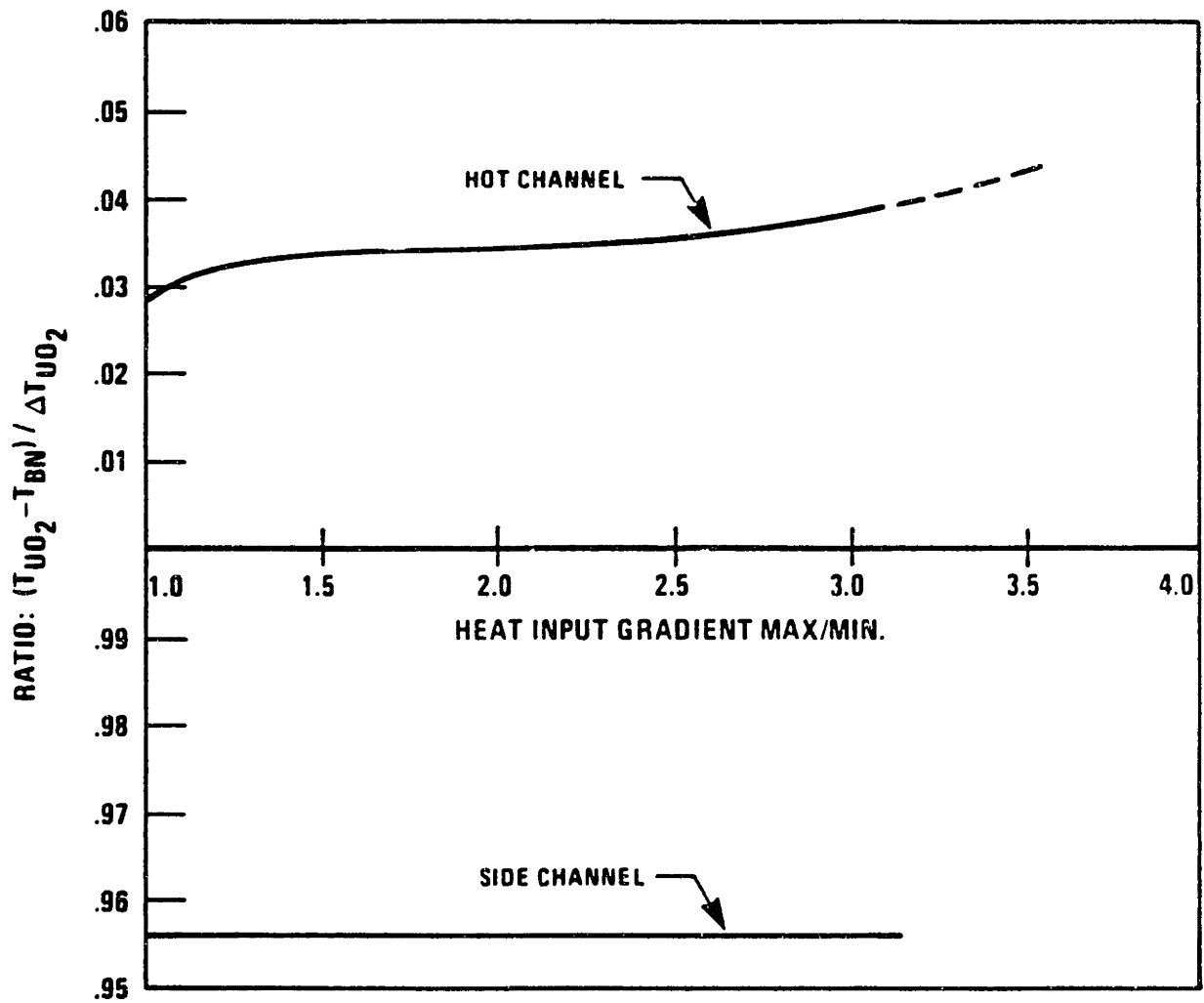
Figure 5.1 Ratio of the Peak Temperature Difference for a
Blanket Assembly (Taken from Reference E-3)

(E-4) reported that in the turbulent flow condition the peak temperature rise measured for the BN simulator rods might be lower than that for UO_2-filled rods by around 3 percent of the average temperature rise. In case of the laminar flow this excess flattening of the peak temperature rise was evaluated as high as 5 to 6 percent. Therefore it appears that Figure 5.1 was calculated for turbulent flow.

The results of references (E-3) and (E-4) were obtained from a conduction code formulated in the following manner (E-5). The calculational geometry was chosen as a zigzag strip along the power skew direction (across flat to flat) with 4 grids in the rod region. The computer code basically solved the conduction equation written in terms of the conductance for each connecting node. The axial convection of sodium flow was modeled as an equivalent axial conductance C_e such as,

$$C_e = 2C_p W \tag{5.1}$$

where C_p = specific heat of sodium

   W = axial mass flow rate

The turbulent mixing and the crossflow mixing by the wire spacers were also modeled as,

$$C_T = \beta C_e \tag{5.2}$$

$$C_W = aC = a \frac{kA}{x} \tag{5.3}$$

where C_T = equivalent conductance due to the turbulence

   β = turbulent mixing paramter

   C_W = equivalent conductance due to the wire sweeping

   a = arbitrary constant

   k = thermal conductivity of the sodium

   A = cross-sectional area normal to the direction of heat flux

x = conductance length

C = radial molecular conductance between nodes

The total lateral conduction input in the code was fC where f was an adjustable factor to account for enhancement due to turbulent mixing and wire wrap crossflow, i.e.,

$$f \equiv \frac{C + C_T + C_W}{C} \qquad (5.4)$$

Temperature distributions for two cases, i.e., BN insulated heater rods and UO_2-filled fuel rods, were obtained using the above equivalent conductance approach, and the temperature difference between two cases at the peak subchannel was plotted with respect to a multiplication factor, f. The results are shown in Figure 5.2. In the laminar flow condition, it was recommended that f be equal to 1 since the heat transfer was assumed to occur entirely by molecular conduction. Then, the percentage temperature difference between BN and UO_2 rod cases was 7.5%. In the turbulent flow condition, f equal to 4 was recommended in order to include the turbulent mixing and the wire sweeping effects. Then the percentage temperature difference became 3.7% which is consistent with the result of Figure 5.1. However, this method based on the equivalent conductance concept has some drawbacks. First, the f value is not known and reflects the uncertainty in the wire sweeping effect. Second, the selected nodal points appear too coarse to accurately evaluate the non-radial heat conduction effect. Most finite difference methods have the same drawback regarding calculation of detailed temperature fields.

To evaluate the non-radial conduction effect through fuel rods or BN rods more correctly, we have developed a computer code which solves the energy equations in 2-dimensional form (r, θ directions) with an approximate analytical method.

POWER SKEW = 2.8/1.

$$\frac{T_{UO_2} - T_{BN}}{T_{out} - T_{in}}$$

WITH GAP CONDUCTANCE

NO GAP CONDUCTANCE

MULTIPLICATION FACTOR, f
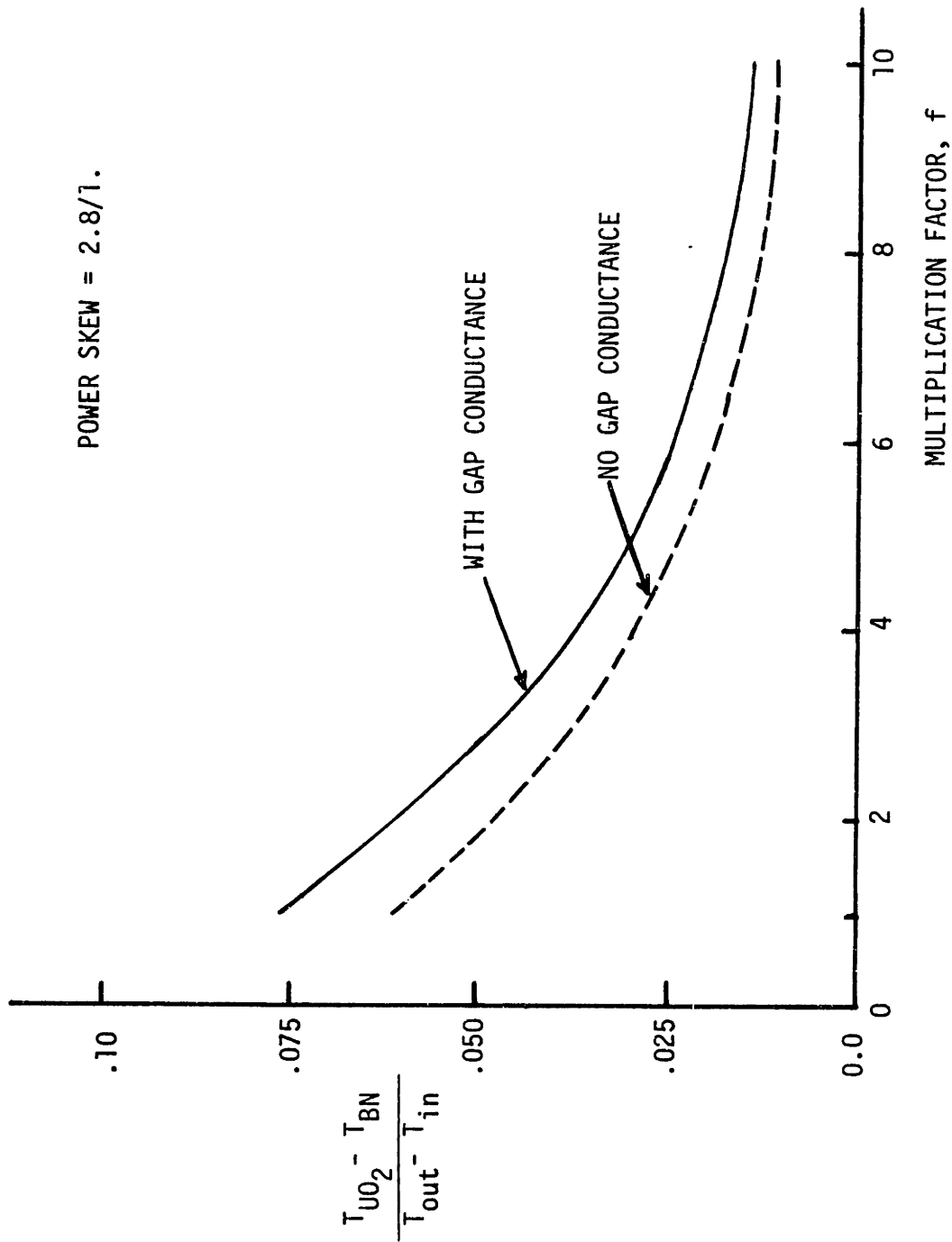
Figure 5.2 Normalized Temperature Difference in the Peak
Subchannel (Taken from Reference E-5)

5.1.3 Scope of Work

The scope of work along with the procedure to attain the stated goal will be presented.

1) The different types of subchannels (unit cells) are identified for the bundle of interest. Governing equation and boundary conditions for a multiregion geometry are set up for each unit cell. Approximate analytical solutions are obtained and the numerical implementation of these solutions is explained step by step. Utilizing these unit cell numerical formulations and an iterative technique for matching the boundary conditions at adjacent cells using the approach of Yeung and Wolf, the composite bundle solution is obtained. The solution method is embodied in a computer code, RODCON.

2) Detailed explanation for the RODCON code is provided including a calculational flow algorithm. Validation of the RODCON code is performed for a unit cell geometry and for a multirod geometry. The unit cell results are compared with the predictions of Nijsing and Eifler (N-1) which include the sophisticated turbulent eddy diffusivity and secondary flow effect. The multirod results are compared with the BODYFIT predictions.

3) In Chapter 6, an energy transfer model for the non-radial heat conduction effect through rods is developed. Parametric studies to determine the unknown coefficients in the suggested model are performed by using the RODCON code. In Chapter 7, the temperature distributions in the rod bundles are predicted by the ENERGY-IV code employing the rod conduction model. The results are compared against all available experimental data.

5.2 Governing Equation

Generally, the detailed temperature distribution within a rod bundle can be obtained by solving all the conservation equations simultaneously. However, this requires tremendous computational effort for a multirod analysis. Since our main purpose is to evaluate the energy transfer through rods in the azimuthal direction, the energy equation was decoupled from the momentum equation by introducing some appropriate assumptions. Then, the energy equation was solved for each material region analytically.

5.2.1 Energy Equation

The schematic geometries for the BN insulated heater rod and for the UO_2-filled fuel rod are depicted in Figure 5.3. The mathematical formulation of the energy equation and its numerical implementation for the UO_2 fuel rod case were presented by Yeung and Wolf (Y-1). In this work, the energy equation was written for the BN insulated heater rod case and an analytical solution for each material region was derived. Unit cell geometry was used to set up the mathematical formulation. The extension to the multirod geometry case by incorporating the boundary matching technique is briefly explained in Section 5.3.1.

The simulated heater rod is composed of electrical heating element, boron nitride (BN) or magnesium oxide (MgO) insulator and stainless steel (SS) cladding as shown in Figure 5.3 (M-2). The general form of the energy equation to be applied to each region is written as,

$$\rho C_p \frac{DT}{Dt} = \nabla \cdot (k \nabla T) + q''' + T\beta \frac{Dp}{Dt} + \mu \Phi* \qquad (5.5)$$

where, ρ = density of the fluid

C_p = specific heat of the fluid

T = temperature

SS CLADDING

UO_2

UO_2 - FILLED FUEL PIN

SS CLADDING

BN (OR MgO) INSULATOR

HEATING ELEMENT
(NICHROME V)
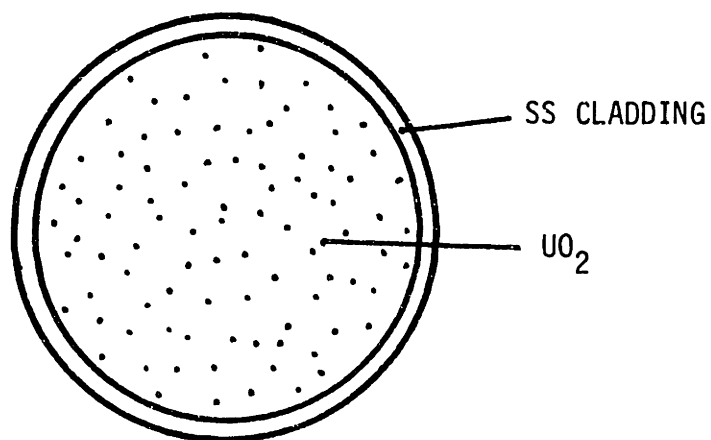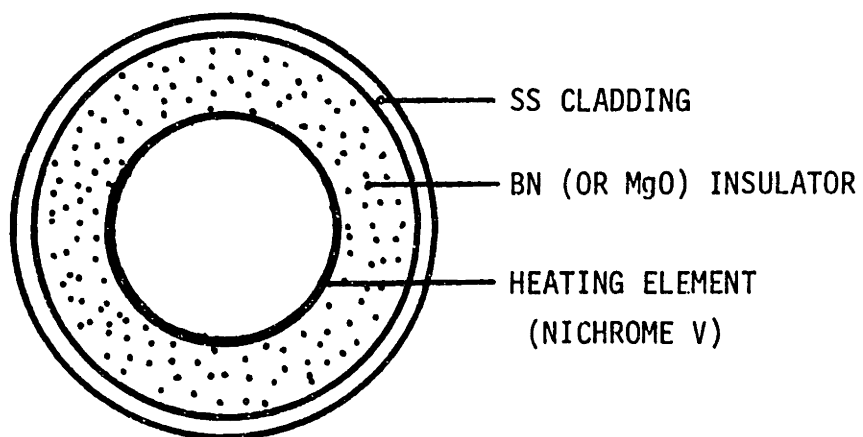
FUEL PIN SIMULATOR

Figure 5.3 Geometry for a UO_2-Filled Fuel Pin and for a BN
Insulated Heater Pin

t = time variable

k = thermal conductivity

q''' = power density

β = thermal expansion coefficient of the fluid

p = pressure

μ = viscosity

Φ* = viscous energy

To simplify Eq. (5.5), the following assumptions are introduced:

(1) Steady state condition is considered.

(2) The fluid is assumed to be incompressible.

(3) Viscous effect is neglected.

(4) The flow is hydrodynamically and thermally fully developed.

(5) Slug flow assumption is used for the velocity distribution.

(6) Thermal conductivity, density and specific heat are constant
    with respect to temperature and position.

(7) Axial heat conduction is negligible compared with radial and
    azimuthal heat conductions.

(8) Heat source with uniform heat flux is located at the inner
    surface of the BN insulator, and no heat is generated in the BN
    insulator or SS cladding.

Using the above assumptions, Eq. (5.5) reduces to the following form in
the cylindrical coordinate system:

$$\rho C_p u \frac{\partial T}{\partial z} = k[\frac{1}{r} \frac{\partial}{\partial r} (r \frac{\partial T}{\partial r}) + \frac{1}{r^2} \frac{\partial^2 T}{\partial \theta^2}] \tag{5.6}$$

where u is the axial velocity of the fluid.

This equation can be applied to each material region. For the BN (or
MgO) insulator or the SS cladding region,

$$\frac{1}{r} \frac{\partial}{\partial r} (r\frac{\partial T}{\partial r}) + \frac{1}{r^2} \frac{\partial^2 T}{\partial \theta^2} = 0 \qquad (5.7)$$

For the Na coolant region,

$$\frac{1}{r} \frac{\partial}{\partial r} (r\frac{\partial T}{\partial r}) + \frac{1}{r^2} \frac{\partial^2 T}{\partial \theta^2} = \frac{\rho C_p u}{k_{Na}} \frac{\partial T}{\partial z} \qquad (5.8)$$

where, k_{Na} = thermal conductivity of the sodium coolant.

By virtue of the assumption of thermally fully developed flow, the temperature gradient $\frac{\partial T}{\partial z}$ can be assumed constant and can be determined from the heat balance of the whole system. The heat balance of the whole system (or bundle) is obtained as,

$$\frac{\partial T}{\partial z} = (\frac{\partial T}{\partial z})_B = \frac{N\bar{q}'}{\rho u_B A_f C_p} \qquad (5.9)$$

Substituting Eq. (5.9) into (5.8) yields,

$$\frac{1}{r} \frac{\partial}{\partial r} (r\frac{\partial T}{\partial r}) + \frac{1}{r^2} \frac{\partial^2 T}{\partial \theta^2} = \frac{N\bar{q}'}{k_{Na} A_f} (\frac{u}{u_B}) \qquad (5.10)$$

where, $\bar{q}'$ = bundle average linear heat rate

N = number of heater rods in the bundle

A_f = total free flow area

u_B = bundle average axial velocity

From Eqs.(5.7) and (5.10), if the above assumptions are valid and the flow split u/u_B is given, the detailed temperature distribution in a rod bundle can be calculated by incorporating appropriate boundary conditions.

5.2.2 Boundary Conditions

The boundary conditions of this problem are continuity of temperature and continuity of heat flux at the interfaces of different material regions. In addition, the heat source distribution should be specified. In order to determine the unknown eigenvalues in the

solutions of the energy equations, the boundary conditions at the cell boundary in the coolant region should be imposed.

The heat source distribution and the continuity conditions for temperature and heat flux are written as:

$$q''(r_o) = \frac{q'}{2\pi r_o} = -k_{BN} \frac{\partial}{\partial r} U(r_o, \theta) \tag{5.11}$$

$$-k_{BN} \frac{\partial}{\partial r} U(a, \theta) = h_g \left[U(a, \theta) - V(a, \theta) \right] \tag{5.12}$$

$$-k_{BN} \frac{\partial}{\partial r} U(a, \theta) = -k_{SS} \frac{\partial}{\partial r} V(a, \theta) \tag{5.13}$$

$$V(b, \theta) = T(b, \theta) \tag{5.14}$$

$$-k_{SS} \frac{\partial}{\partial r} V(b, \theta) = -k_{Na} \frac{\partial}{\partial r} T(b, \theta) \tag{5.15}$$

$$U(r, \theta) = U(r, \theta + 2\pi) \tag{5.16}$$

$$V(r, \theta) = V(r, \theta + 2\pi) \tag{5.17}$$

$$T(r, \theta) = T(r, \theta + 2\pi) \tag{5.18}$$

where U, V and T are the temperatures in the insulator, cladding and coolant regions, respectively, and h_g denotes the gap conductance at the gap between the insulator and cladding regions. Boundary conditions, Eqs. (5.16), (5.17) and (5.18) are required to yield single-valued solutions with respect to the azimuthal direction.

5.2.3 Approximate Analytical Solutions of the Energy Equations

The temperature field of each material region was solved in an analytical way. For the insulator and cladding regions, Eq. (5.7) was solved by the method of separation of variables. The general solution for the BN insulator region yields,

$$U(r, \theta) = A_o + B_o \ln r + \sum_{n=1}^{\infty} \left[(A_n r^n + B_n r^{-n}) \cos n\theta \right.$$

$$\left. + (A_n' r^n + B_n' r^{-n}) \sin n\theta \right] \tag{5.19}$$

For the SS cladding region, the general solution is given in the same form as,

$$V(r,\theta) = C_o + D_o \ln r + \sum_{n=1}^{\infty} \left[(C_n r^n + D_n r^{-n}) \cos n\theta \right.$$

$$\left. + (C_n' r^n + D_n' r^{-n}) \sin n\theta \right] \tag{5.20}$$

For the coolant region, the solution is obtained by solving Eq. (5.10) as,

$$T(r,\theta) = E_o + F_o \ln r + \frac{1}{4} Sr^2 + \sum_{n=1}^{\infty} \left[(E_n r^n + F_n r^{-n}) \cos n\theta \right.$$

$$\left. + (E_n' r^n + F_n' r^{-n}) \sin n\theta \right] \tag{5.21}$$

where, $S \equiv \dfrac{N\bar{q}'}{k_{Na} A_f} \left(\dfrac{u}{u_B} \right)$ \hfill (5.22)

A_o, B_o, A_n, B_n, A_n', B_n', etc. are constants to be determined from the boundary conditions. Substituting Eqs. (5.19), (5.20) and (5.21) into the boundary conditions from Eqs. (5.11) through (5.15) and using the orthogonality of the Fourier sine and cosine series, the above constants are determined as follows:

$$A_o = C_o + \frac{q}{Bi} + q(1-\alpha) \ln a \tag{5.23}$$

$$B_o = -q \tag{5.24}$$

$$D_o = -q\alpha \tag{5.25}$$

$$E_o = C_o - \frac{1}{4} Sb^2 + \left[q\alpha(\beta-1) + \frac{1}{2} Sb^2 \right] \ln b \tag{5.26}$$

$$F_o = -q\alpha\beta - \frac{1}{2} Sb^2 \tag{5.27}$$

and,

$$B_n = A_n r_o^{2n} \tag{5.28}$$

$$C_n = \frac{1}{2} f_n A_n \tag{5.29}$$

$$D_n = \frac{1}{2} b^{2n} g_n A_n \tag{5.30}$$

$$E_n = \frac{1}{4} \left[(1+\beta)f_n + (1-\beta)g_n \right] A_n \tag{5.31}$$

$$F_n = \frac{1}{4} b^{2n} \left[(1-\beta)f_n + (1+\beta)g_n \right] A_n \tag{5.32}$$

where,

$$q = \frac{q'}{2\pi k_{BN}} \tag{5.33}$$

$$Bi = \frac{h_g a}{k_{BN}} \tag{5.34}$$

$$\alpha = \frac{k_{BN}}{k_{SS}} \tag{5.35}$$

$$\beta = \frac{k_{SS}}{k_{Na}} \tag{5.36}$$

$$h = \frac{a}{b} \tag{5.37}$$

$$w = \frac{r_o}{b} \tag{5.38}$$

$$f_n = (1 + \alpha + \frac{n}{Bi}) + (1 - \alpha - \frac{n}{Bi}) \, (\frac{w}{h})^{2n} \tag{5.39}$$

$$g_n = h^{2n}\left[(1 - \alpha + \frac{n}{Bi}) + (1 + \alpha - \frac{n}{Bi}) \, (\frac{w}{h})^{2n}\right] \tag{5.40}$$

B_n', C_n', D_n', E_n' and F_n' are expressed as the exactly same formula as Eqs. (5.28), (5.29), (5.30), (5.31) and (5.32) in terms of A_n' instead of A_n, respectively.

By substituting all the constants determined from the boudnary conditions into the general solutions, the temperature field of each material region is obtained in a dimensionless form as follows:

For the BN insulator region,

$$\frac{U(\rho,\theta)-C}{q\alpha\beta} = \frac{1}{Bi\,\alpha\beta} + \frac{1}{\alpha\beta} \ln (\frac{h}{\rho}) + \sum_{n=1}^{\infty} \, [\frac{Y_n}{n} \, (\rho^n + w^{2n}\rho^{-n}) \cos n\theta$$

$$+ \frac{Y_n'}{n} \, (\rho^n + w^{2n}\rho^{-n}) \sin n\theta \tag{5.41}$$

For the SS cladding region,

$$\frac{V(\rho,\theta) - C}{q\alpha\beta} = -\frac{1}{\beta} \ln \left(\frac{\rho}{h}\right) + \sum_{n=1}^{\infty} \frac{Y_n}{2n} (f_n \rho^n + g_n \rho^{-n}) \cos n\theta$$

$$+ \frac{Y'_n}{2n} (f_n \rho^n + g_n \rho^{-n}) \sin n\theta \qquad (5.42)$$

For the coolant region,

$$\frac{T(\rho,\theta) - C}{q\alpha\beta} = \frac{1}{\beta} \ln h - \left(1 + \frac{1}{I}\right) \ln \rho + \frac{1}{2I} (\rho^2 - 1)$$

$$+ \sum_{n=1}^{\infty} \left[\frac{Y_n}{4n} \left\{((1 + \beta)f_n + (1 - \beta)g_n)\rho^n + ((1 - \beta)f_n \right.\right.$$

$$+ (1 + \beta)g_n)\rho^{-n}\right\} \cos n\theta + \frac{Y'_n}{4n} \left\{((1 + \beta)f_n + (1 - \beta)g_n)\rho^n\right.$$

$$+ ((1 - \beta)f_n + (1 + \beta)g_n)\rho^{-n}\right\} \sin n\theta\right] \qquad (5.43)$$

where,

$$C \equiv C_o - q\alpha \ln a \qquad (5.44)$$

$$\rho = \frac{r}{b} \qquad (5.45)$$

$$Y_n \equiv \frac{nb^n}{q\alpha\beta} A_n \qquad (5.46)$$

$$Y'_n \equiv \frac{nb^n}{q\alpha\beta} A'_n \qquad (5.47)$$

$$I \equiv \frac{q\alpha\beta}{\frac{1}{2}Sb^2} \qquad (5.48)$$

The physical meaning of the constant C can be explained from the temperature solution for the cladding region. The temperature at the cladding surface is obtained by setting ρ equal to h in Eq. (5.42). Then, integrating this equation with respect to angle θ from 0 to 2π (or the angle at the symmetric location) yields,

$$C = \frac{1}{2\pi} \int_0^{2\pi} V(h,\theta) \, d\theta \qquad (5.49)$$

This result shows that the constant C is simply the average temperature at the cladding surface. The constant C cannot be determined by the above boundary conditions. In order to obtain the value of the constant C, a reference temperature such as the average coolant temperature of the unit cell should be given.

The constant I can be rewritten as,

$$I = \frac{q\alpha\beta}{\frac{1}{2}Sb^2} = (\frac{A_f}{N\pi b^2}) \, (\frac{q'}{\bar{q}'}) \, (\frac{u_B}{u}) \qquad (5.50)$$

Thus, I is the multiplication of the ratio of the total flow area to the area occupied by the rods and the peaking factor and the reciprocal of the flow split of the cell to the bundle average velocity.

The temperature field in each material region can be obtained from Eqs. (5.41), (5.42) and (5.43) if the unknown constants Y_n and Y'_n are provided. These unknown constants are determined by the boundary conditions at the cell boundary in the coolant region. Two kinds of boundary condition types can be applied, i.e., Dirichlet and Neumann boundary conditions which specify the temperature and the heat flux at the cell boundary, respectively. At the walls of the side cells and at the symmetric lines, the adiabatic boundary condition, i.e., a Neumann boundary condition, is imposed.

5.3 Multirod Analysis Code, RODCON

In the previous section, the temperature field solution of each region has been obtained by an analytical method. In order to implement it into a numerical computer code, an approximate solution is obtained by truncating the infinite summation to a finite term N. N should be determined so that the residual of the summation is negligibly small.

The RODCON code has been developed by modifying the Yeung and Wolf code (Y-1). The capability to solve the temperature field for the BN rod configuration with different heat source distribution was added. A normalization procedure was implemented so that the temperature fields of each unit cell could be compared with each other. Normalized subchannel temperatures were also evaluated by lumping the detailed temperature distribution.

The RODCON code can analyze a rod bundle with one-twelfth symmetry. As an example, the geometric configuration of a 61-rod bundle is shown in Figure 5.4. A twelfth sector of the rod bundle is divided into a number of small unit cells. The cell boundaries are shown in Figure 5.4 as dashed lines. The boundary conditions to be used in the multirod calculation are also indicated in the figure.

5.3.1 Calculation Procedure

A schematic flow diagram of the RODCON code is presented in Figure 5.5. Input information required for the RODCON code is the geometrical data for a given rod bundle configuration, the thermal conductivities of the constituent materials and the power peaking factor for each heater rod. Input requirements and Fortran listing of the RODCON code are presented in Appendix D.

The calculation procedure can be divided into three steps: unit cell calculation, multirod calculation and normalization of the temperature field.

5.3.1.1 Unit Cell Calculation

The temperature field of each unit cell is obtained by assuming an adiabatic boundary condition at the cell boundary, i.e., each unit
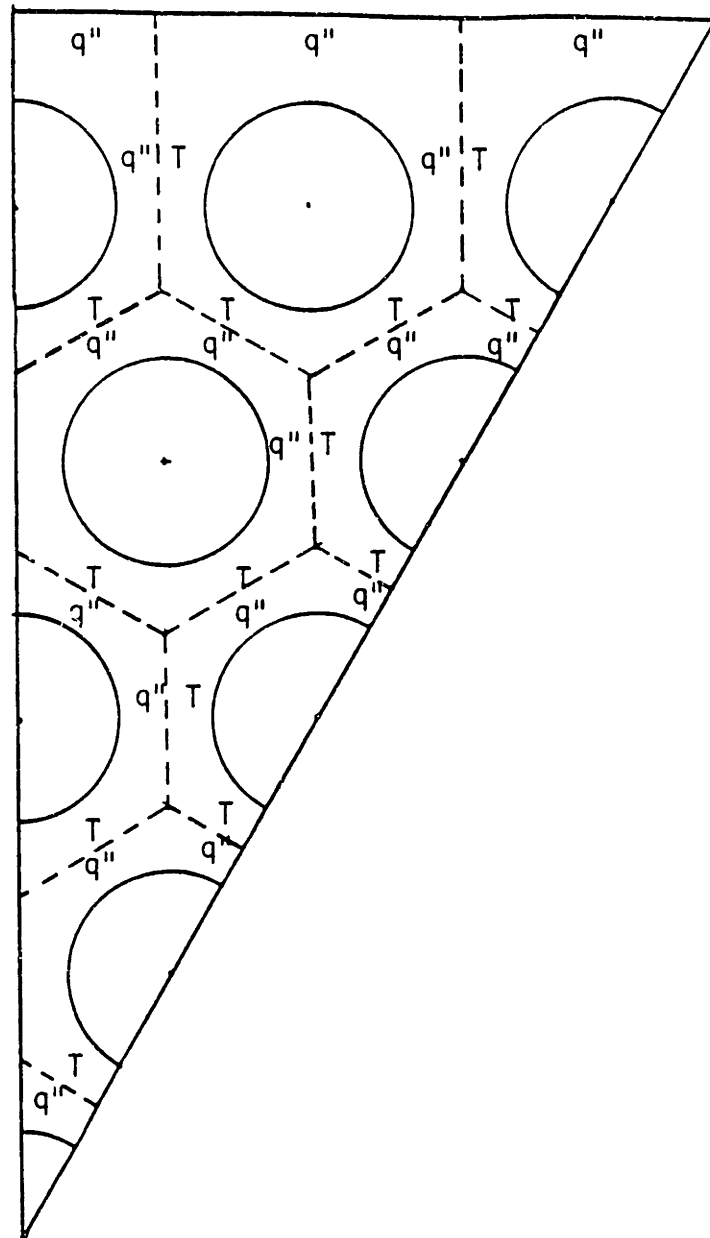
Figure 5.4 1/12 Sector of 61-Pin Bundle Geometry with the
Imposed Boundary Conditions
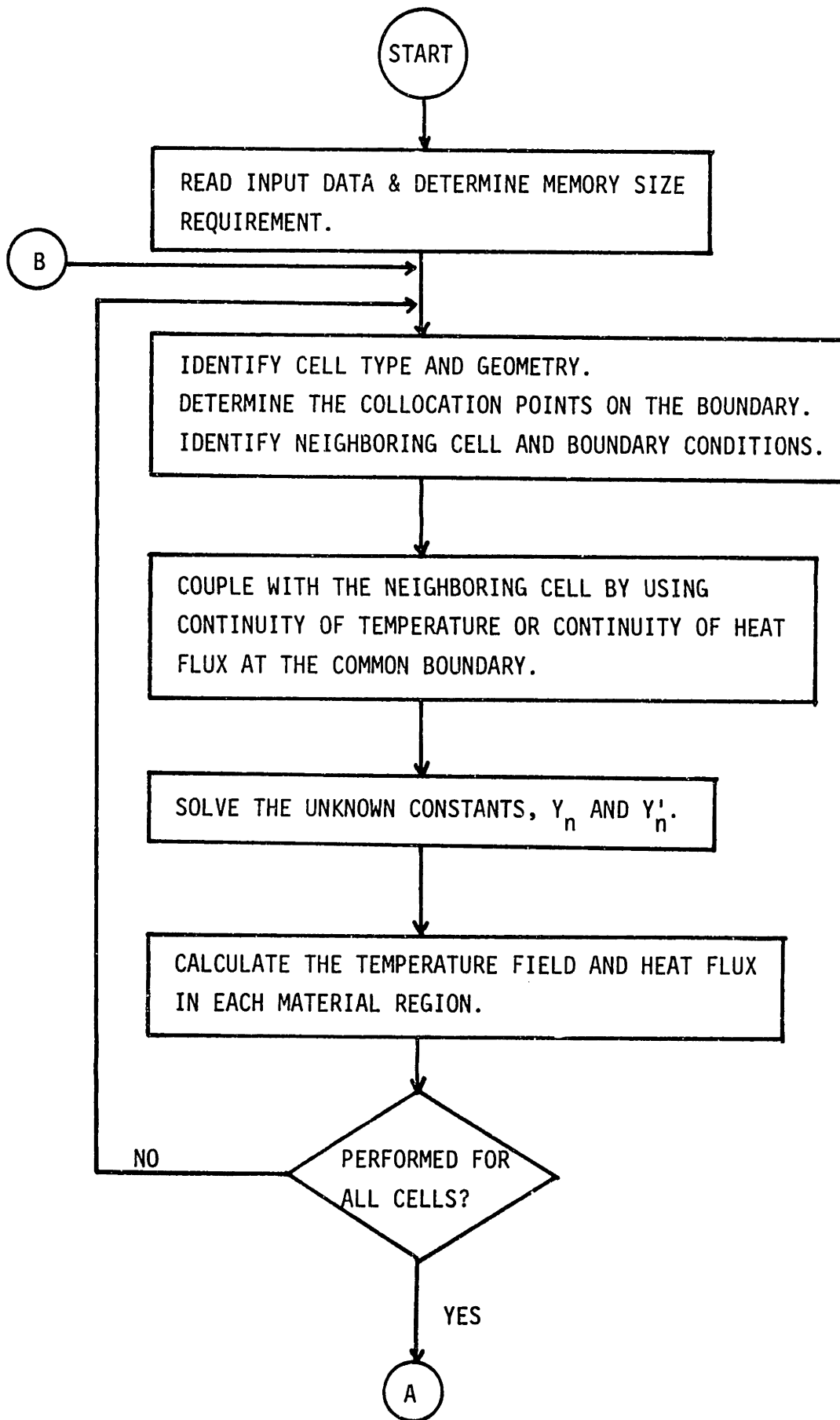
Figure 5.5 Calculational Flow Diagram of the RODCON Code
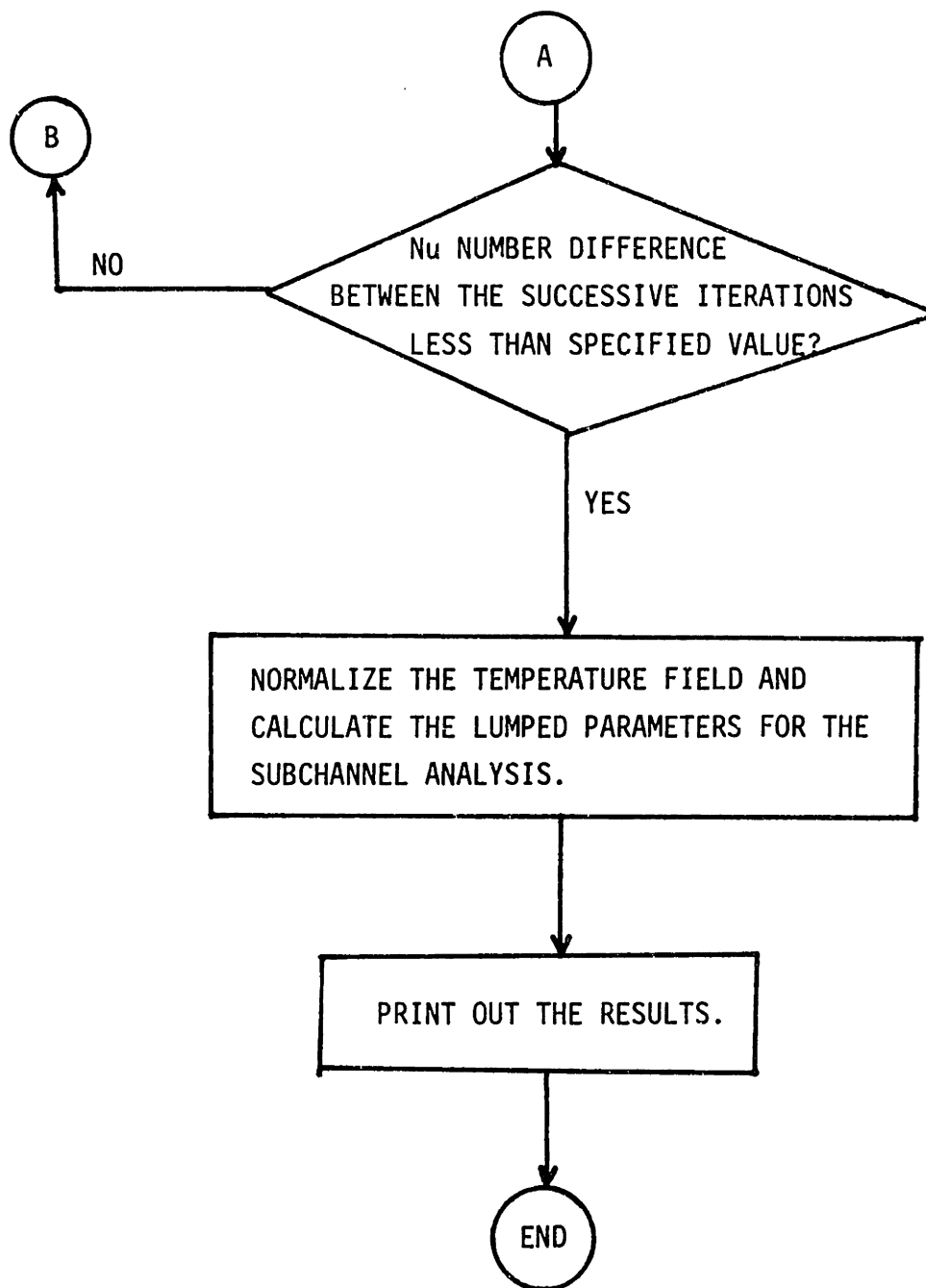
Figure 5.5 (Continued)

cell is an isolated cell. In order to solve the unknown eigenvalues Y_n and Y_n', the number of points at the cell boundary should be chosen to be equal to or more than the number of the unknowns. The Y_n and Y_n' can be determined by solving the system of the linear equations. Once Y_n and Y_n' are obtained, all temperature fields can be determined from Eqs. (5.41), (5.42) and (5.43).

5.3.1.2 Multirod Calculation

The temperature fields obtained from the unit cell calculations result in discontinuity of temperature at the common boundary between neighboring cells. In order to match the temperatures and the heat fluxes at the collocation points on the common boundary, the following iterative method was adapted: A set of the average temperatures of the two neighboring cells at the collocation points on the common boundary is used as a new temperature boundary condition for the calculation of one of two unit cells. Figure 5.4 shows the boundaries of unit cells where the temperature or the heat flux boundary condition is imposed. The new temperature boundary condition leads to a new heat flux distribution at the common boundary. Then, this new heat flux distribution at the common boundary is used as an updated boundary condition to calculate a new temperature field for its neighboring unit cell. This procedure yields new temperature fields for both neighboring cells. The above procedure is repeated iteratively until the discontinuity of temperature at the common boundary is acceptably small. Then, the final temperature field in the rod bundle which satisfies the boundary conditions at all the common boundaries can be obtained.

5.3.1.3 Normalization of Temperature Field

The dimensionless temperature obtained from the aforementioned procedure is the temperature difference relative to the average cladding surface temperature of the unit cell. However, the average cladding surface temperatures for all unit cells are not the same. In order to compare the dimensionless temperature of the unit cell with that of other cells, the temperature difference should be calculated relative to a reference temperature which can be uniquely determined. In this work, the bulk mean coolant temperature of the bundle at a certain axial location is selected as the reference temperature since the bulk mean coolant temperature can be easily obtained from the simple energy balance in the rod bundle. Finally, the subchannel average coolant temperature is calculated by lumping the detailed temperature distribution within the subchannel.

5.3.2 Validation of the RODCON Code

The capability of the RODCON code for the analyses of a unit cell and a multirod geometry were tested against a more sophisticated analytical method including a turbulent model and against a three-dimensional distributed parameter code.

5.3.2.1 Unit Cell Analysis

Nijsing and Eifler (N-1) obtained the temperature field by solving the energy and the momentum equations which include the turbulent eddy diffusivity models. The anisotropic effect of the turbulent eddy diffusivity and the secondary flow effect were also included in the prediction of the velocity field. The flow was assumed thermally and hydrodynamically fully-developed in their approach as well as in the RODCON code.

Comparisons between the RODCON predictions and the results of Nijsing and Eifler's method are shown in Figures 5.6 and 5.7. The RODCON calculations were performed for the same geometrical configuration and material compositions. For the uniform heat flux at the cladding surface, the dimensionless cladding surface temperature distribution of the RODCON code lies between that of the isotropic turbulence case and that of the no turbulence case as shown in Figure 5.6. The RODCON result is quite acceptable for the following reasons: The slug flow model employed in the RODCON code is based on two assumptions, i.e., (a) uniform velocity distribution, (b) neglect of turbulence and secondary flow contribution to heat transport. Assumption (a) flattens the temperature profile within the coolant, while assumption (b) yields less heat transport through the coolant. Thus, it is expected that the cladding surface temperature variation predicted by the slug flow model should be smaller than that predicted by conduction only (with non-uniform velocity distribution). The temperature variation predicted by the slug flow model can be smaller or larger than that predicted by a more realistic analytical model including the turbulence or secondary flow contribution. It depends on the conditions of a given problem.

Figure 5.7 shows the RODCON results of the dimensionless cladding surface temperature distributions for the uniform heat flux condition at the inner cladding and at the inner sodium bond surfaces. The corresponding temperature distributions of the Nijsing and Eifler's method are also drawn in Figure 5.7 for the same heat flux boundary conditions except the result of the multiregion analysis in which a uniform heat source distribution in the fuel region is used instead of
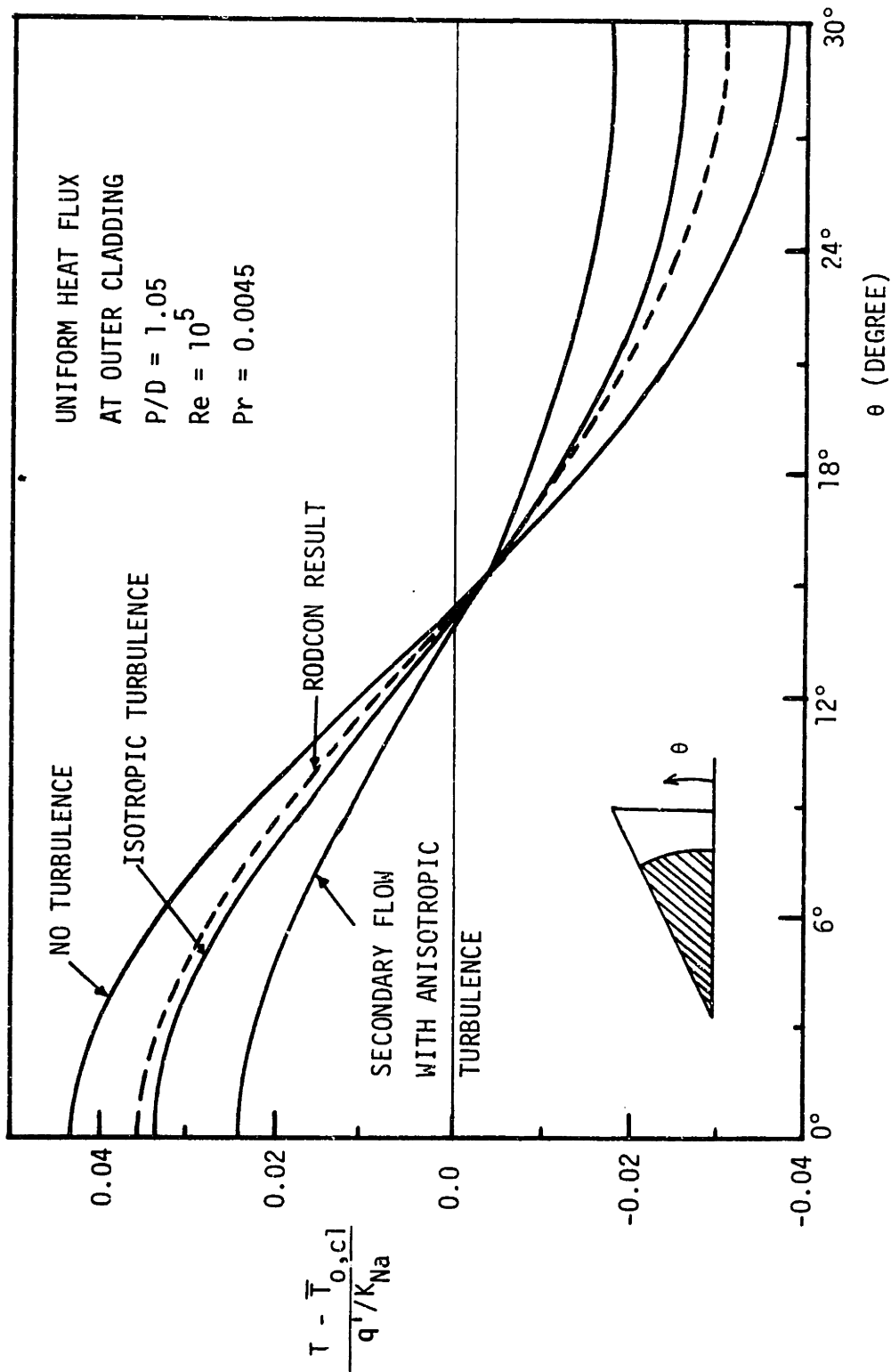
Figure 5.6 Comparisons of Circumferential Cladding Temperature Variation Between the RODCON Predictions and Nijsing and Eifler's Results
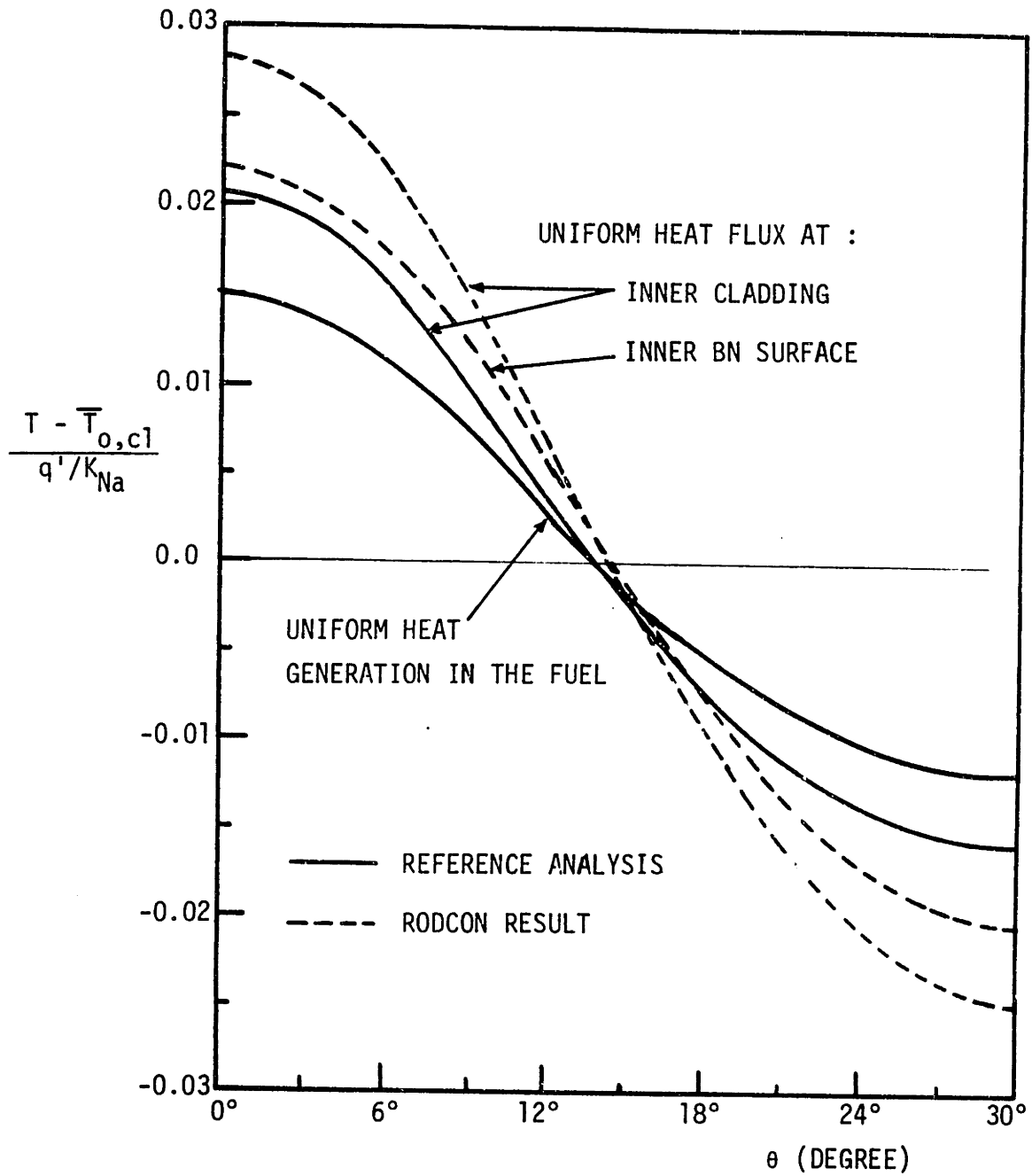
Figure 5.7 Circumferential Cladding Temperature Variation for Different Heat Flux Conditions

the constant heat flux condition at the inner sodium bond. The RODCON predictions of the temperature variation generally overestimate those of the analytical method of Nijsing and Eifler. The reason is, as mentioned before, that the turbulence and the secondary flow effect are not included in the RODCON code.

From this comparison study, it is concluded that the overall prediction of the RODCON code is quite satisfactory for a unit cell analysis.

5.3.2.2 Multirod Analysis

In order to assess the capability of the RODCON code for a multirod analysis, the BODYFIT code was chosen as a benchmark code. The BODYFIT code is a 3-dimensional distributed parameter code for thermal-hydraulic analyses of rod bundles using the technique of boundary-fitted coordinates.

A 7-pin hexagonal rod bundle with sodium as the coolant was chosen for the sample problem. The geometrical parameters and operating conditions (C-4) are summarized in Table 5.1. The coolant temperature variations along the symmetric boundary are plotted in Figure 5.8. The dimensionless temperature rise ΔT^* in the ordinate is defined as,

$$\Delta T^* = \frac{T_i - T_{in}}{T_{out} - T_{in}} \tag{5.51}$$

where T_i is the temperature at the local position, i. T_{in} is the bundle inlet temperature and T_{out} is the temperature at the bundle outlet where the calculations are performed. The prediction obtained by the RODCON code shows good agreement compared with the BODYFIT code. It is observed that the RODCON prediction generally underestimates the ΔT^* at the symmetry boundary. This may originate from the inherent

Table 5.1 Geometrical Parameters and Operating Conditions
of Sample Problem

Rod Diameter, D	0.006 m
Gap between Rods	0.0019 m
Gap between Wall and Rods	0.00116 m
Heated length	0.72 m
Pitch to Diameter Ratio, P/D	1.3167
Cladding Thickness	0.00065 m
Boron Nitride Thickness	0.00075 m
Power Skew, Max/Min	1.2/1.0
Power Density	6.4×10^9 W/m^3
Bundle Inlet Temperature, T_{in}	553°C
Inlet Velocity	2.15 m/sec
Conductivity Ratio, k_{BN}/k_{SS}	0.7813
Conductivity Ratio, k_{SS}/k_{Na}	0.3538
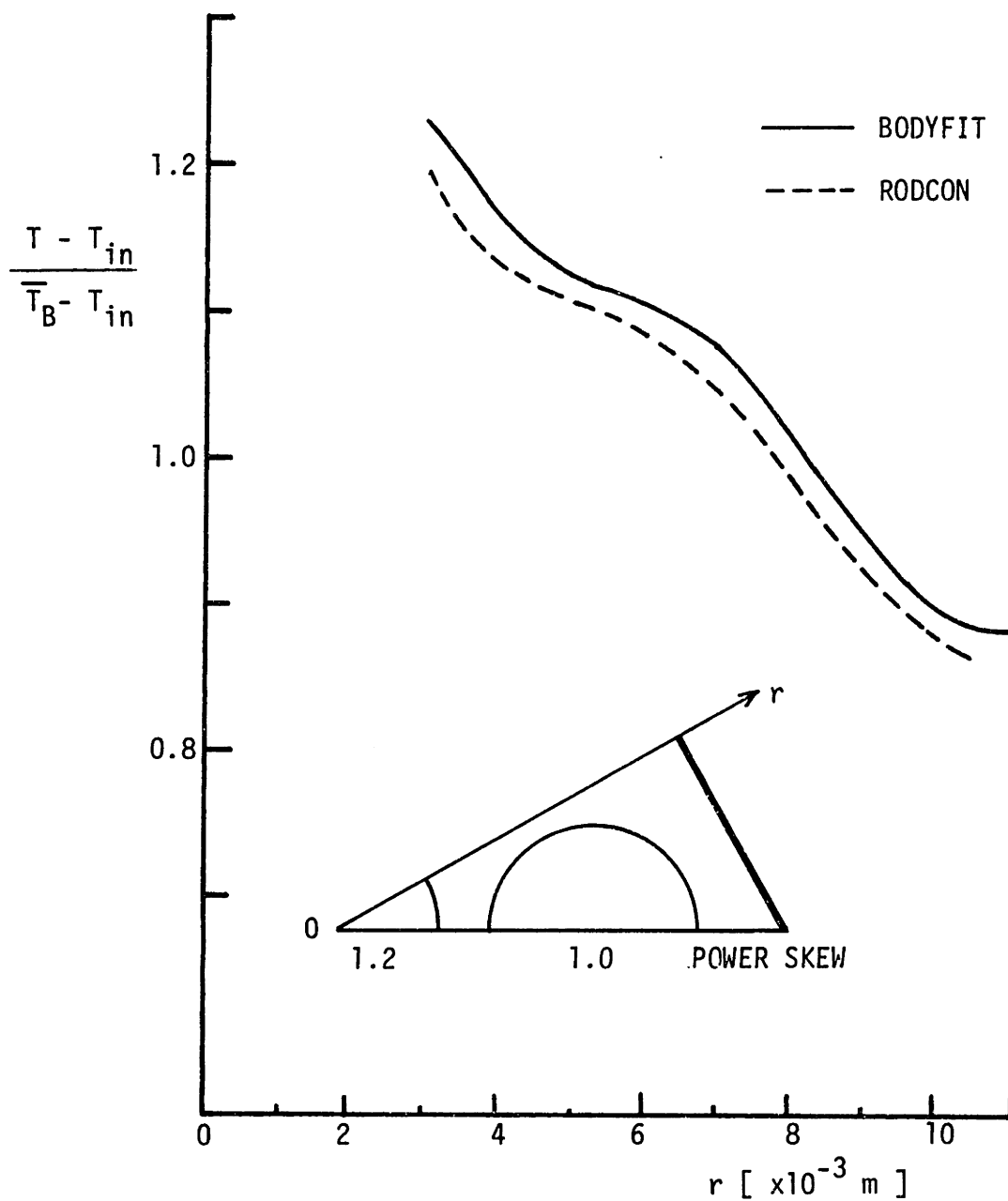
Figure 5.8   Comparison of the Coolant Temperature Profile
Between the RODCON and BODYFIT Predictions

assumption of the slug flow model in the RODCON code. Since the energy mixing by turbulence is not included, the RODCON prediction of the temperature at the boundary away from the heater rod can underestimate it although the uniform velocity assumption flattens the temperature profile. Another possibility is the 2-dimensional nature of the RODCON code which cannot treat the flow developing effect at the entrance region. It is noted that the magnitude of ΔT^* obtained by the RODCON code varies along the axial position although the shape of ΔT^* remains constant in the fully-developed region.

5.4 Conclusions

In order to estimate the non-radial heat conduction effect through the heater rods, the RODCON code was developed based on an approximate analytical method. The analytical temperature solution of each material region was derived. A boundary matching technique was employed for the analysis of a multirod geometry. The RODCON code was tested against a more sophisticated analytical solution for a single cell geometry as well as the results of the BODYFIT code for a multirod geometry. Despite the RODCON assumptions such as the slug flow model for the velocity distribution, it has been proven that the RODCON code is a reliable tool to assess the non-radial heat conduction effect.

CHAPTER 6

THE MODELING OF NON-RADIAL HEAT CONDUCTION THROUGH RODS

6.1 Introduction

In Chapter 5, the general features of the RODCON code were explained and

the importance of the non-uniform heat flux distribution in the analysis of

simulated heater rods was addressed. In addition, the capability and

accuracy of the RODCON code were validated by comparison with the results of

other more sophisticated methods. In this chapter, first, the important

parameters such as thermal conductivities of constituent materials,

temperature distribution within a heater rod and uncertainties involved in

the RODCON code are investigated in detail. Then, a correlation for the

non-radial rod conduction has been developed to provide an additional heat

transfer model for the ENERGY-IV code. Finally, a parametric study to

determine the unknown constants has been performed and the explanation of how

to obtain those values has been provided. In Chapter 7, temperature

distributions in various wire-wrapped rod bundles from the ENERGY-IV code

incorporating the rod conduction model are presented.

6.2 Important Factors in Evaluating the Rod Conduction Effect

6.2.1 Thermal Conductivities of Constituent Materials

The main purpose of the RODCON code development is to evaluate the

non-uniform heat flux distribution at the cladding surface in the simulated

heater rod insulated by boron nitride (BN). The heat flux distribution at

the cladding surface in the actual UO_2-filled fuel rod is usually assumed to

be uniform. This assumption is reasonable since the temperature in the fuel

region is much higher than the surrounding coolant temperature due to the low

thermal conductivity of UO_2 and thus, the heat flux distribution within the fuel region is not affected by the coolant temperature boundary conditions. However, in the BN insulated heater rod, the heat flux distribution is expected to be quite non-uniform due to the high thermal conductivity of BN. This is because the non-radial heat conduction is enhanced by the high thermal conductivity when the surrounding coolant temperature is not uniform. Therefore, it is very important to correctly estimate the thermal conductivities of the constituent materials which are directly related to the non-uniform heat flux distribution.

Several investigators have reported the value of the BN thermal conductivity. Ott and Hedrick (O-2) have calibrated it from heat flux and temperature data obtained in a cylindrical rod geometry. The calibrated BN thermal conductivity and the extrapolated curve for a rod bundle are plotted in Figure 6.1 as a function of BN temperature. The BN thermal conductivity data available in the literature are also presented in Figure 6.1. As one can observe in Figure 6.1, the experimental data are widely scattered for a given temperature. For an example, when the BN temperature is 930°F, the maximmum value of the BN thermal conductivity is 16 Btu/hrft°F while the minimum is 4.8 Btu/hrft°F. Since the BN thermal conductivity depends on the compactness (porosity) of the BN powder, i.e., theoretical density, one reason why the data vary so much may originate from the use of different theoretical density BN material for each measurement.

For our calculation, the ORNL correlation obtained for 92% theoretical density of BN was selected because it presented moderate thermal conductivity in comparison with other data. The correlation is written as:

$$k_{BN} = 12.432481 - 0.002031 \ T \qquad (6.1)$$
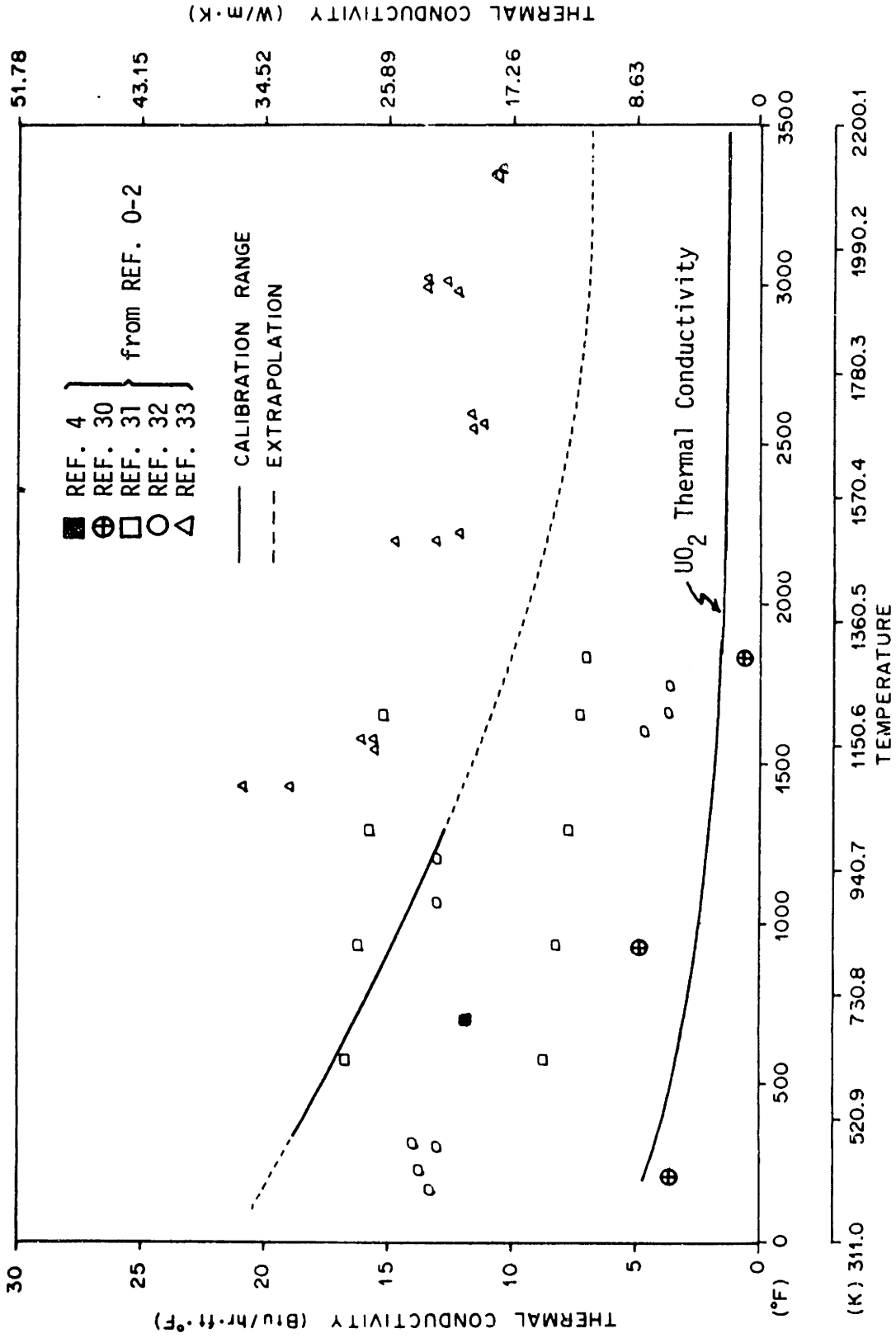
Figure 6.1 Boron Nitride Thermal Conductivity (Taken from Reference 0-2)

where the units of the thermal conductivity are Btu/hrft°F and that of the temperature, T is °F. The range of the data scatter for a certain BN temperature is greater than the range of the thermal conductivity change due to the temperature variation. Thus, the assumption of the constant thermal conductivity with respect to the temperature is acceptable since the uncertainty in the thermal conductivity encompasses the error contributed by ignoring the temperature dependence.

The thermal conductivity of stainless steel which is the cladding material of both the simulated heater rod and the UO_2 fuel rod is comparable to that of BN. Table 6.1 shows the thermal conductivity of SS as a function of SS temperature. The thermal conductivity of UO_2 is very low compared with that of BN or SS. UO_2 thermal conductivity has been well treated in the

Table 6.1 Thermal Conductivity of Stainless Steel-316 (O-2)

Temperature (°F)	k_{SS} (Btu/hrft°F)
400	9.1
450	9.4
500	9.6
550	9.8
600	10.0
650	10.2
700	10.4
750	10.7
800	10.9
850	11.1
900	11.3
950	11.5
1000	11.7

literature. The correlation suggested by Lyons and an International Panel of Experts in 1965 (L-2) was used in our calculation and also plotted in Figure 6.1.

6.2.2 Temperature Distribution within a Heated Rod

It is assumed in the RODCON code that the thermal conductivity is constant within each material zone. Thermal conductivity change with temperature within each material zone may be included if one can solve a non-linear energy equation. Generally, this equation is hard to solve analytically and therefore, we usually rely on numerical methods. The RODCON code cannot incorporate the temperature dependence since an approximate analytical solution method is utilized. Therefore, it is important to determine an average temperature for each material zone to obtain an appropriate thermal conductivity.

The average temperature of each material zone can be calculated from the results of the detailed temperature distribution. The detailed rod radial temperatures will change depending on the boundary conditions imposed or equivalently the size of the calculation regime employed. A unit cell calculation was used instead of a multicell calculation since the improved temperature distribution accuracy is not needed. This is because the uncertainty in thermal conductivity is far greater than the variation in average zone temperatures from the two calculations. The temperature profile was obtained by running the code iteratively so that the thermal conductivity used would correspond to the average temperature. The radial temperature profiles for the BN insulated heater rod and UO_2 rod cases are plotted in Figures 6.2 and 6.3, respectively. Note that the scales of the ordinates are different from each other. The operating conditions and geometry of a sample case are as follows:
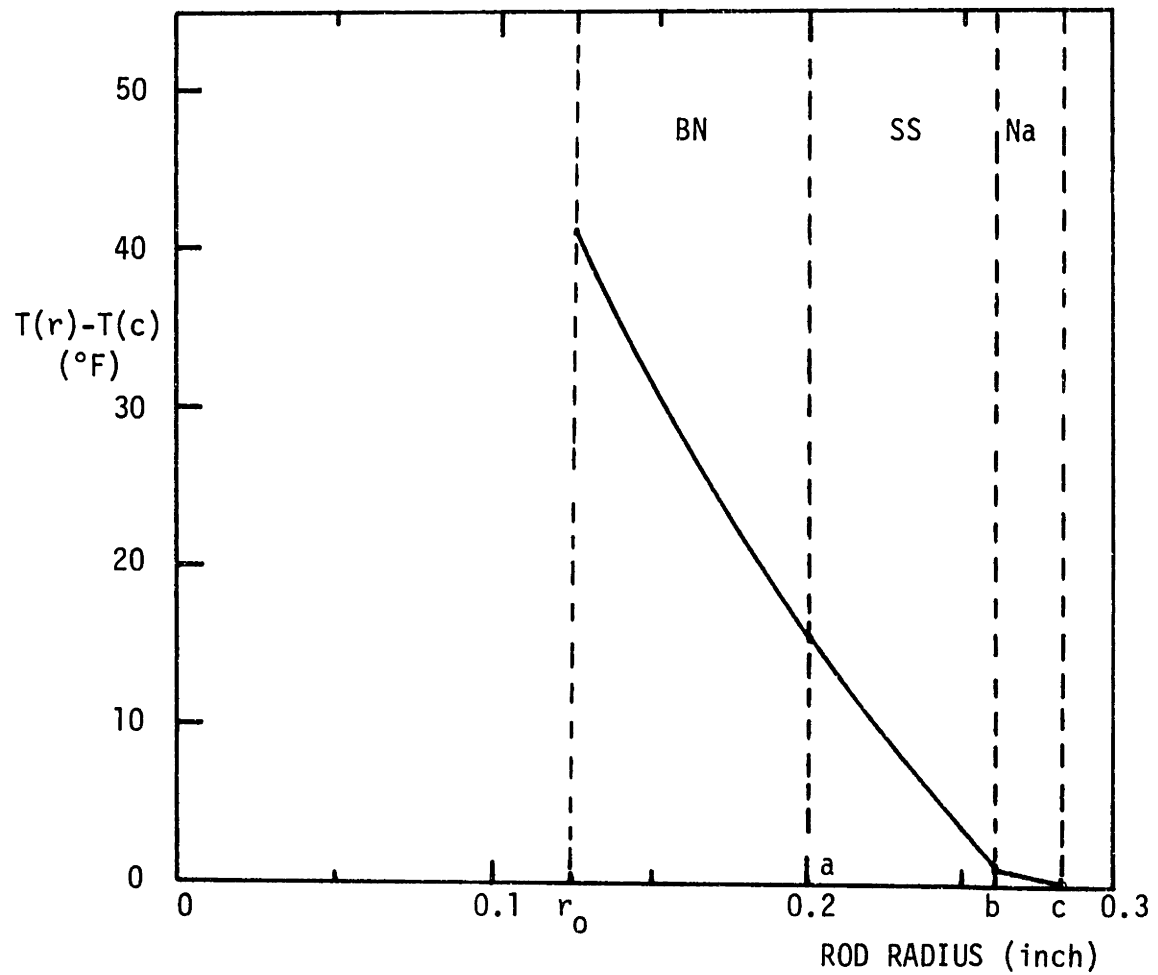
Figure 6.2 Radial Temperature Distribution in a BN Insulated
Heater Rod (q' = 1.143 KW/ft)
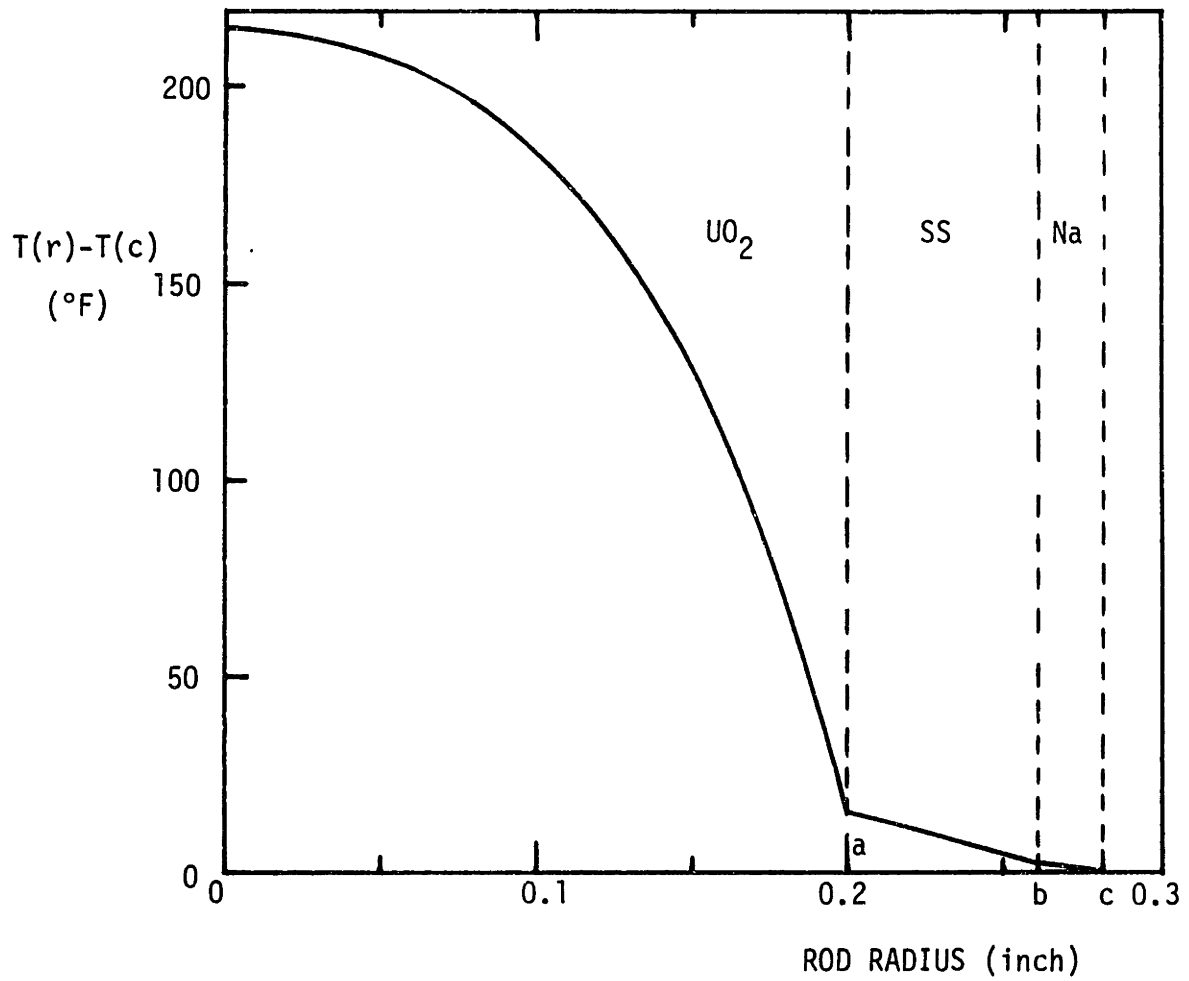
Figure 6.3 Radial Temperature Distribution in a UO_2-Filled Rod
(q' = 1.143 KW/ft)

Rod diameter: 0.519 inches

Cladding thickness: 0.060 inches

Inner diameter of BN: 0.250 inches

Average rod power: 1.143 kw/ft

Reference coolant temperature

(at the outlet):   778°F

The curvatures of the radial temperature profiles are different from each other since it is assumed that heat is generated uniformly at the inside wall of BN insulator for the BN rod case, whereas the heat source in the UO_2 region is uniformly distributed for the UO_2 case. The average temperatures for BN and UO_2 cases are around 805°F and around 960°F, respectively. The average temperature of each material zone is summarized in Table 6.2 for two rod power cases ($\bar{q}'$ = 1.143 kw/ft and 0.147 kw/ft) as examples.

Table 6.2   Average Temperature of Each Material Zone
(for a Blanket Type Rod)

Average Rod Power (kw/ft)	1.143	0.147
Reference Coolant Temperature (°F)	778	775
$\bar{T}_{BN}$ (°F)	805	780
$\bar{T}_{UO_2}$ (°F)	960	800
$\bar{T}_{SS}$ (°F)	786	777

6.2.3 Other Factors to be Considered

In the previous Sections 6.2.1 and 6.2.2, two important parameters, i.e., thermal conductivity and temperature profile were described. In addition, there are several other parameters that affect the RODCON prediction of the temperature profile. These are as follows.

(1) Flow Distribution

The RODCON code employs the slug flow model for the velocity distribution. In the slug flow model, the velocity distribution of each unit cell is assumed to be uniform. Although the RODCON code allows for a flow split between the unit cells, the flow split values correlated for subchannel analysis cannot be directly applied since the unit cell configuration in RODCON is not compatible with the subchannel configuration. Moreover small adjustments in the flow obtained by estimating the flow split appropriate to the unit cell configuration were found to yield only small changes in the coolant temperature distribution.

(2) Gap Conductance between SS Cladding and the UO_2 or BN region

Gap conductance between BN powder and SS cladding is expected be very high due to the negligible gap left from the manufacturing process and the small geometry change induced by heating the heater rod. Thus, it can be assumed that no gap exists between the BN insulator and SS cladding. On the contrary, gap conductance between UO_2 pellet and SS cladding in an actual LMFBR rod is quite low due to the relatively large gap distance provided to accommodate fuel swelling and the fission gas release.

The Biot number for the gap is defined as:

$$Bi \equiv \frac{h_g a}{k_{UO_2}} \tag{6.2}$$

where a is the radius of UO_2 pellet. The gap conductance h_g between UO_2 and SS cladding (E-5) is around 300 $Btu/hrft^2°F$. The corresponding Bi value is 3.3. Based on our calculations, the effect of the gap conductance on the temperature distribution is quite small but it is not negligible.

6.3 Rod Conduction Model

In the lumped parameter analysis, a whole bundle is divided into a number of small meshes (or subchannels) in which mass, momentum and energy equations are written in terms of suitably defined lumped variables. Energy transport between subchannels occurs through the control volume boundaries. The temperature and velocity fields can be predicted well provided that all the energy transfer mechanisms are properly modeled empirically or analytically. Heat conduction through rods, one of the heat transfer mechanisms, should also be correlated to include the effect of non-uniform heat flux distribution at the rod surface which is not negligible when the BN simulated heater rod is employed for out-of-pile tests.

The most desirable method of evaluating the magnitude of heat conduction through rods correctly is to conduct a relevant experiment and develop an empirical correlation based on the experiment. However, it is difficult to experimentally measure the rod conduction effect since the thermal conductivities of the heater rod materials (e.g., BN) cannot be easily determined. Moreover, in order to develop a model in terms of geometrical parameters and thermal conductivities, a great number of experimental case studies should be carried out.

In this research work, a numerical model for the rod conduction effect to be used in the subchannel analysis codes has been developed by modifying the RODCON code.

6.3.1 Model Geometry

For modeling purposes, two adjacent subchannels enclosed by four rods were selected as shown in Figure 6.4. In order to evaluate the detailed temperature and heat flux distribution, the RODCON code which was originally developed for a simulation of a multirod bundle geometry has been modified to deal with this specific geometry. Since the selected geometry is symmetrical along the vertical centerline, the domain of analysis is reduced to half of the full geometry. The cell boundaries are denoted as dashed lines and the boundary condition for each boundary is indicated in Figure 6.4. Here, q" stands for the heat flux boundary condition (Neumann type) and T for the temperature boundary condition (Dirichlet type).

For the symmetry line and the outside boundaries in contact with the surrounding neighboring subchannels, adiabatic boundary conditions are applied. This implies that no heat transfer occurs between these two subchannels and the surrounding subchannels. The above adiabatic boundary condition imposed on the outside boundaries seems to be unreasonable if there exists a strong power skew which leads to significant heat flux across the outside boundaries. The boundary condition effect on the model can be examined by reference to Figure 6.4. When the bundle power is strongly skewed in the direction from high power at G to low power at E, it is expected that heat transfer occurs inward across boundary $\overline{DG}$ and outward across boundary $\overline{DE}$. Then, the subchannel average temperature at high power side increases and that of low power side decreases as drawn schematically in Figure 6.5. This leads to steeper temperature gradient at the subchannel boundary $\overline{DF}$ which corresponds to larger azimuthal heat flux (see Eq. (6.10)) compared to the result with the adiabatic boundary condition. However, the suggested correlation to be proposed in Eq. (6.21) can accommodate this effect since the heat flux is correlated proportional to the subchannel average temperature difference.
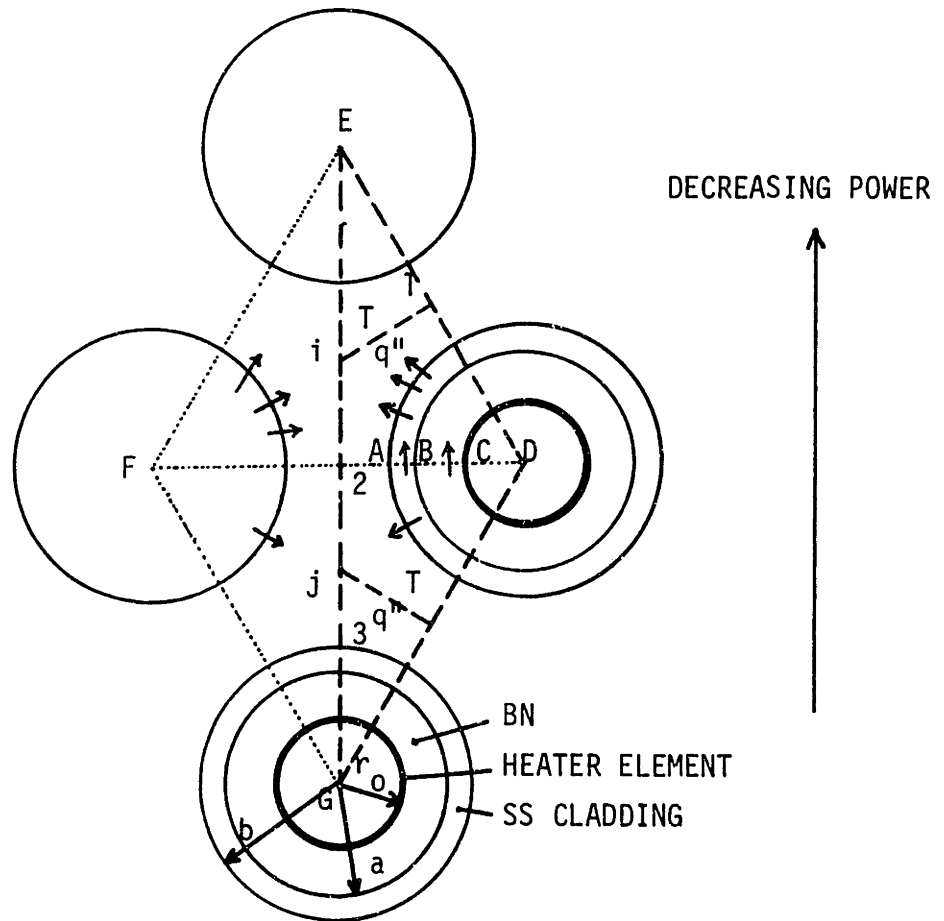
Figure 6.4 Geometry Utilized in the Rod Conduction Modeling
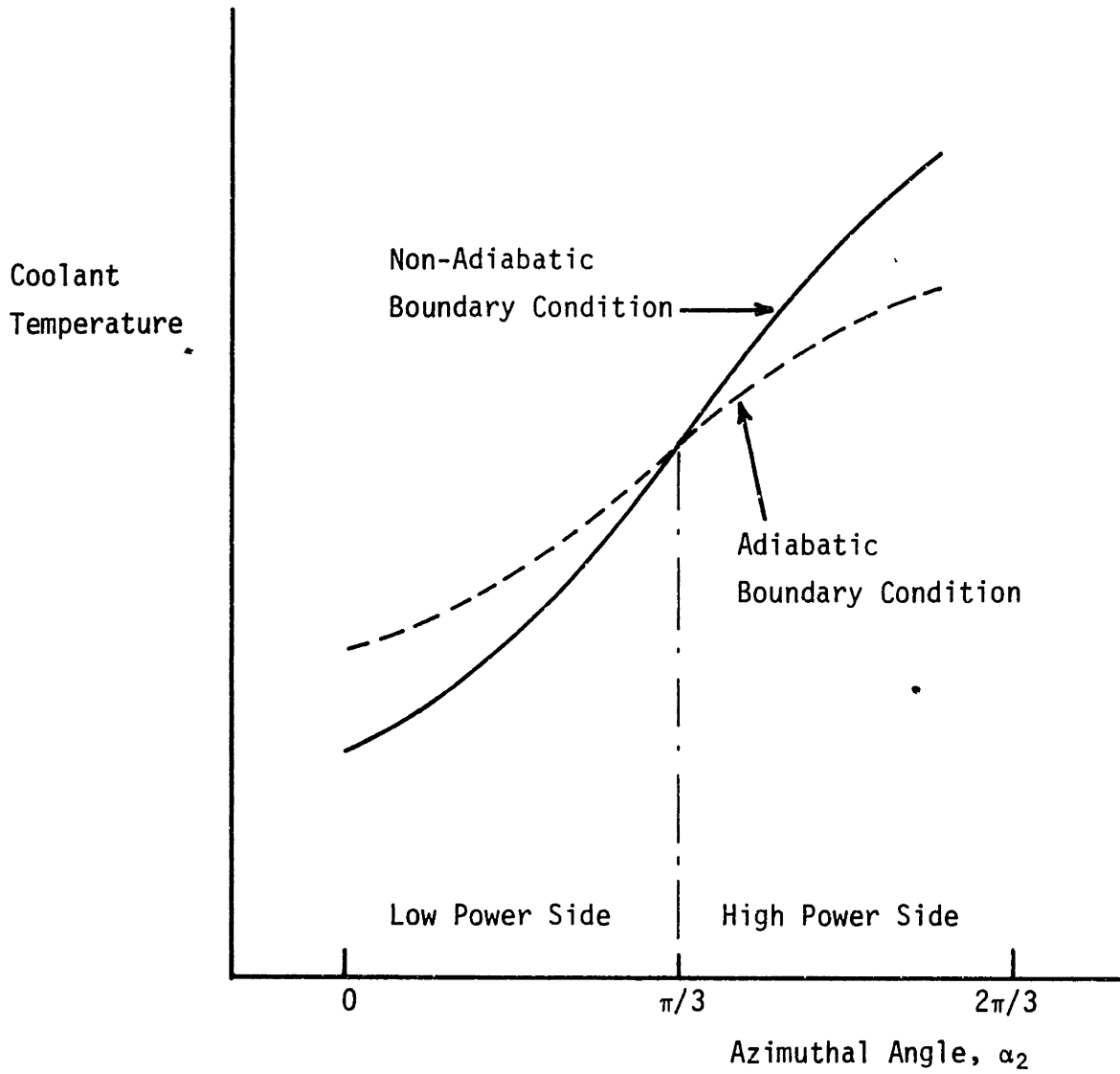
Figure 6.5 Predicted Azimuthal Temperature Profiles Incorporating
Adiabatic versus Non-Adiabatic Boundary Conditions

As shown in Figure 6.4, the selected geometry consists of three unit cells which have different geometrical characteristics from each other. The geometrical parameters of each unit cell are tabulated in Table 6.3. β_i is the vertex angle which is the angle between a reference line and the line connecting the center and the vertex point, i (i = 1, 2 for both cell types 1 and 3, i = 1, 2, 3, 4 for cell type 2). Note that the reference line for each unit cell is defined as the line connecting the center and the vertex point 1. Although the reference line may be drawn arbitrarily, it is convenient to choose the reference line as defined above since the angles start from the reference line with the same counterclockwise orientation. α_j is the normal angle which is the angle between the reference line and the line drawn from the center normal to the cell boundary which is in contact with the neighboring unit cell in the calculational domain. Here j is the cell boundary number (j = 1 for cell types 1 and 3, j = 1, 2, 3 for cell type 2). a_j is the normal distance between the center and the cell boundary.
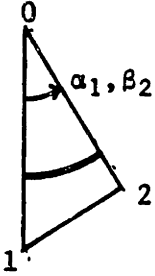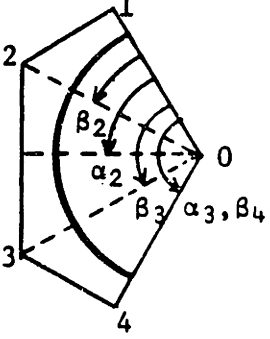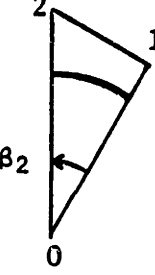
It has to be noted that the geometrical symmetry of a unit cell can yield further simplifications of the temperature field equations. The general solution form for the coolant region (Eq. (5.21)) is written as:

$$T(r,\theta) = E_o + F_o \ln r + \frac{1}{4} Sr^2 + \sum_{n=1}^{\infty} \left[(E_n r^n + F_n r^{-n}) \cos n\theta \right.$$

$$\left. + (E_n' r^n + F_n' r^{-n}) \sin n\theta \right] \tag{6.3}$$

For the cell types 1 and 3 which have (0, $\pi/6$) symmetry, the adiabatic boundary condition should be imposed on the symmetry line and the outside boundaries in contact with the surrounding neighboring subchannels. That is expressed as:

$$\frac{\partial}{\partial \theta} T(r,0) = \frac{\partial}{\partial \theta} T(r, \frac{\pi}{6}) = 0 \tag{6.4}$$

Table 6.3 Geometry and Boundary Conditions of Unit Cells

Cell Number (or Type)	Unit Cell	β_i	α_j	a_j
1		$0, \dfrac{\pi}{6}$	$\dfrac{\pi}{6}$	$\dfrac{P}{2}$
2		$0, \dfrac{\pi}{6}, \dfrac{\pi}{2}, \dfrac{2\pi}{3}$	$0, \dfrac{\pi}{3}, \dfrac{2\pi}{3}$	$\dfrac{P}{2}, \dfrac{P}{2}, \dfrac{P}{2}$
3		$0, \dfrac{\pi}{6}$	0	$\dfrac{P}{2}$

Substituting Eq. (6.3) into Eq. (6.4) gives:

for $\theta = 0$,

$$\sum_{n=1}^{\infty} (E_n' r^n + F_n' r^{-n}) = 0 \qquad (6.5)$$

To satisfy Eq. (6.5) for any values of r, E_n' and F_n' should vanish.

For $\theta = \frac{\pi}{6}$,

$$\sum_{n=1}^{\infty} (E_n r^n + F_n r^{-n}) \sin \frac{\pi}{6}n = 0 \qquad (6.6)$$

To have non-trivial solutions, $\sin \frac{\pi}{6}n$ should vanish. Then,

$$n = 6m, \qquad m = 1, 2, 3, \ldots \qquad (6.7)$$

Finally, the temperature field solution of cell types 1 and 3 is obtained as:

$$T(r,\theta) = E_o + F_o \ln r + \frac{1}{4} Sr^2 + \sum_{n=1}^{\infty} (E_n r^{6n} + F_n r^{-6n}) \cos 6n\theta \qquad (6.8)$$

By applying the same procedure, the temperature field solution of cell type 2 which has $(0, 2\pi/3)$ symmetry can be reduced to the following form:

$$T(r,\theta) = E_o + F_o \ln r + \frac{1}{4} Sr^2 + \sum_{n=1}^{\infty} (E_n r^{3n/2} + F_n r^{-3n/2}) \cos \frac{3n}{2}\theta \qquad (6.9)$$

For the BN and SS regions, the same argument can be applied.

6.3.2 Model Construction

In the previous section, the geometrical consideration of the rod conduction model was presented and the unit cells employed in the RODCON code were described. The rod conduction effect to be modeled is essentially an additional energy transfer mechanism which has not been taken into account in the lumped parameter analysis codes. Most lumped parameter codes assume that the distributed heat source originating from the heated solid rod is proportional to the solid volume occupying the subchannel and non-uniform

distribution of the rod surface heat flux is neglected. As mentioned earlier, the non-radial heat conduction is not negligible if the heater rod is composed of high thermal conductivity materials and a temperature gradient exists between adjacent subchannels.

6.3.2.1 Evaluation of Azimuthal Heat Flux

The amount of heat conducted through the heater rods across the subchannel boundary can be evaluated by calculating the azimuthal heat flux distribution along this boundary. The azimuthal heat flux normal to the radial direction in the cylindrical coordinates is defined as,

$$q''_{azi} = - k \frac{1}{r} \frac{\partial}{\partial \theta} T(r,\theta) \tag{6.10}$$

By substituting Eq. (5.19) into Eq. (6.10), the azimuthal heat flux in the BN insulator region is obtained as,

$$(q''_{azi})_{BN} = - \frac{k_{BN}}{r} \sum_{n=1}^{\infty} \left[- n(A_n r^n + B_n r^{-n}) \sin n\theta + n(A'_n r^n + B'_n r^{-n}) \cos n\theta \right] \tag{6.11}$$

or in dimensionless form,

$$\frac{(q''_{azi})_{BN}}{qk_{BN}/b} = \frac{\alpha\beta}{\rho} \sum_{n=1}^{\infty} \left[Y_n(\rho^n + w^{2n}\rho^{-n}) \sin n\theta - Y'_n(\rho^n + w^{2n}\rho^{-n}) \cos n\theta \right] \tag{6.12}$$

where q has been defined by Eq. (5.33).

The azimuthal heat flux in the SS cladding region can be obtained in a similar way and is written in dimensionless form as,

$$\frac{(q''_{azi})_{SS}}{qk_{BN}/b} = \frac{\beta}{2\rho} \sum_{n=1}^{\infty} \left[Y_n(f_n\rho^n + g_n\rho^{-n}) \sin n\theta - Y'_n(f_n\rho^n + g_n\rho^{-n}) \cos n\theta \right] \tag{6.13}$$

The dimensionless parameters used in the above equations are defined by Eqs. (5.33) through (5.40) and Eqs. (5.44) through (5.48).

The azimuthal heat transfer rate through each region can be evaluated by integrating the azimuthal heat flux in the radial direction over that region. The linear heat transfer rate in the BN region is expressed as,

$$(q'_{azi})_{BN} = \int_{r_o}^{a} (q''_{azi})_{BN} \, dr \qquad (6.14)$$

and in dimensionless form,

$$\frac{(q'_{azi})_{BN}}{qk_{BN}} = \alpha\beta \sum_{n=1}^{\infty} \left[\frac{1}{n} (h^n - w^{2n}h^{-n}) \, (Y_n \sin n\theta - Y'_n \cos n\theta) \right] \qquad (6.15)$$

The linear heat transfer rate in the SS region is written as,

$$(q'_{azi})_{SS} = \int_{a}^{b} (q''_{azi})_{SS} \, dr \qquad (6.16)$$

In a dimensionless form,

$$\frac{(q'_{azi})_{SS}}{qk_{BN}} = \frac{\beta}{2} \sum_{n=1}^{\infty} \frac{1}{n} \left[f_n(1 - h^n) - g_n(1 - h^{-n}) \right] (Y_n \sin n\theta - Y'_n \cos n\theta) \qquad (6.17)$$

Then, total linear heat transfer rate through the rod section (BN + SS) is the sum of the two heat transfer rates and is expressed as,

$$(q'_{azi})_{SUM} = \int_{r_o}^{a} (q''_{azi})_{BN} dr + \int_{a}^{b} (q''_{azi})_{SS} dr \qquad (6.18)$$

which is the sum of Eqs. (6.15) and (6.17) in a dimensionless form.

The azimuthal heat transfer rate of interest is the value at the subchannel boundary, i.e., at the line $\overline{DF}$ shown in Figure 6.4. The angular position of this line is $\pi/3$ from the reference line ($\overline{DE}$) of the cell number 2 (refer to Table 6.3). Total heat transfer rate is two times the value at the line $\overline{AC}$ since the subchannel boundary includes two half rod sections. Then the total linear heat transfer rate through the rods across the subchannel boundary is expressed as,

$$(q'_{azi})_{ROD} = 2(q'_{azi})_{SUM}\Big|_{\theta=\pi/3} \qquad (6.19)$$

and in dimensionless form,

$$\frac{(q'_{azi})_{ROD}}{qk_{BN}} = \sum_{n=1}^{\infty} \frac{1}{n} \left[2\alpha\beta(h^n - w^{2n}h^{-n}) + \beta\{f_n(1 - h^n) - g_n(1 - h^{-n})\} \right]$$

$$\times (Y_n \sin\frac{n\pi}{3} - Y'_n \cos\frac{n\pi}{3}) \qquad (6.20)$$

This value is numerically calculated using the RODCON code.

6.3.2.2 Suggested Correlation

By examining Eq. (6.20), it is found that the heat transfer rate due to the non-radial heat conduction is formulated in terms of the thermal conductivities of the constituent materials, the rod geometry and the temperature distribution implicitly included in the coefficients Y_n and Y_n'. From this observation, the linear heat transfer rate through the rods was correlated by the following form:

$$(q'_{azi})_{ROD} = C_o \left(\frac{k_{BN}}{k_{Na}}\right)^{\alpha} \left(\frac{P}{D}\right)^{\beta} \left(\frac{c}{D}\right)^{\gamma} k_{Na}(T_i - T_j) \qquad (6.21)$$

where c is the gap spacing between rods.

6.3.3 Parametric Study to Determine the Unknown Constants

In order to determine the unknown constants C_o, α, β and γ, parametric studies have been performed for various rod geometries (i.e., P/D ratios) and thermal conductivity ratios. Additionally different power skew conditions were investigated to confirm that the power skew need not be included in Eq. (6.21).

Eq. (6.21) can be written in the following dimensionless form:

$$\dot{Q}_{ROD} = C_o \left(\frac{k_{BN}}{k_{Na}}\right)^{\alpha} \left(\frac{P}{D}\right)^{\beta} \left(\frac{c}{D}\right)^{\gamma} (\theta_i - \theta_j) \qquad (6.22)$$

where

$$\dot{Q}_{ROD} \equiv 2\pi \frac{(q'_{azi})_{ROD}}{\bar{q}'} \tag{6.23}$$

and

$$\theta_i - \theta_j \equiv \frac{2\pi k_{Na}}{\bar{q}'} (T_i - T_j) \tag{6.24}$$

$\bar{q}'$ is the average linear heat transfer rate at the inner surface of BN where the heating elements are located.

Table 6.4 summarizes the cases analyzed in these parametric studies and the numerical results obtained from RODCON runs. The RODCON runs were executed for the power skew condition 1.2/1.0/0.8. Typical values of the WARD blanket rods (E-6) and the ORNL fuel rods (M-2) were used for the thermal conductivity ratio of SS and Sodium (k_{SS}/k_{Na}=0.26), SS cladding thickness to rod radius ratio (a/b = 0.77) and BN to rod radius ratio (r_o/b = 0.48). It should be noted that the constant C_o in Table 6.4 was evaluated after the other unknown constants α, β and γ were determined using least square method. Since the calculated values of C_o for all the cases studied are almost the same ($C_o \simeq 0.52$), it is concluded that the correlation is quite accurate over a wide range of P/D ratios (1.05 $\leq$ P/D $\leq$ 1.4) and thermal conductivity ratios (0.1 $\leq$ $k_{BN}/k_{Na} \leq$ 0.4).

The RODCON calculations were also carried out at other power skew conditions, i.e., 1.1/1.0/0.9 and 1.3/1.0/0.7, but the calculated unknown constants showed almost the identical values. These results have confirmed that the correlation for the rod conduction effect does not depend on the power skew because the subchannel average temperature difference and the heat flux terms in the model may accommodate the power skew.

Table 6.4 Parametric Study Cases for the Power Skew 1.2/1.0/0.8

Cases	Input		Results		
	P/D	k_{BN}/k_{Na}	$\dot{Q}_{ROD}$	$\theta_i - \theta_j$	C_o
1	1.05	0.260	0.1419	0.5039	0.519
2	1.082	0.260	0.1255	0.4563	0.518
3	1.12	0.260	0.1095	0.4105	0.519
4	1.18	0.260	0.0912	0.3584	0.517
5	1.244	0.260	0.0776	0.3204	0.518
6	1.3	0.260	0.0688	0.2964	0.518
7	1.4	0.260	0.0573	0.2667	0.517
8	1.082	0.407	0.1354	0.4111	0.523
9	1.082	0.311	0.1295	0.4383	0.519
10	1.082	0.216	0.1215	0.4744	0.518
11	1.082	0.168	0.1164	0.4973	0.521
12	1.082	0.120	0.1103	0.5247	0.532
13	1.244	0.407	0.0876	0.3016	0.525
14	1.244	0.311	0.0815	0.3131	0.520
15	1.244	0.215	0.0738	0.3275	0.518
16	1.244	0.168	0.0690	0.3363	0.519
17	1.244	0.120	0.0636	0.3464	0.529

The dependence of C_o on the thickness of BN was investigated by varying r_o/b for P/D = 1.082 and 1.244. The results were correlated as,

$$C_o = (0.31)(\frac{r_o}{b})^{-0.7} \qquad (6.25)$$

for the range of $0.4 \leq r_o/b \leq 0.6$.

From the above parametric analysis, the unknown constants were determined, and the correlation for the rod conduction effect was constructed as,

$$\begin{array}{c}\text{Linear Heat Transfer Rate} \\ \text{due to Non-Radial} \\ \text{Rod Conduction}\end{array} = (0.52) (\frac{k_{BN}}{k_{Na}})^{0.38} (\frac{P}{D})^{-1.04} (\frac{c}{D})^{0.016} k_{Na}(T_i - T_j)$$

$$(6.26)$$

This correlation is independent of the power skew.

It is instructive to compare the magnitude of the rod conduction effect with that of the conduction through coolant. The correlation of the conduction through coolant suggested by Cheng (C-1) is:

$$\begin{array}{l}\text{Linear Heat Transfer Rate} \\ \text{due to Conduction through} \\ \text{Na Coolant}\end{array} = \kappa(\frac{c}{\eta})k_{Na}(T_i - T_j)$$

$$= (0.66)(\sqrt{3})(\frac{c}{D})^{0.7} k_{Na} (T_i - T_j) \qquad (6.27)$$

where κ is the conduction shape factor and η the centroidal distance between subchannels. The geometrical parameters were evaluated at the interior subchannels.

The ratio of these two heat conduction mechanisms is defined as R and expressed as:

$$R \equiv \frac{\text{Energy Transfer Rate due to Non-Radial Conduction through BN Insulated Heater Rod}}{\text{Energy Transfer Rate due to Conduction through Na Coolant}}$$

$$= (0.45) (\frac{k_{BN}}{k_{Na}})^{0.38} (\frac{P}{D})^{-1.04} (\frac{c}{D})^{-0.684} \qquad (6.28)$$

R is plotted as a function of thermal conductivity ratio of k_{BN}/k_{Na} in Figure 6.6 for two different P/D ratios. The ratio R of the small P/D geometry is larger than that of the large P/D geometry. The reason is that the cross-sectional area in the rod available for the heat conduction at the subchannel boundary is relatively larger than the heat conduction area through the coolant when the P/D ratio is small. The ratio R increases as the thermal conductivity ratio increases. This agrees with the expectation that the non-radial heat conduction through rods is enhanced by higher BN thermal conductivity.

For the blanket bundle geometry (P/D = 1.082), the ratio R varies from 0.95 to 1.6 as the k_{BN}/k_{Na} ranges from 0.1 to 0.4, respectively. For the fuel bundle geometry (P/D = 1.244), R varies from 0.4 to 0.65 for the same range of the thermal conductivity ratio. These results indicate that the contribution of the rod conduction in the BN insulated heater rod is larger in the blanket and smaller in the fuel geometry than that of the conduction through coolant even though the data scattering of available BN thermal conductivity is considered.

6.4 Summary

(1) The thermal conductivities of the constituent materials of the heater rods were reviewed, and it was found that the experimental data for the BN thermal conductivity were widely scattered for a given temperature. The temperature distribution within a unit cell was calculated to provide a reference temperature used to estimate the thermal conductivity of each material region.

(2) To assess the effect of rod conduction, the RODCON code developed in Chapter 5 was modified so as to predict the temperature and heat flux for
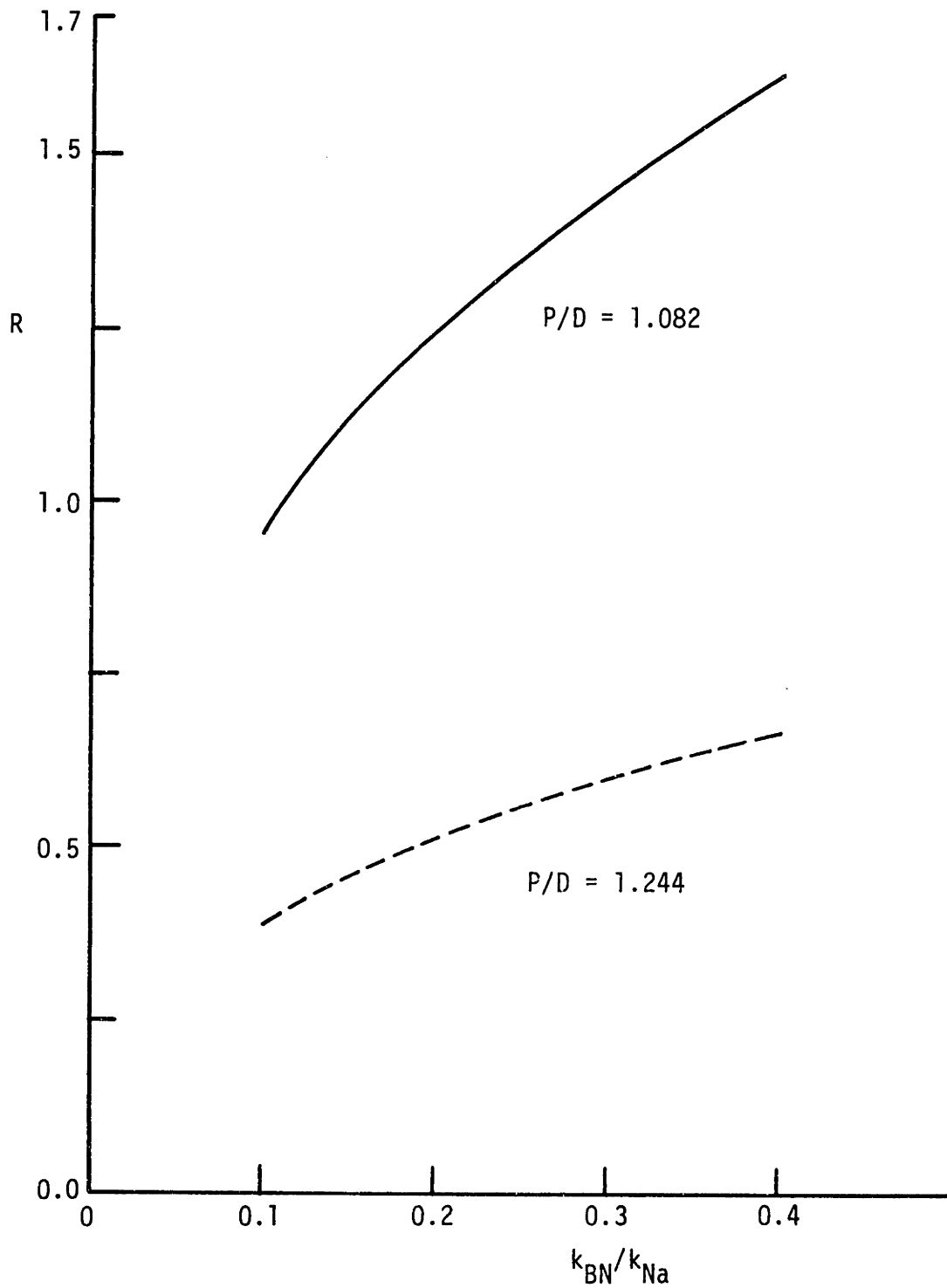
Figure 6.6 Comparison of Energy Transfer Rates due to Non-Radial
Rod Conduction versus Coolant Conduction

a selected geometry. The azimuthal heat flux at subchannel boundary was derived and adopted into the code. A correlation for non-radial rod conduction was suggested in terms of the thermal conductivites, rod geometry (pitch to diameter ratio and gap spacing) and subchannel temperature difference. Parametric studies to determine the unknown constants were performed utilizing the modified RODCON code. The model developed was given in Eq. (6.26). This correlation can be applied to both fuel and blanket bundle geometries irrespective of the flow regime.

CHAPTER 7

VALIDATION OF ROD CONDUCTION MODEL AND RELATIVE IMPORTANCE OF

ENERGY TRANSFER MECHANISMS

7.1 Introduction

The additional energy transfer mechanism in out-of-pile tests of

non-radial heat conduction through rods was discussed in Chapters 5 and

6. The RODCON code was developed to calculate the detailed temperature

and heat flux within rod bundles, which was prerequisite to quantify the

rod conduction effect. Then, a rod conduction model was constructed by

evaluating the azimthual heat transfer rate through rods in a selected

geometry.

In this chapter, the validity of the rod conduction model and the

potential need to account for thermal plume mixing is examined by

comparison of predicted temperature profiles with experimental data from

the out-of-pile tests. The code prediction has been performed by the

ENERGY-IV code (C-1) incorporating the rod conduction model. The relative

importance of wire sweeping including turbulent mixing, convective energy

transfer by flow redistribution, fluid conduction and rod conduction as

mechanisms of energy transfer between subchannels in the mixed convection

condition is investigated.

7.2 Model Adaption to the ENERGY-IV Code

The rod conduction model developed in this research has been applied

to the ENERGY-IV code. ENERGY-IV is a subchannel analysis computer code

which is applicable to both forced convection and mixed convection

conditions. The constitutive correlations such as flow split,

interchannel mixing, edge transverse velocity ratio and conduction shape

factor required for closure in the ENERGY-IV code have been developed by

Cheng (C-1). Uniform heat flux at the rod surface is inherently assumed

in this code, since the power input of each subchannel is evaluated as the

sum of the heat flux multiplied by the surface fraction of the heater rods

occupying the subchannel. However, in the mixed convection condition, the

heat conduction effect through rods becomes important and needs to be

included.

The rod conduction effect has been included in ENERGY-IV by adjusting

the coolant conduction shape factor. The detailed procedure utilized is

as follows. The ratio R of the two heat conduction mechanisms where

conduction through the coolant is the denominator can be obtained from

Eq. (6.28). The total heat conduction which is the sum of the heat

conduction through coolant and through rods equals (1 + R) times the heat

conduction through coolant only. Therefore, if the coolant conduction

shape factor is multiplied by (1 + R), the coolant heat conduction

correlation with the adjusted conduction shape factor can be used to

represent the total heat conduction.

7.3 Test Bundles Used for Validation

The out-of-pile temperature data from the Westinghouse Advance

Reactor Division (WARD) (E-6, E-7, M-1), the Oak Ridge National Laboratory

(ORNL) (M-2) and the Toshiba Corporation (Japan) (N-2) were used to

validate the rod conduction model. The specifications of the test bundles

are summarized in Table 7.1. The WARD bundle simulates the blanket

assembly and the ORNL and Toshiba bundles simulate the fuel assembly. All

tests employed heater rods electrically insulated by boron nitride and

sodium as a coolant.

Table 7.1 Specifications of Test Bundles

Bundle	Number of Rods	D_R (in)	D_W (in)	P/D	W/D	H/D	Heated Length (in)	Axial Power Profile*
WARD 61-Pin	61	0.519	0.037	1.082	1.078	7.7	45.0	Chopped Cosine 1.40/1
ORNL 61-Pin	61	0.230	0.056	1.244	1.244	52.2	36.0	Chopped Cosine 1.38/1
Toshiba 37-Pin	37	0.256	0.052	1.210	1.210	47.2	36.6	Chopped Cosine 1.21/1

* Maximum to Average Power

The cross section of the WARD and ORNL 61-pin bundles including the thermocouple locations is drawn in Figure 7.1. The thermocouples in the WARD bundle were placed along the flat to flat direction, whereas those in the ORNL bundle were positioned along the corner to corner diagonal. For the WARD bundle, the 55" level corresponds to the outlet of the heated zone and the 32" level corresponds to the midplane of the heated zone because of the 9.5" cold entrance length. The temperature data measured at these levels were selected to compare with the code predictions. For the ORNL bundle, the 37" level is the outlet of the heated zone. The temperature data measured at the 37" and 25" levels were used. The power skew was established row-by-row and oriented across the flats of the hexagonal duct for both test bundles. The normalized power of each row for various power skew conditions is shown in Table 7.2. The subchannel identification number used in the ENERGY-IV code for a 61-pin bundle is shown in Figure 7.2.

The cross section of the 37-pin Toshiba bundle is depicted in Figure 7.3. The locations of the thermocouples attached to the heater rods are also indicated in Figure 7.3. The temperature data measured at the 36" level (near the outlet of heated zone) was used for comparison with the code predictions. The power control for this rod bundle was grouped into three separate regions. The normalized power of each region for different power skew cases is given in Table 7.2. The subchannel identification number for the 37-pin bundle is shown in Figure 7.4.

7.4 Temperature Profile Comparisons Between Code Predictions and
     Experimental Data

The operating conditions of the experimental runs used for the validation of the rod conduction model are listed in Table 7.3. One

Row

FACE A
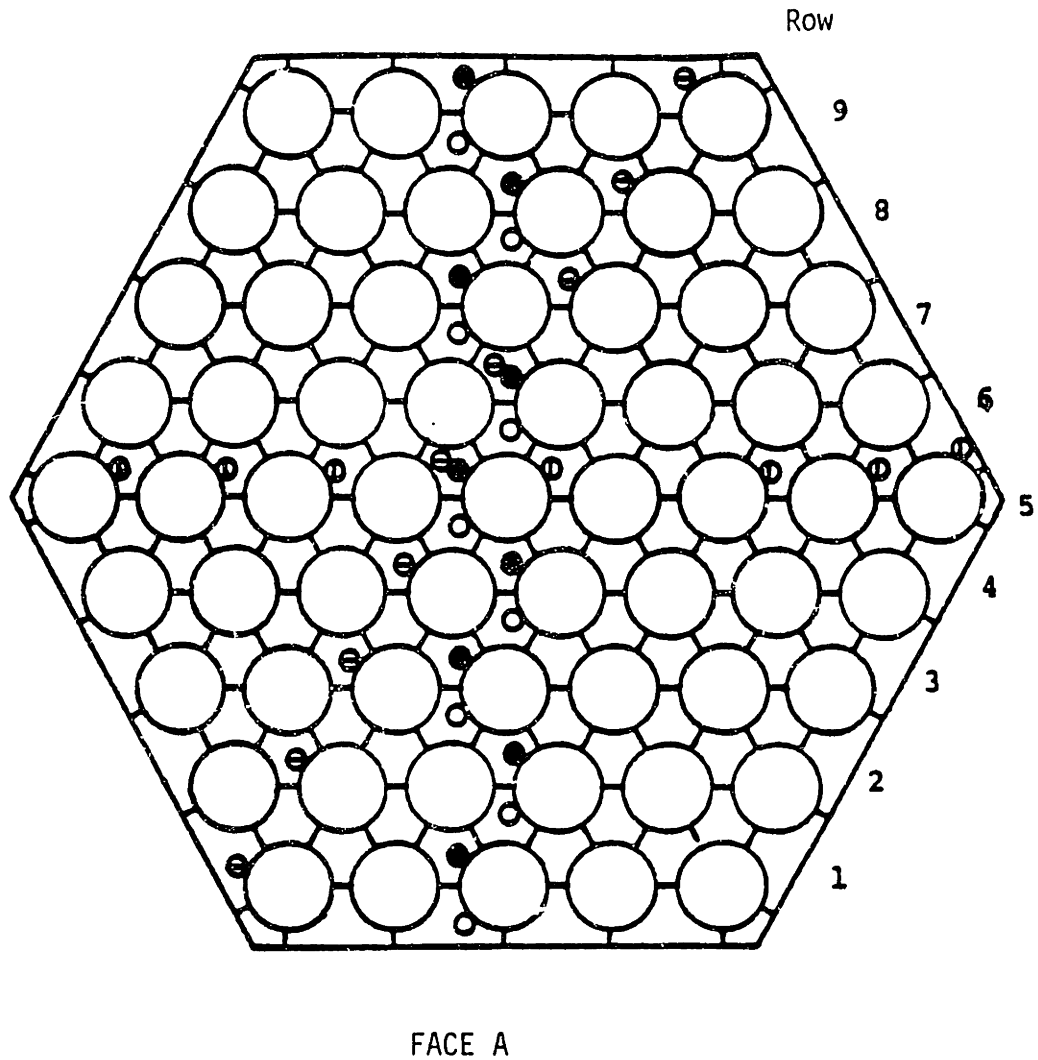
Thermocouple Locations

Level

● 55"   WARD 61-Pin
○ 32",80"

⊖ 25",37"   ORNL 61-Pin
Ⓓ 21"

Figure 7.1   Power Regions and Thermocouple Locations for WARD
and ORNL 61-Pin Bundles

Table 7.2 Normalized Power for Various Power Skew Conditions

Bundle	Power Skew*	Row (or Region)								
		1	2	3	4	5	6	7	8	9
WARD	2.0/1	0.71	0.75	0.80	0.87	0.96	1.06	1.18	1.30	1.45
61-Pin	2.2/1	0.66	0.73	0.78	0.87	0.99	1.14	1.17	1.24	1.46
	2.8/1	0.64	0.68	0.71	0.80	0.88	1.03	1.22	1.47	1.78
	4.3/1	0.50	0.51	0.55	0.68	0.85	1.00	1.37	1.68	2.16
	4.7/1	0.46	0.50	0.52	0.69	0.85	1.06	1.25	1.79	2.18
ORNL	1.5/1	0.79	0.84	0.91	0.95	1.00	1.04	1.10	1.16	1.23
61-Pin	2.0/1	0.68	0.75	0.83	0.92	1.01	1.07	1.16	1.25	1.33
	3.0/1	0.51	0.62	0.74	0.88	1.01	1.12	1.24	1.39	1.50
Toshiba	1.4/1	1.18	1.00	0.84						
37-Pin	2.0/1	1.36	1.00	0.69						

* Maximum to Minimum
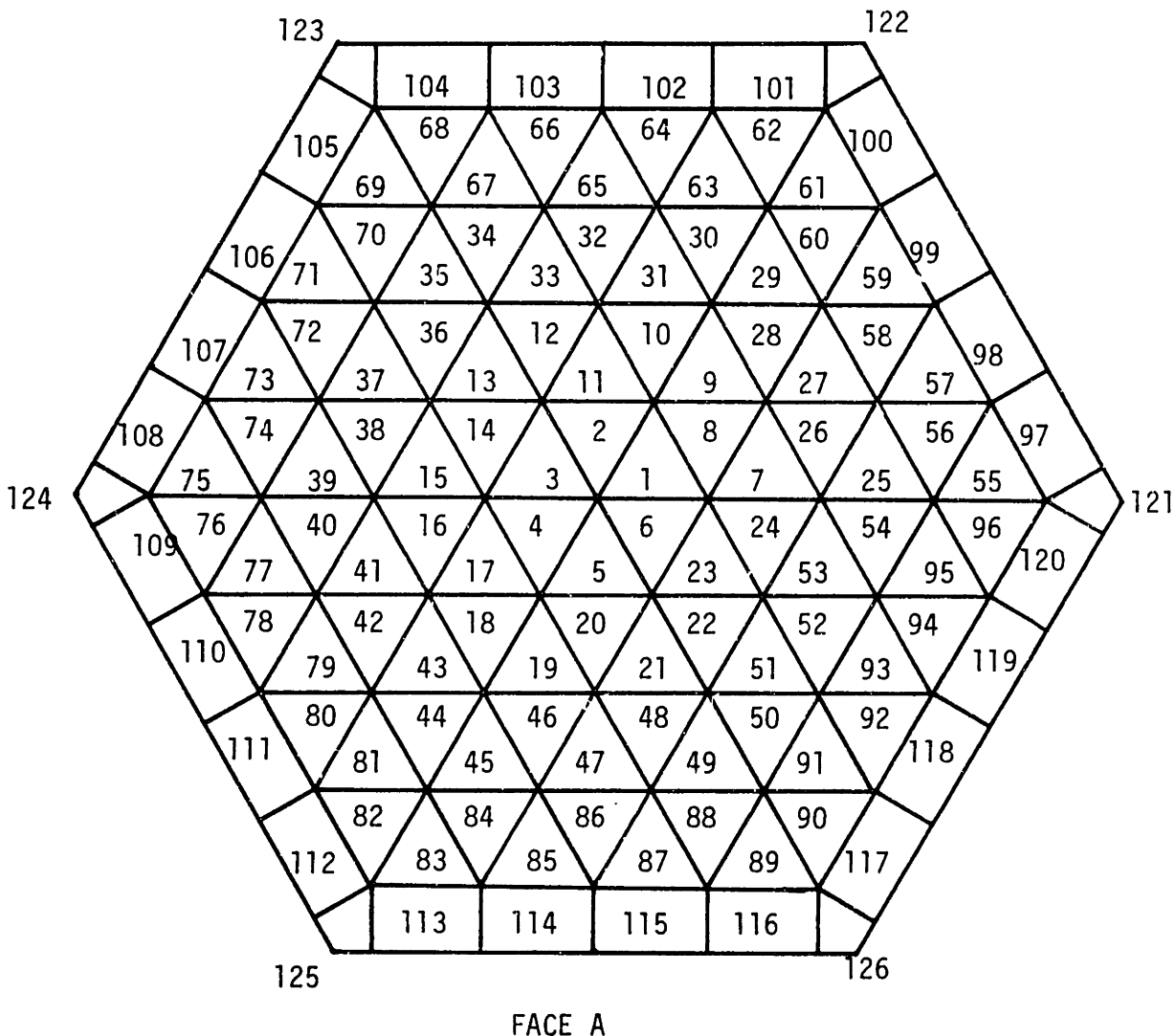
Figure 7.2 Subchannel Identification Number for a 61-Pin Bundle
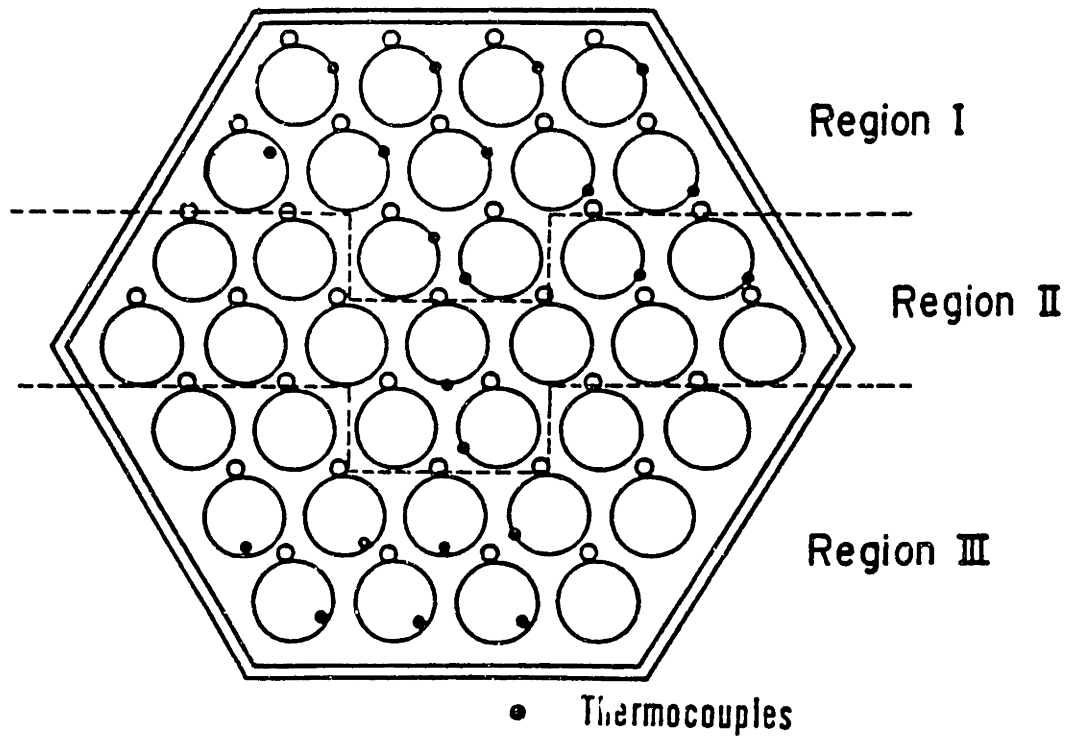
Figure 7.3 Power Regions and Thermocouple Locations for Toshiba 37-Pin Bundle
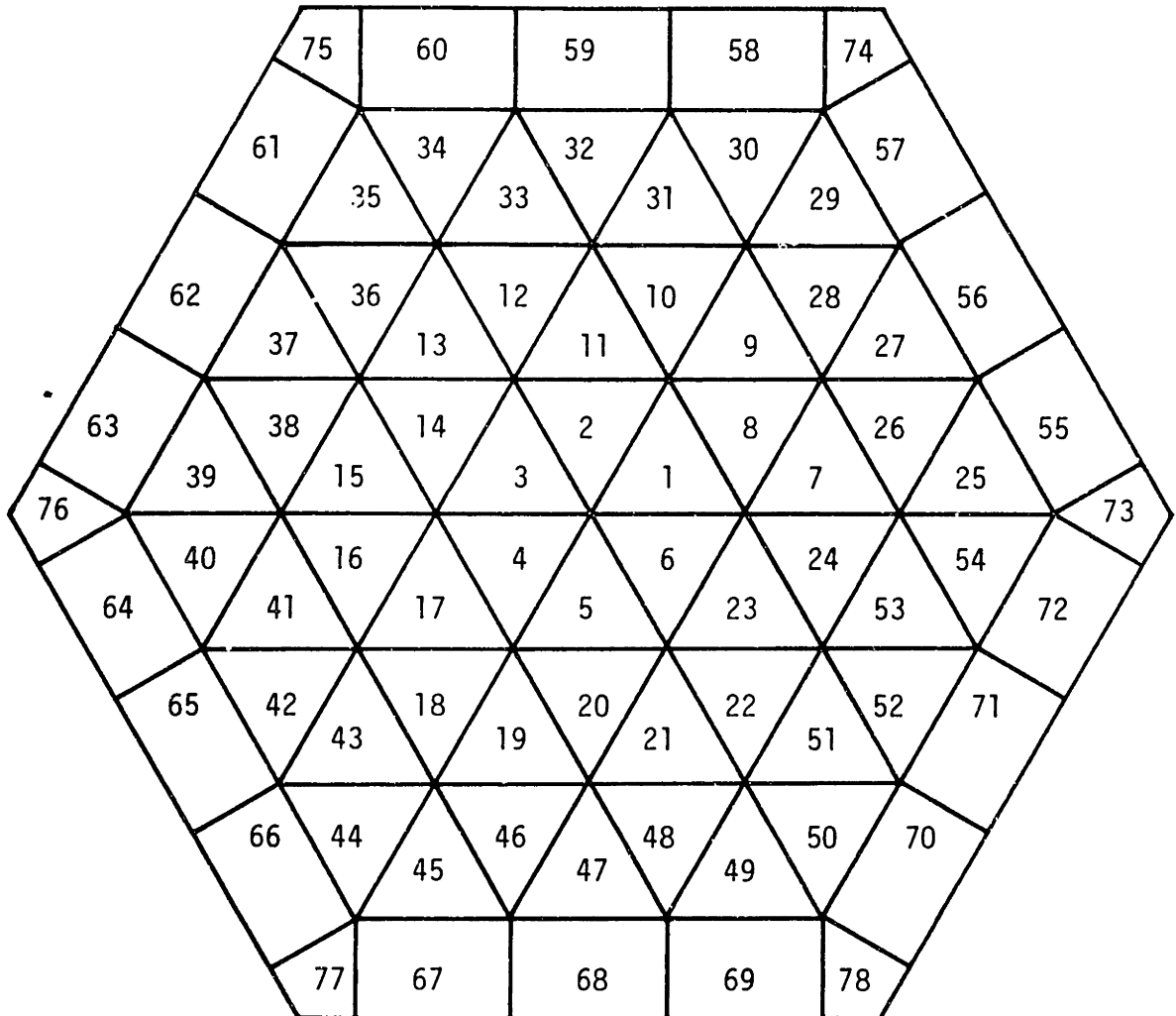
Figure 7.4   Subchannel Identification Number for a 37-Pin Bundle

Table 7.3 Experimental Runs Used for the Validation of the Rod
Conduction Model

Bundle	Run	Bundle Flow Rate (GPM)	Average Rod Power(kw/ft)	Power Skew*	Re_b	$Gr_{\Delta T}$	$\dfrac{Gr_{\Delta T}}{Re_b}$	T_{in} (°F)	ΔT_b^{**} (°F)
WARD	223	36.8	1.143	2.8/1	8950	390	0.04	605	179
61-Pin	227	4.9	0.147	1.0/1	1180	370	0.31	602	172
	401	4.89	0.146	2.0/1	1180	370	0.31	605	171
	720	2.29	0.062	2.2/1	540	320	0.59	581	154
	221	18.1	0.572	2.8/1	4390	400	0.09	600	181
	229	4.8	0.138	2.8/1	1150	350	0.31	598	165
	723	4.35	0.283	4.3/1	1140	960	0.84	597	376
	717	2.11	0.066	4.7/1	500	360	0.72	568	177
ORNL	19-101	103.8	4.518	3.0/1	53300	380	0.007	708	207
61-Pin	12-114	2.22	0.065	1.0/1	1120	250	0.22	722	138
	17-105	4.28	0.278	1.5/1	2310	640	0.28	739	312
	18-105	4.12	0.275	2.0/1	2230	660	0.30	736	321
	19-105	3.96	0.276	3.0/1	2140	680	0.32	729	334
Toshiba	E37P17	16.02	0.477	1.4/1	8250	70	0.009	409	80
37-Pin	C37P06	5.47	0.363	1.0/1	3020	180	0.06	398	179
	E37P13	1.54	0.119	1.0/1	880	230	0.26	404	208
	F37P20	5.24	0.477	1.4/1	3060	280	0.09	400	246
	F37P27	2.85	0.288	1.4/1	1700	330	0.19	400	274
	G37P25	5.24	0.483	2.0/1	3070	290	0.09	399	250
	L37P43	2.39	0.302	2.0/1	1500	460	0.31	401	345

* Maximium to Minimum
** Energy Balance Value

forced convection run for each test bundle was selected to investigate the importance of the rod conduction effect in different convection conditions. For the mixed convection condition, the runs were chosen to accommodate various power skew conditions. The temperature data and the calculation results were represented by a normalized temperature rise, ΔT^*, defined as,

$$\Delta T^* \equiv \frac{T_i - T_{in}}{T_{out} - T_{in}} \tag{7.1}$$

where,

T_i: subchannel average temperature of subchannel i

T_{in}: bundle inlet temperature

T_{out}: bundle outlet temperature

In the following sections, the ENERGY-IV predictions are compared with the experimental data for each test bundle.

(1) WARD Blanket Bundle

Figure 7.5 presents the ENERGY-IV predictions with and without the rod conduction model compared with the temperature data of WARD Run 223 in the forced convection condition. The ENERGY-IV results without the model predict the data well at both measurement levels. The maximum temperature rise at the outlet of the heated zone (55" level) is only overpredicted by 4 % of ΔT^*. However, the prediction with the model shows excellent agreement by reducing the maximum temperature rise at the high power side. The overprediction is merely 0.5%. This result implies that the rod conduction effect exists in the blanket bundle even in the forced convection condition although the magnitude is quite small.

The ratio of temperature rise difference between the predictions without and with the model to that predicted without the model can be expressed as,
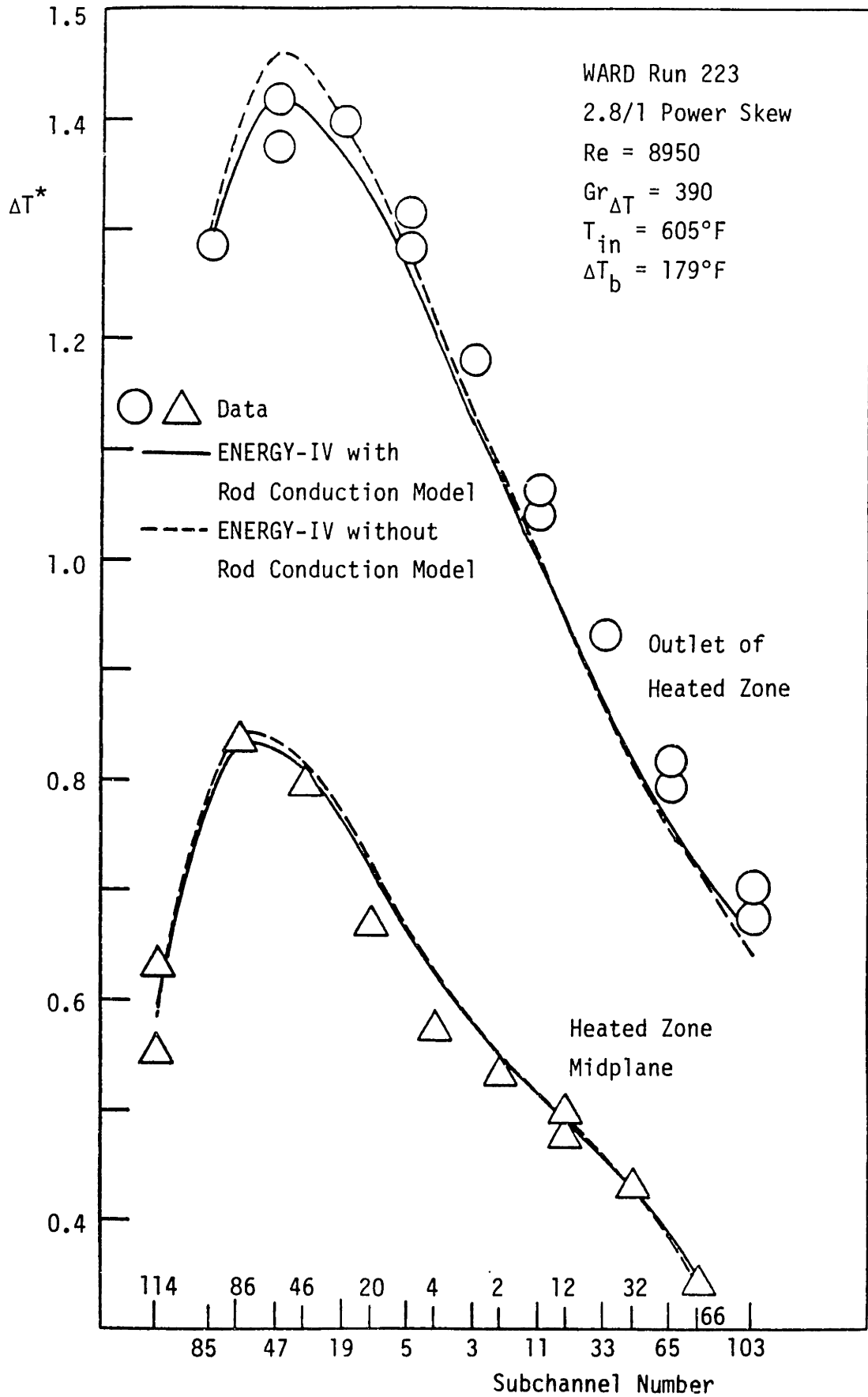
Figure 7.5 Measured and Predicted Temperature Rise for WARD Run 223

$$\frac{\Delta T^*_{UO_2} - \Delta T^*_{BN}}{\Delta T^*_{UO_2}} = \frac{T_{UO_2} - T_{BN}}{\Delta T_{UO_2}} \qquad (7.2)$$

where $\qquad \Delta T_{UO_2} = T_{UO_2} - T_{in} \qquad (7.3)$

$\Delta T^*_{UO_2}$ denotes the normalized temperature rise predicted without the rod conduction model which is consistent with the uniform rod surface heat flux assumption simulating the UO_2 fuel rods

ΔT^*_{BN} refers to the normalized temperature rise predicted with the model for conduction through BN insulated rods.

This ratio is a measure of the rod conduction effect. The ratio for the peak subchannel is 2.4% for this forced convection run. Compared with the estimation by Engel and Markley (E-3) (refer to Figure 6.1), this result is somewhat smaller than their calculated value (3.6%) at 2.8/1 power skew in the forced convection condition.

Figures 7.6, 7.7, 7.8, 7.9, 7.10, 7.11, 7.12 show the ENERGY-IV predictions with and without the rod conduction model compared with the temperature data of WARD Runs 227, 401, 720, 221, 229, 723 and 717, respectively in mixed convection conditions. The power skew ranges from 1/1 to 4.7/1 as shown in Table 7.3. For the uniform power case of Run 227, the ENERGY-IV result without the model substantially overpredicts the temperature rise at the high power subchannels at the outlet of the heated zone. The percent overprediction of the maximum ΔT^*, i.e., the maximum of $(\Delta T^*_{pred} - \Delta T^*_{data})/\Delta T^*_{data}$, is 4.3% (the maximum ΔT^* of the data is 1.09 whereas that of the ENERGY-IV prediction is 1.137). This value corresponds to a 8°F temperature difference. The calculation
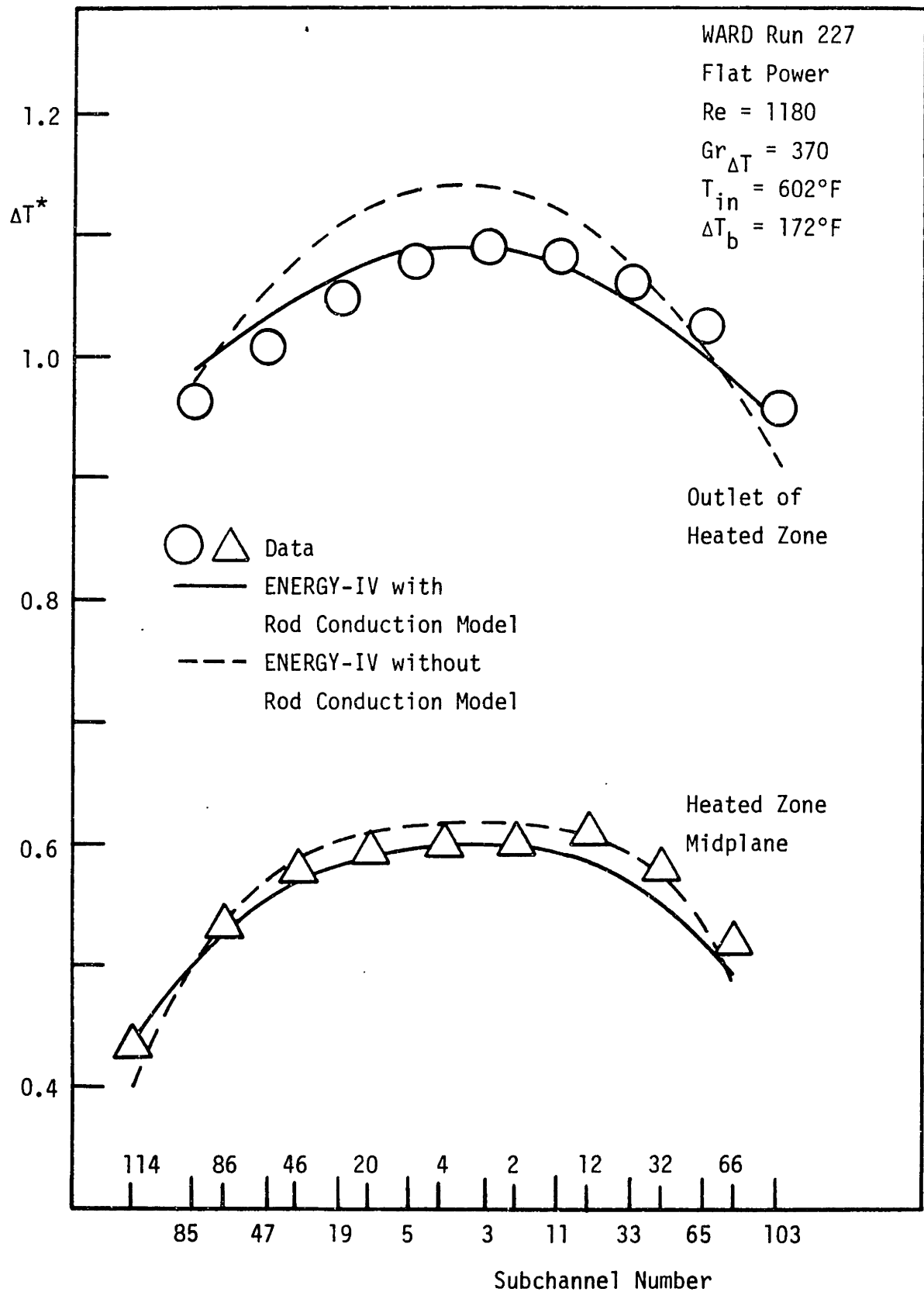
Figure 7.6 Measured and Predicted Temperature Rise for WARD Run 227
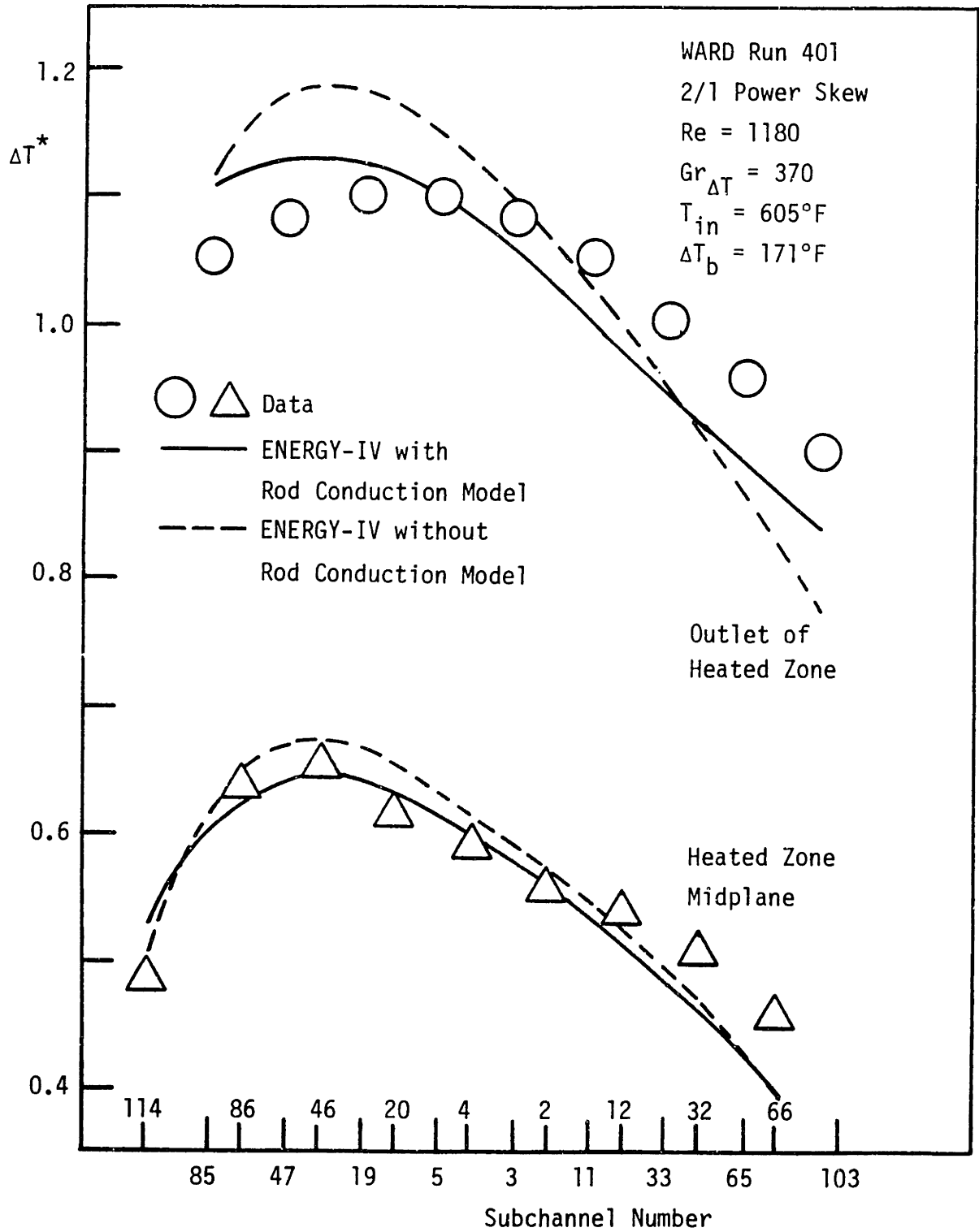
Figure 7.7 Measured and Predicted Temperature Rise for WARD Run 401
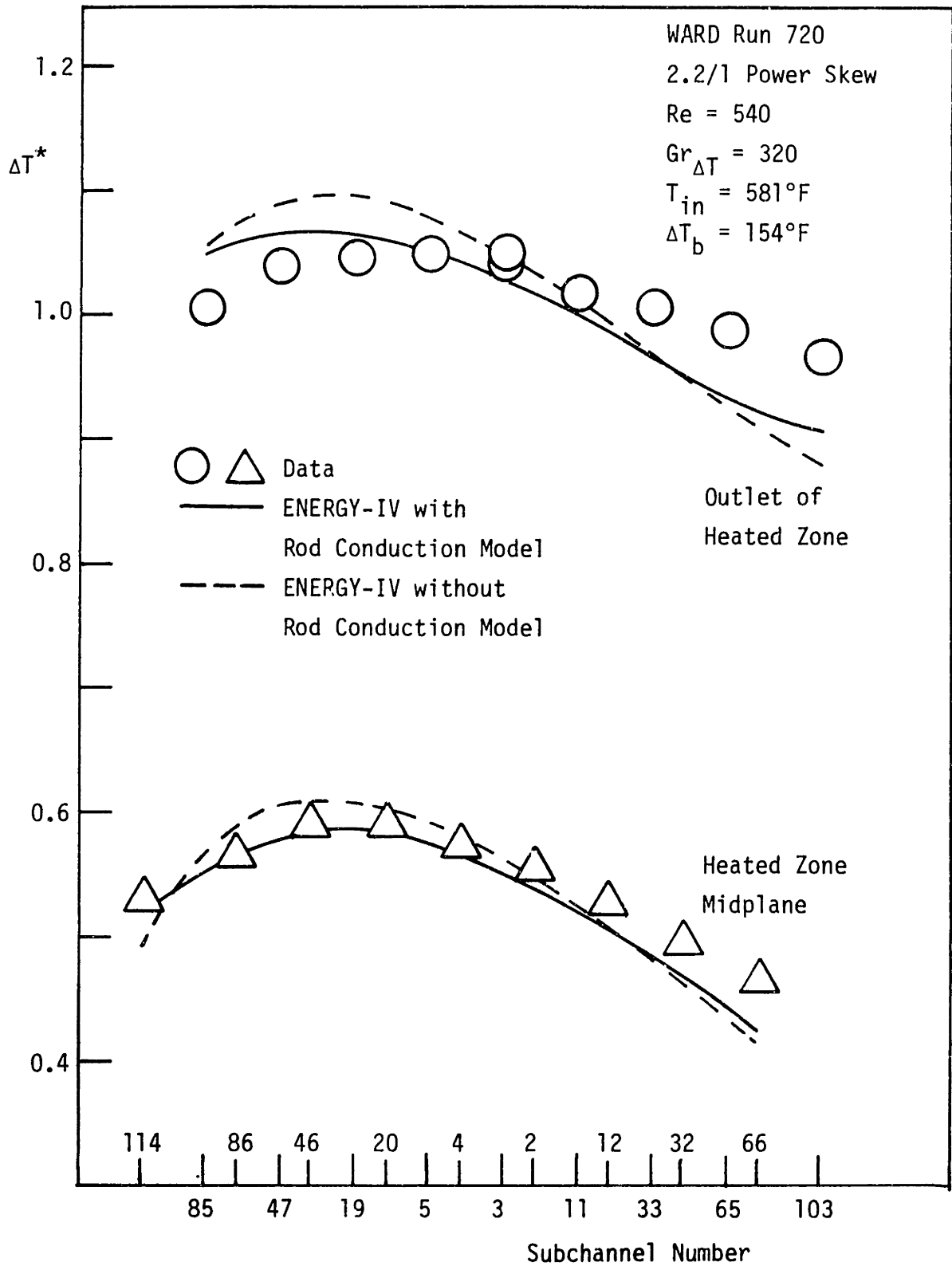
Figure 7.8 Measured and Predicted Temperature Rise for WARD Run 720
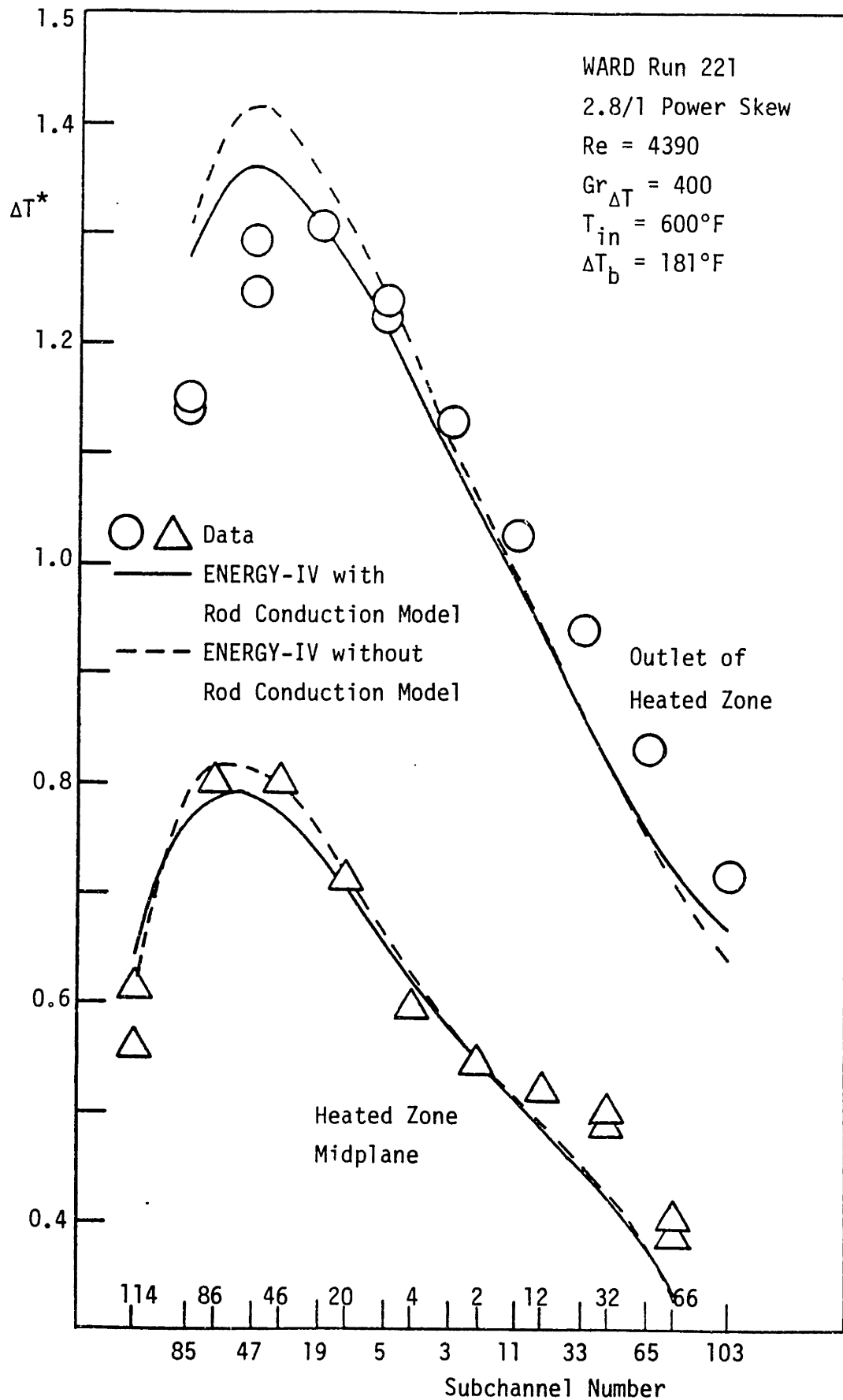
Figure 7.9 Measured and Predicted Temperature Rise for WARD Run 221
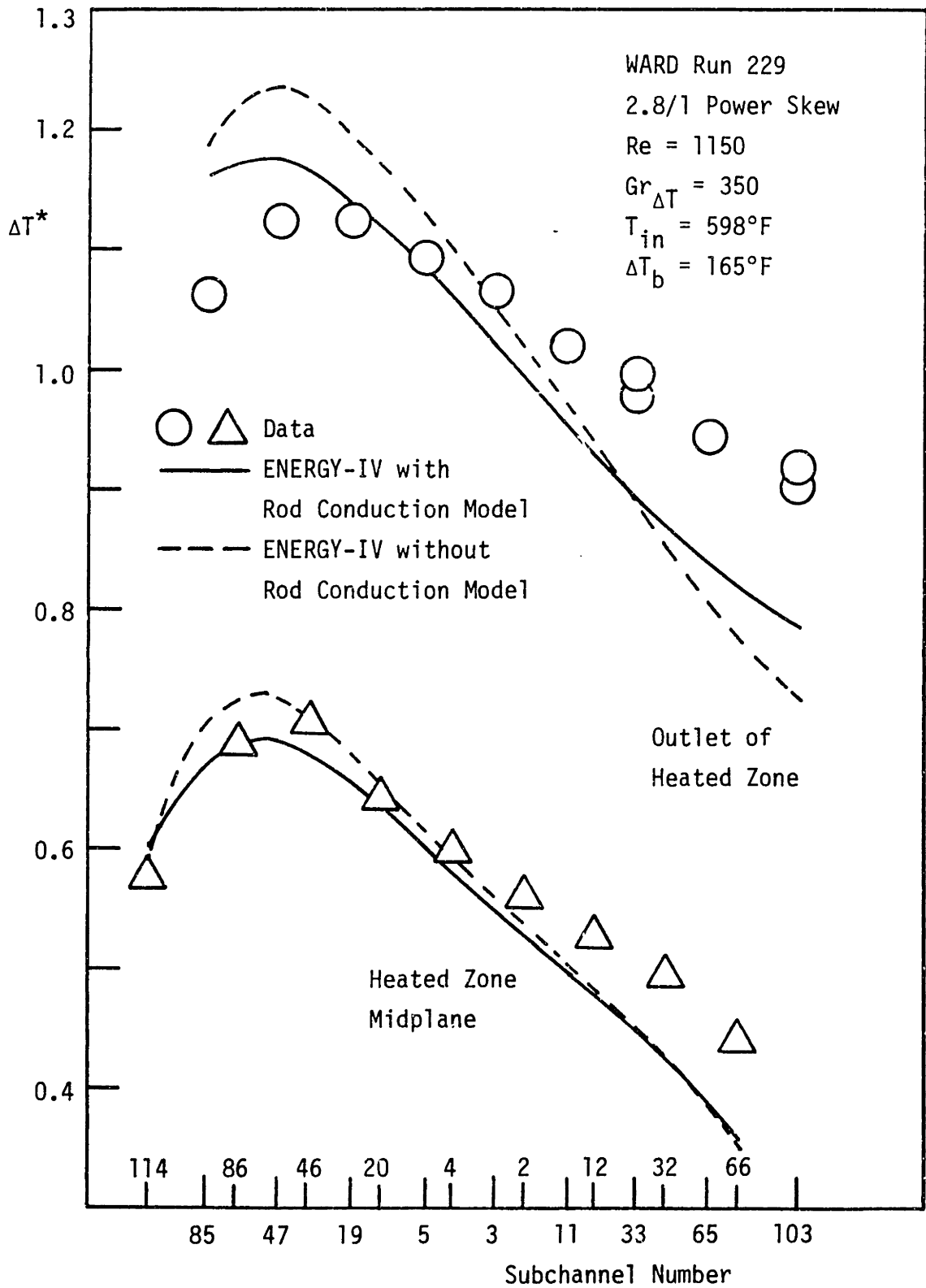
Figure 7.10   Measured and Predicted Temperature Rise for WARD Run 229
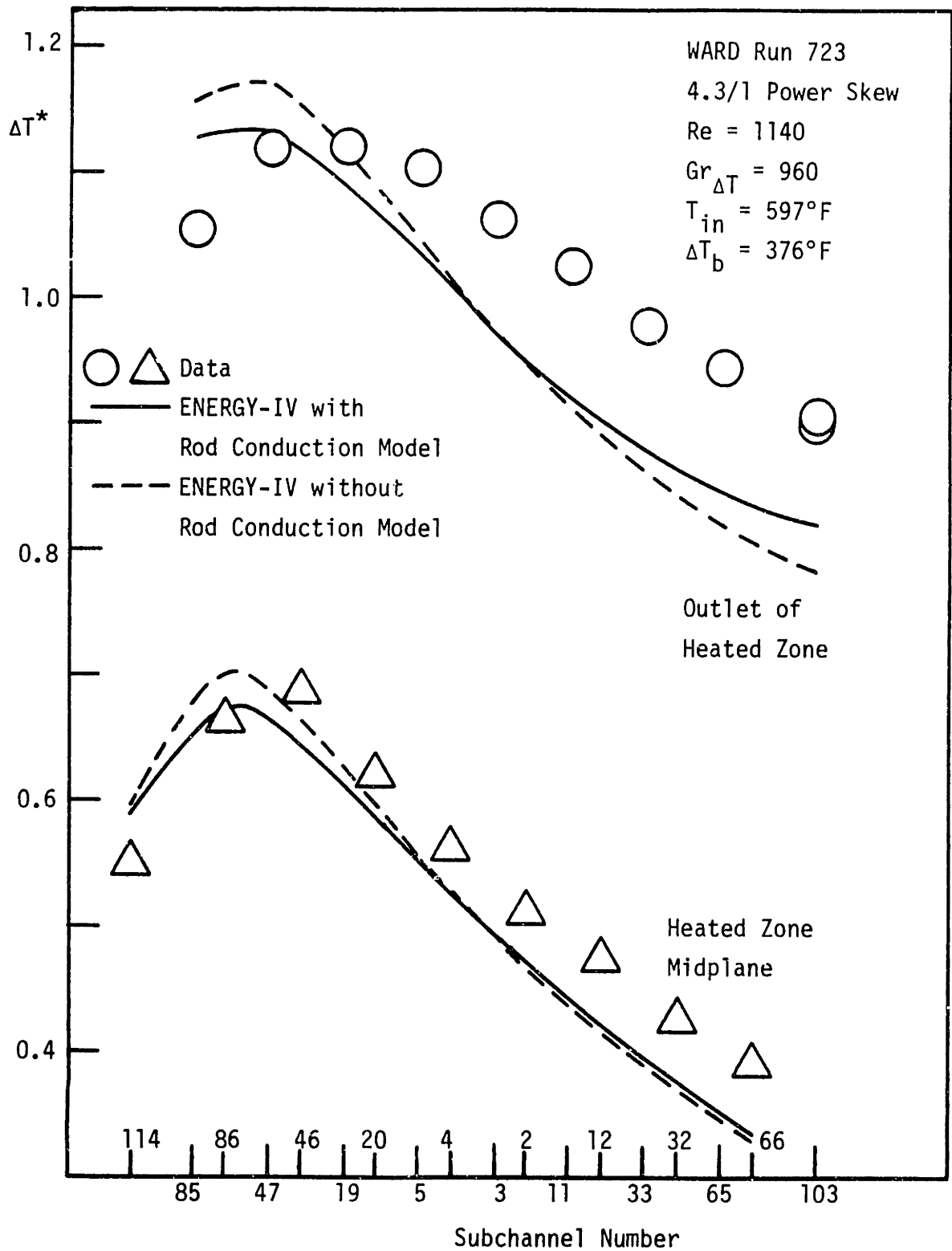
Figure 7.11 Measured and Predicted Temperature Rise for WARD Run 723
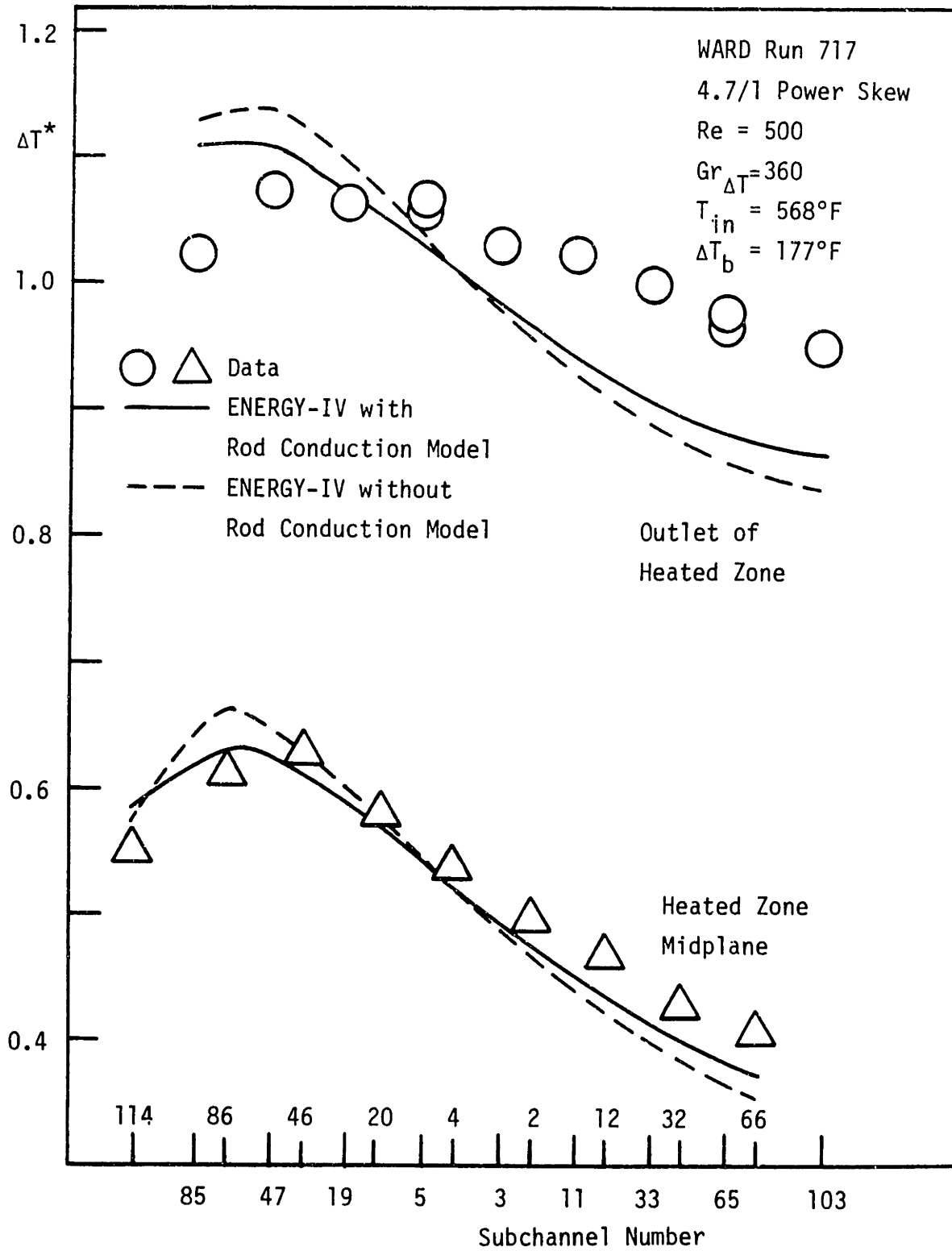
Figure 7.12   Measured and Predicted Temperature Rise for WARD Run 717

results with the model almost perfectly predict the data at the outlet of the heated zone. The perecent ratio of the maximum temperature rise difference between the two predictions is 4.1%. This result is also smaller than the estimated value (5-6%) by Engel and Markley (E-4) in the laminar mixed convection condition.

The rod conduction model was also tested for various power skew conditions. As shown in Figures 7.7 through 7.12, the overpredictions of the maximum ΔT^* in the high power regions and underpredictions of ΔT^* in the low power regions are significantly reduced by incorporating the rod conduction model in the ENERGY-IV code. Table 7.4 summarizes the percent overpredictions of the maximum ΔT^* for both cases (without and with the rod conduction model) indicating substantial decrease of the maximum ΔT^* due to the rod conduction effect.

The ENERGY-IV code predicts ΔT^* quite well at the heated zone midplane. However, although the rod conduction effect is included, the ΔT^*'s in the high power regions are overpredicted and those in the low power regions are significantly underpredicted for all the power skew runs performed at the outlet of the heated zone. This observation infers that another heat transfer mechanism such as thermal plume mixing exists under mixed convections conditions and/or the flow redistribution effects employed in the ENERGY-IV code are not properly modeled. To quantify the thermal plume mixing, an experimental investigation was performed and discussed in Chapter 8. As explained in Chapter 8, a suitable correlation for the thermal plume mixing could not be constructed due to unexpected counterheat flux and abnormal temperature gradient measured at the subchannel boundary. Regarding the flow redistribution due to buoyancy

Table 7.4 Decrease of the Maximum ΔT^* due to the Rod Conduction
Effect in Mixed Convection Conditions

Test	Run	Power Skew	Re_b	$Gr_{\Delta T}$	Percent Overprediction of Max. $\Delta T^{*(1)}$	
					without Rod Conduction	with Rod Conduction
WARD	227	1.0/1	1180	370	4 %	0 %
61-Pin	401	2.0/1	1180	370	7 %	3 %
	720	2.2/1	540	320	4 %	2 %
	221	2.8/1	4390	400	8 %	4 %
	229	2.8/1	1150	350	10 %	5 %
	723	4.3/1	1140	960	5 %	1 %
	717	4.7/1	500	360	6 %	3 %
ORNL	12-114	1.0/1	1120	250	(2)	(2)
61-Pin	17-105	1.5/1	2310	640	2 %	-1 %
	18-105	2.0/1	2230	660	1 %	-1 %
	19-105	3.0/1	2140	680	2 %	-1 %
Toshiba	C37P06	1.0/1	3020	180	2 %	-3 %
37-Pin	E37P13	1.0/1	880	230	1 %	-1 %
	F37P20	1.4/1	3060	280	0 %	-4 %
	F37P27	1.4/1	1700	330	6 %	2 %
	G37P25	2.0/1	3070	290	5 %	-1 %
	L37P43	2.0/1	1500	460	7 %	3 %

(1) Values at the outlet of the test section.

(2) Datashowed a dip in the center region and 5 % discrepancy appeared.

effect, the ENERGY-IV employs a simple model for the energy transfer by the crossflow. This model may result in the poor predictions. However, as will be seen later, the ENERGY-IV results for the ORNL and Toshiba fuel bundles predict the temperature profiles quite well in the mixed convection conditions. Therefore, the poor ENERGY-IV predictions cannot be attributed to the simple model for the energy transfer by the crossflow. Consequently, the thermal plume effect might be significant in the blanket bundle.

The perecent ratios of the maximum temperature rise difference between the two predictions (given in Eq. (7.2)) are 4.1%, 2.5%, 3.6%, 4.8%, ˙3.2% and 2.8% for WARD Run 720 (2.2/1 power skew), 221 (2.8/1), 229 (2.8/1), 723 (4.3/1) and 717 (4.7/1), respectively. These results indicate that the rod conduction effect is independent of power skew.

(2) ONRL Fuel Bundle

Figure 7.13 compares the ENERGY-IV predictions with the data of Run 19-101 in the forced convection condition. The predictions with the rod conduction model and without the model do not reveal significant differences. As will be illustrated later, wire sweeping and turbulent mixing are predominant over the energy transfer by the conduction mechanism at this high flow (Re = 53300), forced convection condition.

Figures 7.14, 7.15, 7.16 and 7.17 present the comparisons between the predictions and the data for Runs 12-114 (flat power), 17-105 (1.5/1 power skew), 18-105 (2/1 power skew) and 19-105 (3/1 power skew) respectively in mixed convection conditions. For these mixed convection runs, the temperature data could not yield the energy balance determined by the power input because of heat loss along the test bundle. The data of ΔT^* in the figures, therefore, were calculated from the temperature data
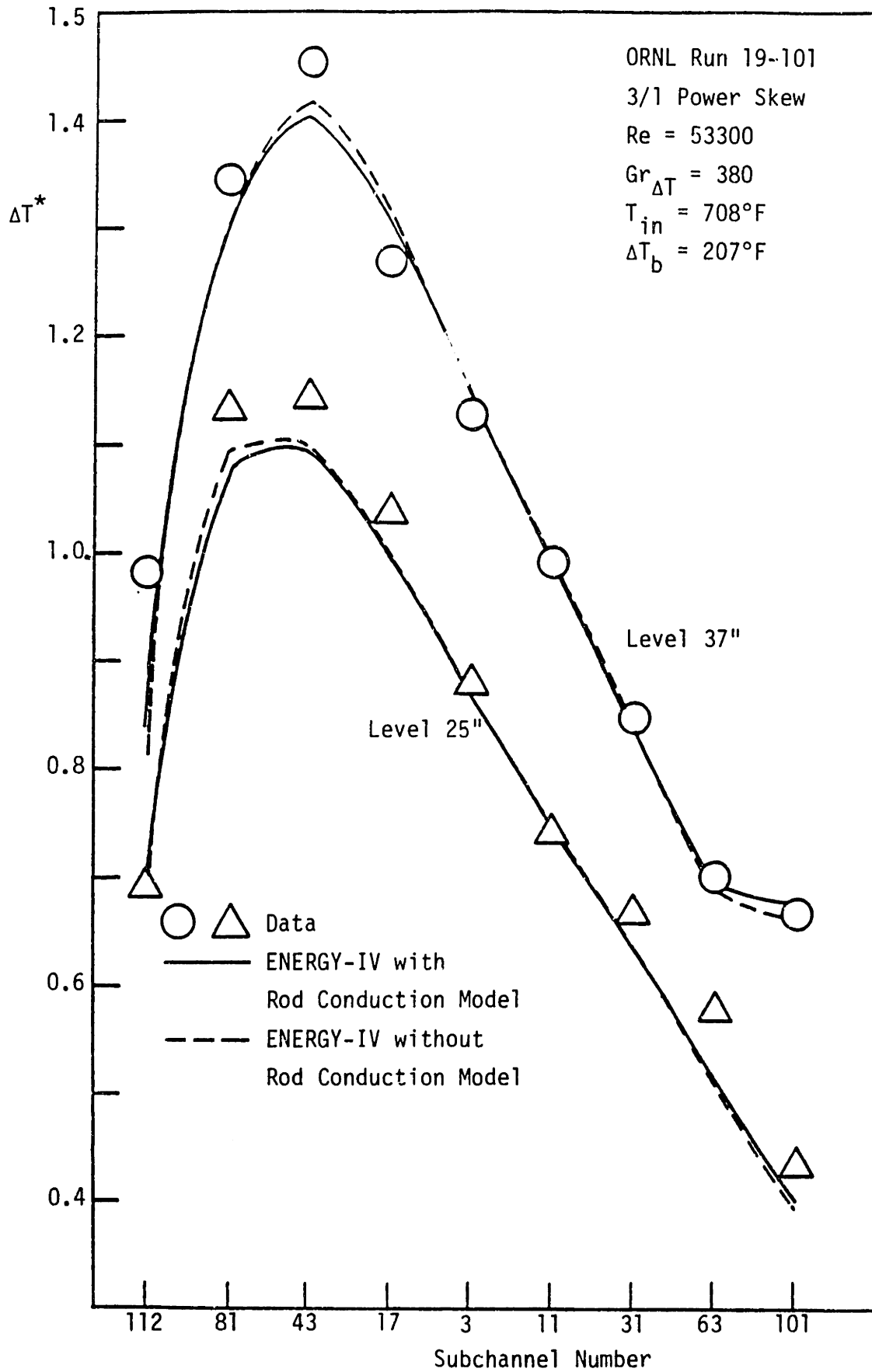
Figure 7.13 Measured and Predicted Temperature Rise for ORNL
Run 19-101
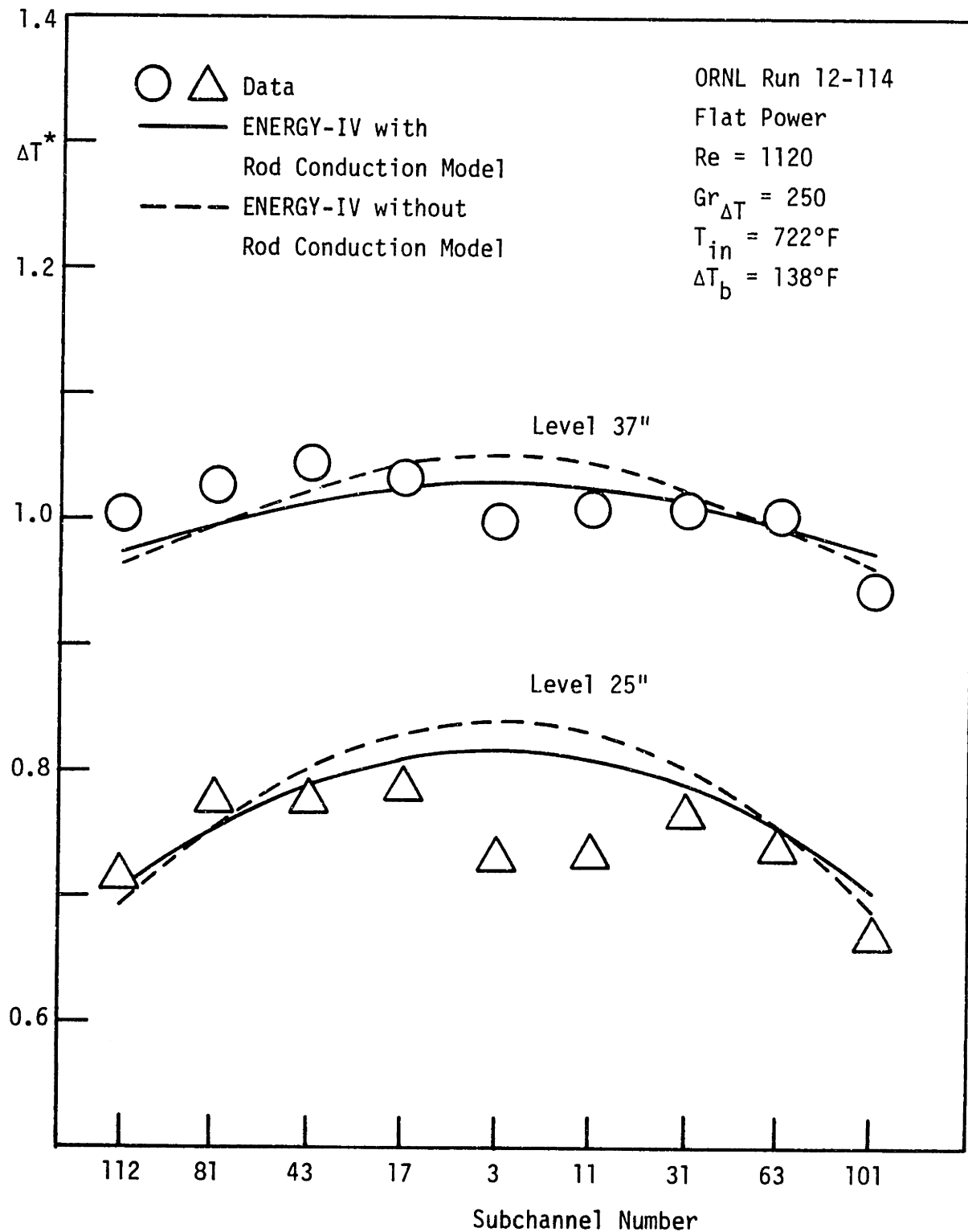
Figure 7.14   Measured and Predicted Temperature Rise for ORNL
Run 12-114
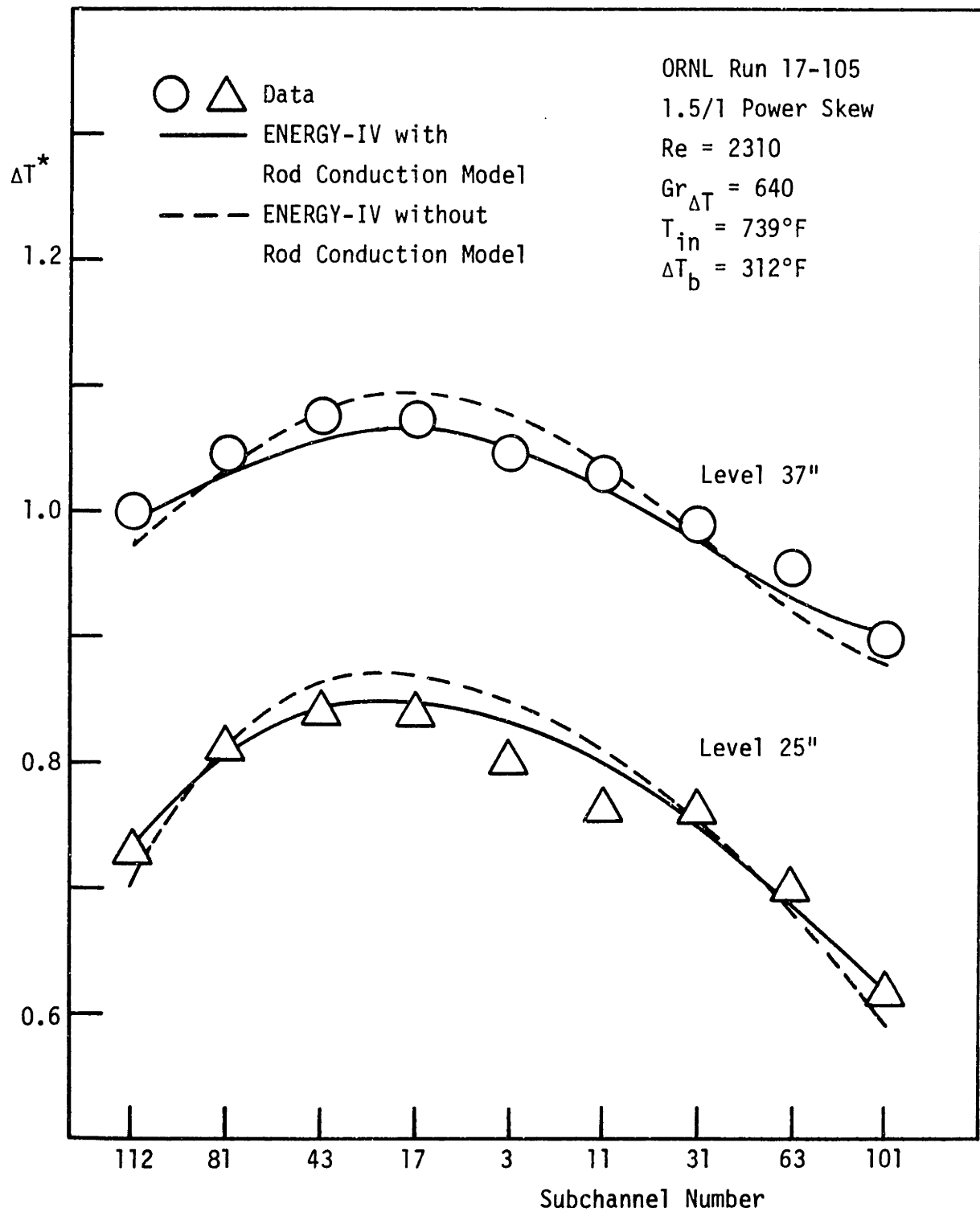
Figure 7.15 Measured and Predicted Temperature Rise for ORNL
Run 17-105
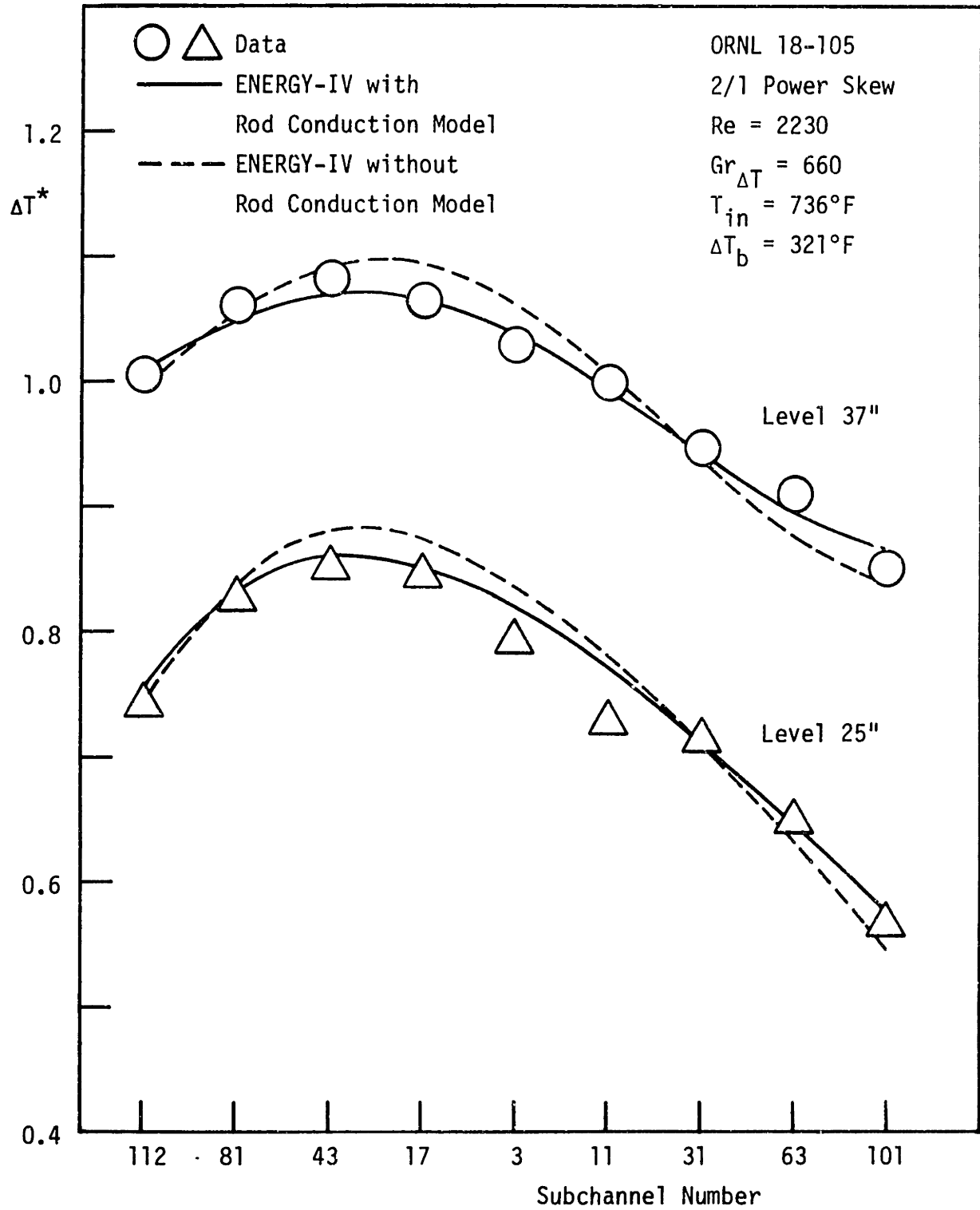
Figure 7.16   Measured and Predicted Temperature Rise for ORNL
             Run 18-105
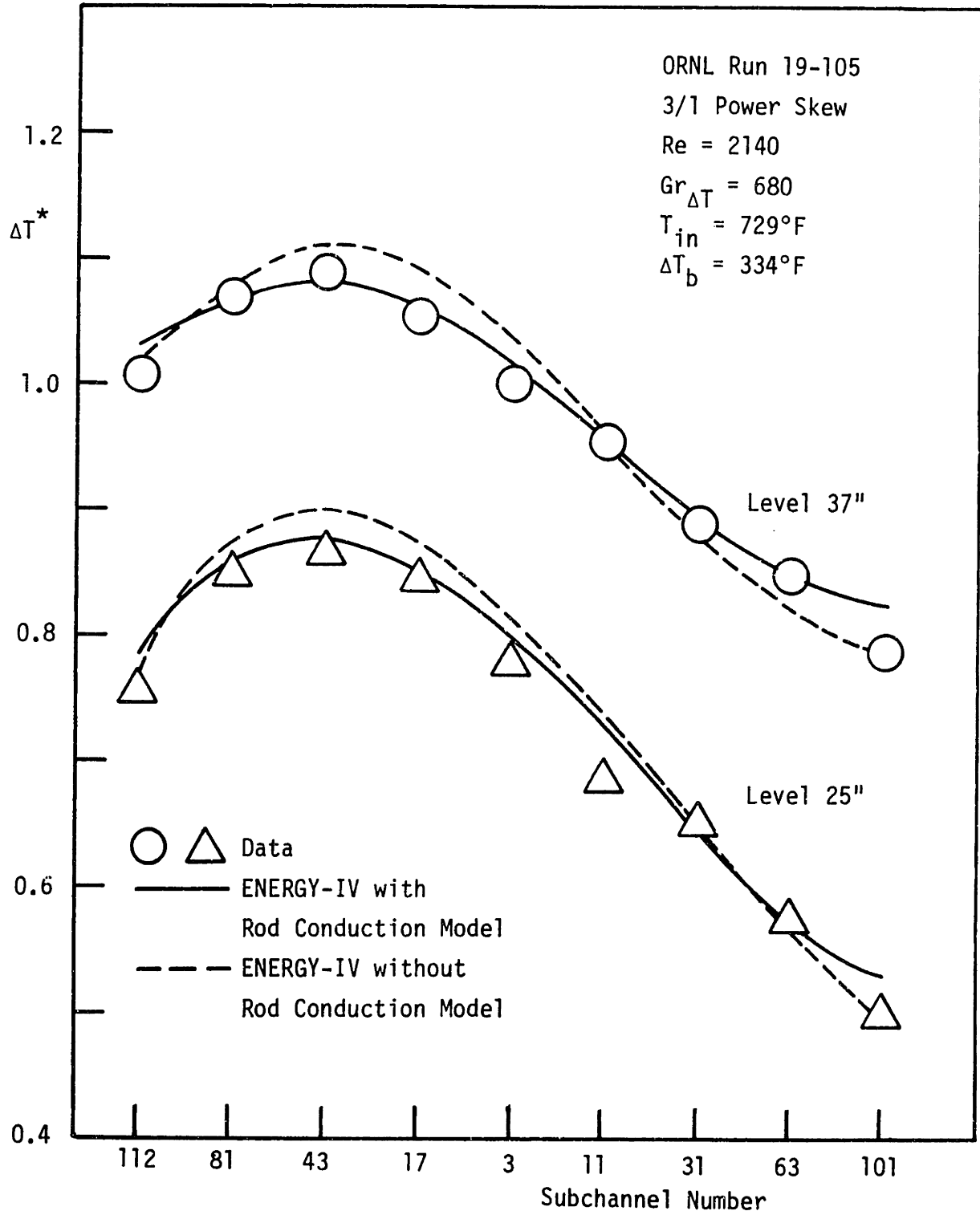
Figure 7.17   Measured and Predicted Temperature Rise for ORNL
Run 19-105

corrected by the energy balance consideration. The detailed procedure

used to correct the ORNL mixed convection data is given in Appendix D.

The code predictions show good agreement with the data for all runs except

Run 12-114 in which the data show a dip in the center region. The

overprediction of the code without the model is around 2% of ΔT_b,

i.e., 6°F. When the rod conduction effect is included, the calculated

results show a slight underprediction of -1% of ΔT_b. The ratio of the

maximum temperature rise difference between the two predictions is 2.5%

for all power skew cases. This result is somewhat small compared with the

values of the WARD blanket bundle (2.5% to about 4.8%). It is explained

by the fact that the relative heat transfer area available for the

conduction through rods to that for the conduction through coolant is

smaller for the fuel type bundle (P/D = 1.244) than for the blanket type

bundle (P/D = 1.082). The overall ENERGY-IV predictions suggest that

there is no thermal plume effect in the ORNL fuel bundle whereas

significant thermal plume effect exists in the WARD blanket bundle.

(3) Toshiba Fuel Bundle

Figure 7.18 illustrates the comparisons between the predictions and

the data for Toshiba Run E37P17 in forced convection condition. The

percent ratio of the maximum ΔT^* difference between the two predictions is

around 3%. In the mixed convection condition, the predictions with the

rod conduction model and without the model are compared with the data for

various power skew cases as shown in Figures 7.19, 7.20 and 7.21. The

decreases of the maximum ΔT^* due to the rod conduction effect are shown in

Table 7.4. The percent ratios of the maximum ΔT^* difference between the

two predictions range from 2% to 5%. However, inclusion of the rod

conduction effect did not always improve the ENERGY-IV predictions. The

ENERGY-IV results with the model showed better predictions for Toshiba
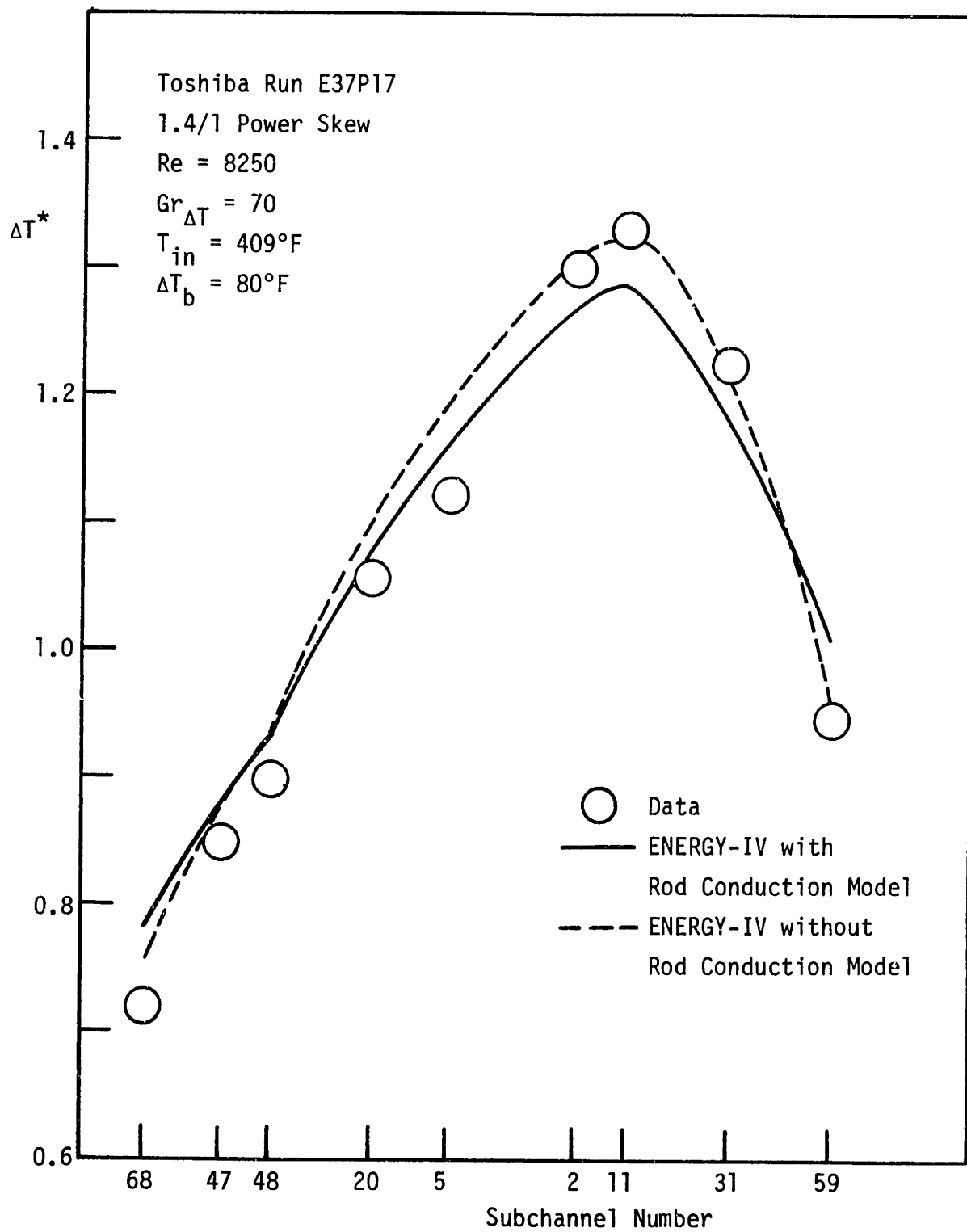
Figure 7.18   Measured and Predicted Temperature Rise at the Outlet
of Heated Zone for Toshiba Run E37P17
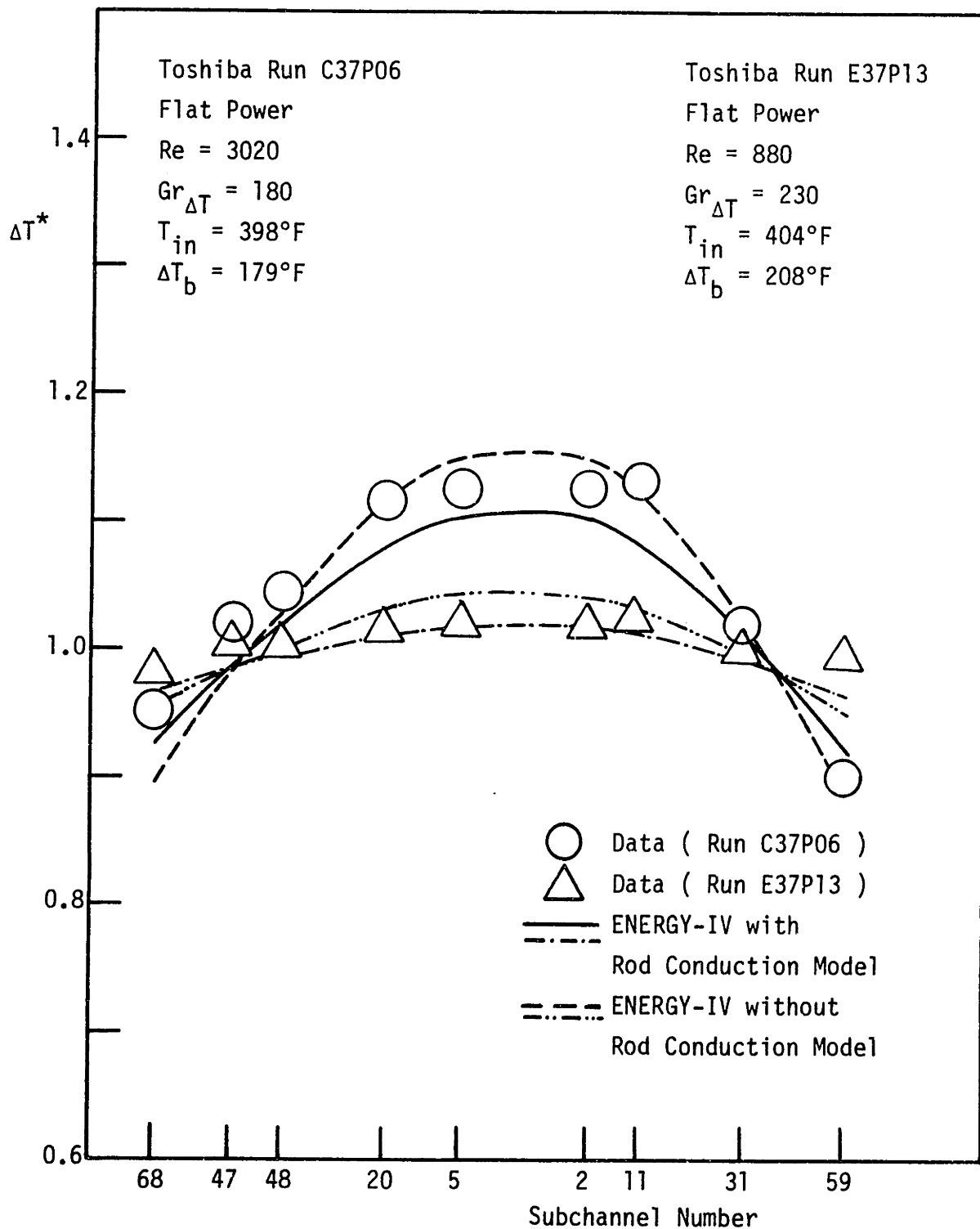
Figure 7.19   Measured and Predicted Temperature Rise at the Outlet
of Heated Zone for Toshiba Runs C37P06 and E37P13
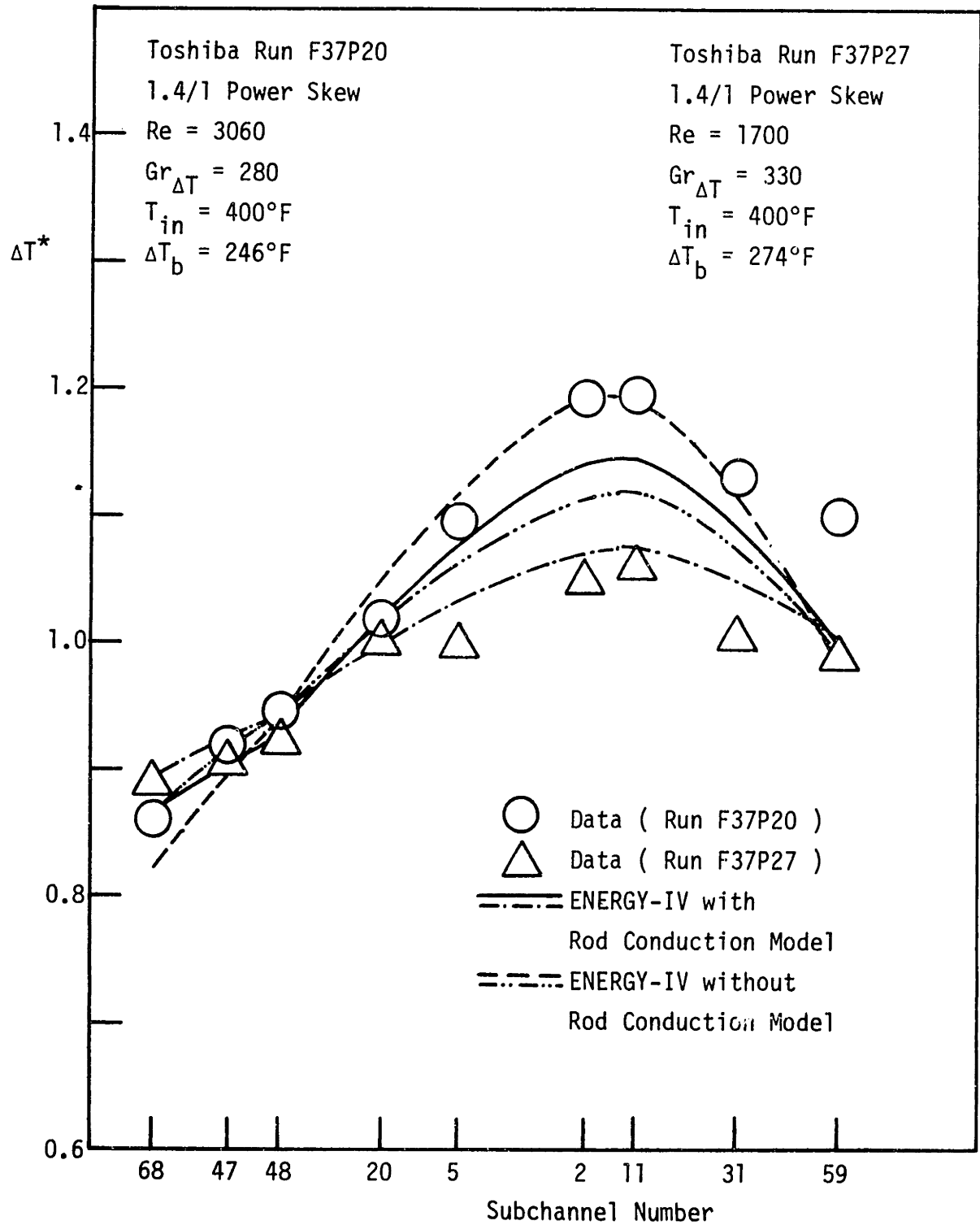
Figure 7.20   Measured and Predicted Temperature Rise at the Outlet
of Heated Zone for Toshiba Runs F37P20 and F37P27
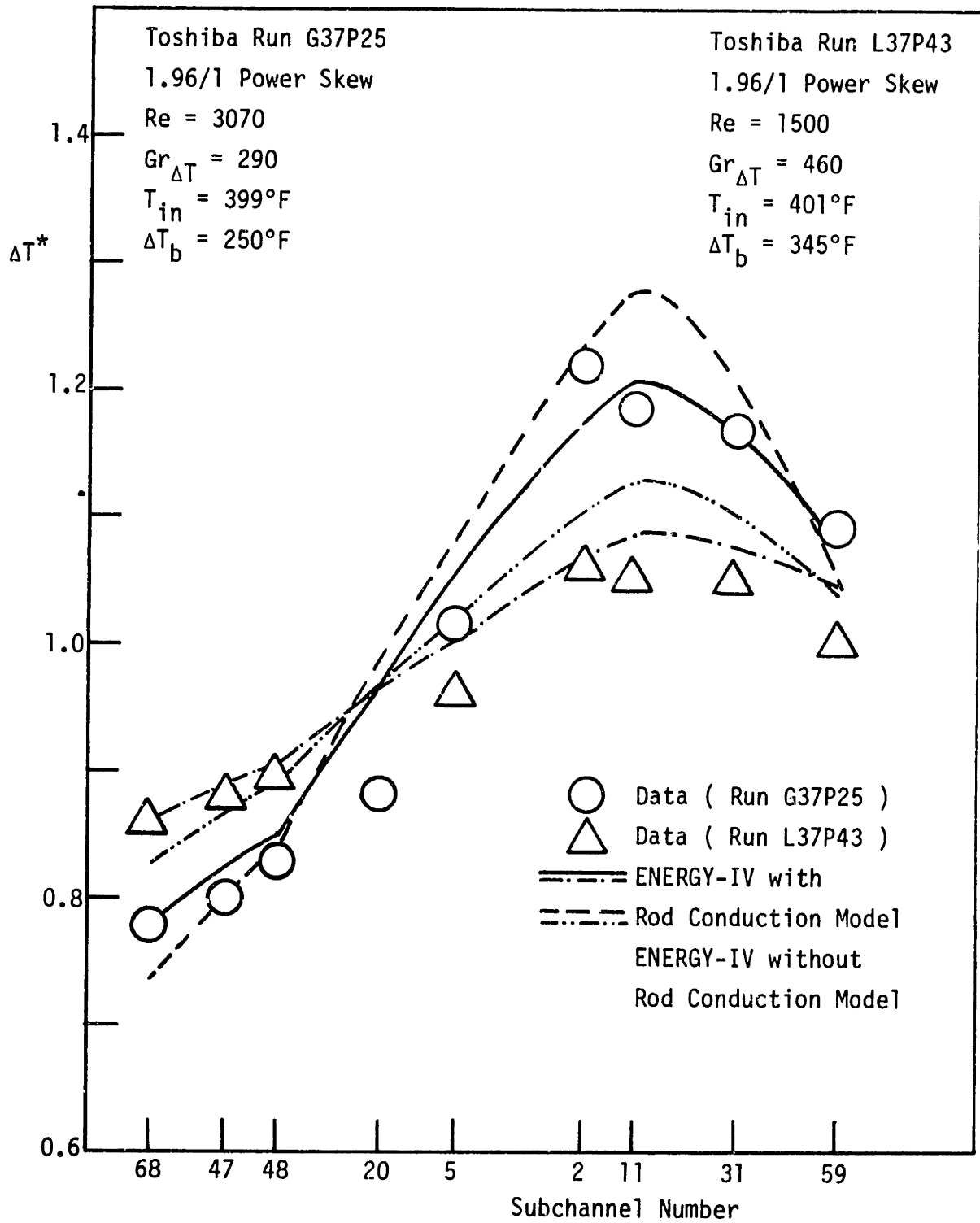
Figure 7.21 Measured and Predicted Temperature Rise at the Outlet
of Heated Zone for Toshiba Runs G37P25 and L37P43

Runs F37P27, G37P25 and L37P43. On the other hand, the ENERGY-IV results without the model predicted better for Toshiba Runs E37P17 and F37P20.

The validation of the rod conduction model has been performed for the three test bundles. The inclusion of the rod conduction effect significantly reduces the difference between the ENERGY-IV predictions and the data. The calculated results with the rod conduction model still overpredict the maximum ΔT^* for the WARD blanket bundle. For the ORNL and Toshiba fuel bundles, the results show almost the same values of the maximum ΔT^* as the data. Consequently, the rod conduction model constructed in this research is reasonably accurate in predicting the rod conduction effect in both fuel and blanket bundles.

7.5 Relative Importance of Energy Transfer Mechanisms

As explained in Chapter 5, the energy transfer mechanisms between subchannels in mixed convection conditions are wire sweeping including turbulent mixing, convective energy transfer by flow redistribution, fluid conduction and rod conduction. In this section, the relative importance of these mechanisms will be investigated, and the regimes in which these parameters are dominant or important will be identified.

Cheng (C-1) constructed relative importance maps in the following manner. A dimensionless parameter relevant to each energy transfer mechanism was established such as a dimensionless effective eddy diffusivity $\varepsilon^*_{1\eta}$ for the wire sweeping including turbulent mixing, a dimensionless thermal diffusivity α^*_1 for the fluid conduction, and a dimensionless thermal plume mixing parameter $\varepsilon^*_{\eta M}$ for the thermal plume mixing. $\varepsilon^*_{\eta M}$ was correlated by matching the ENERGY-IV results to the data. All these three parameters were expressed in terms of Re, $Gr_{\Delta T}$, Pr and geometric parameters (P/D, De, flow area, etc.). Regarding

convective transfer by flow redistribution, since no obvious parameter was found directly comparable to other parameters, a different method was employed to compare the relative importance of energy transfer by flow redistribution to that by wire sweeping through examination of the changes in maximum ΔT^* due to these mechanisms. The relative magnitude of each parameter to $\varepsilon^*_{1\eta}$, then, was calculated to obtain the importance of each energy transfer mechanism. Although this approach is quite straight-forward, it should be noted that the first three parameters are directly comparable to each other but the last parameter, i.e., the relative importance of flow redistribution effect, is not comparable to those parameters since they were not constructed based on the same logic.

In this work, a new rigorous approach is suggested to estimate the relative importance of the energy transfer mechanisms. In addition, the rod conduction effect is included as an additional energy transfer mechanism. The thermal plume mixing is not considered since a relevant correlation could not be obtained as explained in Chapter 8. The importance of each energy transfer mechanism is formulated based on maximum ΔT^*. The reasons are as follows: Maximum ΔT^* is an important parameter regarding safety concerns of the LMFBR core and it is also used to determine the boundaries of the forced, mixed and natural convection regions (E-6, N-2). The effect of each mechanism can be obtained by eliminating each contribution from the total contribution to the maximum ΔT^*.

The relative importance of energy transfer by wire sweeping including turbulent mixing to all energy transfer is defined as,

$$\text{SWEEP} \equiv \frac{1}{A} \left(\text{Max. } \Delta T^* \Big|_{\substack{\text{Mixed Option} \\ \text{with all } - \varepsilon^*_{1\eta}}} - A \right) \qquad (7.4)$$

For convective energy transfer by flow redistribution,

$$FRD \equiv \frac{1}{A} \left(Max. \ \Delta T^* \bigg|_{\substack{\text{Forced Option} \\ \text{with all} - (FR)}} - A \right) \tag{7.5}$$

For fluid conduction,

$$FLUID \equiv \frac{1}{A} \left(Max. \ \Delta T^* \bigg|_{\substack{\text{Mixed Option} \\ \text{with all} - \alpha_1^*}} - A \right) \tag{7.6}$$

For rod conduction,

$$ROD \equiv \frac{1}{A} \left(Max. \ \Delta T^* \bigg|_{\substack{\text{Mixed Option} \\ \text{with all} - (CON)}} - A \right) \tag{7.7}$$

where

$$A \equiv Max. \ \Delta T^* \bigg|_{\substack{\text{Mixed Option} \\ \text{with all}}} \tag{7.8}$$

and FR denotes the flow redistribution effect and CON refers to the rod conduction effect. Max. ΔT^* is the value calculated by the ENERGY-IV at the outlet of the heated zone for each case. Note that the mixed convection option with all energy transfer effects is used as the base case. Each parenthesis refers to the change of the maximum ΔT^* resulting from omitting each effect versus including all energy transfer effects. For a given Re and $Gr_{\Delta T}$ condition, five ENERGY-IV runs are required to calculate the above four relative energy transfer parameters (i.e., SWEEP, FRD, FLUID and ROD).

The method of constructing an importance map as a function of Re and $Gr_{\Delta T}$ is as follows: For a fixed $Gr_{\Delta T}$ (i.e., heat input), ENERGY-IV runs are performed for various Re conditions (i.e., from low rate to high flow rate). Then the boundaries between the regions where the relative energy transfer parameters are significant are identified for the given $Gr_{\Delta T}$. The same procedure is repeated at different but near the

previous $Gr_{\Delta T}$ condition until all the range of $Gr_{\Delta T}$ is covered. The ENERGY-IV runs should be performed with a small interval of Re number near the expected boundary regions. The $Gr_{\Delta T}$ number should not exceed the value where the maximum temperature predicted by the ENERGY-IV equals the sodium saturation temperature.

Figure 7.22 shows the importance map for a blanket bundle constructed utilizing the new approach. In the high Re region (Re $\geq$ 5000), wire sweeping including turbulent mixing is dominant. As Re decreases, rod conduction and fluid conduction become important. At low Re range (Re $\leq$ 1000) flow redistribution dominates over other energy transfer mechanisms. The criterion for importance of rod conduction and fluid conduction was established as a 15% or greater effect with respect to total effect of energy transfer. It is observed that the rod conduction effect is always larger than the fluid conduction effect. The dashed line in Figure 7.22 indicates the boundary where the effects of flow redistribution and wire sweeping including turbulent mixing are the same. For a blanket bundle with $Gr_{\Delta T}$ = 400, which is the typical operating condition of the WARD runs, the rod conduction effect is important in the range of Re = 250 to 5000 whereas the fluid conduction is important between Re = 700 to 3000. Fluid and rod conductions decrease as $Gr_{\Delta T}$ increases. That is because flow redistribution increases as $Gr_{\Delta T}$ increases.

Figure 7.23 shows the relative importance of energy transfer mechanisms for a fuel bundle simulating the ORNL bundle. In this case, the effects of rod conduction and fluid conduction are almost the same. Overall features are the same as those of a blanket bundle. Several higher importance lines (20%, 25%, 30%) are drawn to illustrate the
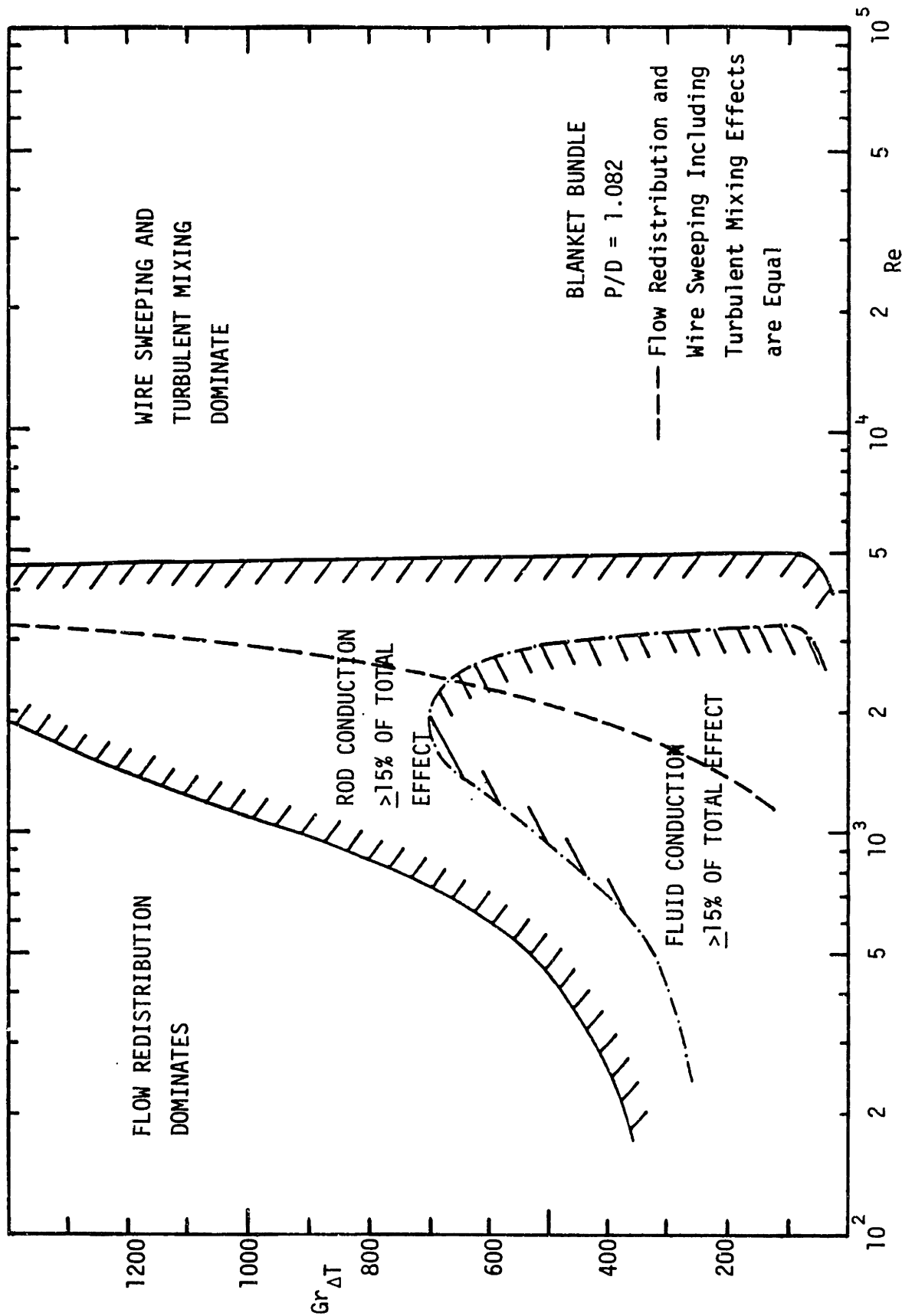
Figure 7.22 Operation Region of Dominance or Significance of Each Energy Transfer Mechanism in a Blanket Bundle
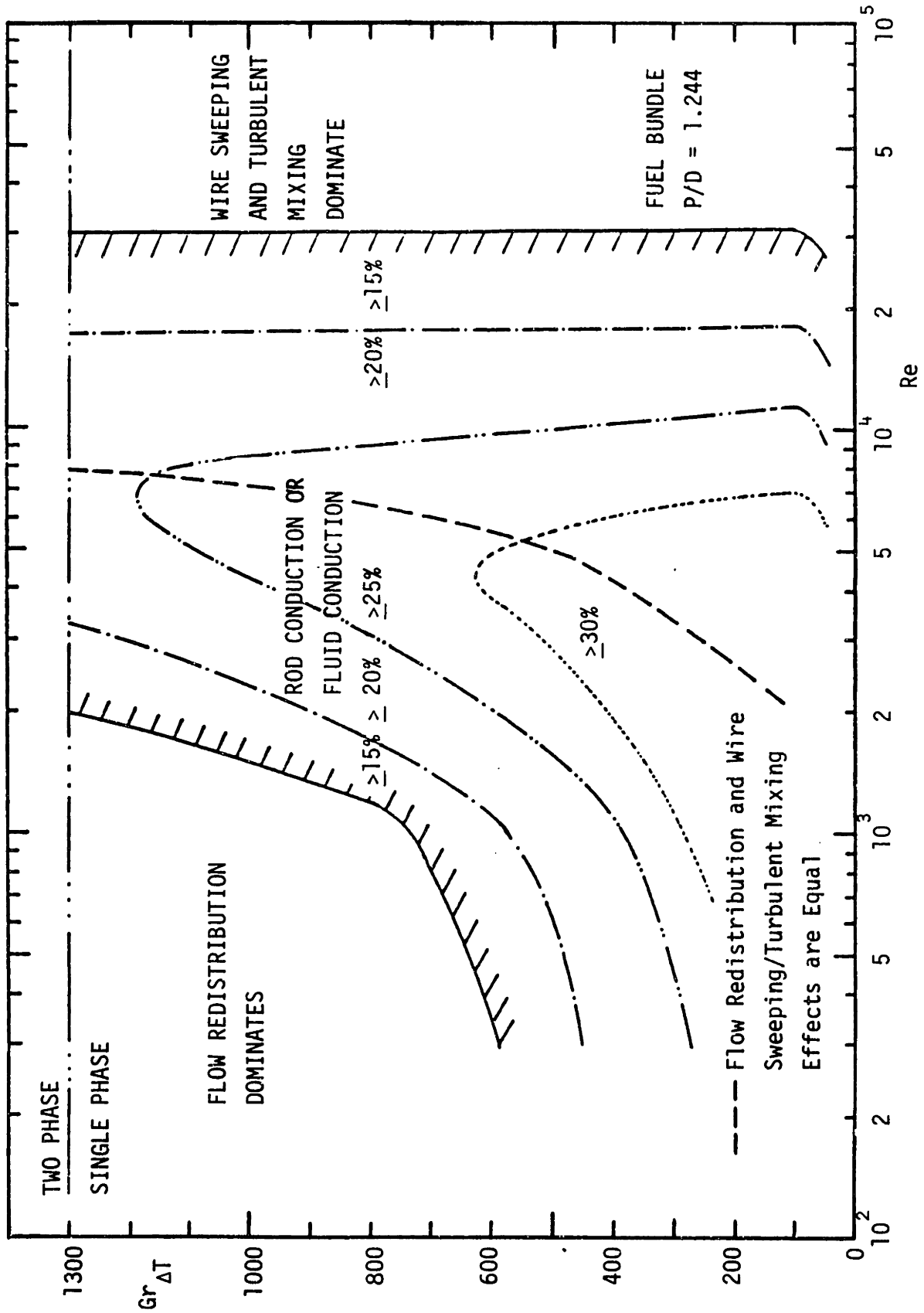
Figure 7.23 Operation Region of Dominance or Significance of Each Energy
Transfer Mechanism in a Fuel Bundle

detailed variation of the importance of the conduction effect. For a fuel bundle with $Gr_{\Delta T}$ = 600, the rod conduction and fluid conduction effects are important ($\geq 15\%$) in the range of Re = 400 to 30000. The maximum value of $Gr_{\Delta T}$ was set to 1300 since the ENERGY-IV predicted the maximum temperature would be higher than the sodium saturation temperature above this $Gr_{\Delta T}$ value.

From Figures 7.22 and 7.23, it is concluded that rod conduction and fluid conduction are important in the mixed convection condition. Flow redistribution dominates in the low Re, high $Gr_{\Delta T}$ region. Wire sweeping including turbulent mixing dominates in the high Re region. These two energy transfer mechanisms have the same importance at the boundary of Re $\approx$ 2500 for a blanket bundle and an Re $\approx$ 6000 for a fuel bundle.

CHAPTER 8

TURBULENT THERMAL PLUME MIXING EXPERIMENT IN

MIXED CONVECTION CONDITIONS

8.1 Introduction

8.1.1 Motivation of Work

In order to predict the temperature field within a rod bundle
correctly, all the energy transfer mechanisms involved in the energy
mixing between subchannels should be considered and modeled properly.
In Chapters 5, 6 and 7, the non-radial rod conduction effect which is
particularly important for the analysis of the out-of-pile test
bundles was investigated. Energy transfer mechanisms involved in
mixed convection conditions were also discussed and the domain where
each energy transfer mechanism was relatively important was
identified.

At low flow, high power conditions (i.e., high $Gr_{\Delta T}/Re$), it
is believed that an additional heat transfer mechanism due to the
so-called thermal plume effect may exist. Thermal plumes in rod
bundles have been visually observed by Bates and Khan (B-4), Symolon
(S-6) and Okada and Todreas (O-3) in their low flow, high power
experiments. In all experiments large temperature fluctuations were
measured at the center of subchannels although the flow Reynolds
number indicated a laminar condition. Several investigators (B-4,
C-1, S-6) have tried to quantify the thermal plume mixing effect by
matching numerical results with experimental data and to correlate it
as a function of bundle dimensionless parameters such as Reynolds
number, Grashof number, power skew and bundle geometry. However,

they did not consider the rod conduction effect which was proven to be important in mixed convection out-of-pile experiments. Moreover, most of the correlations lacked a physical basis and were not experimentally verified. Therefore, it is our purpose to provide fundamental data by directly measuring the turbulent heat transfer induced by the thermal plumes.

8.1.2 Scope

In order to explore the thermal plume mixing effect experimentally, the following work was sequentially executed.

(1) The physics of the thermal plume mixing in rod bundles has been studied and the parameters to be measured have been established.

(2) The test section and other experimental apparatus were designed and constructed.

(3) The velocity fluctuations were measured by a laser Doppler anemometer and the temperature fluctuations measured by a thermocouple. The turbulent heat flux induced by the thermal plumes was obtained by processing these two parameters through turbulence processor devices. The other parameters such as subchannel average temperatures, fluctuation intensities and correlation coefficients were also measured to yield an insight into the physical phenomenon of thermal plume mixing.

(4) The above measurements were performed for different $Gr_{\Delta T}$ and Re conditions as well as various power skew conditions.

8.1.3 Literature Review

The term "thermal plume" is used to describe flow arising from

point or line heat sources when buoyancy is continuously supplied. A sharp boundary exists between the turbulent buoyant fluid (the plume) and the surroundings. The turbulent plume diffuses in the transverse direction through the processes of entrainment of external fluid across this boundary by large turbulent eddies. In a heated rod bundle, it is postulated that the interaction between the thermal boundary layer on a vertically heated rod and the bulk fluid leads to the formation of large hot eddies which diffuse to the cold side. A schematic representation of the thermal plumes is shown in Figure 8.1.

Turbulent thermal plumes were visually observed by Bates and Khan (B-4) in their flow transient experiment in a square-array bare rod bundle in the low Reynolds number region. Based on their observations and analysis of the numerical results, a correlation for the turbulent cross flow mixing rate, W', was suggested as follows,

$$W' = 0.01 \ (\frac{Gr}{Re^2}) \ Q_p \qquad \text{when Re} \leq 450$$

$$= 0 \qquad \text{when Re} > 450 \qquad (8.1)$$

where

$$Gr = \frac{g \beta \Delta T_b D_e^3}{\nu^2}$$

$$Q_p = \frac{\text{high power}}{\text{average power}}$$

Eq. (8.1) is converted into dimensionless form as,

$$\varepsilon_{TM}^* = 1.4 \times 10^4 \ (\frac{Gr_{\Delta T}}{Re^3}) \ Q_p \qquad (8.2)$$

where

$$Gr_{\Delta T} = \frac{g \beta \Delta T_b D_e^4}{\nu^2 L}$$
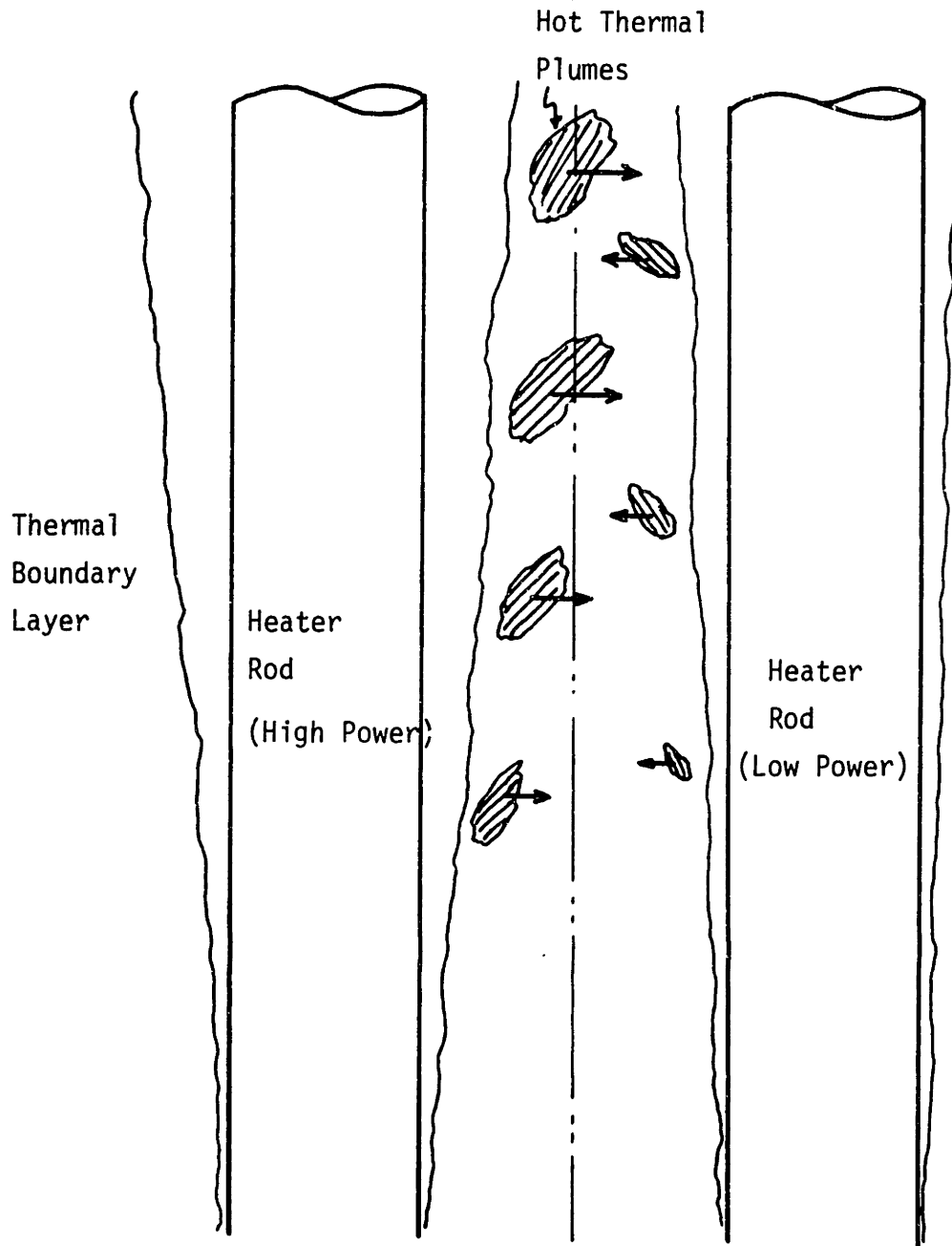
Figure 8.1   A Schematic Representation of the Thermal Plume
Generations

and ε_{TM}^* is the dimensionless thermal plume mixing parameter representing the ratio of the transverse mass flux due to the thermal plumes to the axial mass flux. A detailed description of the definition of ε_{TM}^* will be given in Section 8.2. It was found that numerical COBRA code predictions of their test section behavior could be improved by including the effect of the turbulent mixing due to the turbulent thermal plumes below a Reynolds number of 450.

Symolon (S-6) has suggested a model based on a modified mixing length hypothesis including the buoyancy effect. During his recirculation test, turbulent flow was observed in heated subchannels of thé rod bundle due to instabilities caused by the buoyancy forces. In the unheated subchannels, the flow remained laminar because there were no buoyancy induced instabilities and the Reynolds number was low. A model was developed based on the modified mixing length hypothesis of Oosthuizen (O-4) where the velocity fluctuations produced when a fluid lump moves into a region of a different temperature are assumed due to buoyancy forces. The dimensionless mixing parameter between two subchannels was constructed as:

$$\varepsilon_{TM}^* = 1.75 \frac{D_e}{D_H} \sqrt{\frac{\ell}{D_H}} \sqrt{\frac{Gr_q}{Pr \; Re^{2.4}}} \; Q^* \tag{8.3}$$

where

D_e = bundle hydraulic diameter

D_H = bundle heated diameter

ℓ = centroidal distance between subchannels

Gr_q = Grashof number based on the heat flux = $g\beta q'' D_e^4 / k\nu^2$

Pr = Prandtl number = $C_p \mu / k$

Q^* = minimum power/bundle average power

Substituting the geometrical values of the MIT 4×4 rod bundle against which the model was calibrated, Eq. (8.3) is expressed as,

$$\varepsilon^*_{TM} = 1.1 \left(\frac{Gr_{\Delta T}^{0.5}}{Re^{0.7}}\right) Q^* \qquad (8.4)$$

Utilizing the same mixing length hypothesis, Cheng (C-1) proposed a correlation of the mixing parameter for triangular LMFBR rod bundles. The unknown coefficients were adjusted so that the code predictions of the maximum temperature rises and the shape of the temperature profile showed similar results to the experimental data. The correlation was calibrated as,

$$\varepsilon^*_{TM} = 0.1\left(\frac{c}{D}\right)^{-0.5} \left(\frac{Gr_{\Delta T}}{Re}\right) \qquad (8.5)$$

Cheng found the power skew influence on the thermal plume mixing parameter to be insignificant.

All the above investigations were performed in the rod bundles with square-array or triangular-array geometry in the mixed convection condition. However, as mentioned earlier, these correlations were not constructed based on the experimental measurements of the turbulent heat flux but modeled by matching the numerical results with the velocity or temperature data. No experiment has yet been performed to determine the turbulent heat flux in a rod bundle geometry in the mixed convection condition where the Reynolds number is low (Re<3000) and the power of heated rod is high.

Most of the available thermal plume experiments in the literature were performed with flat plates in the natural convection condition. The majority of the experiments have reported only mean temperature and velocity profiles and local heat transfer rates. A few of them

measured the temperature and velocity fluctuations, the turbulent shear and turbulent heat flux in the fully developed turbulent boundary layers. Lock and Trotter (L-3) using a vertically heated plate measured the fluctuations of the temperature using iron-constantan thermocouple wires. It was found that the temperature fluctuations were of the same order as the mean values in the natural convection region and the scale of turbulence was of the order of the thermal boundary layer thickness in the outer region and decreased sharply near the heated wall. Vliet and Liu (V-1) observed the fluctuations of the velocity using the hydrogen bubble technique in the fully developed turbulent natural convection condition with a vertically heated flat plate. The observations revealed the existence of large turbulent eddies in the region near the wall, as well as in the outer portion of the turbulent boundary layer. It was concluded that these eddies are three-dimensional in nature and are supposed to result from the decay of the vortex street layer structure. Both temperature and velocity fluctuations were investigated by Jaluria and Gebhart (J-1) in a vertical, flat plate in the transition and fully developed turbulent natural convection conditions. Their experiments verified the previous observations and also clarified the transition mechanisms to the fully developed turbulent natural convection flow.

The turbulent heat flux parameters, $\overline{w'T'}$ (turbulent heat flux in the flow direction) and $\overline{u'T'}$ (turbulent heat flux in the direction normal to the wall) in a turbulent natural convection boundary layer

were reported by Smith (S-7) on an isothermal vertical plate in air.
Bill, Jr. and Gebhart (B-5) carried out extensive measurements on the
turbulent heat flux parameters in the transition and the fully
developed turbulent natural boundary layers in a vertically heated
plate. The velocity fluctuations were determined using hot-wire
sensors and the temperature fluctuations were measured using
copper-constantan thermocouples. It was found that both $\overline{u'T'}$ and $\overline{w'T'}$
had a maximum close to the wall and decreased through the boundary
layer. It was also noted that large temperature fluctuations gave
rise to buoyancy concentration, which caused large velocity
fluctuations.

For rod bundle geometry, an experimental investigation with
mercury as the fluid was carried out by Dutton and Welty (D-1). The
heat transfer rates in the natural convection regime were reported as
functions of Nusselt number and Grashof number. They also presented
the temperature disturbances measured near the wall at a subchannel
for different bundle geometries, i.e., P/D = 1.5, 1.3, 1.1 and a
single cylinder. It was found that the amplitudes of the temperature
fluctuations did not change much along the azimuthal coordinate around
the rod for the low Prandtl number fluid. The effect of gap spacing
on the temperature fluctuations was observed as follows. For a single
cylindrical rod, the amplitudes of the disturbances were negligible
for a given Grashof number range. For P/D = 1.5, quite large
amplitudes of the temperature disturbances were encountered. As the
gap spacing was reduced further, the amplitudes and frequencies
decreased until for P/D = 1.1 they were again negligible. Since the
flow regime of this experiment is far below the fully developed

turbulent convection regime, the characteristics of the fully developed turbulent convection flow may be different from the above results.

8.2 Thermal Plume Mixing Parameter

In this section, the definitions of the turbulent heat flux and the thermal plume mixing parameter to be used in the subchannel analysis code, ENERGY-IV, are explained. The schematic geometry considered in this analysis is illustrated in Figure 8.2. The coordinate system and three components of the velocity are also indicated.

The local heat flux across the gap can be expressed as the sum of molecular conduction and turbulent convection through the coolant such as:

$$q''_{ij} = -k(\frac{1}{r} \frac{\partial \bar{T}}{\partial \theta})_{gap} + \rho C_p (\overline{v'T'})_{gap} \qquad (8.6)$$

where the bar (-) denotes the time-average quantity. Note that the component of the velocity fluctuations of interest is in the azimuthal direction normal to the gap.

Heat transport across the gap per unit axial length is written as,

$$q'_{ij} = 2 \int_{D/2}^{P/2} q''_{ij} \, dr \qquad (8.7)$$

From Eqs. (8.6) and (8.7), the linear heat flux due to the turbulent convection only can be written as:

$$q'^*_{ij} = 2 \int_{D/2}^{P/2} \rho C_p (\overline{v'T'})_{gap} \, dr \qquad (8.8)$$
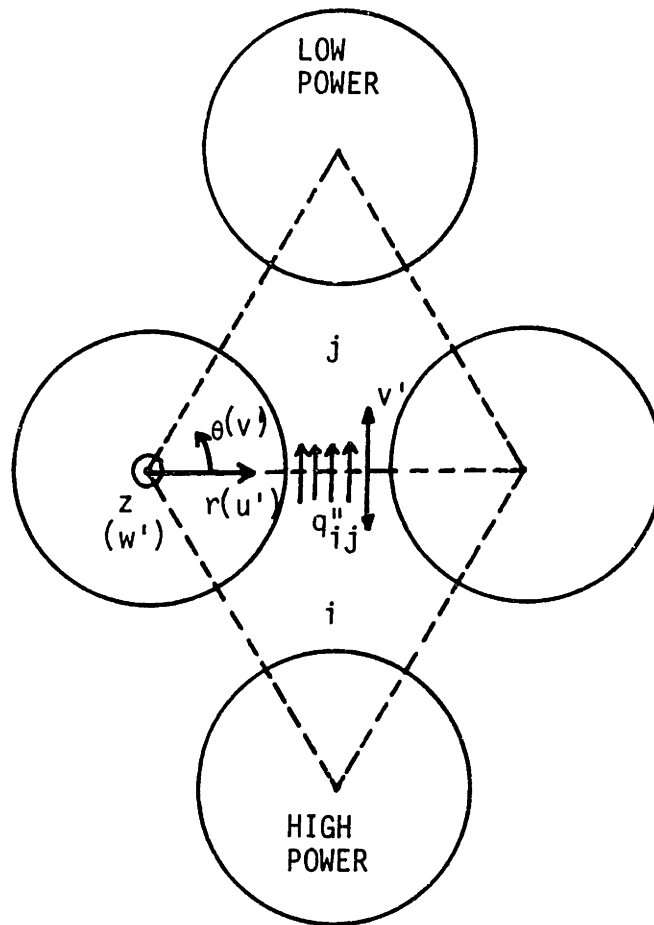
Figure 8.2 Coordinate System and Velocity Fluctuation Components

The turbulent heat flux, $\rho c_p \overline{v'T'}$, is considered to consist of two contributions, i.e., turbulent thermal plumes due to buoyancy effect and natural turbulence due to turbulent shear flow, namely,

$$\overline{v'T'} = (\overline{v'T'})_{\text{Thermal Plume}} + (\overline{v'T'})_{\text{Natural Turbulence}} \qquad (8.9)$$

In our experiment, these two quantities were not separtely measured because the contribution of the natural turbulence is expected to be small at high power conditions compared with that of the thermal plume. In addition, since the natural turbulence due to instability of laminar flow is not usually taken into account for turbulent heat flux correlations, the turbulent heat flux including both contributions may be suitable for modeling purposes.

Utilizing the eddy diffusivity concept, the linear turbulent heat flux is expressed as,

$$q_{ij}'^* = \rho C_p c \varepsilon_{ij} \left(\frac{\overline{T}_i - \overline{T}_j}{\eta_{ij}} \right) \qquad (8.10)$$

where c = gap spacing

η_{ij} = centroidal distance between subchannels i and j

ε_{ij} = eddy diffusivity of heat

The energy transfer between subchannels is also written as,

$$q_{ij}'^* = W_{ij}^{*P} C_p (\overline{T}_i - \overline{T}_j) \qquad (8.11)$$

where W_{ij}^{*P} is the effective mass exchange rate between subchannels i and j due to turbulent thermal plume mixing.

A dimensionless thermal plume mixing parameter, ε^*_{TM}, is defined as,

$$\varepsilon^*_{TM} \equiv \frac{\text{effective transverse mass flux due to thermal plumes}}{\text{axial bundle average mass flux}}$$

i.e.,

$$\varepsilon^*_{TM} = \frac{W^*_{ij} \, P/c}{\rho \bar{w}_b} \qquad (8.12)$$

From Eqs. (8.8) and (8.11), Eq. (8.12) is written as,

$$\varepsilon^*_{TM} = \frac{2}{c \, \bar{w}_b (\bar{T}_i - \bar{T}_j)} \int_{D/2}^{P/2} \overline{(v'T')}_{gap} \, dr \qquad (8.13)$$

In order to get ε^*_{TM} to be applied to the ENERGY-IV code, the turbulent heat flux, $\overline{v'T'}$, should be measured along the gap, and the subchannel average temperatures and bundle average axial velocity should also be obtained. The correlation for the eddy diffusivity of heat can be obtained from Eqs. (8.8) and (8.10) as follows,

$$\varepsilon_{ij} = \frac{2 \, \eta_{ij}}{c(\bar{T}_i - \bar{T}_j)} \int_{D/2}^{P/2} \overline{(v'T')}_{gap} \, dr \qquad (8.14)$$

From Eqs. (8.13) and (8.14) the relationship between the eddy diffusivities is

$$\varepsilon^*_{TM} = \frac{\varepsilon_{ij}}{\bar{w}_b \eta_{ij}} \qquad (8.15)$$

which is consistent with the definition of the dimensionless turbulent diffusivity $\varepsilon^*_{I\eta}$ of Cheng (C-1).

8.3 Experimental Apparatus

8.3.1 Design and Construction of the Test Section

The design goals of the test section were established as follows:

(1) The rod configuration of the test section should be designed to simulate an infinite rod array and to minimize the number of required heater rods. The rod diameter should be large enough so that the velocity and temperature can be measured at several positions along the gap length which is established by the rod diameter and P/D ratio.

(2) To ensure fully developed flow near the exit of the heated section where the measurements were performed, the heated length should be long (i.e., L/D $\geq$ 50) within the limitations of the laboratory space and the apparatus configuration.

(3) The power of the heater rods should be high enough to cover the planned $Gr_{\Delta T}$ ranges. Since heater powers are limited, the total cross-section flow area must be correspondingly limited.

(4) Utilization of existing equipment and facilities should be maximized to reduce the expenditure of purchasing new components. Regarding this, an existing housing duct was used and the diameter of the heater rod was chosen among the manufacturers standard sizes.

Figure 8.3 shows a schematic diagram of the test section. The cross-section of the test section at elevation AA is drawn in Figure 8.4. The test section consisted of the square housing enclosing four heater rods, the bottom plate, top plenum and the flow redistributors which also supported the heater rods. The test section was supported
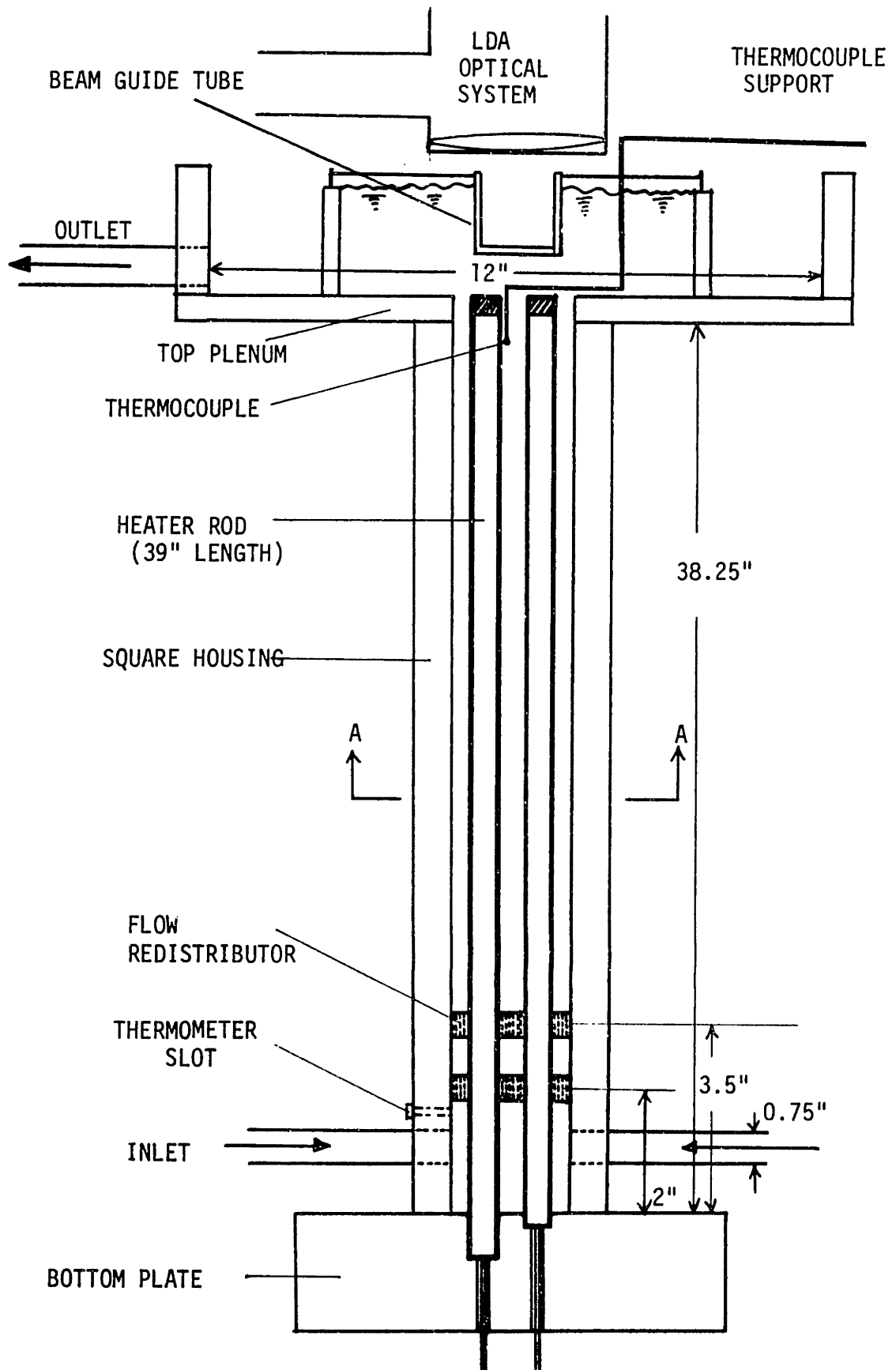
Figure 8.3   Overview of the Test Section
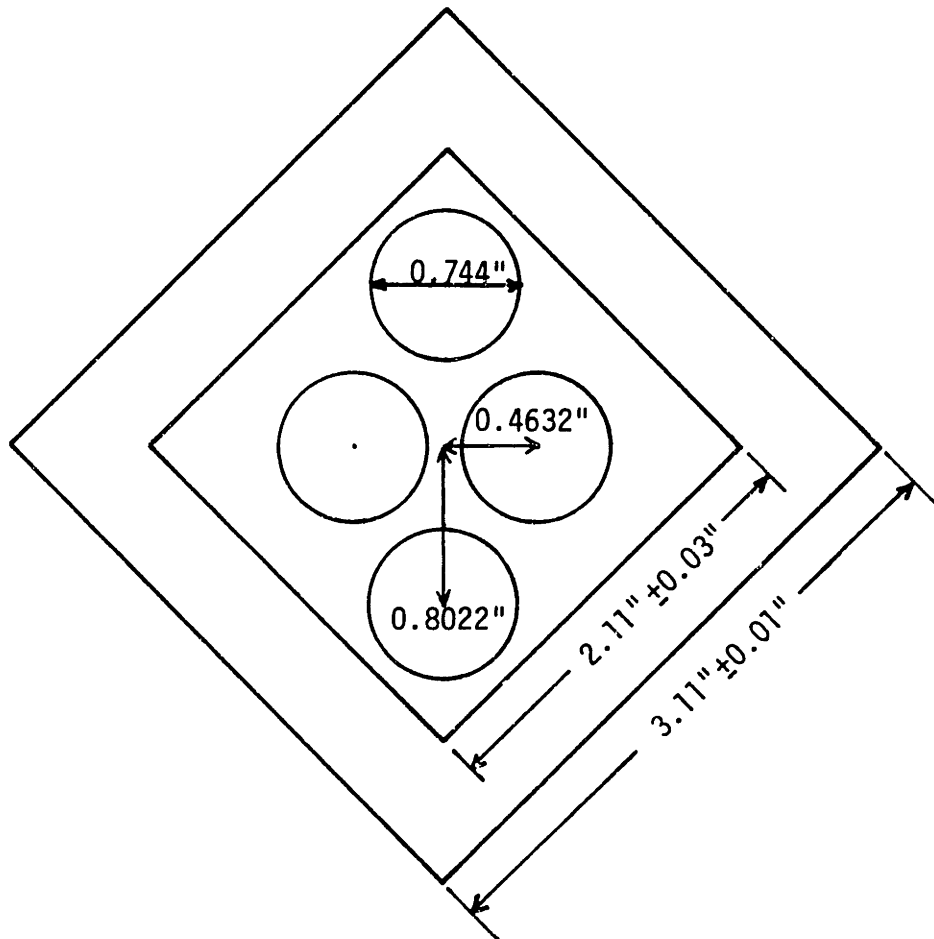
Figure 8.4 Cross-section of the Test Section

by a Dexion frame attached to a traversing system. Thus, the test section could be relocated by adjusting the traversing machine. By doing so, the measurement position could be easily changed to a desired position without readjusting the optical system. The reasons for choosing to move the test section instead of the optical system were as follows: (a) Since the optical system including the laser oscillator was too heavy to place on the traversing machine, and we were especially concerned about the stability of the laser oscillator, it was desirable not to move the optical system. (b) An accurate measurement position could be found by moving the test section with the traversing system, whereas it was difficult to position the optical system exactly if the laser oscillator was fixed and the mirrors and lens only were adjusted.

8.3.1.1 Square Housing

The housing, the shape of which was a square duct, was made of plexiglas. The height of the housing is 38.25" (97.16 cm) and the measured inner dimension is 2.11" ± 0.03" (5.36 cm ± 0.08 cm) square and the outer dimension is 3.11" ± 0.01" (7.90 cm ± 0.03 cm) square. The square housing duct was available from a previous 9-pin (3 x 3 square-array) experiment. The tolerance of the inner dimension was quite large. However, the reduction of the tolerance was difficult since the plexiglas plates comprising the housing duct were tightly glued together. Moreover, the plexiglas plate itself had some tolerance in thickness. Therefore, the existing housing duct was used without any modifications because it was presumed that the tolerance of the housing duct would not greatly affect the thermal-hydraulic characteristics of the interior subchannels of interest.

At the bottom portion of the square housing duct, two holes were drilled on opposite sides for the flow inlet. Pipes with a 0.75" (1.905 cm) inner diameter were fitted to these inlets. The two inlets provide symmetrical flow of the water and smaller flow velocity for each inlet, which aids in reducing the flow non-uniformity at the entrance region. To measure the temperature at the inlet, a small slot was provided for a thermometer at the entrance region. Since the heater rods had a 4" (10.16 cm) unheated zone at the lead wire end side and the thermometer was located at 1.5" (3.81 cm) above the bottom plate, it was believed that the temperature measured at that location correctly represented the inlet temperature of the test section.

8.3.1.2 Heater Rods

The heater rod dimensions were established to fit within the existing square housing duct and to safisfy the geometrical considerations in Section 8.3. Figure 8.4 presents the rod configuration in the square duct. Four heater rods were ordered from RAMA Co. The technical specifications for the heater rods are as follows:

Nominal diameter: 0.75" (1.905 cm)

Actual diameter, D_R: 0.744" ± 0.002" (1.890 cm ± 0.005 cm)

Total length, L_R: 39" (99.06 cm) ± 2%

Heated length, L_H: 34.75" (88.27 cm)

Curvature tolerance: ± 0.002"/ft

Maximum power per rod: 4 kw (at 240 V)

Nominal resistance: 14.4 Ω

The heater rods have a 4" unheated zone at the lead wire end and a

0.25" cold zone at the opposite end of the lead wire end. The lead wire is composed of a 2" solid nickle pin and an 8" flexible lead wire. Figure 8.5 is a schematic diagram of the RAMAROD high temperature cartridge heater supplied by RAMA Co. Note that the resistance wire in the heater rod is coiled circumferentially to provide quite uniform heat flux distribution in the azimuthal direction. The axial heat flux profile of this type of heater rod was examined by Efthimiadis (E-1) using thermocouples attached on the rod surface. It was found that the axial heat flux profile was uniform except for about 1 to 2 cm at the vicinity of both ends of the heated zone.

According to the rod configuration of Figure 8.4, the geometrical characteristics of the test section based on the actual dimensions are:

Pitch to rod diameter ratio, P/D: 1.245

Interior gap distance, D_g: 0.1823" (0.463 cm)

Gap distance between wall and rod surface, D_w: 0.116" (0.295 cm)

Equivalent diameter of the bundle, De_b : 0.610" (1.549 cm)

Equivalent diameter of the interior subchannel, De_i: 0.528" (1.341 cm)

Since the region of interest is the interior gap and subchannels, special attention was given to the dimensions of the interior region.

In order to correctly simulate a multirod bundle assembly, the thermal-hydraulic conditions of the test bundle should be similar to the multirod assembly. In forced convection experiments, the test bundle can be constructed to have the same thermal-hydraulic
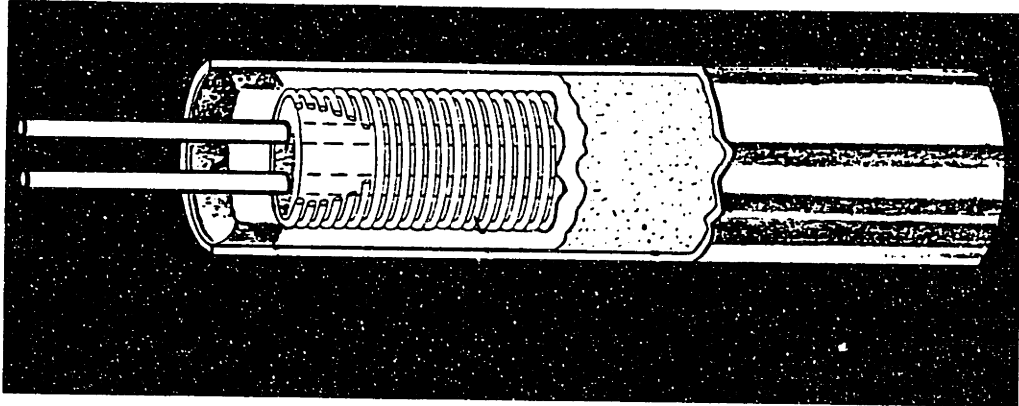
1   The highest quality resistance wire, is evenly coiled and uniformly centered in close proximity to the heater sheath.

2   Magnesium Oxide, compacted to a very high density by proper filling and swaging, forms the heat conducting electrical insulation between the resistance wire and the sheath. The ability of high density MgO to act as a heat conductor and an electrical insulator at high temperatures allows the resistance wire to be in close proximity to the heater sheath. Because of the low temperature drop from resistance wire to sheath, the sheath can be allowed to run hotter without overheating the resistance wire.

3   Incoloy sheath material provides high temperature corrosion resistance and a high emissivity factor. Other materials are available upon request.

4   A moisture and contaminant resistant lava seal is provided as standard. Other seal materials are available.

5   Solid nickel terminal pins are attached to the resistance wire by our patented high temperature connection which makes the RAMAROD superior to other so called high temperature cartridge heaters.

6   All RAMARODS are sealed at the end with a welded metal disc allowing immersion in liquids when required.

Figure 8.5   Heater Rod

conditions as the multirod bundle assembly. However, in mixed convection conditions, the flow redistribution due to buoyancy effect makes the simulation complicated. Therefore, we did not make an effort to have geometric similarity for the hydraulic diameters. Actually, the hydraulic diameter of the interior subchannels (De_i = 0.528") was designed to be a little smaller than that of the side subchannels (De_s = 0.623"). This design concept may be favorable in heated cases since the velocities of the interior subchannels are increased due to the buoyancy effect. Another reason to select the rod diameter of 0.75" (nominal) was that this dimension was a standardized size and no special order was required.

8.3.1.3 Bottom Plate

A schematic representation of the bottom plate is shown in Figure 8.6. It is made of plexiglas with the dimensions of 4.5" x 7.25" (rectangular) and 1.5" (thickness). the housing and the heater rods were placed on the bottom plate. A rubber gasket was inserted between the flange of the housing duct and the bottom plate to seal against water leakage. Four holes were drilled at the bottom plate to support the heater rods and to guide the lead wire. A silicon sealant (RTV106, red) was used to prevent leakage through the holes.

It should be noted that the depth of each hole supporting the heater rod is different since the heater rods have different lengths due to the manufacturing tolerance. Since the measurement was taken near the exit level, it was desirable to have the ends of the heater rods positioned at the same exit level. This was achieved by adjusting the hole depths to accommodate the length differences among the four heater rods.
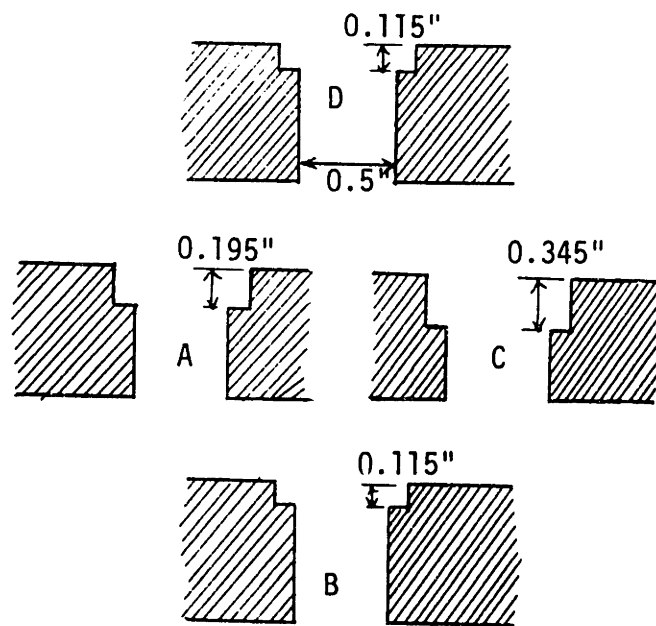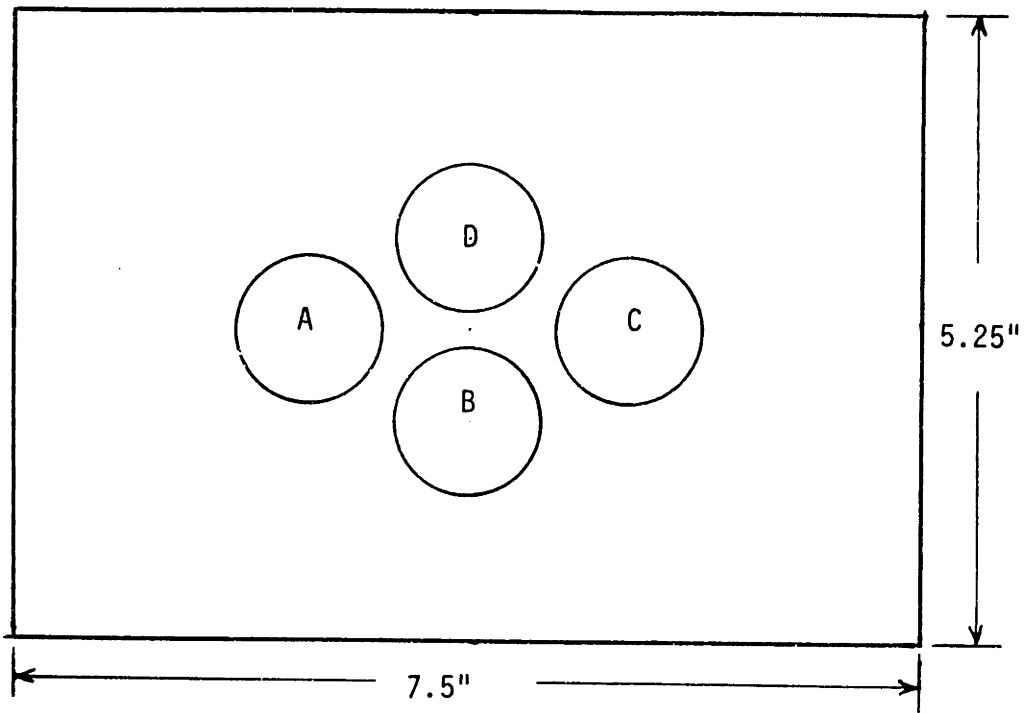
Figure 8.6 Bottom Plate (Top and Side View)

As mentioned earlier, the bottom plate was not fixed to the ground, but it was placed on the supporting frame. This allowed the test section to move three dimensionally relative to the ground, whereas the optical system was fixed to the ground.

8.3.1.4 Top Plenum

Figure 8.7 shows a top view of the top plenum. The material of the top plenum is PVC and it consists of two concentric cylinders and a circular plate connected to the housing. The inner plenum has a 7" inner diameter and is always filled with water during a series of experiments. The water spills over the top flange of the inner cylindèr to the outer plenum and the outlet piping. The reason for submerging the optical system by this inner plenum design is as follows: Two laser beams projected from the top of the test section are refracted with different angles if the water in the top plenum has a free surface. Then, the focussing point is not stationary due to the moving boundary. In order to eliminate the moving boundary at the water surface, a beam guide tube attached to the laser optical system was designed to be submerged as shown in Figure 8.3.

The inner diameter of the outer plenum is 12". The design consideration for the outer plenum is to make its inner diameter as large as possible. This concern comes from the relative position of the outlet of the top plenum to the water level of the tank (see figure 8.9). Due to the configuration of the existing apparatus arrangement the gravitational driving force draining the water from the top plenum to the water tank is not strong enough when the flow rate is high. Therefore, in order to provide enough space for the water to be drained, it is desirable to make a large diameter of the
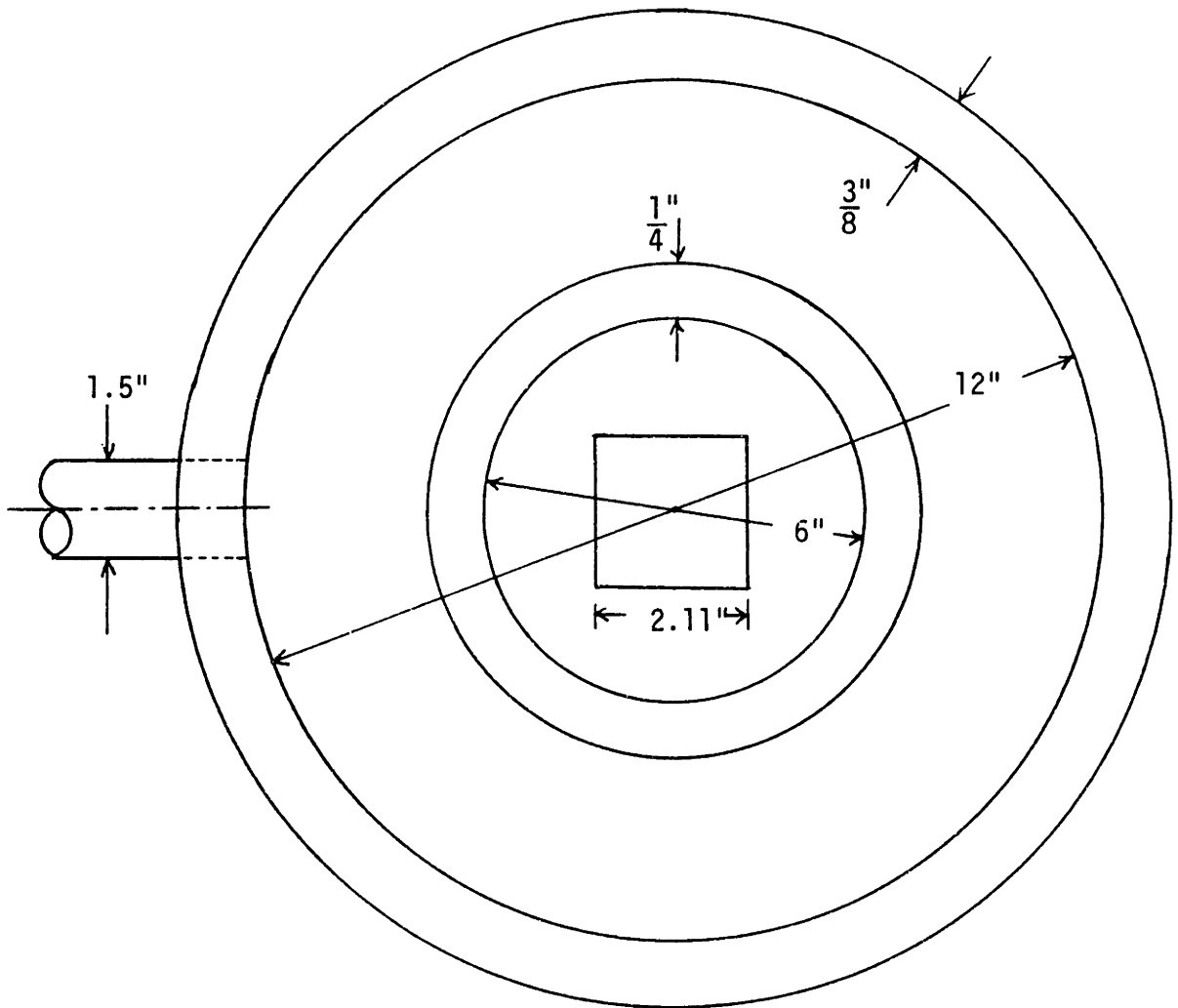
Figure 8.7 Top Plate (Top View)

outer plenum. For the same reason, the outlet pipe attached to the outer plenum was designed to have a large diameter, i.e., a 1.5" inner diameter.

8.3.1.5 Flow Redistributors

The water pumped from the tank flows into the test section through the inlet nozzles located at both sides of the lower end part of the test housing. Thus, it is expected that there is a strong cross flow at the test housing inlet. It is a prerequisite to have a uniform inlet velocity profile to measure the turbulent fluctuations successfully. To fulfill this requirement, two flow redistributors were set up in the entrance region of the test section.

The cross section of a flow redistributor is drawn in Figure 8.8. The flow redistributors were made of plexiglas plate which had many small diameter holes (1/8" to 1/10"). The two flow redistributors were separated by 1.5" in order to align the flow more effectively. The function of the flow redistributors is not only to redistribute the flow but also to position the heater rods at their desired locations. During the construction stage of the test section, it was found that the alignment of the heater rods at their correct positions could not be achieved by only two flow redistributors and bottom holes. Consequently, a supporting frame was installed on the top plenum and welded to the top of the heater rods.

The upper flow redistributor was located just below the beginning of the heated section of the heater rod. It is favorable to position the flow redistributor in the unheated zone since it may otherwise be broken by the radial thermal expansion of the heater rods.
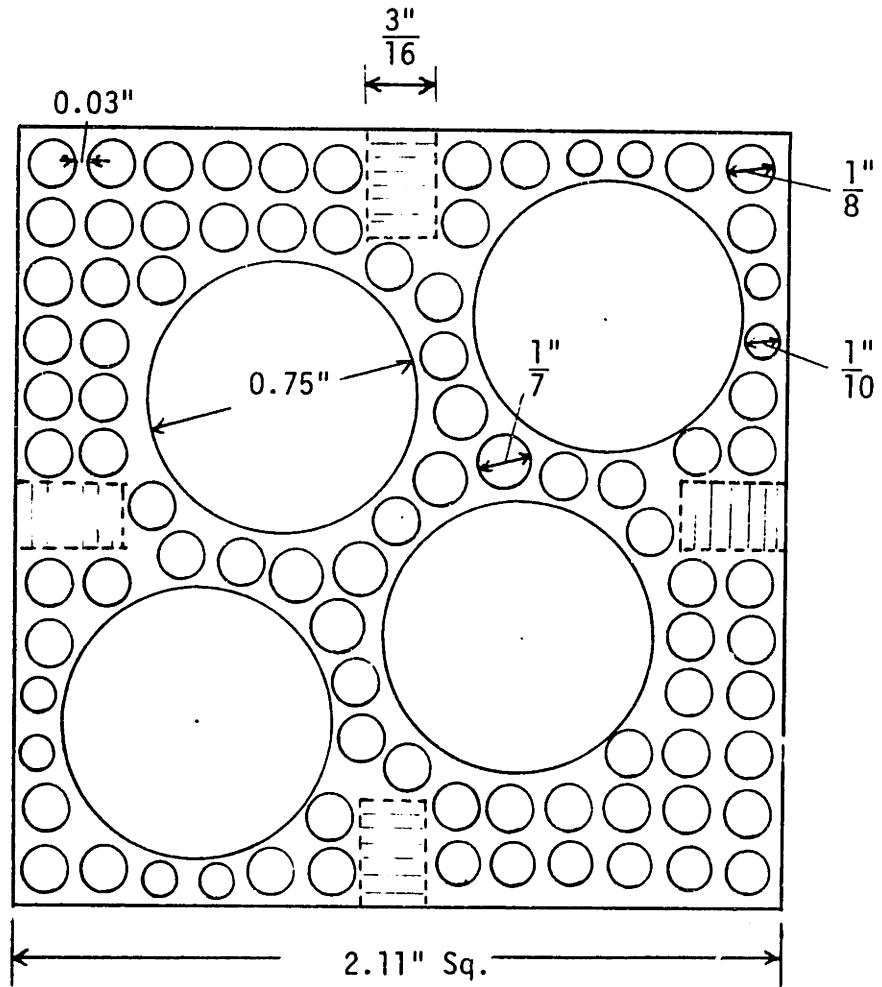
Figure 8.8 Flow Redistributor (0.5" Thickness)

8.3.1.6 Other Components

In order to support the test section, a supporting frame made of Dexion was constructed and attached to the traversing machine through supporting arms. The traversing machine was available in the laboratory. Before the experiments were performed, it was calibrated using a dial gauge with a minumum scale of 0.001".

8.3.2 Flow Loop

A schematic diagram of the loop used in this work is drawn in Figure 8.9. Most of the components of the loop were already built for the high flow turbulent recirculation experiment by Sawdye (S-8). The following parts have been newly added and replaced:

(1) A new test section has been constructed for our turbulent mixing experiment. Consequently, the inlet and outlet piping was replaced to allow connection to the inlet and outlet nozzles of the new test section.

(2) A flowmeter has been added to measure the low flow rate required since the existing two flowmeters were installed for the purpose of measuring high turbulent flow.

(3) Four heater rods were submerged into the water tank in order to degas the water. Each heater rod has a maximum power of 2 kw. Degassing the water is important in the heated experiments. According to our previous experience, it has been observed that many bubbles were generated around the heated rods when the degassing process was not successfully accomplished. These bubbles alter the heat transfer rate and block the flow path between heater rods.
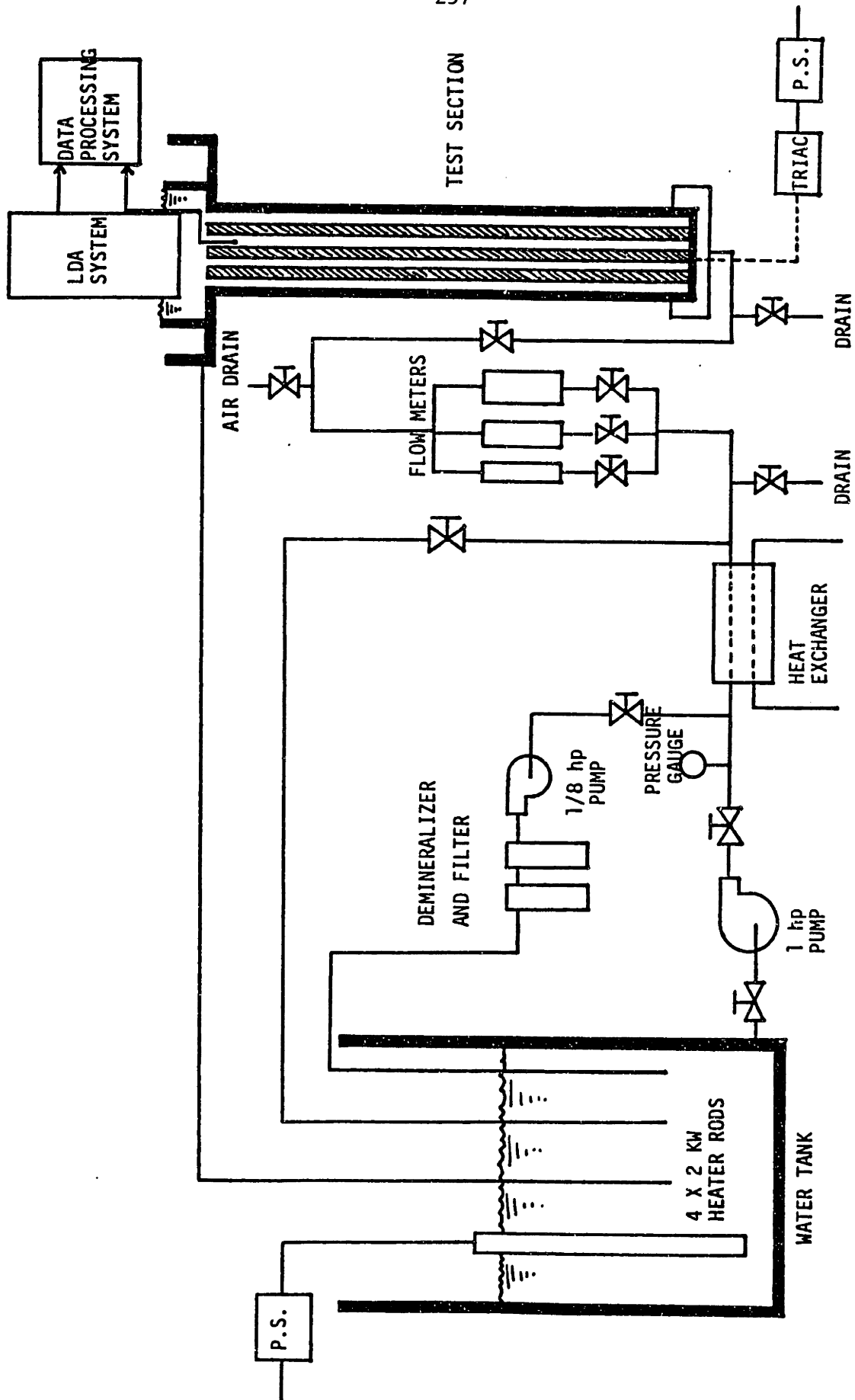
Figure 8.9 Schematic Representation of the Experimental Loop

(4) Two drains have been installed to drain the water from the test section and the water tank. Another purpose of the drain piping is to clean up the loop without passing the water through the test section. (5) In order to remove the air remaining in the pipes, two air relief valves were installed at the top portion of the piping system. Since the location of the pipes after passing through the flowmeters was higher than that of the free water surface of the test section, air always occupied the upper piping if the air was not bled out.

As shown in Figure 8.9, the loop consists of the test section, two flowmeters, a heat exchanger, two pumps, pipings, valves and a water tank. Note that the water loop was arranged as a circulating versus a once-through system. There are three reasons to choose the circulating loop arrangement. First, the capacity of the existing water tank is not large enough to supply degassed water continuously during a series of experiments in a once-through system. Second, the light scattering particles such as SiC dispersed in the water tank to amplify the scattering intensity are expensive. Therefore, it is economical to reuse them by a recirculating loop arrangement. Finally, in the recirculating open loop system, caution should be taken to prevent air from being entrained in the water along the flow path. Regarding that, the outlet pipe of the test section and the by-pass pipe were arranged to be submerged below the water level of the tank.

In the following subsections, the main components of the loop are explained in more detail.

8.3.2.1 Water Tank

The water tank is made of aluminum with the volume of 0.13 m^3 (34 gallons). Its interior was coated with several layers of an epoxy paint to prevent corrosion. Four heater rods (2 kw for each rod) were submerged in the tank. Before commencing the experiments, the water in the tank was degassed to remove the air dissolved in the water. This was accomplished by heating the water to the boiling temperature (bulk water temperature > 95°C). Then this water was cooled to ambient temperature (25°C) by natural convection between the water and the surrounding atmosphere. It took approximately one hour to heat the water to the boiling temperature with these four heater rods and around twenty hours to cool it to ambient. Although the heat exchanger could be used to cool it, it should not be operated at high water temperature (≥ 70°C) because of poor temperature durability of the vinyl tubing connecting the water tank and recirculation pipe.

8.3.2.2 Flowmeters

Two parallel flowmeters were used to cover the flow range of interest. One was a newly installed low flow range meter and the other was an existing high flow range meter. The maximum volume flow rates of the flowmeters provided by the manufacturer are $495 \text{ cm}^3/\text{s}$ (7.84 gpm) and $154 \text{ cm}^3/\text{s}$ (2.44 gpm). The flowmeter measuring low flow rate was calibrated using the classical bucket/stop watch method. The calibration results are shown in Figure 8.10. The measured values present linear behavior with the percent scale indicated on the flowmeter. The maximum flow rate was calibrated as 2.44 gpm identical with the nominal value. The maximum error of this calibration was less than 2.6%.
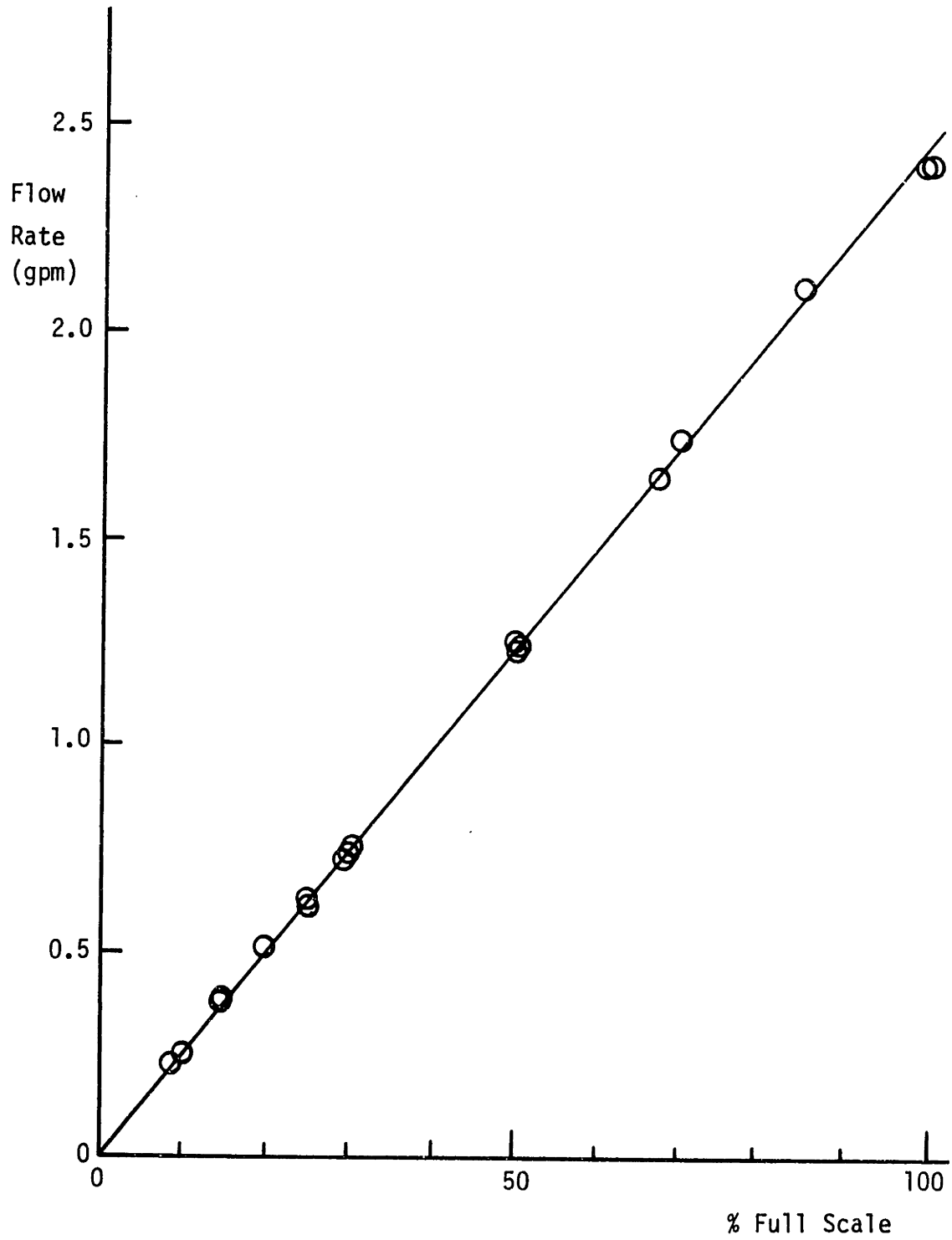
Figure 8.10 Flowmeter Calibration Curve (2.44 gpm Max. Nominal)

8.3.2.3 Pumps

Two pumps were installed to circulate the water in the loop. A one hp pump was used to provide the flow through the test section for the measurements and to clean the loop. The nominal flow rate of this pump is up to 33 gpm. A one-eighth hp pump was used for filtering and demineralization of the water. The nominal flow rate is up to 30 gph. This low power pump was only operated before measurements since the light scattering particles of large diameter might be removed by the filtering system.

8.3.2.4 Heat Exchanger

A heat exchanger was used to maintain constant inlet temperature of the test section. Heat generated in the heater rods and frictional heat from the pump were removed by cold city water passing through the heat exchanger. It was observed that the time to reach a steady state condition was around one hour.

In addition to the above components, there are valves, pipes, and a demineralizer and filter. Special attention was given to choosing the material of the pipings and valves. The valves are all brass to reduce corrosion problems. The piping system consists of brass pipes and vinyl tubing which is also corrosion-resistant. The vinyl tubing was used to provide the flexible connection between the test section and the rigid portion of the loop required for translation of the test section by the traversing machine.

8.3.3 Power Supply System

A power supply system was designed and constructed to heat the heater rods electrically and to control the power of each heater rod

individually. The power supply system consists of four sets of main circuits and gate pulse generating circuits. Figure 8.11 shows a set of the power supply circuit. An r.m.s. voltmeter (DISA 55D35) and an A.C. ammeter were mounted to monitor the power of each heater rod.

Triacs were used to control the power which have the following advantages over the variable voltage transformers such as variacs which are often used as a power controller:

(a) They are quite cheap.

(b) Power levels are preset by toggle switches or a computer.

(c) Transient experiments with variable heater power can be performed if desired.

A triac is a kind of bi-directional thyristor which allows an electric current to flow only when a gate pulse is given. Once the current begins to flow, it continues to flow until the voltage of sinusoidal A.C. power source reaches zero. Detailed descriptions of the principle and function of the triac are given in Appendix F.

By changing the triggering phase angle, the heater power can be controlled. The triggering phase angle is the phase lag of the gate pulse from the zero-crossing point where the A.C. voltage is zero. A gate pulse generating circuit was designed to change the triggering phase angle. It consists of a zero-crossing detector, clock pulse generator, heater selector and trigger pulse generator. The zero-crossing detector generates a pulse whenever the voltage of A.C. power source becomes zero. A quartz crystal oscillator generates clock pulses at 30.72 KHz which are used to perform the count-up operation. The zero-crossing pulses together with the clock pulses
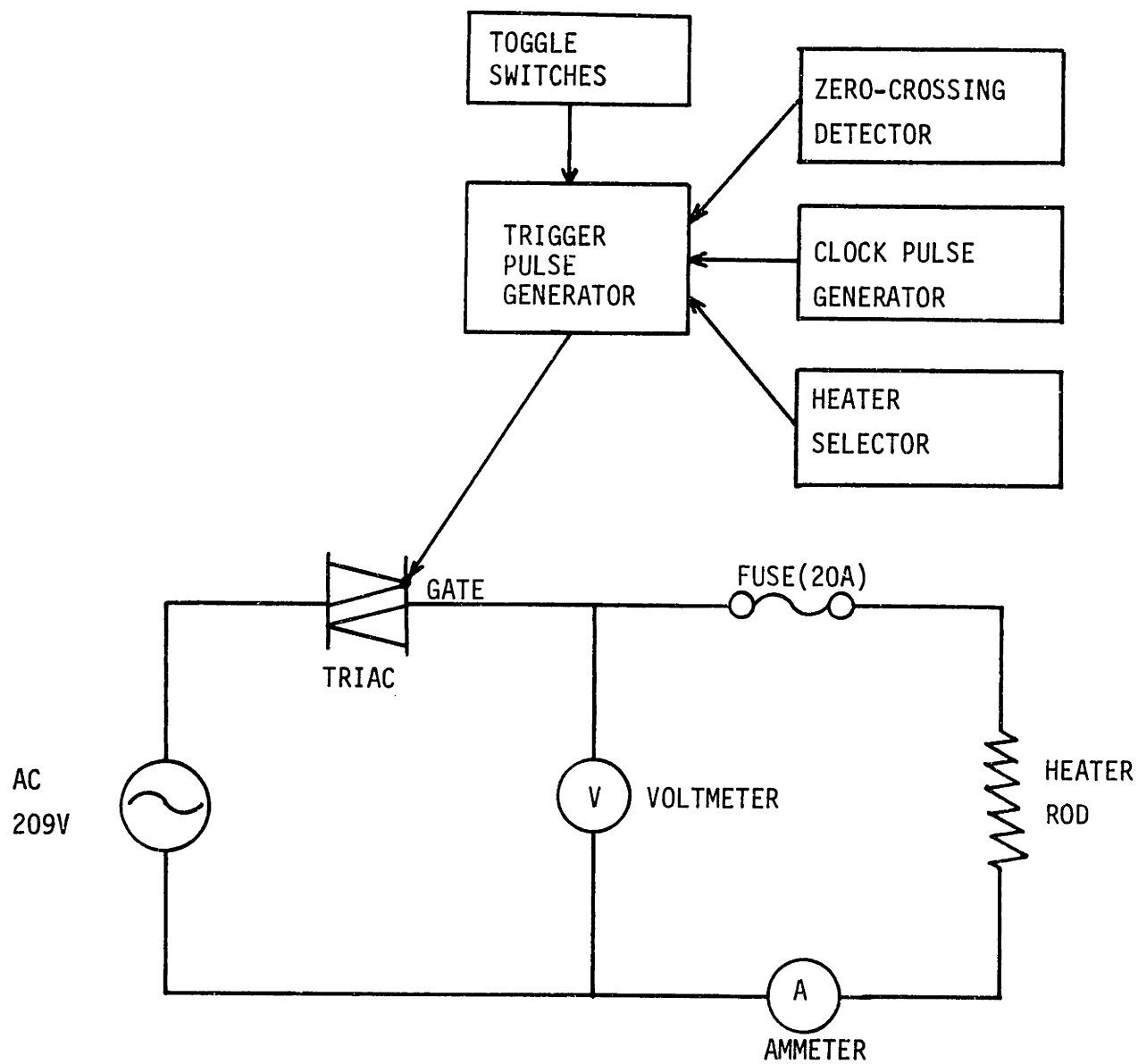
Figure 8.11   Main Circuit and Gate Pulse Generating Circuit

are transmitted to the trigger pulse generator where the gate pulses are generated. The initial data preset by the eight toggle switches are entered into the gate circuit which is chosen by the heater selector. If a computer is used instead of the toggle switches, the heater power can be changed programmably and therefore transient experiments are possible. The circuit diagrams and functions of the gate circuit and power control system are explained in detail in Appendix F.

Figure 8.12 shows the voltages of the heater rod predicted from Eq. (F.5) of Appendix F in comparison with the measured values with the r.m.s. voltmeter. The maximum difference between the theoretical and experimental results was 1.2% of the r.m.s. voltage (209V) of the A.C. power source. This result has proven that the power supply system was designed and constructed correctly.

8.3.4 Laser Doppler Anemometer System

In order to measure the velocity fluctuations of transverse flow between subchannels in the field where the thermal plumes exist, a velocimeter is needed which satisfies the following conditions and characteristics:

(a) The velocimeter is not substantially influenced by the temperature fluctuations of the fluid.

(b) The sensor does not disturb the flow and the temperature fields.

(c) The sensor has the ability to measure low fluid velocity with an average velocity that may be zero.

(d) The sensor can function in a flow passage which is narrow and of complicated shape.
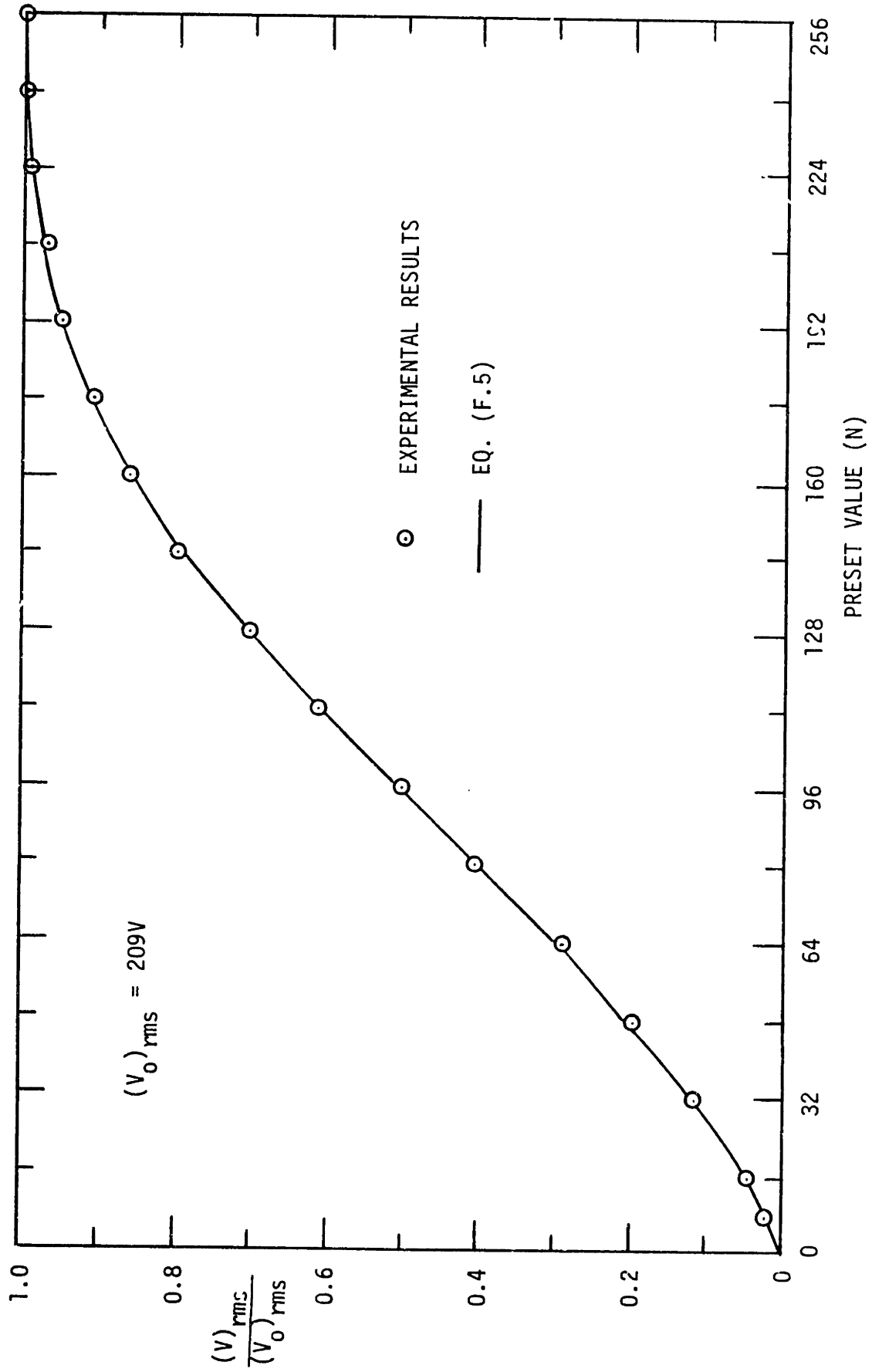
Figure 8.12 Measured and Calculated Heater Rod Voltages Controlled by the Power Supply System

From the above considerations, a laser Doppler anemometer (LDA) was selected. The principles and applications of the LDA have been discussed by Durst et al. (D-2), Drain (D-3) and Carajilescov (C-5) and need not be repeated here.

The laser available for the experiment was a He-Ne unit (Spectra-Physics Model 125) operating at 632.8 mm wavelength. The power of the He-He laser with a plasma current of 32 milliamps was measured to be 15 mW, while the rated power was 50 mW. Since this power was somewhat low for operation with the backscatter mode, silicon carbide powder (mean diameter is 1.5µm with geometric standard deviation of 1.4 and density is 3.2 g/cm^3) was used to increase the scattered light intensity. The concentration of the light scattering particles was selected to provide approximately one particle in the measuring volume. This could be achieved by checking the Doppler signal while adding the particles to the water in the flow loop little by little.

The LDA system was operated in the backscatter mode to measure the transverse velocity component of the fluid flow at the gap at the top of the test section. The laser beam must be projected on the measuring point from the top side to prevent the rods from blocking the beam path. A schematic diagram of the optical system is shown in Figure 8.13. The laser beam was projected from the horizontally set He-Ne laser and directed using two mirrors to enter the beamsplitter (TSI 9115-2) vertically. The beamsplitter had a prism which split the incoming laser beam into two parallel beams of equal intensity. The distance between each split beam and the incoming beam was 25 mm.

MIRROR

LASER
(He-Ne SP-125)

MIRROR

BEAMSPLITTER (TSI 9115-2)

BRAGG CELL

FROM 40 MHz
POWER SOURCE

FREQUENCY
SHIFTER
(TSI 9180-2)

PIN HOLE

BACKSCATTER
MIRROR

RECEIVING
ASSEMBLY
(TSI 9140)

BACKSCATTER
LENS

PHOTOMULTIPLIER
(DISA 55L12)

FILTER

OUTPUT
(TO PRE-
AMPLIFIER)

FRONT LENS ($\begin{matrix} \text{f=103 mm (TSI 9117) or} \\ \text{f=250 mm (TSI 9118)} \end{matrix}$)

V

MEASURING POINT
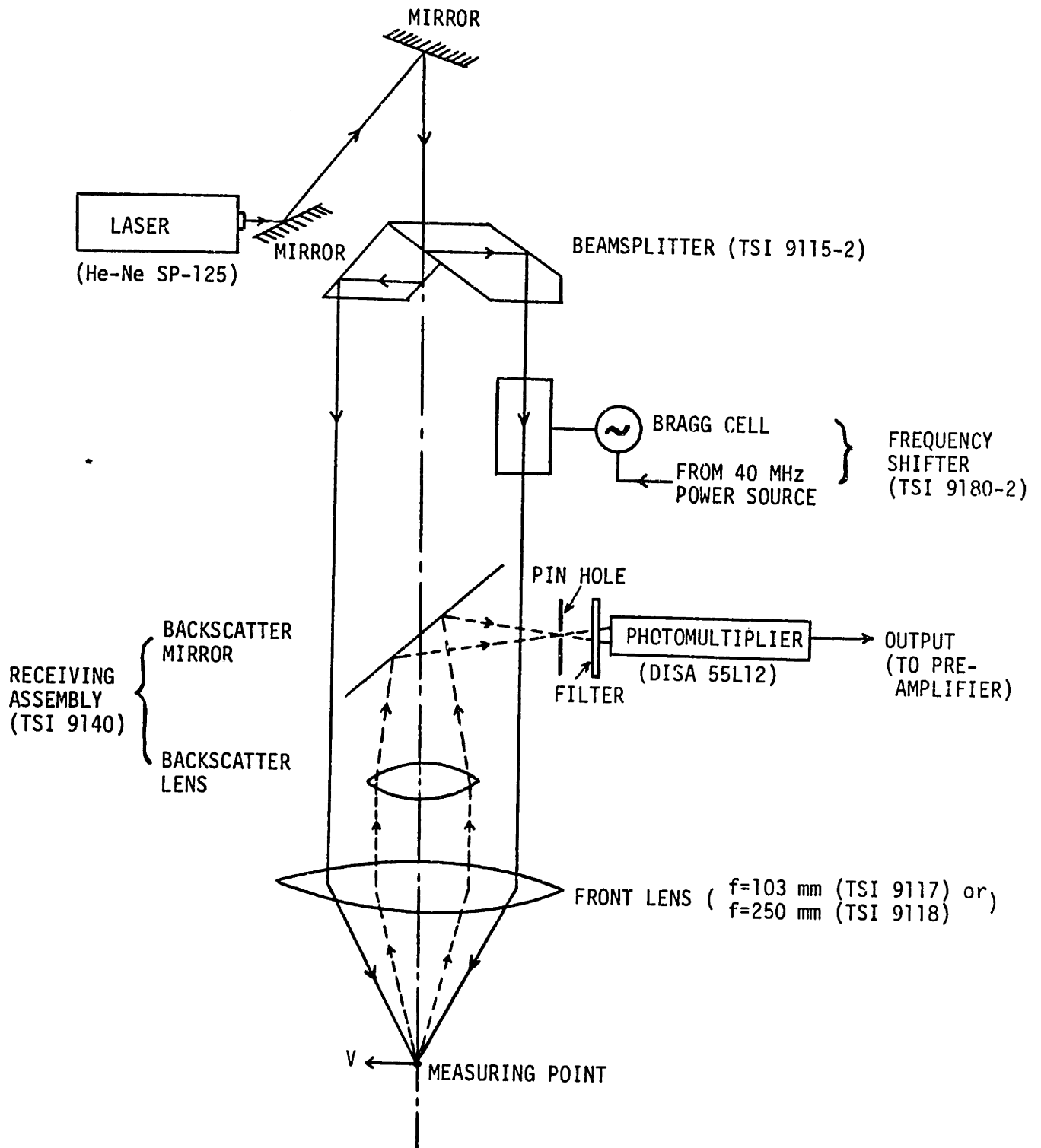
Figure 8.13 Dual Beam Backscatter LDA System

One beam then passed through the Bragg cell (TSI 9180-2), where it suffered a frequency shift of 40 MHZ so that the direction of the flow could be detected. The front lens (f = 103 mm (TSI 9117) and f = 250 mm (TSI 9118)) was used for focusing the incident beams and collecting the backscattered light. The receiving assembly (TSI 9140) had a lens and a mirror which focused the collimated light from the front lens onto a photomultiplier pinhole. The photomultiplier (TSI 9162) was used to detect the Doppler signals and to convert light intensity to electrical current.

The optical system used in the work is a differential or fringe mode system and the Doppler frequency, f_D, is given by:

$$f_D = \frac{2v}{\lambda} \sin \frac{\theta}{2} \tag{8.16}$$

where λ is the wavelength of the laser light, θ the angle between the two incident beams, and v the velocity component perpendicular to the line bisecting the angle between the two incident beams and in the same plane. The measuring volume is considered an ellipsoid which is defined by the $1/e^2$ - intensity boundary. The dimensions of the measuring volume and the calibration factor between measured Doppler frequency and velocity, F ($v = F \cdot f_D$), are shown in Table 8.1. These LDA parameters were obtained for the existing optics.

8.3.5 Thermocouple System

The fluid temperature was measured utilizing a thermocouple probe consisting of 0.003" (0.0076 cm) diameter copper-constantan wires. The time constant of the thermocouple was estimated as less than 0.1 sec (0-5). Since the frequency of the temperature fluctuations due to

Table 8.1   Measuring Volume and Conversion Factor

Front lens f (mm)	dx (mm)	dr (mm)	dz (mm)	F (cm/s/kHz)
103	0.041	0.043	0.17	0.1342
250	0.10	0.10	1.0	0.318

Formulas:

$$dx = \frac{4f\lambda}{\pi di} \; , \quad dy = \frac{dx}{\cos(\theta/2)} \; , \quad dz = \frac{dx}{\sin(\theta/2)} \; ,$$

$$\theta = 2\arctan\left(\frac{D}{2f}\right), \quad F = \frac{\lambda}{2\sin(\theta/2)}$$
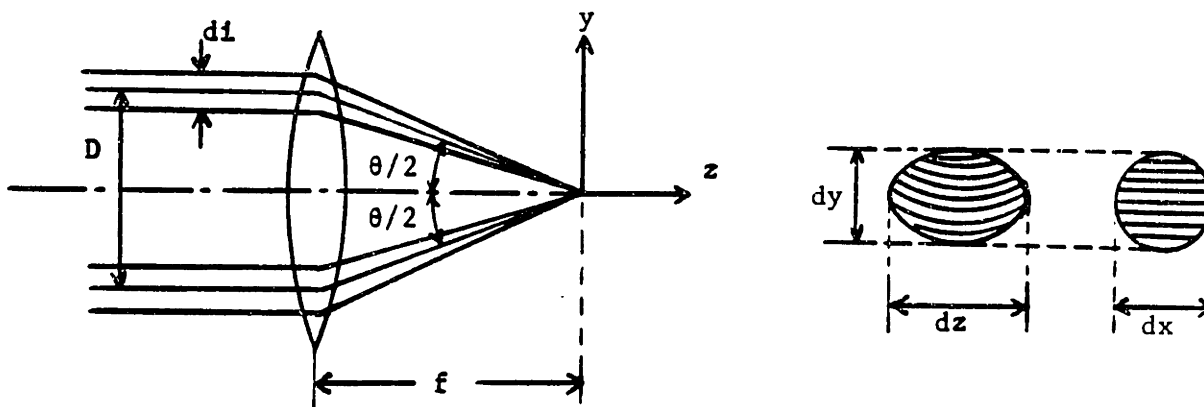
di = $1/e^2$ – diameter of laser beam (= 2 mm)

dx, dy, dz = optical probe volume dimensions

   dy – in measuring direction

   dz – along the optical axis

   dx – normal to dy and dz

D = beam separation (= 50 mm)

f = focal length of front lens

θ = beam intersection angle

λ = laser wavelength (= 632.8 nm)

thermal plumes was observed to be less than 5 Hz, this time constant was sufficient for resolution of the temperature fluctuations.

An ice water filled box was used for the reference junction. A supporting frame was installed to guide the thermocouple wires. Since the supporting frame was fixed on the ground as well as the laser optical system, no adjustment of the thermocouple position was required once the thermocouple probe was positioned close to the measuring volume of the LDA so that the velocity and temperature could be measured at almost the same position. To measure the temperature distribution in the subchannels, the test section was translated to the desired positions.

8.3.6 Signal Processing System

Figure 8.14 shows a block diagram of the signal processing system. Most of the devices were available from previous experiment (S-8) except a DC differential amplifier, low-pass filters and a switch circuit. The electric Doppler signal from the photomultiplier was amplified and transmitted to a mixer of the frequency shifter (TSI 985) to shift the detected signal frequency down into the range required by the velocity range to be measured. This process removed the flow-directional ambiguity, the pedestal signal and the fringe bias as well as compressed the frequency of large turbulent signals. Since the average transverse velocity was small in the experiment, the center frequency of the tracker was adjusted to indicate zero velocity or the frequency of output of the downmix circuit. The tracker frequency ranges used in this experiment were 15 kHz and 50 kHz
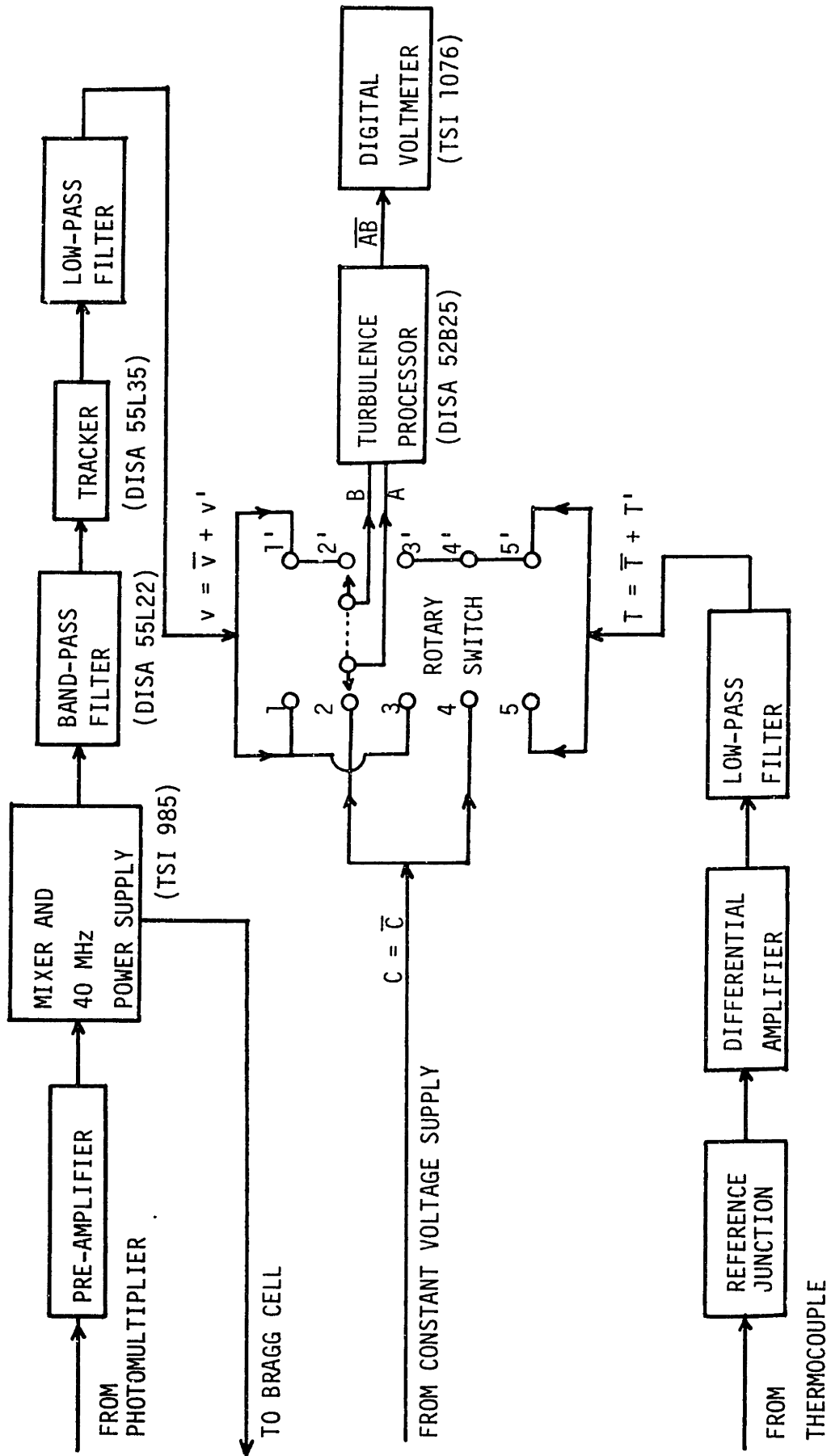
Figure 8.14 Signal Processing System

depending on the magnitude of the velocity fluctuation. The frequency-shifted signal was then delivered to a preamplifier with a bandpass filter (DISA 55L30) to reject white noise and the pedestal voltage and then was processed by a tracker (DISA 55L35). The tracker converted the signal into the voltage directly proportional to the fluid velocity. A low-pass filter was designed to remove Doppler ambiguity due to the change of the amplitude of the laser Doppler signal. The cut-off frequency was established to be 50 Hz since it was observed that the frequency of the velocity fluctuation due to the thermal plume was less than 10 Hz. The attenuation factor of the filter was 0.175, which was measured utilizing a signal generator and a digital voltmeter.

The thermoelectric voltage generated by a thermocouple probe and referenced with an ice junction was amplified by a DC differential amplifier. The amplified voltage was then passed through a low-pass filter. The cut-off frequency of the filter was set to be 50 Hz since the frequency of the temperature fluctuation was also less than 10 Hz. Then the common noise included in the output of the thermocouple could be rejected by the DC differential amplifier and the low-pass filter. The total gain of the amplifier and the filter measured using a low voltage source was 100. Circuit diagrams of DC differential amplifier and low-pass filters for the temperature and velocity are drawn in Appendix G.

The velocity and temperature together with the constant voltage supplied by a DC power source were fed to a turbulence processor (DISA 52B25) through a switch. The turbulence processor was a small analog computer and used as a multiplier in this experiment. When the input

signals were A and B, the output signals of the turbulence processor showed a mean value of AB. The time constant of integration ranged from 0 to 100 sec. As shown in Figure 8.14, a rotary switch was used to select the inputs of the turbulence processor among the five sets of combination of the velocity, temperature and constant voltage. The function of the rotary switch is summarized in Table 8.2. A digital voltmeter (TSI 1076) was used to read the mean output voltage of the turbulence processor.

8.4 Experimental Procedure

The detailed procedure of this experiment can be found in the instruction manual prepared by Nakajima (N-3). In this section, the main procedure for the measurements and data analysis are presented.

8.4.1 Measurement Procedure

The following steps were followed:

(1) The degassed water had been prepared by heating the water in the tank one day before the experiment was performed. The laser was turned on and allowed to operate at least 30 minutes to maximize the laser power. The ice box was prepared and the signal processing system was checked and adjusted.

(2) The pump was turned on and then the flow rate was set to the desired level. The heat exchanger began to operate with maximum capacity.

(3) After confirming that the power control switch was off, the switch for the main power supply was turned on and the powers of the heater rods were preset individually at the approximate desired values. Figure 8.12 was used to set the power level

Table 8.2 Function of Rotary Switch

Turbulence Processor

Switch	Input A B	Output		Information
1 - 1'	v v	$\overline{v^2}$	$(= \overline{v}^{-2} + \overline{v'^2})$	$\overline{v'^2}$
2 - 2'	C v	$C\,\overline{v}$	$\longrightarrow \overline{v}$	
3 - 3'	v T	$\overline{v\,T}$	$(= \overline{v}\,\overline{T} + \overline{v'T'})$	$\overline{v'T'}$
4 - 4'	C T	$C\,\overline{T}$	$\longrightarrow \overline{T}$	
5 - 5'	T T	$\overline{T^2}$	$(= \overline{T}^{-2} + \overline{T'^2})$	$\overline{T'^2}$

(Notes)

$v = \overline{v} + v'$, $T = \overline{T} + T'$

C : Constant voltage supplied by a DC power supply

through the binary toggle switches. Then the main switch of the power control system was turned on, and fine adjustment of the power of each heater rod selected through the heater selector switches was performed. When high power inputs were required, a fan was used to cool the triac circuit to maintain the operating temperature.

(4) The inlet and outlet temperatures were monitored to check when the steady state condition was achieved. It took around one hour for most of the experimental conditions.

(5) The offset value of the turbulence processor was recorded to calibrate the data when its inputs were set to zero. The switches of the DC power supplies were turned on, and the exact voltage of the constant power supply (a dry cell with around 1.5 V) was measured from the output A of the switch box where the low pass filters were placed when the rotary switch was positioned on No.2 or No.4.

(6) The rotary switch was set at No.2. When the photomultiplier was turned off, the output of the tracker indicated the shifted frequency of the frequency shifter which corresponded to the zero velocity. The variable resistance of the differential amplifier for the velocity was adjusted so that the output of the differential amplifier (or the digital voltmeter) was zero. Then the photomultiplier was turned on, and the output voltage of the digital voltmeter was read which yielded the mean velocity as shown in Table 8.2.

(7) The rotary switch was set at No.1. The output voltage showed the sum of $\bar{v}^2$ and $\overline{v'^2}$ from which the velocity fluctuation intensity, $(\overline{v'^2})^{1/2}$, could be obtained.

(8) The rotary switch was then set at No.4. The variable resistance of the differential amplifier for the temperature was adjusted so that the output of the digital voltmeter was zero. By connecting the inputs of the differential amplifier together, the average temperature could be obtained since the offset value corresponded to the actual thermoelectric voltage.

(9) After connecting the inputs to the thermocouple again, the rotary switch was set at No.5. Since the average temperature was forcefully set equal to zero volts in step (8), the output of the turbulence processor showed $\overline{T'^2}$ instead of the sum of $\bar{T}^2$ and $\overline{T'^2}$. This modification was made because of the concern that the magnitude of the temperature fluctuation was quite small compared to that of the average temperature. By eliminating the average component of the temperature, the gain setting of the turbulence processor could be further increased to reduce the measurement error of the fluctuating component.

(10) Elimination of the average component of the velocity was performed for the following reason: If the velocity measured at step (6) and the temperature fluctuation measured at step (8) were used by setting the rotary switch at No.3, the output would be,

$$A \cdot B \approx \overline{(\overline{v} + v')(T')} = \overline{v} \ \overline{T'} + \overline{v'T'}$$

The term, $\overline{v} \ \overline{T'}$, was not exactly zero due to the measurement error. When $\overline{v}$ was quite large, $\overline{v} \ \overline{T'}$ was not negligible. Therefore the following procedure was adopted: After the photomultiplier was turned off and the rotary switch was set at No.2, the Doppler signal processor was placed on the manual position and tuned to indicate the average velocity reading obtained in step (6). Then the variable resistance of the differential amplifier for the velocity was adjusted so that the output voltage became zero. This process resulted in the average velocity equal to zero volts.

(11) Then, the rotary switch was set at No.3. The output of the turbulence processor corresponded to the turbulent heat flux, $\overline{v'T'}$.

For the average temperature measurements only, the steps (1), (2), (3), (4), (5) and (8) were carried out. Throughout this procedure, the gains of the turbulence processor were adjusted to the maximum range possible without overloading the processor.

8.4.2 Data Processing

The Doppler frequency is directly proportional to the fluid velocity as given in Eq. (8.16).

$$f_D = \frac{2v}{\lambda} \sin \frac{\theta}{2} \tag{8.16}$$

The frequency is related to the tracker output voltage as,

$$f_D = \frac{f_{max}}{V_{max}} V_D \tag{8.17}$$

From Eqs. (8.16) and (8.17),

$$V_D = \frac{2}{\lambda} \frac{V_{max}}{f_{max}} \sin\frac{\theta}{2} \, v \qquad (8.18)$$

The output voltage of the turbulence processor is expressed as,

$$V_{out} = G_{Att} \, G_{TP} \, V_D \qquad (8.19)$$

or

$$V_{out} = C_o \, G_{TP} \, v \qquad (8.20)$$

where $\qquad C_o \equiv G_{Att} \frac{2}{\lambda} \frac{V_{max}}{f_{max}} \sin\frac{\theta}{2}$ $\qquad (8.21)$

G_{Att} is the attenuation factor of the filter and differential amplifier and G_{TP} is the gain of the turbulent processor. The measured value of G_{Att} was 0.175. Table 8.3 shows the values of the constant, C_o, for the combinations of the front lens and the tracker frequency range utilized in this experiment. The values in Table 8.1 were used to calculate C_o. The units of V_{out} and v are volts and mm/s, respectively.

The output voltage of the tubulence processor for the temperature measurement is expressed as,

$$V_{out} = G_F \, G_{TP} \, T \qquad (8.22)$$

G_F is the gain of the DC differential amplifier and filter, and T the thermoelectric voltage of the thermocouple in voltage units. The conversion table between the output voltage reading of the digital voltmeter and the desired parameters is shown in Table 8.4. The change of the thermelectric voltage with respect to the temperature is almost linear within the experimental range (50°F to 100°F). Therefore, the following relation was used to convert the voltage to degrees: 0.025 mV = 1°F.

Table 8.3   Conversion Constant, C_o

f_{max} \\ lens	103 mm	250 mm
15 KHz	0.087	0.0367
50 KHz	0.026	0.011

Table 8.4   Conversion Table of the Voltage Reading

Switch No.	Multiplication A B	Voltage Reading, V_{Read} $(=V_A \cdot V_B)$ [Volts^2]
1	v − v	$C_o^2 \dfrac{G_A G_B}{10} (\overline{v^2} + \overline{v'^2})$
2	C − v	$C_o \dfrac{G_A G_B}{10} \overline{Cv}$
3	v' − T'	$10\, C_o G_A G_B \overline{v'T'}$
4	C − T	$10\, G_A G_B \overline{CT}$
5	T' − T'	$10^3 G_A G_B \overline{T'^2}$

8.5 Experimental Conditions

The experimental conditions have been established to simulate the operating conditions of the available rod bundle temperature data (M-2, N-2) and cover the range in which the thermal plume phenomenon was expected to be observed. This range was between the flow redistribution and the natural turbulent flow dominant zones. The triangular-array with P/D = 1.245 was chosen to simulate a fuel type LMFBR assembly.

The following flow and power conditions were originally planned:

Flow rate : $200 \leq Re \leq 3000$

Power level : $0 \leq Gr_{\Delta T} \leq 1500$ or $0 \leq Gr_{\Delta T}/Re \leq 7.5$

Power skew : Various power skew conditions

Flow condition : Steady state, fully developed turbulent flow

However, the poor Doppler signal made the high power experiments impossible because of the spatial and temporal fluid density variation along the laser beam path. In high power cases, large temperature fluctuations due to the thermal plumes led to fluid density variations, and in turn, variations of the refractive index of water. These refractive index changes distorted the laser beams, which resulted in two effects : no focal point, i.e., no Doppler signal and uncertainty of the measuring volume position. In order to reduce these two effects, a laser beam guide tube was placed close to the measuring point to shorten the laser beam path in water. In addition, to reduce the no focal point effect a front lens with a longer focal length (f = 250 mm) was employed to increase the size of the measuring volume. Table 8.1 shows that the size of the measuring volume obtained by the front lens of f = 250 mm is around 20 times larger

than that obtained by the front lens of f = 103 mm. Then the focal point could be formed although the beam paths were slightly shifted. In spite of these efforts, all the proposed ranges could not be covered.

To check symmetry of the test section, reverse power skew condition was also tested. According to our measurements of temperature profile within subchannels, the symmetry requirement was not satisfied. The reason was not clear, but it might come from the non-uniform heat flux or incorrect alignment of the heater rods.

Fully developed turbulent flow conditions were chosen because inclusion of the developing effect of the turbulent boundary layer together with the transition from laminar to turbulent would have required much more data since the entrance length must be adjusted and the transition mechanism must also be clarified.

The operating conditions actually performed are summarized as,

Flow rate : $200 \leq Re \leq 900$

Power level : $0 < Gr_{\Delta T} \leq 450$ or $0 < Gr_{\Delta T}/Re \leq 1.8$.

Detailed operating conditions are presented in Appendix H.

8.6 Results

Prior to the measurements, the sign of the velocity was established by the following two observations. When the laser beams were focused on a solid surface and the solid was moved in either direction, the tracker output reading became positive or negative depending on the direction of movement. A second observation was that the direction of the fringe movement, which was opposite to that of the fluid velocity, was indicated in the Bragg cell. For presentation purposes, the coordinate system was taken as shown in Figure 8.2,

where the positive direction of the transverse velocity component was taken from the high to the low power side. Although this sign convention was opposite to the sign of the tracker output reading, this convention yielded easier interpretation of the experimental data.

The errors associated with the velocity and temperature measurements were estimated based on the error analysis methods of other investigators (S-8, C-5). The main sources of error and the estimated values were identified as follows:

(a) Error due to flow rate variation : about 3%

(b) LDA electronics error : about 3%

(c) Error due to finite integration time of the turbulence processor: about 5% (about 10% for $\overline{v'T'}$)

(d) Error in geometric arrangement of heated rods : about 10%

(e) Thermocouple error : about 3% (or $\pm$ 1.5°F) based on reference temperature of 32°F (for $\overline{T}$) and about 20% for T'

Utilizing the above error components the errors of the average and fluctuation of the velcocity, i.e., $\overline{v}$ and $\overline{(v'^2)}^{1/2}$, were estimated as 12% $(\sqrt{(3)^2 + (3)^2 + (5)^2 + (10)^2})$. The errors of the average and fluctuation of the temperature were 3% and 21% $(\sqrt{(5)^2 + (20)^2})$, repectively. The error of the turbulent heat flux measurements was estimated as 25% $(\sqrt{(3)^2 + (3)^2 + (10)^2 + (10)^2 + (20)^2})$.

The database obtained is summarized in Appendix H. Run 1 through Run 20 were executed utilizing the front lens of f = 103 mm while Run 21 through Run 45 were executed using the front lens of f = 250 mm. The velocities and turbulent heat fluxes measured in Runs 1 to 20 were not used in this analysis because the Doppler signals were not

monitored correctly and thus an error larger than that estimated above might be involved.

(1) Turbulent Heat Flux ($\overline{v'T'}$) at the Center of the Gap

Figure 8.15 shows the turbulent heat flux, $\overline{v'T'}$ (actually turbulent heat flux is defined as $\rho C_p \overline{v'T'}$), measured at the gap center for various Re and $Gr_{\Delta T}$ conditions. For the case of Re = 240, the turbulent heat flux monotonically increases when $Gr_{\Delta T}/Re$ increases. This result is coincident with our expectation that turbulent thermal plumes transfer energy from the high to the low power side and the energy mixing increases as $Gr_{\Delta T}/Re$ increases. For other flow rate cases, the turbulent heat flux increases in the range of small $Gr_{\Delta T}/Re$ values and then decreases. Further, as $Gr_{\Delta T}/Re$ continues to increase, the turbulent heat flux decreases to zero and then changes sign (from positive to negative). The negative heat flux means that turbulent thermal plumes transfer heat from low to high power side, i.e., against the power skew. This is an unexpected result. The physical reason for this result is not yet clear.

The existence of this kind of counterflux was observed experimentally and predicted by several investigators (L-4, D-4). LaRue and Libby (L-4) measured the counterflux of helium in the turbulent boundary layer with slot injection of helium. Negative values of $\overline{c'T'}$, where c was the helium concentration, were observed in the region of high density turbulence. They presumed that dynamic coupling between the velocity and scalar fields might be involved, but no satisfactory explanation was available. Deissler (D-4) presented
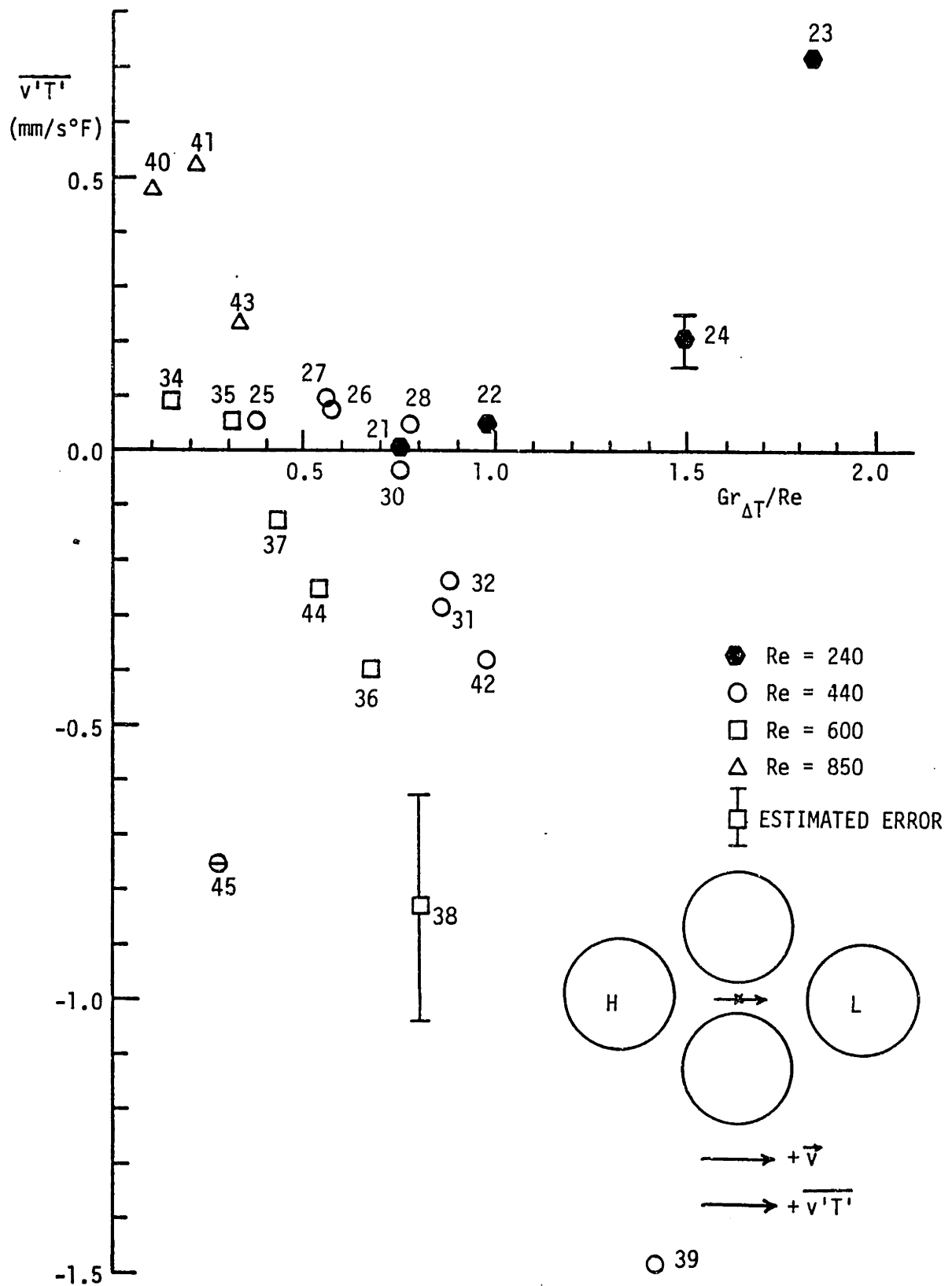
Figure 8.15 Turbulent Heat Flux Measured at the Gap Center

an analytical prediction of the covariance of the axial velocity and temperature, $\overline{w'T'}$, in the flow field where the gravity force and axial temperature gradient exist. He showed that the turbulence could transfer heat against a temperature gradient even when a large temperature gradient existed, and postulated that it was caused by the action of the buoyancy force on turbulent eddies. It was also mentioned that a pressure gradient could cause heat to transfer against a temperature gradient. For our experimental case, the counterflux may be caused by the pressure difference, density variation or simply the reverse temperature gradients at the gap relative to the power skew direction to be presented in the next section. These possibilities are further examined in Section 8.7.

The estimated error ranges are indicated for several data points. The limiting condition which could be achieved using our existing apparatus due to deterioration of the Doppler signals was at the highest $Gr_{\Delta T}/Re$ for each Re range. The criterion for signal deterioration was established as the condition when the Doppler signal observed by an oscilloscope stayed at the zero value for an appreciable amount of time.

(2) Temperature Profile

As seen in Eq. (8.13), subchannel average temperatures must be measured to evaluate the thermal plume mixing parameter. If the temperature and axial velocity distributions within subchannels were measured, the subchannel average temperatures could be calculated correctly. However, the axial velocity distribution throughout the subchannels could not be measured with our existing apparatus. Instead, the temperatures of six points selected within a subchannel

were measured and an arithmetic mean was used for the estimation of the subchannel average temperature. The locations of the measuring points (denoted as "x") are indicated in Figure 8.16.

The temperature profiles along the symmetry line (normal to the gap distance) are shown in Figures 8.17, 8.18, 8.19 and 8.20 for different flow conditions, i.e., Re = 240, 440, 600 and 850 respectively. The power skew of each run is also presented in the figures. It should be noted that the temperatures at two points located at both sides of the symmetry line were also measured to evaluate the subchannel average temperature although they are not shown in the figures. For the case of Re = 240, the temperatures near the gap at the high power side are higher than those at the low power side. However, for other cases, although the subchannel average temperatures at the high power side are higher than those at the low power side, the temperatures near the gap at the high power side are generally lower than those at the low power side.

Table 8.5 compares the sign of the measured $\overline{v'T'}$ and the direction of the local temperature gradient. Two features of these data are

(a) Heat transfer is expected in the direction of the power skew. Consequently the sign of $\overline{v'T'}$ should be positive. However many runs exhibit negative values of $\overline{v'T'}$ indicative of heat transfer from the cooler to the hotter subchannel.

(b) For all runs the measured local temperature gradient and the measured $\overline{v'T'}$ do not indicate consistent directions of heat transfer. In some runs while $\overline{v'T'}$ is positive, the local
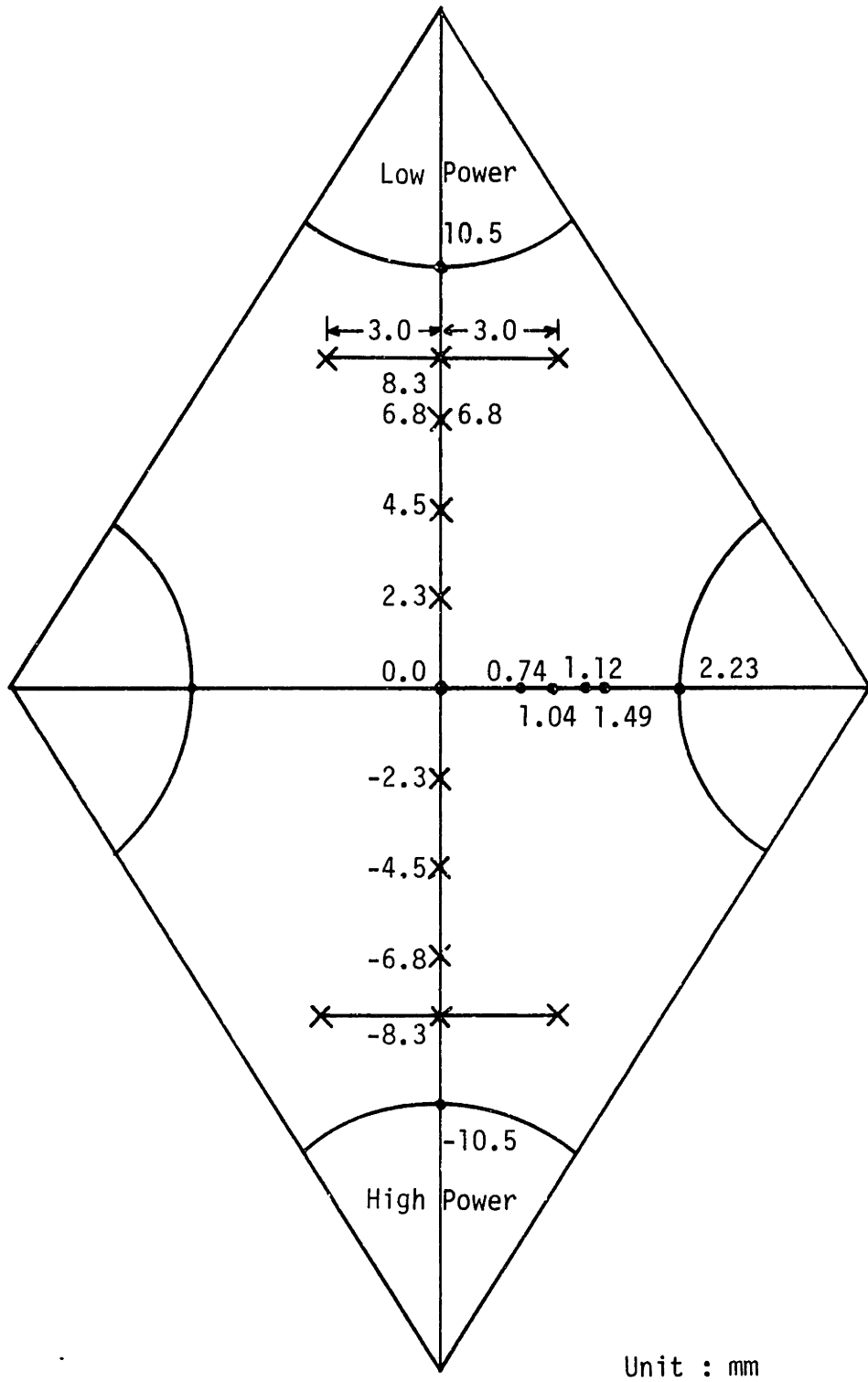
Figure 8.16   Locations of Temperature Measuring Points
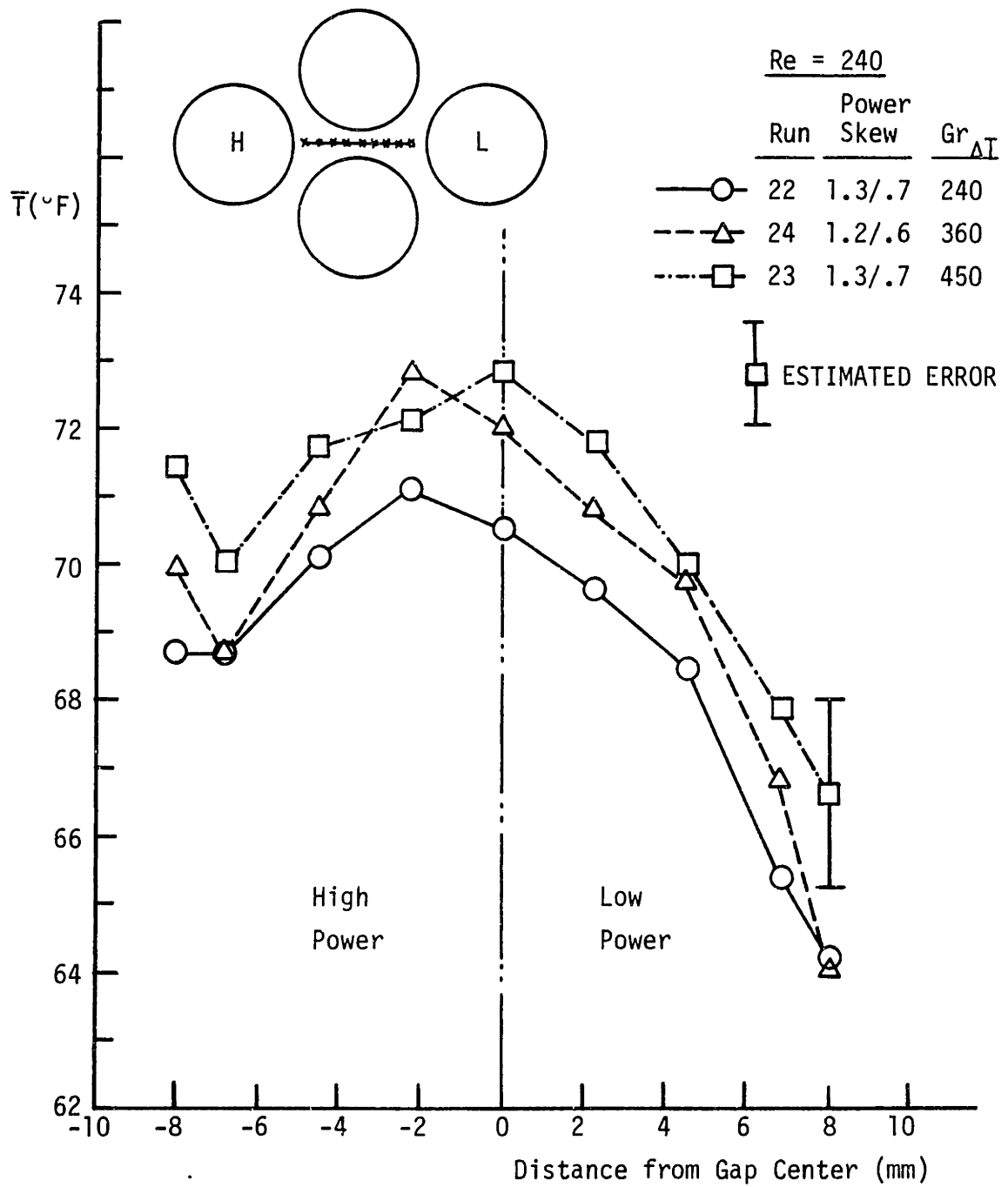
Figure 8.17   Temperature Profile Measured Along the Symmetry Line
(Re = 240)
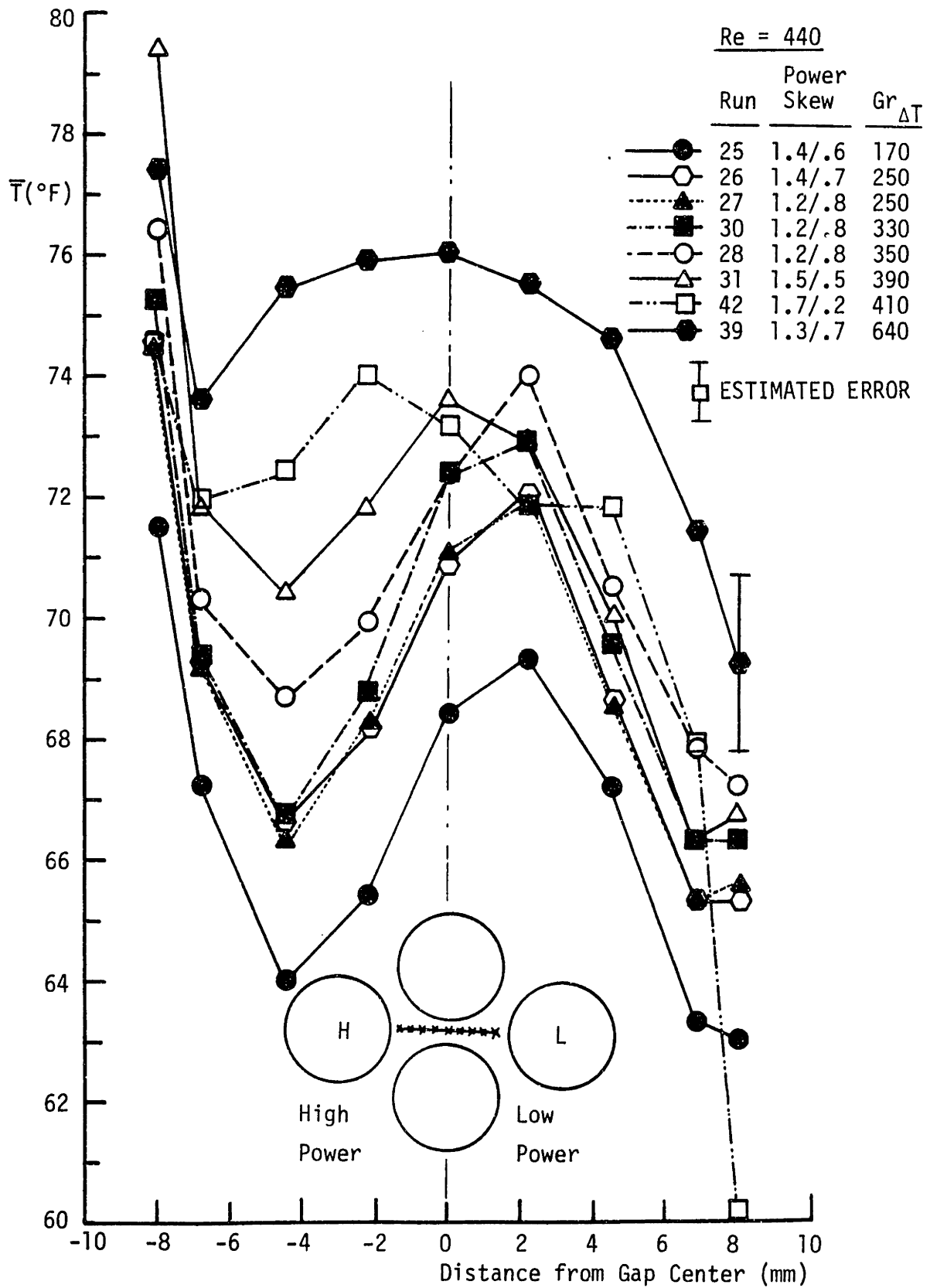
Figure 8.18 Temperature Profile Measured Along the Symmetry Line
(Re = 440)
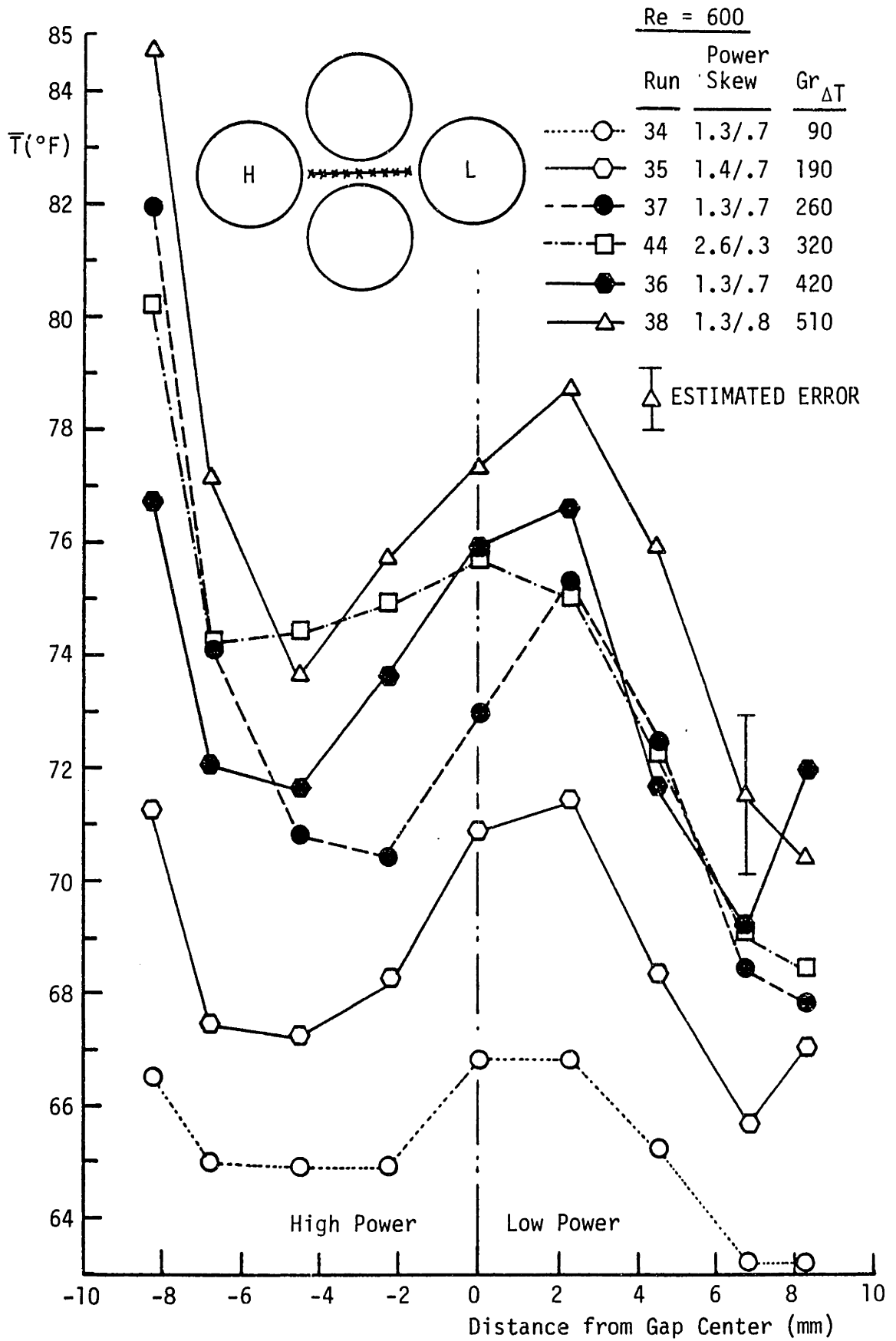
Figure 8.19 Temperature Profile Measured Along the Symmetry Line (Re =600)
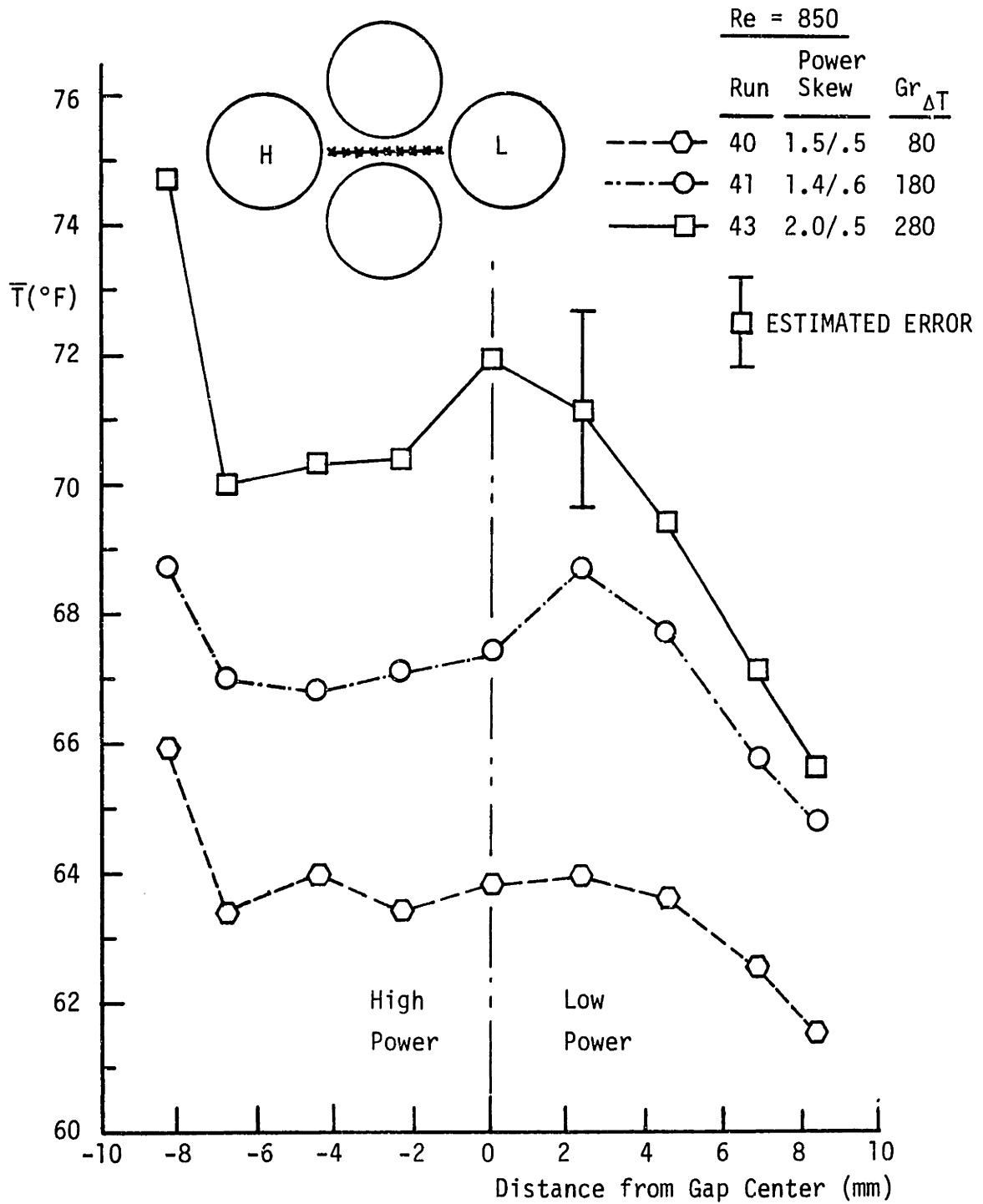
Figure 8.20 Temperature Profile Measured Along the Symmetry Line
(Re = 850)

Table 8.5 Comparisons Between the Sign of $\overline{v'T'}$ and the Local

Temperature Gradient

Re	Run	sign of $\overline{v'T'}$	Local Temperature Gradient Relative to Power Skew Direction
240	22	+	same
	24	+	same
	23	+	zero gradient
	21	+	N/A
440	25	+	opposite
	26	+	opposite
	27	+	opposite
	28	+	opposite
	30	−	opposite
	31	−	opposite
	42	−	same
	39	−	zero gradient
	45	−	same
600	34	+	opposite
	35	+	opposite
	37	−	opposite
	44	−	opposite
	36	−	opposite
	38	−	opposite
850	40	+	zero gradient
	41	+	opposite
	43	+	opposite

Convention is that + $\overline{v'T'}$ is heat transfer in Power Skew Direction

temperature gradient is opposite to the power skew direction (i.e., cases 25, 26, 27, 28, 34, 35, 41 and 43). This asymmetry in results suggests that large scale eddies are responsible for the direction of heat transfer, not the local gap temperature gradient.

A special power skew was tested. Figure 8.21 shows the power skew and the temperature profile of Run 45. Two rods near the gap were not heated to eliminate the generation of an abnormal temperature gradient at the gap due to unsymmetric heater rod heat flux distribution. As shown in Figure 8.15, the sign of $\overline{v'T'}$ of Run 45 is still negative, although the temperature gradient at the gap is the same direction as the power skew.

(3) Turbulent Thermal Plume Mixing Parameter, ε^*_{TM}

The turbulent thermal plume mixing parameter ε^*_{TM} defined in Eq. (8.13) was estimated from the measured turbulent heat flux and subchannel average temperatures. The turbulent heat flux measured at the gap center was used assuming uniform distribution along the gap. The actual distribution for a sample case is presented in the following section. ε^*_{TM} is plotted as a function of $Gr_{\Delta T}/Re$ in Figure 8.22. The overall trend of ε^*_{TM} is similar to that of $\overline{v'T'}$. Due to the counterflux problem a reasonable correlation of ε^*_{TM} could not be formulated although this was our primary goal.

(4) Velocity and Temperature Fluctuations

$(\overline{v'^2})^{1/2}$ measured at various Re and $Gr_{\Delta T}$ conditions is shown in Figure 8.23. For the high flow rate range (Re $\geq$ 600), significant
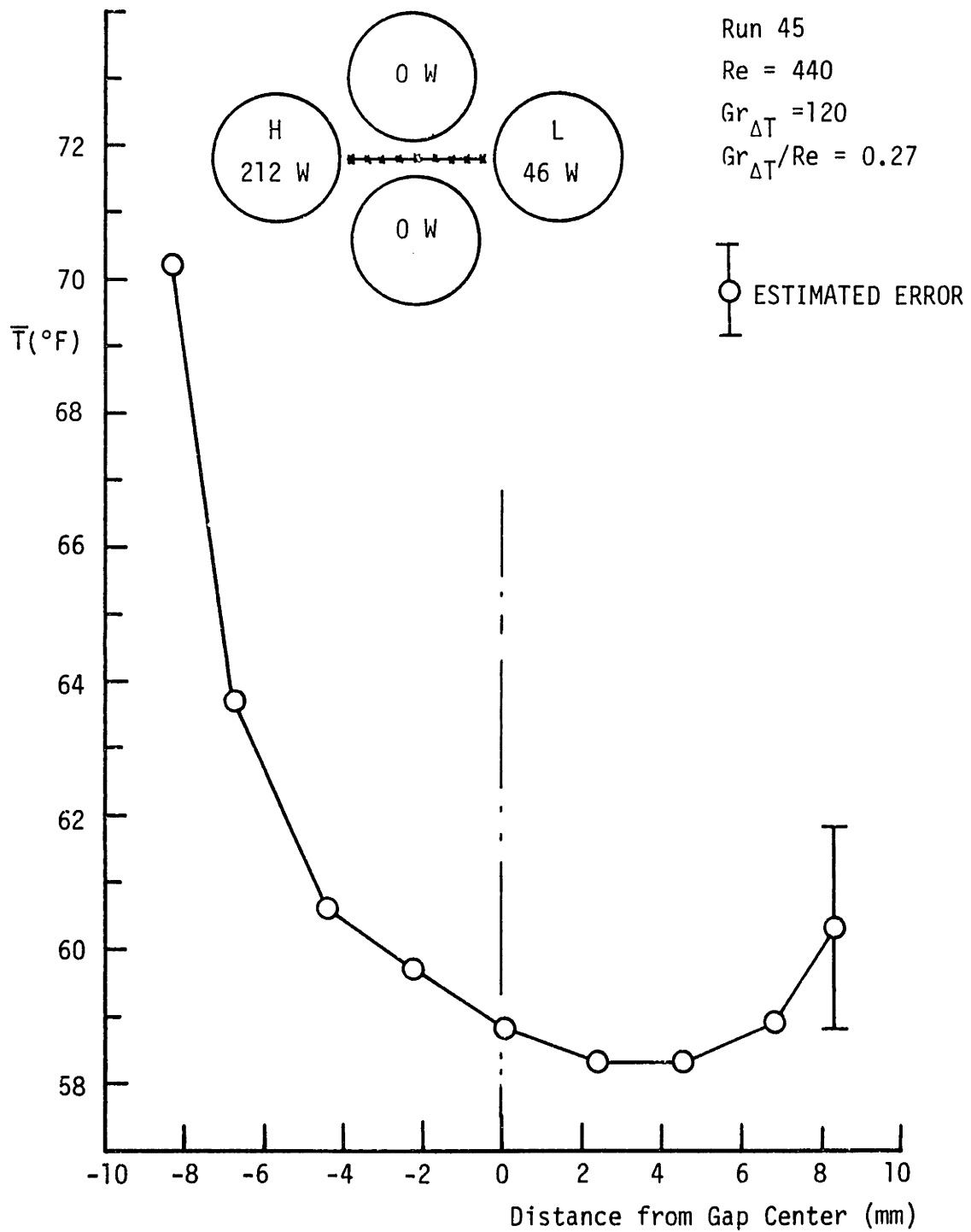
Figure 8.21   Temperature Profile Measured Along the Symmetry Line
for Run 45 (Re = 440)
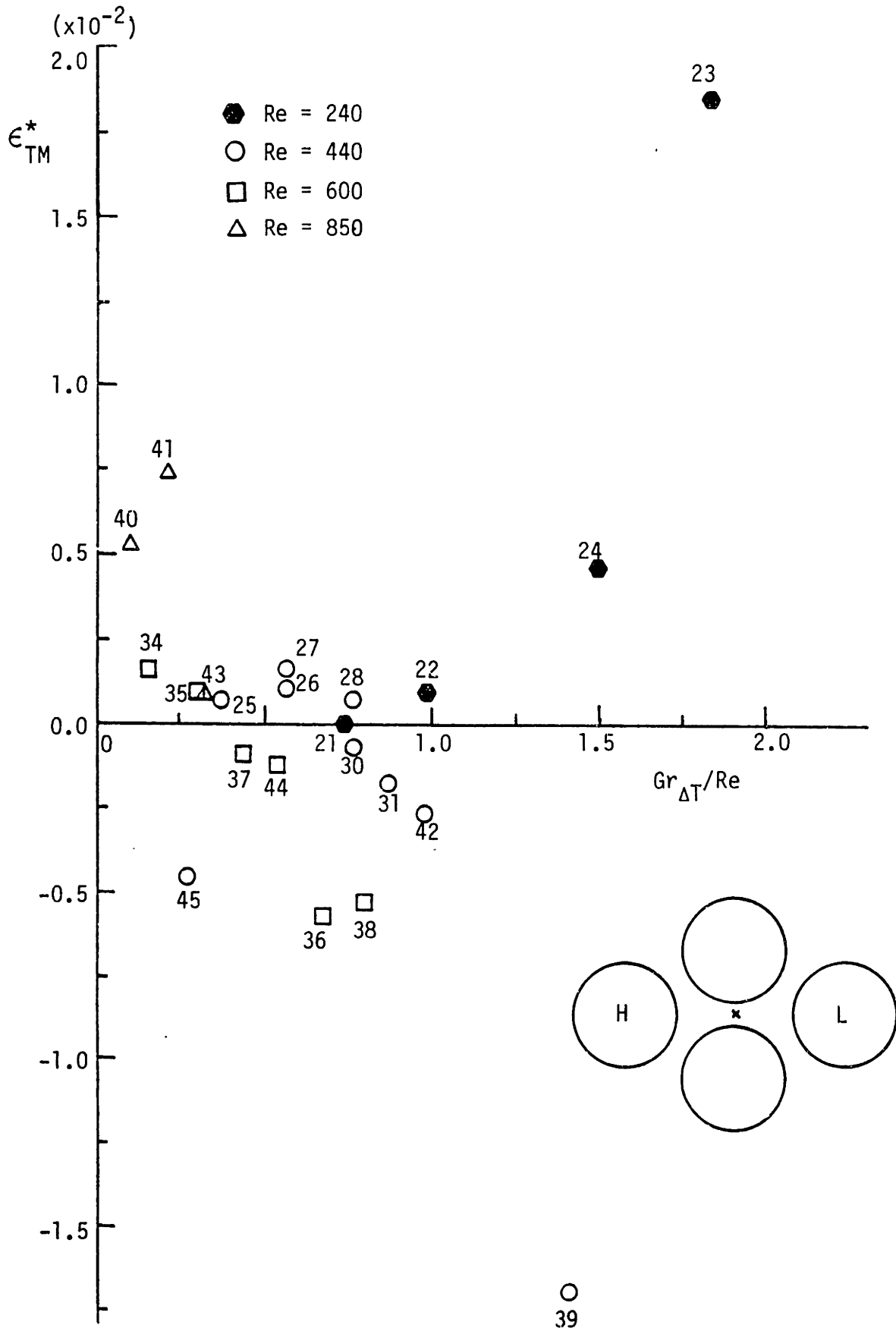
Figure 8.22 Turbulent Thermal Plume Mixing Parameters
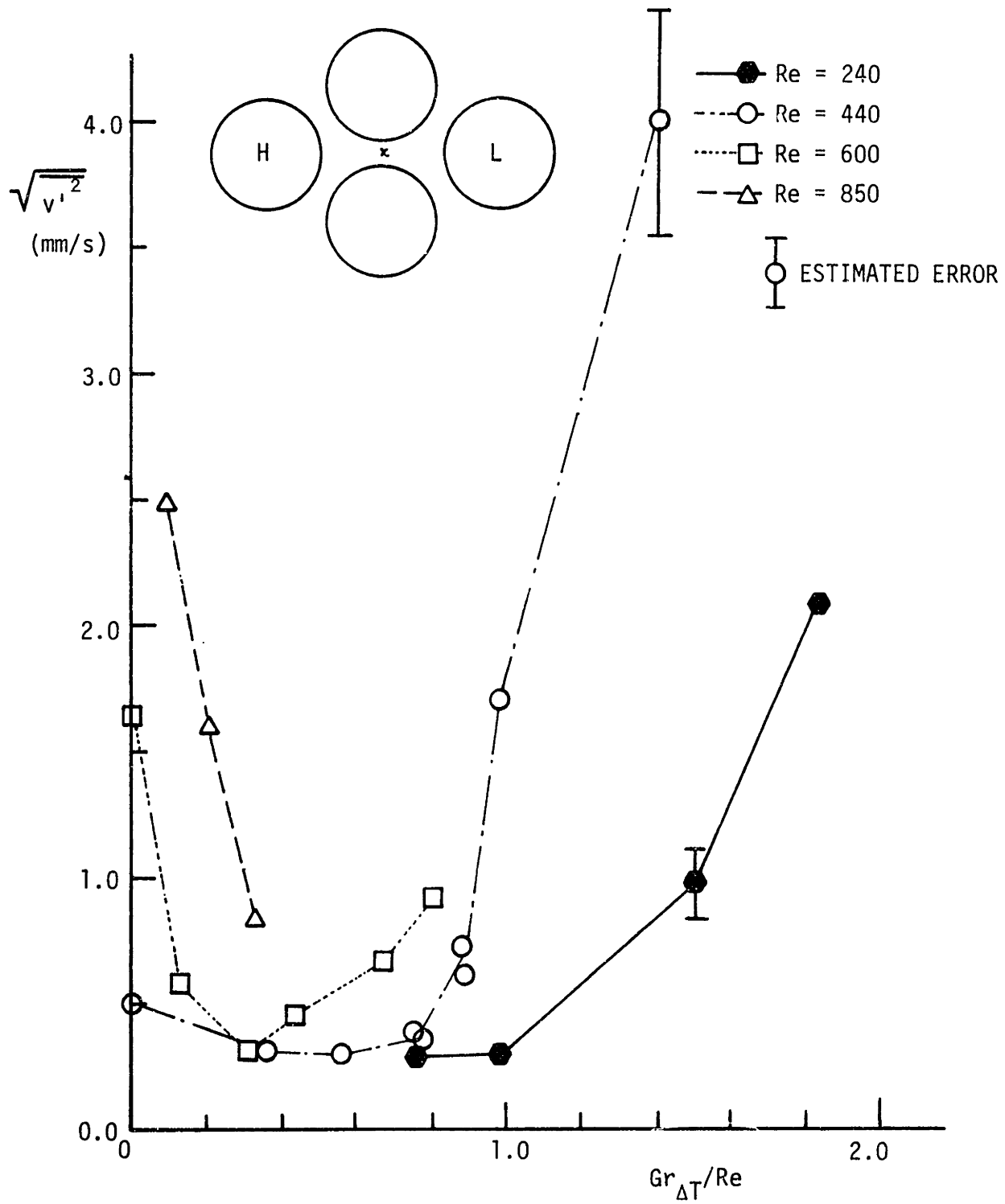
Figure 8.23   Velocity Fluctuations Measured at the Gap Center

fluctuations are observed even in the unheated condition. As $Gr_{\Delta T}$

increases, the fluctuations are reduced which appears to be a kind of

laminarization of the transverse velocity. The reason for this

behavior is not clear.

The r.m.s. values of temperature fluctuations, $(\overline{T'^2})^{1/2}$, are

shown in Figure 8.24. $(\overline{T'^2})^{1/2}$ increases quite linearly as

$Gr_{\Delta T}/Re$ increases. Further increase of the $Gr_{\Delta T}/Re$ leads to

leveling off the $(\overline{T'^2})^{1/2}$. Figure 8.25 presents the curve of onset of

the temperature fluctuations and indicates the domain where the

temperature fluctuations were observed. This result provides the

minimum condition to be satisfied for the thermal plume mixing.

The figure also shows the onset of the thermal plume mixing as a

function of Re and $Gr_{\Delta T}$. The criterion for the onset of the

thermal plume mixing was established as the $\overline{v'T'}$ measured at the gap

center being greater than 0.05 mm/s·°F. It was also observed that the

onset of temperature fluctuations and thermal plumes did not

significantly depend on the power skew.

(5) Correlation Coefficient, R

The correlation coefficient, R, is defined as

$$R = \frac{\overline{v'T'}}{(\overline{v'^2})^{1/2}(\overline{T'^2})^{1/2}} \quad \text{where} \quad 0 \le |R| \le 1$$

R is a measure of degree of the correlation between velocity

fluctuations and temperature fluctuations. The values of $|R|$ measured

at the gap center are plotted in Figure 8.26. The results of $|R|$

ranging from 0.1 to 0.5 are quite reasonable compared with other
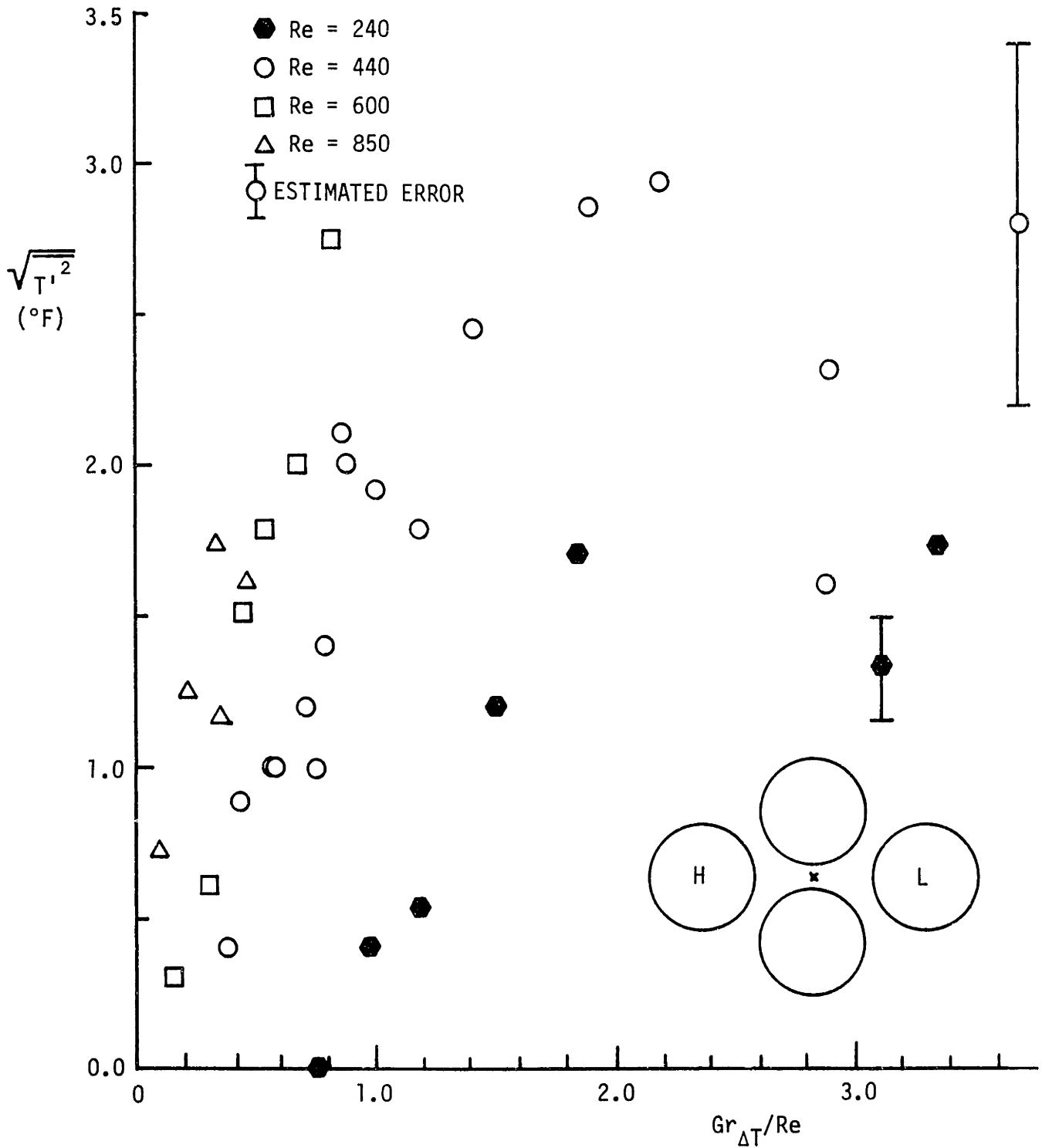
Figure 8.24   Temperature Fluctuations Measured at the Gap Center
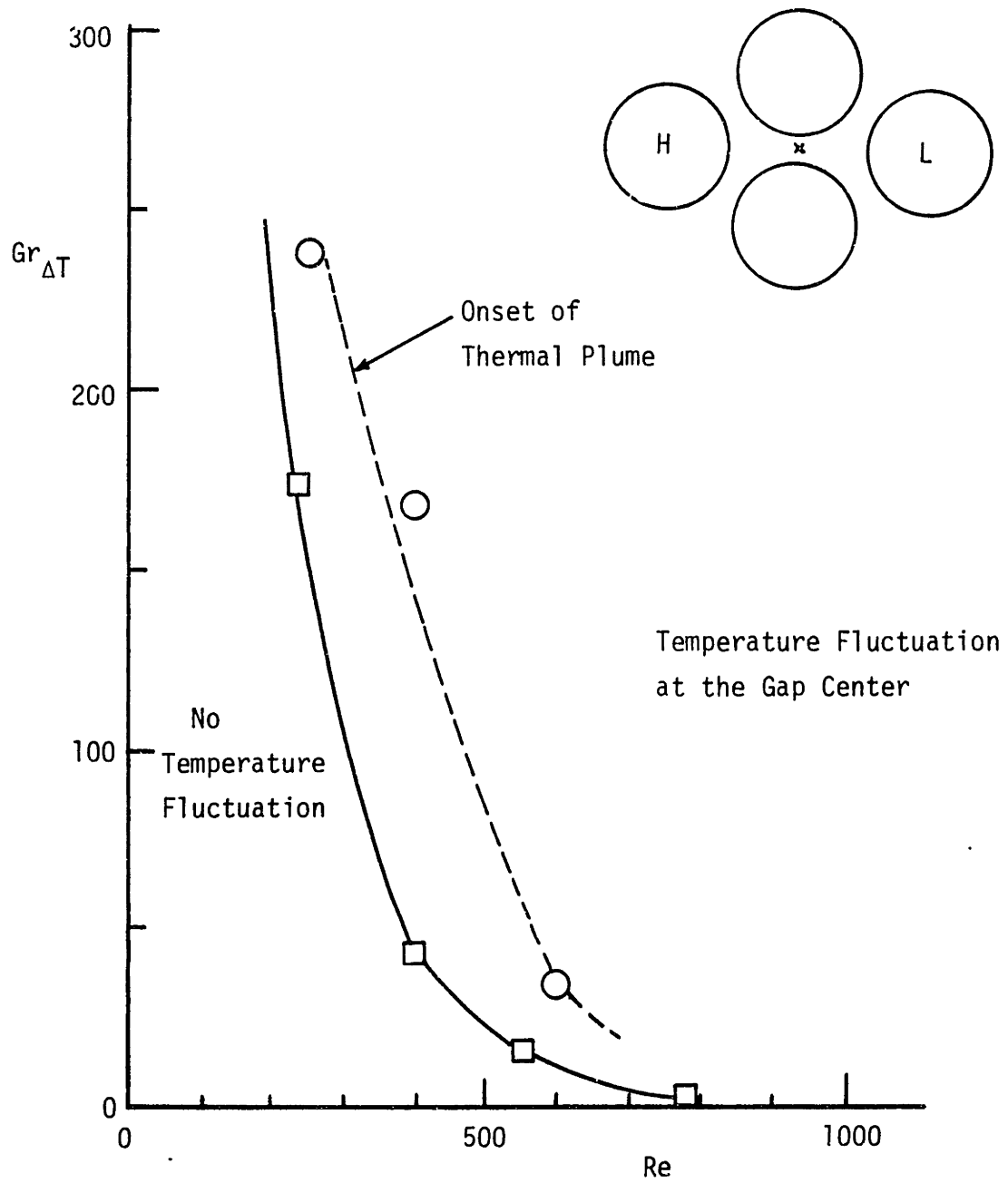
Figure 8.25 Onset of the Temperature Fluctuation and Thermal Plume
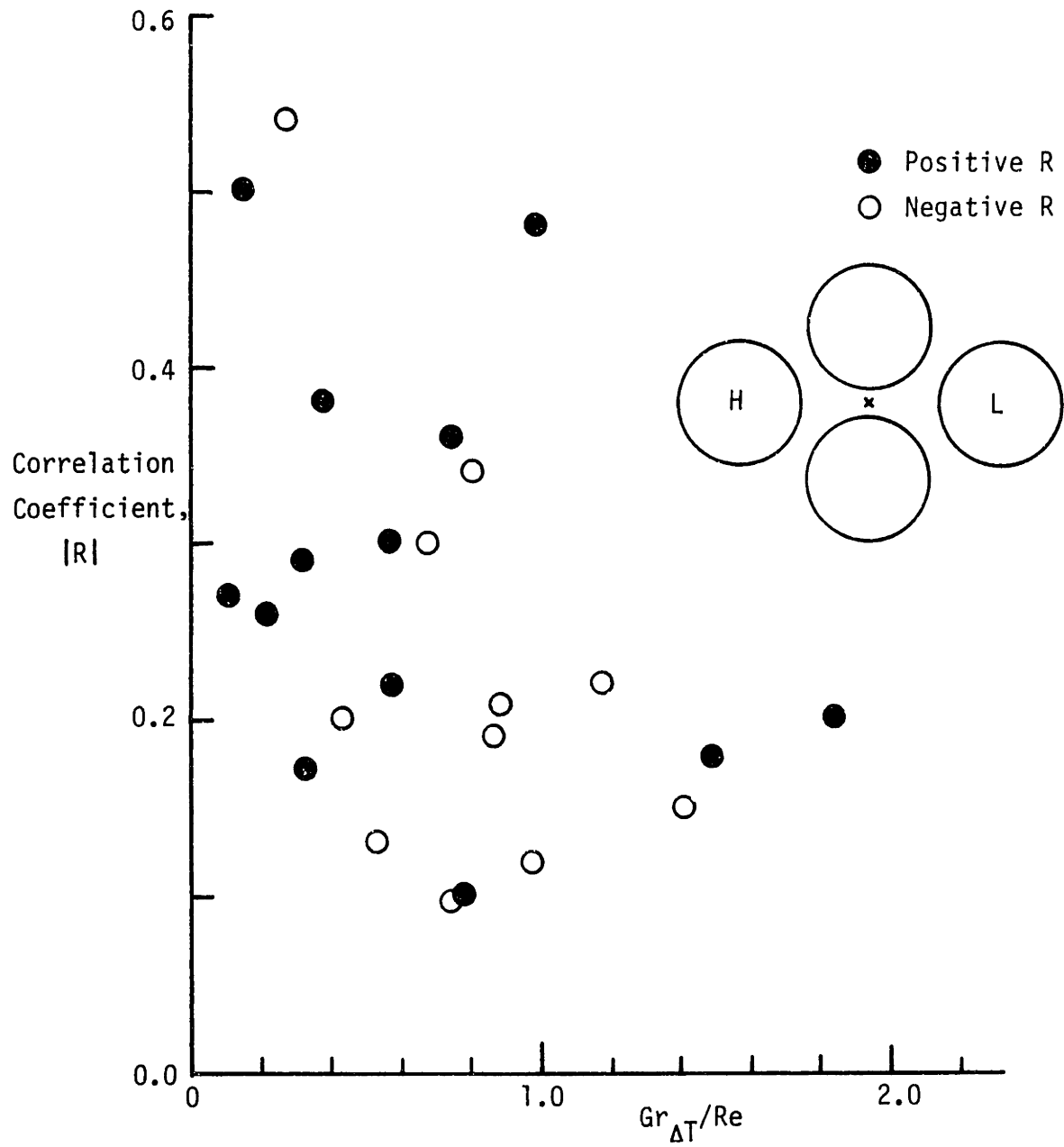
Figure 8.26 Correlation Coefficient Obtained at the Gap Center

experimental data (L-5, B-5).

(6) The Parameters, $\overline{v'T'}$, $\bar{v}$, $\bar{T}$, $(\overline{v'^2})^{1/2}$ and $(\overline{T'^2})^{1/2}$, Measured Near

Gap Region

Run 44 (Re = 610, $Gr_{\Delta T}$ = 320, power skew = 2.69/0.34) was

performed to examine the parameters in detail. Figure 8.27 shows

$(\overline{T'^2})^{1/2}$ together with $\bar{T}$ along the symmetry line. The temperature

fluctuations at the high power side are generally larger than that at

the low power side. It is also observed in Figure 8.27 that large

fluctuations exist near the centers of the subchannel while small

fluctuations exist near the gap. $\overline{v'T'}$, $\bar{v}$, $\bar{T}$, $(\overline{v'^2})^{1/2}$ and $(\overline{T'^2})^{1/2}$

measured at three points near the gap along the symmetry line are

presented in Figure 8.28. These parameters were also measured along

the gap as shown in Figure 8.29. The distribution of $\overline{v'T'}$ indicates

that $\overline{v'T'}$ has a large negative value near the gap center and gradually

approaches zero from the middle position between gap center and rod

wall. The parameters $\bar{v}$ and $(\overline{v'^2})^{1/2}$ near the gap center are larger

than those near the wall. The parameters close to the wall could not

be measured since the beam path was blocked by the rod. The same

measurements were also carried out for Run 22 (Re = 240, $Gr_{\Delta T}$ =

240, power skew = 1.33/0.65). As shown in Figure 8.30, $\overline{v'T'}$ is always

positive along the gap and the maximum value is obtained at the gap

center. The above two runs show the similar distributions of the

parameters studied except the sign of $\overline{v'T'}$ is different.
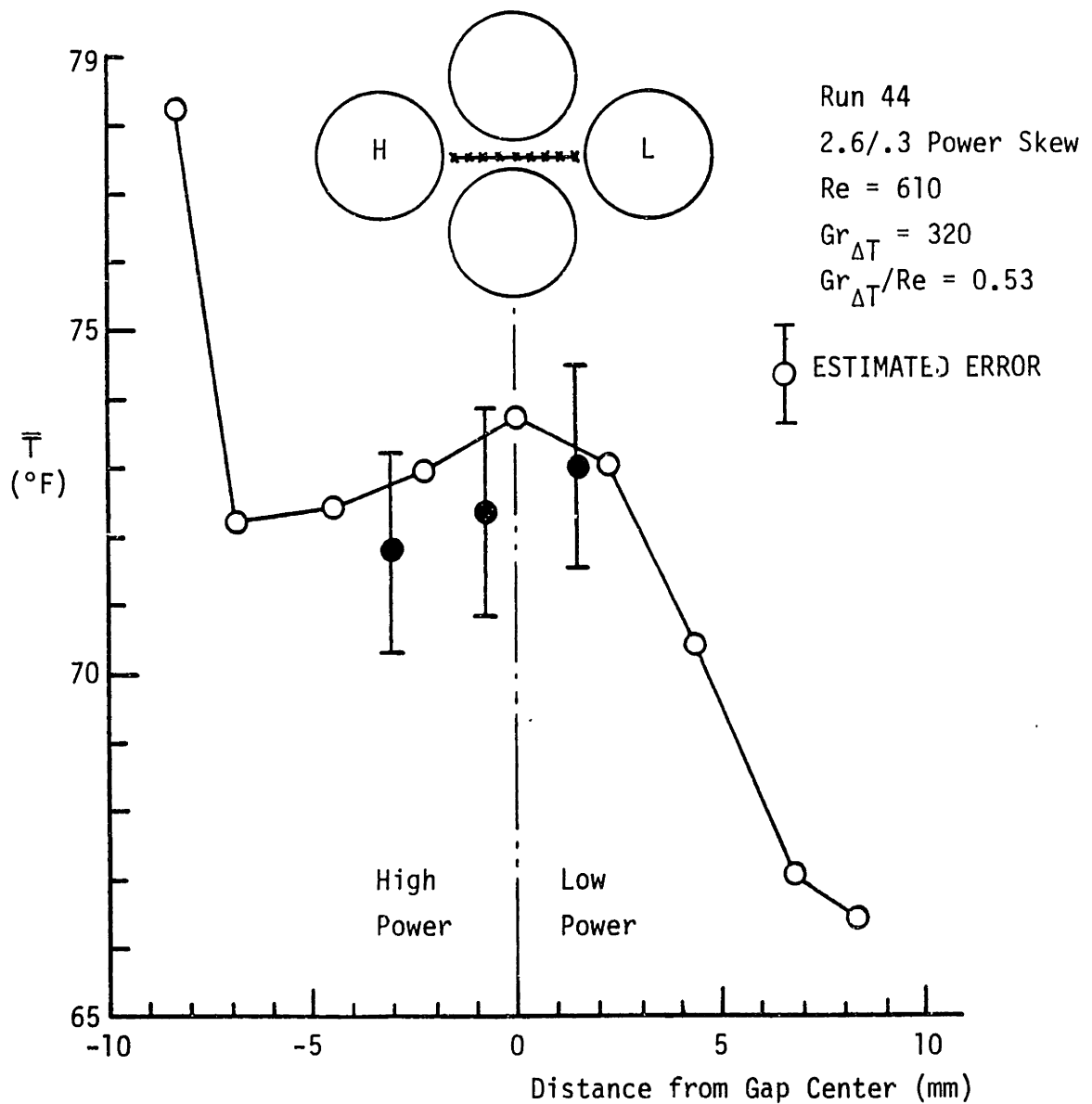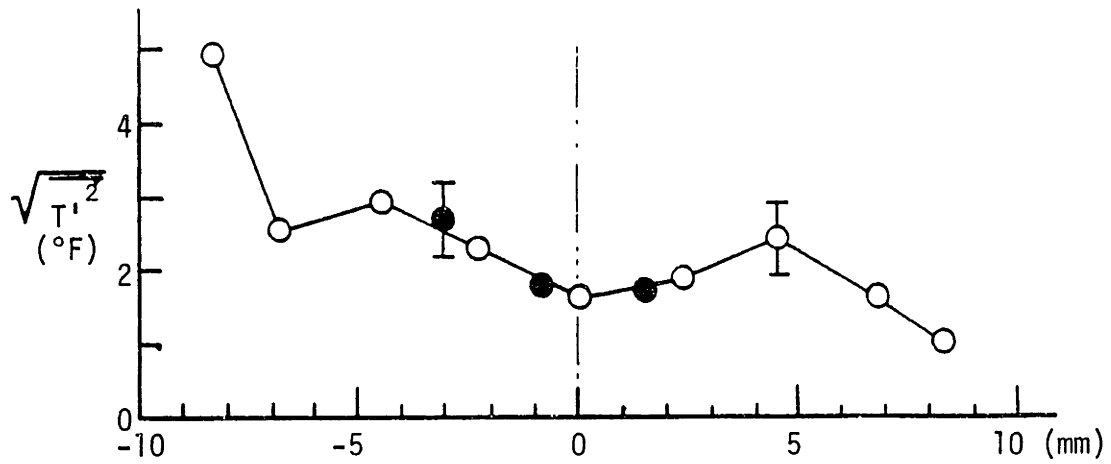
Figure 8.27 Temperature Profile and Fluctuations Measured Along the Symmetry Line for Run 44

Run 44

2.6/.3 Power Skew

Re = 610

$Gr_{\Delta T}$ = 320

$Gr_{\Delta T}/Re$ = 0.53

⊖ ESTIMATED ERROR
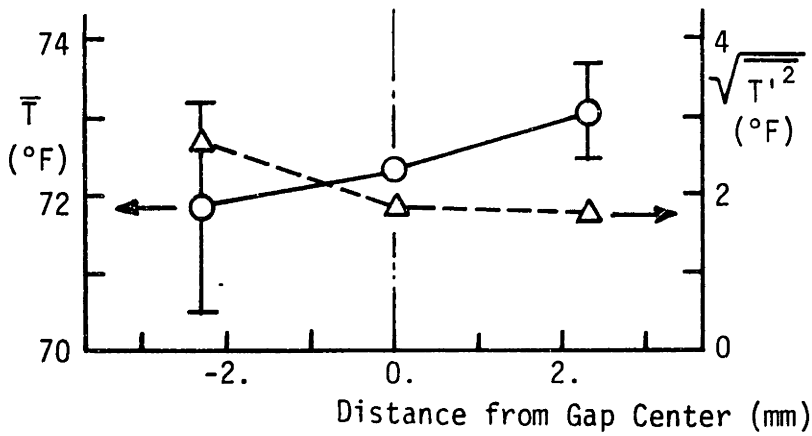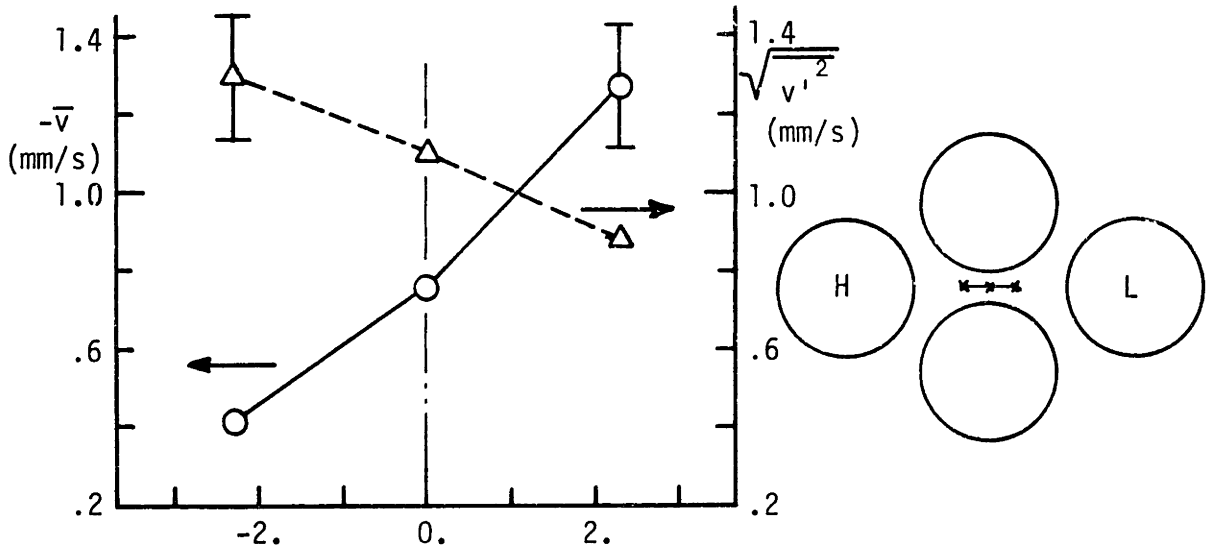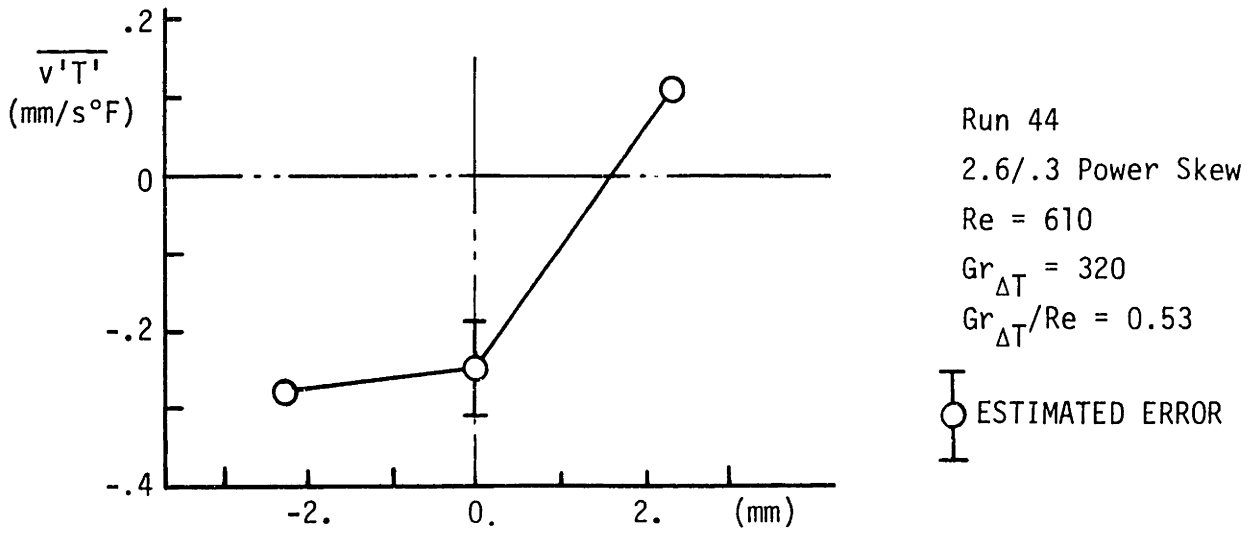
Figure 8.28   Parameters Measured Along the Symmetry Line near
Gap Region for Run 44
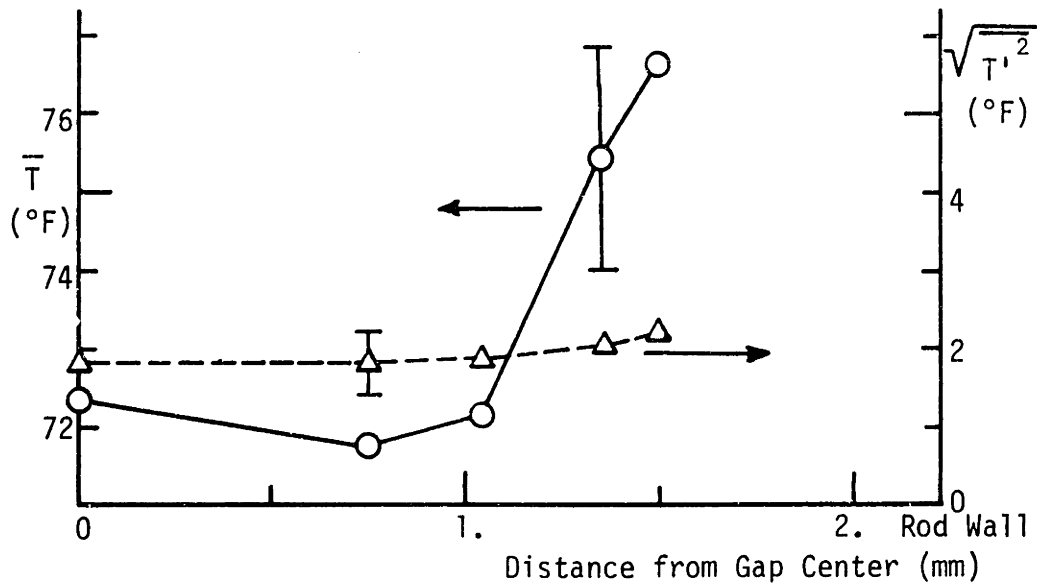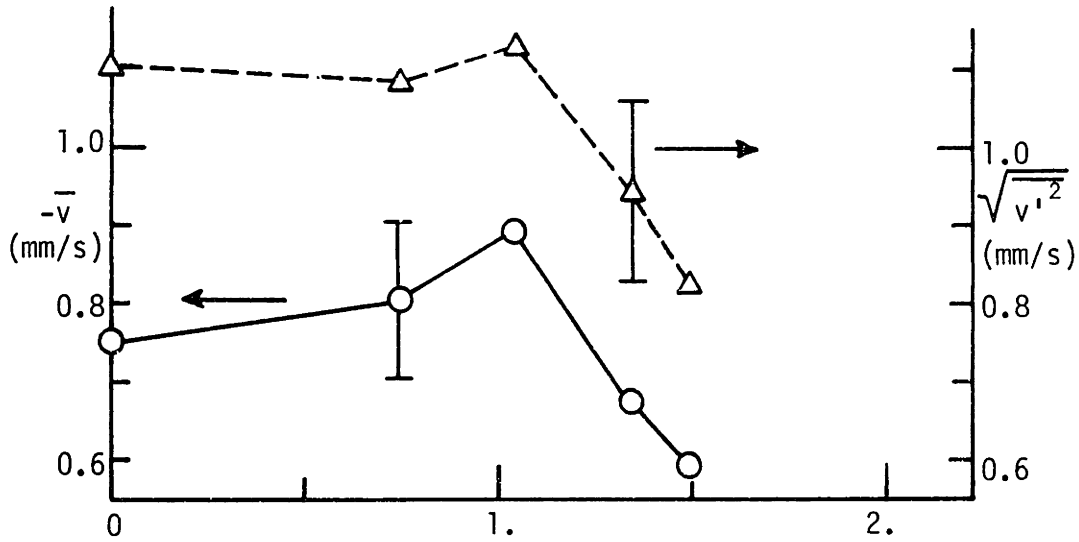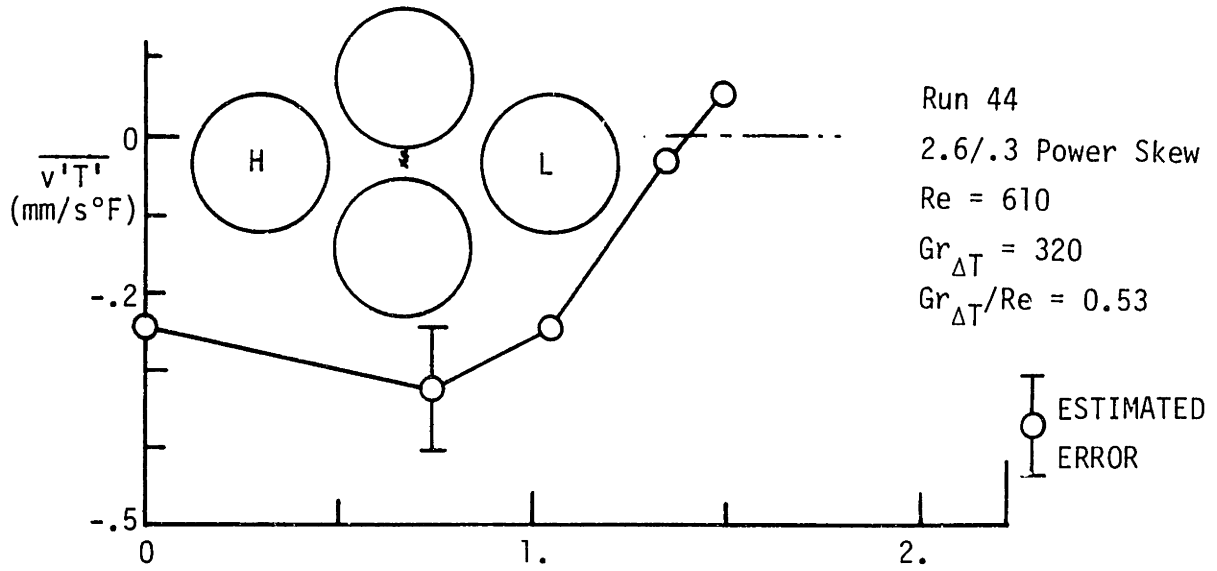
Figure 8.29   Parameters Measured Along the Gap for Run 44
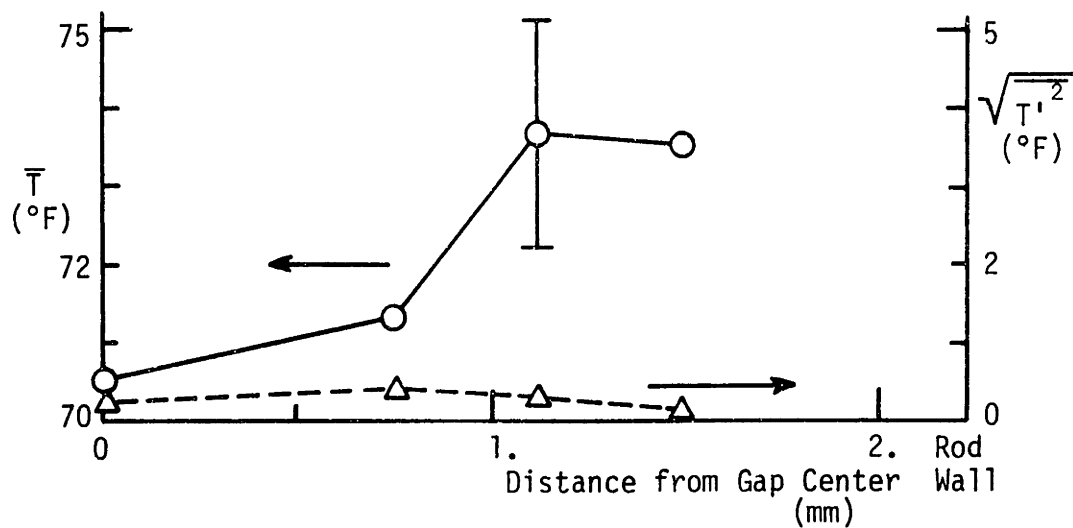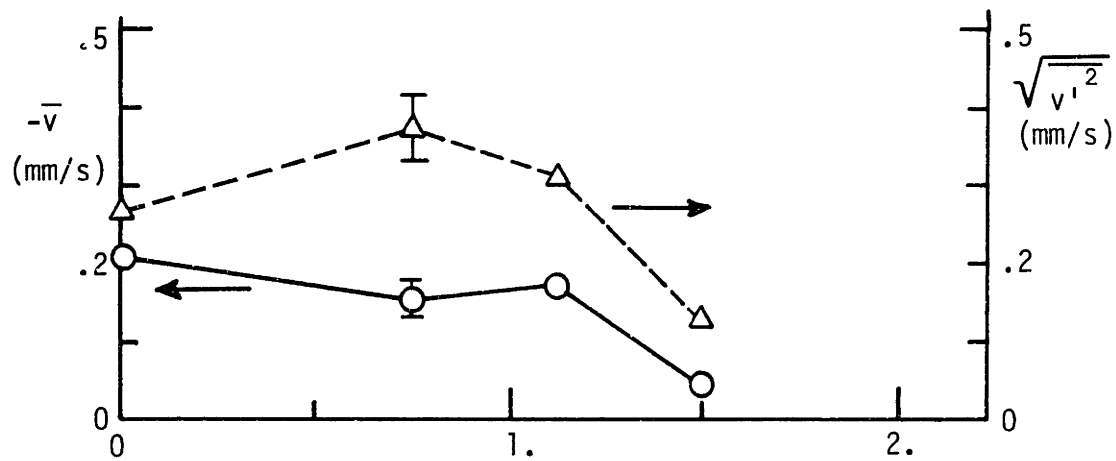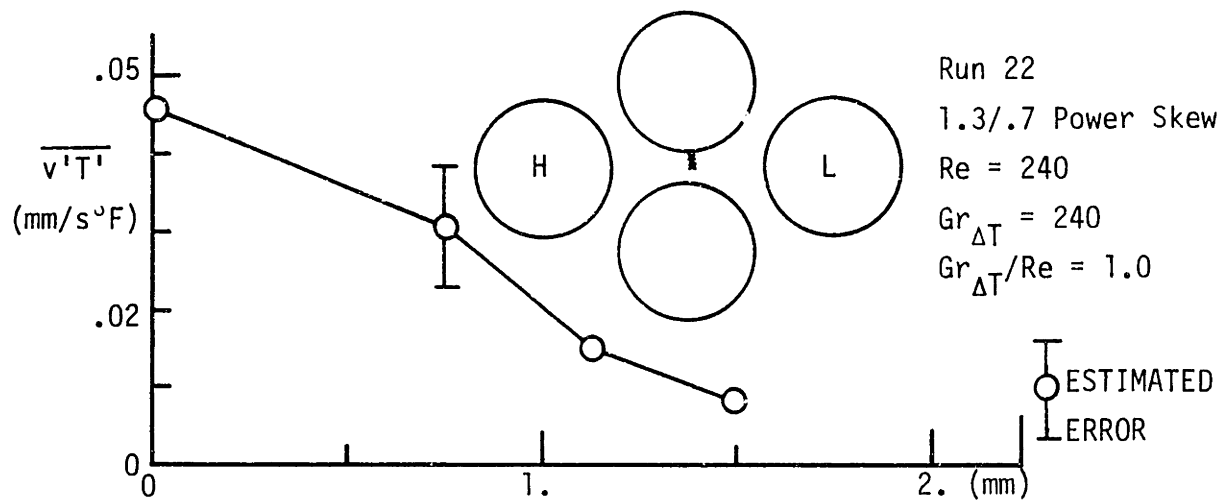
Figure 8.30 Parameters Measured Along the Gap for Run 22

8.7 Discussion

(1) Negative Turbulent Heat Flux

As mentioned before, several possible causes of the counterflux observed for cases of Re $\geq$ 440 can be identified. First, the pressure difference between two subchannels may vary with time due to the instability of laminar flow. The variation of the pressure difference will affect the motion of turbulent eddies. If the pressure force acts in the direction opposite to that in which an eddy begins to move, the sign of the velocity fluctuation might be changed without necessarily changing the sign of the corresponding temperature fluctuation. Next the heat flux may directly follow the temperature gradient. For the counterflux case, this means that the temperature gradient is opposite to the power skew direction. As discussed in Section 8.6(2), this is not always true, such as the cases when the turbulent heat flux is positive while the temperature gradient is opposite. However, if the size of the thermal plume, i.e., the scale of turbulent eddies depends on the heat input, (i.e., $Gr_{\Delta T}$) and decreases as $Gr_{\Delta T}$ increases, the turbulent heat flux can change sign from positive to negative as $Gr_{\Delta T}$ increases. This logic however cannot explain the result of Runs 42 and 45 (negative heat flux but the direction of the temperature gradient is the same as that of power skew).

Another possibility can be drawn from the spiral structure of the thermal plume. The spiral nature of a starting plume which is the region of buoyant fluid resulting from the initiation of heating of an infinite fluid was observed by Tanny and Shlien (T-3) in their flow

visualization experiments. Assuming that the structure of turbulent thermal plume is similar to that of the starting plume, a hypothesized structure of the thermal plume is schematically depicted in Figure 8.31. The arrows show the flow direction around the thermal plume. Above the plume the transverse velocity is directed toward the high power region due to flow redistribution effects, i.e., v is negative. Just before the thermal plume arrives at the measuring point, v' becomes positive but fluid temperature still maintains approximately the ambient temperature. When the thermal plume is passing the measuring point, the fluid temperature will increase but significant opposite flow by the swirl of thermal plume may lead to negative v'. Then overall $\overline{v'T'}$ may exhibit a negative value. This kind of thermal plume behavior was observed by examining the velocity and temperature signals through the oscilloscope. Figure 8.32 shows a schematic representation of the variation of the velocity and temperature fluctuations deduced from observation of a single heated rod. The large peaks of velocity and temperature seem to be due to thermal plumes. A sudden increase of the velocity precedes the peak, while the temperature does not change significantly. Then, a temperature peak is followed by a velocity peak which corresponds to the opposite flow region of the thermal plume. This results in large negative heat flux. However, since the counterflux of heat did not occur for all experimental conditions, this hypothesis may be limited to high Re and $Gr_{\Delta T}$ conditions.

308
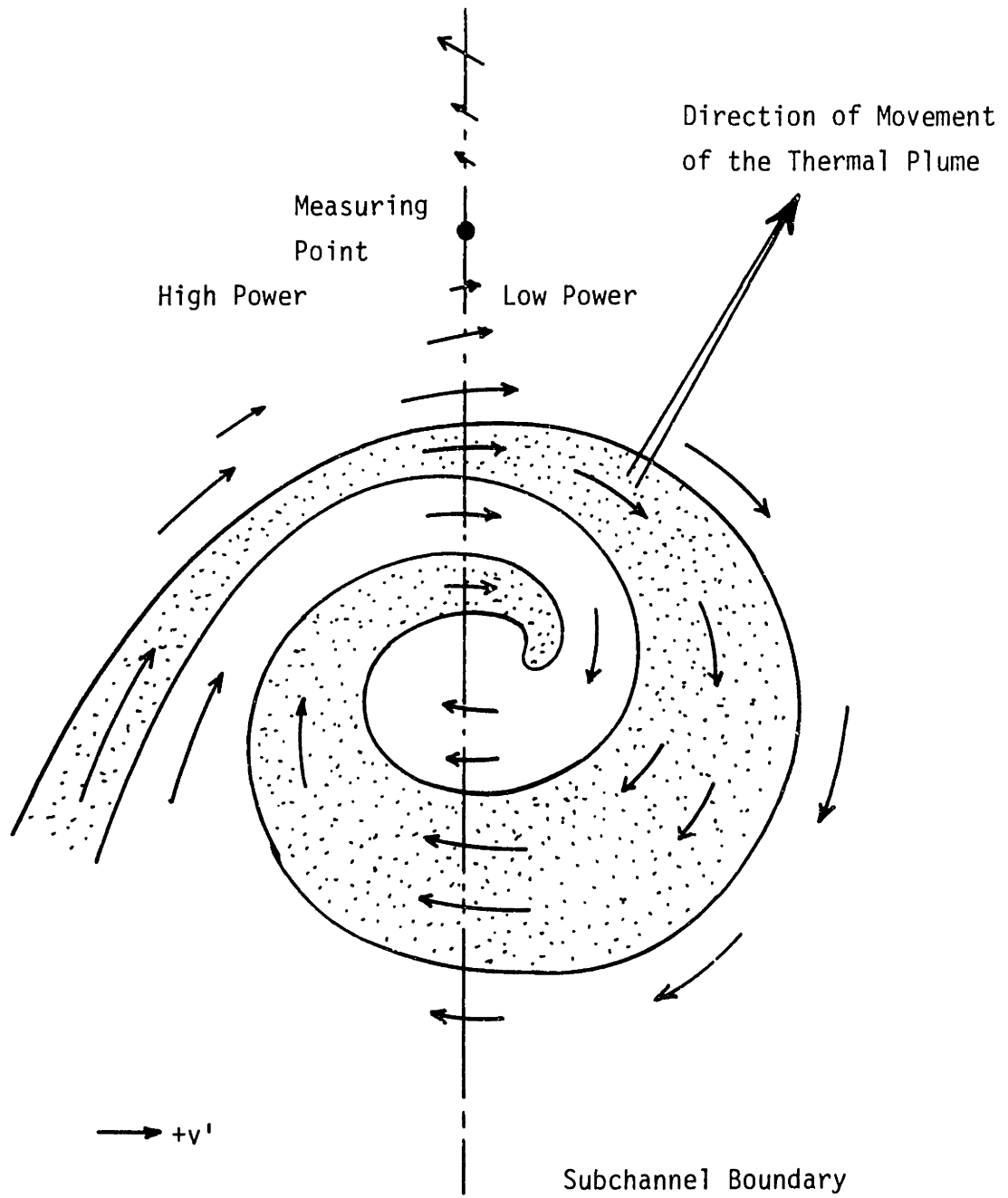
Figure 8.31   Thermal Plume Structure and Flow Pattern
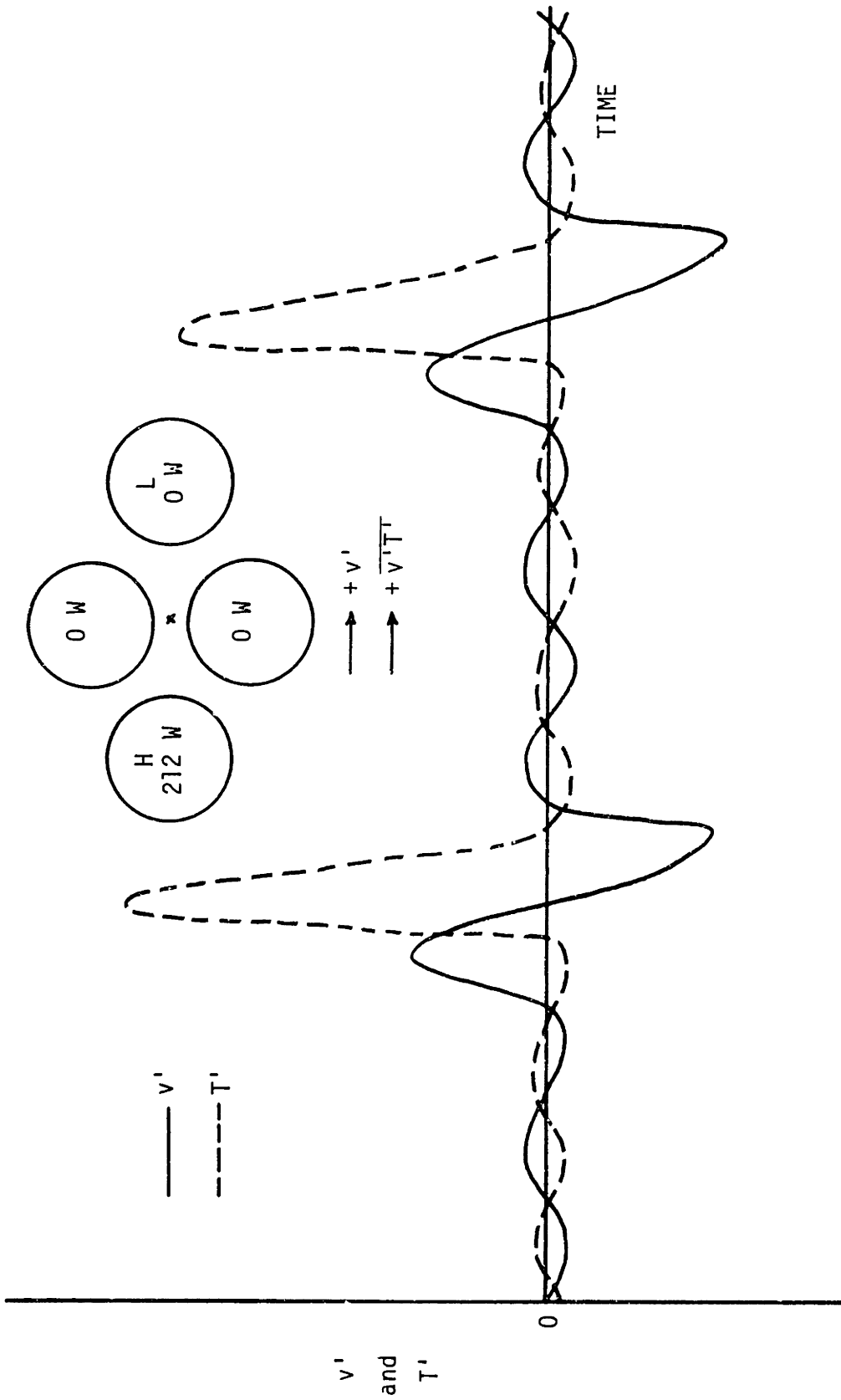
Figure 8.32 Schematic Drawing of Time-Variation of the Velocity
and Temperature at the Gap Center

(2) Temperature Profile

It was pointed out that in most of the experimental cases the temperature gradient at the gap was oppositely directed to the power skew. The reason might come from non-uniform heat flux at the rod surface and/or incorrect geometry of the test section. The effect of non-uniform heat flux distribution was examined using the RODCON code explained in Chapter 5. Since the heater rods utilized MgO (k = 2.9 W/m°K) as the insulation material and Incoloy (k = 11.5 W/m°K) as the cladding material, it is expected that significant non-radial rod conduction might exist. The code predictions and the experimental data for Run 27 are shown in Figure 8.33. For this RODCON case the resulting rod surface non-uniform heat flux distribution is about 8%. A hump at the gap was predicted by the code by inclusion of the rod conduction effect. This result is consistent with the experimental data. It implies that the effect of rod conduction is quite significant on the temperature profiles in our experiments.

(3) Turbulent Heat Transfer vs. Fluid Conduction

The relative magnitude of the turbulent heat flux to the fluid conduction was evaluated to determine its contribution to total heat transfer. Total heat transfer between subchannels is equal to the sum of fluid conduction and turbulent heat flux, i.e.,

$$q'' = - k\nabla T + \rho C_p (\overline{v'T'})$$

Then the ratio of the turbulent heat flux to the fluid conduction is,

$$R = \frac{\overline{v'T'}}{\frac{k}{\rho C_p} \nabla T} \approx \frac{\overline{v'T'}}{\alpha \frac{\Delta \overline{T}}{\eta}}$$
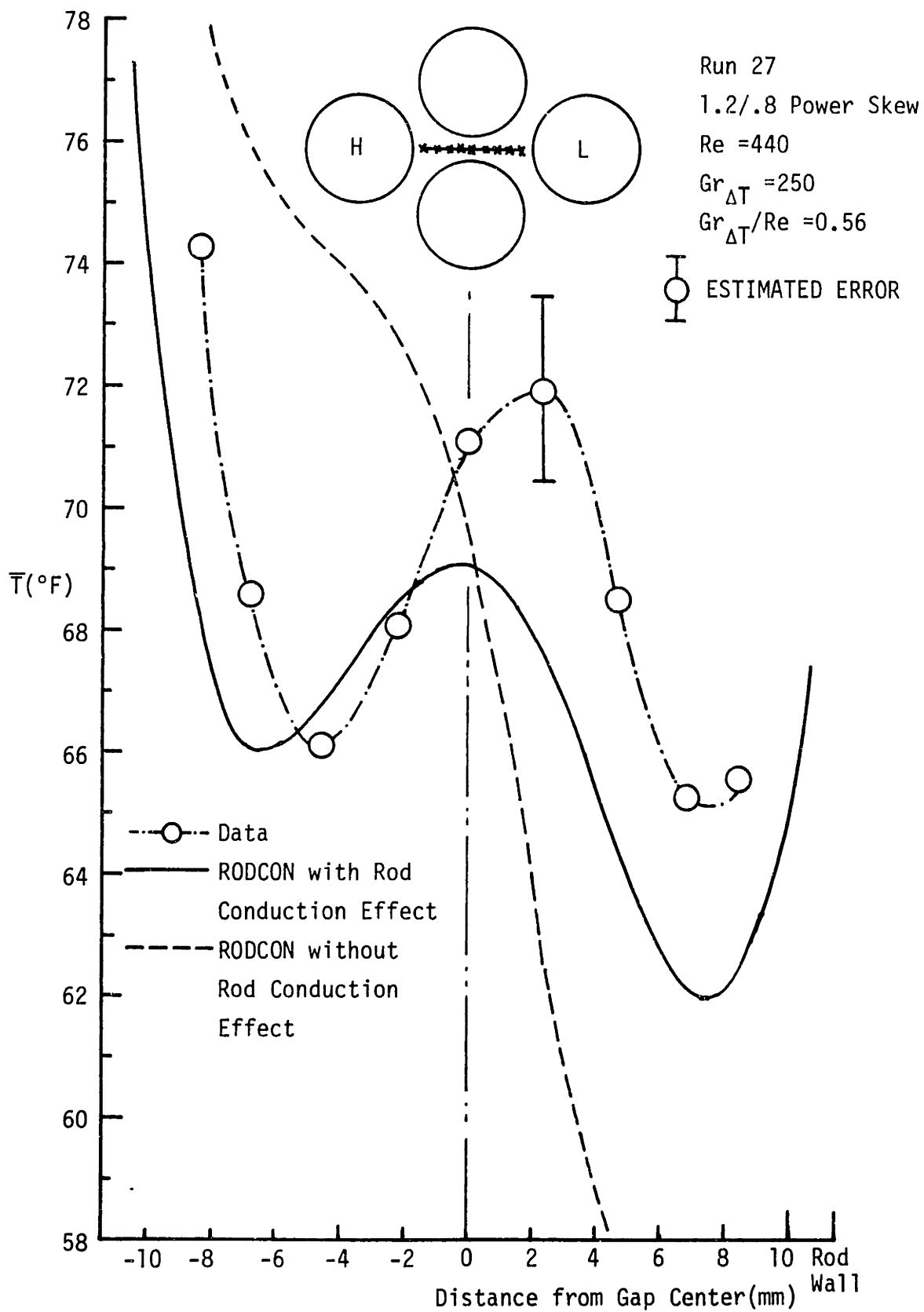
Figure 8.33   Measured and RODCON Predicted Temperature Profile
Along the Symmetry Line for Run 27

where $\alpha = \dfrac{k}{\rho C_p}$; thermal diffusivity of the fluid

$\quad\quad$ ($\alpha = 1.45\times10^{-7} m^2/s$ for water at $20°C$)

$\Delta\bar{T}$; subchannel average temperature difference

η ; subchannel centroidal distance

As an example, for Run 26,

$$\overline{v'T'} = 6.9\times10^{-5} \ m/s\cdot°F$$

and

$$\frac{\Delta\bar{T}}{\eta} = \frac{2°F}{1.36\times10^{-2} \ m} = 147 \ °F/m$$

Then,

$$R = \frac{6.9\times10^{-5}}{(1.45\times10^{-7})(147)} \simeq 3$$

Therefore, the magnitude of the turbulent heat flux is comparable to that of the fluid conduction in water.

If $\overline{v'T'}$ in sodium is assumed to be the same as that in water, then under the same temperature gradient,

$$\alpha = 6.7\times10^{-5} \ m^2/s \ (for \ sodium \ at \ 380°C)$$

$$R = \frac{6.9\times10^{-5}}{(6.7\times10^{-5})(147)} \simeq 0.007$$

This result shows that the turbulent heat flux in sodium may be quite small compared with the fluid conduction even if an order of magnitude of error is allowed.

(4) Comparisons with Other Predictions of ε^*_{TM}

Figure 8.34 compares ε^*_{TM} measured in this experiment with other predictions. The prediction of Bates and Khan (B-4) was deduced from their low flow turbulent mixing correlation given in Eq. (8.2) and operating condition. The WARD and ORNL estimations were obtained by evaluating the magnitude of an additional mixing required to match
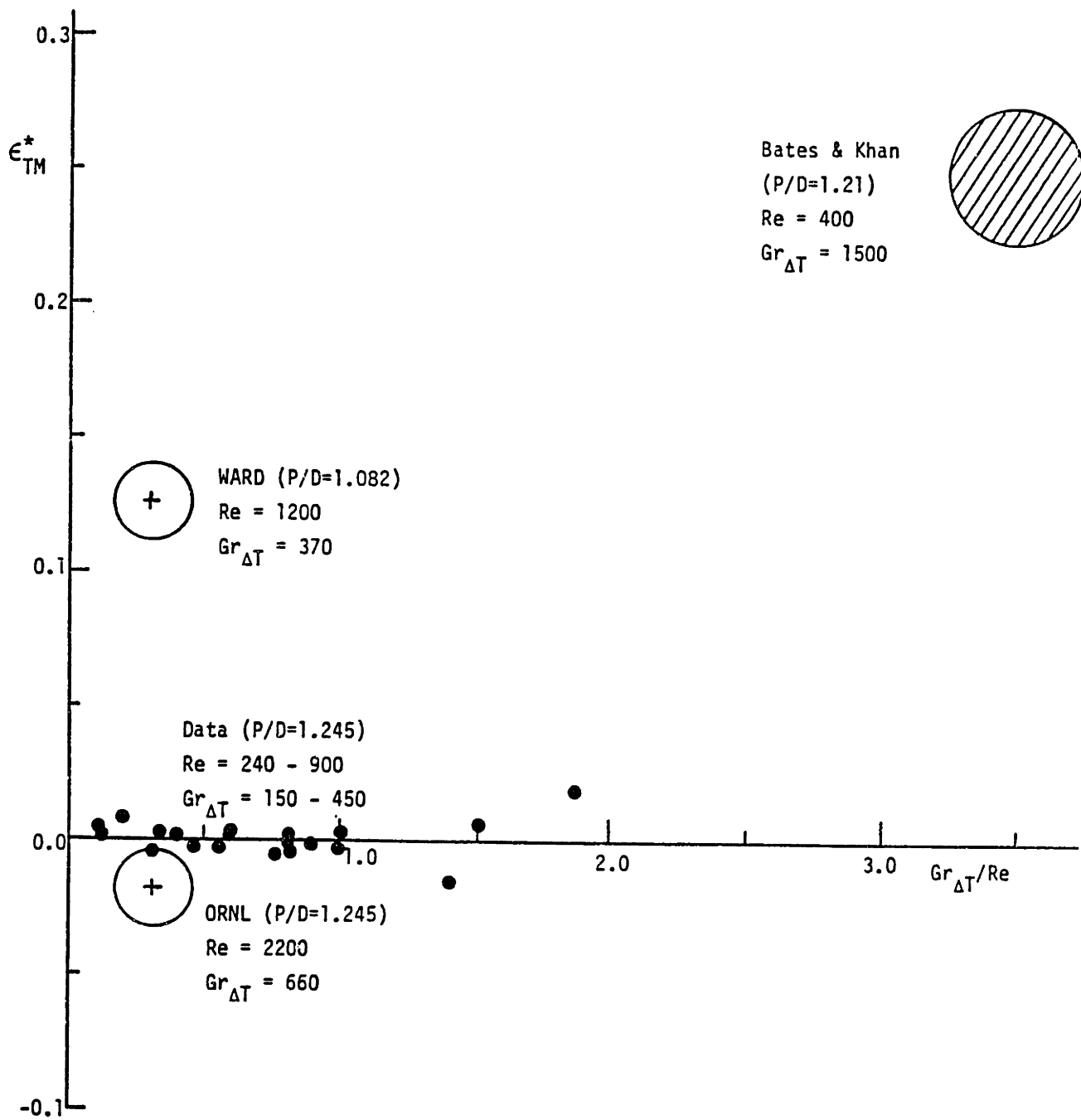
Figure 8.34   Comparisons of Measured ϵ^*_{TM} with Other Predictions

their data with the ENERGY-IV results including the rod conduction effect. As shown in Table 7.4, the WARD blanket bundle reveals around 3% overprediction of maximum ΔT^*, corresponding to $\varepsilon^*_{TM} = 0.125$, while the ORNL fuel bundle reveals 1% underprediction corresponding to $\varepsilon^*_{TM} = -0.019$. The measured data are seen to be very small compared with other predictions.

8.8 Conclusions

The experimental investigation of the turbulent thermal plumes in a triangular rod array (P/D = 1.245) has been performed to measure the turbulent heat transfer between subchannels and to provide information on the thermal plume behavior at the gap. The magnitude of the turbulent heat flux measured was comparable to that of molecular conduction of water. However, for application to the sodium case, it was expected that the turbulent heat flux relative to the fluid conduction might be quite small due to the high thermal conductivity of sodium and the smearing effect of the temperature fluctuations.

Counterflux heat transfer, i.e., heat flux directed against the power skew was observed. The turbulent heat flux changed sign from positive to negative as $Gr_{\Delta T}/Re$ increased when $Re \geq 400$, while it monotonically increased as $Gr_{\Delta T}/Re$ increased when $Re = 240$. The possible causes addressed were the pressure variation with time due to instability of laminar flow, the temperature gradient oppositely directed to the power skew or the spiral structure of the thermal plume. A correlation for the turbulent thermal plume mixing parameter could not be constructed due to the unexplained counterflux phenomena and the measured abnormal temperature gradient at the gap.

CHAPTER 9

CONCLUSIONS AND RECOMMENDATIONS

9.1 Conclusions

The conclusions of this study are as follows.

(1) Porous Body Analysis in Wire-Wrapped Rod Bundles

The governing conservation equations of the porous body approach were derived. An alternative definition of the distributed resistance force was proposed as given in Eq. (2.30) based on physical reasoning. A pressure model consistent with this alternative distributed resistance was suggested, and a comparison study with other existing models for the pressure term was executed. Although the superiority of the suggested pressure model could not be verified by the error analysis due to the limitation of the one dimensional cases examined, the suggested model is recommended since any spatial correlation for numerical application is not required and the approximations to derive this model were minimized.

(2) Selection of an Optimum Control Volume Layout

Practical limitations and approximations required for numerical implementation of the porous body approach were identified and compared with those of the subchannel analysis method. Proper choice of a porous body control volume is important to minimize the errors resulting from the approximations and thus improve accuracy of the flow and pressure field predictions. Based on computing time and accuracy, the staggered half-pin layout was selected as the optimum control volume layout. The selection basis is summarized in Table 3.3. The geometrical configuration of the staggered half-pin layout is very similar to that of the subchannel analysis control volume.

(3) Distributed Resistance Models for the Porous Body Analysis

Distributed resistance models for the porous body analysis were developed to account for the presence of the wire spacer in wire-wrapped rod bundle. These models were formulated in terms of distributed resistance forces as a function of flow velocity and control volume geometry. The distributed resistance models were incorporated into a porous body code, THERMIT, particularly for the staggered half-pin layout and axial mesh size equal to H/12, where H is the wire-wrap lead length. The THERMIT predictions were compared with velocity and pressure field data under turbulent flow conditions. Overall prediction of the velocity field was quite satisfactory. The swirl flow behavior at the side subchannels was predicted consistently with the experimental data. The pressure field prediction showed qualitative agreement with the data although quantitative comparisons could not be made because of different flow velocity conditions. From these comparison studies, it is concluded that the staggered half-pin layout is an appropriate choice and the distributed resistance models developed for the porous body analysis are suitable for wire-wrapped rod bundle analysis.

(4) Non-Radial Rod Conduction

Also investigated was non-radial heat conduction through heater rods, which is an additional energy transfer in simulated heater rod fabricated with high thermal conductivity insulator material (i.e., Boron Nitride). A multirod analysis computer code, RODCON, was developed utilizing the iterative boundary matching approach of Yeung and Wolf to estimate the non-radial rod conduction effect. This code

was tested against more sophisticated methods such as BODYFIT code. The temperature and heat flux distributions predicted by the RODCON yielded satisfactory results compared with those of the above methods.

(5) Rod Conduction Model and Validation

A correlation for the non-radial heat conduction through heater rods was proposed in terms of azimuthal heat transfer rate, thermal conductivities, subchannel geometry (P/D and c/D ratios) and subchannel average temperature differences. The unknown constants of this correlation were calibrated utilizing the RODCON code which was modified to calculate the azimuthal heat flux in a geometry particularly chosen for modeling purposes. The calibrated rod conduction correlation is given in Eq. (6.26).

This model was adapted to a subchannel analysis code, ENERGY-IV. The effect of the non-radial rod conduction was examined by comparing the temperature profiles predicted by the ENERGY-IV with this model and without the model. The predictions were also compared against all available experimental data of out-of-pile tests. The results showed that inclusion of the rod conduction effect significantly reduced the difference between the ENERGY-IV prediction and the data. The reduction of the maximum ΔT^* was of 4% of ΔT_b in blanket bundles and was of 3% in fuel bundles under mixed convection conditions. However, the calculated results with the model still overpredicted the maximum ΔT^* by 3% for blanket type bundle. On the other hand, the results showed almost the same values as the data for fuel type bundle.

(6) Relative Importance of Energy Transfer Mechanisms

Four energy transfer mechanisms, i.e., wire sweeping including turbulent mixing, convective heat transfer by flow distribution, fluid

conduction and rod conduction in mixed convection conditions were

compared based on the effect of each mechanism on maximum ΔT^*. The

region in which each mechanism was significant was drawn as a function

of Re and $Gr_{\Delta T}$ numbers for a blanket and a fuel bundle as shown in

Figures 7.22 and 7.23 respectively. Wire sweeping including turbulent

mixing was dominant in Re $>$ 5000 for blanket bundle and Re $>$ 30000 for

fuel bundle irrespective of $Gr_{\Delta T}$ number. Flow redistribution was

dominant in Re $<$ 500 (at $Gr_{\Delta T}$ = 500) for blanket bundle and Re $<$ 1000

(at $Gr_{\Delta T}$ = 700) for fuel bundle. Flow redistribution became more

important as $Gr_{\Delta T}$ increased. Fluid conduction and rod conduction

were significant (greater than 15% of total effect) in the range of

500 $<$ Re $<$ 5000 (at $Gr_{\Delta T}$ = 500) for blanket and 1000 $<$ Re $<$ 30000

(at $Gr_{\Delta T}$ = 700) for fuel bundle.

(7) Turbulent Thermal Plume Mixing Experiment

An enhanced energy mixing by turbulent thermal plumes was

experimentally investigated. A test section of a triangular rod array

(P/D = 1.245) was constructed and a power supply system to control the

power of heater rods individually was designed utilizing triacs.

Turbulent heat flux induced by the thermal plume and other physical

parameters were measured at the gap between subchannels at various Re

and $Gr_{\Delta T}$ conditions. Relative magnitude of the measured turbulent

heat flux to fluid conduction in water was approximately of the same

order. When Re = 240, the turbulent heat flux monotonically increased

as $Gr_{\Delta T}$ increased. On the other hand, when Re $\geq$ 400, positive

heat flux for low $Gr_{\Delta T}$ range and negative for high $Gr_{\Delta T}$ range

were measured. This negative heat flux, so-called counterflux heat

transfer, corresponds to the heat transfer from the low power to the

high power side. Further, in many experimental runs, the temperature

gradient at the gap was opposite to the power skew direction.

Therefore, a suitable correlation for the turbulent thermal plume

mixing parameter could not be constructed due to this unexplained

counterflux phenomenon and the abnormal temperature gradient measured

at the gap.

9.2 Recommendations for Future Work

(1) Distributed Resistance Model Validation

To validate the distributed resistance model developed for porous

body analysis and calibrate the undetermined constant to apply to wide

variety of bundle geometry and flow conditions, more THERMIT

calculations should be performed. Since each run requires substantial

computing time because of slow convergence rate, development of a

numerical scheme to accelerate the convergence should precede further

efforts to validate the model.

(2) Thermal Plume Mixing Experiment

Based on the analysis of the experimental results obtained and

the problems encountered in this experiment, the following work is

recommended to provide a basis for further modeling of turbulent

thermal plumes.

(a) The turbulent heat flux measurement should be extended to higher

$Gr_{\Delta T}$ and Re conditions. The operating conditons were limited by

the poor Doppler signal due to large density variation at high

$Gr_{\Delta T}$ conditions. The Doppler signal can be improved by reducing

the laser beam path length in the liquid. Thus it is recommended that

a beam guide tube be used having the shape of a tapered cylinder.

This shape will also minimize the flow disturbance.

(b) A counter for the Doppler signal, if available, is better than the tracker for the high power experiment. Since the counter counts the signals only when the laser beam is scattered by the seeded particle, it can eliminate the drop-out problem of the Doppler signals.

(c) A new design of the heater rods is suggested to reduce the effect of the non-uniform heat flux and the conduction through heater rods. The heater is composed of a conducting tube through which electrical current passes. Material selection and dimensions for the heater are described in Appendix I.

(d) To investigate the geometry dependence, i.e., P/D ratio, of the thermal plume mixing, measurements on a blanket type assembly (P/D = 1.08) must be performed. Larger diameter heater rods (D greater than or approximately equal to 1 inch) should be used to achieve the physically required gap width. The test section should be redesigned to accommodate the four larger heaters and should be accurately fabricated to minimize the tolerances. According to the estimation using RODCON code, the heat flux deviation of 1% due to manufacturing tolerance yields a change of subchannel average temperature of around 1°F.

(e) The supporters of the heaters at the top plenum should be constructed to allow thermal expansion of the heaters. The supporters should not disturb the flow significantly.

(f) The axial velocity should be measured to determine a reasonable subchannel average temperature and to check for symmetry of the test section. The axial velocity just above the end of the heater can be measured by projecting the laser beam horizontally. This can be

accomplished by either utilizing a transparent plenum wall or placing a mirror on the top plate to change the beam direction.

(g) An on-line printer or a microcomputer is required to record the signals of the velocity and temperature fluctuations as sketched in Fig. 8.32. These signals will provide information on the time scale, i.e., frequencies of the velocity and temperature fluctuations and hence permit a better understanding of the physical characteristics of the thermal plumes to be developed.

(h) As mentioned before, reduction of the transverse velocity fluctuations was observed at low $Gr_{\Delta T}$ and high Re number regions. The reason for this laminarization phenomenon should be explored.

REFERENCES

B 1   Bear, J., <u>Dynamics of Fluids in Porous Media</u>, American Elsevier
      Co., New York, 1972.

B-2   Bartholet, R.G., et al., "Clinch River Breeder Reactor Plant.
      11:1 Scale Wire-Wrapped Rod Bundle Air Flow Tests, Interior
      Subchannels," WARD-D-108, Westinghouse, November 1975.

B-3   Bartholet, R.G., et al., "CRBRP. 11:1 Scale, Wire-Wrapped Rod
      Bundle Air Flow Test, Side Subchannels," WARD-D-0129,
      Westinghouse, January 1976.

B-4   Bates, J.M. and Khan, E.U., "Investigation of Combined Free and
      Forced Convection in a 2×6 Rod Bundle During Controlled Flow
      Transients," AIChE Symposium Series, Heat Transfer, Orlando,
      1980.

B-5   Bill, Jr., R.G. and Gebhart, B., "The Development of Turbulent
      Transport in a Vertical Natural Convection Boundary Layer," Int.
      J. Heat Mass Transfer, Vol. 22, 1979.

C-1   Cheng, S.K., "Constitutive Correlations for Wire-Wrapped
      Subchannel Analysis under Forced and Mixed Convection
      Conditions," Ph.D. Thesis, Department of Nuclear Engineering,
      Massachusetts Institute of Technology, September 1984.

C-2   Chen, Y.R., Ip, K. and Todreas, N.E., "Velocity Measurements in
      Edge Suchannels of Wire-Wrapped LMFBR Fuel Assemblies,"
      COO-2245-11TR, Department of Nuclear Engineering, Massachusetts
      Institute of Technology, September 1974.

C-3   Chen, G.C-J, et al., "BODYFIT-1FE: A Computer Code for
      Three-Dimensional Steady-State/Transient Single-Phase Rod-Bundle
      Thermal-Hydraulic Analysis," NUREG/CR-1874, ANL-80-127, 1980.

C-4   Chen, B.C-J., Personal communication to T.S. Ro, 1985.

C-5   Carajilescov, P., "Experimental and Analytical Study of Axial
      Turbulent Flows in an Interior Subchannel of a Bare Rod Bundle,"
      Ph.D. Thesis, Department of Nuclear Engineering, Massachu. :tts
      Institute of Technology, March 1975.

D-1   Dutton, J.C. and Welty, J.R., "An Experimental Study of Low
      Prandtl Number Natural Convection in an Array of Uniformly Heated
      Vertical Cylinders," J. Heat Transfer, August, 1975.

D-2   Durst, F., Melling, A. and Whitlaw, J.H., <u>Principles and Practice
      of Laser-Doppler Anemometry</u>, Academic Press Ltd., London, 1976.

D-3   Drain, L.E., <u>The Laser Doppler Technique</u>, John Wiley and Sons
      Ltd., England, 1980.

D-4   Deissler, R.G., "Turbulence in the Presence of a Vertical Body
      Force and Temperature Gradient," J. Geophysical Research, Vol.
      67, No.8, July 1962.

E-1   Efthimiadis, A., "Mixed Convection and Hydrodynamic Modeling of
      Flows in Rod Bundles," Ph.D. Thesis, Department of Nuclear
      Engineering, Massachusetts Institute of Technology, June 1984.

E-2   Ebeling-Koning, D.B. and Todreas, N J., "Hydrodynamics of Single
      and Two-Phase Flow in Inclined Rod Arrays," DOE/ER/12075-2TR,
      Department of Nuclear Engineering, Massachusetts Institute of
      Technology, September 1983.

E-3   Engel, F.C. and Markley, R.A., "Paramater Studies of Peak
      Temperature Rise for LMFBR Blanket Rod Bundles," Nuclear
      Engineering and Design, Vol. 68, 1981.

E-4   Engel, F.C., Minushkin, B., Atkins, R.J. and Markely, R.A.,
      "Characterization of Heat Transfer and Temperature Distributions
      in an Eiectrically Heated Model of an LMFBR Blanket Assembly,"
      Nuclear Engineering and Design, Vol. 62, 1980.

E-5   Engel, F.C., Personal communication to N.E. Todreas, 1985.

E-6   Engel, F.C., Markley, R.A., and Bishop, A.A., "The Effects of
      Radial Heat Flux Gradients and Flow Regimes on the Peak Sodium
      Temperature Rise in Wire-Wrapped Rod Bundles," ANS Topical
      Meeting, Kiamesha Lake, September 1982.

E-7   Engel, F.C., Markley, R.A. and Minushkin, B., "Temperature
      Profiles in Natural and Forced Circulation of Sodium Through a
      Vertical LMFBR Blanket Test Assembly," AIChE Symposim Series,
      Milwaukee, 1981.

G-1   Gunter, A.Y. and Shaw, W.A., "A General Correlation of Friction
      Factors for Various Types of Surfaces in Crossflow," ASME
      Transactions, Vol. 67, 1945.

G-2   Grafham, D.R. and Golden, F.B., SCR Manual, Prentice-Hall Inc.,
      6th ed., 1982.

J-1   Jaluria, Y. and Gebhart, B., "On Transition Mechanisms in
      Vertical Natural Convection Flow," J. Fluid Mech., Vol. 66, part
      2, 1974.

L-1   Lafay, J., Menant, B. and Barroil, J., "Local Pressure
      Measurements and Peripheral Flow Visualization in a Water 19-Rod
      Bundle Compared with FLICA IIB Calculations: Influence of Helical
      Wire-Wrap Spacer System," AIChE-ASME Heat Transfer Conference,
      San Francisco, ASME paper 75-HT-22, August 1975.

L-2   Lahey, R.T. and Moody, F.J., The Thermal Hydraulics of a Boiling
      Water Nuclear Reactor, American Nuclear Society, Illinois, 1977.

L-3   Lock, G.S.H. and Trotter, F.J. deB., "Observations on the
      Structure of a Turbulent Free Convection Boundary Layer," Int.
      J. Heat Mass Transfer, Vol. 11, 1968, pp.1225-1232.

L-4   LaRue, J.C. and Libby, P.A., "Measurements in the Turbulent
      Boundary Layer with Slot Injection of Helium," The Physics of
      Fluids, Vol. 20, No.2, February 1977.

L-5   Liburdy, J.A., Groff, E.G. and Faeth, G.M., "Structure of a
      Turbulent Thermal Plume Rising Along an Isothermal Wall," J. Heat
      Transfer, Vol. 101, May 1979.

M-1   Markley, R.A. and Engel, F.C., "Blanket Sodium Heat Transfer Test
      Data and Evaluation," LMFBR Core T&H Information Meeting,
      Monterey, March 1981.

M-2   Morris, R.H. et al., "Single-Phase Sodium Tests in a 61-Pin
      Full-Length Simulated LMFBR Fuel Assembly-Record of Phase 1
      Experimental Data for THORS Bundle 9," ORNL/TM-7315, August 1980.

M-3   Matsui, N., "Fundamentals of DC Motor Control by Microcomputer,"
      Denshi Kagaku, in Japanese, November 1983, pp.14-18.

M-4   Markus, J., Guidebook of Electronic Circuits, McGraw-Hill, 1975.

N-1   Nijsing, R. and Eifler, W., "Temperature Fields in Liquid-Metal-
      Cooled Rod Assemblies," Progress in Heat and Mass Transfer, Vol.
      7, 1973.

N-2   Namekawa, F., Ito, A. and Mawatari, K., "Experimental Modeling
      and Simulation Criteria for Thermal Hydraulics in Rod Bundles
      during Buoyancy Induced Flow," IAHR Specialists Meeting,
      Richland, August 1984.

N-3   Nakajima, T., "Instruction Manual for Velocity and Temperature
      Measurements," To be published, Department of Nuclear
      Engineering, Massachusetts Institute of Technology, 1986.

O-1   Ohtake, T., Urawashi, S. and Takahashi, K., "Velocity
      Measurements in the Subchannel of the Wire-Spaced Subassembly,"
      Nuclear Technology, Vol. 30, September 1976.

O-2   Ott, L.J. and Hedrick, R.A., "ORTCAL - A Computer Code for THTF
      Heated Rod Thermocouple Calibration," NUREG/CR-0342,
      ORNL/NUREG-51, 1979.

O-3   Okada, T. and Todreas, N.E., "Mixed Convection Flow Experiments
      in Wire-Wrapped Bundles," PNC/MIT-13TR, Department of Nuclear
      Engineering, Massachusetts Institute of Technology, September
      1984.

O-4   Oosthuizen, P.H., "Turbulent Combined Convective Flow over a
      Vertical Plane Surface," 5th International Heat Transfer
      Conference, Tokyo, 1974.

O-5 Omega Engineering, Inc., Temperature Measurement Handbook and Encyclopedia, 1985.

P-1 Patankar, S.V., Numerical Heat Transfer and Fluid Flow, Hemisphere Publishing Co., 1980.

R-1 Reed, W.H., et al., "THERMIT: A Computer Program for Three-Dimensional Thermal-Hydraulic Analysis of Light Water Reactor Cores," EPRI NP-2032, September 1981.

R-2 Row, D.S., "COBRA-IIIC: A Digital Computer Program for Steady-State and Transient Thermal-Hydraulic Analysis of Nuclear Fuel Elements," BNWL-1695, Battelle Pacific Northwest Laboratories, Richland, WA, March 1973.

R-3 Roidt, R., Carelli, M.D. and Markley, R.A., "Experimental Investigations of the Hydraulic Field in Wire-Wrapped LMFBR Core Assemblies," Nuclear Engineering and Design, Vol. 62, 1980.

S-1 Sha, W.T. and Chao, B.T., "Local Volume-Averaged Transport Equations for Single-Phase Flow in Regions Containing Fixed, Dispersed Heat-Generating (or Absorbing) Solids," NUREG/CR-1969, ANL-80-124, April 1981.

S-2 Sha, W.T., et al., "COMMIX-1: A Three-Dimensional Transient Single-Phase Component Computer Program for Thermal Hydraulic Analysis," NUREG/CR-0415, ANL-77-96, 1978.

S-3 Slattery, J.C., Momentum, Energy and Mass Transfer in Continua, McGraw-Hill, 1972, pp. 198-244.

S-4 Sarno, A., Gori, P. and Andalo, G., "Local Pressure and Velocity Measurements in a Water 19-Rod Bundle Using a Wire Wrap Spacer System," Paper for IWCFR-Specialist's Meeting on Thermodynamics of FBR Fuel Subassemblies under Nominal and Non-Nominal Operating Conditions, Karlsruhe, February 1979.

S-5 Schor, A.L., "A Four-Equation Two-Phase Flow Model for Sodium Boiling Simulation of LMFBR Fuel Assemblies," Ph.D. Thesis, Department of Nuclear Engineering, Massachusetts Institute of Technology, 1982.

S-6 Symolon, P.D., "Mixed Convection in Vertical Rod Bundles," Ph.D. Thesis, Department of Mechanical Engineering, Massachusetts Institute of Technology, 1982.

S-7 Smith, R.R., "Characteristics of Turbulence in Free Convection Flow Past a Vertical Plate," Ph.D. Thesis, University of London, Queen Mary College, 1972.

S-8 Sawdye, R.W., "Measurement and Simulation of a Three-Dimensional Turbulent Recirculating Flow," Ph.D. Thesis, Department of Nuclear Engineering, Massachusetts Institute of Technology, May 1985.

T-1   Todreas, N.E., 22.313 Class Notes, Chapters 17 and 18, Department
      of Nuclear Engineering, Massachusetts Institute of Technology.

T-2   Todreas, N.E., 22.313 Class Notes, Chapter 19, Department of
      Nuclear Engineering, Massachusetts Institute of Technology.

T-3   Tanny, J. and Shlien, D.J., "Velocity Field Measurements of a
      Laminar Starting Plume," Phys. Fluids, Vol. 28, No.4, April 1985.

T-4   Texas Instruments Inc., The TTL Data Book for Design Engineers,
      2nd ed., 1981.

V-1   Vliet, G.C. and Liu, C.K., "An Experimental Study of Turbulent
      Natural Convection Boundary Layers," J. of Heat Transfer,
      November, 1969.

W-1   Whitaker, S., "Diffusion and Dispersion in Porous Media," AIChE

      Journal, Vol. 13, No. 3, 1967, pp. 420-427.

W-2   White, F.M., Viscous Fluid Flow, McGraw-Hill, 1974, p. 210.

Y-1   Yeung, M.K. and Wolf, L. "A Multicell Slug Flow Heat Transfer
      Analysis of Finite LMFBR Bundles," COO-2245-68TR, Department of
      Nuclear Engineering, Massachusetts Institute of Technology, 1978.

APPENDIX A

Distributed Resistance in the Control Volume Approach

The volume-averaged momentum equation is given in Eq.(2.5) and rewritten as,

$$\gamma_V \frac{\partial}{\partial t} {}^i\langle \rho \vec{v} \rangle + \frac{1}{V}\int_{A_f} \rho \vec{v}(\vec{v} \cdot \vec{n}) \; dA = \langle \rho \vec{g} \rangle - \nabla\langle p \rangle$$

$$+ \nabla \cdot \langle \overline{\overline{\tau}} \rangle + \frac{1}{V}\int_{A_{fs}} (-p\vec{n} + \overline{\overline{\tau}} \cdot \vec{n}) \; dA \qquad (A.1)$$

As discussed in Section 2.5.2, the resistance force term should be redefined so that it can be also applied in the limiting cases. The limiting cases in the flow field analysis may be;

1) No fluid motion: If $\vec{v} \to 0$, $\vec{R} \to 0$.

2) Viscous friction is negligible (inviscid flow approximation):

   If $\mu \to 0$, $\vec{R} \to 0$.

Since the resistance force is conventionally correlated based on $\vec{v}$ and μ as Eq.(2.28), $\vec{R}$ should approach zero for these limiting cases.

Next we propose an approach to handle these limiting cases. The physical phenomenon which contributes to the form drag is the wake formulation generated by the boundary layer separation. If no wake is formed such as in the above limiting cases or when the flow area gradually converges, the form drag does not exist. Thus, the resistance force can be expressed as the following:

   Resistance Force = (Friction drag due to the viscous stress over

   the solid surface) + (Form drag resulting from the

   pressure difference produced by the boundary layer

   separation (i.e., wake formation)).

The calculation of the form drag in an analytical way is difficult. Usually it is obtained by measurement. In a heuristic way without rigorous mathematical verification, let us modify the momentum equation (Eq.(A.1)) and the definition of $\vec{R}$ to achieve our goal. A schematic diagram of the pressure distribution on the solid surface is shown in Figure A.1. The pressure at the wall can be written as,

$$P_{wake} = P_{no\ wake} - \Delta P_{wake} \qquad (A.2)$$

where,

$P_{no\ wake}$; Pressure distribution in case of the ideal flow

(no wake downstream of the obstacle)

P_{wake}; Actual pressure distribution, i.e., p in Eq.(A.1)

ΔP_{wake}; Difference between the actual pressure and

$P_{no\ wake}$

For the limiting cases in which no wake is generated, $\Delta P_{wake} = 0$ since $P_{wake} = P_{no\ wake}$. We can now define the resistance term and re-express the momentum equation consistent with this definition. The resistance force term can be defined as,

$$\int_{V_f} \vec{R}'dV \equiv \int_{A_{fs}} (\overline{\overline{\tau}}\cdot\vec{n} + \Delta P_{wake}\ \vec{n})\ dA \qquad (A.3)$$

where $-\int_{A_{fs}} (\overline{\overline{\tau}}\cdot\vec{n})dA$ is the friction drag force and $-\int_{A_{fs}} (\Delta P_{wake}\vec{n})dA$ is the modified form drag force.

This definition of the resistance force satisfies the limiting cases. Using Eq.(A.3), the momentum equation (Eq.(A.1)) becomes,

$$\gamma_V \frac{\partial}{\partial t}\ {}^{1}\langle\rho\vec{v}\rangle + \frac{1}{V} \int_{A_f} \rho\vec{v}(\vec{v}\cdot\vec{n})\ dA = \langle\rho\vec{g}\rangle - \nabla\langle p\rangle + \nabla\cdot\langle\overline{\overline{\tau}}\rangle$$

$$+ \frac{1}{V}\int_{A_{fs}} (-P_{no\ wake}\ \vec{n})\ dA + \frac{1}{V} \int_{V_f} \vec{R}'dV \qquad (A.4)$$
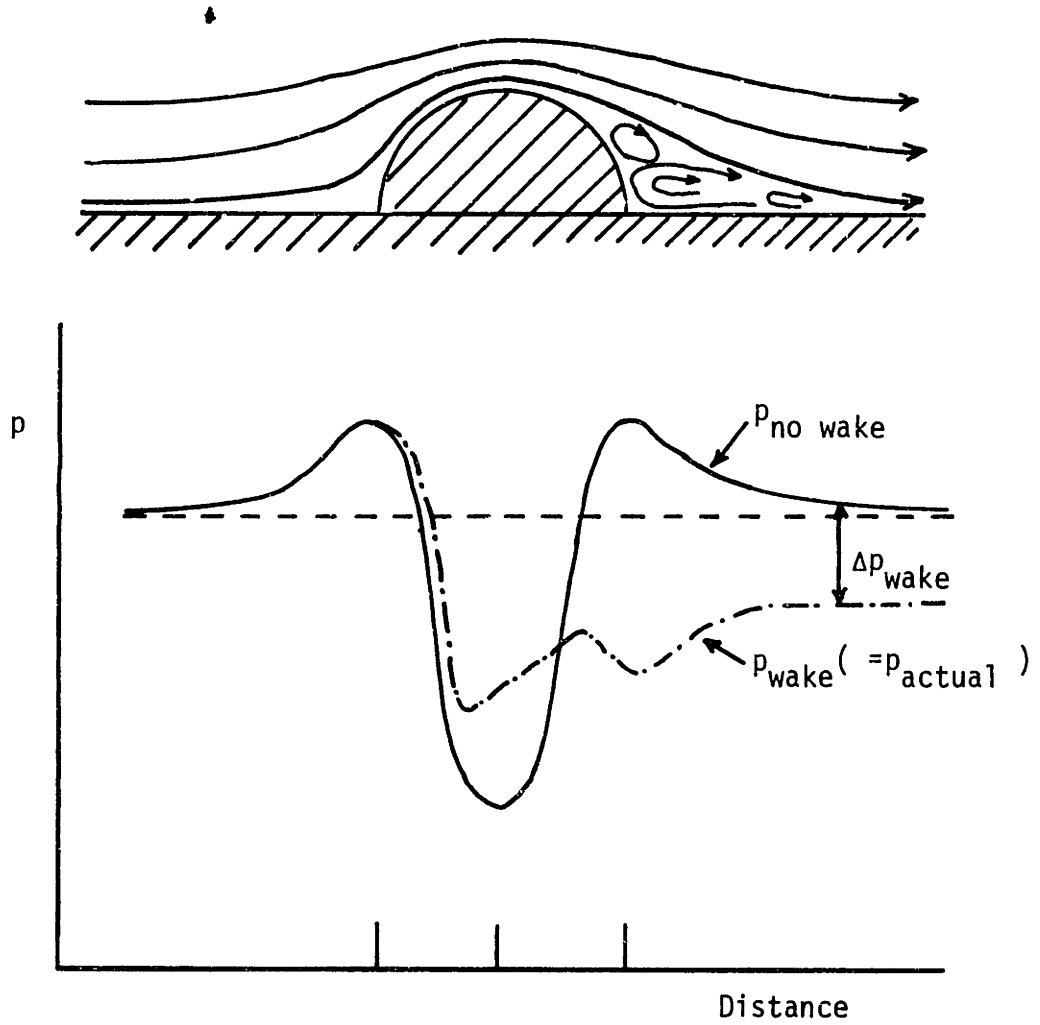
Figure A.1   Pressure Distribution in Case of Flow Past an Obstacle

The term $\frac{1}{V}\int_{A_{fs}} (-p_{no\ wake}\ \vec{n})dA$ cannot be evaluated analytically in terms of the actual pressure p and geometrical parameters without further assumptions for general cases.

Here, two special cases are introduced to illustrate how to estimate the term. If the flow area on either side of the control volume is the same and obstacles generating the wake are completely surrounded by the control volume boundary (Fig. A.2), $\frac{1}{V}\int_{A_{fs}} (-p_{no\ wake}\ \vec{n})dA$ is negligible as one can deduce from Fig. A.1 since $p_{no\ wake}$ is symmetric about the obstacle. Then Eq. (A.4) yields

$$\gamma_V \frac{\partial}{\partial t} \frac{1}{i}\langle\rho\vec{v}\rangle + \frac{1}{V}\int_{A_f} \rho\vec{v}(\vec{v}\cdot\vec{n})\ dA = \langle\rho\vec{g}\rangle - \nabla\langle p\rangle + \nabla\cdot\langle\bar{\bar{\tau}}\rangle + \frac{1}{V}\int_{V_f} \vec{R}'\ dV \quad (A.5)$$

For the other case when the wake region in a control volume is assumed to be small compared with total control volume or when no wake is generated although the flow area on either side of the control volume is different for either case, the pressure distribution without wake formation can be approximated equal to the actual pressure, i.e.,

$$p_{no\ wake} \approx p_{wake} \equiv p \qquad\qquad (A.6)$$

Then Eq. (A.4) is written as,

$$\gamma_V \frac{\partial}{\partial t} \frac{1}{i}\langle\rho\vec{v}\rangle + \frac{1}{A}\int_{A_f} \rho\vec{v}(\vec{v}\cdot\vec{n})\ dA = \langle\rho\vec{g}\rangle - \nabla\langle p\rangle + \nabla\cdot\langle\bar{\bar{\tau}}\rangle$$

$$+ \frac{1}{V}\int_{A_{fs}} p\ \vec{n}\ dA + \frac{1}{V}\int_{V_f} \vec{R}'dV \qquad (A.7)$$

$$= \langle\rho\vec{g}\rangle - \langle\nabla p\rangle + \nabla\cdot\langle\bar{\bar{\tau}}\rangle + \frac{1}{V}\int_{V_f} \vec{R}'dV \qquad (A.8)$$

For the two limiting cases explained in Section 2.5, Eq. (A.8) should be used.
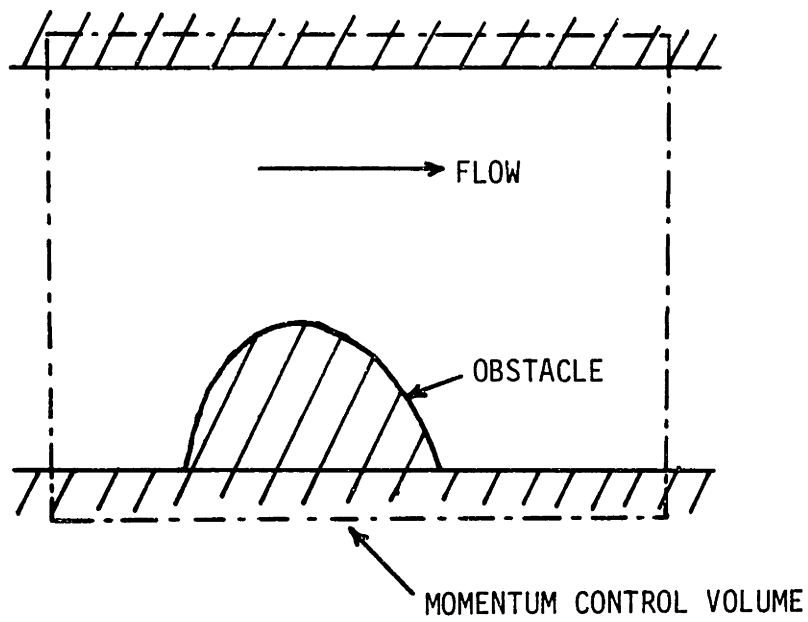
Figure A.2   Control Volume Having Equal Flow Area on Either
           Side with an Obstacle

APPENDIX B

Algebraic Details of the Analytical Solution of the Pressure Term

Throughout the following examples, incompressible fluid is assumed, i.e., $^i\langle\rho\rangle = {}^i\{\rho\} = \rho$.

B.1   Example 1

(a)   COMMIX Model

From Eq. (2.55),

$$^i\langle p\rangle_i = \frac{1}{V_{f_i}} \int p(x) A_f(x) dx \tag{B.1}$$

$p(x)$ is obtained from the Bernoulli equation:

$$p(x) = p_i + \rho g x \tag{B.2}$$

and the free flow area is given as,

$$A(x) = g - \frac{b-a}{h} x \tag{B.3}$$

Then,

$$^i\langle p\rangle_i = \frac{1}{bh} \int_{-h/2}^{h/2} (p_i + \rho g x)(b - \frac{b-a}{h} x) dx$$

$$= p_i - \frac{1}{12} \frac{b-a}{b} \rho g h$$

and

$$^i\langle p\rangle_{i+1} = \frac{1}{ah} \int_{h/2}^{3h/2} (p_i + \rho g x)(b - \frac{b-a}{h} x) dx$$

$$= p_i + (\frac{13}{12} - \frac{1}{12} \frac{b}{a}) \rho g h$$

Then the analytical solution of the pressure drop is

$$\Delta(^i\langle p\rangle)_{analy} = {}^i\langle p\rangle_{i+1} - {}^i\langle p\rangle_i$$

$$= \rho g h \left(1 - \frac{1}{12} \frac{(b - a)^2}{ab}\right) \qquad (2.56)$$

B.2 Example 2

(a) COMMIX Model

Analytical expression of the pressure is given as

$$p(x) = P_i + \frac{1}{2} \rho u_i^2 - \frac{1}{2} \rho u(x)^2 \qquad (B.4)$$

and from continuity,

$$u(x) = \frac{b}{A(x)} u_i \qquad (B.5)$$

Substituting Eqs. (B.3), (B.4) and (B.5) into Eq. (B.1),

$$^i\langle p \rangle_i = \frac{1}{bh} \int_{-h/2}^{h/2} \left(P_i + \frac{1}{2} \rho u_i^2 - \frac{1}{2} \rho u(x)^2\right) A(x) dx$$

$$= P_i + \frac{1}{2} \rho u_i^2 - \frac{1}{bh} \frac{1}{2} \rho u_i^2 \int_{-h/2}^{h/2} \frac{b^2}{\left(b - \frac{b - a}{h} x\right)} dx$$

$$= P_i + \frac{1}{2}\rho u_i^2 + \frac{1}{2}\rho u_i^2 \frac{b}{b - a} \ln \frac{a + b}{3b - a}$$

Using the same procedure as above,

$$^i\langle p \rangle_{i+1} = P_i + \frac{1}{2} \rho u_i^2 + \frac{1}{2} \rho u_i^2 \frac{b^2}{a(b - a)} \ln \frac{3a - b}{a + b}$$

Since the analytical solution of the pressure drop is given as

$$\Delta(^i\langle p \rangle)_{analy} = {}^i\langle p \rangle_{i+1} - {}^i\langle p \rangle_i$$

Eq. (2.64) is fully obtained.

(b) Area Model

The analytical solution of the area averaged pressure is expressed as,

$$^{ix}\{p\}_i = P_i$$

$$^{ix}\{p\}_{i+1} = P_i + \frac{1}{2} \rho u_i^2 - \frac{1}{2} \rho u_{i+1}^2$$

Then the continuity ($u_{i+1}a = u_i b$), the pressure drop is

$$\Delta(^{ix}\{p\}_{analy} = \frac{1}{2} \rho u_i^2 [1 - (\frac{b}{a})^2] \tag{2.67}$$

APPENDIX C

Fortran Listing of Subroutine FWALL

```
C                    DISTRIBUTED RESISTANCE CALCULATION
C
C                         THERMIT4E   VERSION
C      ************************************************************
       subroutine fwall (FWV,FWL,IMOM,VXL,VYL,VZL,CFV,CFL,
      1      PA,ALPA,ROVA,ROLA,VISVA,VISLA,XAREA,YAREA,XVOL,YVOL,
      2      ZVOL,XDE,YDE,ZDE,XYDZ,ZDZ,I,JJ,NSTEP)
C      ************************************************************
C COMPUTES WALL FRICTION AND FORM LOSS USING DISTRIBUTED RESISTANCE
C FORCE MODEL DEVELOPED BY TAE SUN RO ON OCTOBER, 1984
C INPUT;
C     IMOM       INDEX FOR A SPECIFIC MOMENTUM CALCULATION
C         =1     X-MOMENTUM
C         =2     Y-MOMENTUM
C         =3     Z-MOMENTUM
C     VXL        X-COMPONENT (U) OF AVERAGE VELOCITY OF STAGGERED MESH
C     VYL        Y-COMPONENT (V) OF AVERAGE VELOCITY OF STAGGERED MESH
C     VZL        Z-COMPONENT (W) OF AVERAGE VELOCITY OF STAGGERED MESH
C OUTPUT;
C     FWL        DISTRIBUTED RESISTANCE OF LIQUID (FORCE/FLUID VOLUME)
C     FWV        =0 ( PRESENT VERSION )
C     --------------------------------------------------------
C     I                                                      I
C     I    AXIAL MESH = H/12,   XY MESH NUMBERS = 66         I
C     --------------------------------------------------------
       IMPLICIT REAL*8 (A-H,O-Z)
       COMMON /fricin/ DIAR,DIAW,PIRW,AREAG,SLXY,STX,STY,COEFP
       COMMON /fricfc/ FCON(8)
       DIMENSION XLENG(12,66),YLENG(12,66),ZLENG(12,66)
       DIMENSION XYANGLE(12),ZANGLE(12)
       DIMENSION XROD(66),YROD(66),ZROD(66)
       DIMENSION XWALL(66),YWALL(66),ZWALL(66)
C     --------------------------------------------------------------
C THE FOLLOWING DATA SET REPRESENTS WIRE LENGTH OF STAGGERED MESHES
C     --------------------------------------------------------------
       DATA ((XLENG(J,I),J=1,12),I=1,66) /
      1    36*0.,6*0.,3*1.,12*0.,3*1.,6*0.,3*1.,12*0.,3*1.,6*0.,
      2    3*1.,12*0.,3*1.,48*0.,6*0.,3*1.,6*0.,3*1.,3*0.,6*1.,
      3    3*0.,3*1.,6*0.,3*1.,3*0.,6*1.,3*0.,3*1.,6*0.,3*1.,
      4    3*0.,6*1.,3*0.,3*1.,3*0.,9*0.,3*1.,24*0.,6*0.,
      5    3*1.,3*0.,3*0.,3*1.,3*0.,6*1.,3*0.,3*1.,6*0.,3*1.,
      6    3*0.,6*1.,3*0.,3*1.,6*0.,3*1.,3*0.,6*1.,3*0.,3*1.,
      7    6*0.,3*1.,3*0.,6*1.,3*0.,3*1.,12*0.,3*1.,15*0.,
      8    3*1.,6*0.,3*1.,3*0.,3*1.,6*0.,3*1.,3*0.,6*1.,
      9    3*0.,3*1.,6*0.,3*1.,3*0.,6*1.,3*0.,3*1.,6*0.,3*1.,
      a    3*0.,6*1.,3*0.,3*1.,6*0.,3*1.,3*0.,6*1.,36*0.,3*1.,
      b    6*0.,3*1.,3*0.,3*1.,6*0.,3*1.,3*0.,6*1.,3*0.,3*1.,
      c    6*0.,3*1.,3*0.,6*1.,3*0.,3*1.,6*0.,3*1.,3*0.,6*1.,
      d    60*0.,3*1.,6*0.,3*1.,12*0.,3*1.,6*0.,3*1.,12*0.,
      e    3*1.,6*0.,3*1.,9*0.,24*0. /
       DATA ((YLENG(J,I),J=1,12),I=1,66) /
      1    160*0.,4*1.,6*0.,2*1.,4*0.,2*1.,2*0.,2*1.,2*0.,4*1.,
      2    2*0.,2*1.,2*0.,2*1.,4*0.,2*1.,2*0.,2*1.,2*0.,4*1.,
      3    2*0.,2*1.,2*0.,2*1.,4*0.,2*1.,2*0.,2*1.,8*0.,
```

```
4    2*1.,40*0.,4*1.,4*0.,
5    2*0.,2*1.,4*0.,2*1.,2*0.,2*1.,2*0.,4*1.,2*0.,2*1.,
6    2*0.,2*1.,4*0.,2*1.,2*0.,2*1.,2*0.,4*1.,2*0.,2*1.,
7    2*0.,2*1.,4*0.,2*1.,2*0.,2*1.,2*0.,4*1.,2*0.,2*1.,
8    2*0.,2*1.,4*0.,2*1.,2*0.,2*1.,8*0.,2*1.,16*0.,4*1.,4*0.,
9    2*0.,2*1.,4*0.,2*1.,2*0.,2*1.,2*0.,4*1.,2*0.,2*1.,
a    2*0.,2*1.,4*0.,2*1.,2*0.,2*1.,2*0.,4*1.,2*0.,2*1.,
b    2*0.,2*1.,4*0.,2*1.,2*0.,2*1.,2*0.,4*1.,2*0.,2*1.,
c    2*0.,2*1.,4*0.,2*1.,2*0.,2*1.,2*0.,4*1.,2*0.,2*1.,
d    2*0.,2*1.,4*0.,2*1.,2*0.,2*1.,8*0.,2*1.,16*0.,4*1.,4*0.,
e    2*0.,2*1.,4*0.,2*1.,2*0.,2*1.,2*0.,4*1.,2*0.,2*1.,
f    2*0.,2*1.,4*0.,2*1.,2*0.,2*1.,2*0.,4*1.,2*0.,2*1.,
g    2*0.,2*1.,4*0.,2*1.,2*0.,2*1.,2*0.,4*1.,2*0.,2*1.,
h    2*0.,2*1.,4*0.,2*1.,2*0.,2*1.,8*0.,2*1.,40*0.,4*1.,4*0.,
i    2*0.,2*1.,4*0.,2*1.,2*0.,2*1.,2*0.,4*1.,2*0.,2*1.,
j    2*0.,2*1.,4*0.,2*1.,2*0.,2*1.,2*0.,4*1.,2*0.,2*1.,
k    2*0.,2*1.,4*0.,2*1.,2*0.,2*1.,8*0.,2*1.,24*0. /
  DATA ((ZLENG(J,I),J=1,12),I=1,31) /
1    24*0.,5*0.,.5,1.,.5,11*0.,.5,1.,.5,7*0.,.5,1.,.5,0.,
2    .5,1.,.5,7*0.,.5,1.,.5,7*0.,.5,1.,.5,0.,
3    .5,1.,.5,7*0.,.5,1.,.5,11*0.,.5,1.,.5,41*0.,
4    .5,1.,.5,7*0.,.5,1.,.5,0.,.5,1.,.5,3*0.,
5    .5,1.,.5,0.,.5,1.,.5,0.,.5,1.,.5,1.,.5,0.,.5,1.,.5,
6    0.,.5,1.,.5,0.,.5,0.,.5,1.,.5,0.,.5,1.,.5,0.,.5,1.,.5,
7    1.,.5,0.,.5,1.,.5,0.,.5,1.,.5,0.,.5,0.,
8    .5,1.,.5,0.,.5,1.,.5,0.,.5,1.,.5,1.,.5,
*    5*0.,.5,1.,.5,0.,.5,9*0.,
9    .5,1.,.5,17*0.,.5,1.,.5,7*0.,.5,1.,.5,0.,.5,1.,.5,2*0.,
a    0.,.5,1.,.5,0.,.5,1.,.5,0.,.5,1.,.5,
b    1.,.5,0.,.5,1.,.5,0.,.5,1.,.5,0.,.5,
c    0.,.5,1.,.5,0.,.5,1.,.5,0.,.5,1.,.5,
d    1.,.5,0.,.5,1.,.5,0.,.5,1.,.5,0.,.5,
e    0.,.5,1.,.5,0.,.5,1.,.5,0.,.5,1.,.5,
f    1.,.5,0.,.5,1.,.5,0.,.5,1.,.5,0.,.5,
h    0.,.5,1.,.5,0.,.5,1.,.5,0.,.5,1.,.5,5 /
  DATA ((ZLENG(J,I),J=1,12),I=32,66) /
i    1.,.5,5*0.,.5,1.,.5,0.,.5,9*0.,.5,1.,.5,3*0.,
j    .5,1.,.5,6*0.,0.,.5,1.,.5,0.,.5,1.,.5,4*0.,
k    1.,.5,0.,.5,1.,.5,0.,.5,1.,.5,0.,.5,
l    0.,.5,1.,.5,0.,.5,1.,.5,0.,.5,1.,.5,
m    1.,.5,0.,.5,1.,.5,0.,.5,1.,.5,0.,.5,
n    0.,.5,1.,.5,0.,.5,1.,.5,0.,.5,1.,.5,
o    1.,.5,0.,.5,1.,.5,0.,.5,1.,.5,0.,.5,
p    0.,.5,1.,.5,0.,.5,1.,.5,0.,.5,1.,.5,
q    1.,.5,0.,.5,1.,.5,0.,.5,1.,.5,0.,.5,
r    0.,.5,1.,.5,5*0.,.5,1.,.5,1.,.5,9*0.,.5,15*0.,
s    .5,1.,.5,6*0.,0.,.5,1.,.5,0.,.5,1.,.5,4*0.,
t    1.,.5,0.,.5,1.,.5,0.,.5,1.,.5,0.,.5,
u    0.,.5,1.,.5,0.,.5,1.,.5,0.,.5,1.,.5,
v    1.,.5,0.,.5,1.,.5,0.,.5,1.,.5,0.,.5,
w    0.,.5,1.,.5,0.,.5,1.,.5,0.,.5,1.,.5,
x    1.,.5,0.,.5,1.,.5,0.,.5,1.,.5,0.,.5,
y    0.,.5,1.,.5,5*0.,.5,1.,.5,1.,.5,9*0.,.5,39*0.,
z    .5,1.,.5,6*0.,0.,.5,1.,.5,8*0.,
```

```
      1     1.,.5,0.,.5,1.,.5,5*0.,.5,0.,.5,1.,.5,8*0.,
      2     1.,.5,0.,.5,1.,.5,5*0.,.5,0.,.5,1.,.5,8*0.,
      3     1.,.5,9*0.,.5,24*0. /
C     --------------------------------------------------------------
C     DATA SET FOR ROD FRACTION OF STAGGERED MESH
C     --------------------------------------------------------------
      DATA (XROD(I),I=1,66)/
      1     3*0.,6*.25,4*0.,.25,6*.5,.25,2*0.,.25,8*.5,
      2     .25,0.,.25,8*.5,.25,2*0.,.25,6*.5,.25,4*0.,
      3     6*.25,2*0. /
      DATA (YROD(I),I=1,66)/
      1     13*0.,.3,.4,.6,.4,.6,.4,.3,3*0.,
      2           .3,.4,.6,.4,.6,.4,.6,.4,.3,.0,
      3           .3,.4,.6,.4,.6,.4,.6,.4,.6,.4,.3,0.,
      4           .3,.4,.6,.4,.6,.4,.6,.4,.3,3*0.,
      5           .3,.4,.6,.4,.6,.4,.3,2*0. /
      DATA (ZROD(I),I=1,66)/
      1     2*0.,.15,.2,.3,.2,.3,.2,.15,3*0.,.15,.35,5*.5,
      2     .35,.15,0.,.15,.35,7*.5,.35,.15,.15,.35,7*.5,
      3     .35,.15,0.,.15,.35,5*.5,.35,.15,3*0.,.15,.2,.3,.2,
      4     .3,.2,.15,2*0. /
C     --------------------------------------------------------------
C     DATA SET FOR DUCT WALL AREA
C     --------------------------------------------------------------
      DATA (XWALL(I),I=1,66) /
      1     3*0.,1.1909,4*.5938,1.1909,4*0.,1.1875,6*0.,
      2     1.1875,2*0.,1.1875,8*0.,1.1875,0.,1.1875,8*0.,
      3     1.1875,2*0.,1.1875,6*0.,1.1875,4*0.,
      4     1.1909,4*.5938,1.1909,2*0. /
      DATA (YWALL(I),I=1,66) /
      1     13*0.,1.4878,5*.5938,1.4878,3*0.,1.1875,7*0.,
      2     1.1875,0.,1.1875,9*0.,1.1875,0.,1.1875,7*0.,1.1875,
      3     3*0.,1.4878,5*.5938,1.4878,2*0. /
      DATA (ZWALL(I),I=1,66) /
      1     2*0.,.894,5*.5938,.894,3*0.,.994,.1935,5*0.,
      2     .1935,.994,0.,.994,.1935,7*0.,.1935,2*.994,
      3     .1935,7*0.,.1935,.994,0.,.994,.1935,5*0.,.1935,
      4     .994,3*0.,.894,5*.5938,.894,2*0. /
C     --------------------------------------------------------------
C     WIRE DIRECTIONS OF STAGGERED MESHES
C     --------------------------------------------------------------
      DATA (XYANGLE(J),J=1,12) /
      1     7.,9.,11.,-11.,-9.,-7.,-5.,-3.,-1.,1.,3.,5. /
      DATA (ZANGLE(J),J=1,12) /
      1     8.,10.,12.,-10.,-8.,-6.,-4.,-2.,0.,2.,4.,6. /
C     ***********************************************************************
      PHI=3.1415927
      SL=SLXY
      PI=PIRW
      VAXL=ABS(VXL)
      VAYL=ABS(VYL)
      IF(VAXL .GE. 1.E-18 .AND. VAYL .GE. 1.E-18) GO TO 70
      IF(VAXL .LT. 1.E-18 .AND. VAYL .LT. 1.E-18) VL2=VZL**2
      IF(VAXL .LT. 1.E-18 .AND. VAYL .GE. 1.E-18) VL2=VAYL**2+VZL**2
```

```
      IF(VAXL .GE. 1.E-18 .AND. VAYL .LT. 1.E-18) VL2=VAXL**2+VZL**2
      GO TO 90
   70 VL2=VXL**2+VYL**2+VZL**2
   90 CONTINUE
      VL=SQRT(VL2)
      J=JJ-1
      IF(J .EQ. 0) J=12
      AA=FCON(1)
      RECRA=FCON(2)
      BB=FCON(3)
      CC=FCON(4)
      DD=FCON(5)
      RECRT=FCON(6)
      EE=FCON(7)
      FF=FCON(8)
C **********************************************************************
C X-DIRECTION DISTRIBUTED RESISTANCE
C **********************************************************************
      IF(IMOM .NE. 1) GO TO 100
      VXTEMP=VXL
      IF(NSTEP .LE. 20) GO TO 15
      IF(VXL .GT. -1.E-10 .AND. VXL .LT. 0.) VXL=-1.E-10
      IF(VXL .LT. +1.E-10 .AND. VXL .GE. 0.) VXL=+1.E-10
   15 CONTINUE
      IF(VXL .EQ. 0.) GO TO 50
      IF(XVOL .EQ. 0.) GO TO 50
      AWROD=PHI*DIAR*XYDZ*XROD(I)
      AWIRE=PHI*DIAW*XYDZ/COS(PI)
      AWIRE=AWIRE*XLENG(J,I)
      AWALL=1.E-4*XWALL(I)
      AWSUB=AWROD+AWALL
      AWTOT=AWROD+AWIRE+AWALL
      IF(AWTOT .EQ. 0.) GO TO 50
C --------------------------------------------------------------------
C X COMPONENT FORCE OF RODS
C --------------------------------------------------------------------
      VXG=VXL*XAREA/AREAG
      IF(XAREA .LT. AREAG) VXG=VXL
      XDV=4.*XVOL/AWTOT
      REX=ROLA*XDV*ABS(VXG)/VISLA
      IF(REX .LE. RECRT) FRICL=DD/REX
      IF(REX .GT. RECRT) FRICL=EE/REX**FF
      COEF1=XDV**.4*SL**.6/STX
      FRX=.125*FRICL*ROLA*VXG*ABS(VXG)*COEF1*AWSUB
C --------------------------------------------------------------------
C  TANGENTIAL FORCE OF WIRE SPACERS
C --------------------------------------------------------------------
      IF(AWIRE .LT. 1.E-20) GO TO 20
      REXV=ROLA*XDE*VL/VISLA
      IF(REXV .LE. RECRA) FRICA=AA/REXV
      IF(REXV .GT. RECRA) FRICA=BB/REXV**CC
      ANGLE=XYANGLE(J)*PHI/12.
      VLCOS=VXL*SIN(PI)*COS(ANGLE) + VYL*SIN(PI)*SIN(ANGLE)
     1       + VZL*COS(PI)
```

```
      FWT=.125*FRICA*ROLA*VL*VLCOS*AWIRE
C ----------------------------------------------------------------
C  NORMAL FORCE OF WIRE SPACERS
C ----------------------------------------------------------------
      VN=-VXL*COS(PI)*COS(ANGLE) - VYL*COS(PI)*SIN(ANGLE)
    1    + VZL*SIN(PI)
      REVN=ROLA*XDE*ABS(VN)/VISLA
      IF(REVN .LT. 1.) REVN=1.
      CD=1.+10./REVN**.6667
      FWN=.5*CD*COEFP*ROLA*VN*ABS(VN)*DIAW*XYDZ*XLENG(J,I)/COS(PI)
      GO TO 40
   20 FWT=0.
      FWN=0.
   40 CONTINUE
      FXTOT=FRX+(FWT*SIN(PI)-FWN*COS(PI))*COS(ANGLE)
      RESX=FXTOT/XVOL
      FWL=RESX/VXL
      GO TO 60
   50 FWL=0.
   60 CONTINUE
      FWV=0.
      VXL=VXTEMP
      RETURN
C ****************************************************************
C  Y-DIRECTION DISTRIBUTED RESISTANCE
C ****************************************************************
  100 CONTINUE
      IF(IMOM .NE. 2) GO TO 200
      VYTEMP=VYL
      IF(NSTEP .LE. 20) GO TO 115
      IF(VYL .GT. -1.E-10 .AND. VYL .LT. 0.) VYL=-1.E-10
      IF(VYL .LT. +1.E-10 .AND. VYL .GE. 0.) VYL=+1.E-10
  115 CONTINUE
      IF(VYL .EQ. 0.) GO TO 150
      IF(YVOL .EQ. 0.) GO TO 150
      AWROD=PHI*DIAR*XYDZ*YROD(I)
      AWIRE=PHI*DIAW*XYDZ*YLENG(J,I)/COS(PI)
      AWALL=1.E-4*YWALL(I)
      AWSUB=AWROD+AWALL
      AWTOT=AWROD+AWIRE+AWALL
      IF(AWTOT .EQ. 0.) GO TO 150
C ----------------------------------------------------------------
C  Y COMPONENT FORCE OF RODS
C ----------------------------------------------------------------
      VYG=VYL*YAREA/AREAG
      IF(YAREA .LT. AREAG) VYG=VYL
      YDV=4.*YVOL/AWTOT
      REY=ROLA*YDV*ABS(VYG)/VISLA
      IF(REY .LE. RECRT) FRICL=DD/REY
      IF(REY .GT. RECRT) FRICL=EE/REY**FF
      COEF2=YDV**.4*SL**.6/STY
      FRY=.125*FRICL*ROLA*VYG*ABS(VYG)*COEF2*AWSUB
C ----------------------------------------------------------------
C  TANGENTIAL FORCE OF WIRE SPACERS
```

```
C  ------------------------------------------------------------
       IF(AWIRE .LT. 1.E-20) GO TO 120
       REYV=ROLA*YDE*VL/VISLA
       IF(REYV .LE. RECRA) FRICA=AA/REYV
       IF(REYV .GT. RECRA) FRICA=BB/REYV**CC
       ANGLE=XYANGLE(J)*PHI/12.
       VLCOS=VXL*SIN(PI)*COS(ANGLE) + VYL*SIN(PI)*SIN(ANGLE)
     1       + VZL*COS(PI)
       FWT=.125*FRICA*ROLA*VL*VLCOS*AWIRE
C  ------------------------------------------------------------
C  NORMAL FORCE OF WIRE SPACERS
C  ------------------------------------------------------------
       VN= -VXL*COS(PI)*COS(ANGLE) - VYL*COS(PI)*SIN(ANGLE)
     1     + VZL*SIN(PI)
       REVN=ROLA*YDE*ABS(VN)/VISLA
       IF(REVN .LT. 1.) REVN=1.
       CD=1.+10./REVN**.6667
       FWN=.5*CD*COEFP*ROLA*VN*ABS(VN)*DIAW*XYDZ*YLENG(J,I)/COS(PI)
       GO TO 140
   120 FWT=0.
       FWN=0.
   140 CONTINUE
       FYTOT=FRY+(FWT*SIN(PI)-FWN*COS(PI))*SIN(ANGLE)
       RESY=FYTOT/YVOL
       FWL=RESY/VYL
       GO TO 160
   150 FWL=0.
   160 CONTINUE
       FWV=0.
       VYL=VYTEMP
       RETURN
C  ****************************************************************
C   Z-DIRECTION DISTRIBUTED RESISTANCE
C  ****************************************************************
   200 CONTINUE
       IF(IMOM .NE. 3) GO TO 999
       IF(VZL .EQ. 0.) GO TO 250
       IF(ZDE .EQ. 0.) GO TO 250
       AWROD=PHI*DIAR*ZDZ*ZROD(I)
       AWIRE=PHI*DIAW*ZDZ*ZLENG(J,I)/COS(PI)
       AWALL=1.E-4*ZWALL(I)
       AWSUB=AWROD+AWALL
       AWTOT=AWSUB+AWIRE
       IF(AWTOT .EQ. 0.) GO TO 250
C  ------------------------------------------------------------
C   AXIAL FORCE OF RODS
C  ------------------------------------------------------------
       REV=ROLA*ZDE*VL/VISLA
       IF(REV .LE. RECRA) FRICA=AA/REV
       IF(REV .GT. RECRA) FRICA=BB/REV**CC
       FRA=.125*FRICA*ROLA*VZL*VL*AWSUB
C  ------------------------------------------------------------
C   TANGENTIAL FORCE OF WIRE SPACERS
C  ------------------------------------------------------------
```

```
      IF(AWIRE .LT. 1.E-20) GO TO 220
      ANGLE=ZANGLE(J)*PHI/12.
      VLCOS=VXL*SIN(PI)*COS(ANGLE) + VYL*SIN(PI)*SIN(ANGLE)
     1      + VZL*COS(PI)
      FWT=.125*FRICA*ROLA*VL*VLCOS*AWIRE
C    ----------------------------------------------------------------
C    NORMAL FORCE OF WIRE SPACERS
C    ----------------------------------------------------------------
      VN= - VXL*COS(PI)*COS(ANGLE) - VYL*COS(PI)*SIN(ANGLE)
     1      + VZL*SIN(PI)
      REVN=ROLA*ZDE*ABS(VN)/VISLA
      AVN=ABS(VN)
      REVN=ROLA*ZDE*AVN/VISLA
      IF(REVN .LT. 1.E-4) GO TO 210
      CD=1.+10./REVN**.6667
      FWN=.5*CD*COEFP*ROLA*VN*AVN*DIAW*ZDZ*ZLENG(J,I)/COS(PI)
      GO TO 240
  210 FWN=5.*COEFP*ROLA**.3333*VISLA**.6667*AVN**.3333*VN/
     1      ZDE**.6667*AWIRE/PHI
      GO TO 240
  220 FWT=0.
      FWN=0.
  240 CONTINUE
      FZTOT=FRA+FWT*COS(PI)+FWN*SIN(PI)
      RESZ=FZTOT/ZVOL
      FWL=RESZ/VZL
      GO TO 260
  250 FWL=0.
  260 CONTINUE
      FWV=0.
      RETURN
  999 WRITE(6,1000)
 1000 FORMAT(1H1,//////,5X,"NO FLAG FOR MOMENTUM CALCULATION")
      END
```

APPENDIX D

D.1 Input Data Description of the RODCON Code

The input format used in the RODCON code is free format except the title card.

Group 1   Title description, format 20A4

Group 2   Run option : indi, ivel, imix, iprint

    indi   = option for the cell geometry
            = 0, uniform heat generation in the fuel region
            = 1, uniform heat flux at the inner BN surface
    ivil   = option for the flow split
            = 1, equal flow split
            = 2, flow split as $u = (D_e/De_T)^{5/7}$
    imix   = option for the energy mixing
            = 0, no mixing
            = 1, mixing included
  iprint   = option for the printout
            = 0, print both temperature and heat flux
            = 1, print only temperature field

Group 3   Integer parameter: ni, nk, mmax, it, nt

    ni   = maximum number of the collocation points
    nk   = maximum number of terms
  mmax   = geometry option
            = 0, unit cell
            = 1, 7-pin bundle
            = 2, 19-pin bundle
            = 3, 37-pin bundle
            = 4, 61-pin bundle
            = 5, 91-pin bundle
    it   = maximum number of iterations
    nt   = maximum number of the angular intervals to be printed

Group 4   Geometry parameters: pd, t, h, ve, daw, da, bis

    pd   = P/D, pitch to diameter ratio
    t   = a/b, clad inner to outer radius ratio
    h   = ro/b, BN inner to clad outer radius ratio
    ve   = dimensionless wall distance
   daw   = BN (or fuel) to clad thermal conductivity ratio
    da   = clad to coolant thermal conductivity ratio
   bis   = dimensionless gap conductance at the BN (or fuel) and clad interface

Group 5   Power peaking factors: q(k)

D.2 Fortran Listing of the RODCON Code

```
c  **************************************************
c
c        RODCON is a computer code to solve detailed
c         temperature distribution in rod bundle.
c        The RODCON code was modified from the code of
c        Yeung and Wolf by Tae Sun Ro on March, 1985
c
c  **************************************************
c
c        1/12 rod bundle simulation
c
       implicit real*8 (a-h,o-z)
       double precision pi
       common /inter/ indi,ivel,imix,iprint,ntitle(20)
       common /bun1/ w(10),z(10)
       common /bun2/ daw,da,pd,t,ve,bis,pi,yt,dh,eps,h
       common /bun3/ q(12),mt(12)
       common /split/ uint,uedge,ucorn,aedgew,aedgei,acorn,aint
       common /temp/ tht(13)
       dimension a(7000)
       pi=3.1415926536
       eps=1.0d-12
c -----------------------------------------------
c     Read Input Data
c -----------------------------------------------
       read(5,100) (ntitle(i),i=1,20)
 100   format(20a4)
       read(5,*) indi,ivel,imix,iprint
       read(5,*) ni,nk,mmax,it,nt
       read(5,*) pd,t,h,ve,daw,da,bis
c -----------------------------------------------
c  z(i) = Roots of the Legendre Polynomials
c -----------------------------------------------
       z(1)=0.14887
       z(2)=-z(1)
       z(3)=0.4334
       z(4)=-z(3)
       z(5)=0.67941
       z(6)=-z(5)
       z(7)=0.86506
       z(8)=-z(7)
       z(9)=0.97391
       z(10)=-z(9)
c -----------------------------------------------
c  w(i) = Weights of the Gauss-Legendre Quadrature
c -----------------------------------------------
       w(1)=0.29552
       w(2)=w(1)
       w(3)=0.26927
       w(4)=w(3)
       w(5)=0.21909
       w(6)=w(5)
       w(7)=0.14945
       w(8)=w(7)
       w(9)=0.066671
       w(10)=w(9)
       if(mmax .eq. 0) go to 20
       go to (1,2,3,4,5) mmax
 1     kk=2
       go to 10
```

```
   2 kk=4
     go to 10
   3 kk=6
     go to 10
   4 kk=9
     go to 10
   5 kk=12
     go to 10
  20 kk=1
  10 continue
     read(5,*) (q(k),k=1,kk)
     if(ivel .ne. 0) go to 40
     read(5,*) uint,uedge,ucorn
  40 continue
     mz=(nk*(nk+1))/2
     mk=nk-1
     rod=1.0
     if(mmax .eq. 0) go to 30
     do 7 k=1,mmax
   7 rod=rod+6.*k
  30 continue
     af=(mmax*pd*1.732/2.+ve/2.)*(mmax*pd+ve/1.732)-rod*pi/12.
     yt=af/(rod*pi/12.)
     dh=af/(rod*pi/12.+(mmax*pd+ve/1.732)/2.)
     if(mmax .eq. 0) dh=12.*af/pi
     jphi=10
     jyj=jphi+ni
     jgjn=jyj+ni
     jr=jgjn+ni*nk
     jgtg=jr+nk
     jaux=jgtg+mz
     jdy=jaux+mk
     jr1=jdy+kk*nk
     jyp=jr1+nk
     jgp=jyp+ni
     jx=jgp+ni*nk
     jf=jx+nk
     jg=jf+nk
     jdf=jg+nk
     jdg=jdf+kk*nk
     jb=jdg+kk*nk
c
     call couple(mmax, ni,nk,mz,mk,kk,a(jphi),a(jyj),a(jgjn),a(jr),a(jg
    1tg),a(jaux),a(jdy),a(jr1),a(jyp),a(jgp),a(jx),a(jf),a(jg),
    2 a(jdf),a(jdg),it,nt)
c
     if(imix .eq. 0) go to 999
c
     call subchannel
c
 999 stop
     end
c
c *************************************************************************
     subroutine couple(mmax, ni,nk,mz,mk,kk,phi,yj,gjn,r,gtg,aux,dyn,r1
    1,yp,gp,x,fn,gn,dfn,dgn,it,nt)
c *************************************************************************
c
     implicit real*8 (a-h,o-z)
     common /inter/ indi,ivel,imix,iprint,ntitle(20)
```

```
      common /bun1/ w(10),z(10)
      common /bun2/ daw,da,pd,t,ve,bis,pi,yt,dh,eps,h
      common /bun3/ q(12),mt(12)
      common /split/ uint,uedge,ucorn,aedgew,aedgei,acorn,aint
      common /temp/ tht(13)
      dimension phi(ni),yj(ni),gjn(ni,nk),r(nk),gtg(mz),aux(mk),dyn(kk,n
     1k),r1(nk),x(nk),yp(ni),gp(ni,nk),fn(nk),gn(nk),dfn(kk,nk),
     2 dgn(kk,nk)
      dimension at3(12),afa(12),adu(12),adg(12,31),ara(12,31),
     1          atv(12,31),aq1(12,31),atc2(12,31),aq2(12,31),
     2          atk2(12,31),aq3(12,31),icount(12,6),tb(12,6),
     3          aa(12),aa1(12),ca(12),aflow(12),zcon(12),velo(12),
     4          btk2(12,31),btc2(12,31),btv(12,31),dt(12)
      dimension atbn1(12,31),atbn2(12,31),btbn1(12,31),btbn2(12,31)
      dimension ai(8),al(8),ab(8),ai1(8),al1(8),ab1(8),ap(8),mj(10)
      dimension tnorm(12,12),nois(12)
c
      write(6,100) (ntitle(i),i=1,20)
      if(mmax .eq. 0) go to 1060
      go to (1010,1020,1030,1040,1050) mmax
 1010 write (6,101)
      go to 1060
 1020 write(6,102)
      go to 1060
 1030 write(6,103)
      go to 1060
 1040 write(6,104)
      go to 1060
 1050 write(6,105)
 1060 write(6,1070) indi,ivel,imix,iprint,ni,nk,mmax,it,nt
      write(6,1080) pd,t,h,ve,daw,da,bis,(q(k),k=1,kk)
      if(ivel .eq. 0) write(6,1090) uint,uedge,ucorn
      write(6,106) ni,nk,it
      write(6,111) pd,t,ve
      write(6,118) h
      write(6,112) daw,da,bis
      write(6,114)
      write(6,273) z
      write(6,115)
      write(6,273) w
  100 format(1h1,//,2x,20a4,//,1x," listing of input parameters",
     1 //)
  101 format("   7-rod anaysis ",/)
  102 format("  19-rod anaysis ",/)
  103 format("  37-rod anaysis ",/)
  104 format("  61-rod anaysis ",/)
  105 format(" 91-rod anaysis ",/)
  106 format("   max no of points= ",i5,5x," max no of terms =   ",
     1 i5,5x,"  no of iterations = ",i5,5x,/)
  111 format(" p/d = ",f12.5,5x," a/b = ",f12.5,5x," 2w/d = ",
     2 f12.5,/)
  112 format(" kf/k = ",f12.5,5x," k/kc = ",f12.5,5x," bis = ",
     1       e12.5,/)
  114 format(" roots of legendre polynomials ",/)
  115 format(/," weights of gauss-legendre quadrature ",/)
  118 format(" r1/b= ",f12.5,/)
 1070 format(1h0,3x," Input Data ",/,5x,9(i5,3x),/)
 1080 format(5x,6(f12.5),/,5x,e12.5,5x,12(f12.5),/)
 1090 format(5x,3(f12.5,5x))
c
```

```
      if(mmax .eq. 1) kmax=2
      if(mmax .eq. 2) kmax=4
      if(mmax .eq. 3) kmax=6
      if(mmax .eq. 4) kmax=9
      if(mmax .eq. 5) kmax=12
c
c      start of iteration
c
      do 911 ij=1,12
      do 911 jk=1,6
      tb(ij,jk)=0.
      icount(ij,jk)=0
  911 continue
      do 1000 ki=1,it
      if(ki .ge. it) write(6,121) ki
  121 format(1h1," iteration ",i5,/)
      mm=mmax
 2000 nn=mm
c
c       cell identification
c
 3000 call type (mm,nn,mmax,k,ik,cf,xc,yc,ax)
      call chan (k,ik,is,ai,al,ab,u)
      call pdtn (ik,is,mj,np,lf)
      if(mmax .eq. 0) u=1.
      if(ki .eq. 1) u=1.
      nf=lf
      call ntb (mmax,ik,jb)
      if(ki.gt.1) nf=lf-jb
      if(ik .ge. 7) nf=nf/2
      mt(k)=nf
      ynt=yt*q(k)/u
      if(ki-1) 7,7,8
    7 do 9 n=1,nk
      a=cf*n
      call coeff(a,cn1,cn2)
      dfn(k,n)=cn1
      dgn(k,n)=cn2
    9 continue
    8 do 10 n=1,nk
      fn(n)=dfn(k,n)
   10 gn(n)=dgn(k,n)
      if(ki .ge. it) write(6,122) k,ik,q(k),u
      if(ki .eq. it) velo(k)=u
  122 format(///," cell ",i4,5x," type ",i5,5x," heat rate=",
     1    f10.4,5x," flow = ",f10.4,/)
c
c       determination of collocation points
c
      call points (is,np,mj,ai,al,ab,phi)
      jj=0
      ic=1
      do 4000 i=1,is
      jm=mj(i)
c
c           identifying neighboring cell and boundary condition
c
      if(mmax .eq. 0) go to 307
      call neigh (mmax,mm,nn,ik,i,m1,n1)
      go to 308
```

```fortran
      307 m1=-1
          n1=-1
      308 continue
          if(m1-mm) 300,320,310
      300 ib=1
          go to 350
      310 ib=2
          go to 350
      320 if(n1-nn) 330,330,340
      330 ib=1
          go to 350
      340 ib=2
      350 if((m1.eq.-1.).and.(n1.eq.-1.)) ib=0
          if(ki.eq.1) ib=0
          if(ib.eq.0) go to 63
          call type (m1,n1,mmax,k1,ik1,cf1,x1,y1,a1)
          call chan (k1,ik1,is1,ai1,al1,ab1,u1)
          if(ki .eq. 1) u1=1.
          yt1=yt*q(k1)/u1
          nf1=mt(k1)
          do 22 n=1,nf
          r(n)=dyn(k,n)
          if(ik-7) 22,210,210
      210 r(nf+n)=dyn(k,nf+n)
       22 continue
          do 74 n=1,nf1
          r1(n)=dyn(k1,n)
          if(ik1-7) 74,76,76
       76 r1(nf1+n)=dyn(k1,nf1+n)
       74 continue
c
c         construction of the coefficient matrix
c
       63 do 61 j=1,jm
          jp=j+jj
          rh=ai(i)/dcos(phi(jp)-al(i))
          if(ib-1) 60,78,78
       78 xx=xc+rh*dcos(phi(jp)+ax)
          yy=yc+rh*dsin(phi(jp)+ax)
          rh1=dsqrt((xx-x1)**2+(yy-y1)**2)
          ph1=-1.*a1+datan((yy-y1)/(xx-x1))
          if((xx-x1).le.0.0) ph1=-1.*a1+pi+datan((yy-y1)/(xx-x1))
          if(ib-1) 73,73,75
c
c            coupling by using continuity of temperature
c
       73 call temp (3,ik,cf,nf,r,ynt,rh,phi(jp),tt)
          call temp (3,ik1,cf1,nf1,r1,yt1,rh1,ph1,t1)
          vind=0.
          if(indi .eq. 0) vind=1./(bis*da*daw)
          yj(jp)=.5*(tt*q(k)+t1*q(k1))-q(k)*((rh**2-1.)/(2.*ynt)-(1./ynt+1.)
        1    *dlog(rh)+dlog(t)/da-vind)
          if(jb.eq.0) go to 34
          do 36 nb=1,jb
          if(nb.eq.ic) go to 31
          gjn(jp,nb)=0.0
          go to 36
       31 gjn(jp,nb)=1.0
       36 continue
       34 do 62 n=1,nf
```

```
      a=cf*n
   62 gjn(jp,n+jb)=(fn(n)*rh**(-a)+gn(n)*rh**a)*dcos(a*phi(jp))*
     1              q(k)/a
      if(ik .lt. 7) go to 61
      do 27 n=1,nf
      a=cf*n
   27 gjn(jp,nf+jb+n)=(fn(n)*rh**(-a)+gn(n)*rh**a)*dsin(a*phi(jp))*
     2                q(k)/a
      go to 61
   75 i1=1
   82 if(ph1-ab1(i1+1)) 80,80,81
   81 i1=i1+1
      go to 82
c
c         coupling by using continuity of heat flux
c
   80 call flux (3,ik1,cf1,nf1,r1,yt1,al1(i1),rh1,ph1,q2n)
      q2n=q2n*q(k1)/q(k)
      go to 77
   60 q2n=0.0
   77 if(indi .eq. 0)
     2yj(jp)=((1.+1./ynt)-(rh**2)/ynt)*dcos(phi(jp)-al(i))+rh*q2n
      if(indi .eq. 1) yj(jp)=((1.+1./ynt)-(rh**2)/ynt)*dcos(phi(jp)
     3        -al(i))+rh*q2n/h
      if(ki-1) 52,52,54
   52 continue
      do 29 n=1,nf
      a=cf*n
      aph11=(a-1.)*phi(jp)+al(i)
      aph12=(a+1.)*phi(jp)-al(i)
   29 gjn(jp,n)=gn(n)*rh**a*dcos(aph11)-fn(n)*rh**(-a)*dcos(aph12)
      if(ik .lt. 7) go to 61
      do 28 n=1,nf
      a=cf*n
      aph11=(a-1.)*phi(jp)+al(i)
      aph12=(a+1.)*phi(jp)-al(i)
   28 gjn(jp,nf+n)=gn(n)*rh**a*dsin(aph11)-fn(n)*rh**(-a)*dsin(aph12)
      go to 61
   54 do 32 nb=1,jb
   32 gjn(jp,nb)=0.0
      do 72 n=1,nf
      a=cf*n
      aph11=(a-1.)*phi(jp)+al(i)
      aph12=(a+1.)*phi(jp)-al(i)
   72 gjn(jp,n+jb)=gn(n)*rh**a*dcos(aph11)-fn(n)*rh**(-a)*dcos(aph12)
      if(ik .lt. 7) go to 61
      do 19 n=1,nf
      a=cf*n
      aph11=(a-1.)*phi(jp)+al(i)
      aph12=(a+1.)*phi(jp)-al(i)
   19 gjn(jp,nf+jb+n)=gn(n)*rh**a*dsin(aph11)-fn(n)*rh**(-a)*
     1                dsin(aph12)
   61 continue
      if(ib.eq.1) ic=ic+1
 4000 jj=jj+mj(i)
c
c         solving the unknown vector
c
      call size (ni,nk,mk,mz,np,lf,gjn,yj,gp,yp,gtg,aux,eps,r)
      if(ki .ge. it) write(6,401)
```

```fortran
  401 format(/," coefficients for the fourier series ",/)
      if(ki .ge. it) write(6,273) (r(n),n=1,lf)
      do 21 n=1,nf
      dyn(k,n)=r(n+jb)
      x(n)=r(n+jb)
      if(ik-7) 21,23,23
   23 dyn(k,nf+n)=r(jb+nf+n)
      x(nf+n)=r(jb+nf+n)
   21 continue
      if(ki .lt. it) go to 15
c
c         determination of nusselt no
c
      call tavg (1,is,ab,ik,nf,fn,gn,x,ai,al,cf,ynt,t3,fa)
      vind=0.
      if(indi .eq. 0) vind=1./(da*daw*bis)
      du=2./(dlog(t)/da-vind-t3)
      write(6,51) t3,fa,du
      at3(k)=t3
      afa(k)=fa
      adu(k)=du
   51 format(/," t mean = ",f12.5,5x," area = ",f12.5,5x,
     1   " nu = ",f12.5)
c
c         azimuthal distribution of temperature and heat flux
c
  650 format(/," azimuthal distribution of temperature and heat flux ")
  651 format(/,1x," deg.   c/b      tembn in    tbn half ",1x,
     1         "tclad  in  tclad out      t(c)         q(c)    ",/)
  654 format(/,1x," deg.   c/b      tclad in   qclad in ",1x,
     1         "tclad out  qclad out      t(c)         q(c)    ",/)
      i=1
      do 65 j=1,nt
      ph=(j-1)*(ab(is+1)-ab(1))/(nt-1)
      if(ph.gt.ab(i+1)) i=i+1
      ra=ai(i)/dcos(ph-al(i))
      fs=t
      halfh=h+0.5*(t-h)
      if(iprint .eq. 1) call temp(1,ik,cf,nf,x,ynt,h,ph,tbn1)
      if(iprint .eq. 1) call temp(1,ik,cf,nf,x,ynt,halfh,ph,tbn2)
      call temp (2,ik,cf,nf,x,ynt,fs,ph,tv)
      call temp (2,ik,cf,nf,x,ynt,1.d0,ph,tc2)
      call temp (3,ik,cf,nf,x,ynt,ra,ph,tk2)
      call flux (1,ik,cf,nf,x,ynt,al(i),fs,ph,q1)
      call flux (2,ik,cf,nf,x,ynt,al(i),1.d0,ph,q2)
      call flux (3,ik,cf,nf,x,ynt,al(i),ra,ph,q3)
      dg=ph*180./pi
      if(mmax .eq. 0 .and. iprint .eq. 0)
     1write(6,117) dg,ra,tv,q1,tc2,q2,tk2,q3
      if(mmax .eq. 0 .and. iprint .eq. 1)
     1  write(6,117) dg,ra,tbn1,tbn2,tv,tc2,tk2,q3
      adg(k,j)=dg
      ara(k,j)=ra
      atv(k,j)=tv
      aq1(k,j)=q1
      atc2(k,j)=tc2
      aq2(k,j)=q2
      atk2(k,j)=tk2
      aq3(k,j)=q3
      atbn1(k,j)=tbn1
```

```
      atbn2(k,j)=tbn2
      if(j .eq. 1) go to 65
      if(ph .eq. ab(i+1)) go to 65
      icount(k,i)=icount(k,i)+1
      tb(k,i)=tb(k,i)+tk2
   65 continue
      write(6,700)
  700 format(/," calculational results for lumped parameter ",/)
      nij=0
      do 15 i=1,is
c
c         lumped temperature calculation for subchannel geometry
c
      ap(1)=ab(i)
      ap(2)=al(i)
      if(dabs(ap(1)-ap(2)).le.1.0d-3) go to 107
      call tavg (i,i,ap,ik,nf,fn,gn,x,ai,al,cf,ynt,t1,f1)
      write(6,153) i,ap(1),ap(2),f1,t1
      nij=nij+1
      if(k .eq. kmax .and. nij .eq. 1) acorn=f1
      if(k .eq. kmax .and. nij .eq. 2) aedgew=f1
      if(k .eq. kmax .and. nij .eq. 3) aedgei=f1
      if(k .eq. kmax .and. nij .eq. 4) aint=f1
      tnorm(k,nij)=t1
  107 ap(1)=al(i)                                          .
      ap(2)=ab(i+1)
      if(dabs(ap(1)-ap(2)).le.1.0d-3) go to 15
      call tavg (i,i,ap,ik,nf,fn,gn,x,ai,al,cf,ynt,t2,f2)
      write(6,153) i,ap(1),ap(2),f2,t2
      nij=nij+1
      if(k .eq. kmax .and. nij .eq. 1) acorn=f2
      if(k .eq. kmax .and. nij .eq. 2) aedgew=f2
      if(k .eq. kmax .and. nij .eq. 3) aedgei=f2
      if(k .eq. kmax .and. nij .eq. 4) aint=f2
      tnorm(k,nij)=t2
  153 format(1x," side",i2,1x," from",f8.4,1x,"to",f8.4,
     1    1x," area =",f8.4,1x," tavg = ",f8.4)
   15 continue
      if(ki .ge. it) nois(k)=nij
   14 nn=nn-2
      if(nn) 142,3000,3000
  142 mm=mm-1
      if(mm) 1000,2000,2000
 1000 continue
c
c         normalization procedure
c
c
c
      if(mmax .eq. 0) go to 890
      if(mmax .eq. 1) go to 811
      dt(1)=q(1)*tb(1,1)/dble(icount(1,1))-q(2)*tb(2,4)/
     1      dble(icount(2,4))
      dt(2)=q(2)*tb(2,2)/dble(icount(2,2))-q(3)*tb(3,1)/
     2      dble(icount(3,1))
      if(mmax .eq. 2) go to 812
      dt(3)=q(3)*tb(3,2)/dble(icount(3,2))-q(4)*tb(4,3)/
     1      dble(icount(4,3))
      if(mmax .eq. 3) go to 813
      dt(4)=q(3)*tb(3,3)/dble(icount(3,3))-q(5)*tb(5,6)/
     2      dble(icount(5,6))
```

```fortran
      dt(5)=q(5)*tb(5,2)/dble(icount(5,2))-q(6)*tb(6,3)/
     1        dble(icount(6,3))
      dt(6)=q(5)*tb(5,4)/dble(icount(5,4))-q(7)*tb(7,1)/
     2        dble(icount(7,1))
      if(mmax .eq. 4) go to 814
      dt(7)=q(7)*tb(7,2)/dble(icount(7,2))-q(8)*tb(8,5)/
     1        dble(icount(8,5))
      dt(8)=q(8)*tb(8,2)/dble(icount(8,2))-q(9)*tb(9,3)/
     2        dble(icount(9,3))
      if(mmax .eq. 5) go to 815
      dt(9)=q(7)*tb(7,3)/dble(icount(7,3))-q(10)*tb(10,6)/
     3        dble(icount(10,6))
      dt(10)=q(8)*tb(8,3)/dble(icount(8,3))-q(11)*tb(11,6)/
     1        dble(icount(11,6))
      dt(11)=q(11)*tb(11,2)/dble(icount(11,2))-q(12)*tb(12,3)/
     2        dble(icount(12,3))
      go to 820
  811 dt(1)=q(1)*tb(1,1)/dble(icount(1,1))-q(2)*tb(2,3)/
     1        dble(icount(2,3))
      go to 820
  812 dt(3)=q(3)*tb(3,2)/dble(icount(3,2))-q(4)*tb(4,2)/
     1        dble(icount(4,2))
      go to 820
  813 dt(4)=q(3)*tb(3,3)/dble(icount(3,3))-q(5)*tb(5,5)/
     1        dble(icount(5,5))
      dt(5)=q(5)*tb(5,2)/dble(icount(5,2))-q(6)*tb(6,2)/
     1        dble(icount(6,2))
      go to 820
  814 dt(7)=q(7)*tb(7,2)/dble(icount(7,2))-q(8)*tb(8,4)/
     1        dble(icount(8,4))
      dt(8)=q(8)*tb(8,2)/dble(icount(8,2))-q(9)*tb(9,2)/
     2        dble(icount(9,2))
      go to 820
  815 dt(9)=q(7)*tb(7,3)/dble(icount(7,3))-q(10)*tb(10,5)/
     1        dble(icount(10,5))
      dt(10)=q(8)*tb(8,3)/dble(icount(8,3))-q(11)*tb(11,5)/
     1        dble(icount(11,5))
      dt(11)=q(11)*tb(11,2)/dble(icount(11,2))-q(12)*tb(12,2)/
     2        dble(icount(12,2))
  820 continue
      asum=0.
      aa(1)=0.
      if(mmax .gt. 2) go to 835
      ijmax=kmax-1
      do 830 ij=1,ijmax
      asum=asum+dt(ij)
  830 aa(ij+1)=asum
      go to 836
  835 do 837 ij=1,3
      asum=asum+dt(ij)
  837 aa(ij+1)=asum
      aa(5)=aa(3)+dt(4)
      aa(6)=aa(5)+dt(5)
      if(mmax .le. 3) go to 836
      aa(7)=aa(5)+dt(6)
      aa(8)=aa(7)+dt(7)
      aa(9)=aa(8)+dt(8)
      if(mmax .lt. 5) go to 836
      aa(10)=aa(7)+dt(9)
      aa(11)=aa(8)+dt(10)
```

```
      aa(12)=aa(11)+dt(11)
  836 continue
      do 840 ij=1,kmax
  840 aa1(ij)=aa(ij)-dt(1)
      fatot=0.
      do 845 ij=1,kmax
  845 fatot=fatot+afa(ij)*velo(ij)
      do 847 ij=1,kmax
  847 aflow(ij)=afa(ij)*velo(ij)/fatot
      zfl=0.
      zfl1=0.
      do 850 ij=1,kmax
      zfl=zfl+aa(ij)*aflow(ij)
  850 zfl1=zfl1+aa1(ij)*aflow(ij)
      ca(1)=aa1(1)-zfl1
      do 860 m=2,kmax
  860 ca(m)=aa(m)-zfl
      cacon=0.
      do 870 ij=1,kmax
  870 cacon=cacon+aflow(ij)*q(ij)*at3(ij)
c
      do 880 ij=1,kmax
      zcon(ij)=ca(ij)-cacon
      do 880 j=1,nt
      btk2(ij,j)=zcon(ij)+q(ij)*atk2(ij,j)
      btc2(ij,j)=zcon(ij)+q(ij)*atc2(ij,j)
      btv(ij,j)=zcon(ij)+q(ij)*atv(ij,j)
      btbn1(ij,j)=zcon(ij)+q(ij)*atbn1(ij,j)
      btbn2(ij,j)=zcon(ij)+q(ij)*atbn2(ij,j)
  880 continue
      do 890 ij=1,kmax
      write(6,931) ij
      write(6,932)
      if(iprint .eq. 0) write(6,654)
      if(iprint .eq. 1) write(6,651)
      do 897 j=1,nt
      if(iprint .eq. 0) write(6,117) adg(ij,j),ara(ij,j),btv(ij,j),
     1     aq1(ij,j),btc2(ij,j),aq2(ij,j),btk2(ij,j),aq3(ij,j)
  897 if(iprint .eq. 1) write(6,117) adg(ij,j),ara(ij,j),btbn1(ij,j),
     2     btbn2(ij,j),btv(ij,j),btc2(ij,j),btk2(ij,j),aq3(ij,j)
  890 continue
      write(6,898)
  898 format(/," conversion constants,  b-q.a ",/)
      do 899 ij=1,kmax
      iss=nois(ij)
      do 951 j=1,iss
  951 tnorm(ij,j)=zcon(ij)+q(ij)*tnorm(ij,j)
      write(6,943) ij,zcon(ij),q(ij)
      write(6,944) (tnorm(ij,j),j=1,iss)
  899 continue
  943 format(3x,"cell",i2,3x,"zcon=",e12.5,3x,"q=",f10.4)
  944 format(1x,6(4x,f8.4))
  932 format(/," normalized temperature distribution ")
  931 format(/," cell number performed normalization ",1x,i2)
  117 format(1x,f5.1,f7.3,6f11.5)
  273 format(8(2x,e12.5))
      if(imix .eq. 0) go to 999
c
c     subchannel analysis preparation
c
```

```fortran
c
      tht(1)=(tnorm(1,1)+tnorm(2,5)+tnorm(2,6))/3.
      tht(2)=(tnorm(2,3)+tnorm(2,4)+tnorm(3,1))/3.
      tht(3)=(tnorm(2,1)+tnorm(2,2)+tnorm(3,2)+tnorm(3,3)+tnorm(4,5)
     1       +tnorm(4,6))/6.
      tht(4)=(tnorm(3,6)+tnorm(5,10)+tnorm(5,11))/3.
      tht(5)=(tnorm(3,4)+tnorm(3,5)+tnorm(4,3)+tnorm(4,4)+tnorm(5,1)
     2       +tnorm(5,12))/6.
      tht(6)=(tnorm(4,1)+tnorm(4,2)+tnorm(5,2)+tnorm(5,3)+tnorm(6,5)
     3       +tnorm(6,6))/6.
      tht(7)=(uint*(tnorm(5,8)+tnorm(5,9))+uedge*tnorm(7,1))/
     4       (2.*uint+uedge)
      tht(8)=(uint*(tnorm(5,6)+tnorm(5,7))+uedge*(tnorm(7,2)+tnorm(7,3)
     5       +tnorm(8,8)+tnorm(8,9)))/(2.*uint+4.*uedge)
      tht(9)=(uint*(tnorm(5,4)+tnorm(5,5)+tnorm(6,3)+tnorm(6,4))
     6       +uedge*(tnorm(8,1)+tnorm(8,10)))/(2.*uedge+4.*uint)
      tht(10)=(uint*(tnorm(6,1)+tnorm(6,2))+uedge*(tnorm(8,2)
     7        +tnorm(8,3))+ucorn*(tnorm(9,4)+tnorm(9,5)))/
     8        (2.*uint+2.*uedge+2.*ucorn)
      tht(11)=(aedgew*(tnorm(7,5)+tnorm(8,6))+aedgei*(tnorm(7,4)
     9        +tnorm(8,7)))/(2.*aedgew+2.*aedgei)
      tht(12)=(uedge*(aedgew*tnorm(8,5)+aedgei*tnorm(8,4))
     1        +ucorn*(aedgew*tnorm(9,2)+aedgei*tnorm(9,3)))/
     2        ((uedge+ucorn)*(aedgew+aedgei))
      tht(13)=tnorm(9,1)
      write(6,973)
  973 format(1x,"dimensionless subchannel average temperature, thete",
     1  /,3x,"i",5x,"theta",/)
      write(6,974) (i,tht(i),i=1,13)
  974 format(3x,i2,f12.4,/)
c
  999 continue
      return
      end
c ***********************************************************
      subroutine size (ni,nk,mk,mz,np,nc,gjn,yj,g,y,gtg,aux,eps,r)
c ***********************************************************
      implicit real*8 (a-h,o-z)
      dimension gjn(ni,nk),yj(ni),y(np),g(np,nc),gtg(mz),aux(mk),r(nk)
      do 10 j=1,np
      y(j)=yj(j)
      do 10 n=1,nc
   10 g(j,n)=gjn(j,n)
      call gtprd (g,y,r,np,nc,1)
      call mata (g,gtg,np,nc,0)
      call dgels (r,gtg,nc,1,eps,ier,aux)
      return
      end
c ***********************************************************
      subroutine type (m,n,mmax,k,ik,cf,xc,yc,ax)
c ***********************************************************
      implicit real*8 (a-h,o-z)
      common /bun2/ daw,da,pd,t,ve,bis,pi,yt,dh,eps,h
      if(m-1) 30,40,50
   50 m1=m-1
      jsum=0
      do 15 j=1,m1
   15 jsum=jsum+j/2+1
      k=2+n/2+jsum
      go to 25
```

```fortran
   40 k=2
      go to 25
   30 k=1
   25 if(m.eq.0) go to 2
      if(m.eq.mmax) go to 4
      if(m.eq.1) go to 3
      if(n.eq.0) go to 8
      if(n.eq.1) go to 9
      if(n.eq.m) go to 10
      ik=9
      go to 20
    8 ik=6
      go to 20
    9 ik=10
      go to 20
   10 ik=5
      go to 20
    4 if(n.eq.0) go to 5
      if(n.eq.m) go to 7
      if(n.eq.1) go to 6
      ik=7
      go to 20
    7 ik=2
      go to 20
    6 ik=8
      go to 20
    5 ik=3
      go to 20
    3 ik=4
      go to 20
    2 ik=1
   20 cf=1.0
      if(ik.eq.1) cf=6.0
      xc=n*pd
      yc=m*2.*pd*dsin(pi/3.)
      ax=-1.*pi/2.
      if(m.eq.n) ax=pi/3.
      return
      end
c     ***********************************************************
      subroutine chan (k,ik,is,ai,al,ab,u)
c     ***********************************************************
      implicit real*8 (a-h,o-z)
      common /inter/ indi,ivel,imix,iprint,ntitle(20)
      common /bun2/ daw,da,pd,t,ve,bis,pi,yt,dh,eps,h
      common /bun3/ q(12),mt(12)
      common /split/ uint,uedge,ucorn,aedgew,aedgei,acorn,aint
      dimension ai(10),al(10),ab(10)
      if(ivel .ne. 0) go to 20
      if(aint .eq. 0.) go to 20
      u1=uint
      u2=(3.*uint*aint+uedge*(aedgew+aedgei))/(3.*aint+aedgew+
     1    aedgei)
      u3=(ucorn*acorn+2.*uint*aint+uedge*(aedgew+aedgei))/(acorn
     2    +2.*aint+aedgew+aedgei)
   20 continue
      go to (1,2,3,4,4,6,7,7,9,9),ik
    1 is=1
      ai(1)=pd
      al(1)=0.
```

```fortran
      ab(1)=0.0
      ab(2)=pi/6.
      d=(3.464*pd**2-pi)/pi
      if(ivel .eq. 0) u=u1
      go to 500
    2 is=3
      ai(1)=ve
      ai(2)=pd
      ai(3)=pd
      al(1)=pi/6.
      al(2)=pi*12./18.
      al(3)=pi
      ab(1)=0.
      ab(2)=al(1)+datan(ai(2)/ai(1))
      ab(3)=5.*pi/6.
      ab(4)=pi
      af=(pd+ve/1.732)*(1.732*pd/2.+ve/2.)-pd**2/3.464-pi/2.
      d=af/(pi/2.+(pd+ve/1.732)/2.)
      if(ivel .eq. 0) u=u3
      go to 500
    3 is=3
      ai(1)=pd
      ai(2)=pd
      ai(3)=ve
      al(1)=pi/6.
      al(2)=pi/2.
      al(3)=pi
      ab(1)=0.
      ab(2)=pi/3.
      ab(3)=pi/2.+datan(ve/ai(2))
      ab(4)=pi
      d=(pd*(1.732*pd/2.+ve)-pi/2.)/(pi/2.+pd/2.)
      if(ivel .eq. 0) u=u2
      go to 500
    4 is=4
      do 12 i=1,is
      ai(i)=pd
   12 al(i)=(i-1)*pi/3.
      ab(1)=0.
      ab(2)=pi/6.
      ab(3)=pi/2.
      ab(4)=5.*pi/6.
      ab(5)=pi
      d=(3.464*pd**2-pi)/pi
      if(ivel .eq. 0) u=u1
      go to 500
    6 is=3
      ab(1)=0.
      do 13 i=1,is
      ai(i)=pd
      al(i)=(i-1)*pi/3.+pi/6.
   13 ab(i+1)=pi*i/3.
      d=(3.464*pd**2-pi)/pi
      if(ivel .eq. 0) u=u1
      go to 500
    7 is=5
      ai(1)=pd
      ai(2)=pd
      ai(3)=ve
      ai(4)=pd
```

```fortran
      ai(5)=pd
      al(1)=pi/6.
      al(2)=pi/2.
      al(3)=pi
      al(4)=3.*pi/2.
      al(5)=11.*pi/6.
      ab(1)=0.
      ab(2)=pi/3.
      ab(3)=pi/2.+datan(ve/pd)
      ab(4)=2.*pi-ab(3)
      ab(5)=5.*pi/3.
      ab(6)=2.*pi
      d=(pd*(1.732*pd/2.+ve)-pi/2.)/(pi/2.+pd/2.)
      if(ivel .eq. 0) u=u2
      go to 500
    9 is=6
      ab(1)=0.
      do 14 i=1,is
      ai(i)=pd
      al(i)=pi*(i-1)/3.+pi/6.
   14 ab(i+1)=pi*i/3.
      d=(3.464*pd**2-pi)/pi
      if(ivel .eq. 0) u=u1
  500 continue
      if(ivel .eq. 1) u=1.
      if(ivel .eq. 2) u=(d/dh)**(5./7.)
      return
      end
c     ***********************************************************
      subroutine pdtn (ik,is,mj,np,nf)
c     ***********************************************************
      dimension mj(10)
      go to (1,2,3,4,4,6,7,7,9,9),ik
    1 mj(1)=4
      go to 100
    2 mj(1)=8
      mj(2)=6
      mj(3)=4
      go to 100
    3 mj(1)=8
      mj(2)=6
      mj(3)=4
      go to 100
    4 mj(1)=4
      mj(2)=8
      mj(3)=8
      mj(4)=4
      go to 100
    6 mj(1)=8
      mj(2)=8
      mj(3)=8
      go to 100
    7 mj(1)=8
      mj(2)=6
      mj(3)=8
      mj(4)=6
      mj(5)=8
      go to 100
    9 do 20 i=1,6
   20 mj(i)=8
```

```fortran
  100 np=0
      do 16 i=1,is
   16 np=np+mj(i)
      nf=np*2/3
      return
      end
c
c
      subroutine ntb (mmax,ik,jb)
c
      go to (1,2,3,4,5,6,7,8,9,10) ik
    1 jb=0
      return
    2 jb=2
      if(mmax.eq.1) jb=1
      return
    3 jb=1
      return
    4 jb=1
      return
    5 jb=2
      return
    6 jb=1
      return
    7 jb=3
      return
    8 jb=2
      return
    9 jb=3
      return
   10 jb=2
      return
      end
c
c
      subroutine points (isd,ni,nj,ai,al,ab,phi)
c
      implicit real*8 (a-h,o-z)
      common /bun2/ daw,da,pd,t,ve,bis,pi,yt,dh,eps,h
      common /bun3/ q(12),mt(12)
      dimension ai(10),al(10),ab(10),xs(10),ys(10),nj(10)
      dimension phi(ni)
      isc=isd+1
      xs(1)=ai(1)/dcos(al(1))
      ys(1)=0.
      do 150 i=2,isc
      xs(i)=(ai(i-1)/dcos(ab(i)-al(i-1)))*dcos(ab(i))
  150 ys(i)=(ai(i-1)/dcos(ab(i)-al(i-1)))*dsin(ab(i))
      k=1
      do 120 i=1,isd
      nis=nj(i)
      do 120 j=1,nis
      x=((nis-j+.5)*xs(i)+(j-.5)*xs(i+1))/nis
      y=((nis-j+.5)*ys(i)+(j-.5)*ys(i+1))/nis
      if(y) 10,10,20
   10 if(x.ge.0.) phi(k)=2.*pi+datan(y/x)
      if(x.lt.0.) phi(k)=pi+datan(y/x)
      go to 120
   20 if(x.ge.0.) phi(k)=datan(y/x)
      if(x.lt.0.) phi(k)=pi+datan(y/x)
```

```fortran
  120 k=k+1
      return
      end
c
c
      subroutine neigh (mmax,m,n,ik,is,mm,nn)
c
      go to (1,2,3,4,4,6,7,7,9,9),ik
    1 mm=m+1
      nn=n+1
      return
    2 go to (11,12,13),is
   11 mm=-1
      nn=-1
      return
   12 mm=m
      nn=n-2
      if(mmax.eq.1) mm=-1
      if(mmax.eq.1) nn=-1
      return
   13 mm=m-1
      nn=n-1
      return
    3 go to (14,15,16),is
   14 mm=m-1
      nn=n+1
      return
   15 mm=m
      nn=n+2
      return
   16 mm=-1
      nn=-1
      return
    4 go to (17,18,19,20),is
   17 mm=m+1
      nn=n+1
      return
   18 mm=m+1
      nn=n-1
      return
   19 mm=m
      nn=n-2
      if(ik.eq.4) mm=-1
      if(ik.eq.4) nn=-1
      return
   20 mm=m-1
      nn=n-1
      return
    6 go to (21,22,23),is
   21 mm=m-1
      nn=n+1
      return
   22 mm=m
      nn=n+2
      return
   23 mm=m+1
      nn=n+1
      return
    7 go to (24,25,26,27,28),is
   24 mm=m-1
```

```fortran
      nn=n+1
      return
   25 mm=m
      nn=n+2
      return
   26 mm=-1
      nn=-1
      return
   27 mm=m
      nn=n-2
      if(ik.eq.8) mm=-1
      if(ik.eq.8) nn=-1
      return
   28 mm=m-1
      nn=n-1
      return
    9 go to (29,30,31,32,33,34),is
   29 mm=m-1
      nn=n+1
      return
   30 mm=m
      nn=n+2
      return
   31 mm=m+1
      nn=n+1
      return
   32 mm=m+1
      nn=n-1
      return
   33 mm=m
      nn=n-2
      if(ik.eq.10) mm=-1
      if(ik.eq.10) nn=-1
      return
   34 mm=m-1
      nn=n-1
      return
      end
c
c
      subroutine gtprd (a,b,r,n,m,l)
c
      implicit real*8 (a-h,o-z)
      dimension a(1),b(1),r(1)
      ir=0
      ik=-n
      do 10 k=1,l
      ij=0
      ik=ik+n
      do 10 j=1,m
      ib=ik
      ir=ir+1
      r(ir)=0.
      do 10 i=1,n
      ij=ij+1
      ib=ib+1
   10 r(ir)=r(ir)+a(ij)*b(ib)
      return
      end
c
```

```fortran
c
      subroutine mata (a,r,n,m,ms)
c
      implicit real*8 (a-h,o-z)
      dimension a(1),r(1)
      do 70 k=1,m
      kx=(k*k-k)/2
      do 70 j=1,m
      if(j-k) 10,10,70
   10 ir=j+kx
      r(ir)=0.
      do 60 i=1,n
      if(ms) 20,40,20
   20 call loc (i,j,ia,n,m,ms)
      call loc (i,k,ib,n,m,ms)
      if(ia) 30,60,30
   30 if(ib) 50,60,50
   40 ia=n*(j-1)+i
      ib=n*(k-1)+i
   50 r(ir)=r(ir)+a(ia)*a(ib)
   60 continue
   70 continue
      return
      end
c
c
      subroutine loc (i,j,ir,n,m,ms)
      ix=i
      jx=j
      if(ms-1) 10,20,30
   10 irx=n*(jx-1)+ix
      go to 36
   20 if(ix-jx) 22,24,24
   22 irx=ix+(jx*jx-jx)/2
      go to 36
   24 irx=jx+(ix*ix-ix)/2
      go to 36
   30 irx=0
      if(ix-jx) 36,32,36
   32 irx=ix
   36 ir=irx
      return
      end
c
c
      subroutine dgels (r,a,m,n,eps,ier,aux)
c
      dimension a(1),r(1),aux(1)
      double precision r,a,aux,piv,tb,tol,pivi,eps
      if(m) 24,24,1
    1 ier=0
      piv=0.d0
      l=0
      do 3 k=1,m
      l=l+k
      tb=dabs(a(l))
      if(tb-piv) 3,3,2
    2 piv=tb
      i=l
      j=k
```

```fortran
    3 continue
      tol=eps*piv
      lst=0
      nm=n*m
      lend=m-1
      do 18 k=1,m
      if(piv) 24,24,4
    4 if(ier) 7,5,7
    5 if(piv-tol) 6,6,7
    6 ier=k-1
    7 lt=j-k
      lst=lst+k
      pivi=1.d0/a(i)
      do 8 l=k,nm,m
      ll=l+lt
      tb=pivi*r(ll)
      r(ll)=r(l)
    8 r(l)=tb
      if(k-m) 9,19,19
    9 lr=lst+(lt*(k+j-1))/2
      ll=lr
      l=lst
      do 14 ii=k,lend
      l=l+ii
      ll=ll+1
      if(l-lr) 12,10,11
   10 a(ll)=a(lst)
      tb=a(l)
      go to 13
   11 ll=l+lt
   12 tb=a(ll)
      a(ll)=a(l)
   13 aux(ii)=tb
   14 a(l)=pivi*tb
      a(lst)=lt
      piv=0.d0
      llst=lst
      lt=0
      do 18 ii=k,lend
      pivi=-aux(ii)
      ll=llst
      lt=lt+1
      do 15 lld=ii,lend
      ll=ll+lld
      l=ll+lt
   15 a(l)=a(l)+pivi*a(ll)
      llst=llst+ii
      lr=llst+lt
      tb=dabs(a(lr))
      if(tb-piv) 17,17,16
   16 piv=tb
      i=lr
      j=ii+1
   17 do 18 lr=k,nm,m
      ll=lr+lt
   18 r(ll)=r(ll)+pivi*r(lr)
   19 if(lend) 24,23,20
   20 ii=m
      do 22 i=2,m
      lst=lst-ii
```

```
              ii=ii-1
              l=a(lst)+.5d0
              do 22 j=ii,nm,m
              tb=r(j)
              ll=j
              k=lst
              do 21 lt=ii,lend
              ll=ll+1
              k=k+lt
   21         tb=tb-a(k)*r(ll)
              k=j+1
              r(j)=r(k)
   22         r(k)=tb
   23         return
   24         ier=-1
              return
              end
c
c
              subroutine tavg (k1,k2,ab,ik,nf,fn,gn,x,ai,al,cf,
     1          ynt,t3,fa)
c
              implicit real*8 (a-h,o-z)
              common /inter/ indi,ivel,imix,iprint,ntitle(20)
              common /bun2/ daw,da,pd,t,ve,bis,pi,yt,dh,eps,h
              dimension x(nf),fn(nf),gn(nf)
              dimension ab(10),ai(10),al(10)
              dtan(x)=dsin(x)/dcos(x)
              suma=0.
              sumb=0.
              sumc=0.
              sumy=0.
              i=1
              do 31 l=k1,k2
              call simps (simpa,ab(i),ab(i+1),nf,fn,gn,x,ai(l),al(l),
     1          cf,ynt,ik,1)
              suma=suma+(simpa*ai(l)**4)
              call simps (simpb,ab(i),ab(i+1),nf,fn,gn,x,ai(l),al(l),
     1          cf,ynt,ik,2)
              sumb=sumb+(simpb*ai(l)**2)
              call simps (simpc,ab(i),ab(i+1),nf,fn,gn,x,ai(l),al(l),
     1          cf,ynt,ik,3)
              sumc=sumc+simpc
              sumy=sumy+ai(l)*ai(l)*(dtan(ab(i+1)-al(l))-dtan(ab(i)-al(l)))
   31         i=i+1
              fa=(sumy-(ab(i)-ab(1)))/2.
              vind=0.
              if(indi .eq. 0) vind=1./(bis*da*daw)
              t3=-1./(2.*ynt)+dlog(t)/da-vind
              t3=t3+((suma-(ab(i)-ab(1)))/(8.*ynt)-(ynt+1.)*(sumb+
     1          (ab(i)-ab(1)))/(4.*ynt)+sumc)/fa
              return
              end
c
c
              subroutine simps (simp,xa,xb,nk,fn,gn,r,ai,al,cf,ynt,
     1          ik,ja)
c
              implicit real*8 (a-h,o-z)
              common /bun1/ w(10),z(10)
```

```fortran
      common /bun2/ daw,da,pd,t,ve,bis,pi,yt,dh,eps,h
      dimension r(nk),fn(nk),gn(nk)
      sump=0.
      do 2 i=1,10
      ph=(z(i)*(xb-xa)+(xa+xb))/2.
      go to (10,11,12,13),ja
   10 y=(1./dcos(ph-al))**4
      go to 2
   11 y=(2.*dlog(ai/dcos(ph-al))-1.)/(dcos(ph-al)**2)
      go to 2
   12 y=0.
      do 21 n=1,nk
      a=cf*n
      ap=ai/dcos(ph-al)
      g=gn(n)/(a+2.)*(ap**(a+2.)-1.)
      if(a.eq.2.) go to 22
      f=fn(n)/(2.-a)*(ap**(2.-a)-1.)
      go to 25
   22 f=fn(n)*dlog(ap)
   25 y=y+(g+f)*r(n)/a*dcos(a*ph)
      if(ik-7) 21,23,23
   23 y=y+(g+f)*r(nk+n)/a*dsin(a*ph)
   21 continue
      go to 2
   13 rh=ai/dcos(ph-al)
      call flux (3,ik,cf,nk,r,ynt,al,rh,ph,q2)
      y=q2*ai/(dcos(ph-al)**2)
    2 sump=sump+w(i)*y
      simp=sump*(xb-xa)/2.
      return
      end
c
c
      subroutine temp (ja,ik,cf,nk,r,ynt,p,ph,tdmp)
c
      implicit real*8 (a-h,o-z)
      common /inter/ indi,ivel,imix,iprint,ntitle(20)
      common /bun2/ daw,da,pd,t,ve,bis,pi,yt,dh,eps,h
      dimension r(1)
      go to (2,3,4),ja
    2 sumv=0.
      do 10 n=1,nk
      a=cf*n
      if(indi .eq. 0) sumv=sumv+r(n)*p**a*dcos(a*ph)/a
      if(indi .eq. 1)
     1sumv=sumv+r(n)*(p**a+h**(2.*a)*p**(-a))*dcos(a*ph)/a
      if(ik-7) 10,12,12
   12 if(indi .eq. 0) sumv=sumv+r(nk+n)*p**a*dsin(a*ph)/a
      if(indi .eq. 1)
     2sumv=sumv+r(nk+n)*(p**a+h**(2.*a)*p**(-a))*dsin(a*ph)/a
   10 continue
      if(indi .eq. 0) tdmp=sumv+(1.-(p/t)**2)/(2.*da*daw)
      if(indi .eq. 1)
     1tdmp=sumv+dlog(t/p)/(da*daw)+1./(da*daw*bis)
      return
    3 sumt=0.
      do 20 n=1,nk
      a=cf*n
      if(indi .eq. 0) go to 50
      s1=(1.+daw+a/bis+(1.-daw-a/bis)*(h/t)**(2.*a))*p**a
```

```fortran
      s2=((1.-daw+a/bis)*t**(2.*a)+(1.+daw-a/bis)*h**(2.*a))*p**(-a)
      go to 60
   50 s1=(1.+daw+a/bis)*p**a
      s2=(1.-daw+a/bis)*t**(2.*a)/(p**a)
   60 continue
      sumt=sumt+(s1+s2)*r(n)*dcos(a*ph)/(2.*a)
      if(ik-7) 20,22,22
   22 sumt=sumt+(s1+s2)*r(nk+n)*dsin(a*ph)/(2.*a)
   20 continue
      if(indi .eq. 0) tdmp=sumt+(dlog(t/p))/da-1./(bis*da*daw)
      if(indi .eq. 1)
     1tdmp=sumt+dlog(t/p)/da
      return
    4 sum=0.
      do 30 n=1,nk
      a=cf*n
      call coeff(a,fn,gn)
      sum=sum+(gn*p**a+fn*p**(-a))*r(n)*dcos(a*ph)/a
      if(ik-7) 30,32,32
   32 sum=sum+(gn*p**a+fn*p**(-a))*r(nk+n)*dsin(a*ph)/a
   30 continue
      vind=0.
      if(indi .eq. 0) vind=1./(bis*da*daw)
      tdmp=sum+(p**2-1.)/(2.*ynt)-(1./ynt+1.)*dlog(p)+
     3     dlog(t)/da-vind
      return
      end
c
c

      subroutine flux (ja,ik,cf,nk,r,ynt,al,p,ph,q2)
c
      implicit real*8 (a-h,o-z)
      common /inter/ indi,ivel,imix,iprint,ntitle(20)
      common /bun2/ daw,da,pd,t,ve,bis,pi,yt,dh,eps,h
      dimension r(nk)
      go to (1,2,3) ja
c
c
c        heat flux within the fuel or bn region
c
    1 sum1=0.
      do 10 n=1,nk
      a=cf*n
      ap=a*ph
      if(indi .eq. 0) al=p**a
      if(indi .eq. 1)
     3al=p**(a-1.)-h**(2.*a)*p**(-a-1.)
      sum1=sum1+r(n)*al*dcos(ap)
      if(ik-7) 10,12,12
   12 sum1=sum1+r(nk+n)*al*dsin(ap)
   10 continue
      if(indi .eq. 0) q2=1.-da*daw*sum1
      if(indi .eq. 1)
     1q2=h/p-da*daw*h*sum1
      return
c
c        heat flux within the clad (ss) region
c
    2 sum2=0.
      do 20 n=1,nk
```

```fortran
      a=cf*n
      if(indi .eq. 0) go to 50
      s1=1.+daw+a/bis+(1.-daw-a/bis)*(h/t)**(2.*a)
      s2=(1.-daw+a/bis)*t**(2.*a)+(1.+daw-a/bis)*h**(2.*a)
      go to 60
   50 s1=1.+daw+a/bis
      s2=(1.-daw+a/bis)*t**(2.*a)
   60 continue
      sum2=sum2+r(n)*(s1*p**(a-1.)-s2*p**(-a-1.))*dcos(a*ph)/2.
      if(ik-7) 20,22,22
   22 sum2=sum2+r(nk+n)*(s1*p**(a-1.)-s2*p**(-a-1.))*dsin(a*ph)/2.
   20 continue
      q2=1./p-da*sum2
      if(indi .eq. 1) q2=q2*h
      return
    3 suma=0.
      sumb=0.
      do 30 n=1,nk
      a=cf*n
      call coeff(a,fn,gn)
      suma=suma+r(n)*(gn*p**(a-1.)-fn*p**(-1.-a))*dcos(a*ph)
      sumb=sumb-r(n)*(gn*p**a+fn*p**(-a))*dsin(a*ph)
      if(ik-7) 30,33,33
   33 suma=suma+r(nk+n)*(gn*p**(a-1.)-fn*p**(-1.-a))*dsin(a*ph)
      sumb=sumb+r(nk+n)*(gn*p**a+fn*p**(-a))*dcos(a*ph) .
   30 continue
      if(indi .eq. 1)
     1q2=sumb*dsin(ph-al)*h/p-(suma+p/ynt-(1.+1./ynt)/p)*
     1    dcos(ph-al)*h
      if(indi .eq. 0) q2=sumb*dsin(ph-al)/p-(suma+p/ynt
     2      -(1.+1./ynt)/p)*dcos(ph-al)
      return
      end
c
c
      subroutine coeff(a,fn,gn)
c
c
c     determine fn and gn
c
      implicit real*8 (a-h,o-z)
      common /inter/ indi,ivel,imix,iprint,ntitle(20)
      common /bun2/ daw,da,pd,t,ve,bis,pi,yt,dh,eps,h
      if(indi .eq. 0) go to 10
      x=1.+daw+a/bis+(1.-daw-a/bis)*(h/t)**(2.*a)
      y=(1.+daw-a/bis)*h**(2.*a)+(1.-daw+a/bis)*t**(2.*a)
      go to 20
   10 x=1.+daw+a/bis
      y=(1.-daw+a/bis)*t**(2.*a)
   20 continue
      gn=.25*((1.+da)*x+(1.-da)*y)
      fn=.25*((1.-da)*x+(1.+da)*y)
      return
      end
c
c
c
c *********************************************************
      subroutine subchannel
c *********************************************************
```

```
      implicit real*8 (a-h,o-z)
      common /inter/ indi,ivel,imix,iprint,ntitle(20)
      common /temp/ tht(13)
      common /bun2/ daw,da,pd,dumt,ve,bis,pi,yt,dh,eps,dumh
      common /split/ flow1,flow2,flow3,aedgew,aedgei,acorn,aint
      dimension b(13,13),c(13),q(13)
      dimension told(13),thtnew(13),t(13),tn(13),del(13)
c
      data root3 /1.7320508/
c
c
c       read input data for subchannel analysis
c
      read(5,*)  hleng,diam,aflow1,aflow2,aflow3,vb
      read(5,*)  eps1,eps2,ckappa,alpha,cll
      read(5,*)  qk,tin,tb
      read(5,*)  ipq,itermax,epsdel
      if(ivel .ne. 0) read(5,*) flow1,flow2,flow3
c
      cgap=(pd-1.)*diam
      dgap=(ve-1.)*diam/2.
      eta11=pd*diam/root3
      eta12=(ve*diam/2.+eta11)/2.
      eta22=pd*diam
      eta23=(pd+.5*ve/root3)/2.
      do 10 i=1,13
  10  told(i)=qk*tht(i)+tb
c
c
      fa1=flow1*aflow1
      fa2=flow2*aflow2
      fa3=flow3*aflow3
      ua=8.*fa1+2.*fa2+.5*fa3
c
      p1=cgap*hleng/aflow1
      p2=ckappa*alpha/(flow1*vb*eta11)
      c1=p1*p2
      q(1) = (1.+c1)*told(1)-c1*told(2)-tin
      q(2) =-c1*told(1)+(1.+3.*c1)*told(2)-2.*c1*told(3)-tin
      q(3) =-c1*told(2)+(1.+2.*c1)*told(3)-c1*told(5)-tin
      if(ipq .eq. 1)  q(3)=-2.*c1*told(2)+(1.+3.*c1)*told(3)
     1                     -c1*told(5)-tin
      q(4) = (1.+3.*c1)*told(4)-2.*c1*told(5)-c1*told(7)-tin
      q(5) =-c1*told(3)-c1*told(4)+(1.+3.*c1)*told(5)-c1*told(6)-tin
      q(6) =-c1*told(5)+(1.+2.*c1)*told(6)-c1*told(9)-tin
      if(ipq .eq. 1)  q(6)=-2.*c1*told(5)+(1.+3.*c1)*told(6)
     2                     -c1*told(9)-tin
      q(7) =-c1*told(4)+(1.+3.*c1)*told(7)-2.*c1*told(8)-tin
      q(9) =-c1*told(6)-c1*told(8)+(1.+3.*c1)*told(9)-c1*told(10)-tin
      p3=p2*eta11/eta12
      c11=p1*p3
      q(8) =-c1*told(7)+(1.+2.*c1+c11)*told(8)-c1*told(9)-c11*told(11)
     1      -tin
      q(10) =-c1*told(9)+(1.+c1+c11)*told(10)-c11*told(12)-tin
      if(ipq .eq. 1)  q(10)=-2.*c1*told(9)+(1.+2.*c1+c11)*told(10)
     3                     -c11*told(12)-tin
      p4=cgap*hleng/aflow2
      p5=ckappa*alpha/(flow2*vb*eta12)
      c12=p4*p5
      p6=dgap*hleng/aflow2
```

```
      p7=p5*eta12/eta22
      c2=p6*p7
      p8=p7*eta22/eta23
      c23=p6*p8
      p9=dgap*hleng/aflow3
      p10=p8*flow2/flow3
      c3=p9*p10
      q(11)=-c12*told(8)+(1.+c12+c2+c22)*told(11)-(c2+c22)*told(12)
     2      -tin
      q(12)=-c12*told(10)-c2*told(11)+(1.+c12+c2+c23+c22)*told(12)
     3      -(c22+c23)*told(13)-tin
      q(13)=-(c3+c33)*told(12)+(1.+c3+c33)*told(13)-tin
c
      write(6,301) p1,p2,p3,p4,p5,p6,p7,p8,p9,p10
  301 format(5e14.4)
      write(6,302) c1,c11,c12,c2,c23,c3
  302 format(6e13.4)
      write(6,303) (q(i),i=1,13)
  303 format(7e11.4)
c
c
      c1=p1*(p2+eps1)
      c11=p1*(p3+eps1)
      c12=p4*(p5+eps1*flow1/flow2)
      c2=p6*(p7+eps2)
      c23=p6*(p8+eps2)
      c3=p9*(p10+eps2*flow2/flow3)
      c22=p6*c11
      c33=p9*c11*flow2/flow3
c
      write(6,304) c1,c11,c12,c2,c23,c3,c22,c33
  304 format(4e15.4)
c
      do 20 i=1,13
      do 20 j=1,13
   20 b(i,j)=0.0
      b(1,1)=1.+c1
      b(1,2)=-c1
      b(2,1)=-c1
      b(2,2)=1.+3.*c1
      b(2,3)=-2.*c1
      b(3,2)=-c1
      b(3,3)=1.+2.*c1
      b(3,5)=-c1
      b(4,4)=1.+3.*c1
      b(4,5)=-2.*c1
      b(4,7)=-c1
      b(5,3)=-c1
      b(5,4)=-c1
      b(5,5)=1.+3.*c1
      b(5,6)=-c1
      b(6,5)=-c1
      b(6,6)=1.+2.*c1
      b(6,9)=-c1
      b(7,4)=-c1
      b(7,7)=1.+3.*c1
      b(7,8)=-2.*c1
      b(8,7)=-c1
      b(8,8)=1.+2.*c1+c11
      b(8,9)=-c1
```

```
      b(8,11)=-c11
      b(9,6)=-c1
      b(9,8)=-c1
      b(9,9)=1.+3.*c1
      b(9,10)=-c1
c
      b(10,9)=-c1
      b(10,10)=1.+c1+c11
      b(10,12)=-c11
      b(11,8)=-c12
      b(11,11)=1.+c12+c2+c22
      b(11,12)=-c2-c22
      b(12,10)=-c12
      b(12,11)=-c2
      b(12,12)=1.+c12+c2+c23+c22
      b(12,13)=-c22-c23
      b(13,12)=-c3-c33
      b(13,13)=1.+c3+c33
c
      if(ipq .ne. 1) go to 120
      b(3,2)=-2.*c1
      b(3,3)=1.+3.*c1
      b(6,5)=b(3,2)
      b(6,6)=b(3,3)
      b(10,9)=b(3,2)
      b(10,10)=1.+2.*c1+c11
  120 continue
c
c     write(6,305)
c 305 format(1x,//,1x,"elements of B matrix",/)
c     do 50 i=1,13
c  50 write(6,306)  (b(i,j),j=1,13)
  306 format(13f6.2)
      do 30 i=1,13
   30 c(i)=q(i)+tin
c
c
c
c
c        Gauss-Seidel iterative method
c
      ni=0
      do 70 i=1,13
   70 t(i)=tb
  510 continue
      tn(1)=(c(1)-b(1,2)*t(2))/b(1,1)
      tn(2)=(c(2)-b(2,1)*tn(1)-b(2,3)*t(3))/b(2,2)
      tn(3)=(c(3)-b(3,2)*tn(2)-b(3,5)*t(5))/b(3,3)
      tn(5)=(c(5)-b(5,3)*tn(3)-b(5,4)*t(4)-b(5,6)*t(6))/b(5,5)
      tn(4)=(c(4)-b(4,5)*tn(5)-b(4,7)*t(7))/b(4,4)
      tn(6)=(c(6)-b(6,5)*tn(5)-b(6,9)*t(9))/b(6,6)
      tn(7)=(c(7)-b(7,4)*tn(4)-b(7,8)*t(8))/b(7,7)
      tn(8)=(c(8)-b(8,7)*tn(7)-b(8,9)*t(9)-b(8,11)*t(11))/b(8,8)
      tn(9)=(c(9)-b(9,6)*tn(6)-b(9,8)*tn(8)-b(9,10)*t(10))/b(9,9)
      tn(10)=(c(10)-b(10,9)*tn(9)-b(10,12)*t(12))/b(10,10)
      tn(11)=(c(11)-b(11,8)*tn(8)-b(11,12)*t(12))/b(11,11)
      tn(12)=(c(12)-b(12,10)*tn(10)-b(12,11)*tn(11)-b(12,13)*
     1         t(13))/b(12,12)
      tn(13)=(c(13)-b(13,12)*tn(12))/b(13,13)
c
      do 80 i=1,13
```

```fortran
   80 del(i)=dabs(tn(i)-t(i))/dabs(tn(i))
      do 85 i=1,13
      if(del(i) .gt. epsdel) go to 500
   85 continue
      go to 600
  500 do 90 i=1,13
   90 t(i)=tn(i)
      ni=ni+1
      write(6,310) ni,(t(i),i=1,13)
  310 format(1x,i3,/,(1x,7f11.3))
      if(ni .gt. itermax) go to 600
      go to 510
  600 continue
      write(6,200)
  200 format(1x,"  temperature profile included wire pumping and"
     1     ," turbulent effect",/,3x,"i",3x,"temperature,T(i)",/)
      write(6,210) (i,tn(i),i=1,13)
  210 format(3x,i2,6x,f10.4)
c
c
      usum=.5*(tn(1)+tn(2)+tn(4)+tn(7))+tn(3)+tn(5)+tn(6)+tn(8)
     1     +tn(9)+tn(10)
      uasum=fa1*usum+fa2*(tn(11)+tn(12))+.5*fa3*tn(13)
      tbpred=uasum/ua
      tbdif=(tbpred-tb)/tb
      write(6,215) tbpred,tbdif
  215 format(/,3x,"Tb - prediction =",f10.3,/,3x,"Tb - error =",
     1     e12.5)
c
c
      do 40 i=1,13
   40 thtnew(i)=(tn(i)-tb)/qk
      write(6,220)
  220 format(1x,//,1x, " dimensionless temperatures",/)
      write(6,210) (i,thtnew(i),i=1,13)
      stop
      end
```

APPENDIX E

Correction of ORNL 61-Pin Bundle Data

The ORNL temperature data obtained in mixed convection conditions (Test 17 Run 105, Test 18 Run 105 and Test 19 Run 105) have revealed an energy balance problem. The measured temperature rise $(T_{out} - T_{in})$ for the three runs were 291°F, 289°F and 290°F while the predicted temperature rises from energy balance considerations without heat loss were 312°F, 321°F and 334°F, respectively. These results suggested that substantial heat loss might have occurred along the bundle length since the outlet temperature was measured at the bundle exit, 24 inches downstream from the end of the heated section.

In order to estimate the average temperature at the 37" level where the subchannel temperature measurements were performed, the following correction method was introduced. Figure E.1 shows the schematic diagram of the ORNL bundle. The parameters in the figure represent,

T_{in}: Bundle inlet temperature

T_{37}: Average temperature at the 37" level

T_{exit}: Bundle exit temperature

Q_{in}: Total heat input over the heated section

Q_{L1}: heat loss in region 1 (from inlet to the 37" level)

Q_{L2}: Heat loss in region 2 (from the 37" level to the exit)

H_1: Height of region 1 (=37")

H_2: Height of region 2 (=24")

Simple heat balance for this bundle yields,

$$\dot{m}C_p (T_{bal} - T_{37}) = Q_{L1} \qquad (E.1)$$

$$\dot{m}C_p (T_{bal} - T_{exit}) = Q_{L1} + Q_{L2} \qquad (E.2)$$
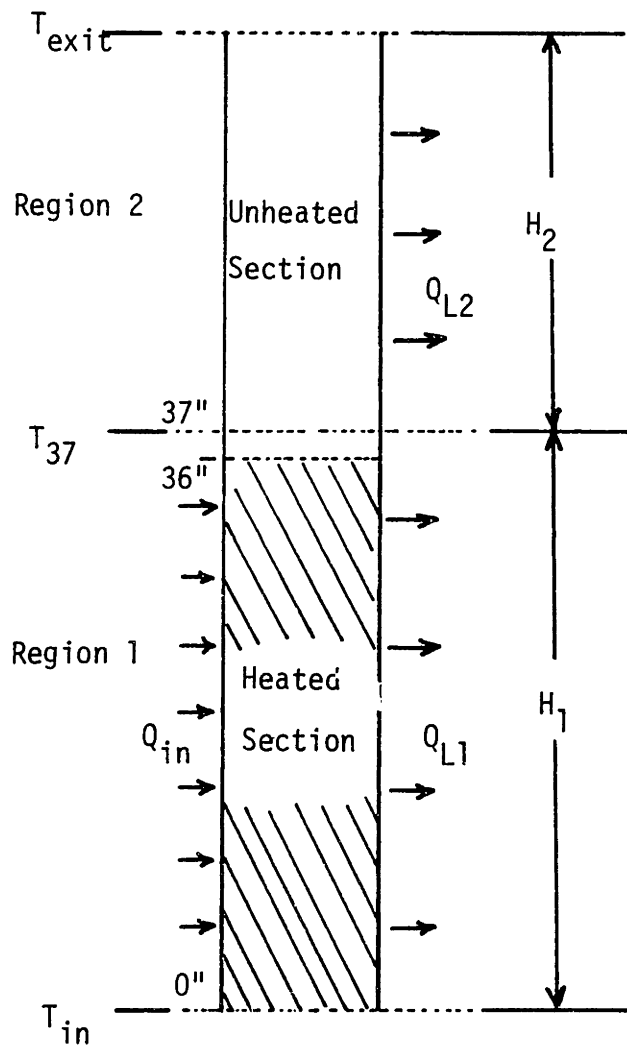
Figure E.1 Test Section of ORNL Fuel Bundle

where

$\dot{m}$: Mass flow rate of the bundle

C_p : Specific heat

T_{bal} : Average temperature at the 37" level obtained assuming no heat loss.

The heat loss of each region can be expressed as,

$$Q_{L1} = \bar{h}_1 H_1 P (\bar{T}_1 - T_a) \qquad (E.3)$$

$$Q_{L2} = \bar{h}_2 H_2 P (\bar{T}_2 - T_a) \qquad (E.4)$$

where,

$\bar{h}_i$: Average heat transfer coefficient over the region i (i = 1,2)

P : Bundle perimeter

$\bar{T}_i$: Average temperature of region i

T_a : Ambient temperature surrounding the bundle.

If T_a is assumed to be quite small compared to the fluid temperature,

i.e., $T_a \ll \bar{T}_i$ and $\bar{h}_1$ is assumed to be equal to $\bar{h}_2$, then

$$Q_{L1} = CH_1 \bar{T}_1 \qquad (E.5)$$

$$Q_{L2} = CH_2 \bar{T}_2 \qquad (E.6)$$

From Eqs. (E.3) and (E.4), the heat loss over the region 1 can be expressed as,

$$Q_{L1} = \frac{H_1 \bar{T}_1}{H_1 \bar{T}_1 + H_2 \bar{T}_2} (Q_{L1} + Q_{L2}) \qquad (E.7)$$

Substituting Eqs. (E.1) and (E.2) into Eq. (E.7) yields,

$$T_{37} = T_{bal} - \frac{H_1 \bar{T}_1}{H_1 \bar{T}_1 + H_2 \bar{T}_2} (T_{bal} - T_{exit}) \qquad (E.8)$$

In order to obtain T_{37}, the average temperatures $\bar{T}_1$ and $\bar{T}_2$ should be determined in a proper way. If the temperature profile is assumed to be linear axially, one can assume that,

$$\bar{T}_1 = \frac{T_{in} + T_{bal}}{2} \qquad (E.9)$$

$$\bar{T}_2 = \frac{T_{bal} + T_{exit}}{2} \qquad (E.10)$$

Using Eqs. (E.9) and (E.10), T_{37} can be obtained from Eq. (E.8). Then $\bar{T}_1$ and $\bar{T}_2$ are estimated again as,

$$\bar{T}_1 = \frac{T_{in} + T_{37}}{2} \qquad (E.11)$$

$$\bar{T}_2 = \frac{T_{37} + T_{exit}}{2} \qquad (E.12)$$

Then T_{37} can be calculated more correctly. The above iteration proceeds until the change of T_{37} between the successive iterations is acceptably small.

Once T_{37} is evaluated, one can calculate the dimensionless temperature rise ΔT^*, defined as,

$$\Delta T^* = \frac{T - T_{in}}{T_{out} - T_{in}} \qquad (E.13)$$

by using the calculated average outlet temperature T_{37} for T_{out} instead of the bundle exit temperature T_{exit}.

The calculated results of T_{37} for the three runs are as follows:

For Test 17 Run 105, $T_{37} = 1039°F$.

For Test 18 Run 105, $T_{37} = 1039°F$.

For Test 19 Run 105, $T_{37} = 1038°F$.

APPENDIX F

Principles and Circuit Diagrams of the Power Supply System

F.1 Principles of Triacs

F.1.1 Thyristors

As shown in Figure F.1, a thyristor is a type of switch through which an electric current begins to flow from the anode to the cathode only when a gate pulse is given. Once the current begins to flow, the thyristor maintains its function as a diode and the current flows until the anode voltage, V_i, reaches zero. We can, therefore, control the heater power by giving a gate pulse which has a phase lag of α from the zero-crossing point where the anode voltage is zero. The phase lag, α, is called the trigger angle.

F.1.2 Triacs

Figure F.1 shows that less than half of the A.C. power source is available, since the thyristor does not let the current flow while the anode voltage is negative. This shortcoming can be improved by utilizing a triac instead of a thyristor. A triac is a bi-directional thyristor, in which gate pulses turn the device on for load current in either direction. Figure F.2 shows the operation principle of the triac.

The heater power, W, is given as a function of the triggering phase angle, α, as:

$$W = \frac{1}{\pi} \int_0^{\pi} \frac{V_{TR}^2}{R} \, d\theta = \frac{V_o^2}{\pi R} \int_{\alpha}^{\pi} \sin^2\theta \, d\theta$$

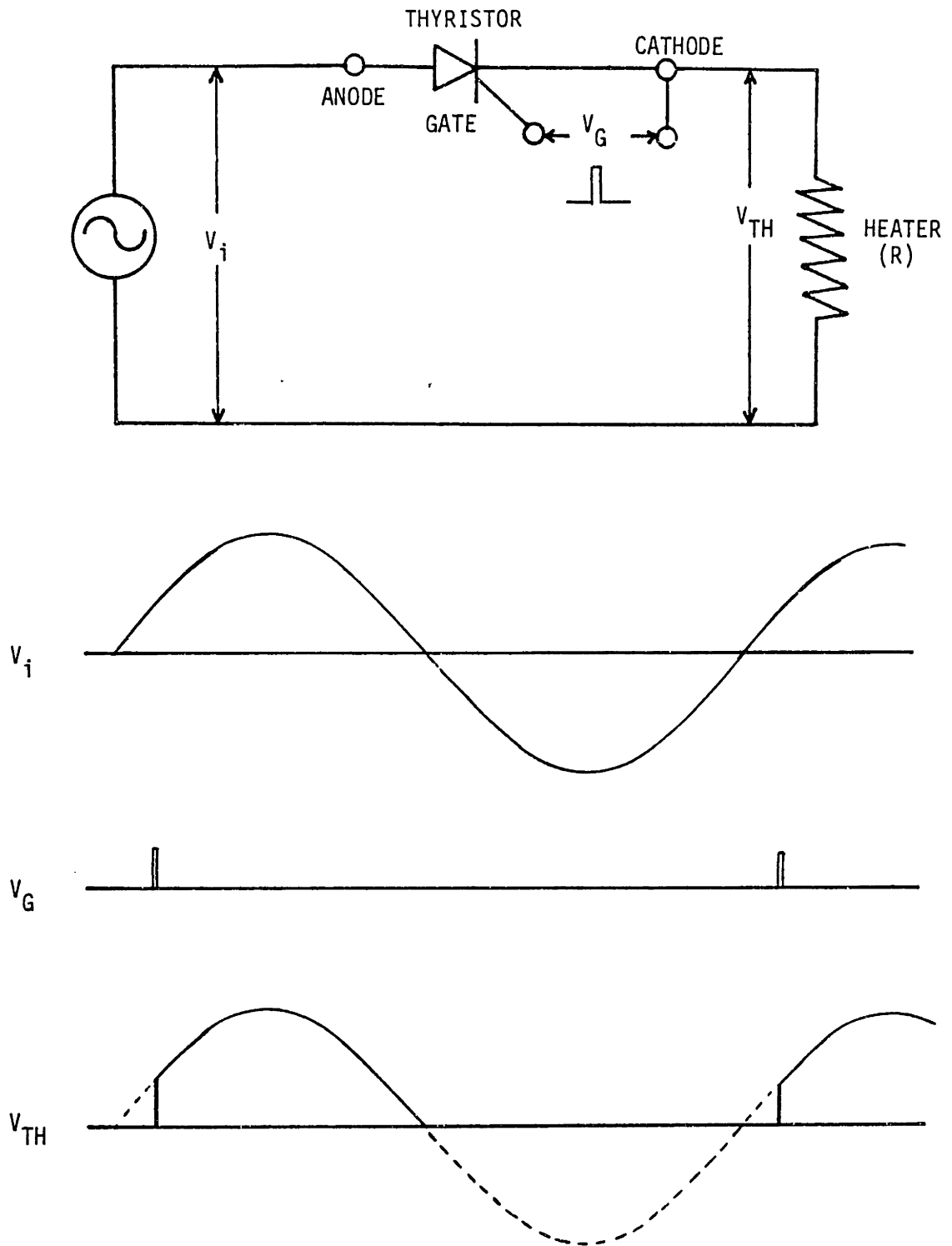$$= \frac{V_o^2}{2\pi R} \left[(\pi - \alpha) + \frac{1}{2} \sin 2\alpha \right] \qquad\qquad (F.1)$$
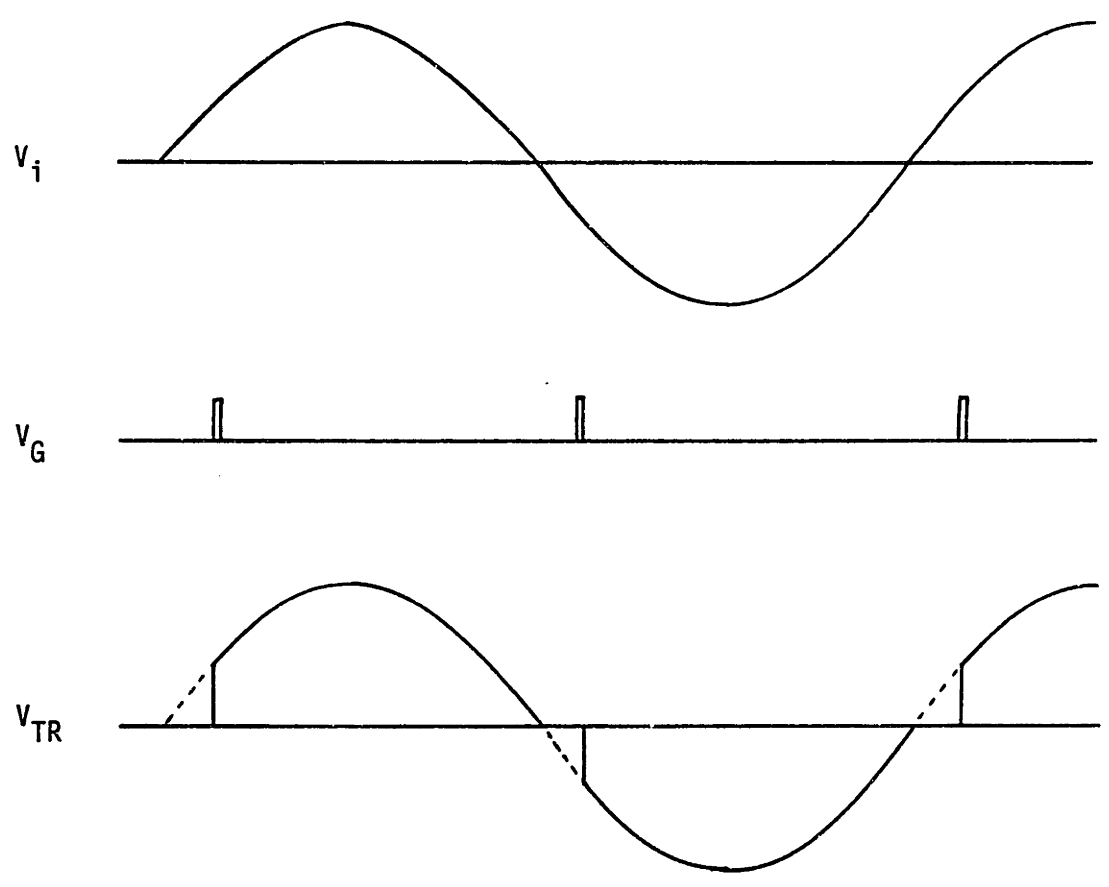
Figure F.1 Principle of Thyristor
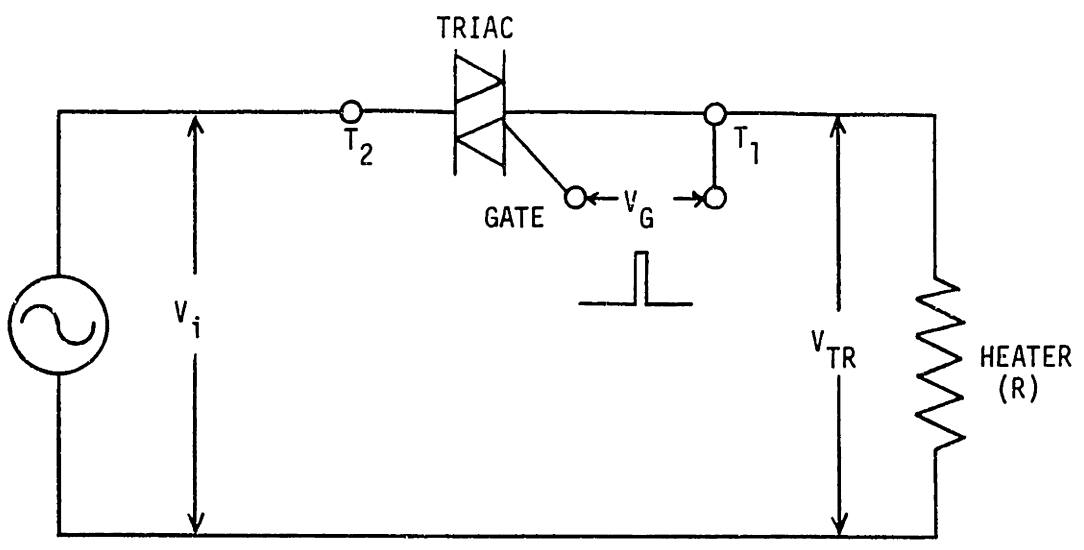
Figure F.2 Priciple of Triac

where we assumed $V_i = V_0 \sin\theta$ and $\theta = \omega t$. The symbols ω and V_0 are respectively the angular frequency and the peak voltage of the A.C. power source, while t is the time and R the electric resistance of the heater rod. If the power source is used directly for heating, the heater power, W_0, is

$$W_0 = \frac{1}{\pi} \int_0^\pi \frac{V_i^2}{R} \, d\theta = \frac{V_0^2}{2R} \qquad (F.2)$$

Eq. (F.1) then becomes,

$$\frac{W}{W_0} = (1 - \frac{\alpha}{\pi}) + \frac{1}{2\pi} \sin 2\alpha, \qquad (F.3)$$

or

$$\frac{(V)_{rms}}{(V_0)_{rms}} = (\frac{W}{W_0})^{1/2} = \left[(1 - \frac{\alpha}{\pi}) + \frac{1}{2\pi} \sin 2\alpha\right]^{1/2}, \qquad (F.4)$$

where $(V)_{rms}$ and $(V_0)_{rms}$ are the root mean square values of the voltage which correspond to W and W_0, respectively. The control system for the heater power therefore requires a gate circuit which can change the phase angle of triggering continuously and electronically.

F.2 Gate Circuit

An electronic circuit to change the triggering phase angle of α, namely a gate circuit, is required to control the heater power. If high precision of the controller is desired, a digital gate circuit will be better than an analog circuit, because the analog circuit has inherent drift of current.

F.2.1 TTL Programmable Counter '193

One of the methods to design a digital gate circuit is the use of a programmable counter (M-3). Figure F.3 shows an outline of the programmable 4-bit binary counter '193 (T-4). The data outputs can be

Figure F.3 4-Bit Counter, '193

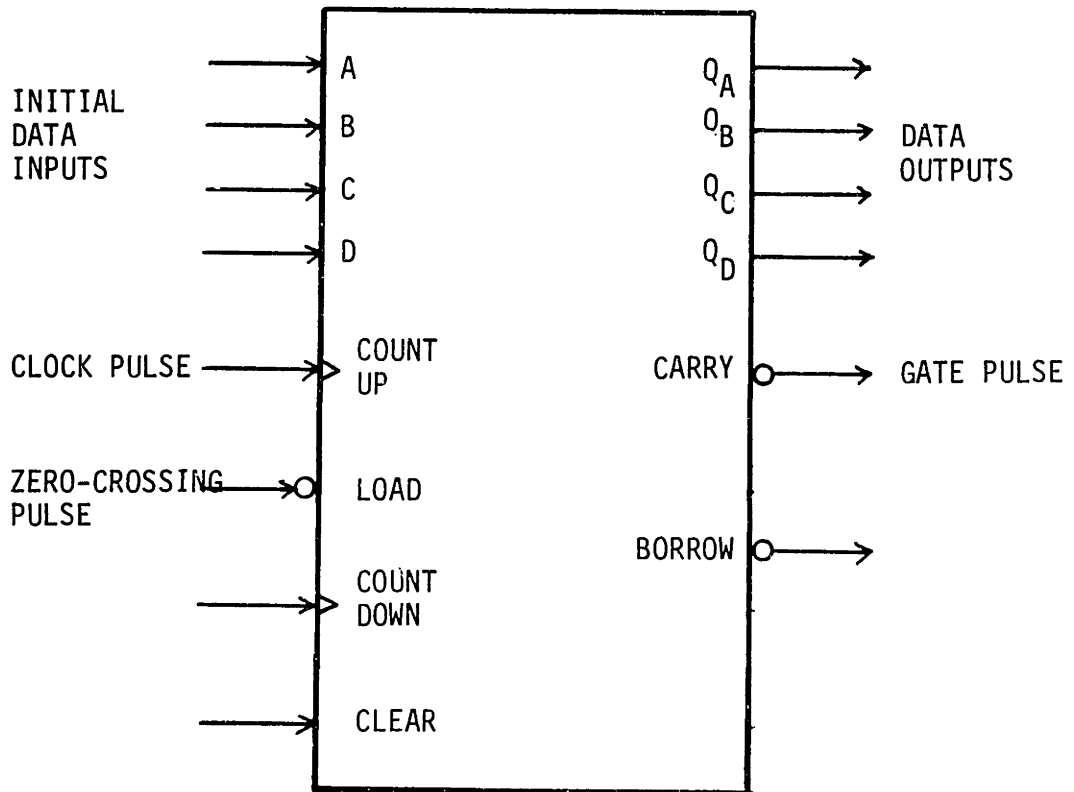preset to either level by entering the desired initial value at the data inputs when the load input is low. Count-up is then performed by a train of clock pulses and the carry output produces a pulse when the counter overflows. Typical operation sequences of the '193 are shown in Figure F.4.

In the case where the initial data are loaded at every zero-crossing of the A.C. power source and the count-up is performed by a clock signal with a prescribed frequency, the carry output can be used as a trigger pulse. The triggering phase angle is given by the difference in time between the zero-crossing pulse and the carry pulse. The trigger angle, α, is therefore determined by the initial data loaded at the zero-crossing.

F.2.2 Digital Gate Circuit

Figure F.5 shows an example of digital trigger circuit having a 4-bit programmable counter '193 and its timing chart. The toggle switches are used to enter the initial data at the data inputs. In order to cover the half period of the A.C. power source with four bits, sixteen clock-pulses ($=2^4$) are required for the half period. Assuming that the frequency of the power source is 60 Hz, the frequency of the clock-pulse oscillator is:

$$f_c = 60 \times 2 \times 16 = 1920 \ (Hz)$$

Let us assume that we have a zero-crossing detector which gives a pulse whenever the voltage of the A.C. power source becomes zero. Using the zero-crossing pulses as a load signal in the circuit shown in Figure F.5, the initial data are set at the zero-crossing. The carry signal is generated in the latter half of the overflowed clock pulse after the count-up is performed. Reforming and amplifying the carry signal, we can use it as a gate signal. The triggering phase angle corresponding to the heater power level is then controlled by the toggle switches.
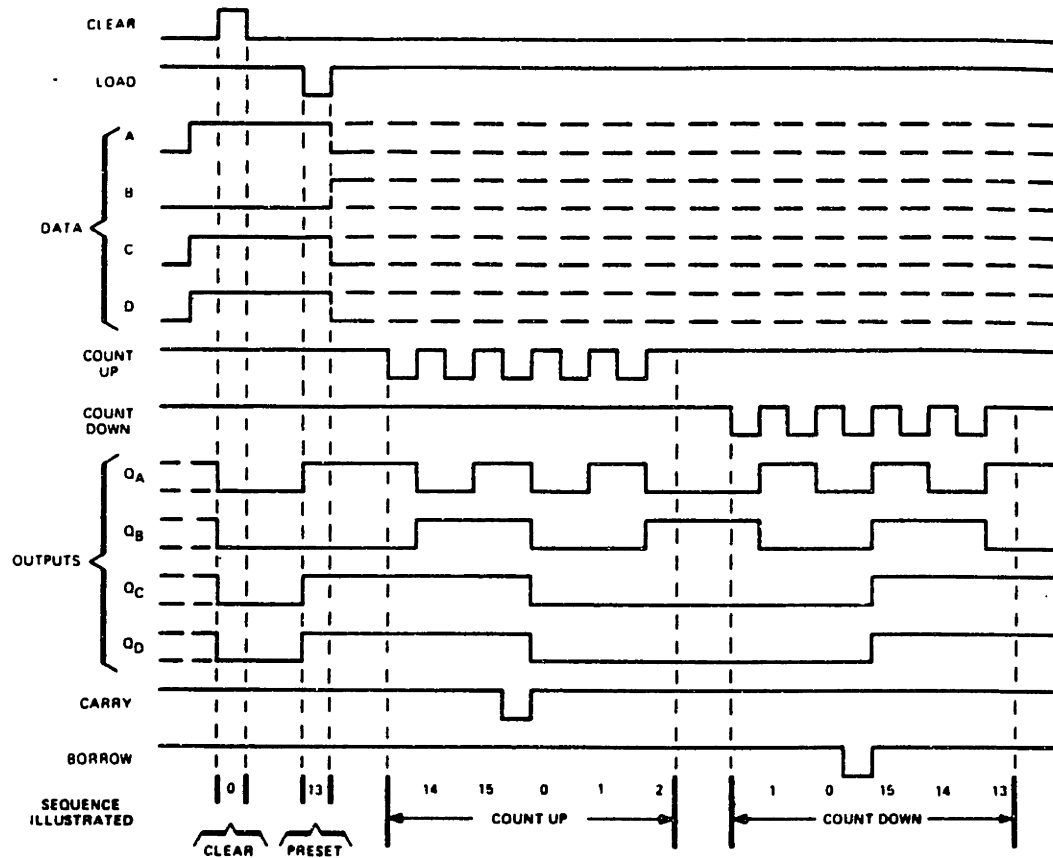
Figure F.4 Typical Clear, Load, and Count Sequences
(Taken from Reference T-4)
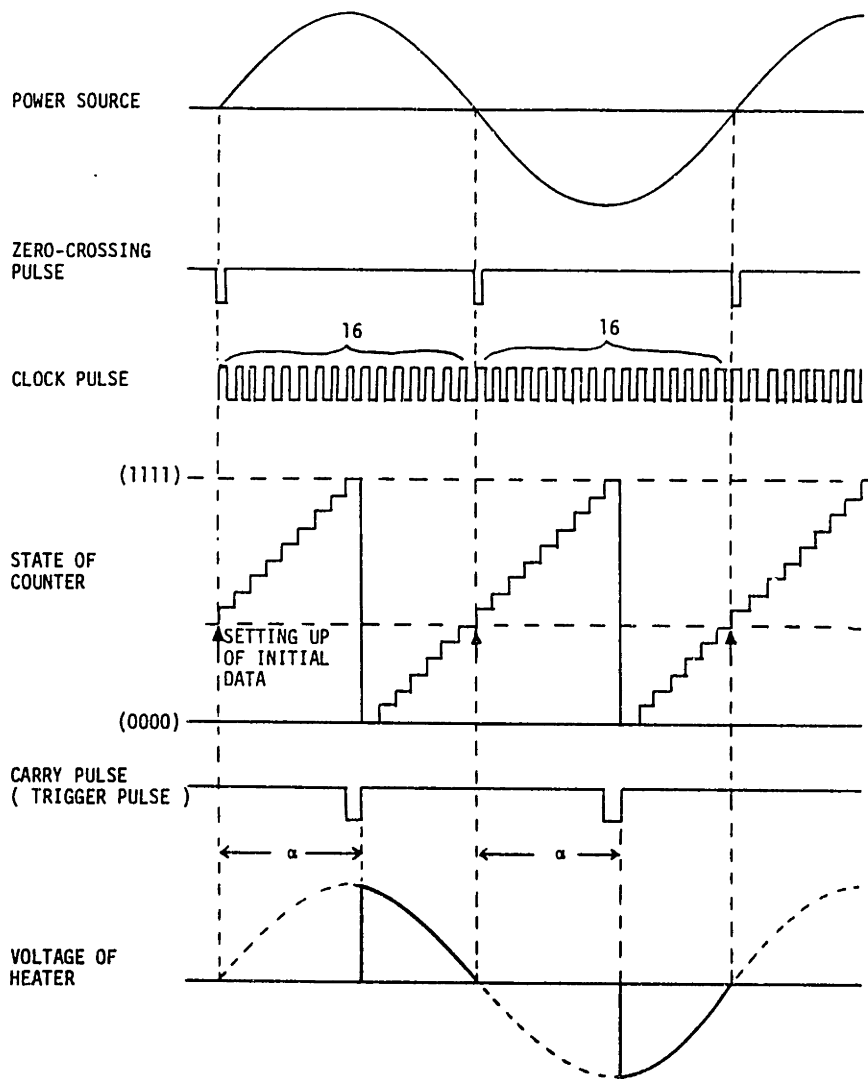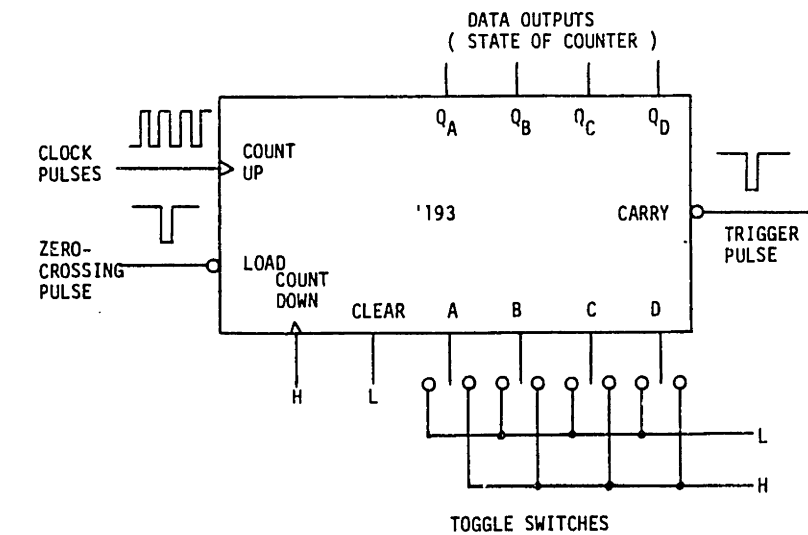
Figure F.5 Timing Chart of the Gate Circuit

Since sixteen clock pulses are assigned to a half period of the A.C. power source in the circuit, the phase angle per clock pulse is

$$\theta_c(4) = \frac{180°}{2^4} = 11.25° \text{ or } 0.1963 \text{ rad}$$

This means that the triggering phase angles are given as integer valuestimes 11.25°.

In the case of $\alpha = 90°$ and $(V_0)_{rms} = 220$ V, $(V)_{rms}$ are given from Eq. (F.4) as:

$$(V)_{rms} (90°) = 155.5 \text{ V}$$

$$(V)_{rms} (90° + 11.25°) = 135.0 \text{ V}$$

One bit of the initial data inputs therefore corresponds to 20.5 V (= 155.5 - 135.0). To improve the resolution of the trigger angle, the bit number of the initial data inputs should be increased . When an 8-bit counter, for example, is used, the phase angle per clock pulse becomes:

$$\theta_c(8) = \frac{180°}{2^8} = 0.703° \text{ or } 0.0123 \text{ rad}$$

One bit of the initial data inputs corresponds to 1.2 V under the same conditions as before.

F.3 Power Supply System

Figure F.6 shows the power supply circuit for each heater rod which has an 8-bit programmable counter consisting of two 4-bit counters, '193 (M-3). The octal latch circuit, '373, is used as a memory of the initial data. The flip-flop, '74, changes the pulse width of the carry signal of the '193 so that the width of the gate pulse may coincide with the period in which the triac stays on. The main electric line, namely the A.C. 209 V line in our laboratory, has a voltage change of more than ± 100 V at 60 Hz against the ground as a standard, while the voltage of the TTL
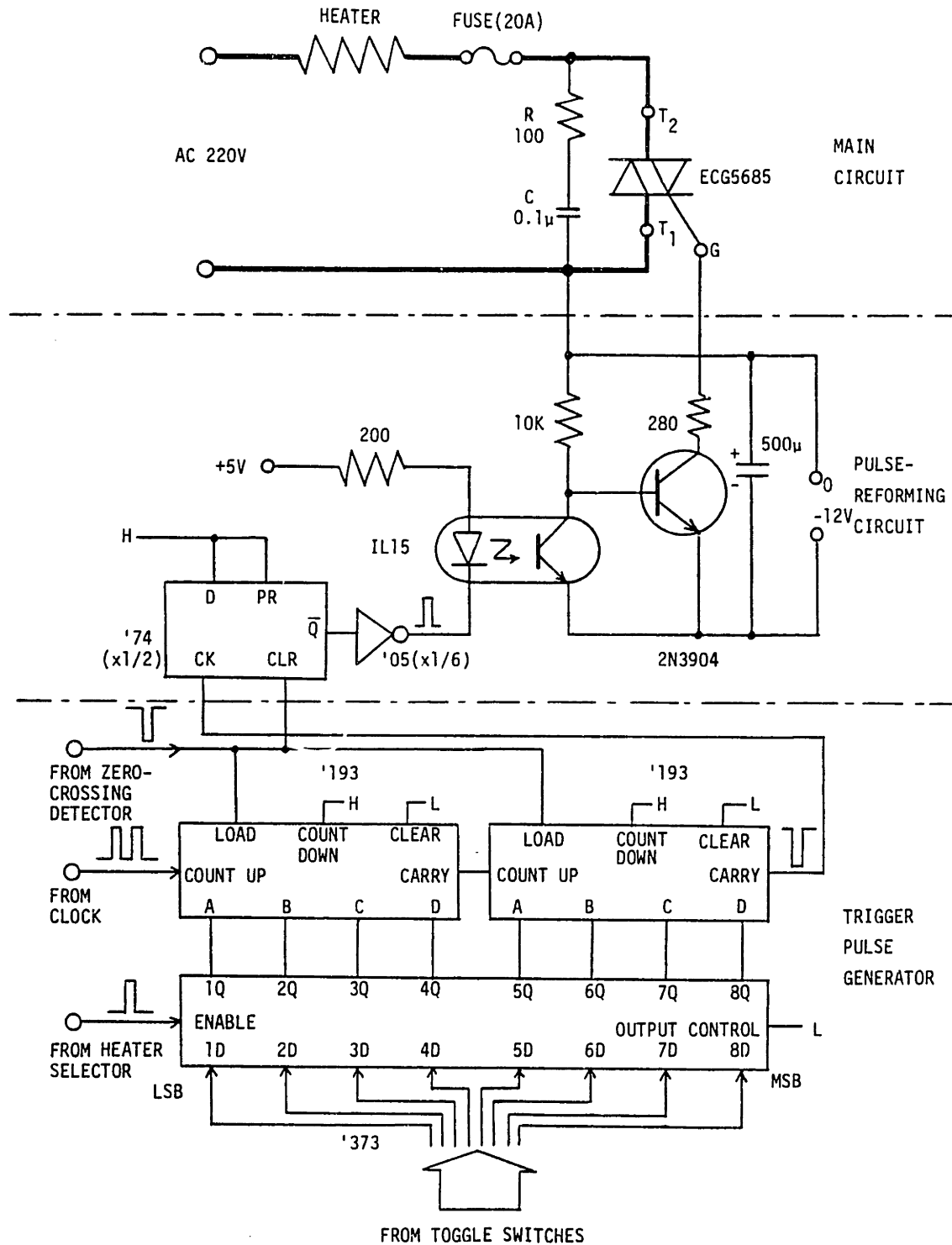
Figure F.6 Power Supply Circuit

integrated circuits is less than 5 V. The optical coupler, IL15, makes safe switching of the heater rod with IC logic signals. Low logic input of the buffer with open-collector, '05, turns off the coupler, making the transistor, 2N3904, saturate and turns on the triac, ECG5685, to energize the heater rod (M-4). The triac remains on until the first zero-crossing after the gate pulse is given. The resistor, R, and the capacitor, C, in the main circuit are used to protect the triac by suppressing transient voltage levels which exceed the normal repetitive peak voltage applied to the triac (G-2).

The control system of the power supply circuits is shown in Figure F.7. A quartz crystal oscillator generates clock pulses at 30.72 KHz (= 60 Hz x 2 x 2^8). A toggle switch is used to control the main currents flowing through the heater rods by switching the clock pulses on and off. The zero-crossing pulses produced by the voltage comparators, NTE834, together with the clock pulses, are sent to each power supply circuit which is shown in Figure F.6. The initial data preset by the eight toggle switches enter into one of the latch circuits in Figure F.6 which is chosen by the heater selector.

In the present power supply system, the triggering phase angle, α, is expressed by the preset data, N, as follows,

$$\alpha = \frac{2^8 - N}{2^8} \pi$$

Eq. (F.4) then becomes,

$$\frac{(V)_{rms}}{(V_o)_{rms}} = \left[\frac{N}{256} - \frac{1}{2\pi} \sin\left(\frac{N}{128} \pi\right) \right]^{1/2} \qquad (F.5)$$
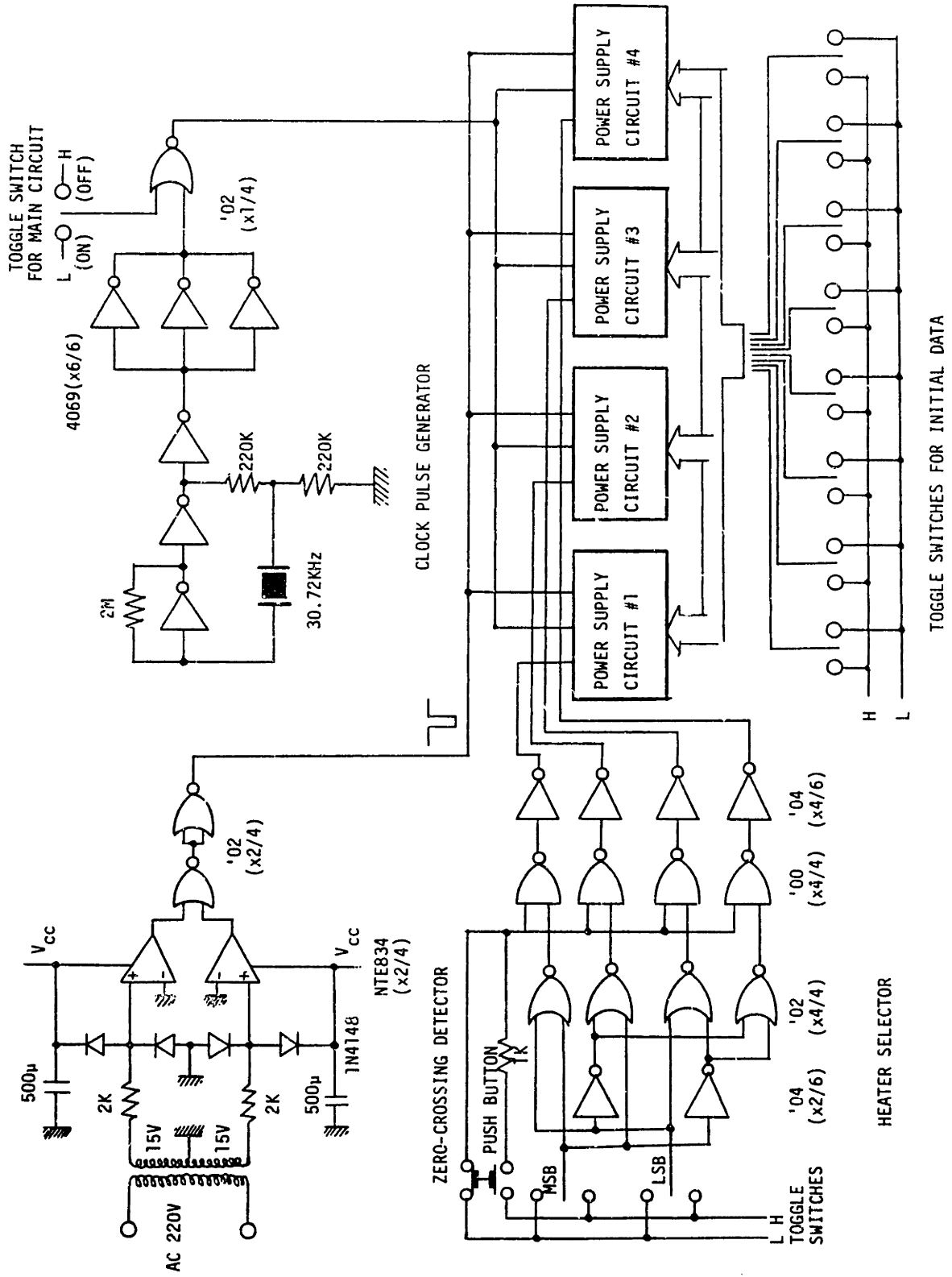
Figure F.7 Power Supply Control System

APPENDIX G

Circuit Diagrams of the Low-Pass Filters

.

Figure G.1 Circuit Diagram of the Low-Pass Filter for the Velocity Measurement

LOW-PASS FILTER

DIFFERENTIAL AMPLIFIER
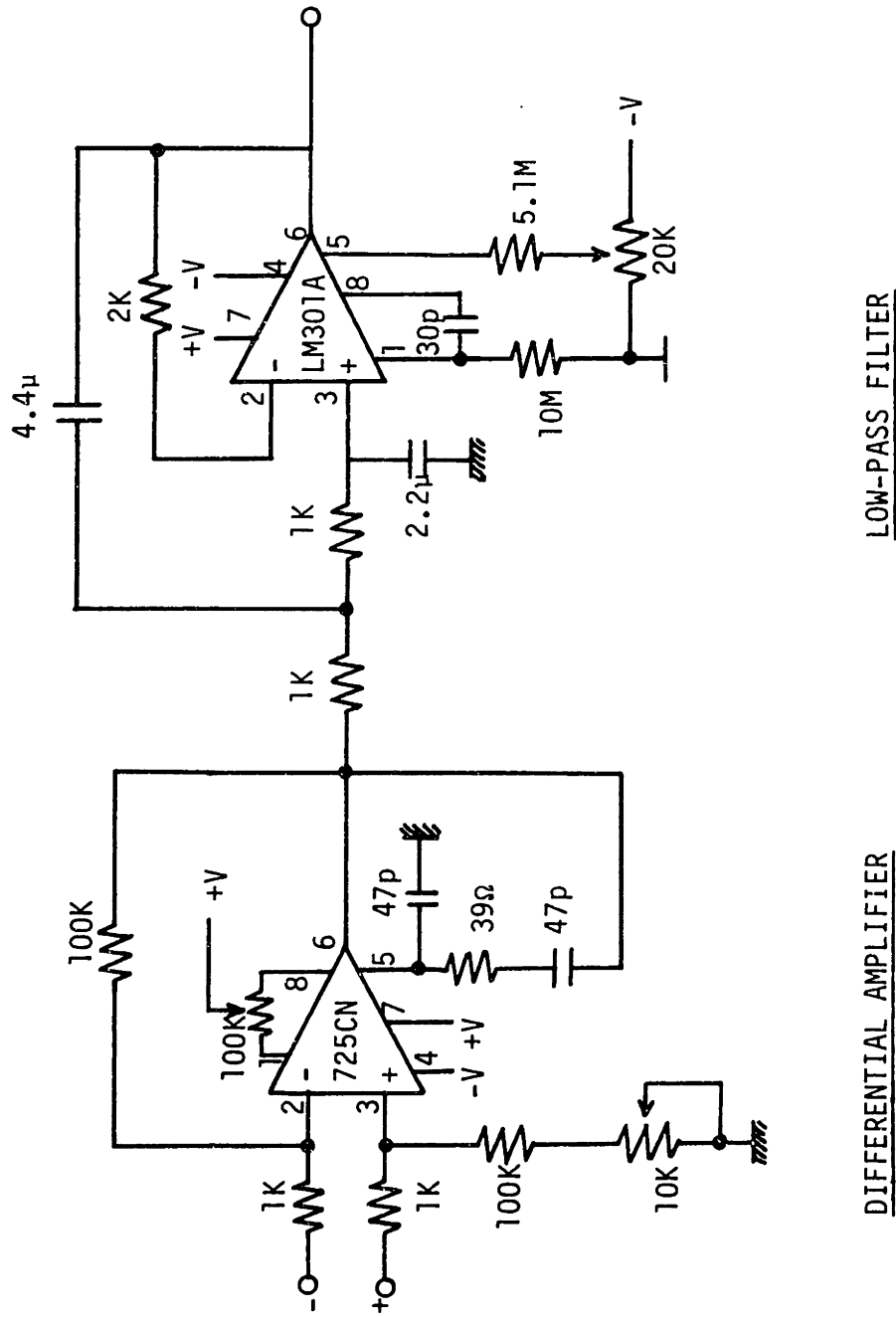
Figure G.2 Circuit Diagram of the Amplifier and Low-Pass Filter
for the Temperature Measurement

APPENDIX H

Database of the Thermal Plume Mixing Experiment

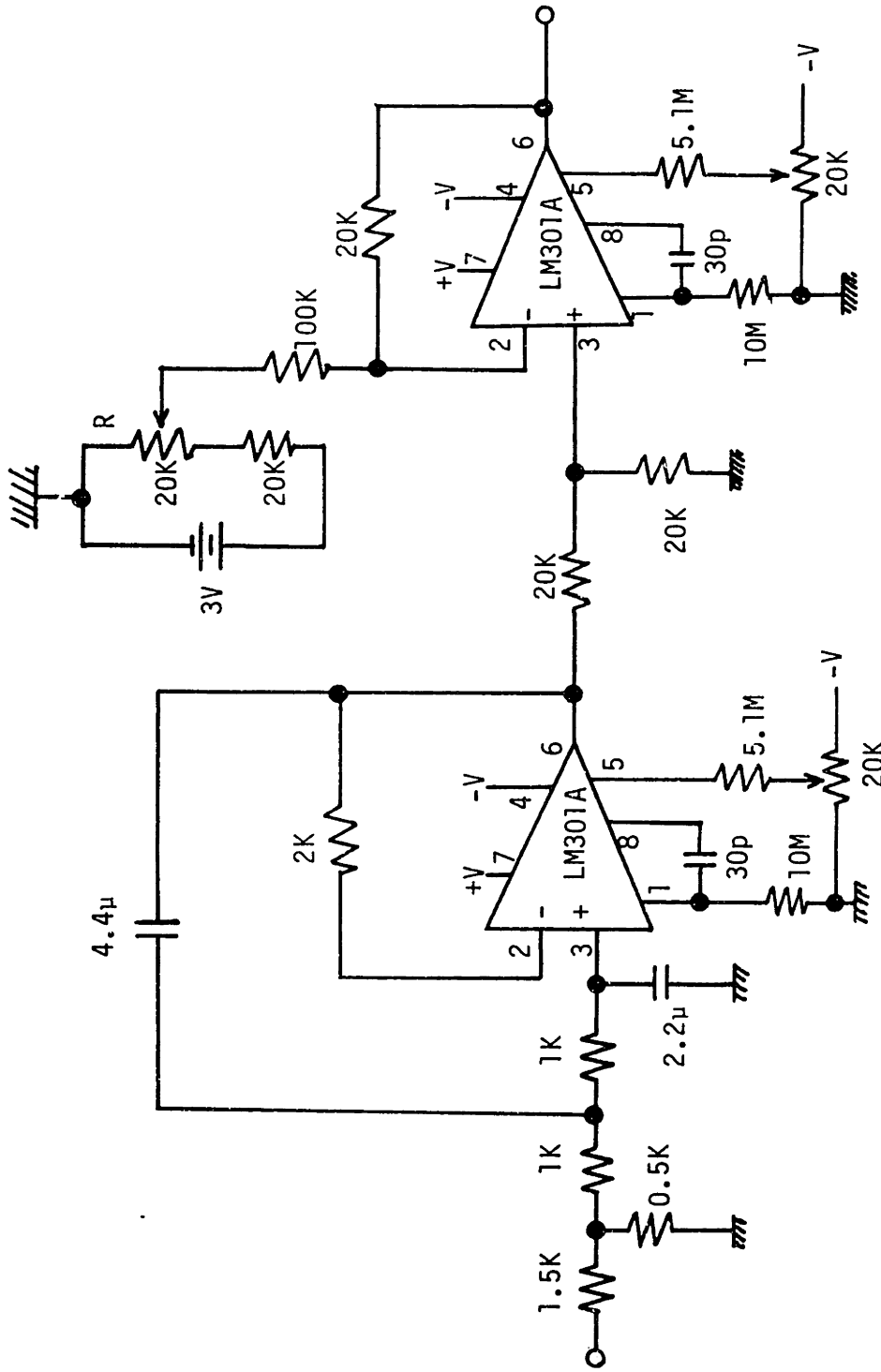| Run	Flow (%Fs)	Total Power (W)	Power skew	T_{in} (°F)	T_{out} (°F)	ΔT_b (°F)	Re	$Gr_{\Delta T}$	$Gr_{\Delta T/Re}$
1	30.6	299	.82/1.19	64.8	69.5	4.7	406	289	0.71
2	60.2	520	.81/1.15	64.2	69.0	4.8	793	287	0.36
3	19.5	422	.78/1.19	65.0	77.0	12.0	272	912	3.35
4	19.3	414	1.24/.82	65.5	76.5	11.0	270	836	3.10
5	19.1	617	1.20/.80	65.5	82.6	17.1	277	1520	5.49
6	32.0	688	.78/1.17	65.6	76.6	11.0	447	840	1.88
7	93.9	798	.79/1.17	65.4	69.7	4.3	1254	272	0.22
8	20.0	176	.69/1.36	64.8	69.8	5.0	266	311	1.17
9	31.5	463	.79/1.25	64.4	72.0	7.6	425	498	1.17
10	31.6	245	.75/1.24	63.8	67.0	3.2	409	175	0.43
11	31.0	994	.79/1.20	63.8	79.7	15.9	437	1256	2.87
12	60.5	765	.81/1.22	63.0	69.0	6.0	790	346	0.44
13	30.3	1251	.80/1.23	64.6	83.0	18.4	439	1615	3.68
14	91.0	794	.79/1.16	62.2	66.5	4.3	1161	224	0.19
15	31.1	858	.77/1.21	62.3	75.8	13.5	424	926	2.18
16	93	1400	0.8/1.2	61.6	68.4	6.8	1198	369	0.31
17	94.4	817	0.51/1.49	60.5	64.6	4.1	1175	192	0.16
18	31	986	.77/1.20	60.8	78.2	17.4	425	1222	2.88
20	34	1059	.71/1.32	60.6	65.3	4.7	1367	225	0.16
21	18.9	118	.49/1.51	59.8	63.7	3.9	233	174	0.75
22	19.2	183	.65/1.33	61.0	65.8	4.8	242	237	0.98
23	19.0	305	.65/1.31	60.4	68.8	8.4	243	445	1.83
24	19.0	248	.60/1.24	60.2	67.3	7.1	240	358	1.49
25	36.4	240	.57/1.43	59.1	63.0	3.9	444	166	0.37
26	35.8	365	.65/1.36	59.8	65.2	5.4	445	252	0.57
27	35.7	367	.78/1.21	59.4	64.8	5.4	442	246	0.56
28	35.7	430	.79/1.19	60.3	67.2	6.9	452	348	0.77
29	34.8	427	.79/1.21	59.8	66.5	6.7	437	325	0.74
30	34.8	427	.79/1.21	59.8	66.5	6.7	437	325	0.74
31	35.1	526	.49/1.45	59.4	67.3	7.9	442	388	0.88
32	34.7	516	1.41/0.5	59.6	67.2	7.6	437	375	0.86
33	31.5	463	.79/1.25	64.4	72.0	7.6	425	498	1.17
34	49.1	182	.67/1.29	58.6	60.8	2.2	588	86	0.15

Run	Flow (%Fs)	Total Power (W)	Power skew	T_{in} (°F)	T_{out} (°F)	ΔT_b (°F)	Re	$Gr_{\Delta T}$	$Gr_{\Delta T/Re}$
35	49.1	364	.66/1.36	59.1	63.4	4.3	600	186	0.31
36	49.1	753	.69/1.31	60.6	68.6	8.0	629	424	0.67
37A	49.2	563	.68/1.33	59.6	65.6	6.0	613	282	0.46
37	49.3	563	.68/1.33	59.7	65.3	5.6	613	261	0.43
38	49.3	960	.77/1.25	60.8	70.0	9.2	639	512	0.80
39	34.8	755	.69/1.30	60.7	71.7	11.0	456	642	1.41
40	69.6	287	.49/1.50	58.8	60.8	2.0	835	79	0.095
41	69.8	589	.57/1.37	58.8	63.0	4.2	850	177	0.21
42	33.7	566	.18/1.66	58.8	67.3	8.5	422	410	0.97
43	69.8	914	.52/1.95	59.6	65.6	6.0	869	282	0.32
44	49.1	753	.34/2.60	59.1	66.0	6.9	611	323	0.53
45	36.6	258	46/0/212	58.0	61.1	3.1	438	120	0.27

Run	$\overline{v}$ (mm/s)	v'^2 (mm/s)	$\overline{T}$ (mV)	T'^2 (mV)	$\overline{v'T'}$ (mm/s mV)	R	T_H (mv)	T_C (mV)	ϵ_{TM}^* ($\times 10^{-2}$)
1	0.10	0.32	0.951	0.027	0.00292	0.339	0.943	0.888	.197
2	0.17	0.85	0.885	0.026	-.00422	-0.190	0.911	0.882	-.276
3	0.52	3.55	0.983	0.039	.0284	0.206	1.005	1.006	—
4	0.05	2.64	1.001	0.030	.00422	0.053	1.003	0.998	—
5	-0.23	2.10	1.122	0.036	.00806	0.107	1.126	1.121	—
6	-0.03	2.25	1.064	0.064	-.00729	0.051	1.041	1.007	-.760
7	0.04	1.09	0.898	0.030	-0.00345	-0.105	0.916	0.895	-.199
8	0.20	0.35	0.939	0.012	-0.00385	-0.912	0.893	0.841	-.421
9	0.85	2.12	0.975	0.040	-0.0100	-0.118	0.996	0.913	-.531
10	0.53	0.61	0.940	0.020	- .00539	-0.440	0.898	0.862	-.540
11	1.76	5.34	1.094	0.052	-0.0754	-0.269	1.125	1.103	-12.6
12	0.33	1.02	0.914	0.036	- .00269	-0.23	0.959	0.902	-.088
13	0.87	4.43	1.171	0.063	- .0632	-0.226	1.175	1.174	—
14	0.55	5.46	0.819	0.031	-0.0115	-0.068	0.859	0.850	—
15	0.83	6.63	1.020	0.066	-0.0207	-0.047	1.027	1.022	—
16							0.932	0.894	
17	0.	2.14	0.816	0.037	- .0112	- .14	0.819	0.788	-.00435
18	0.40	5.41	1.022	0.037			1.040	1.017	
20	0.82	3.61	0.778	0.033	- .0073	- .06	0.799	0.771	-.00271
21	0.34	0.28	0.816	0.0	0.0	—	—	—	—
22	0.21	0.27	0.845	0.008	- .00103	- .48	0.810	0.745	-0.95×10^{-3}
	0.15	0.37	0.864	0.015	- .00069	- .12	gap (0.347^{mm})		
	0.17	0.31	0.916	0.011	- .00034	- .10	gap (-0.025^{mm})		
	0.05	0.13	0.914	0.005	- .00017	- .29	gap (-0.397^{mm})		
23	0.33	2.08	0.897	0.038	- .0161	- .20	0.850	0.798	-1.86×10^{-2}
24	0.18	0.97	0.880	0.026	- .0046	- .18	0.826	0.767	-0.47×10^{-2}
25	0.24	0.31	0.799	0.0095	- .00112	- .38	0.781	0.740	-0.085×10^{-2}
26	0.11	0.30	0.855	0.023	- .00155	- .22	0.839	0.793	-0.11×10^{-2}
27	0.09	0.30	0.859	0.023	- .00206	- .30	0.831	0.793	-0.17×10^{-2}
28	0.05	0.34	0.886	0.031	- .00103	- .10	0.879	0.838	- .080
29	0.37	0.43	0.899	0.014	- .00215	- .36	—	—	—
30	0.22	0.39	0.885	0.023	+ .00086	+ .096	0.849	0.814	+ .080
31	0.17	0.60	0.848	0.044	+ .0054	+ .21	0.909	0.812	+ .180

Run	$\bar{v}$ (mm/s)	v'^2 (mm/s)	$\bar{T}$ (mV)	T'^2 (mV)	$\overline{v'T'}$ (mm/s mV)	R	T_H (mv)	T_C (mV)	ε_{TM}^* (x10^{-2})
32	0.14	0.72	0.880	0.048	+ .0065	+ .19	0.841	0.835	—
33	0.29	0.71	0.885	0.037	+ .0057	+ .22	0.996	0.913	+.248
34	0.22	0.57	0.712	0.007	- .0020	- .50	0.691	0.663	-.165
35	0.16	0.31	0.810	0.013	- .0012	- .29	0.772	0.741	-.090
36	0.42	0.67	0.922	0.045	+ .0090	+ .30	0.881	0.845	+.579
	0.32	0.64	0.894	0.053	+ .0033	+ .10⁻	sym (9.87^{mm})		
	0.64	0.70	0.944	0.036	+ .0057	+ .23	sym (12.13^{mm})		
37A	0.33	0.39	0.880	0.030	+ .0044	+ .37	—	—	—
37	0.20	0.44	0.855	0.034	+ .0030	+ .20	0.896	0.824	+.096
38	0.21	0.93	0.954	0.060	+ .0188	+ .34	0.976	0.894	+.528
39	0.78	3.99	0.969	0.055	+ .0335	+ .15	0.951	0.886	+1.68
40	0.84	2.47	0.695	0.016	- .0106	- .27	0.706	0.673	-.525
41	0.75	1.58	0.775	0.028	- .0117	- .26	0.778	0.752	-.733
42	0.50	1.71	0.912	0.043	+ .0087	+ .12	0.901	0.790	+.265
43	0.27	0.79	0.855	0.039	- .0052	- .17	0.873	0.784	-.095
44	0.75	1.10	0.886	0.040	+ .0057	+ .13	0.924	0.809	+.115
	0.80	1.08	0.873	0.040	+ .0073	+ .17	gap (0.347)^{mm}		
	0.89	1.13	0.882	0.042	+ .0057	+ .12	gap (0.05)^{mm}		
	0.67	0.94	0.955	0.045	+ .0008	+ .02	gap (-0.25)^{mm}		
	0.59	0.82	0.983	0.048	- .0011	- .03	gap (-0.397)^{mm}		
	0.41	1.29	0.874	0.060	+ .0063	+ .08	sym (8.4^{mm})		
	1.26	0.88	0.901	0.038	- .0024	- .07	sym (13.0^{mm})		
45	0.38	2.05	0.585	0.015	+ .0171	+ .54	0.713	0.596	+.454

APPENDIX I

Heater Tube Approaches

In order to eliminate the non-uniform heat flux problem caused by heat conduction through rods, heater tubes are suggested instead of heater rods. Design constraints from the experimental operating conditions are

- Maximum required heater power: 3000 W

    (Corresponding $Gr_{\Delta T} \approx 1500$ for uniform power case)

- Minimum rod diameter: 0.75 inches (1.905 cm)

- Maximum rod length: ≈ 1.2 m

I.1. Direct Resistance Heating

(a) Hollow Rod

Constraint: 209 Volts power source stepped by commercial variac

to 200 amps, 0 to about 240 volts.

This constraint using SS-304 with highest resistivity ($\rho = 7.2 \times 10^{-7}$ ohm·m) require a wall thickness of 0.015 inches or less. This is obtained by the following:

Resistance is given as,

$$R = \frac{\rho \ell}{A_x}$$

where R: resistance (ohm), ρ: resistivity(ohm m),

    A_x: cross-sectional area of hollow rod (m^2),

    ℓ: rod length (m).

Minimum resistance required by the constraint is

$$R = \frac{P}{i^2} = \frac{3000}{200^2} = 0.075 \text{ ohm}$$

and

$$A_x = \frac{\rho \ell}{R} = \frac{(7.2 \times 10^{-7})(1.2)}{0.075} = 1.15 \times 10^{-5} \text{ m}^2$$

Then the maximum thickness of the tube is

t = 0.00038 m (0.015 inches).

(b) Conducting Fluid

Saturated NaCl solution as a conducting fluid requires a high voltage variable power source, i.e., 6 amps. 500 volts. This result is obtained by the following:

Resistance of the NaCl solution is

$$R = \frac{\rho \ell}{(\frac{\pi}{4})D^2} = 80 \text{ ohm}$$

where, ρ = 0.044 ohm m for NaCl solution

ℓ = 0.915 m

D = 1 inch (=0.0254 m) for rod diameter

Then

$$i = (\frac{P}{R})^{1/2} = (3000/80)^{1/2} \simeq 6 \text{ amps}$$

and V $\simeq$ 500 volts

I.2. Fluid Heating

Another approach is to pass the hot water through the tube. The maximum power achieved by this approach is 1350 W per rod. This result is obtained by the following:

$$Q = h \, \pi \, D \, \ell \, (T_H - T_c)$$

where h: heat transfer coefficient of the tube wall (neglecting

the thermal resistances at the inner wall and tube)

T_H: temperature (about 210°F) of hot water passing

through the tube

T_c: bulk coolant temperature ($\approx$ 60°F)

and

$$\frac{hDe}{k} = 3.66 \text{ (for laminar flow)}$$

Therefore,

$$h \simeq \frac{(3.66)(0.364)}{(0.53/12)} \approx 30 \text{ (Btu/hr ft}^2 \text{ °F)}$$

for D_e = 0.53" based on an interior subchannel with

triangular array and P/D = 1.18.

Then,

Q = (30)(π)(1/12)(1.2/.305)(210-60)

= 4600 BTU/hr

= 1350 W